Prediction of the Residual Strength of Liquefied Soils

by

Chwen-Huan Wang

A dissertation submitted in partial fulfillment of the
requirements for the degree of

Doctor of Philosophy

University of Washington

2003

Program Authorized to Offer Degree: Civil and Environmental Engineering

UMI Number: 3091088

UMI®

ProQuest Information and Learning Company
300 North Zeeb Road
P.O. Box 1346
Ann Arbor, MI 48106-1346

Doctoral Dissertation

University of Washington
Graduate School

This is to certify that I have examined this copy of a doctoral dissertation by

Chwen-Huan Wang

and have found that it is complete and satisfactory in all respects,
and that any and all revisions required by the final
examining committee have been made.

Chair of Supervisory Committee:

Steven L. Kramer

Reading Committee:

Pedro Arduino

Robert D. Holtz

Steven L. Kramer

Greg R. Miller

Date: June 12, 2003

University of Washington

Abstract

Prediction of the Residual Strength of Liquefied Soils

by Chwen-Huan Wang

Chairperson of the Supervisory Committee

Professor Steven L. Kramer

Department of Civil and Environmental Engineering

Soil liquefaction has led to extensive damage to buildings, bridge, and lifelines in past earthquakes. While the effects of liquefaction can be manifested in many ways, the most devastating are in the form of flow slides. Flow slides can move at high speeds for distances of hundreds of meters, and destroy everything in their path. They have been observed in both natural and man-made soils, and can be triggered by many types of events of which earthquake shaking is only one.

Evaluation of the potential for flow slide development requires evaluation of the residual strength of liquefied soil. This problem has been one of the most difficult in geotechnical earthquake engineering because the residual strength is difficult to be measured accurately. Empirical procedures based on back-calculation of residual strength from flow slide failures have been developed and used widely. These approaches suffer from (1) only a limited number of flow slide case histories available, (2) some cases have little quantitative data, and (3) the process involves assumptions. These factors introduce considerable unquantified uncertainty into the predicted residual strengths.

A new approach to the back-calculation of residual strength from flow slide case histories has been developed. The approach objectively and consistently identify and quantify the most significant uncertainties in the parameters through the back-

calculations by the Monte Carlo simulation. Each flow slide case history is represented by a joint probability density function of penetration resistance and residual strength, rather than by a single deterministic data point as in previous analyses. By applying this methodology to some well-documented case histories, and applying its basic principles to other case histories, a database of residual strength data was developed. Using basic principles of soil mechanics, the approach that residual strength is related to penetration resistance was found to be consistent with field data.

A predictive model for residual strength was developed. It allows estimation of the conditional probability distribution of residual strength given corrected standard penetration test resistance. It allows engineers to determine the probability of a given residual strength value being exceeded for a given average standard penetration resistance.

TABLE OF CONTENTS

Page

LIST OF FIGURES

Figure Number | Page

LIST OF TABLES

Table Number | Page

Acknowledgements

The works involved in this study was finically supported by the Washington State Department of Transportation, the Pacific Earthquake Engineering Research (PEER) Center, and the John R. Kiely Professorship. Their devotions in this project are greatly appreciated.

In the extensive Ph.D. study, Professor Steven L. Kramer fully devoted his intelligence and kindness to provide guidance for author's works. The author sincerely cherishes the knowledge and wisdom gained by following Professor Kramer's supervision. Additional appreciations from author are to thank the devotions from Professors Pedro Arduino, Robert D. Holtz, and Gregory R. Miller, for their helpful discussions and reviewing the manuscript. Besides, it was delightful to enjoy the professors' vivid spirits that are always the main source to hold the Geotech Family together.

Further appreciations to Ms. Marcia Buck, Mr. Ken Knowlan, Ms. Carole McCutcheon, Ms. Renate Staub, Ms. Arla Webb, their helps brought peace to author's intense academic life.

Friendship was another main source that supported author's will to arrive the end of this long journey. For those people in the department, in the Seattle, and all around the world, your warmhearted friendships are always remembered.

To my parents and sister

Chapter 1

Introduction

Soil liquefaction, which can cause sudden loss of soil strength, often produces devastating, unrecoverable losses of human life and property. The magnitude and nature of these losses can be strongly influenced by the residual strength of the liquefied soil. Over recent decades, researchers have made a number of important advances in the evaluation of the residual strength of liquefied soil. Among these researchers, Seed (1987) presented a pioneering strategy to identify a relationship between standard penetration test (SPT) resistance and residual strength. The relationship was based on back-calculation of the stability of flow-slide case histories, and has been widely implemented in engineering practice. For engineering practice, establishment of this relationship allows engineers to use the most common in-situ soil exploration technique -- SPT -- to estimate the residual strength of liquefaction-susceptible soil. However, Seed's process for evaluating residual strength required a number of assumptions that were mostly based on professional and judgment from his lifetime of experience, which is nearly impossible for successors in this line of work to match. For this reason, it is desirable, in the interests of both the engineering practice and analytical research, to establish a guideline that produces the relationship between the SPT resistance and the residual strength from a systematic back-analysis process.

The objective of this research is to establish a procedure for rational, objective, and systematic back-analysis of the residual strength from a series of flow-slide case histories. The procedure is intended to recognize, and account for, the numerous sources of uncertainty that vary widely from one case history to another. The effects of uncertainty in the parameters involved in the back-analysis process will be characterized using Monte Carlo analyses. The Monte Carlo analysis describes each parameter by using a large number of random values of a predetermined probability distribution. In each simulation, the back-analysis process first samples the parameter values from their probability distributions, and then estimates the corresponding residual strength from the limit-equilibrium slope stability analysis. For each flow-slide case history, the relationship established between the representative SPT resistance and the back-calculated residual strength will be described by a cloud of points, instead of a single point as produced Seed's and related procedures. This procedure will provide statistical significance (mean and standard deviation values) to the relationship between SPT resistance and residual strength.

An important part of the residual strength back-analysis process is identification of the correct geometry of the slope for back-analysis. The geometry used in the limit-equilibrium slope stability analysis should be corrected to eliminate impact of inertial effects (kinetic energy). Kinetic energy is produced by movement of the failed materials, the velocity of which increases and the then decreases during the deformation process. In conventional back-analysis procedures, upper and lower bounds of residual strength are usually characterized by the back-calculation using the pre- and post-failure geometries, respectively. Without involving the deformation process in the evaluation, the back-calculation of those two geometries cannot produce an accurate result when kinetic energy is significant. In this research, a procedure will be established to estimate the geometry that is unaffected by inertial effects.

After analyzing all available flow-slide case histories, this research will be able to provide a database that illustrates the relationship between SPT resistance and residual strength. This procedure will help the future user employ the SPT resistance to estimate a probability distribution for residual strength. The user can then decide what level of risk he/she is willing to accept for design or evaluation, and use the residual strength probability distribution accordingly.

Chapter 2 presents case studies of several major earthquakes that occurred in the twentieth century. The seismological characteristics of each earthquake event and its significant ground damage are presented, with particular attention to soil liquefaction-related failures. The following sections in this chapter introduce the terminology of soil liquefaction and its classical laboratory observations. Several typical soil liquefaction-related phenomena are introduced as examples.

Chapter 3 describes the behavior of liquefied soil at the micro- and macro-scale levels. Because liquefaction-susceptible material is usually granular (sandy), the soil matrix comprising liquefiable soil and other materials can be treated as a particulate assembly. During soil liquefaction, at the micro-scale level, the particulate behavior within an assembly is introduced according to the inter-particle and particle-fluid interactions. At the macro-scale level, the behavior of debris-flow material is presented as an extreme case of soil liquefaction. The flow behavior is examined according to the strong agitation within the particle-fluid mixture.

Chapter 4 explains various approaches to evaluate the residual strength of liquefied soil. This chapter begins with a review of flow-slide failure. The knowledge learned from studies of the particulate flow and the debris-flow failure helps to understand the initiation and failure process of flow-slide failure. The following sections introduce the current methods of evaluating residual strength using both laboratory and analytical approaches.

Chapter 5 describes the approach that used in this research. The proposed objective is to establish a systematic process for establishing the residual strength of liquefied soil based on actual flow-slide case histories. This systematic process will be implemented with Monte-Carlo-based analyses to account for the effects of uncertainty in each parameter on the results of the back-analyzing process. In each case history, the proposed procedure will produce a joint probability density function for SPT resistance and residual strength/normalized residual strength ratio, along with statistical parameters (e.g. the mean value and the standard deviation) of the representative SPT resistance and the back-analyzed residual strength/normalized residual strength ratio of liquefied soil. A database will be assembled after combining results from all back-analyses of flow-slide case histories, and other soil liquefaction-induced failures.

Chapter 6 presents the application of those procedures that has been described in the preceding chapter, which included the procedures used to perform Monte Carlo simulations of flow slide case histories for the purpose of investigating the effects of uncertainties in input parameters on uncertainty in the residual strength of the soil. In this chapter, the Wachusett Dam case history is first demonstrated as a detailed example for this new approach. The following sections summarize other significant case histories. Finally, procedures for estimation of the uncertainty in residual strength for smaller and less well-documented case histories are presented.

Chapter 7 presents the regression analyses that are employed to characterize the trend and scatter in the relationship between the residual strength and SPT resistance. Ultimately, procedure for estimating conditional probability density function (upon SPT resistance) for residual strength will be developed.

Chapter 8, the last chapter, first gives a brief introduction of the needs of engineers to have a systematically produced database in order to make the best estimate the residual strength of liquefied soils. A summary of each chapter is made to introduce the background knowledge for people to understand the phenomenon of soil liquefaction, and the systematical approach that has been established in this study. The last part of this chapter gives conclusions that summarize the results, followed by the recommendations for the future research.

Chapter 2

Soil Liquefaction

2.1 INTRODUCTION

Soil liquefaction involves the interaction between soil particles and interstitial water. This interaction can lead to loss of soil strength and triggering of failure. Earthquakes, construction loads, or natural causes such as heavy rainfall can initiate soil liquefaction. Soil liquefaction commonly causes building and bridge failures, roadway and dam deformation, slope failures, and lifeline damages. Some very serious damage, such as large area of landslides and debris flows, or the collapses of earth dams can occur due to flow slides. Each of these failures produces a different level of hazard, from loss of structure serviceability to loss of human life. Prevention of on these disasters requires tremendous efforts from engineers and researchers.

In recent decades, geotechnical engineers and researchers have devoted tremendous effort to the evaluation and prevention of soil liquefaction-induced failures. Adequate procedures have been developed to explain and evaluate the liquefaction potential. These empirical and experimental procedures are built on in-situ testing, laboratory experiments, and analytical work. In-situ testing, such as the standard penetration test (SPT) and the cone penetration test (CPT), helps engineers to understand the strength and other characteristics of soil. Laboratory testing, such as static and cyclic triaxial tests, provides information on the behavior of soil from initial static condition, through initiation of liquefaction, and finally to the post-liquefaction condition. Knowledge gained from the in-situ and laboratory testing can be used to analyze soil behavior in real case history studies. Based on the knowledge to date, most liquefaction phenomena can be reasonably evaluated and prevented.

This chapter presents an overview of soil liquefaction. It starts by showing some case studies of earthquake-induced liquefaction failures. These cases give a good picture of how soil liquefaction causes great damage. The following sections explain the terminology and evaluation of susceptibility for soil liquefaction. The main focus is to illustrate the mechanism of how the soils react with water in laboratory and field conditions, thus causing liquefaction phenomena. The last section of this chapter describes several typical types of failure that are caused by soil liquefaction.

2.2 SOIL LIQUEFACTION CASE STUDIES

2.2.1 Alaska Earthquake, 1964

The Alaska earthquake, the second largest earthquake in this century, struck Alaska area in March 27, 1964. The moment magnitude was estimated as 9.2, while the largest earthquake in this century was the 1960 Chile earthquake with moment magnitude of 9.5. The epicenter of the Alaska earthquake was of 61.04°N and 147.73°W, which was about 10 km east of the mouth of College Fjord, approximately 90 km west of Valdez and 120 km east of Anchorage. The focal depth was estimated to be 20 to 50 km.

The subduction tectonic zone covers the area of the Gulf of Alaska and the Aleutian Islands. At the boundary between the North American plate and the Pacific plate, the tectonic movement accumulated 5 to 7 cm per year of strain energy. That explains why approximately 6 percent of world's largest shallow earthquakes were located in this region (Bartlett and Youd, 1992), e.g. the moment magnitude of 9.1 in 1957 and the moment magnitude of 8.7 in 1965. For the 1964 event, the fault rupture propagated toward southwest at speed of 3 km per second (Bartlett and Youd, 1992). The total rupture length was about 600 to 800 km.

Although Anchorage was 120 km away from the epicenter, it and its surrounding area sustained severe damages. A strong tsunami attacked the Gulf of Alaska and the Prince William Sound region. The costal area suffered loss of life and damage to surface structures and lifeline facilities. In downtown Anchorage, the earthquake destroyed about 30 city blocks. Some of the devastation was caused by landslides. Several huge landslides at Turnagain Heights and Government Hill devastated large area of personal and public properties, and closed many schools. In soil liquefaction hazard areas, lateral spreading damaged numerous railroad and highway bridges, and roadways. The following is a case study for lateral spreading related damage.

2.2.1.1 Snow River

The Snow River is located about 35 km away from the epicenter of the 1964 Alaska earthquake. The ground motion lasted about 90 seconds and reached about 0.4 g (Bartlett and Youd, 1992). The local soil condition and the characteristics of earthquake motion damaged several bridges by lateral spreading.

The alluvial plain of the Snow River was covered by glacial and alluvial deposits. Site investigation revealed that granular soils dominated the subsurface to depths of 50 m (Ross et al., 1973). Around Bridge No. 605A, the loose deposit of silty sands extended the upper 30 m. The average SPT-N value was about 11 blows per foot (Bartlett and Youd, 1992; Ross et al., 1973).

At the time of the earthquake, the newly constructed highway bridge No. 605A had 4 of 6 concrete piers completed (Bartlett and Youd, 1992; Ross et al., 1973). All of those piers showed displacement, settlement, and rotation following the earthquake. One pier sustained 2.4 m displacement toward the Kenai Lake. Another one had 15 degrees of rotation. Other bridges, No. 603, No. 604, No. 605, and No. 606, suffered similar damages on piers and decks. Figure 2-1 shows the damage of No. 605 bridge.

2.2.2 Niigata Earthquake, 1964

A magnitude 7.5 earthquake struck Niigata, Japan, in 1964. The epicenter, located at 38°21'N and 139°11'E, was 22 km off the coast near Awa Island. The focal point of fault rupture was about 40 km deep (Hamada, 1992).

The large area which suffered earthquake damage included Niigata City through Yamagata and Akita Prefectures (Hamada, 1992). Soil liquefaction was the major cause for the substantial disaster. Hamada (1992) summarized the major damage in Niigata City: structural failures caused by foundation failures, sub-surface structures damaged by buoyancy of liquefied soils, and retaining structure failures caused by increasing earth pressure and reduced soil strength.

Earthquake motion was recorded in two monitoring stations in Niigata City. One station was on the roof of building and the other was in the basement. Both of those stations were in the Kawagishi-Cho. Because Kawagishi-Cho sustained serious damage from liquefaction, liquefied soil behavior can be seen in the recorded acceleration data. In the first 7 seconds of record, when the soil was not liquefied, the predominant period was 0.2 second with amplitude of 0.05g. During the time of 7 to 11 seconds, the maximum acceleration values were 0.159g in the basement and 0.184g on the roof, with a predominant period of 0.8 seconds. This behavior showed the soils were softened after liquefaction and then amplified the ground motion intensity.

Most failures in Niigata City were concentrated along the Shinano River. After the earthquake, both right and left riverbanks moved toward the river. Sand boils and surface cracking were observed near the banks. Large displacement (lateral spreading) along the banks caused serious damage to bridge structures. The river was built following the old river channel. The right (northwest direction) bank was basically the old riverbank. The left (southeast direction) bank was built on the old natural levee of river. In-situ testing showed the liquefiable layer was inclined toward the river center from both banks. However, the left bank showed a softer and thicker liquefiable soil layer, which induced more serious damages than the right bank did.

Three representative cases are discussed as follows.

2.2.2.1 Kawagishi-Cho Buildings

In the city of Kawagishi-Cho, the earthquake caused serious ground displacement, sand boils, and surface cracking. The maximum ground displacement reached about 11 m in some locations. Among these failures, the foundation failure of several apartment buildings was observed in this area.

The strength reduction of the weakened liquefied soil induced bearing capacity failure for many buildings. Several apartment buildings in this area tilted severely and almost laid on the ground because of the lost foundation bearing capacity (Figure 2-2). Despite this, the apartment structures themselves were relatively intact.

2.2.2.2 NHK Building

In 1985, about twenty years after the Niigata earthquake, the foundation of NHK building was excavated for reconstruction. All pile foundation supports that had been excavated were found to have been completely fractured (Figure 2-3). The fractures were found in two positions: 2.5 to 3.5 m from the upper end and 2.0 to 3.0 from the bottom (Hamada, 1992).

The local soil type was loose sand with SPT-N values from 5 to 10 blows per foot in the upper 10 m. Observations from the ground movement showed that the maximum horizontal displacement was about 2.0 m. It was concluded that the movement of liquefied soils caused flexural failure of the pile foundations at the top and bottom of the liquefied layer.

2.2.2.3 Showa Bridge

The Showa Bridge was simply built on columns supported by driven steel pipe piles. The length of piles was about 25 m, about 14 m of which was penetrated in soils. Several minutes after the earthquake, five spans between the center and left bank collapsed and became partially submerged in the river (Figure 2-4). Initially, the damage was suspected to be caused by the structural dynamic repose. However, after one pile support was extracted and examined, it was determined that the soil liquefaction was the main reason for bridge damage.

The extracted pile was bent toward the river center about 7 to 8 m below the riverbed. This depth coincided the bottom of the liquefiable soil layer. Observation showed that the lateral spreading around the bridge abutment on left bank had about a 3 m ground displacement toward the river. It was concluded that the soil liquefaction caused the bending of the pile supports, and the collapse of the bridges.

2.2.3 San Fernando Earthquake, 1971

This earthquake occurred on February 9, 1971 in the San Fernando area. The epicenter was located at 34°24'N and 118°23.7'W, which was 13 km north-northwest of San Fernando. The focal depth was 8.4±4 km (Bolt and Gopalakrishnan, 1975). The magnitude was 6.4 on the Richter scale. The earthquake was felt in southern California, western Arizona, and southwestern Nevada (Coffman et al., 1982). Surface faulting was observed within the San Fernando and Sylmar communities (O'Rourke et al., 1992).

The San Fernando earthquake was particularly important because it generated many strong motion records. The total number of recording stations was 241, 175 of which were in downtown Los Angeles (Cloud and Hudson, 1975). The recording station at the Pacoima Dam, which was 8 km south of the epicenter and 4 km north of the surface faulting, was the nearest recording to the epicenter (O'Rourke et al., 1992). This record showed a peak acceleration of 0.72 g in the vertical direction and 1.25 g in the horizontal direction. The recorded motion in downtown Los Angeles, which is 28 km south of the epicenter, had a peak acceleration of 0.27 g in the horizontal direction. One important recording was at the Lower San Fernando dam because of its catastrophic flow slide type failure. The recording station, which was 17 km south of the epicenter, showed 0.55 to 0.6 g at dam abutment.

In this event, ground failures including ground deformation, slope failure, sand boils, surface cracking, and lateral spreading. In this section, two cases of soil liquefaction-related failure, the Lower San Fernando Dam and the San Fernando Valley Juvenile Hall, are discussed below.

2.2.3.1 Lower San Fernando Dam

The Lower San Fernando Dam located near the Van Norman Lakes was one of three earth dams that impounded water from the lake (Scott, 1971). The epicenter was about 8.5 miles from the Lower San Fernando Dam and produced a peak ground acceleration of 0.55 to 0.6 g. The earth-filled dam collapsed in the flow slide type of failure about 20 to 30 seconds after the earthquake motion (Seed et al., 1988). Figure 2-5 shows an aerial photo of the post-failure condition of the dam. After the slide ended, the freeboard was about 5 feet, in which 35 feet before the failure (Seed et al., 1975a). The toe of upstream embankment moved about 100 feet toward the reservoir. In order to prevent water flowing into the downstream residential area, dam operators took 4 days to pump out water to a safe elevation.

The investigation of Seed and his colleagues (Lee et al., 1975; Seed et al., 1973; Seed et al., 1975a, b) showed that the embankment of the Lower San Fernando Dam rested on the alluvium that consisted of stiff clay with lenses of sand and gravel. The construction of the Lower San Fernando Dam, accomplished by hydraulic filling the lower portion, lasted from 1912 to 1915 . The upper portion was built by dry and rolled filling in 1924 and between 1929 to 1930.

A series of excavation had been carried out by Seed and his colleges (Lee et al., 1975; Seed et al., 1973; Seed et al., 1975a). In-situ sampling and trenches identified soil types among the slide debris. Huge blocks of intact soil were found within the slide debris. Those soil blocks mainly consisted of clay and fill from the upper portion of embankment. Further in-situ sampling and testing also found disturbance among the hydraulic fills located in the lower central of embankment. The alluvium foundation and a thin layer of hydraulic fills above the foundation had been found undisturbed.

According to those evidences, the failure was initiated by the soil liquefaction in the hydraulic fills. Because of the sudden drop of soil strength in this region, after the initiation of liquefaction, the process of regaining stability from surrounding soils induced the large deformation of embankment. The post-failure investigation revealed that embankment soils had been broken into big intact soil blocks floating and sliding along the liquefied hydraulic fills. Several in-situ tests also explored the intrusion of liquefied hydraulic fills between intact soil blocks. It proved that the hydraulic fills had been liquefied into fluid-like materials.

2.2.3.2 San Fernando Valley Juvenile Hall

San Fernando Valley Juvenile Hall is located about 7.5 miles south of the epicenter and about 2.5 miles northwest of the surface faulting. After the earthquake, a large lateral spread caused ground and structure damage to the facility. From the overall movement of the lateral spreading, the displacement was moving toward the Upper Van Norman Reservoir. Figure 2-6 shows cracks and ground deformation caused by lateral spreading.

The surface rupture extended about 4000 feet, and was 900 feet wide (Fallgren and Smith, 1973). This area stretched from Juvenile Hall to the Sylmar Converter Station at the edge of Upper Van Norman Reservoir. At the Juvenile Hall site, the underlying bedrock was about at 100 feet depth. Streamflow and mudflow accumulated in the alluvium deposits above the bedrock. Fallgren and Smith (1973) reported that bucket-auger borings had been carried out to a depth of 80 feet. A layer of loose silty sand of 10 feet thick had been discovered at a depth of 20 feet. Combined with the observations of sand boils, this loose silty sand layer initiated soil liquefaction and caused lateral spreading.

2.2.4 Loma Prieta Earthquake, 1989

The Loma Prieta earthquake struck California in October 17, 1987. The magnitude of this earthquake was 7.0 in the Richter Magnitude and 7.1 in the surface wave magnitude. The epicenter was located approximately 16 km northeast of Santa Cruz or approximately 30 km south of San Jose, which is 37.037°N and 121.883°W (Seed et al., 1990).

The focal point of Loma Prieta earthquake was within the San Andreas Fault, which is a strike-slip fault separating the Pacific Plate and the North American Plate. The rupture length of this event was approximately 45 km. The initial rupture was located at depth of 18 km. Over the next 7 to 10 seconds, the fault ruptured approximately 20 km to the north and 20 km to the south. The rupture propagated toward the surface and stopped at a depth of 5 to 7 km.

The location of the epicenter was outside any metropolitan area. The nearest massive failure inside a large city was Santa Cruz, which was about 10 miles away. Despite its distance, because of the local geology variation, or the local site effect, some of the metropolitan area was serious damaged. Another example of this effect took place in the San Francisco area, which is located about 60 miles away from the epicenter. Some metropolitan areas suffered serious ground failures and structural damage. The PGA values on rock in the San Francisco Bay area were approximately 0.06g to 0.12g. For locations with hydraulic–filled materials underlain with soft to medium stiff clay, the PGA values reached 0.16g to 0.33g (Seed et al., 1990). The local site effect played an important role in this earthquake destruction.

2.2.4.1 Marina District

Located about 40 miles from the epicenter, the relatively moderate earthquake motion nevertheless caused widespread damage to ground and structures. The damage included sand boils, ground deformation, lateral spreading, foundation failure, structure failure, and lifeline failure. The reason for those failures can be traced back through the history of this region.

At the end of nineteenth century, Marina bay was filed with dumped consisting of loose sands. The materials used for placement were from adjacent sand dunes. In the twentieth century, in order to provide sufficient land for 1915 Panama Pacific Exposition, the current Marina District was hydraulically filled with loose silty sands. The hydraulic fills extended to the seawall built in 1899. The original soils below the filled sands were medium-to-soft clay. Figure 2-7 shows the old shoreline and seawall. The enclosed area was the hydraulic fill, which suffered serious soil liquefaction damage during the 1989 earthquake.

When the earthquake waves propagated to the local bedrock, the soft clay modified the wave characteristics by increasing the period and amplifying the magnitude. This local effect caused both soil liquefaction hazards and the structural damage.

2.2.4.2 Treasure Island

To host the 1939 Golden Gate Exposition, Treasure Island was constructed as a man-made island in the center of San Francisco Bay. Rock dikes were placed to form the perimeter of Treasure Island after which the interior was hydraulically filled by sands and silty sands. The infilled materials were dredged from the seabed at several locations (Figure 2-8) in the bay.

Numerous failures occurred after the earthquake. Lateral spreading and settlement occurred surrounding the perimeter of island. Sand boils were a widespread problem, which caused a large ground deformation. The maximum settlement at the levee reached 2 feet (Seed et al., 1990). Besides damages caused by soil liquefaction, structural damages and lifeline failures were serious as well.

The amplification from the local site effect was reflected from the local PGA values. The maximum PGA from a nearby rock island, Yerba Buena Island, was 0.067g. However, the maximum PGA observed at Treasure Island reached 0.16g.

2.2.5 Kobe Earthquake, 1995

The Kobe (Hyogoken-Nanbu) earthquake struck the metropolitan area of Kobe in 1995. This was the most destructive earthquake in Japan since the Kanto earthquake that struck Tokyo and Yokohama in 1923. The epicenter was located at 34.60°N and 135.00°E with focal depth of 14 km. The location is 20 km southwest of downtown Kobe, between the northeast of Awaji Island and the mainland (Akai et al., 1995). The moment magnitude was estimated at 6.9.

The tectonic rupture was located between the North American plate and the Eurasian plate. The focal mechanism was right-lateral strike-slip faulting on a rupture area of 30 km to 50 km long and 15 km wide. With the average slip of 1.1 to 1.9 m on fault plane, the seismic moment was estimated as 2.5×10^{26} dyne-cm (Akai et al., 1995). The same tectonic mechanism had caused several severe earthquakes in the history of this region: the 1891 Nobi earthquake, with a magnitude of 8; the 1927 Tango earthquake, with a magnitude of 7.3; the 1943 Tottori earthquake, with a magnitude of 7.2; and the 1948 Fukui earthquake, with a magnitude of 7.1 (Kanamori, 1995).

The Kobe area sustained serious damages in the 1995 earthquake. The downtown of Kobe was about 20 km from the initial rupture. Near-fault activity produced strong earthquake motion. In this event, there were four major ruptures in the sequence. The directivity of rupture was toward the downtown of Kobe, which accumulated the energy in this event. Because of the directivity effect, the velocity profiles of the earthquake motion had brief and large amplitude. For example, velocity reached 175 cm/sec at Takatori in western Kobe (Akai et al., 1995). Finally, the local site effect contributed amplification effect to the earthquake motion. For example, the PGA value reached 0.8 g on alluvial sites in Kobe and Nishinomiya while the PGA value was about 0.3 g at rock sites (Akai et al., 1995).

2.2.5.1 Port Island

The construction of Port Island was a two-phase sequence. The first phase took 15 years and ended in 1981. The second phase was supposed to be completed in 1996, a plan which was terminated because of the earthquake. The construction involved dumping fills to form the island and compacting the surface soils. A series of caisson-type quay walls retained the fill at the perimeter of the island. However, the effort of compaction could only density the upper few meters of the 12 m-thick fills. The fill materials were residual soil formed by weathering of granite from adjacent mountains. The soil profiles of this material included small gravels, sands, and silts. SPT-N values showed that blow counts were 5 to 10 per foot for this layer, which indicated a high possibility of liquefaction.

The Port Island suffered serious damages along the perimeter of island. The lateral spreading extended about 3 km from the waterfront to inland. The width was several kilometers along the bay. The lateral spreading damaged the port facilities including quay walls, buildings, and cargo cranes (Figure 2-9). For those deep foundations near the bay, the force of lateral spreading sheared the connection between piles and pile cap.

Inland of Port Island, liquefaction caused surface deformation, ground cracking, and sand boils. The overall performance of structures was relatively acceptable. However, the ground settlement caused problems in foundation performance. Some pile-supported structures elevated above surface while the foundations were still intact. Some small structures on shallow foundation showed minor tilting because of differential settlement.

2.2.6 Nisqually Earthquake, 2001

A major earthquake struck northwest of Washington State on February 28, 2001. The moment magnitude was 6.8 and the epicenter was located at 47.149°N and 122.727°W, with a depth of 52 km. This location is near the Nisqually River delta, about 18 km northeast of the city of Olympia, 24 km southwest of Tacoma, and 58 km southwest of Seattle.

The hypocenter of the Nisqually earthquake was located within the Juan de Fuca Oceanic plate which subductes beneath the North American Plate within the Cascadia Subduction Zone. The fault plane orientation has a strike of 357° and dips to the east at 69°. Several major earthquakes have occurred within relatively the same vicinity. The magnitude 6.2 earthquake in 1939 and the magnitude 6.4 earthquake in 1946 both had epicenters located within approximately 60 km of the Nisqually earthquake epicenter. The Olympia earthquake of 1949, magnitude 7.1, was initiated by the same fault rupture. In another more recent event in 1999, the Satsop earthquake, with moment magnitude 5.8, occurred about 60 km west of the Nisqually earthquake.

The ground motion of the Nisqually earthquake was moderate throughout the Puget Sound area. Only two stations showed peak ground acceleration (PGA) exceeding 0.25g. The PGA in the Seattle metropolitan area ranged from 0.02g to 0.22g. Some high acceleration values were concentrated south of downtown Seattle in the vicinity of the Duwamish River. At the end of nineteenth century, this area was hydraulically filled with sandy materials. Hydraulic fills have since been found to be highly liquefiable. The soft liquefiable soils tend to amplify the earthquake motion, which caused the high earthquake intensity in south of downtown Seattle. Another area with high PGA was where the Seattle Fault runs underneath the city. Some inspectors observed chimney separation from houses around the Seattle area. Incidents of separation grew larger along the Seattle Fault. It has been suspected that this phenomenon was due to trapped earthquake wave energy between ground surface and fault plane, which caused more damage than in adjacent areas. When comparing the PGA values in the Seattle area, which is 58 km away from the epicenter, with the PGA values in Tacoma area, which was 24 km away from the epicenter, it was found that Tacoma had smaller acceleration values. The average PGA value in Tacoma area was about 0.04g to 0.06g. Possible causes for this phenomenon could be the local site effect or the earthquake ray path mechanism. However, further research will be required to identify those points.

A large amount of liquefaction was observed around the Puget Sound area. Several cases are summarized here for detailed illustration.

2.2.6.1 Capitol Lake, Washington

The 2001 Nisqually earthquake caused sand boils, landslides, and lateral spreading along the perimeter of Capitol Lake. Most of the landslides were located in a remote area. However, most of the lateral spreading sites were under the local access roads along Capitol Lake. All those damaged roads were closed after the earthquake for repair operations.

At the end of nineteenth century, the water level at the lake was lower than the current condition. Most of the area that currently is submerged in the lake was lowland that had no man-made structures or agriculture. The soils in this area could be described as slurry. The water level was raised to its current level when a dam was built in the 1920s. At present, the main purposes of Capitol Lake are water storage and recreational parks. Because the soils are weak and highly liquefiable, any structure built above the soft soils would easily be damaged when soils are liquefied.

Deschutes Parkway suffered serious damage from lateral spreading in the Nisqually Earthquake. The entire section between the south end of Highway 101 and north end of the Fourth Avenue Bridge had to be closed because of severe lateral spreading. Most of the pavement was broken into pieces. Some portions of the roadways settled about 3 to 5 inches. Several sinkholes were seen on the roadway (Figure 2-10). The largest one was approximately 8 feet in diameter and 5 feet in depth. Numerous sand boils occurred along the railroad track next to the Deschutes Parkway. One location near the Fourth Avenue Bridge was found to have sand boils extending more than 20 feet in length along the abundant railroad.

Several landslides were observed around Capitol Lake. One 400-foot-long landslide was located on the northeast side of the lake. This slide area was all natural material. Some flow-slide type failures occurred along the banks of Capitol Lake near the south of downtown Olympia. The flow slide site was a recreational park. Failure caused a roadway embankment to collapse and flow into the reservoir.

2.2.6.2 South of Downtown Seattle

The area to the immediate south of downtown Seattle is known as the Duwamish River valley. During 1890 to 1930, when demand for land increased, this area was hydraulically filled. Both natural deposits and man-made fills in this area are loose and saturated. When the earthquake waves reached this area, the soft soil conditions amplified the wave motion and produced some damage.

Sand boils were observed in many locations: Harbor Island, Alaskan Way Viaduct, Amtrak car wash facilities, Boeing Field, and the Union Pacific train yard. Between Utah Avenue south and First Avenue south, ground deformation caused cracking between the ground surface and buildings (Figure 2-11). In the same area, some buildings suffered serious damages, such as the Seattle Chocolates and the Starbucks Corporation buildings.

2.2.6.3 Sunset Lake, Washington

Sunset Lake is located inside a mobile home park in Tumwater, Washington. After the earthquake, liquefaction caused a serious lateral spreading along the west side of lake (Figure 2-12). A larger number of sand boils occurred along the perimeter of lake. Most of the diameters of sand boils were less than 1 foot. Several large sand boils with a diameter of approximately 3 feet were located at the toe area of the lateral spreading.

The 1999 Satsop earthquake had also caused a small lateral spread along the south side of lake. Some riprap had been placed on this previous failure to stabilize the slope. Only a small deformation occurred at this site after the Nisqually earthquake. The current lateral spreading extended from the front yard of mobile homes cross the roadway and then into the lake. The progressive failure type has been reported for this site.

In the glacier period, this area was covered by a huge amount of glacier. Before the establishment of this mobile home park, Sunset Lake was a mining site and a dumping site for construction of Interstate Highway 5. Several SPTs and CPTs have been conducted since the earthquake. The in-situ testing data revealed the geology profiles in this area.

Based on the SPT test that carried out at the toe of lateral spread, the uncorrected SPT-N values were 1 to 2 blows per foot in the upper 15 to 20 feet. A 2 to 4 ft thick layer of peat was encountered at depth about 20 feet. The SPT blowcount increased to 15 to 20 below this peat layer. Medium to coarse silty sands comprised the major portion layer immediately above and below this peat layer. The interface between the upper loose sands and the peat layer was the possible sliding plane after liquefaction occurred.

2.3 BEHAVIOR OF LIQUEFIABLE SOILS

2.3.1 Liquefaction Phenomena in Early Laboratory Testing

Liquefaction is initiated when saturated sandy material loses a great portion of its shear resistance and then collapses in the form of liquid-like material. The triggering of liquefaction can be caused by monotonic or dynamic loading. When the loading on the soil is applied is so quickly that no water is able to migrate, the loading is referred as undrained loading. During this period, the interaction between soil particles and interstitial water tends to reduce the contact force between soil particles. The diminishing contact force among particles contributes the overall loss of integrity, or strength, of the whole soil matrix. The term "soil matrix" is defined as the space containing varied size of soil particles, interstitial water, and air. In soil liquefaction evaluation, the soil matrix is regarded as saturated, which means there is no air in matrix. When the loading condition refers to monotonic loading, it indicates the loading is continuously increased or decreased. The term dynamic loading refers to seismic loading (an earthquake event) or cyclic loading.

For natural soil deposits or man-made earth structures, the composition of the soil matrix has unique characteristics compared to the soils in other locations. Miura et al. (1997) identified the factors that contribute the mechanical behavior of sands (Figure 2-13). Two groups of properties were included in these categories: primary properties and secondary properties. The primary properties describe the fundamental characteristics of soil particles; e.g. mineralogy, grain density, shape, and grain size distribution. The secondary properties describe the changeable properties of the soil matrix; e.g. packing, void ratio, bulk density, and moisture content. These two groups compose the physical properties, index properties, and chemical properties. The environmental conditions, such as stress, strain, and drainage, also play an important part in affecting the mechanical properties of sands. Even identical mineral composition and grain size distribution, varied secondary properties and environmental conditions always lead to different mechanical properties of sands. For liquefiable soil investigations, secondary properties and environmental condition show a great influence on the liquefaction susceptibility evaluation and the liquefaction post-failure evaluation.

After liquefaction has been initiated and soil matrix transforms into a fluid-like material, all the bonding history has been destroyed and rearranged (Kramer, 1996). Casagrande (1936) used the term "flow structure" to describe the conditions that existed in the liquefied soil. Casagrande (1976) postulated that when flow structure developed, soil particles are constantly rotating related to all surrounding particles in order to maintain a minimum frictional resistance. This agitation forms a chain reaction of particle movement and spreads the flow structure within the flowing liquefied soil. After the movement is terminated, the liquefied soil structure has been totally rearranged and then densified due to dissipation of excessive pore water pressure. As indicated by Castro and Poulos (1977), the development of soil liquefaction is affected by the initial conditions, including the void ratio, confining pressure, and shear stress.

A series of drained and strained-controlled triaxial tests had been conducted by Casagrande (1936) to study the basic behavior of sands. The sand specimens were prepared in loose and dense conditions under the same effective confining stress. For dense specimens, initially the deviator stress increased because of the higher stiffness provided by the interlocked particle geometry. After the deviator stress reached a certain peak value, the value dropped and eventually reached a constant value. The volume of dense specimen increased, or dilated, as it approaching the peak deviator stress and then dropped to a certain value as the deviator stress remained constant. For loose specimens, the deviator stress increased and reached a constant value accompanied by volume contraction to a certain value. Figure 2-14 shows that, under the same initial effective confining stress, the dense and loose specimen eventually approached the same volume, or the same void ratio at large strains. This special void ratio value was named the critical void ratio. After several tests with different initial confining stress, the critical void ratio line was established by connecting the locus of each test.

When Casagrande carried out those tests, the technology was not able to measure the change in pore water pressure during testing. However, he predicted that the tendency of changing volume during the drained test would result in the changing of pore water pressure during an undrained test. For the loose specimens, the tendency for contraction would produce positive excessive pore water pressure during undrained test. When the excess pore water pressure reached a certain value, the soil specimen would collapse and initiate static liquefaction (triggered by monotonic loading). For the dense sample, the tendency to dilate would create negative pore water pressure in the specimen, which increased the effective confining stress and also the shear strength. Under this condition, there would be no static liquefaction. Figure 2-15 summarizes the behavior of loose and dense sands under drained and undrained conditions. By knowing the critical void ratio line and the initial condition, one can predict the tendency to contract or dilate during the drained test, and the tendency to generate positive or negative pore water pressure during the undrained test. The critical void ratio line also marks the boundary between susceptibility and non-susceptibility of occurrence of static liquefaction. When the initial saturated soil condition falls above the line, it indicates contractive behavior of static liquefaction. For those that plot below the line, the dilative behavior produces non-susceptibility to static liquefaction.

When soil structures, e.g. earth dams, suffer damage because of soil liquefaction, the weight of the soil structure itself is the driving force that can cause continuous deformation. Casagrande (1976) indicated that the strain-controlled test would mislead the prediction because constant strain rate did not resemble the natural failure process. In 1938, Fort Peck Dam suffered liquefaction damage and collapsed during construction. The embankment was hydraulically filled loosely with silty sands. During construction, dumping loads generated high excessive pore water pressure in hydraulic fills and this initiated static liquefaction. Investigation showed that, the initial condition of liquefied soil located below the critical void ratio line created from the results of strain-controlled tests, which suggested that no initiation of static liquefaction would occur. This failure revealed the discrepancy of the strain-controlled drained triaxial test.

In order to simulate the constant weight involved in the natural failure process, Castro (1969) conducted stress-controlled triaxial tests with pore water pressure measurement, which was the first time flow structure was achieved in laboratory. In Figure 2-16, tests A, B, and C represent low, intermediate, and high initial relative density, respectively. For a loose specimen, Specimen A showed a peak deviator stress at a small axial strain and then collapsed at large strain because of static liquefaction. This occurrence was termed strain-softening behavior. The positive excessive pore water pressure continuously increased after peak deviator stress and reached a constant value that created low effective confining stress and low shear strength at large strain. For a dense specimen, Specimen C initially contracted with increasing excessive pore water pressure at small axial strain and then dilated with decreasing excessive pore water pressure at large axial strain. This occurrence was called strain-hardening behavior. At the end of the test, Specimen C showed high shear strength because of high value of effective confining stress. For the intermediate relative density, Specimen B showed peak deviator stress at small axial strain and produced strain-softening behavior for a limited period of time. At large strain, Specimen B dilated and produced strain-hardening behavior. This type of behavior was described as limited liquefaction because the drop of shear strength that produced temporary instability was followed by dilation

Based on the stress-controlled undrained triaxial tests, the critical void ratio line was plotted below and roughly parallel to the line plotted from the strain-controlled drained triaxial test. Reviewing the case of Fort Peck Dam by using the new test conclusion, the initial condition plotted above the critical void ratio line and that indicated the flow structure (static liquefaction) could be actually achieved by a stress-controlled undrained triaxial test.

2.3.2 Liquefiable Soil Behavior in Recent Research

Soil liquefaction involves a complicated series of mechanisms between particles and fluids, and the overall behavior of the soil matrix. Over the past few decades, people have gained enormous knowledge of the initiation of soil liquefaction and the post-liquefaction phenomena. However, because different conclusions were made by different researchers, people have been confused by the terminology to recognize soil liquefaction and its related phenomena. Before marching into any further subject in this dissertation, this section explains the terms of liquefaction terminology and its related behavior in laboratory observations.

2.3.2.1 Liquefaction Classification

Mogami and Kubo introduced the term of "liquefaction" in 1953. In recent years, more information about soil liquefaction has been discovered, including the liquefaction initiation process and the failure phenomena of soil liquefaction. The initiation of soil liquefaction can be triggered by static force (construction, water table fluctuation, and heavy rainfall) and dynamic force (earthquake). Combining different initial conditions (void ratio and stress conditions) with single or multiple triggering sources, the failure phenomena can be varied in degree of hazard. Kramer (1996) classified the liquefaction phenomena into two groups: flow liquefaction and cyclic mobility.

Flow liquefaction only occurs in saturated, loose, sandy soils. The triggering sources can be static or dynamic forces. However, after the triggering sources bring soil to the point that initiates liquefaction, the subsequent damages are only produced by the driving force of its own weight. For loose sandy soils, the contractive behavior produces shear strength under a liquefied condition that is lower than the static shear stress caused by its own body weight. In order to maintain static equilibrium, usually a large amount of deformation occurs after soil liquefaction. One example of the effects of flow liquefaction is formation of a flow slide. This kind of hazard usually involves a large damaged area with a large amount of soil volume, e.g. the failure of Lower San Fernando Dam in San Fernando earthquake, 1971.

Cyclic mobility, compared to flow liquefaction, can be triggered in saturated, loose-to-dense soils. After dynamic force brings the stress condition to the point of a zero effective stress condition, there is no dramatic collapse because the static shear stress is lower than the strength of liquefied soils. However, continuous dynamic force and driving force from soil weight can produce different degrees of deformation of the softened soil. For gentle sloping ground, lateral spreading can create damages in roadway, buildings, or adjacent facilities, e.g. the failure of Deschutes Parkway in the Nisqually earthquake, 2001. For level ground, the dynamic force induces upward seepage flow, generated by the dissipation of excessive pore water pressure because of soil liquefaction. This type of post-earthquake damage produces ground settlement, flooding, and sand boils, e.g. the ground settlement in the south of downtown Seattle in the Nisqually earthquake, 2001.

Usually, the occurrence of flow liquefaction is less common than the event of cyclic mobility. The reason for this is that cyclic mobility can be initiated in a broad range of soil conditions, including the initial stress condition and the initial void ratio. However, even with few occurrences, the occurrence of flow liquefaction nearly always creates severe damage. Cyclic mobility, on the other hand, can produce serious damages (large area of lateral spreading) or minor damages (sand boils). For the susceptibility of liquefaction evaluation, both flow liquefaction and cyclic mobility must be seriously considered.

2.3.2.2 Terminology of Soil Liquefaction

In laboratory testing for soil liquefaction evaluation, the behavior of liquefiable soils shows a diverse stress-strain relationship because of soil physical properties and environmental properties. In order to help further understand the liquefaction phenomena in the laboratory, this section defines the terms in soil behavior. Because the focus of this dissertation is flow liquefaction, the nomenclature illustration concentrates on the monotonic loading of triaxial test.

As mentioned in the previous section, flow liquefaction occurs with a sudden drop in the shear strength of the liquefied soil. The loss of equilibrium initiates large deformations driven by static stresses resulting from the soil weight. In laboratory testing to produce flow liquefaction, the peak shear stress is usually mobilized at small strain range, e.g. 2 to 8%. However, a more complicated transition in the stress state has been observed in the post-peak process. This section concentrates in two strain regions: intermediate strain region and large strain range. The value of strain is difficult to specify for each range. Generally, the intermediate strain range refers to the post-peak strain to about 15% of shear strain. The large strain range is a more contested range of values. Several reasons contribute to the capability of mobilizing soil specimen to large strain: physical properties of particle (size and surface texture) and testing device characteristics (boundary condition, type of loading, and size effect between soil particle and device). Verdugo and Ishihara (1996) identified the larger strain region of Toyoura sand started from 26% in axial strain. However, because of the specific type of sand used in their research, and the boundary problem of reaching large strain by using triaxial test, the large strain range is not specified for general conditions at this point.

2.3.2.3 Shear Strength in the Large Strain Region

Despite the varied amount of strain occurring in this region, flow structure has been developed with constant shearing and a saturated undrained condition. Because of the destruction of the original history and structure, the relationship between shear stress and void ratio is unique at the large strain region. The steady state deformation (Castro and Poulos, 1977; Poulos, 1981) is defined as a stress-controlled condition in which the soil matrix flows continuously with constant shear stress, constant effective confining stress, constant volume, and constant velocity. With satisfaction of these conditions, the shear strength of liquefied soil at steady state deformation was termed the "steady state strength".

Kramer (1996) introduced a three-dimensional steady state plot to illustrate soil liquefaction behavior (Figure 2-17). The steady state line is produced by connecting the locus points of the relationship between void ratio and effective confining stress under steady state deformation. This relationship is demonstrated from the space of effective confining stress, shear stress, and void ratio. This plot also shows the projection from three-dimensional space to two-dimensional plane, which are void ratio and shear stress, void ratio and effective confining, and shear stress effective confining stress.

Beside the term of "steady state strength", several other terms have been used to define the shear strength at large strain region: "residual strength" (Seed, 1987) and "critical strength" (Stark and Mesri, 1992). In the Workshop on Shear Strength of Liquefied Soils (Stark et al. 1997), the in-situ liquefaction flow failure has been further recognized as influenced by boundary conditions, spatial soil property variation, drainage or void ratio redistribution, flow duration or strain rate, and initial stresses. In this workshop, the shear strength at large strain was termed as "apparent flow resistance", "mobilized steady state strength", and "apparent or mobilized residual strength". For all those stipulations, the emphasis is to satisfy the theoretical terminology, laboratory testing conditions, and in-situ conditions.

For research in this dissertation, the term "residual strength" is chosen to represent the shear strength for liquefied soil at large strain. Residual strength was first introduced by Skempton (1964) to represent the large strain strength for overconsolidated cohesive soils. Over four decades, residual strength has been widely utilized in academic research and practical soil strength evaluation. For soil liquefaction evaluation, the term "residual strength" is applied by referring to following conditions. First, to evaluate residual strength, it satisfies the steady state deformation as described by Castro and Poulos. Second, this term implies some in-situ and laboratory circumstance: boundary conditions, spatial soil property variation, partially-drained conditions, stress conditions, and loading conditions. Last, though it is important to reproduce the steady state deformation in the laboratory, it is necessary to know the maximum value of strain in the field to estimate the residual strength. For each type of soil, the sufficient strain to produce steady state deformation sometime does not match the actual maximum strain that is observed in the real soil liquefaction event. In order to make the proper decision on residual strength value, it is important to use the shear strength value that corresponded to the field maximum strain for evaluation in each case.

In overall, the definition of residual strength emphasizes conditions of field soil liquefaction. During an evaluation of liquefied soil strength, computer simulation and laboratory testing, the depositional conditions, stress conditions, and loading conditions should closely match the field conditions.

2.3.2.4 Nomenclature in Soil liquefaction

Yoshimine and Ishihara (1998) developed a framework to define and explain the terms of soil liquefaction. Figure 2-18 shows idea laboratory-testing results of soil liquefaction. The nomenclature in this section is based on their framework.

In order to compare soil behaviors under varied initial void ratio, the same initial confining stress was used for four groups in Figure 2-18. With a low initial void ratio, the stress-strain curve shows dilation in the strain-hardening behavior. With higher initial void ratio, the stress-strain curve shows a temporary reduction in effective confining stress, but shear stresses do not drop. Ishihara et al. (1975) labeled this point "phase transformation", at which soil shows a transition from contraction to dilation. As initial void ratio keeps increasing, a temporary steady state appears in phase transformation. Alarcon-Guzman et al. (1988) termed this phenomenon as "quasi-steady state", in which the shear stress is temporarily constant. For all three demonstrations above, the soil behavior at large strain is named "ultimate steady state". When the initial void ratio is increased to a certain value (a very loose condition), the stress-strain curve shows a peak stress followed by a sudden strain-softening behavior. In this case, the soil behavior at large strain is named "critical steady state", in which soils show no tendency of dilation in either the effective confining stress or the shear stress. Figure 2-19 summarizes the four soil behaviors in the effective confining stress and void ratio space. The ultimate steady state line and phase transformation line are produced by connected locus points of ultimate steady state and phase transformation respectively.

2.3.3 Summary of Behavior of Liquefiable Soils

On the micro scale, soil liquefaction is initiated by interaction between soil particles and interstitial water. The contraction tendency in an undrained condition generates positive excessive pore water pressure that reduces the contact force between particles. When the amount of contact force reduction reaches a certain level, in macro-scale, the soil matrix shows initiation of liquefaction that leads to further failures. However, under certain conditions, the soil behavior will show dilation that induces negative pore water pressure. The tendency of dilation produces high effective stress that increases the stability of the soil matrix.

Yamamuro and Covert (2001) demonstrated these behaviors in three schematic stress paths shown in Figure 2-20. The three effective stress paths were tested in an undrained triaxial test on clean sand specimens with the same initial void ratio and different initial confining stresses. The soil specimen under low initial confining stress showed dilation after it passed the phase transformation point. The negative excessive pore water pressure produced the stable behavior, which referred to the increasing shear strength with increasing effective confining stress. For a soil specimen tested under medium confining stress, when the stress condition arrived the quasi-steady state, the low effecting stress and low shear stress brought the specimen into the temporary instability. This temporary instability could produce damage until the following dilation that regained stability. When the initial confining stress was higher than a certain value, the specimen showed a continuous contraction that caused an increase in excessive pore water pressure. Liquefaction was induced under this condition. For all three specimens, the final positions on stress path space converged to roughly the same point, which is the steady state condition. This point can also be referred to as the critical void ratio, based on Casagrande.

2.4 EVALUATION OF LIQUEFACTION HAZARDS

A proper procedure to evaluate liquefaction hazards involves three major steps (Kramer, 1996; Kramer and Elgamal, 2001). The first step is to determine the susceptibility to liquefaction. The Japanese Geotechnical Society (1998) listed three major characteristics of liquefiable soil conditions: the loose sandy deposits, shallow water table with saturated ground surface, and sufficient high earthquake intensity with sufficient long duration. For static liquefaction, the third characteristic can produce a sufficient magnitude of static loading. Besides these characteristics, historical observations and geologic conditions should be evaluated. The second step is to evaluate the potential of initiation of liquefaction when the soil condition is susceptible for liquefaction. When monotonic or dynamic force brings the soil stress state to a liquefaction-susceptible condition, the liquefaction can be initiated if the force is higher than the soil liquefaction resistance. Otherwise, the soil will not be liquefied. The third step is to evaluate the potential of damage when the second step shows the possibility of initiation of soil liquefaction. The evaluation of damage is based on the performance of soils, soil-supported structures, and adjacent facilities. If a severe damage is expected, or damages will be located at sensitive area, e.g. highly populated area, a proper (conservative or high cost) design should be planned. In area where a small level of damage is expected, a less conservative or low-cost design can be carried out.

This section concentrates on illustrating the susceptibility of liquefaction and the initiation of liquefaction.

2.4.1 Susceptibility of Liquefaction

2.4.1.1 Historical Characteristics

Field observations recording earthquake hazards date back to ancient times. Paleoseismologists dated the 1700 Cascadia Great Earthquake based on the observation of a tsunami from Japan (Sasake et al., 1996) and observation of a local depositional trend on the Washington and Oregon coasts (Jacoby et al., 1997). For liquefaction evidence, historical records showed that the effect of seismic-induced liquefaction had been confined within a particular distance to the source. Kuribayashi and Tasuoka (1975) compiled the liquefaction hazards database using earthquake damage in Japan. The database provided an empirical relationship between the earthquake magnitude and the epicentral distance indicating the greatest distance of liquefaction occurrence. Ambraseys (1988) further compiled a worldwide database of liquefaction occurrences for 137 shallow seismic events. The database involved the liquefaction-related ground failure including lateral spreads, loss of bearing capacity, ground settlement, sand boils, and mud volcanoes. However, flow slide type failure on sloping ground was excluded from this database. Ambraseys believed that the seismic shaking only provided the initiation of failure; retrogressive type failure in flow slide was developed by the static force, but not seismic force.

Figure 2-21 shows the plot of relationship between the maximum epicentral distance of a liquefied site and moment magnitude of a seismic event. The solid dots and hollow dots show the liquefaction events and non-liquefaction events respectively. The dividing line provides a helpful estimation of liquefaction occurrences in seismic events. Nevertheless, when soil and structure serviceability is taken into consideration, the dividing line should relay on the degree of liquefaction hazards. For example, Youd and Perkins (1978) recommended that 4 inches was the threshold vertical and horizontal displacement for ground failure that caused structural damage. It will be more valuable to use this criterion to correlate between earthquake magnitude and liquefaction-induced structural damages.

2.4.1.2 Geologic Characteristics

The Japanese Geotechnical Society (1998) provided a geomorphological classification to evaluate liquefaction susceptibility. The highest liquefaction potential group included reclaimed fill, present and old riverbeds, young natural levee, and interdune lowland. The locations with moderate liquefaction potential group included non-interdune lowland, fan, natural levee, sand dune, flow plain, and beach. The lowest liquefaction potential group was located at terrace, hill, and mountain. For example, the south of downtown Seattle is the old riverbed of the Duwamish River. The flow of river carried sandy materials and thus the same materials were deposited in current location. The nature of loose deposits was the main characteristic that induced soil liquefaction. Furthermore, the inter-layered silty materials can decrease the speed of excessive pore water dissipation, which further amplified the effect of liquefaction. Therefore, these soils would be classified as being highly susceptible to liquefaction.

A specific example of geology characteristics of man-made structures that show high liquefaction susceptibility is the hydraulic fill soil structure. For a hydraulic fill transported to the site in the form of slurry, the borrowed materials are excavated by hydraulic dredging and expelled at the site to be filled, during construction. For earth dams, the suspension flows toward the center of dam, with coarse particles settling to form the outer shells and the fine materials form the central core pool (Perloff and Baron, 1976). The hydraulic filled shells are poorly-graded, loose, sandy materials, which combined with the saturated condition of seepage flow, is highly susceptive to soil liquefaction.

2.4.1.3 Spatial and Probabilistic Characteristics

Youd and Perkins (1978) proposed a soil liquefaction evaluation approach based on the correlation between geologic settings and levels of seismic shaking. The damage concerns of geology and seismology were provided by separate maps; the combination of two maps provided the probability concepts of liquefaction-induced ground failures. The first map, the ground failure opportunity, provided the rate of occurrence and the intensity of a seismic event within a specific area. By given a period of time, the occurrence of liquefaction-induced ground failure was provided in terms of probability.

The second map, the ground failure susceptibility, provided the function of geologic materials in an area with the likelihood of liquefaction-induced ground failure because of seismic events. This function required the geologic setting and the correlations between geologic settings and liquefaction susceptibility. Based on the opportunity and susceptibility of ground failure, the combined map, the ground failure potential map, was able to provide site-specific liquefaction evaluation. Furthermore, Youd and Perkins (1987) established a system to characterize ground failure displacement of sloping Late Holocene fluvial deposits. The soil deposits of Holocene age are highly susceptive to soil liquefaction. The term "liquefaction severity index" was introduced to provide a quantitative value of lateral spreading displacement. It was generated from a database of magnitudes of earthquakes and distances of failures from the seismic sources. This technique was valuable for preliminary planning of liquefaction-induced ground failure. However, for a detailed investigation or specific project, additional geotechnical investigations should be planned.

For specific site-response evaluation, great effort is required to determine the quality and quantity of spatial variation on the soil properties. The Geographic Information System (GIS) provides a systematic platform to carry out those efforts. GIS is designed to work with data referenced by spatial or geographic coordinates (Star and Estes, 1990). For geotechnical investigation, GIS provides the ability to interpolate the spatial soil property evaluation with a rapidly updating and expanding database. Figure 2-21 shows a sample GIS map of liquefaction hazard potential evaluation. This specific map provides the potential of severity of liquefaction damages for a specific seismic event. This database included the probabilistic occurrence of a seismic event with the sites geotechnical investigation data, e.g. the SPT results and the CPT results. The results presented an interactive liquefaction ground failure quantity, e.g. ground displacement can be determined.

For engineering practice, the quantitative assessment is important for liquefaction-induced failure evaluation. With the historical seismic hazard data, the failure assessment can be produced by applying regression technique of a large database. Bartlett and Youd

(1992) developed empirical expression of lateral spreading case histories, relating ground displacement to numbers of source and site parameters. The in-situ testing data, such as SPT and CPT, were also utilized for liquefaction-induced failure evaluation. Juang et al. (1999) presented an in-situ test mapping function for liquefaction safety evaluation. Obtained from deterministic method, the mapping function related factor of safety to the probability of liquefaction, inferred from field liquefaction failure database. Their successive efforts (Chen and Juang, 2000; Juang et al., 2000a, b; Juang et al., 2001; and Juang and Jiang, 2000) involved in-situ testing data (SPT, CPT, and shear wave velocity) with the deterministic and probabilistic method for liquefaction potential assessment.

2.4.2 Initiation of Liquefaction

As discussed in Section 2.3.2.1, liquefaction phenomena can be classified into two categories: flow liquefaction and cyclic mobility. The occurrence of both requires some sort of triggering source. Cyclic mobility is one of the most important geotechnical problems caused by dynamic loading, such as earthquakes. Flow liquefaction, on the other hand, can be initiated by both dynamic loading and monotonic loading. Monotonic loading known to have triggered flow liquefaction includes construction dumping, underwater soil deposition, deposition of tailings materials, ground water table fluctuation, and surface water runoff. Some analysis showed that the creep effect of embankment cohesive materials could trigger flow liquefaction because of strain-softening behavior in liquefiable soils (Kramer, 1985). Beside earthquakes, other dynamic loads that can initiate flow liquefaction include tidal change, traffic vibration, geophysical exploration, and blasting.

This section introduces the loading conditions that trigger flow liquefaction and cyclic mobility in soil stress space, followed by the illustrations of the post-liquefaction phenomena.

2.4.2.1 Causes of Liquefaction

Monotonic Loading

Historically, a number of hydraulic-filled dams or tailings dams have failed when part of the soil structure liquefied and produced flow liquefaction. This is due to the nature of loose saturated sandy material common in these types of structure. Figure 2-23 shows five undrained stress-controlled triaxial tests with the same initial void ratio but different initial effective confining stresses. With low initial effective confining stress, Specimen A exhibits dilative behavior until it reaches the steady state point. For intermediate initial effective confining stress, the stress path shows phase transformation (Specimen B) and quasi-steady state (Specimen C) and reaches the steady state point. When the initial effective confining stress is higher than a certain value, the specimen shows continuously contractive behavior until it reaches the steady state point. The projection of the five tests on the *e-p'* space (shown as a steady state line) indicates Specimens A and B fall into the dilative behavior region and Specimens C, D, and E fall into the contractive behavior region. Because they have the same initial void ratio, the five specimens arrive at the same steady state point with the same effective stress conditions. Furthermore, the residual strength is the same for all five specimens.

An example of typical flow liquefaction soil behavior observed in the laboratory is shown in Figure 2-24. The specimen was initially consolidated at Point A and then subjected to an undrained stress-controlled triaxial test. Since the initial condition falls into the contractive behavior region above the steady state line, positive excessive pore water pressure (u_{excess}) develop with increasing axial strain (ε_a). The peak soil strength is mobilized at Point B, which occurs at the small axial strain. At this point, the unstable structure of the soil skeleton collapses, and the strength of the soil decreases. After Point B, the excess pore water pressure keeps increasing until Point C, in which the effective stress reduces close to zero because of high excessive pore water pressure. The required testing time from Point A to Point B usually takes minutes, but the time from Point B to

Point C may take only a fraction of a second. It is because under the stress-controlled condition, the constant loading forces the liquefied soil to form a stable condition with low residual strength, which is consistent with the process of steady state deformation. The soil matrix starts to break down after Point B; hence, Point B is the point that flow liquefaction was initiated.

The flow liquefaction surface, in Figure 2-23, is defined by connecting the initiation of flow liquefaction points, such as Point B in Figure 2-24. The flow liquefaction surface marks the boundary of the stable and unstable stress states in the soil matrix. In the stress path space, when an undrained test with contractive behavior passes the flow liquefaction surface, flow liquefaction will start to develop with eventual shearing of constant value of residual strength. This surface, which marks the boundary between stable and unstable states, can be applied to the monotonic and cyclic loading condition (Kramer, 1996).

The permanent strain that develops during this process occurs mainly after the stress path passes the flow liquefaction surface. Usually the strain level required to mobilize the peak strength of soil is only a few percent or less. When the soil matrix starts to break down and rearrange itself, it requires a huge amount on strain to reach another equilibrium state because of the low residual strength of liquefied soils.

Cyclic Loading

Consider two triaxial specimens with the same initial void ratio that are anisotropically consolidated to the same initial confining stress with initial static shear stress (τ_{static}), which is higher than the residual strength (S_r). One specimen is subjected to monotonic loading and the other to cyclic loading in order to demonstrate the soil behavior under different loading condition (Figure 2-25a). The specimen subjected to monotonic loading in a undrained stress-controlled condition becomes unstable after reaching the flow liquefaction surface, Point B, and moves toward the steady state point,

Point C, with soil strength equal to residual strength. When the other specimen is subjected to cyclic loading with undrained stress-controlled condition, the effective stress path progresses toward the left and reaches the flow liquefaction surface. At Point D, this specimen becomes unstable and rapidly moves to the steady state point, Point C. Comparing the monotonic loading and cyclic loading conditions, even when the stress conditions at Points B and D are different, but with the same initial stress conditions and initial void ratio, the two specimens arrive the same point at the steady state deformation.

Another aspect of cyclic loading is observed when the value of the initial shear stress is lower than the residual strength of the liquefied soil (Figure 2-25b). When cyclic loading is applied to the specimen, the stress path moves to the left and approaches the point where effective stress is zero. As the pressures build up, the stress path eventually oscillates around the zero effective stress condition. The zero effective stress condition was referred to as "initial liquefaction" by Seed and Lee (1966). However, it should not be thought that the soils have no shear strength. During a dynamic event, the soils can be agitated to the point of zero effective stress. After the dynamic event is terminated, the soils are subjected to their own weight and the weight of any structures they support, which is referred to the monotonic loading. After initial liquefaction, subsequent monotonic loading causes the soil to dilate and eventually reach the steady state point by following the drained failure envelope.

For seismic events, permanent strain caused by dynamic loading can develop in increments from each loading cycle. For level ground sites, the damage can be mainly due to vertical settlement during the excess pore water dissipation period. For sloping ground sites, however, the permanent strain can be large because the soil weight causes incremental downslope movement in each cycle. Even when the dynamic loading is terminated, because of the low residual strength value, some permanent strain can occur when soils deform under their own weight.

2.4.2.2 Flow Liquefaction

Flow liquefaction is initiated when the shear stress required to maintain static equilibrium is greater than the residual strength of a liquefied soil, as indicated in the shaded zone in Figure 2-26a. When the initial field stress condition falls in this shaded zone, both monotonic loading and cyclic loading can trigger flow liquefaction. However, the initiation of flow liquefaction requires undrained loading strong enough to make the stress state reach the flow liquefaction surface (FLS).

Kramer and Seed (1988) demonstrated a series of undrained stress-controlled triaxial tests on Sacramento River Fine Sand for evaluation of flow liquefaction resistance. In the beginning, soil specimens were isotropically or anisotropically consolidated under varied levels of initial shear stress. Even though all specimens were initially consolidated under the same effective confining stress, because of varied levels in initial shear stress, the results showed varied levels of final deviator stress required for initiation flow liquefaction. Figure 2-27 shows the plot of initial stress conditions (shear stress over effective confining stress) versus stress conditions at the initiation of flow liquefaction. The presented stress conditions were on a plane inclined at 45° from the minor principal stress axis. The ratio of shear stress and effective confining stress was termed "principle effective stress ratio". When the initial principal effective stress ratio was zero (no initial shear stress), the final principal effective stress ratio was about 0.2 to 0.3. For the case with initial principal effective stress ratio of about 0.6, however, an increase of only about 0.1 was required to initiate flow liquefaction. This demonstrated that when the stress condition is near the initiation of flow liquefaction, or near the flow liquefaction surface in stress path, only a small amount of undrained loading may be required to raise pore water pressure and produce flow liquefaction.

2.4.2.3 Cyclic Mobility

When the static shear stress is lower than the residual strength of liquefied soils, the building up of pore water pressure occurs in a process termed "cyclic mobility". The shaded zone in Figure 2-26b indicates the initial stress conditions under which that cyclic mobility is produced. This shaded zone indicates that cyclic mobility can occur in both loose and dense soils.

Depending on the magnitude of initial shear stress and the magnitude of cyclic loading, cyclic mobility can be classified into three cases. The term stress reversal is defined as the difference of initial static shear stress (τ_{static}) and the cyclic shear stress (τ_{cyclic}). The first case, when $\tau_{static} - \tau_{cyclic} > 0$ (no stress reversal) and $\tau_{static} + \tau_{cyclic} < S_r$ (no exceedence of residual strength), the effective stress path moves to the left until it reaches the drained failure envelope. Further excitation from cyclic loading can only make the effective stress path oscillate on the envelope. In this case, the effective stress never reaches zero, and the resulting strains are relatively small. The second case has no stress reversal but does have an excess of residual strength, i.e. $\tau_{static} + \tau_{cyclic} > S_r$. When the effective stress path crosses the flow liquefaction surface, temporary instability is created, with possible significant permanent strain accumulation. The last case is when $\tau_{static} - \tau_{cyclic} < 0$, which refers to the stress reversal condition. The stress reversal effect causes the effective stress path to move to the left with both compression and extension in each cycle. When the effective stress path reaches the zero effective stress point, the stress path starts to oscillate along the effective failure envelope. Cyclic mobility with stress reversal has been shown to build up excess pore water pressure faster than when no stress reversal occurs. The reason is that extension loading causes soil particles to densify (contract) themselves more when they go through a period of zero shear stress, i.e. stress reversal. As the consequence, the soils subjected to the stress reversal condition usually exhibit large permanent deformation.

2.5 EFFECTS OF LIQUEFACTION

Laboratory element testing of undisturbed or reconstructed samples provide fundamental knowledge of soil liquefaction. Under field conditions, more complicated situations will be involved in the initiation of soil liquefaction and in the post-initiation soil behavior. The factors that affect the occurrence of soil liquefaction in field can be the pore water pressure dissipation, localized low permeability barrier, fissures or localized weak zone, field stress condition, spatial variation of soil properties, local site effect on dynamic loading, and the characteristics of disturbance that trigger soil liquefaction. After liquefaction has been initiated, the post-failure process can be affected by the boundary conditions along the liquefied zone (energy dissipation, material transportation or exchange along boundaries), geometry of liquefied zone and surrounding area (level or sloping ground causing different phenomena), and excessive pore water dissipation during the failure process.

As a result of these variations in field conditions, the effects of soil liquefaction are introduced based on the soil liquefaction classification: flow liquefaction and cyclic mobility. Soils subjected to flow liquefaction failure usually involve large areas of soil mass movement, such as a large landslide or flow slide on sloping ground or man-made retaining structures and embankments. Cyclic mobility type of failures can range from minor to serious damage. On level ground, the process of pore water dissipation creates ground deformation followed by possible damage to soil-supported structures. On sloping ground, dynamic loading can cause accumulated strain and produce lateral spreading. This section looks into the details of several typical liquefaction-induced failures, ranging from minor damage such as sand boils to serious damage such as ground distortion, lateral spreading, and flow slides.

2.5.1 Sand Boils

Sand boils are probably the most commonly seen effect of soil liquefaction. Dynamic loading induces high excess pore water pressure in loose, saturated soils.

During and after the loading period, the high excessive pore water pressure creates a hydraulic gradient that causes water to flow from the high pore water pressure zone to the low pore water pressure zone, which usually generates a upward flow toward the ground surface. In the field, the underground soils usually contain fissures, cracks, and local weak zones, in which water finds its path to dissipate pressure. When the excess pore water pressure creates low effective stress at the liquefied area, the disturbed soil matrix can flow with water to ground surface because the high velocity of water flow creates enough momentum to carry soil particles.

A number of factors can affect the occurrence of sand boils. The characteristics of dynamic loading, such as intensity and duration, will influence the magnitude of excess pore water pressure. The geologic conditions of the liquefied area provide the possibility of occurrence of sand boils appearing on ground surface. These are geology conditions that include the depth of ground water table, depth and thickness of liquefied soils, soil permeability, and intactness of overlaying soil layers (Kramer, 1996). A good example of sand boils occurred at the Sunset Lake, Washington, during the Nisqually Earthquake, 2001. After the 6.8 magnitude earthquake, numerous sand boils had been found surrounding the lake. The intensity and duration was high enough to induce high excessive pore water pressure. The local soils were coarse to medium size sandy soils filling the upper 15 to 20 feet with single digit SPT blow count. Combining with the high ground water table, it created a great opportunity for sand boils occurrence.

For engineering practice, sand boils do not produce great damage to ground surfaces or structures. However, this phenomenon provides information on locating the liquefiable zone and benefits further assessment of soil liquefaction hazards.

2.5.2 Ground Distortion

Soil liquefaction-initiated ground distortions include settlement and structural damage above and under the ground surface. The damage caused by ground distortions result from the dynamic loading that increases pore water pressures. When dry soils are subjected to dynamic loading, settlement is generally complete right after the loading stops. For saturated soils, dissipation of excess pore water pressure is required, so the time to reveal ground settlement depends on the permeability of soil, the stiffness of overlaying soils, and traveling path for water-soil migration. After the water pressure reaches equilibrium state in the post-liquefied zone, the reduction of water volume causes densification in the post-liquefied zone; hence, the ground settlement is the result of the dissipation of excess pore water. Subjecting to soil-supported structure, such settlement can cause damage to soil-supported foundations and overlying structures. For a deep foundation (e.g. pile foundation), ground settlement can expose the pile cap and/or piles themselves, which decreases the supporting capacity of piled foundation. For a shallow foundation, ground settlement may cause differential settlement damage foundation and upper structure.

When the soil strength decreases to the residual strength, the reduction in soil strength may produce several other ground distortion problems. The foundation system may lose a great amount of bearing capacity. Consequently, structures subside and tilt, and even plunge into the ground. Underground facilities, such as lifelines, underground tanks, and underground pipelines, may suffer breakages because of loss of support from surrounding soils.

2.5.3 Lateral Spreading

When soils undergo cyclic mobility, the low effective stress due to increasing pore water pressure can cause local loosening of liquefied soil. Furthermore, because the high hydraulic gradient, water tends to flow and accumulate at the top of the liquefied layer, especially with a less permeable overlaying layer (Fiegel and Kutter, 1994; Kramer, 1996; Kokusho, 1999; Kokusho and Fujita, 2002). This action of accumulating water will further weaken the top of liquefied soil and cause breakage of overlaying layer.

When this situation occurs on gentle sloping ground, such as a river bank, this tendency is amplified with existence of initial shear stress. Considerable strain can be accumulated during dynamic loading along the loosened liquefied soils. Lateral spreading is created by surficial layers sliding along the locally loosened liquefied soils. The surficial layers usually show fissures and scarps between broken soil blocks. With the movement toward the down slope, a shear zone along the perimeter of spreading zone, a vertical and horizontal displacement between soil blocks, and a compressed sliding toe area are often observed. In some cases, the delayed effect from slow dissipation of pore water pressure can cause progressive failure that causes the lateral spreading area to extend in the uphill direction.

The soil movement involved in lateral spreading produces a great threat to ground structures and underground facilities. The lateral soil movement can induce a large bending moments in pile foundations that penetrate the liquefied zone. The bending moment is especially concentrated at the interface (between liquefied and non-liquefied zone) where sliding occurs, producing fractures of piles and reducing bearing capacity. For underground facilities, the portion that falls inside the spreading zone can be carried away with moving soils and disconnected their functions.

2.5.4 Flow Slide

Under an undrained stress-controlled triaxial test, when the initial shear stress is higher than the residual strength of liquefied soil, flow liquefaction is triggered when the soil stress conditions reach the flow liquefaction surface in the effective stress path space, which is followed by a collapse because of sudden drop of soil strength. In field case histories, when soil structures, such as earth dam and roadway embankment, are subjected to dynamic or monotonic loading, a similar situation may occur.

Flow slide is a flow liquefaction related failure, initiated when the soil structure loses its original static equilibrium because of the sudden drop in shear strength of the liquefied soils. In order to reach another form of equilibrium, the soil structure collapses under its own weight. After the initiation of flow liquefaction, the failure process is driven by soil body weight rather than by dynamic stresses. In most flow slide case histories, intact and non-liquefied surficial soils are fractured into blocks that float on the liquefied soil. The major source of resistance, therefore, would be the residual strength of the liquefied soil. As the soil mass deforms, kinetic energy resulting from the traveling velocity of soil mass increases and then decreases as the soil regains stability. A famous flow slide case history is the collapse of Lower San Fernando Dam after the San Fernando Earthquake, 1971. A summary of this flow-slide failure was presented in Section 2.2.6.

2.6 SUMMARY OF SOIL LIQUEFACTION

This chapter provided an introduction of soil liquefaction behaviors in a macro-scale study of laboratory testing and field conditions. From the soil liquefaction case histories, liquefaction-induced hazards can produce minor or major damage. Preventing liquefaction-related hazards started to attract people's attentions about 40 years ago. The pioneering works of Casagrande and Castro lead people to understand the typical behavior of soil liquefaction. The reason for soil liquefaction failures had been determined to be caused by loss of soil strength after an increase of pore water pressure.

Further research has revealed that soil liquefaction can be classified in to two groups: flow liquefaction and cyclic mobility. The distinction between these two groups is the initial stress conditions in effective stress path space. The flow liquefaction type of failure can be initiated by both monotonic loading and dynamic loading. The consequence after the initiation of flow liquefaction involves the sudden drop of soil shear strength to the residual strength. The failures caused by flow liquefaction usually involve serious hazards, such as flow slides. Unlike flow liquefaction, cyclic mobility can only be triggered by dynamic loading, but it can occur in both loose and dense soils. The failures caused by cyclic mobility can range from slight damage to serious hazard. During cyclic mobility failure, the permanent strain is accumulated during dynamic loading cycles. For certain field conditions, such as sloping ground, the accumulated strain can be tremendous.

In order to prevent soil liquefaction hazards, evaluation of liquefaction hazards is important. The susceptibility of liquefaction can first be evaluated based on the historical characteristics, geology characteristics, and spatial and probabilistic characteristics. After the location has been evaluated as liquefaction susceptible, the potential for initiation of liquefaction needs to be further analyzed. The procedure involves evaluation of the level of sources that can trigger liquefaction as flow liquefaction or cyclic mobility. When a location is identified as likely for the initiation of liquefaction, the next assessment is to evaluate the effects of liquefaction occurrence. From an engineering standpoint, the design for liquefaction resistance requires knowledge of damage severity and serviceability after damages.

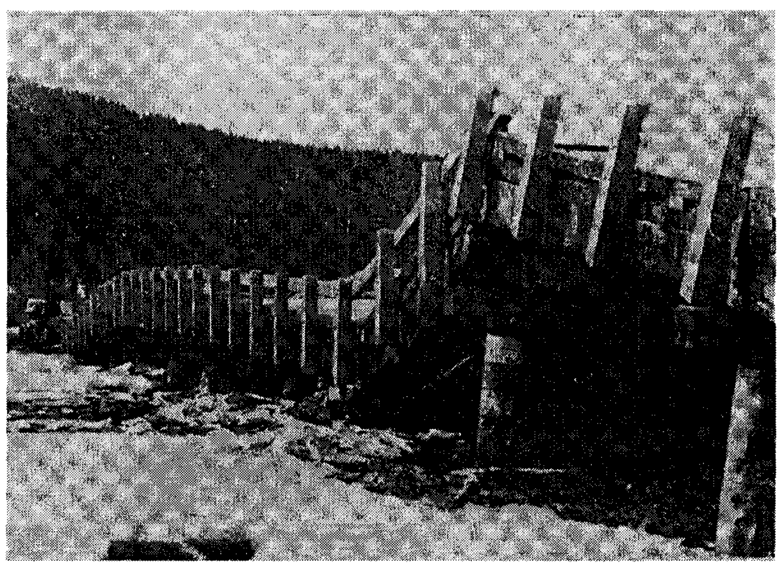

Figure 2-1 No. 605 Bridge, Snow River, Alaska (Ross et al., 1969).

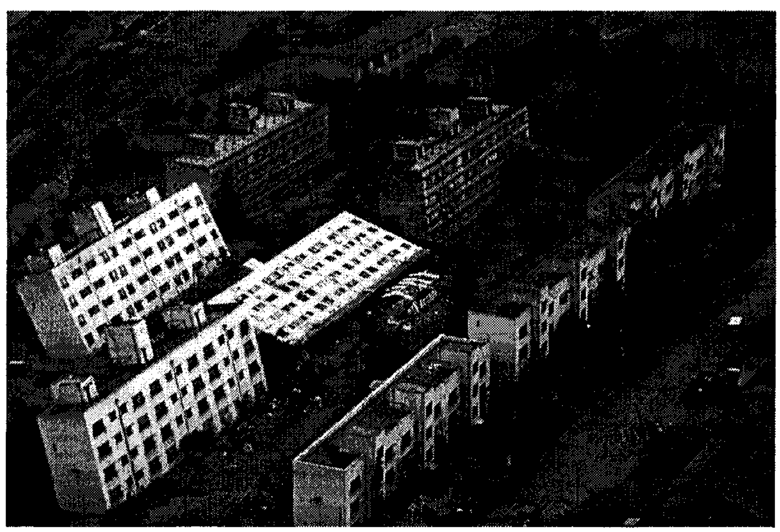

Figure 2-2 Kawagishi-Cho Buildings, Japan (Steinbrugge Collection).

Figure 2-3 NHK Building, Japan (Hamada, 1992).

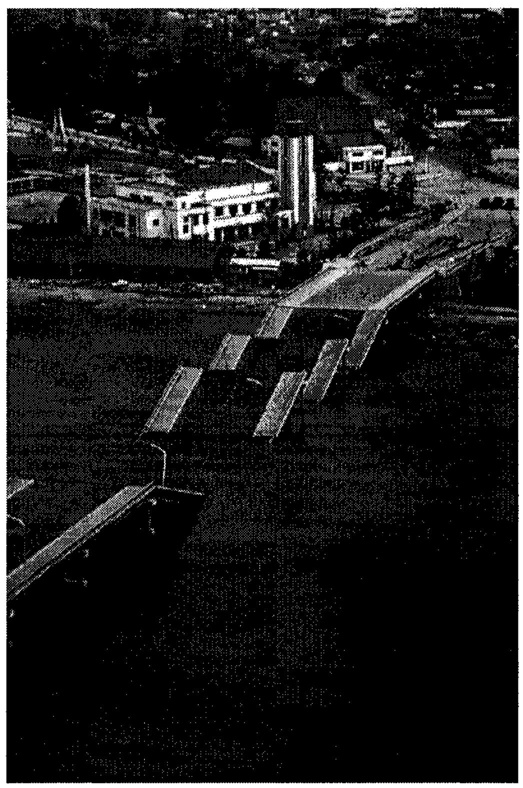

Figure 2-4 Showa Bridge, Japan (Steinbrugge Collection).

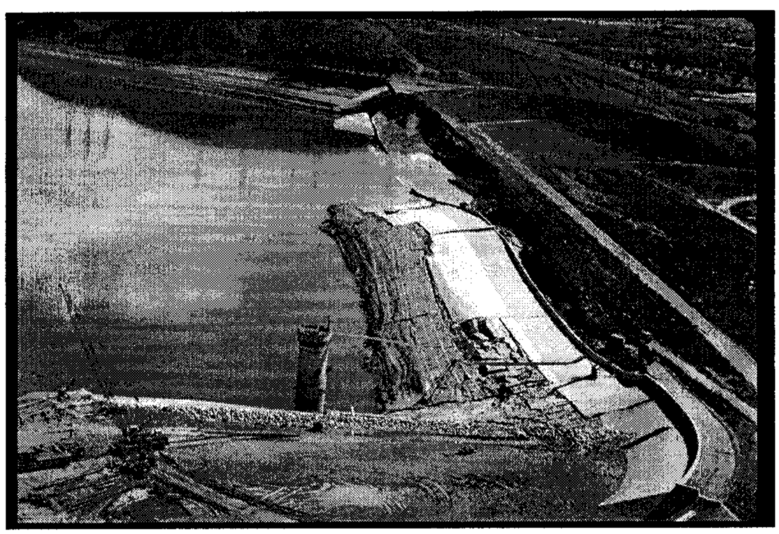

Figure 2-5 Lower San Fernando Dam, California (Steinbrugge Collection).

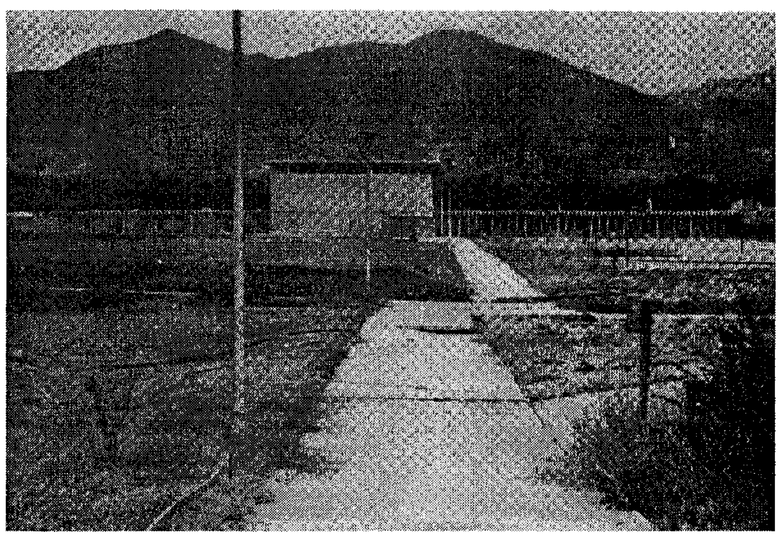

Figure 2-6 San Fernando Valley Juvenile Hall, California (Thompson, 1973)

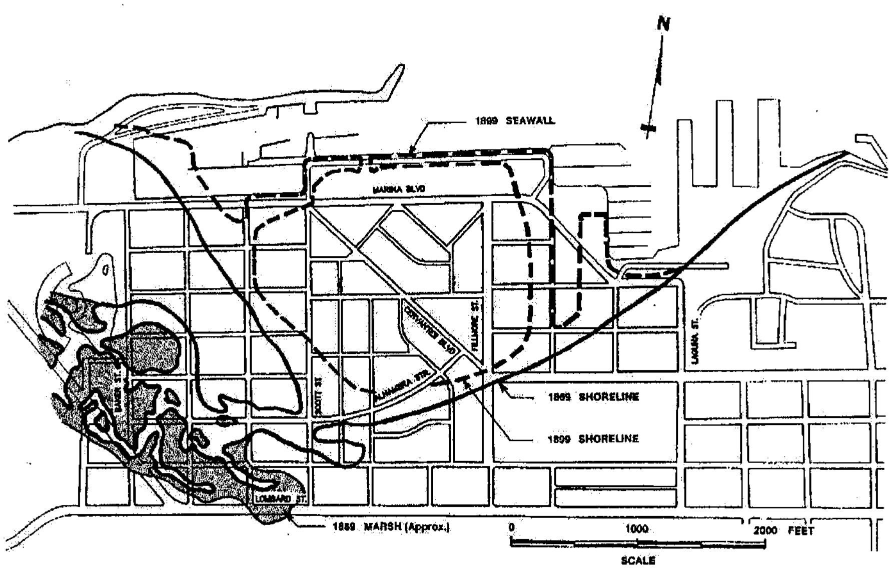

Figure 2-7 Marina District, California (Seed et al., 1990).

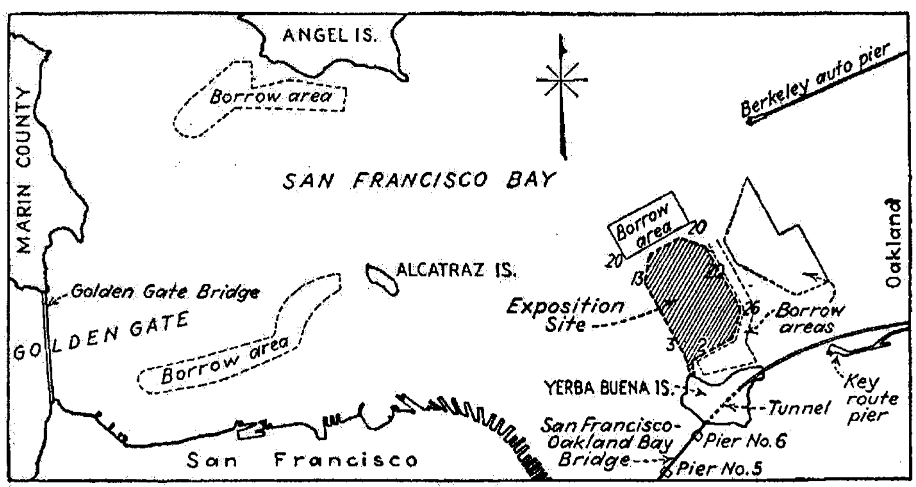

Figure 2-8 Treasure Island, California (Seed et al., 1990).

Figure 2-9 Port Island, Japan (Steinbrugge Collection).

Figure 2-10 Capitol Lake, Washington.

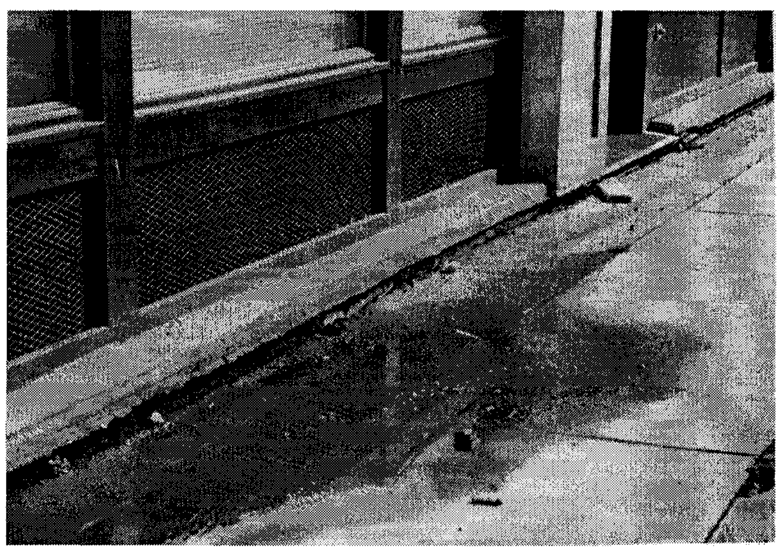

Figure 2-11 South of Downtown Seattle, Washington.

Figure 2-12 Sunset Lake, Washington.

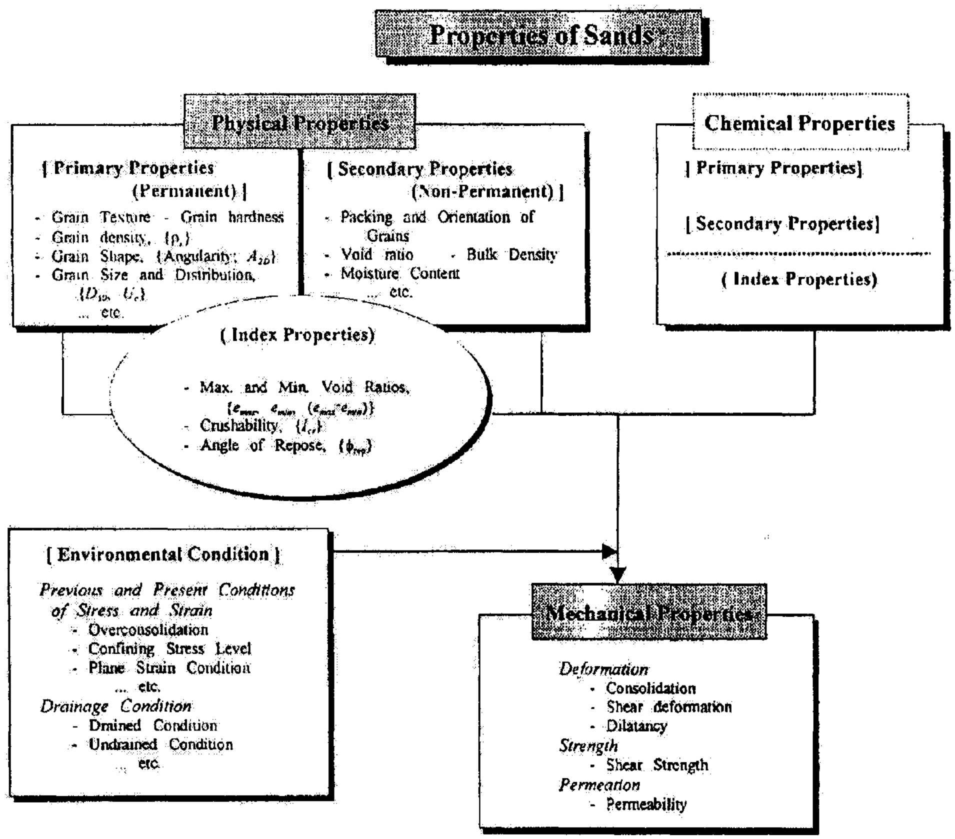

Figure 2-13 Categorization of mechanical properties of sands (Miura et al., 1997).

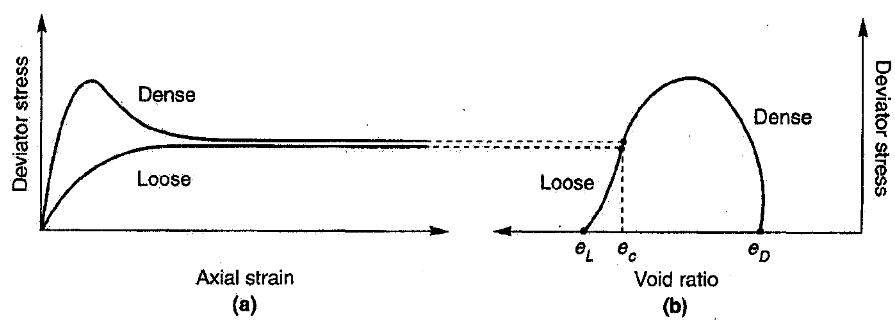

Figure 2-14 At the same effective confining pressure, (a) stress-strain and (b) stress-void ratio for loose and dense sands under drained condition (Kramer, 1996).

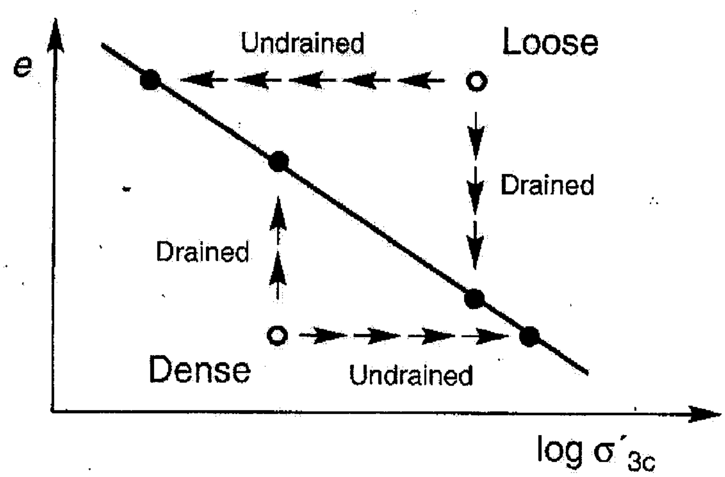

Figure 2-15 Behavior of loose and dense sands under drained and undrained condition (Kramer, 1996).

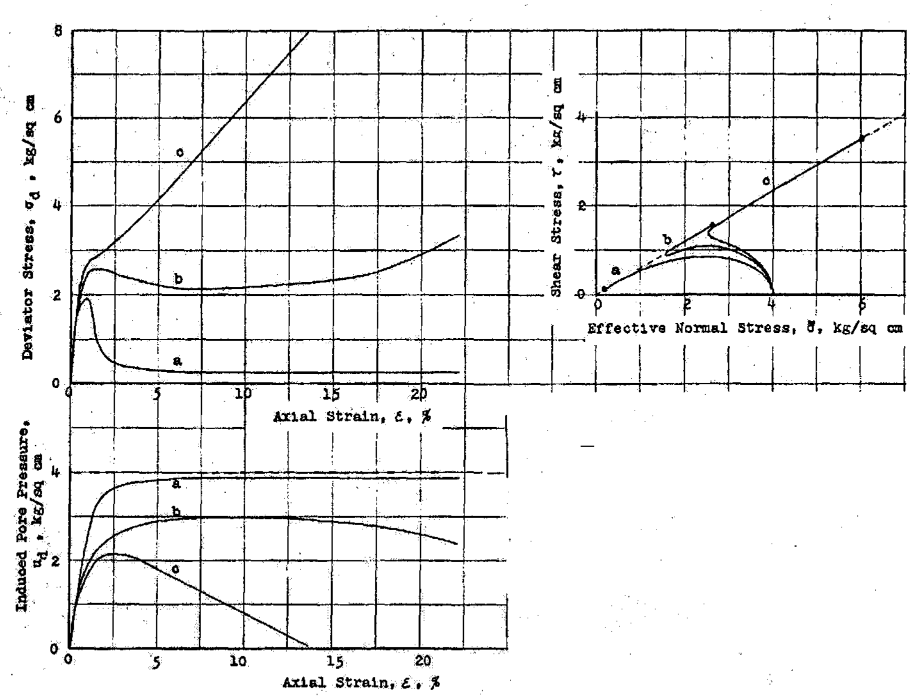

Figure 2-16 Typical stress-controlled undrained triaxial test results by Castro (1969).

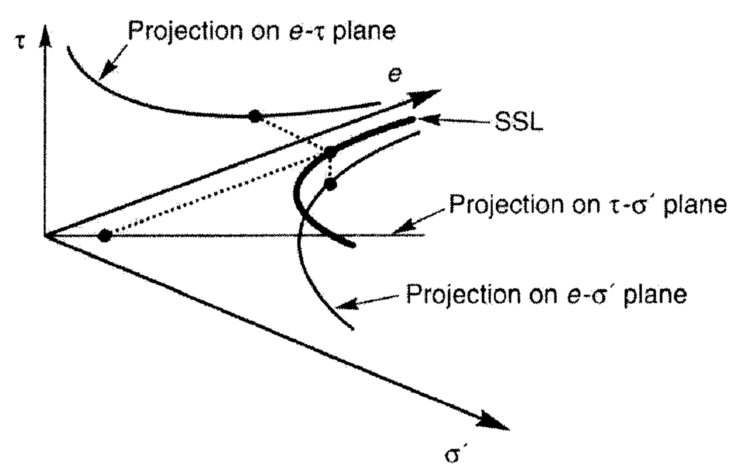

Figure 2-17 Three-dimensional steady state line (Kramer, 1996).

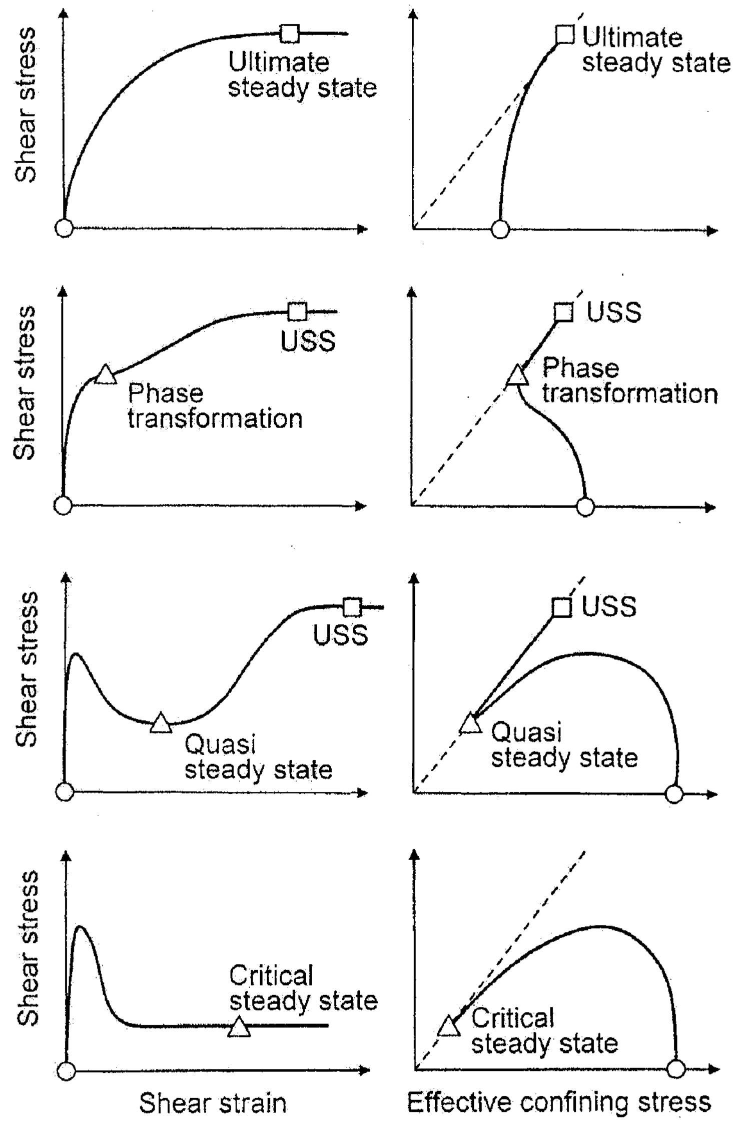

Figure 2-18 Soil Behavior of undrained triaxial test (Yoshimine and Ishihara, 1998).

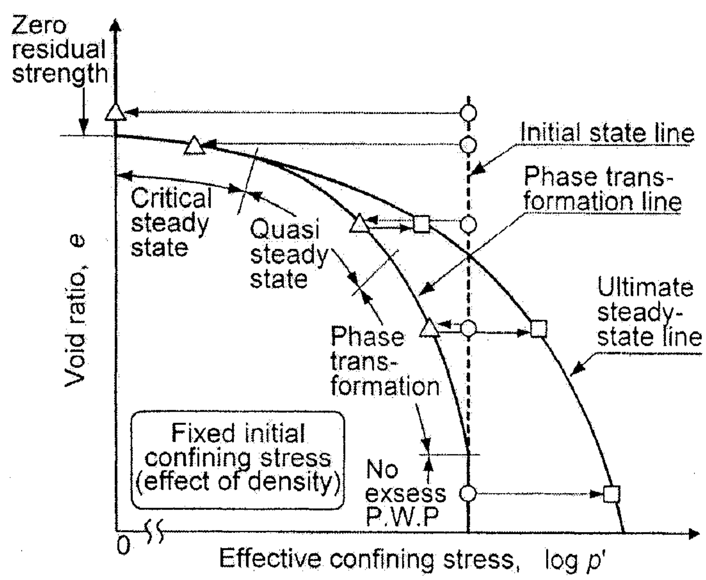

Figure 2-19 Summary of soil behavior in effective confining stress and void ratio space (Yoshimine and Ishihara, 1998).

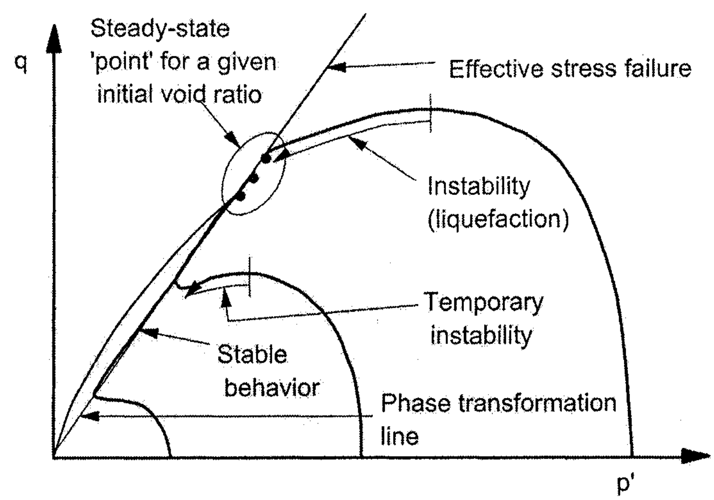

Figure 2-20 Undrained behaviors of loose clean sand under constant initial void ratio with varied initial confining stresses (Yamamuro and Convert, 2001).

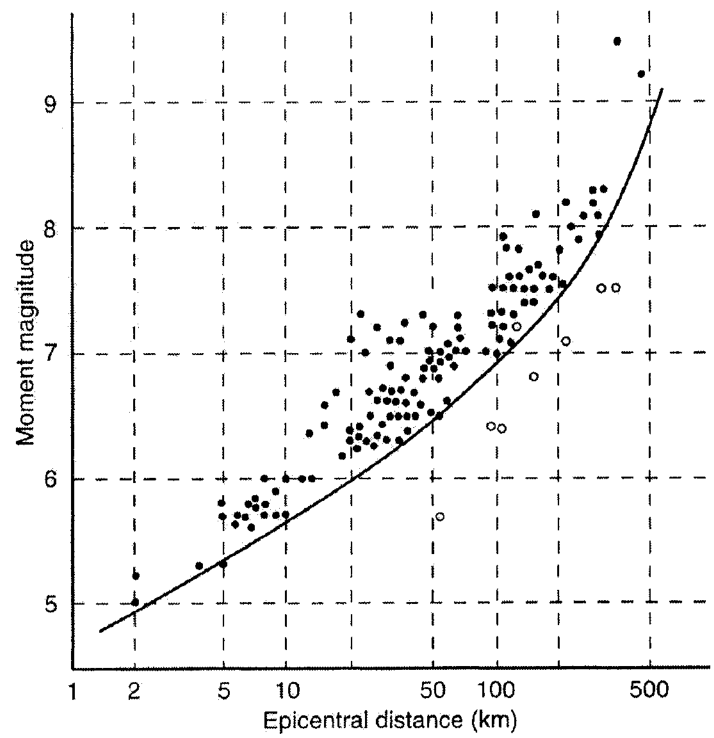

Figure 2-21 Relationship between the maximum epicentral distance of liquefied site and the moment magnitudes of seismic events (after Ambraseys, 1988).

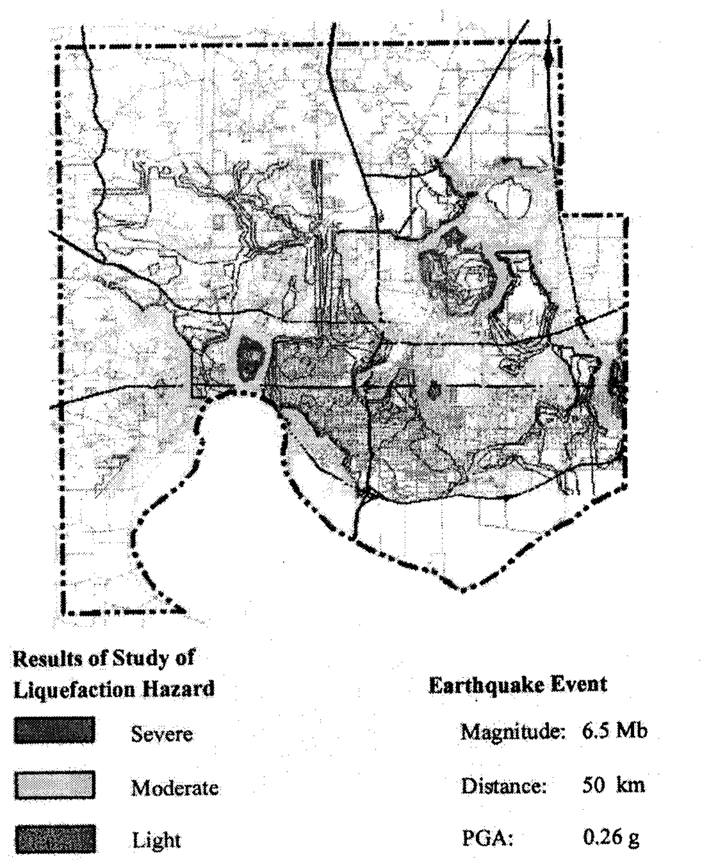

Figure 2-22 An example of GIS map for the potential of the liquefaction-induced ground failure. (Frost et al., 1997).

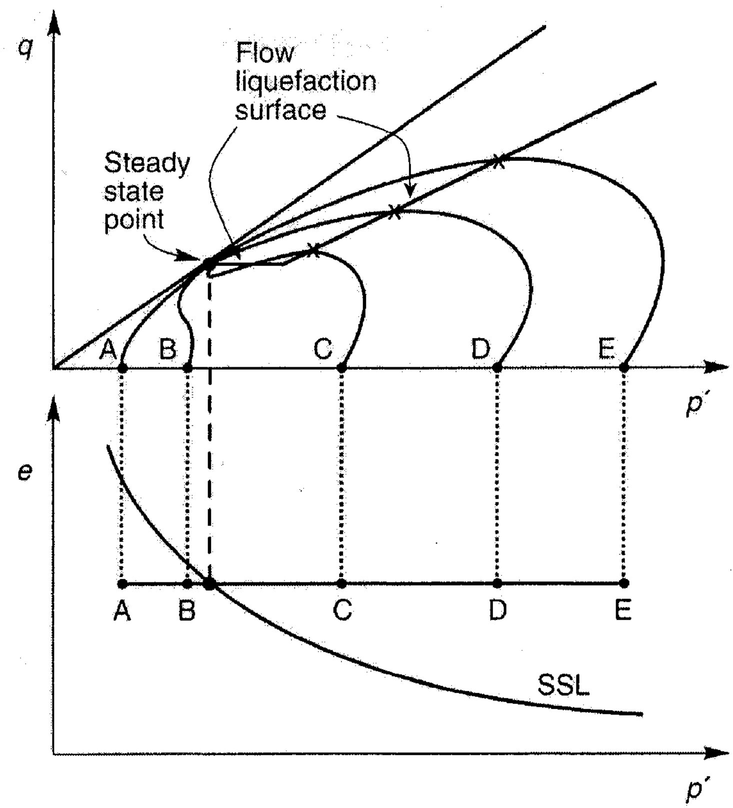

Figure 2-23 Liquefaction induced by monotonic loading (after Kramer, 1996).

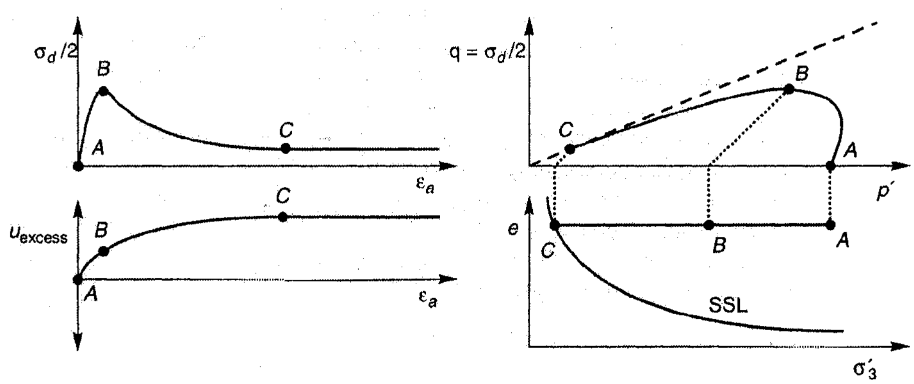

Figure 2-24 Behavior of flow liquefaction under monotonic loading in undrained stress-controlled triaxial test (Kramer, 1996).

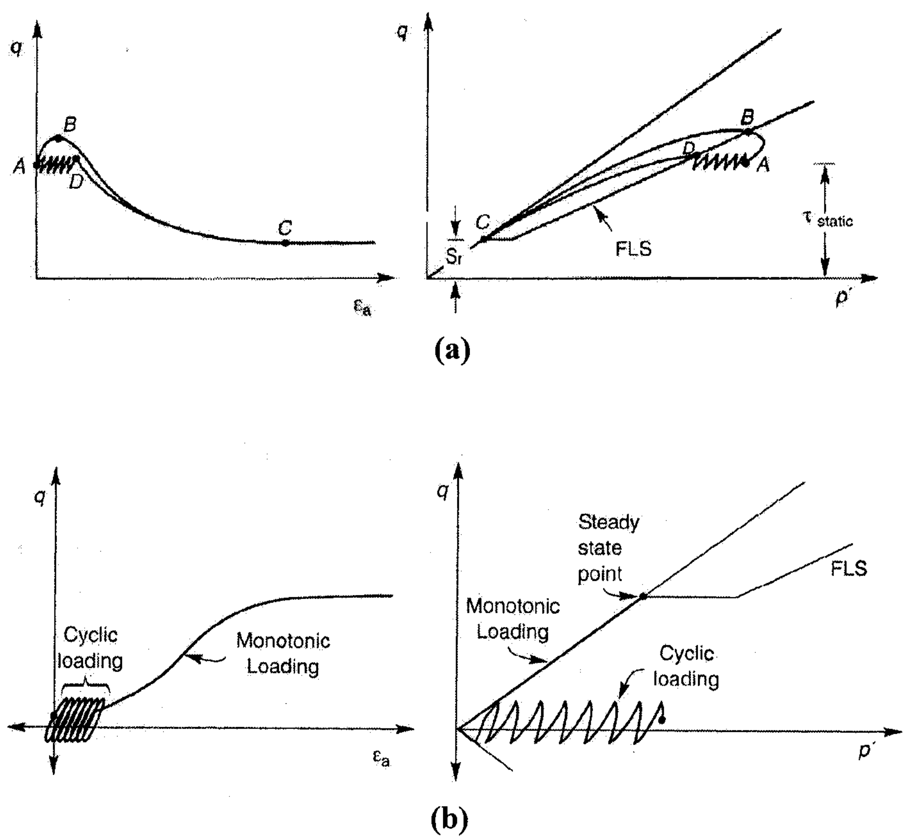

Figure 2-25 Liquefaction induced by cyclic undrained stress-controlled triaxial test, when (a) initial shear stress is greater than residual strength (b) initial shear stress is less than residual strength (after Kramer, 1996).

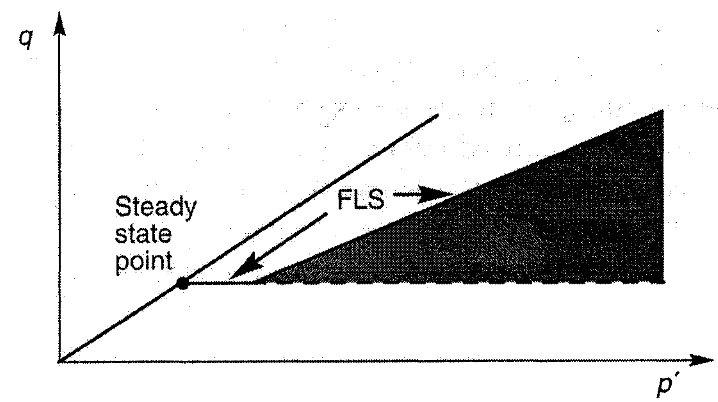

(a)

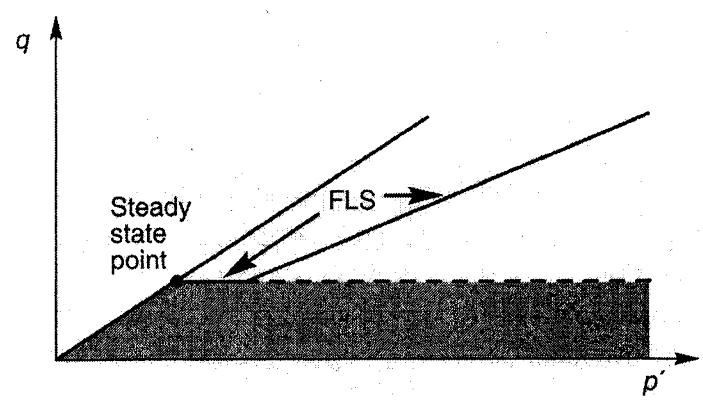

(b)

Figure 2-26 Zones of liquefaction classification (a) flow liquefaction and (b) cyclic mobility (Kramer, 1996).

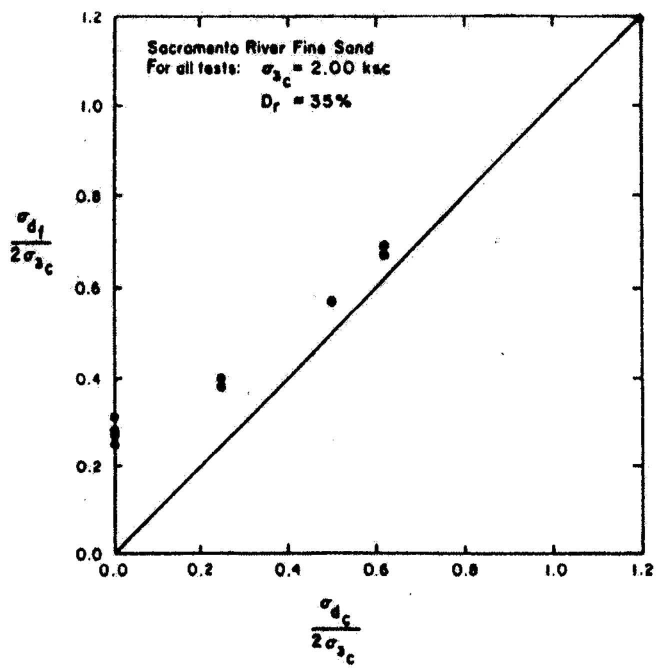

Figure 2-27 Influence of initial shear stress on initiation of flow liquefaction of Sacramento River Sand (Kramer and Seed, 1988).

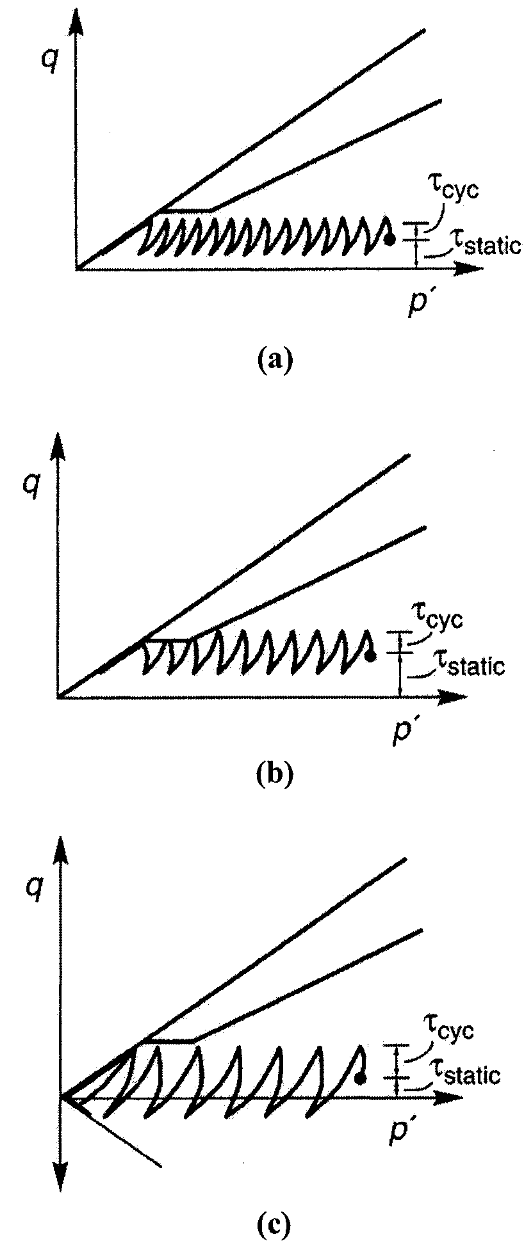

Figure 2-28 Three cases of cyclic mobility (a) no stress reversal and no excess of residual strength, (b) no stress reversal with temporary excess of residual strength, and (c) stress reversal with no excess of residual strength (Kramer, 1996).

Chapter 3

Flow Failure Research

3.1 INTRODUCTION

Geotechnical materials include a wide range of particle sizes, from very small (clay), to very large particles, such as rock blocks. In both analytical and laboratory approaches, the mechanical properties of geotechnical materials have been analyzed in two major systems: the micro-scale system and the macro-scale system. The analytical approach in macro-scale system involves the constitutive modeling, while accounting properly for boundary conditions. To solve geotechnical problems, common analytical methods include the finite element method and the finite difference method. In the laboratory approach to evaluate soil behavior on the macro-scale level, remolded and undisturbed soil specimens have been tested with various loading conditions, boundary conditions, and drainage conditions. On the micro-scale level, the mechanical behaviors are governed by the inter-particle forces, interstitial fluids, and particle-fluid interactions. Because liquefiable soils are composed of sand particles, the concept of this chapter is to study the behaviors of sand-like particles (particulate material) interacting with interstitial fluids.

Oda and Iwashita (1999) introduced a scheme to explain the relationship between local micro-scale behavior of particulate material and the global constitutive relations in the macro-scale system (Figure 3-1). In the micro-scale system, the movement among particles produces inter-particle contact forces, which can displace particles from their original positions. This rearranging of particle positions further alters the contacts among particles and the contact forces. While the measurement is made from the macro-scale behaviors, the stress and strain fields result from averaging of the movement and contact of all particles. In the reverse direction of the averaging effect, the localization process confirms that the macro-scale system provides an overall environmental alteration to strain and stress conditions thereby affecting particle behavior. This scheme explains the basic concept of examining the particulate behaviors on both micro and macro scales.

This chapter starts with a review of particulate flow behavior from the micro-scale point of view. The sources of shear strength in the particulate matrix are introduced with examples of testing verification. Further illustrations of particulate flows include stress development in particle matrix, stress dilatancy, particle localization, and particle crushing effect. The second section presents a review of debris flow phenomena that illustrates the overall behavior of particulate flow in the macro scale. The process of debris flow involves the strong agitation of the particle-fluid interaction, which represents an extreme case of soil liquefaction. The purpose of this chapter is to review soil liquefaction-related phenomena from a simple case of particle assembly to the complicated case of debris-flow mixtures.

3.2 PARTICULATE FLOW

Particulate (granular or particle) flow is influenced by the two-phase structure of the soil: the solid phase (particulate materials) and the void phase (fluids and gases). Jaeger and Nagel (1992) indicated that the mechanical properties of particulate flow are dominated by their dynamic characteristics. In the void phase, thermal motion produces a drift velocity of the small particle, even in the static state. When dynamic agitations are applied to the void phase, interaction between solid and void phases generates further fluctuations besides the interstitial fluid turbulence. While the solid phase is subjected to some previous composition history, the arching effect within the particle packing provides a distinction between the solid phase and the void phase. The flow characteristics in the solid phase are initially determined by the geometry of particle packing and bonding history (e.g. chemical and physical conditions). Under further excitation such as sound propagation and vibrations, the dynamic characteristics of the solid phase are determined by the contact collisions within the random particle packing. Because the contacts between particles are randomized, the determination of particle collisions is controlled by the spatial variations of particle configuration. On the macro-scale level, therefore, the space occupancy of the solid and/or void phase decides the mechanics behaviors. For example, the stress conditions are estimated from inter-particle collisions when the solid phase occupies most of space.

3.2.1 Particle Matrix Study

As classified by Santamarina et al. (2001), particulate materials appear in soils (in geotechnical engineering); unconsolidated sediments (in petroleum geomechanics); food grains (in food science); composites, ceramics, and sintered materials (in materials science); crushed rock (in mining science); granular packing of catalyzers (in chemical engineering); asphalt and cement (in infrastructure); and filters (in water treatment). For the current research of the soil liquefaction in geotechnical engineering, the concentration of study is on granular material such as sandy liquefiable materials.

3.2.1.1 Particle Fabric Formation

Section 2.3.1 introduced the factors that contribute the mechanical characteristics of sands, including physical properties, chemical properties, mechanical properties, and environmental conditions. At any spatial location within the soil matrix, the material composition may differ in the particle type (mineral property) and the geology variation (layered deposition). To recognize the characteristics of soil behaviors, it is beneficial to understand the geological history of soil deposits. The local soil matrix formation is contributed from geology formation, residual deposition, transported agents, and weathering procedure (Mitchell, 1993; Santamarina et al., 2001). The geology of soil deposit formation affects the basic mineral characteristics and crystallization structure of particle. Because the new earth crust was produced from the cooling process of the molten rock magma, the chemical properties are strongly affected by the cooling rate. For example, quartz, the main composition of sand, starts to crystallize when the temperature drops below 573°C. The crystallization structure cannot be well created without the proper cooling rate. After forming the local geology, the residual deposit refers to the soils that have inherent properties from the parent material, such as chemical properties, climate, topography, and drainage conditions. Some soils are subjected to transportive agents, such as glacier, water, and wind. Soils, or rocks, that had been transported from their original locations and developed different deposits may be altered in size, shape, and surface texture. During or at the end of transporting, material sorting may create a gradient of particle sizes along the path.

Weathering is a destructive procedure that usually produces new deposits from the process of physical and chemical alteration (Mitchell, 1993). The physical alteration can involve unloading on the surface of deposits, and reducing pressure or temperature within the subsurface materials. When the surface loads have been altered, the reactions within subsurface materials can include thermal expansion and contraction, renewal of crystallization, and organic activity. The chemical process of weathering is mainly affected by water activity. The chemical reaction between mineral and water, e.g. hydrolysis, changes the basic mineral structure. The result of the weathering procedure alters the mineral compositions, soil deposition, and particle shape and size.

Soils are the final products of all those actions. From the history of soil formation, factors such as particle size, particle gradation, and surface texture can be the result of weathering and/or transporting processes. The stiffness of particles is affected by the properties of the original materials and by chemical alteration. In the micro scale of soil liquefaction evaluation, inter-particle and particle-fluid interactions can be affected by those factors.

3.2.1.2 Particle Movement in Fluid Space

The stress conditions developed within a particulate flow result from particle contacts, interstitial fluid turbulence, and particle-fluid interaction. A simple way to explain the conditions is to imagine the movement of a single particle through a fluid. According to the particle velocity, the particle-fluid interaction can be classified

(Heiskanen, 1993) as the laminar stage, the transitional stage, and the Newtonian flow (steady fluctuation) stage. In the laminar stage, with low particle velocity, the fluid streamlines are smooth and return to their original positions after the particle passes. When particle velocity gradually increases, the fluid streamlines fluctuate behind the passing particle because the particle inertia force generates drag forces between the particle and the fluid. The transition stage refers to the starting of the fluid fluctuations without reaching a steady condition. After the particle velocity reaches a certain level, the fluid turbulence caused by the particle inertia force remains steady, even with increasing particle velocity. This steady condition is termed as the Newtonian flow or the steady fluctuation stage. In this single-particle system, the stress components that contribute to the overall system include interstitial fluid turbulence, or the surficial stresses on the particle caused by particle-fluid interaction, rotation momentum of particle, and the stress components inside the particle that are produced by the surficial stresses.

When two particles move in opposite directions within the same fluid space, the response of the system is more complicated then the single-particle system. In Figure 3-2, Bingham (1922) illustrated a typical condition of the two-particle system. Before the collision occurs between two particles, each particle moves individually with the same stress conditions as the one described in the single-particle system. One difference is the amplified surficial stresses when two particles approach each other. As two particles initiate contact, the collision produces three stress components: a normal stress on the contact surface, a shear stress on the contact surface, and rotational momentum related to the other particle. At the brief moment of contact, those two particles move as one unit because the normal and shear stress components overwhelm the rotational momentum. The collision is terminated when the normal and shear stresses decrease and then cause separation between particles. One thing that should be noted is the vectors of particle movement are altered after separating from collision (Figure 3-2a and Figure 3-2d). In a multi-particle system, a random process of collisions should be deemed due to this vector change.

This two-particle system is the most basic representation of the particulate flows. The overall energy consumption in a particle-fluid system is caused by fluid turbulence, surficial stresses on particles, internal stresses in particles, and collision stresses that include normal and shear stress, and rotation momentum. Some further complications may be involved in the behavior of the particulate flows, such as random inter-particle collisions, particle-fluid interactions, boundary effects, and the various properties of particle itself (e.g. stiffness, shape angularity, and surface roughness).

3.2.2 Testing Verifications

To explain the phenomenon of particulate flow, the small-scale laboratory experiments have been created to explain the behaviors of the large-scale flow in a natural environment. Bagnold (1954) performed the pioneering work in laboratory observation of particulate flow. His work showed that the mechanical properties of particulate flows are dominated by particle collisions or fluid turbulence. Savage and colleagues (Savage and Jeffrey, 1981; Jenkins and Savage, 1983; Savage and McKeown, 1983; Savage and Sayed, 1984; and Hanes and Inman, 1985a, b) developed another laboratory device to identify particulate flow behaviors in the 1980s. They also developed a series of analytical verifications to explain the flow characteristics. Those two groups of testing verification used both man-made and natural particles.

3.2.2.1 Bagnold

To estimate the stress conditions in a particle-fluid matrix undergoing shearing, Bagnold (1954) invented a procedure for evaluating stresses based on the particle inertia and fluid viscosity effects, and found that one or the other could dominate the soil response. In the region of particle inertia domination, stresses were generated predominantly from inter-particle collisions at high particle concentrations (ratio of volume occupied by particles over the total volume) or high shearing rate. Both of these conditions provided high collision frequency, which then produced considerable inter-particle stress in the normal and shearing directions. In Bagnold's conceptual model, collisional stresses were generated between well-ordered particle layers. The applied shearing force caused one layer of particles to overtake another layer, creating collisions between the particles. He concluded that the shear stress, T, dominated by inter-particle collision in the form as

$$T \propto \sigma(\lambda D)^2 (\frac{dU}{dy})^2 \tag{3.1}$$

where σ is particle density, D is particle diameter, λ is a particle concentration-related parameter, and dU/dy is shearing rate.

When the applied shear force or the particle concentration in the particle-fluid matrix was low, fluid viscosity, or interstitial turbulence, dominates the stress conditions. In the region of fluid viscosity domination, normal and shear stresses of mixture were generated through fluid turbulence and particle-fluid interaction effects. When the experiment was conducted with a low concentration and a low shearing rate, Bagnold neglected the particle collisional force. As a result, the fluid agitation produced by particle movement and interstitial fluid turbulence constituted the overall stress condition. He presented the form of shear stress dominated by fluid viscosity as

$$T \propto \lambda^{\frac{3}{2}} \eta \frac{dU}{dy} \tag{3.2}$$

where   is fluid viscosity coefficient.

Bagnold developed a cylindrical viscometer-type device to verify the behavior of the particle-fluid matrix and its stress conditions in the laboratory. This device had two concentric cylindrical drums that created an annular space that was filled by the particle-fluid mixture (Figure 3-3). The stationary inside drum (flexible smooth wall) was supported by a spring calibrated to measure torque, while the outside drum (rigid smooth wall) could be rotated by applying torque. The particles were spherical droplets of a mixture of paraffin wax and lead stearate with a constant diameter of 0.132 cm. To prevent the effect of radial acceleration, the particle density was the same as the fluid density. Initially, only fluids were poured in the annular space between the two drums. Particles were then added into fluids to test the strength of the particle-fluid mixture with different particle concentrations and shearing rates. Typical test results are shown in Figure 3-4. The symbol C is another particle concentration-related parameter. Increasing values of particle concentration resulted from increasing numbers of particle in the mixture. T and P referred to shear stress and normal stress, respectively.

In Figure 3-4, for high particle concentration ($\lambda > 12$) or high shearing rate, Bagnold indicated the stress components (T/λ and P/λ) had linear relationships with $(dU/dy)^2$. When the particle concentration was low ($\lambda < 12$) or the mixture was agitated by the low shearing rate, the stress components became proportional to dU/dy.

3.2.2.2 Savage Group

Following Bagnold's idea of testing particle-fluid mixture in a viscometer type device, Savage and McKeown (1983) modified a viscometer to test the normal and shear stresses of a particle-fluid mixture. In Bagnold's testing, the rigid outside drum and the flexible inner drum were used to test particles with constant diameter. In Savage and McKeown's tests, the device had rigid inside and outside drums to test particle sizes ranging from diameter of 0.097 cm to 0.178 cm. The particles were made of polystyrene and had a spherical shape. In order to evaluate boundary effects, they also established experiments with smooth sidewall and the rough sidewalls to evaluate their interaction with the particle-fluid mixture. The results revealed important information on boundary effects interfering with the various particle concentrations. With increasing particle concentration, severe slipping had been observed between particles and walls in the smooth-walled testing group. In the rough-walled testing group, the rough interior grabbed particles during drum rotation. When tests were conducted with high particle concentration, the formation of a rigid non-flow zone with shear bands was discovered near the rough walls. In this case, the actual sheared zone was smaller than the dimensions of the annular space. The inter-particle collisions were produced in a randomly order within this inter-locked shear bands; hence, the normal and shear stresses showed highly fluctuated values. Overall, the normal and shear stresses of the rough-walled test group showed higher magnitudes of stress components than the smooth-walled test group did.

In 1984, Savage and Sayed developed a new annular shear cell to test dry cohesionless granular material (Figure 3-5). The annular shearing cell was composed of an upper plate fixed on a central shaft and a lower rotating plate that contained the sample space. Dry particles were placed in the annular sample space and sheared in a two-dimensional horizontal plane. Inside the annular sample space, the top and bottom surfaces were glued with sandpaper to grab particles, while the vertical inside and outside annular walls were finished as smoothly as possible to minimize resistance to particle slipping. The tested materials included spherical beads made of polystyrene and glass, and crushed walnut shells in angular shapes. Hanes and Inman (1985a; 1985b) modified the device to be able to retain water in the sample space. The particles tested in this modified version included spherical glass beads with diameters ranging from 0.1 cm to 0.2 cm, and natural well-rounded quartz sand with a mean diameter of 0.055 cm.

Several important conclusions were made from the dry and the saturated annular shear testing. First, observations of the normal and shear stresses generally agreed with the particle inertia domination model in Bagnold's experiments. At lower particle concentration (higher than the particle concentration of fluid viscosity domination group in Bagnold's tests) or low shearing rate, the normal and shear stresses were proportional to dU/dy. At higher particle concentrations or at high shearing rates, the stresses were proportional to the shearing rate raised to a power less than two. Second, the smooth-sidewall design allowed particles to slip relatively well along the boundary but also contributed to particle circulation inside the sample space, which was described as secondary particle movement. In order to monitor this secondary particle movement, a small amount of colored particles was placed on the bottom corner of sample space during sample preparation. Figure 3-6 shows the horizontal and vertical cross-sections of the sample space after the shearing test. The colored particles indicated that the particles had outward and circumferential velocity components accompanied by upward motions. This secondary particle movement also formed a gap at the inside corner near the top surface, especially for those tests with lower particle concentrations. Third, when all the tests were conducted with the low initial normal stress, the ratio of particle size to device size was observed to be a variable that influenced the thickness of the locked shearing zone. This effect caused the actual shearing to take place only in a portion of the sample space. In order to eliminate the forming of locked shearing zone, the minimum ratio of the sample depth to the particle diameter was required to be 10 (Savage and Sayed, 1984) or 5 to 15 (Hanes and Inman, 1985b). Last, the normal and shear stresses in the saturated tests were lower than in the dry tests. Hanes and Inman (1985a; 1985b) suspected that the difference was produced by damping effects from the fluid viscosity.

In the analytical approaches to particulate flow, following Bagnold's efforts, Savage group made revisions on the evaluation of the particle collision mechanism. In Bagnold's particle inertia domination model, the chance of particle collisions was initiated by sliding between well-ordered particle layers. The particle diameter, inter-particle space, and shearing rate controlled the frequency of collision. To improve the model to represent random particle movement within particulate flows, Savage and Jeffrey (1981) assigned Maxwellian distribution functions to particle spatial location, particle velocity distribution, and particle-paired spatial distribution to estimate particle velocities. In this step of formulation, the particle collision was restricted to single-collisions of particle pairs, which considered no multi-collision among particles at one time. Another important factor in Bagnold's model was the momentum transfer involved in particle collisions, which only considered kinetic energy (particle velocity). Jenkins and Savage (1983) deliberated the term of particle collision with balance of mass, linear momentum and fluctuation kinetic energy, internal stress conditions of particle, energy flux, and energy dissipation. This schematic approach represented a valuable improvement over the development of Bagnold's model. A further improvement was proposed by Hanes and Inman (1985b) to include the effects of particle spinning, particle surficial friction, and multiple particle collisions.

3.2.3 Behavior of Particulate Matrix

Section 3.2.1.1 discussed the particle fabric of soils from the geologic viewpoint. Various geologic factors can cause inhomogeneous properties in particle size, particle surface texture, and particle packing. Each of those inhomogeneities can lead to variations in stress conditions and contribute to failure at different stress levels. In the current evaluation of particulate matrix behavior, specific interests are on particle packing, stress conditions on particle collisions, and the development of failure of the particulate level.

3.2.3.1 Particle Assembling

For liquefiable soils, the most common parameters used to characterize the manner in which the particles are arranged are void ratio and relative density. In the particle packing of natural soil, smaller size particles can fit in voids among larger particles during the initial deposition or other agitation sources. When the soil matrix is composed of particles with many different sizes, the voids created by larger particles can be filled with smaller particles. As a result, the soil may have high density and a low void ratio. A soil matrix with poorly (uniformly) graded particle sizes, on the other hand, is more likely to have low density and a high void ratio.

To illustrate the significance of particle packing, Figure 3-7 shows five ideal packings with single-sized spherical particles. The properties of five packings are listed in Table 3-1. In this table, the contact point refers to the number of contacts for each particle to surrounding particles. The number of contact points increase when void ratio decreases, which indicates that space occupied by particles increases as well. The importance of the contact point number is that each contact contributes resistance to deformation under loading conditions. This resistance can be related to Bagnold's model of particle inertia domination that states the stress conditions are created from particle collisions.

When real soils are deposited, the particle packing is diverse due to various particle sizes, shapes, particle-surface textures, orientations, and environmental factors such as deposition history. Oda and Iwashita (1999) indicated the following factors that describe the features of particle assembly. First, the orientation of non-spherical particles is important. During shearing of a particle assembly, the spatial variation of particle shapes and particle orientations may have a strong influence on the failure mechanism. Oda and Koishikawa (1977) showed that the deposition process tends to produce soil structure with long axes lying horizontally. The inherent anisotropy affects particle movement during the shearing process, as demonstrated by sliding in the weak zone. Second, the local void ratio is an important factor of failure development. By measuring the overall external dimensions of the experimental specimen, the void ratio value only represents the global, or average, distribution of the void space within the particle matrix. The localized void structure can affect the process of pore water pressure migration and the stress redistribution during failure. Third, the fabric of particle matrix and subsequent contact between particles affects the development of stress conditions. In naturally-developed soil deposits, the randomness of the assembling process produces far more complicated schemes than the ideal packings shown in Figure 3-7. To simulate micro-mechanical response, techniques that track particle movement and the inherent contacts between particles must be used. Finally, stress conditions can create particle aggregations in the matrix. Oda and Kazama (1998) observed the development of column-like structures in cylindrical specimens during compressive shearing tests. The column-like structures led failure to be concentrated in a localized shear band. To summarize, Maeda et al., (1995) suggested that the nature of the particle assembly affects particle matrix behavior in terms of dilatancy, anisotropy, stiffness, strength, and compressibility.

Researches (Dobry and Ng, 1992; Ng and Lin, 1993; Ng, 1994; Lin and Ng, 1997; Ng, 1999) used spherical and elliptical particles to create numerical simulations in two- and three-dimensional arrays. Simulations were able to establish micro-scale structure development, stress development, and spatial variation of particle orientation.

3.2.3.2 Strength Development of Geotechnical Material

In Bagnold's studies, the sources of strength in the particle-fluid matrix were considered to result from inter-particle collisions and fluid viscosity. The degree to which strength is influenced by particle collisions or fluid viscosity depends on the relative space occupied by the particles and fluids. In geotechnical materials, particles such as rocks, sands, silts, and clays control mechanical behavior. Water, the interstitial fluid, has an effect on the development of effective stresses and can also provide seepage forces. To gain more insight into strength development of geotechnical materials, this section concentrates on the interactions among particles.

The shear resistance of particulate materials is usually expressed in terms of the friction angle, ϕ. Taylor (1948) interpreted the shear resistance of soils as rolling friction, sliding friction, and shear resistance against interlocked particles. Terzaghi et al. (1996) also characterized the friction angle as resulting from inter-particle sliding friction and geometrical interference. Inter-particle sliding friction can be described as the contact shear resistance caused by particle surface roughness. Geometrical interference is contributed by stress dilatancy (particle climbing) and rearrangement (particle pushing). The stress components of geometrical interference are contributed from the contact normal stress and the contact rotational momentum. When the particle matrix is under static conditions, contact normal stress and shear stress establish the static force equilibrium mobilized by a small amount of strain. After static equilibrium has been destroyed, plastic flow occurs in the matrix in concentrated shear bands or zones with large amounts of localized shear strain. In the case of non-spherical particles, the load increment tends to rearrange particles that are located along the localized shearing zones with particle long axes parallel to the local sliding direction. At that moment, most of the shear strength is contributed by contact shear friction and somewhat by contact normal stress. Tamura and Yamada (1996) used a two-dimensional rigid-plastic analysis to show that particle rearrangement dominated the small strain response until localized shear zones appeared in the large strain period with continuously sliding along localized bands.

To summarize the stress components on the micro-scale level, the inter-particle stresses can be classified into three groups, termed the contact normal stress, the contact shear stress, and the contact rotational momentum (Figure 3-8a). Figure 3-8b shows the comparison among three contact interactions with the strain indicator versus the stress indicator. The contribution of each of the stiffness of the soil is ranked from high to low as the contact normal stress, the contact shear stress, and the contact rotational momentum. When two particles collide into each other, Hertz's theory (Hertz, 1896) indicates the initial small contact area develops very high contact normal stress. Any successive incremental load increases the contact area and reduces the contact normal stress. A higher load increment is required to achieve the same amount of deformation increment as the previous load increment does. Therefore, the load-deformation response is non-linear. From the stress-strain response, the deformation may reach the limit of material elasticity and initiate plastic deformation. While the contact normal force is initiated between two particles, the tangential force produces the contact shear force at contact surface. Slipping may occur when the contact shear stress exceeds the maximum shear resistance between two particles. Mindlin's theory (Mindlin, 1949) indicates that this is a non-elastic process with unrecoverable energy loss. The maximum shear resistance on contact depends on the roughness of the surface texture and on particle angularity. After slipping occurs between particles, the movement causes rearrangement among particle assembly. The contact rotation indicates the capability of particles to rearrange their positions. Santamarina et al. (2001) suggested the term "frustration" (the force that prevents the particle to rearrange itself) that may occur among rolling particles and reduce the capability of rotation. The occurrence of frustration depends on the numbers of contact points. For a densely filled particle matrix, a large number of contact points between particles increases the occurrence of frustration.

Particulate flows under rapid plastic shearing usually show stress fluctuations. Shearer and Schaeffer (1997a; 1997b) used a simple discrete model with frictional spring-sliders to simulate particles in sustained rapid shearing. Their results showed that stress fluctuation dramatically increased when the distance between frictional sliders decreased. In the three-dimensional particle space, materials with higher density show larger magnitude stress fluctuations because of the higher frequency of inter-particle collisions. Other factors, such as shearing rate, particle size, and particle angularity, can also affect the amount of stress fluctuations. Under high shearing rates, particles quickly adjust their positions and increase the chance of random collisions. For particles of larger size, the locally instant dilation (climbing among localized particles) causes sudden increase and decrease of stress magnitude. Particle angularity increases the chance of interlocking among particles. To break the interlocking requires more energy consumption from the applied shear force. Between the periods of breaking and reestablishing interlocked geometry, the process of rearrangement can play an important role in the stress fluctuations.

3.2.3.3 Stress Dilatancy

Stress dilatancy occurs within the particle packing when particles rearrange themselves by climbing over others. To explain the geometry rearrangement, Santamarina et al. (2001) postulated frictionless spherical particles packing in a cubic-tetrahedral matrix to demonstrate the stress dilatancy. In Figure 3-9a, the tangential force, T, in the three-particle assembly requires a displacement to mobilize the upper particle to overcome the lower particles by subjecting them to the normal force, N. The required tangential force is $N \times \tan\alpha$, even with no inter-particle friction. For this geometry $\alpha = 30°$, therefore, the angle of dilation is 30° for this specific case. In the plane-strain case, Figure 3-9b demonstrates the possible movement near the shear surface. When the particles are in irregular shapes, the local angle of dilation changes with particle packing geometry, particle size, and particle shape. The overall angle of dilation results from the contributions of local dilation and particle rearrangement (sliding and rotation) sequence as well.

Rowe (1962) explained the stress dilatancy of the particle matrix based on a pure frictional mechanism. He used various regular particle-packing assemblies, such as two-dimensional cubic-tetrahedral, three-dimensional pyramidal, and three-dimensional tetrahedral, to estimate the tendency for stress dilatancy. Rowe concluded that the stress ratio at peak strength and subsequent deformation followed the equation

$$\sigma'_1 / \sigma'_3 = \tan\alpha \times \tan(\Phi_\mu + \beta) \tag{3.3}$$

where σ'_1 is the effective major principal stress, σ'_3 is the effective minor principal stress, α is particle geometrical interlocking angle in the minor principal stress direction, β is the particle geometrical interlocking angle in the effective major principal stress direction, and Φ_μ is the particle surficial friction angle. In laboratory observations, Rowe estimated dilation testing random packings of irregular cohesionless particles, such as steel balls, glass ballotini, and sands, in triaxial compression. He suggested that the angle of dilation should lie in the range of

$$\Phi_{\mu} \leq \Phi'_{dl} \leq \Phi'_{cv} \tag{3.4}$$

where Φ'_{dl} is the dilation angle, and Φ'_{cv} is the friction angle at constant volume shearing after the peak strength, which implies the steady state of deformation. Further research (Li et al., 1999; Wan and Guo, 1999; Li and Dafalias, 2000) suggested that the stress dilatancy was also affected by density, effective confining stress, and stress path.

Rowe (1962) derived an energy consumption ratio, E, in terms of the effective major principal stress to the effective minor principal stress as

$$E = \frac{\tan(\Phi_{\mu} + \beta)}{\tan\beta} = \frac{\sigma'_1}{\sigma'_3(1 + {d\varepsilon_v}/{d\varepsilon_1})} \tag{3.5}$$

where $d\varepsilon_v$ and $d\varepsilon_l$ are the rates of volumetric strain and effective major principal strain, respectively. This equation assumed that sliding took place in the direction of minor principal stress, β. When the equation is applied to the random particle packings, Rowe used the minimum of the energy ratio, $dE/d\beta = 0$, to conclude that when $\beta = (45° - \Phi_{\mu}/2)$, the energy ratio can be expressed as

$$\frac{\sigma'_1}{\sigma'_3(1 + {d\varepsilon_v}/{d\varepsilon_1})} = \tan^2(45° + {\Phi_{\mu}}/{2}). \tag{3.6}$$

Oda and Iwashita (1999) simplified this expression to the form of

$$\tau = \sigma \tan(\Phi_\mu + \nu) \tag{3.7}$$

in direct shear test, where σ is the normal stress, τ is the shear stress, and ν is the dilatancy coefficient (rate of dilatancy associated with shear deformation).

3.2.3.4 Void Redistribution and Development of Shear Zones

Despite the boundary conditions of laboratory testing devices, homogeneously deposited specimens usually show uniform deformation within the entire specimen in the early stage loading. After the specimens reach the peak stresses, however, localized shear zones may start to develop. This tends to lead to further shearing concentration within the localized area. The subsequent loading after peak stresses causes a non-uniform distribution of void ratio within the test specimen. When the stress condition reaches the state of plastic flow, shearing only takes place in localized shear zones. The void ratio in the localized shear zones is usually higher than other places within specimen as a result of the local stress dilatancy. During laboratory testing for soil liquefaction evaluation, void ratio has been shown to be one of the major factors that affects residual strength. However, by measuring the overall void ratio, evaluations may be misled by the localized liquefaction within a small portion of specimen. The importance of understanding void ratio redistribution and localization of shear zones allows geotechnical engineers to gain more insight into failure development, and to understand the mechanism of localized shearing failure observed in liquefaction-related failures and laboratory testing.

The stress-strain relation of the particle matrix can be described in terms of strain-hardening and strain-softening behavior. Before the stress-strain curve reaches its peak condition, shear stress is resulted from inter-particle contacts with relative displacement among particles. When one region in the matrix approaches its peak stress condition, the rate of deformation in this region tends to decrease until the surrounding region reaches a similar stress condition (Santamarina et al, 2001). In other words, the strain-hardening behavior tends to support the development of a homogenous stress condition. When parts of the particle matrix passes their peak shear stress with further straining, however, strain-softening behavior transfers part of stresses to neighboring area and produces progressive failure (Santamarina et al, 2001). Once localized, highly-deformed zones are created, the action of seeking resistance to stresses propagates and enlarges the localized failure area. Expansion of localized failure zones stops when the stresses distribute to the region that stress-dilatancy cannot be further mobilized. During the period of progressive failure due to strain-softening behavior, shear deformation is concentrated in localized failure zones.

Recent technology allows researchers to examine particle movement on a micro scale. Based on observations made by X-ray on specimens from two-dimensional compression testing, Oda et al. (2001) summarized the behavior of particles under monotonic loading condition in two stages. In the first stage, the void ratio values are uniformly distributed throughout the entire specimen. With increased loading, the contact forces transmitted from particle-to-particle establish the major principal stresses within the specimen. Figure 3-10a shows the particles that have high contact stresses with black dots. With increased loading, column-like aggregations begin to develop because of the strengthening in the major principal stress direction and loosening in the minor principal stress direction. In monotonic triaxial testing, Frost and Jang (2000) specified that, because of the restraints at the top and bottom of triaxial specimen, void ratio starts to increase at the center of specimen, and then this tendency migrates toward the top and bottom ends. When the amount of particle contact is reduced in the minor principal stress direction that establishes the concentrated straining zones, the locally-concentrated high void ratio values induce highly anisotropic stress conditions. Before reaching the peak stress condition, the anisotropy induces further stress dilatancy by increasing the area of shear zones and by displacing particles toward the slip direction. In the second stage, when stresses reach peak values, the column-like structures start to collapse (buckling) and initiate plastic flow concentrated in the localized shear zones.

Figure 3-10b shows the particles with high contact stresses have established the column-like structures before collapsing. Large concentrations of voids can be seen along the shear zone I and II. Wong (2000) conducted a series of monotonic triaxial tests on Athadasaca oil sand to observe the void ratio variation inside the specimen. Figure 3-11a shows an enlarged section of the undisturbed specimen before testing. Particles shown in gray are uniformly distributed throughout the specimen. Figure 3-11b shows a shear zone with large voids, which are caused by the local stress dilatancy in dark color. To demonstrate the variation of void distribution within samples, Oda and Kazama (1998) conducted testing on void ratio change on localized shear zones and observed some surprising results. With an initial sample void ratio of 0.63 for Toyoura sand, the measured void ratio values at shear zones ranged from 1.01 to 1.13, which were higher than the maximum void ratio of 0.973.

The particle movement surrounding shear zones is mainly dominated by local anisotropy (Oda and Iwashita, 1999). When the particle assembly has been established, non-spherical particles are oriented with their long axes perpendicular to gravity, which is the cause of initial anisotropy. When the loading produces localized shear zones, anisotropy is further induced when non-spherical particles rotate and adjust their long axes parallel to the slip direction within shear zones (Oda and Kazama, 1998). The result of this particle adjustment affects shearing conditions in two ways. First, the amount of stress dilatancy is decreased because the particle rearrangement reaches the steady state and produces plastic flow near shear zones. The frictional resistance at this moment mainly depends on the particle surficial frictional resistance. Second, even after the plastic flows near shear zones have been terminated, the anisotropy cannot be recovered because of permanent particle rearrangement. When the same particle matrix is subjected to the subsequent monotonic or dynamic loading, the initiation of failure will still be concentrated in the previously established shear zones (Oda et al., 2001).

Through the establishment of column-like structures, the lost contacts in the minor principal stress direction causes voids within shear zones to grow. Before the column-like structures are destroyed by buckling, stress dilatancy is the main factor that causes localized shear zones to grow in the major principal stress direction. Researchers have reported different values of the width of localized shear zones (Roscoe, 1970; Mandl et al., 1977; Oda et al., 1982; Scarpelli and Wood, 1982; Műhlhaus and Vardoulakis, 1987; Bardet and Proubet, 1991; Oda and Kazama, 1998; Wong, 2000). For example, the shear zones that developed in the Toyoura sands have average width of 7 to 8 times the mean particle size (D_{50}) (Oda and Kazama, 1998; Oda and Iwashita, 1999). Factors that affect the growth of localized shear zones are suspected to include the history of deposition, bonding history, particle size, particle angularity, and particle surface texture.

By using the Laser-Aided Tomography (LAT) method (Konagai et al., 1992; Konagai and Tamura, 1992; Ortiz et al., 1992; Konagai and Rangelow, 1994), the dynamic response of the particle matrix has been observed at the micro-scale level. In this test, the particle matrix is composed of crushed optical glass submerged in a liquidwith the same refraction index as the crushed glass, so that the glass particles are invisible when immersed. Observations were aided by shooting intense laser-light sheets (LLS) through the particle matrix. Because the particle surface had been oxidized so the refraction index was slightly different from the intact glass. As a result, particles surfaces become visible in the plane of the LLS (Figure 3-12a). To visualize the particle behavior of a rock-filled dam under dynamic loading, an embankment model was conducted under dynamic excitation on the shaking table with LAT. The embankment model was built with screened particles sized between 2 mm and 5 mm. Sinusoidal base excitation was then applied to the submerged slope. The surface of the model started to slide when the amplitude of base excitation exceeded a certain threshold value (Figure 3-12b). Observations showed that with increasing amplitude and frequency, the depth of sliding surface increased with growing localized slipping zones. Particles outsides the slipping zones were relatively intact with a small amount of movement. The particle movement that was measured from particles above the slipping zones showed an increment of deformation in the vertical direction, which indicates that stress dilatancy has occurred when the particles are slipping under dynamic excitations.

3.2.3.5 Particle Crushing

Particle contact forces (in the normal or shear directions) may significantly increase when particles are subjected to large stress dilatancy or high confining stresses. When forces exceed the elastic limit of the particle itself, the plastic deformation or even particle crushing may occur. For example, soils within large earth-filled dam may show particle crushing because of the high stress condition. Consequently, particle crushing may affect the permeability of soils in earth-filled dam. The purposes of soil particle gradation in the earth-filled dam is designed for retaining particle migration and providing adequate seepage flows. In time, the seepage flow can be affected as well, resulting high pore water pressures accumulating inside dam.

The physical meaning of particle crushing is the breakage of particles that produce smaller particles that increase the chance of particle contact points. An example of change in grain size distribution due to particle crushing is shown in Figure 3-13. The figure shows that, with various initial confining stresses, the amount of particle crushing increases with increased confining stress. The grain size distribution shifts toward the region of well-graded grain size distribution after the compression test. Lade et al. (1996) indicated that, with similar initial confining stresses, a drained test produced more particle crushing than an undrained test. To shear particles under drained conditions, contraction or dilation tends to increase particle contact stresses without inducing excess pore water pressure change. Under undrained conditions, however, contractive behavior produces positive excess pore water pressures that decrease the particle contact stresses.

Stress dilatancy is usually related to the geometry of the particles in the soil matrix. With larger particles, stress dilatancy increases with following increment of shear strength. Owing to particle crushing with increasing stresses, the average particle size decreases, resulting in a condition of decreasing stress dilatancy. However, Lee and Seed (1967) observed that the shear strength increased even with decreasing stress dilatancy under high stresses. They indicated the increased strength was caused by particle crushing that produced more particle contacts.

Several techniques have been used to quantify the amount of particle breakage. The most common technique is based on the grain size distribution (Lee and Farhoomand, 1967; Marsal, 1967; Hardin, 1985; Lade et al., 1996). In order to compare the difference between the initial and the final grain size distributions, a specific grain size or a range of grain size is selected. Another key factor that can indicate the degree of crushing is the difference of particle surface area before and after particle crushing (Miura and O-Hara, 1979; Ueng and Chen, 2000). A more advanced method is based on the energy consumption during testing (Miura and O-Hara, 1979; Lade et al., 1996; Ueng and Chen, 2000). In mechanical behavior, the total energy consumption is divided into components associated with elastic work and plastic work. By changing the volumetric strain and the axial strain, the energy is contributed by the plastic work in breaking particles.

3.2.4 Summary of Particulate Flows

Particulate flows are composed of small individual particles, which interact with each other and with the interstitial fluids. For soil liquefaction evaluation, the mechanical behavior of sand particles mixed with water is major concerns. Particle interaction effects can be illustrated with a simple composition, such as one particle motion and two-particle interaction. A multi-particle mechanism was introduced in the experimental and analytical approach by the Bagnold and Savage groups. Their work provided a good fundamental knowledge of inter-particle, interstitial fluid, and particle-fluid interactions. Further reviews of mechanical behaviors on particle packings introduce inter-particle stresses (normal, shear, and rotation), void redistribution and occurrence of localized shear zones, stress dilatancy, and particle crushing. The review provides knowledge of particle behavior at the micro-scale level for further understanding of the macro-scale phenomena, such as debris flows and flow slides.

3.3 DEBRIS FLOW

The phenomenon of debris flow involves a process in which large volumes of water and poorly sorted earth materials surge downslope in channels or on flat surfaces with extremely high velocities. The strong agitation of water among particles creates high pore water pressures; hence, the behavior of debris flow can be seen as an extreme occurrence of soil liquefaction. The earth materials involved in debris flows can be fractured rocks, boulders, sands, silts, and clays. The destructive force, of a debris flow, resulting from the large flow volume of heavy material moving of high speed, can even carry tree trunks, cars, and houses. Takahashi (1981) classified several types of subaerial massive sediment movement and indicated the typical travel speed of debris flows as ranging from 0.5 to 20 m/sec. Some debris flow velocities have been reported as high as 30 m/sec (Major and Pierson, 1992). Iverson (1997) reported the flow volume may exceed 10^9 m^3 and release more than 10^{16} Joule of potential energy. The kinetic energy, which is the function of velocity and mass, carried by flow can not only destroy every object along the path, but also affect large areas before the debris flow reaches its final resting position. Debris flows have also been described as mudflows, mudslides, earth flows, mud spreads, mudspates, debris torrents, hyperconcentrated flows, and lahars (Iverson, 1997; Johnson, 1965; Johnson and Rodine, 1984).

Middleton and Hampton (1976) distinguished between debris flows and the particulate flows based on their mechanical properties of generating stresses. Among particulate flows with various particle sizes, stresses are generated from particle collisions that are mainly dominated by large particles. For debris flows, on the other hand, the turbulence among the interstitial water provides important influence on strength to interact with suspended particles. Particles with smaller size, such as clays, silts, and sands, can also alter the interaction behavior between solid particles and water, such as increasing the viscosity of particle-water mixture to produce an influence on overall stress behavior.

This section begins with an introduction to the morphologic features of debris flows. The flow deposit is presented in longitudinal and cross sections. The second part introduces the occurrence of debris flows, including the process of initiation, flow in motion, and process of deposition. The third part is an observation of experimental debris-flow flumes made by United States Geological Survey (USGS) investigators. Successful observations have been made on initiation, flow, and deposition. The last part is to summarize the terms used to define the material strength of a moving debris flow.

3.3.1 Debris Flow Morphology

When a debris flow has been initiated, the water within the soil must be sufficient to provide continuous mobility to transport materials in flow (Takahashi, 1978; Takahashi, 1981; Iverson et al., 1997). The mixture of water and earth materials usually flows within relatively confined channels in the beginning, and then is deposited on a flat surface (Johnson, 1965; Johnson, 1970). Figure 3-14 shows an aerial photography of debris-flow deposits in the Death Valley National Monument, California. Debris flow was transported inside the narrow channel (on the top of figure) and deposited on the flat alluvial fan. The confined space of the channel leads to a large flow thickness with high kinetic momentum that allows flow to travel a great distance. Throughout the transportation process, materials are deposited along the flow path. At the same time, erosion caused by dragging force along the flow bed and sidewalls can also scour in-situ soil to increase the volume of the flow mixture (Iverson, 1997). When the debris flow reaches a flat surface, the mixture tends to spread out, slow down, and decrease in thickness. At this stage, fewer materials are dragged into the flow, while more material is deposited on the flow bed. The dry outer perimeter is usually deposited in the form of a dam-like structure to retain materials when debris flows reach the resting position (Johnson and Rodine, 1984). Figure 3-15 shows a picture of the outer edge of the debris-flow deposit, occurred in Panamint Valley, California. The thickness of this deposit was about 1 m.

The action of inverse grading within a debris flow suspends large particles near the surface and front of the flow, while finer particles flow close to the flow bed and distal end (Takahashi, 1980). The effect of erosion and deposition produces a sub-transporting motion that allows particles to be recirculated within the mixture (Hutter, 1999). Figure 3-16 shows particle recirculation appears in two regions. The front nose area, or snout, usually contains large particles because of their high downslope velocities. Recirculation in this area is caused by the collisions among particles within the flow mixture. The water content at this frontal region is usually low, or the material may be even dry (Johnson, 1965; Johnson, 1970; Takahashi, 1991). The main body of the debris flow is composed of finer material behind the frontal nose area. The water content in the main body is usually high and reaches a state of liquefaction (Takahashi, 1991; Iverson, 1997). However, stresses from particle collisions and fluid turbulence are usually extremely erratic. Continuous recirculation among this region is a crucial factor in maintaining a fully-developed flow motion involving the steady exchanging of particles between flow deposition and boundary scour.

Figure 3-17a shows a longitudinal section and a cross section of a debris flow in motion. The longitudinal section of debris flow is comprised of a large wave with several superimposed small waves. Usually smaller waves travel in higher velocities than the speed of the debris flow itself due to the recirculation of the soil-water mixture within the flow. In channeled flow, the agitated mixture moves laterally and creates lateral depositions along boundaries. The lateral depositions are composed by the materials that snout first delivers; they are then overridden by succeeding materials in the body of flow (Johnson, 1965; Johnson, 1970). The amount of lateral deposition can be huge, especially at curves in a channeled flow because of the tangential movement of the mixture (Figure 3-17b). After the waves reach a flatter surface near the bottom of the channel, the decreasing volume of the mixture reduces the kinetic momentum, which then reduces the erosive force along the flow bed. Comparing to the larger particles found in side and frontal deposits, medial depositions in the flow bed are mainly composed of finer materials carried by the distal end of the flow. When the frontal surges carry large particles, the recirculation of finer particles among flow main body lose the ability to erode more particles from the bed and side walls. Instead, the reduced kinetic energy leads to separation of the large and small particles. The consequence is the smaller particles settle along the path after the passing of larger particles.

Johnson and Rodine (1984) provided field methods to estimate properties of debris-flow materials based on observations of residual deposits within flow channels and alluvial fans deposited on flat surface at the base of the flow. Those observations include the thickness of residual deposits, the largest boulders and blocks the flow could carry, and the angle of tilt of the debris flow as it passes a curved channel (β, indicated in Figure 3-17b). Debris properties that can be estimated by this approach include material density, shear strength, cohesion, friction angle, viscosity, and flow rate.

3.3.2 Occurrence of Debris Flow

Slope instability caused by the 1999 Chi-Chi earthquake, which struck central Taiwan with 7.2 magnitude, produced tremendous debris-flow hazards during the following rainy season. From a geological point of view, Taiwan is dominated by the Central Mountains which run from north to south. The major rivers of Taiwan run radially toward the ocean from the mountains. The river channels in the mountains are usually steep and short, which can produce water flowing through with high velocity in a short time. After the strong seismic motions, large-scale landslides produced unstable slopes with loose soils and no and removed the vegetation that normally provides surface protection from rainfall. During the rainy seasons following the earthquake, heavy rainfall created strong surface erosion and carried earth materials with water. Many debris flows were observed within hours following heavy rainfall. This delayed effect could be caused by the surface infiltration or the rising ground water table that softened the surficial soils. In the rainy season of 2001, two years after the Chi-Chi earthquake, debris flows with high intensity and covering large areas struck Taiwan during and after several typhoons. The flows wiped out roadways, railroads, buildings, and several villages. After the flows stopped, the large volumes of mud and objects that had carried created environmental problems in residential areas and also public facilities. The debris flows caused great property damage and human life loss in Taiwan.

Observations of debris flow occurrence bring out several aspects that need to be discussed in depth. The following discussions concentrate on the mechanism of debris flow initiation, flow in motion, and deposition process.

3.3.2.1 Initiation of Debris Flow

The initiation of a debris flow can come from many sources: landslides triggered by liquefaction and surface water runoff, collapsed dams, excess surface water runoff, and ground water table fluctuation inside a slope (Takahashi, 1978; Takahashi, 1981; Takahashi, 1991). The common factor of those causes is the interaction among earth material with a relatively large supply of water. Water plays an important role in the initiation of a debris flow, including weakening the soil through increased pore water pressures due to ground water table fluctuation and surface water infiltration, and through seepage forces. Sources of water supply that can initiate debris flows are rains, snow-melt water, and other excess water supplies (Iverson, 1997). In some cases, evidence from field observations shows that hydraulic conditions can be strongly affected by water trapped in fractures and macro-porous substrate (Iverson et al, 1997).

The variation of slope inclination also has a great influence on debris flows triggered by water. Slope angles of debris flow range from 25° to 45° (Iverson et al, 1997). When water accumulates on a gentle slope, slope remains stable under static conditions because the stresses associated with the weight of the soil and water does not exceed the shear strength of the soil. However, accumulation of water and earth materials on a gentle surface can result in flows with a sufficient high velocity to apply large shear stresses to the underlying ground surface. The kinetic momentum of the moving mixture increases the surface dragging force and hence increases the applied shear stresses on surface layer. The underlying surface layer can then be scoured away with the debris flow when the applied shear stress exceeds soil strength to a certain depth. At this point, debris flows are initiated because excess surface water runoff on gentle slope. In the cases of steep slopes, the initially high shear stress condition in soils creates high anisotropic stresses. Slope can be fragile from surface water runoff and pore water fluctuation. The mechanism of surface runoff on a steep slope is similar to that on a gentle slope. The pore water fluctuation due to water table fluctuation and surface infiltration may decrease the effective stresses and weaken the soil matrix, which then triggers debris flows because the high anisotropy of the steep slope. In the case of a gentle slope, because of the low anisotropic stress condition, the pore water pressure fluctuation followed by the effective stress reduction may not be able to trigger debris flows (Takahashi, 1978; Takahashi, 1981; Iverson et al., 1997).

Soil liquefaction can occur under undrained conditions when loose soils suffer a reduction in strength under monotonic loading. For dense soils, monotonic loading causes the soil to dilate, leading to increased strength. However, observations have shown that under extensional monotonic loading, even densely-filled slopes can exhibit contractive behavior and then mobilize debris flows (Iverson and LaHusen, 1993). Under dynamic conditions, some debris flows have originated from relatively dense slopes. Iverson et al. (1997) summarized the dynamic causes that triggered debris flows under densely-filled slope. Dynamic conditions allow growth of fluctuations in particle stress and fluid stress; therefore, random particle velocities increase with stress fluctuations. This behavior is particularly important for large particles (e.g. fractured rocks) that tumble down from steep slopes (Plafker and Ericksen, 1978). Another cause is the dynamic excitation that alters the stress from the pre-failure static conditions. Pore water pressure fluctuations, accompanied by the anisotropic stresses, propagate on discrete failure surfaces and change effective stresses. This pore water pressure migration leads to the potential for soil liquefaction with initiation of debris flows (Iverson and LaHusen, 1989).

Takahashi (1978; 1991) illustrated the stress distribution in sediments due to surface water runoff. Figure 3-18 shows infinite slopes with loose granular materials in a uniformly-filled surface layer, in which Cases (a), (b), and (c) have little cohesional resistance and Cases (d), (e), and (f) have significant cohesion. Surface water with thickness, h_0, flows parallel to the slope. The pore water pressure is under the hydrostatic condition that produces no seepage force. In Figure 3-18, τ_s and τ_L represent the applied shear stress and the soil resistance, respectively; a_L indicates the depth of failure when τ_s exceeds τ_L.

In Cases (a), (b), and (c) that has little cohesional resistance in surface layer, once the material is scoured by the flow, the scoured materials will be totally mixed with flow mixture without retaining their original shapes. In Case (a), τ_s is higher than τ_L within the entire surface layer, but not the stiff stratum. After the debris flow is initiated, the entire surface layer will be carried away and mix with the debris flow. Compared with Case (a), surface layer in Case (c) has higher τ_L than τ_s below depth a_L. The force carried by debris flow can only scour the materials above depth a_L and mix them into flow. However, when τ_s increases, the scouring depth a_L increases until the entire surface layer is removed. Under this circumstance, with the increasing intensity of water runoff or the growing of flow body, τ_s may eventually exceed τ_L in the stiff stratum. Case (b) shows the situation that debris flow scours the entire surface layer and also part of the stiff stratum.

When the surface layer has relatively significant cohesional resistance, Cases (d), (e), and (f), the mixing process shows different pattern compared to the process of Cases (a), (b), and (c). In Case (d), the cohesional resistance maintains the material above depth a_L in relatively intact condition, while the materials below depth a_L are sheared because τ_s is higher than τ_L. In the early development of debris flow, the materials above a_L may be suspended above flow and as surface blocks. Further water supply and kinetic momentum may destroy these suspended blocks and mix them into debris flows. Cases

(e) and (f) illustrate the cases with strong cohesional resistance in the surface layer. When the debris flow produces a sufficient τ_s, the action of scouring may extend to the stiff stratum, as illustrated in Case (e). In Case (f), on the contrary, the entire surface layer and the stiff stratum remain stable because τ_s is less than τ_L.

Another important factor in the initiation of debris flow is water infiltration followed by water table fluctuation. Iverson (2000) developed theoretical models to predict variations in debris flows initiated from landslides. These variations included topographic, geological and hydraulic variables, and changes in land use. He utilized parameters such as hydraulic diffusivity, rainfall intensity, and rainfall duration to evaluate the response with time when an infinite slope is subjected to potential failure. He assessed the influence of rainfall on near-surface ground water pressures in slopes based on a rectangular Cartesian coordinate system (Figure 3-19a). The inflow to a specific location was controlled by surface topography to produce an existing flow path in the region. In Figure 3-19b, two points labeled as coordinates of (x, y) have different inflow areas, labeled by A with shaded zones. The calculation scheme involved time-marching evaluations of the temporal and spatial distribution of pore water pressure considering infiltration and the consequential reduction of factor of safety within the slope. Figure 3-19c shows results of an example event based on this process. The prediction reveals that during the intense rainfall on the pre-wetted soils, debris flows can be triggered from the increase of excess pore water pressures from the surface layer. In this scenario, the infiltration is provided by an intense rainfall that lasts about 10 minutes. During the infiltration period, Figure 3-19c indicates that the failure propagates rapidly toward the underlying soils. At the end of rainfall (t = 10 minutes), the factor of safety drops below one for those soils above the depth of 0.4 m. After rainfall stops, factor of safety increases to more than one in the shallow depth. The soils in deeper depth, however, still shows low factor of safety because of the remaining water infiltration.

3.3.2.2 Debris Flow in Motion

After the driving stresses exceed the shear resistance of soils, totally or partially saturated soils can start to dilate (as observed in Konagai's experiments) within limited and localized sheared zones (as observed in Oda's experiments). With continuous saturation from surface infiltration or ground water table fluctuation, the driving forces that have been amplified by kinetic momentum change the failure mode from localized shearing to widespread, distributed deformation. Consequently, the downslope movement transforms the soil-water mixture into a debris flow (Iverson 1997; Iverson et al, 1997). Takahashi (1991) characterized the mixing process in two categories. The first category refers to densely-packed earth materials that initially move downslope as intact blocks. The water content of the blocks themselves is not sufficient to fill the increased voids. An extra water supply is required to fully loosen the blocks and produce a fluidized mixture. Examples for this category can be landslide blocks, collapsed dams, and unstable gully beds. The second category includes loosely-filled earth materials that collapse and transform directly to debris flows. In this case, the water content of the earth materials is high enough to fill the increased void volume during motion.

Driven by the body mass, the momentum to maintain the volume of flow depends on the velocity fluctuation within the flowing material. The term granular temperature, T, is used to characterize the fluctuation of particle velocities about their mean velocities (Campbell, 1990; Iverson, 1997; Iverson et al, 1997):

$$T=\left\langle \left(\vec{v}-v_x\right)^2 \right\rangle \tag{3.8}$$

where $\vec{v}$ is the instantaneous velocity of a particle, v_x is its average downslope velocity; and $\langle\ \rangle$ denotes the ensemble average of all particles. Within mobilized flows, granular temperature measures the level of agitation of particles due to fluid turbulence. The importance of granular temperature can be demonstrated in several phenomena (Iverson, 1997; Iverson et al., 1997). First, widespread slips outside the mobilized mixture have behaviors that are strongly affected by granular temperature. With high granular temperature within a flow, interaction between the flow and its boundaries may remove sufficient boundary material to increase the size of the flow. Second, granular temperature also indicates the level of bulk mixture density and the ability of particles to avoid interlocking and to move past one another. The highly-agitated particles that are suspended by the non-equilibrium fluid pressures further enhance the mobility of the fully-developed debris flows. The fluidity of debris flows generally increases with increasing granular temperature and decreasing mixture concentration. As a result, the tendency for particle interlocking is reduced because of the widespread mixing action within the flow. Overall, a fully-developed debris flow has a high intensity of granular temperature.

While the flow mixture is fully developed, interaction among fluids and particles may produce particle segregation. The dynamic sieving effect is often as producing particle segregation in the dry material under dynamic excitation. When the composition of materials includes various sizes of particles, smaller particles are easy to fit in the voids among the larger particles under dynamic excitation. The excitation causes larger particles move upward while the smaller particles move downward, providing a phenomenon termed as a reversed gradient. Takahashi (1991) described the formation of a reversed gradient in a steady debris flow with inter-particle action and fluid-particle interaction. The submerged body weight produces a downward force on an individual particle. Inter-particle collisions were described in terms of layers of particles sliding over each other. During steady-state movement, the particle was subjected to collision forces from both the layer above and the layer below. At the same time, the movement of particles produced a drag force within the surrounding fluids. Combining those factors, the equation of motion showed that the upward movement of particles with relatively large diameters was more likely than adjacent smaller diameter particles.

3.3.2.3 Deposition of Debris Flow

Particle settling and erosion both occur during the movement of a debris flow. When their rates are equal, the flow slide maintains a constant volume. When the kinetic momentum decreases, however, the amount of material deposited on the flow bed or the side walls exceeds the amount of material that is removed by erosion and carried into the flow. The flow starts to lose kinetic momentum when the granular temperature of coarse material drops at the snout and margins (Iverson, 1997). At those locations, coarse materials form levees at the outer rims that impede the wet finer materials from forming a dam. With some residual kinetic momentum in the finer interior materials, the dry outer deposits can still be overridden and then recirculated into flow. When the flow arrives at its final resting position, the inner materials may still have high pore water pressures. A consolidation process then occurs as the water pressure from inner materials dissipates toward the outer boundaries. The mechanical behavior of the flow is then transformed from a fluid-like material to a solid-like material.

3.3.3 Observations from Experimental Debris-Flow Flumes

USGS built the experimental flume model in order to study the behaviors of debris flow (Iverson et al., 1992; Iverson, 1997; Iverson et al., 1997; Reid et al., 1997). Because of a lack of observations of natural debris flows, the USGS experiments provided important information for understanding and analyzing the occurrence of debris flows. As shown in Figure 3-20, three experiment flumes (Experiments I, II, and III) were assembled with the similar materials and dimensions. The homogeneous and isotropic slopes were made by placing sand and fine gravel inside the retaining wall by using a front-end loader and hand shovels. The procedure was considered to have produced no obvious layering or large voids within the soil. All the soils were retained behind 0.65 m high wall and in the 2 m wide, 95 m long channel. Instrumental clusters were placed at deep (*d*), intermediate (*i*), and shallow (*s*) positions. Each cluster contained a tensiometer tip, a time-domain reflectrometry (TDR) probe, and dynamic pore-pressure sensors. Besides these clusters, an extra tensiometers (w) was arranged to monitor the change of pressure head near the retaining wall. The surface displacement was monitored by the extensometer ($E1$ and $E2$).

The objective of the experiment was to monitor flow failures triggered by different hydrologic conditions. Experiment I was injected water from water injection channel to form a phreatic surface among slope. A stable phreatic surface (20 to 30 cm beneath the surface) was established by adjusting the inflow and the draining outflow rates. The water content within the saturated soils was measured at 40%. The hydrologic condition of Experiment II was created by sprinkling water on the top of the slope at a moderate rate of 50 mm/hr. Before failure occurred, a wedge of wet soil was produced in front of the retaining wall. The water content was measured at about 40% in this region. The soil density was reported to be denser in Experiment II, compared to Experiments I and III. Experiment III used high-intensity sprinkling on the slope surface. Initially, the intensity of sprinkling was adjusted to 100 mm/hr in order to saturate the soil. The water infiltration produced a water content of 35% after about an hour. However, a steady phreatic surface was not reached before failure occurred. After 10 minutes of no water supply from sprinkling water, failure was triggered intentionally by increasing the sprinkling intensity to 200 mm/hr. Figure 3-20 shows the approximate location of phreatic surface in the slope for Experiments I and II.

Figure 3-21 shows surface displacement and pore water pressure developing immediately before the debris flow was triggered. In Experiment I, a stable phreatic surface was maintained by the inflow water supply embedded under the slope. The upward flow of water initially raised the pore water pressure around the water injection channel. When the rupture suddenly occurred, the pore water pressure spontaneously increased at the shallow, intermediate, and deep measurement points. This reflected a widespread failure triggered suddenly by liquefaction of the soils. Compared to the sudden rupture observed in Experiment I, the moderate-sprinkling rate of Experiment II initially produced a shallow sliding layer, as shown in Figure 3-20. About a second after the development of initial shallow failure, the slope rupture retrogressed in the upslope direction and induced large area of block-by-block failure. However, the failed mass did not retrogress to the bottom of the slope. The instrumental measurement showed that the increase in pore water pressure mostly appeared in the midslope region. In Experiment III, the failure was induced by soil liquefaction with strain-softening behavior. The failure was initiated by the weight of water and soil that produced a high driving stress along the interface between the soil and the flume bed. Contraction of the soil due to initial sliding was suspected to cause the rising of pore water pressure. A deep sliding surface was then induced along the flume bed toward the end of flume channel, indicating a large amount of soil involved in the sliding area. In this experiment, the failure mechanism was contributed by the initial excess driving stress followed by strain-induced liquefaction.

This series of debris-flow flume experiments revealed the importance of hydrologic conditions on the triggering of debris flow failure. In Experiment I, the failure was initially induced by the upward inflow from the water injection channel. This represented the debris-flow failure induced by the seepage force from the phreatic surface. In Experiment III, even though a stable phreatic surface was never established, a large rupture was triggered by the body weight with following soil liquefaction. This experiment corresponds to debris flows induced by surface water infiltration, such as after the heavy rainfall. A common observation from those two experiments was the change of the pore water pressure. In Experiments I and III, the sudden rupture of soil in the flume was accompanied by a sudden, spontaneous increase in pore water pressure. Soil liquefaction was observed as the triggering failure mechanism. Furthermore, even though zero pore pressure was recorded in the shallow depth prior to failure, those sensors reported a tremendous increase of measurements during flow failure. This evidence shows the pore water was able to migrate into those regions that are previously non-liquefied. In Experiment II, the moderate sprinkling was not able to establish strong seepage force or to increase the body weight by sufficient surface water infiltration. Only a shallow failure was triggered with locally increased pore water pressure. This type of debris flow can be found from soil loosening at a shallow depth because of the water runoff on slope.

3.3.4 Shear Resistance of Debris-Flow Materials

Experimental and analytical results have shown several important factors that characterize the stress conditions of debris-flow materials. In order to mobilize the flow, the driving stress has to exceed the yield strength. Following the initiation of flow, the shear strength of the flow mixture results from contributions from particle collisional resistance and fluid viscosity. Major and Pierson (1992) compiled experimental data and showed that the general power law model (Van Wazer et al., 1963) well represented the relation between the shear stress and the shearing rate. The model was formulated in the form of

$$\tau = \Psi + m\dot{\gamma}^n \tag{3.9}$$

where τ is the shear strength, Ψ is the yield strength, m and n are constants, and $\dot{\gamma}$ is the shear strain rate.

For flows with low sediment concentration, the soil behavior can be expressed as a Newtonian fluid, in which the shear strength is only the function of the shearing rate. When the sediment concentration increases, as in the case of material such as debris flows, the shear strength is also a function of the yield strength. For a non-Newtonian fluid, Equation (3.9) can be simplified to the Bingham fluid in the form of

$$\tau = \tau_y + \eta\dot{\gamma} \tag{3.10}$$

where τ_y is the yield strength, and is the viscosity of the material. Equation (3.10) expresses the shear strength of the mixture with high sediment concentration that linearly relates to the shearing rate after driving stress exceeds the yield strength.

In the field, the fluid phase of a debris flow consists of water and fine materials such as clay, silt, and sand. The fluid phase in the flow usually transports larger particles and produces high granular temperature. When Equation (3.10) describes the general movement of flow, an extra term is required to describe the turbulence created by larger particles and the dispersive forces among the fluid phase. O'Brien and Julien (1985) proposed the quadratic rheological model:

$$\tau = \tau_y + \eta\dot{\gamma} + \xi\dot{\gamma}^2 \tag{3.11}$$

where ξ is a turbulence-dispersion parameter. The value of the turbulence-dispersion parameter is related to the thickness of the flow and the sediment concentration. This model was validated by Julien and Lan (1991) with compiled experimental results.

To further elaborate on Equation (3.11), Takahashi (1993) and Takahashi et al. (1997) improvised the shear strength of the debris-flow materials in motion as

$$\tau=\tau_y+G\eta\frac{du}{dz}+K\sigma_p d^2 \left(\frac{du}{dz}\right)^2 +\sigma_d l^2 \left(\frac{du}{dz}\right)^2 \tag{3.12}$$

where G and K are the coefficients, u is the velocity at height z, σ_p is the density of particle, d is the particle diameter, σ_d is the density of flow mixture, and l is the mixing length of flow. Because the mechanical behaviors of debris flow are considered to be dominated by the particle collisions, the character of particle movement combined with the velocity component should be separated from the overall velocity profile. Equation (3.12) divides the term of turbulence and dispersion into terms of particle movement and overall flow movement.

Iverson et al. (1997) explained that the initiation of debris flow is mobilized from the widespread Coulomb failure followed by soil liquefaction. The granular temperature in flow mixture is then agitated among downslope movement. Combining with the Coulomb failure criteria, Johnson (1970) proposed the Coulomb-viscous model in the form of

$$\tau = c + \sigma_n \tan\varphi + \eta\dot{\gamma} \tag{3.13}$$

where c is the cohesional resistance; σ_n is the vertical stress of varied depth in flow; and φ is the friction angle of the granular material. In Equation (3.13), the yield strength -- Coulomb failure criteria -- is characterized by the cohesional and frictional resistance of the debris-flow material. The equation can also be used to describe the shear strength at various depths within the flow. Unlike Equation (3.13), Takahashi et al. (1997) characterized the yield strength into three terms:

$$\tau_y = c + \sigma_n \tan\varphi + \tau_B \tag{3.14}$$

where τ_B is the yield strength of the interstitial fluid. For a flow with a low sediment concentration, such as a mud flow, the fluid phase of flow may produce a relatively essential strength from turbulence and interaction with larger particles.

3.3.5 Summary of Debris Flow

From the single-particle movement to the multiple particle-interaction system, the phenomenon of debris flow demonstrates a system with random particle collision and interior materials interacting with materials on exterior boundaries. The fluid phase in debris-flow material provides the suspension and turbulence required to transport larger particles. This highly-agitated fluid pressure produces an extreme case of the soil liquefaction.

This section describes the possible mechanism of the initiation of debris flow, the transportation of debris flow materials, and the in eventual deposition. In the absence of data from the natural occurrence of debris flow, the documentation of USGS experimental debris-flow flumes provided important validations of initiation, stress distribution, and pore water pressure fluctuations.

Finally, this section summarized models for characterization of the shear strength of debris-flow material. To characterize the non-Newtonian material, Equations (3.9) to (3.14) describe shear strengths that combine the yield strength and interaction among fluid phase and particles. The yield strength is represented by the Coulomb failure criteria that explains the flow failure, from the initiation of the localized failure zone to the widespread flow movement. During the debris-flow motion, the inter-particle collision and fluid turbulence are described by the velocity profile throughout the flow combined with material properties.

3.4 SUMMARY OF FLOW FAILURE RESEARCH

Soil liquefaction-related phenomena refers to granular soils that fail because of high pore water pressures. The post-liquefaction failure often involves large deformation with the enormous concomitant hazards. The focus of this research is on flow slide failure, the failure that usually involves a large volume of soil mass displaced to the severely deformed post-failure geometry. In order to understand the failure mechanics on the micro-scale level, this chapter starts from the particle interaction among the simple particle assembly. The analytical and experimental scenarios are introduced by the studies made by the Bagnold and Savage groups. The particulate assembly is further studied in its stress development, stress dilatancy, void redistribution and shear zone development, and particle crushing.

As an extreme case of liquefaction-related phenomena, the debris-flow failure demonstrates an excellent application of particulate assembly interacting with interstitial fluid. The process of debris-flow failure is introduced through the initiation of failure, debris-flow material in motion, and deposition. The well-documented study of intentionally induced debris flow failure was reported from USGS experiments. Besides the experimental study, the analytical study evaluated the shear strength of flow material based on the strength parameters (cohesional and frictional resistance) and the shearing rate profiles (velocity and turbulence).

Overall, this chapter has provided a review of the flow behavior of liquefied soil. After the initiation of soil liquefaction, the liquefied material is usually smeared by its own weight or by the non-liquefied material above it. Within a liquefied material, the shear strength is influenced by the inter-particle collisions, the interstitial fluid viscosity, and the particle-fluid interaction. Examining soil behavior on both the micro and the macro scale provides a better concept of how to evaluate the residual strength of the liquefied material.

Type of Packing	Contact Points	Void Ratio
Simple Cubic	6	0.91
Cubic-Tetrahedral	8	0.65
Tetragonal-Sphenodial	10	0.43
Pyramidal	12	0.34
Tetrahedral	12	0.34

Table 3-1 Properties of assembly in the ideal packing by the single-sized particle (after Mitchell, 1993).

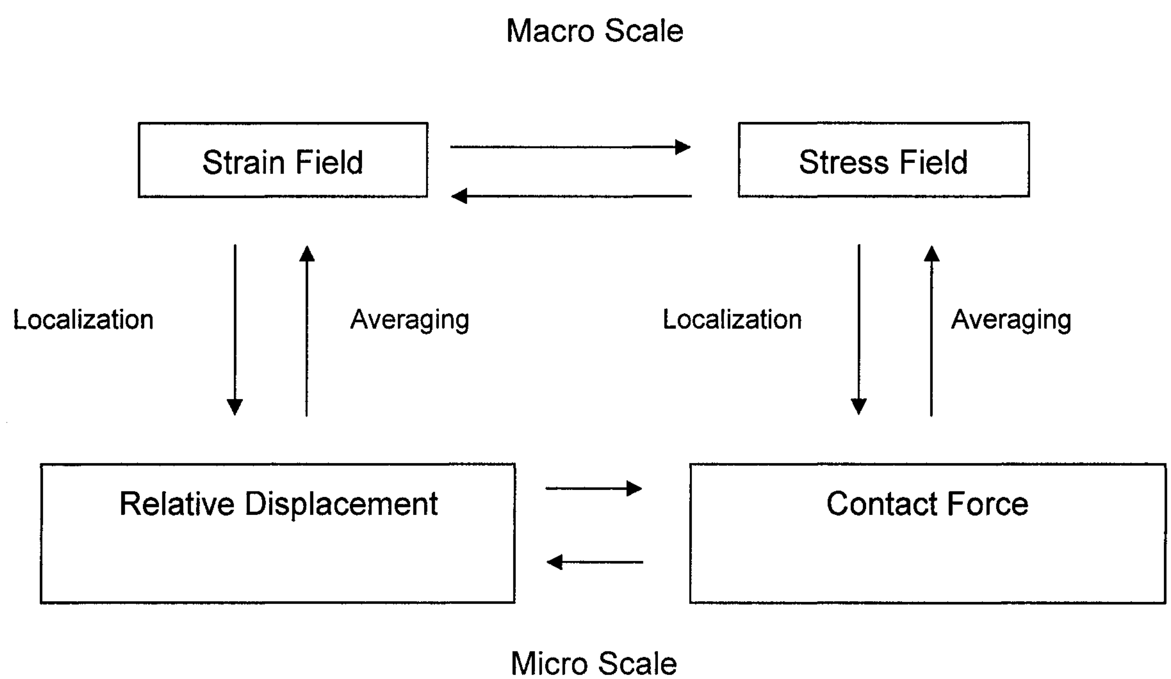

Figure 3-1 Scheme of particulate materials in the macro scale and the micro scale (after Oda and Iwashita, 1999).

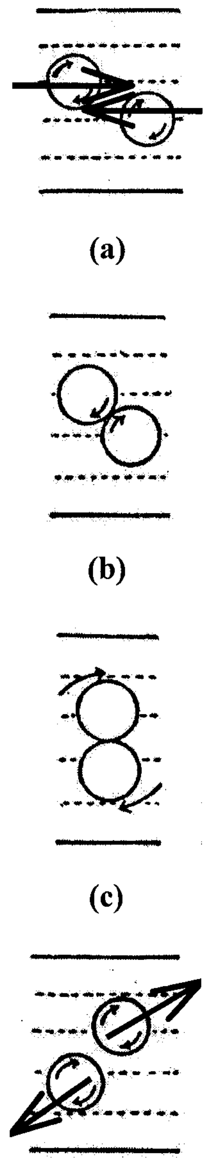

(a) (b) (c) (d)

Figure 3-2 Collision between two particles, (a) before collision, (b) initial contact, (c) two-particle movement, and (d) after collision (after Bingham, 1922).

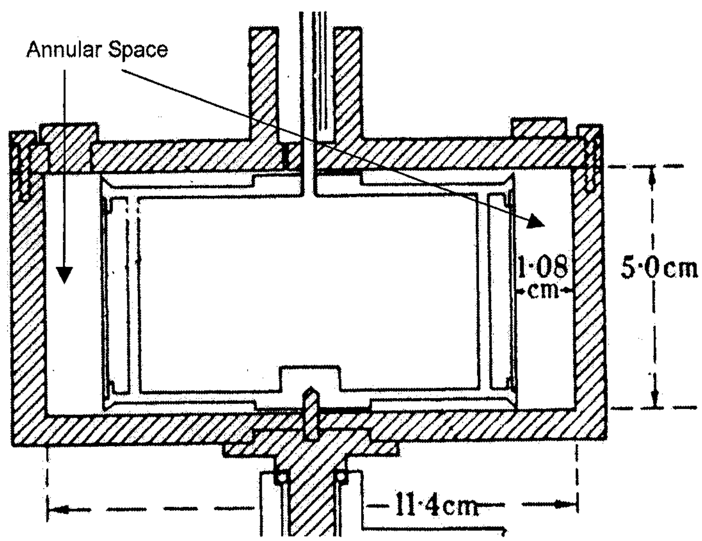

Figure 3-3 Particle-fluid mixture testing device made by Bagnold (after Bagnold, 1954).

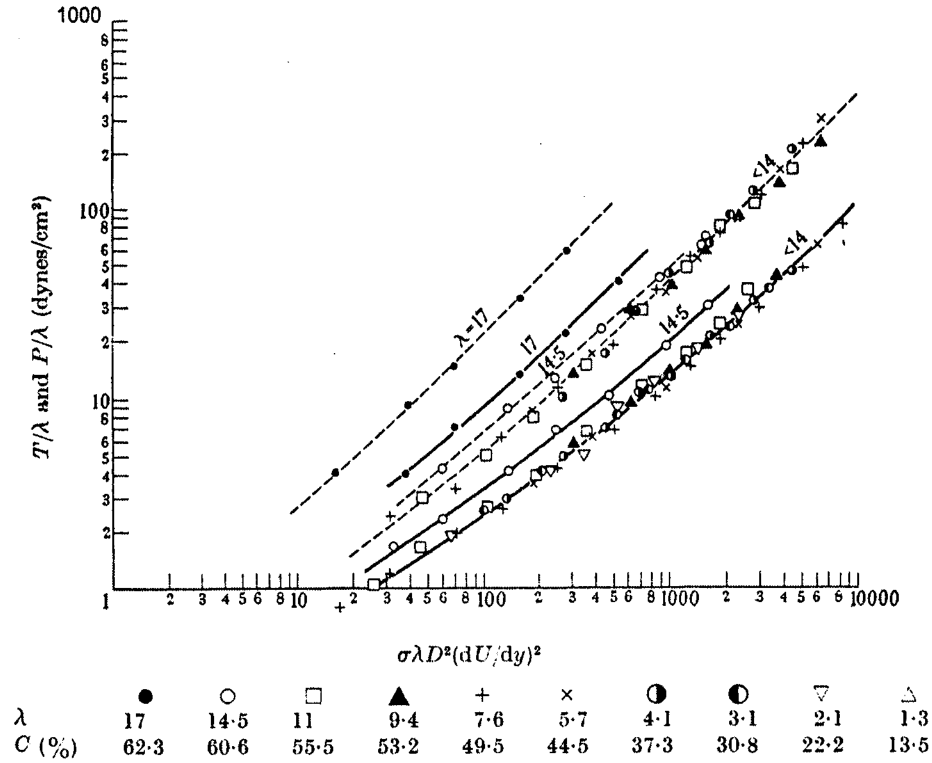

Figure 3-4 Particulate flow testing results from Bagnold (1954). Solid line indicates the bulk shear stress term and dotted line indicated the bulk normal stress term.

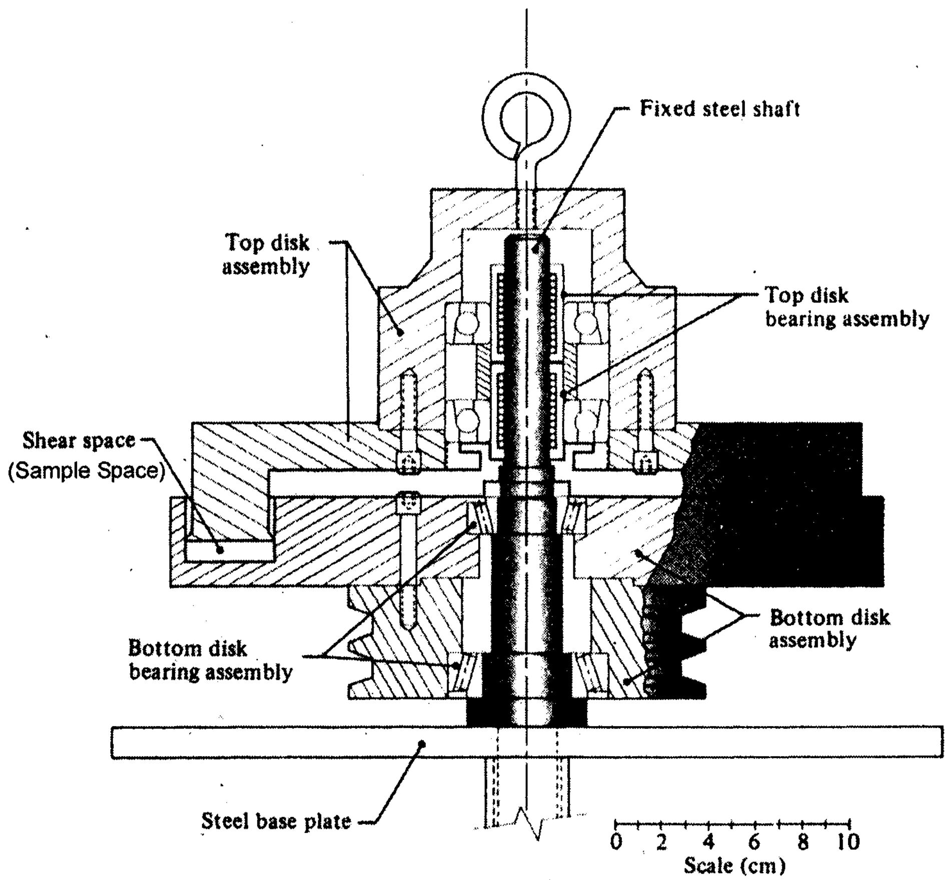

Figure 3-5 Annular shear cell made by Savage and Sayed (after Savage and Sayed, 1984)

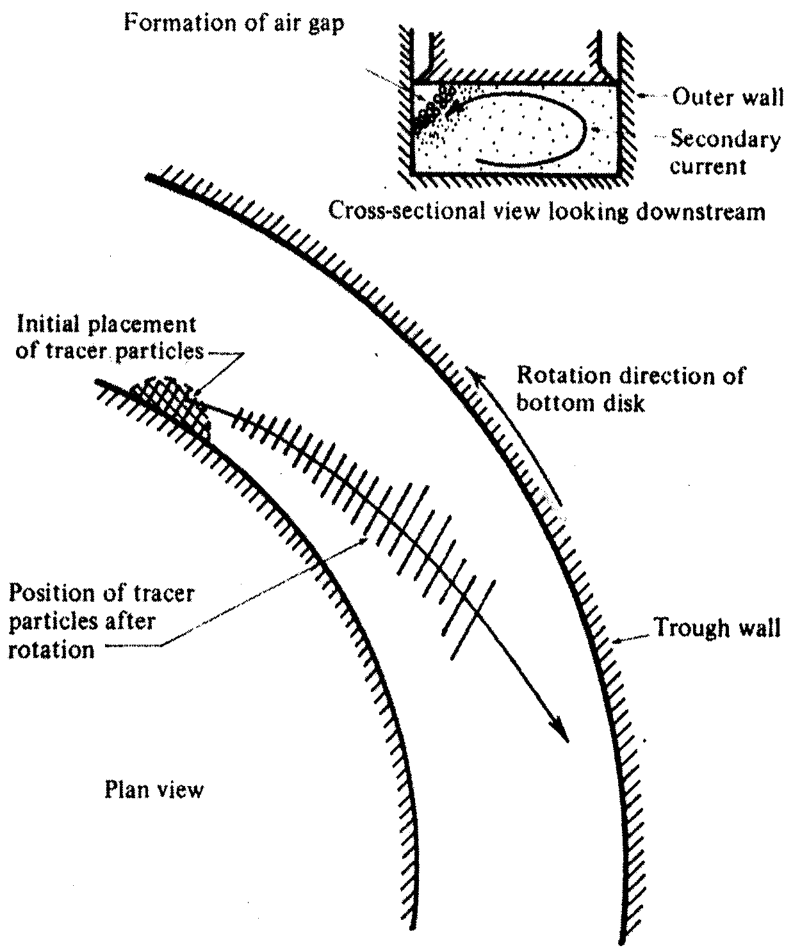

Figure 3-6 Secondary particle movement in annular shear cell (after Savage and Sayed, 1984).

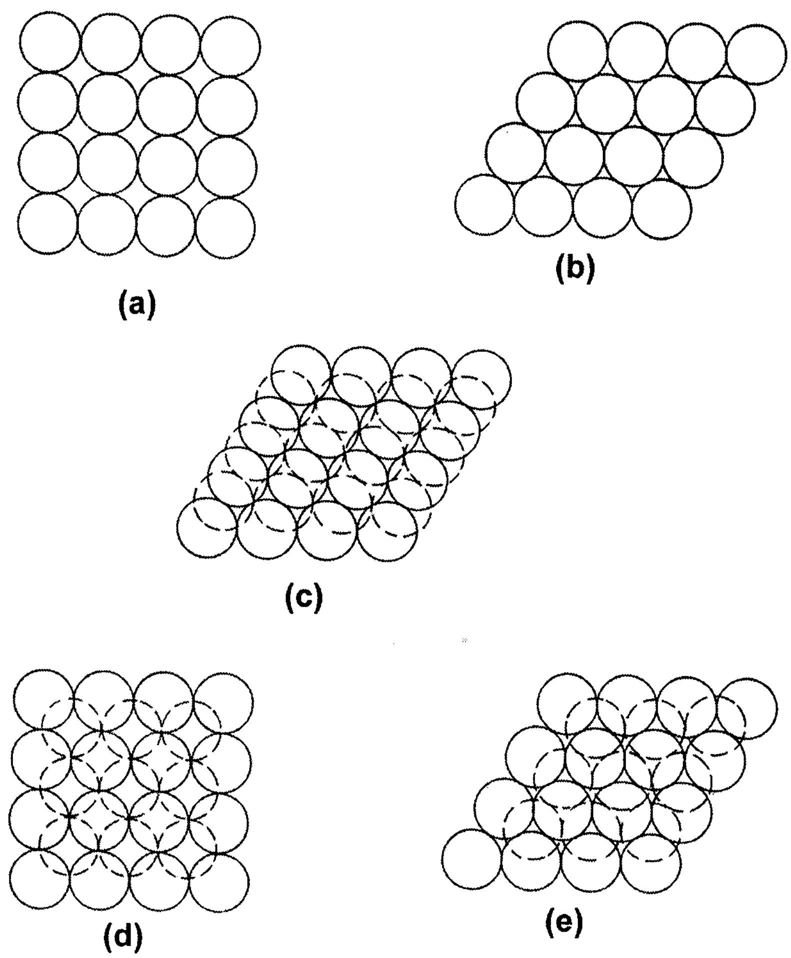

Figure 3-7 Single-sized particle assembly in ideal packing, (a) simple cubic, (b) cubic-tetrahedral, (c) tetragonal-sphenoidal, (d) pyramidal, and (e) tetrahedral (Mitchell, 1993).

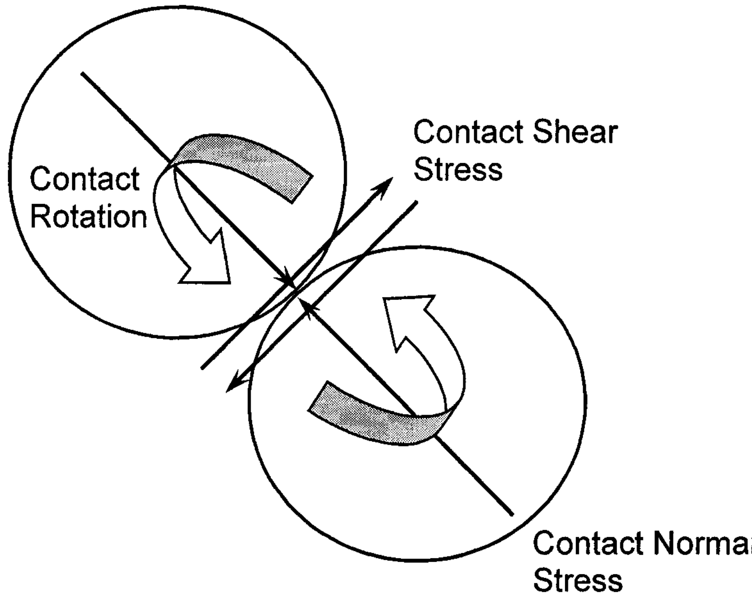

(a)

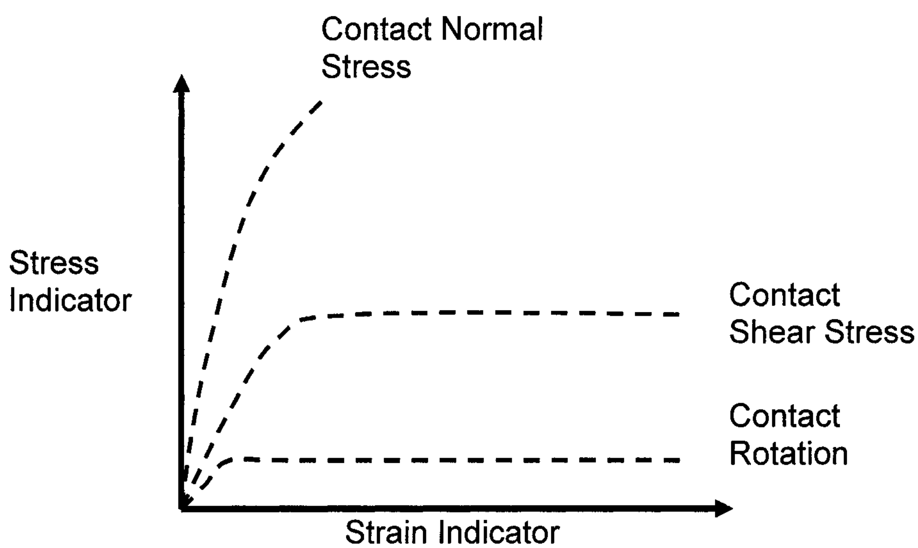

(b)

Figure 3-8 Inter-particle collision, (a) stress components and (b) relations between the stress indicator and the strain indicator.

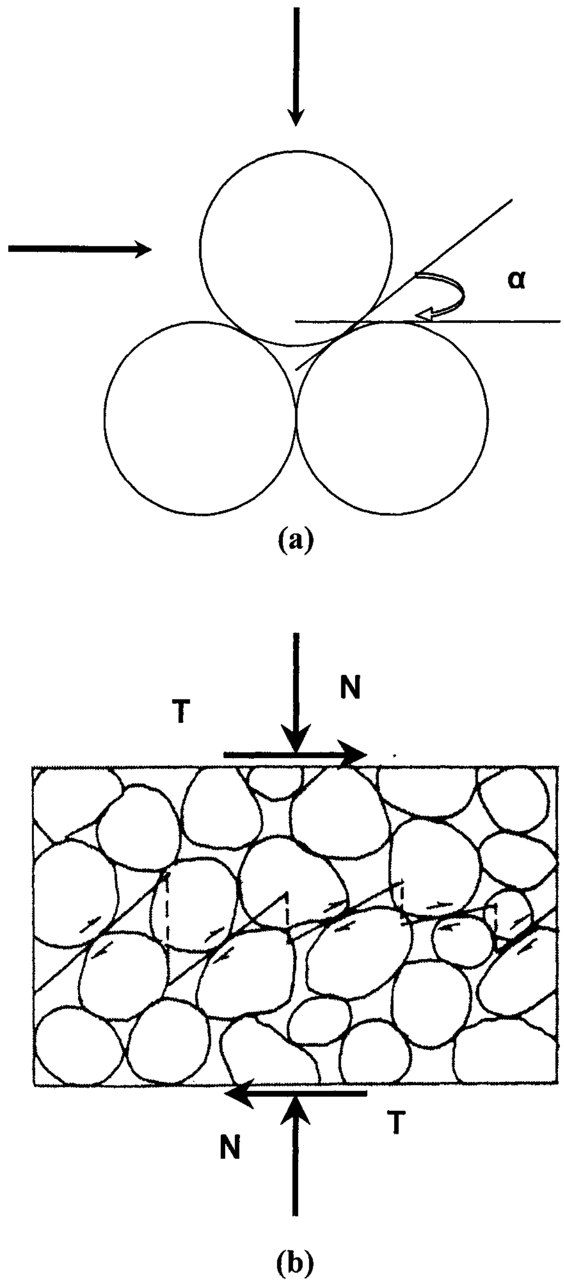

Figure 3-9 Particles dilation illustrations in (a) simple model (after Santamarina et al., 2001) and (b) simple shear test (after Oda and Iwashita, 1999).

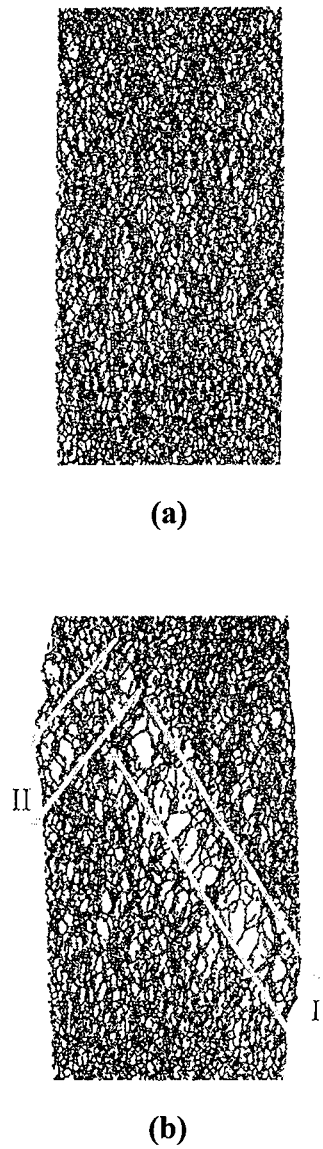

Figure 3-10 Development of column-like structure in the two-dimensional compression test, (a) before peak stress condition and (b) after peak stress condition (Iwashita and Oda, 1999).

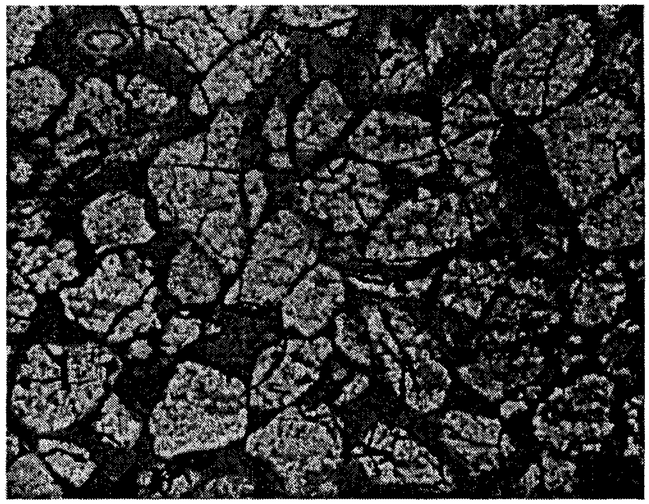

(a)

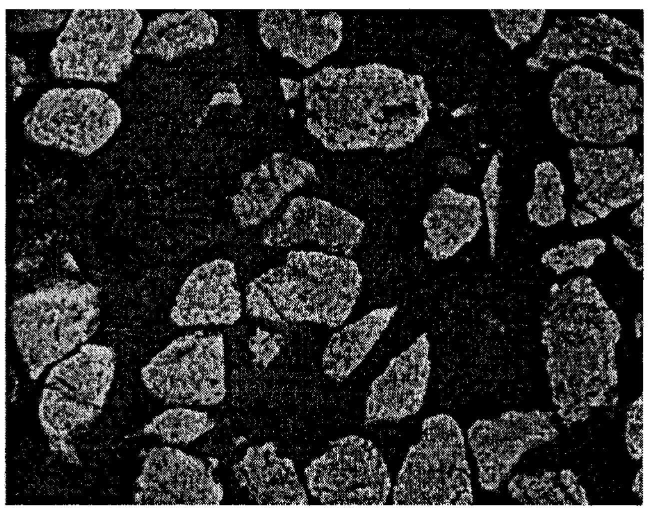

(b)

Figure 3-11 Images of sand particles (gray) and voids (black) in triaxial compression test, (a) after sample preparation and (b) inside shearing zone (Wong, 2000)

(a)

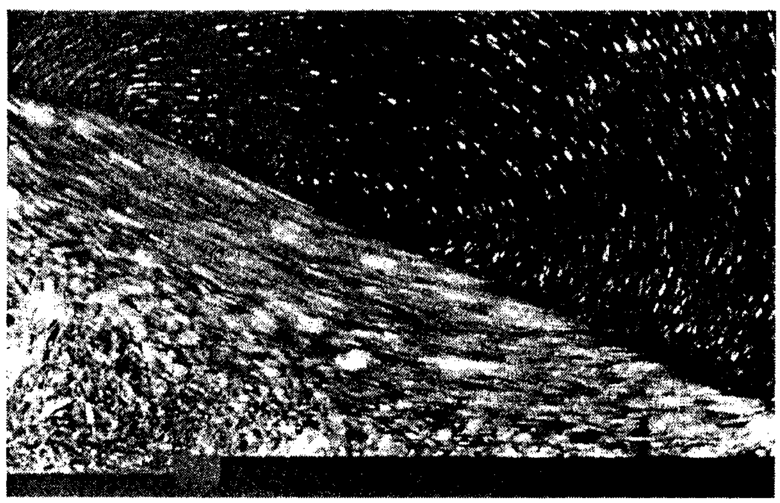

(b)

Figure 3-12 Lased-Aided Tomography for observation of particle matrix under dynamic base excitations, (a) an enlarged view of particles and (b) observation of dynamic response inside the embankment (Konagai et al., 1992).

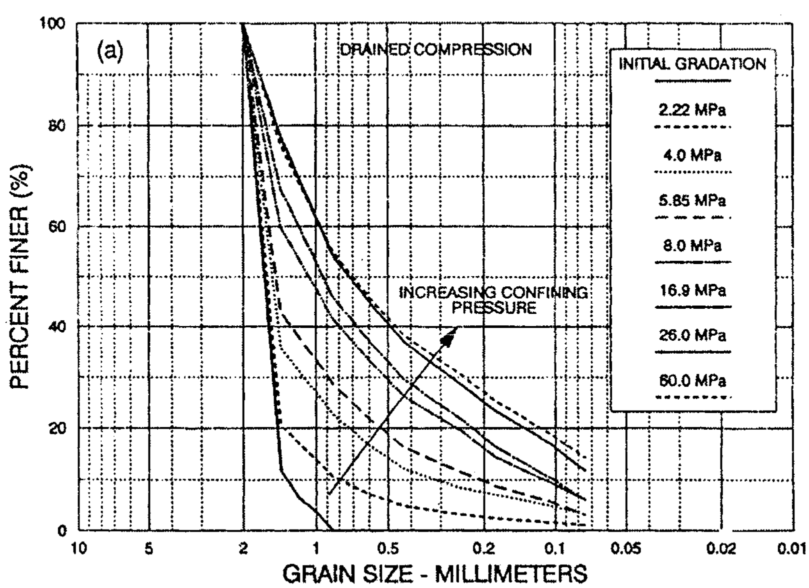

Figure 3-13 Shifting of grain size distribution due to particle crushing in drained triaxial compression test (Lade et al, 1996).

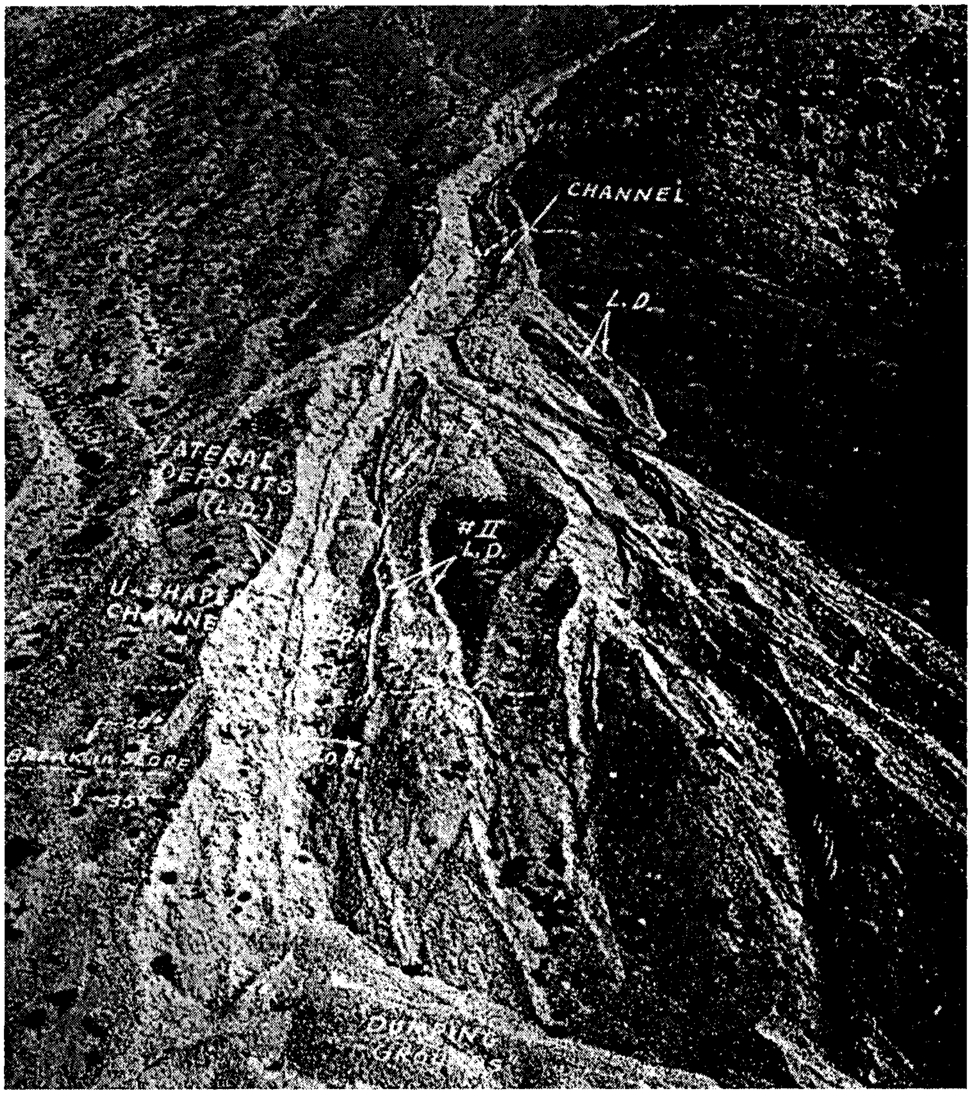

Figure 3-14 Aerial photography of debris-flow deposits near Klare Spring, Death Valley National Monument, California (Johnson, 1970).

Figure 3-15 Outer edge of debris-flow deposits in Surprise Canyon, Panamint Valley, California (Johnson and Rodine, 1984).

132

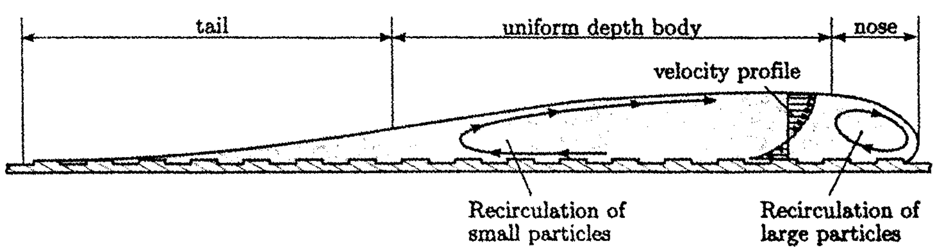

Figure 3-16 Particle recirculation in debris flow (after Hutter, 1999).

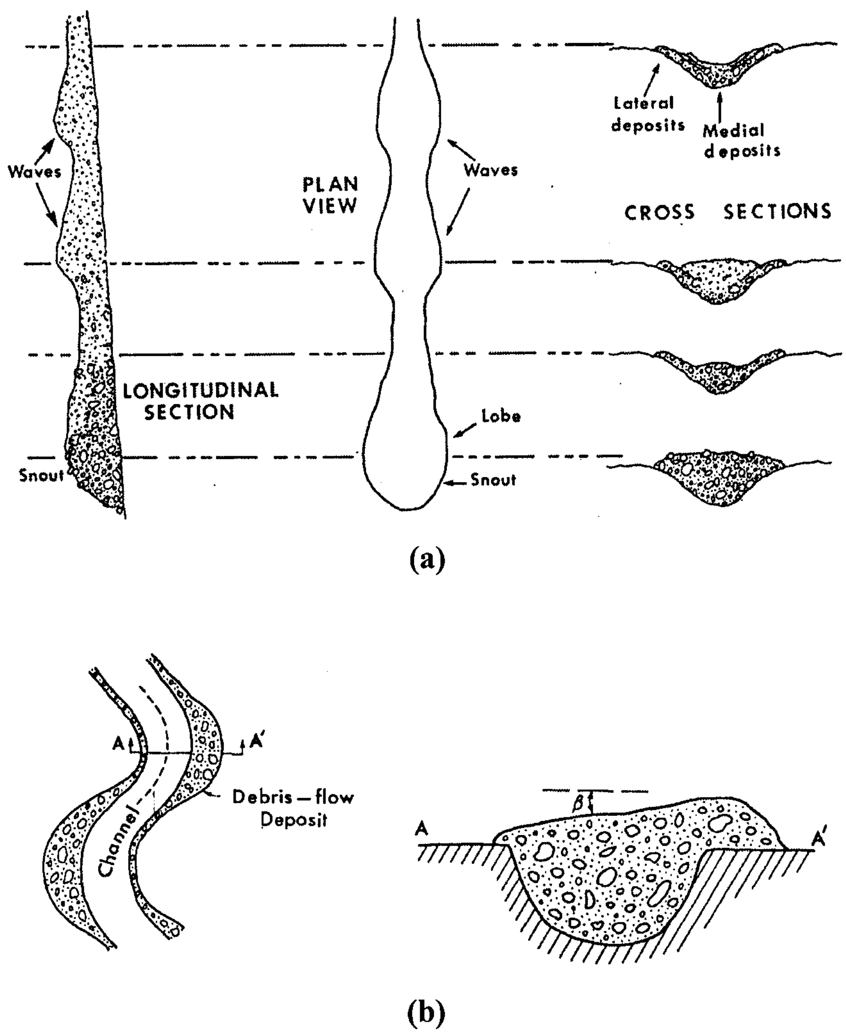

Figure 3-17 Morphology of debris flow, (a) straight channel flow and (b) curved channel flow (after Johnson and Rodine, 1984)

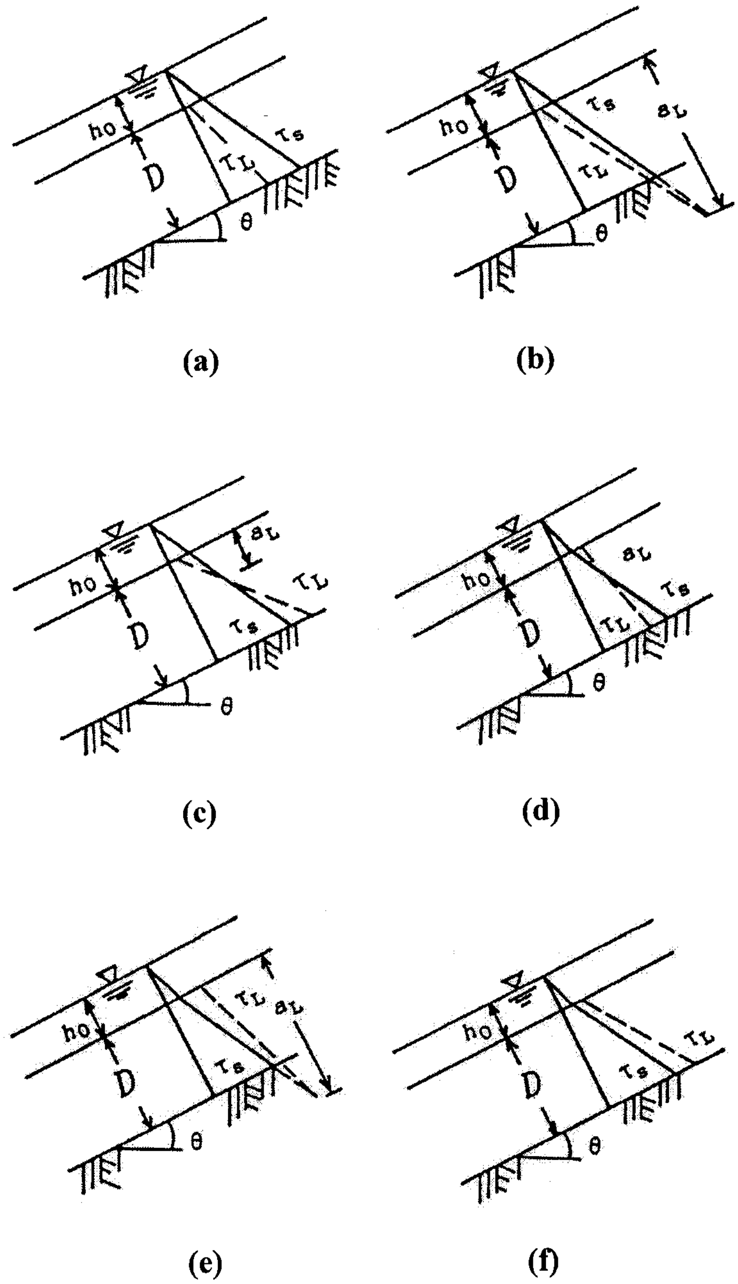

Figure 3-18 Stress distribution in sediments with surface water runoff (Takahashi, 1991).

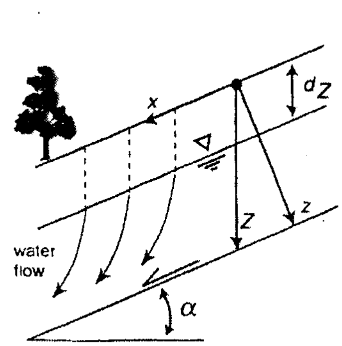

(a)

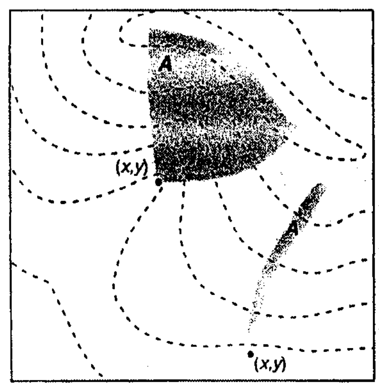

(b)

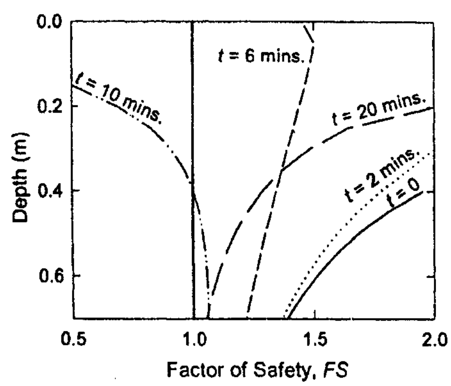

(c)

Figure 3-19 Water infiltration on slope (a) local condition, (b) surface topography, and (c) an example scenario showing evaluation of factor of safety within depth in various time frames (Iverson, 2000).

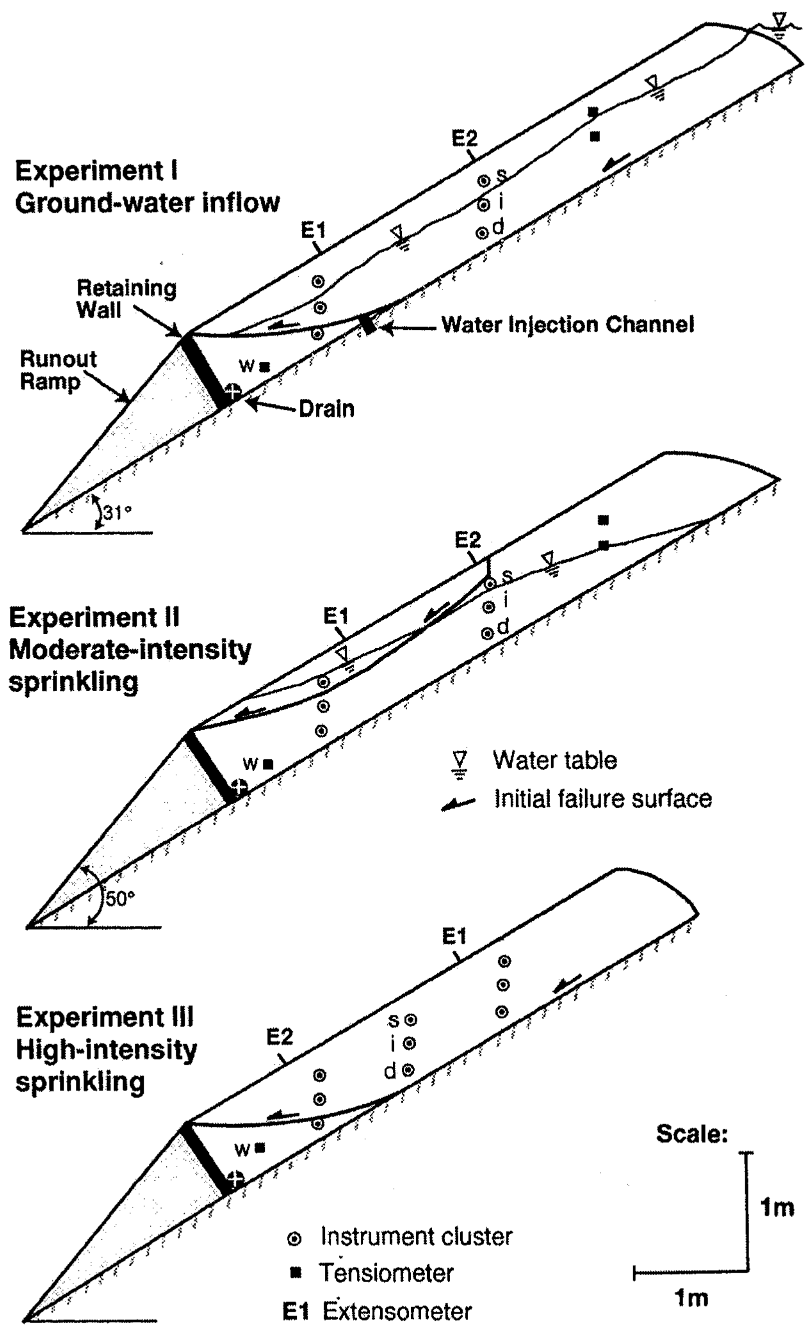

Figure 3-20 Schemes of USGS experimental debris-flow flumes (Reid et al., 1997).

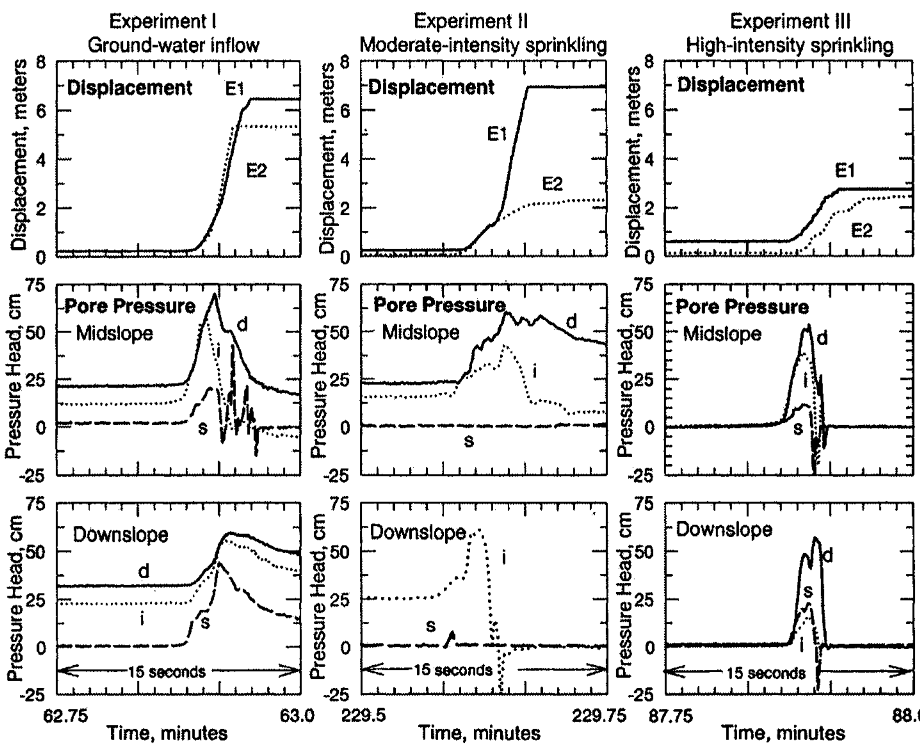

Figure 3-21 Surface displacement and pore water pressure responses during failure of USGS experimental debris-flow flumes (Reid et al., 1997).

Chapter 4

Residual Strength of Liquefied Soil

4.1 INTRODUCTION

The importance of the residual strength of liquefied soil results from the catastrophes that can occur when the strength of a soil deposit is reduced from its pre-liquefied strength to a lower post-liquefied strength. Chapter 3 reviewed the particle-fluid interactions that produce material strength in simple particle assemblies at the micro-scale level. At the macro-scale level, the complicated behavior of debris flows was also been introduced as an extreme case of soil liquefaction. Chapter 3's illustrations of particle-fluid interaction on the micro- and the macro-scale level provide fundamental knowledge of the mechanisms in the soil liquefaction, the initial process of soil liquefaction, and the kinetic momentum of the moving liquefied materials.

This chapter begins with the phenomenon of flow-slide failure to demonstrate the pronounced effect of the soil liquefaction. The possible failure mechanisms of flow slides are introduced. The following section describes factors that can potentially affect the residual strength of liquefied soil, classified according to their effect on soil behavior. Numerous approaches to evaluate the residual strength have been proposed, and this chapter reviews the laboratory-based and field-based approaches for doing so.

4.2 FLOW-SLIDE FAILURE

The term "flow-slide failure" describes the extremely large deformations caused by the soil liquefaction. When the shear strength of a liquefied soil is suddenly reduced, much of the resistance provided by the non-liquefied and liquefied materials is lost and the soil can fail to maintain equilibrium in its original geometry. The driving stress, produced by the weight of the structure itself and possible boundary surcharges, overcomes the soil resistance and initiates deformation. During the motion of a flow-slide failure, non-liquefied soils are often broken into blocks, which remain relatively intact while suspended within the liquefied soil. The liquefied soils are driven by the soil weight and behave as fluid-like material. The failed soil structure regains stability once the kinetic energy dissipates with the deformation process.

Although it is difficult to create field conditions in the laboratory, one technique continues to deliver useful data. Seed (1987) presented a procedure to evaluate the residual strength by a back-calculation procedure using case histories of embankments that had suffered flow-slide failures. The benefit of using actual flow-slide failures to back-calculate the residual strength is that the back-calculated residual strength faithfully represents the actual field conditions. The factors that affect the back-calculation procedure of the flow-slide failure are boundary conditions, geometry of soil structure, and soil properties. In order to understand the process of flow-slide failures, this section introduces triggering mechanisms and the soil behaviors that lead to the occurrence of flow-slide failures. The technique continues to be valuable, and will be of future use in the analysis of liquefaction-susceptible materials.

4.2.1 Initiation of Flow-Slide Failure

Historical records of flow-slide failures reveal that soils can be liquefied by static loading -- construction dumps or creep from constant loads -- or cyclic loading -- earthquake events or tidal wave fluctuations. Reports show that liquefiable soils are commonly described as fine sands with uniform particle size gradation relatively low densities. These are characteristic of flow slides in costal areas (Kramer, 1988). In laboratory testing, this type of soil has been observed to exhibit contractive behavior under undrained loading conditions. Contractive behavior causes the soil structure to be densified by exterior loading or its own weight. In the particulate assembly, the strength of the overall structure depends on the contact points among particles. Shearing deformations produce contractive behavior in a loosely-filled soil structure. However, an undrained soil structure resists compaction by building up the pore water pressure.

Therefore, particle movement temperately attempts to transfer the driving shear stresses from the contact points among particles to the interstitial water. However, because the interstitial water has no capability to sustain the driving shear stresses, the soil structure starts to deform in order for particles to reestablish contacts and regain resistance. Under this circumstance, regaining a stable structure requires a large deformation.

In a structure that suffers flow-slide failure, the deformation usually begins in the liquefiable zone, or even a portion of the liquefiable zone. The existence of the locally expanded area may be the cause for this localized deformation. Iwashita and Oda (1999) observed the development of the column-like structure (Figure 3-10) in the drained, two-dimensional compression test. A similar behavior also can be expected to occur in field. Accompanied by the initial establishing of in-situ stress condition, a certain area within soil structure (e.g. slope) dilates in volume because of the local stress-anisotropy. Since liquefiable soils often have relatively high permeability, long period of consolidation process allows water to fill those expanded voids below the ground water table. As a result, the volume dilation caused by the initial consolidation creates the localized loose, saturated regions that are more susceptible to liquefaction than other liquefiable soils in the surrounding area.

When a monotonic load or cyclic load is applied to the soil structure, this volume-dilated area can be the origin of the soil liquefaction. The tendency of failure then propagates toward the surrounding soils to regain equilibrium condition (Fig 4-1). The soil behaviors following this localized liquefaction can be referred to as the strain-hardening and strain-softening stages. In the initial strain-hardening stage, the deformation propagates toward the surrounding soils and uses the strength of those soils for stabilization. As the surrounding soils compensate for the strength lost in the initial liquefied zone, they suffer a limited amount of deformation with partial damage. Liquefaction is contained, and surrounding soil dissipates the excess pore water pressure. Strain-hardening behavior begins, reuniting particles and establishing a stable force equilibrium condition.

Much more severe deformation can occur in a different situation. When significant driving stress is imposed on a liquefiable area quickly, excess pore water pressure cannot dissipate, creating an undrained condition. The resulting strain-softening behavior can initiate a progressive failure. Moreover, the rapid movement of excess liquefied soil may produce additional soil liquefaction that further weakens the structure. This type of progressive failure amplifies the amount of deformation. Strain-softening behavior can lead to expansion of the initially liquefied area. Accompanying the deformation, momentum (and kinetic energy) increases, which further extends the deformation process to produce considerable damage. The flow-slide deformations that are then observed results from the combined effect of the strain-softening behavior and the kinetic energy.

4.2.2 Kinetic Energy of the Flow-Slide Material

Kinetic energy is critical to evaluate the deformation process of many flow-slide failures, particularly those involving large volumes of soil. After soil liquefaction begins, because water has no capability to sustain shear stress, the initial stable force equilibrium is destabilized when the tendency of contractive behavior attempts to transfer stress from the particle contacts to the interstitial water. When this instability propagates and forms a larger liquefied area, the unbalanced force (the difference between the driving stress and the soil resistance) leads to the development of large deformation. Because a large amount of unbalanced force is produced in the initiation of the failure, the kinetic energy plays an important factor in accelerating the failure debris. This section explains the effects of the kinetic energy on the micro- and macro-scale levels.

4.2.2.1 Kinetic Effect at the Micro Scale

The initiation of soil liquefaction prevents the rearrangement of inter-particle contacts because the undrained condition prohibits change in volume. Without reestablishing contacts, particles can only drift in the interstitial water under the driving stresses. Particle drifting produces two effects that prolong the failure process by accumulating an adequate amount of kinetic energy. The first effect, based on Newton's second law of motion, assumes that unbalanced forces accelerate the particles to create kinetic energy. The kinetic energy displaces particles in the liquefied area and produces further random particle movement (particle collision). This randomization of particle movement triggers progressive failure that involves other particles and expands the liquefied area. The growth of the liquefied area, caused by kinetic energy, can be explained by the concept of the granular temperature (Equation 3.8) that maintains the stability of flow motion. The second effect is that when the particle movement is amplified by the kinetic energy, excess pore water pressure expands toward surrounding, potentially liquefiable regions. With the increasing area that sustains the driving stresses under the undrained condition, the region of the strain-softening materials is enlarged. This further decreases the capability of the slope to maintain stability.

During a flow-slide failure, the kinetic energy that amplifies the deformation process may eventually dissipate in several ways. The unbalanced force that produces the kinetic energy gradually decreases because the deformed geometry can no longer provide sufficient driving stresses to accelerate the deformation process. Furthermore, drainage at the perimeter of the liquefied area will eventually allow the excess pore water pressure to dissipate during failure. In this situation, particles reestablish contacts and regain strength. In a manner similar to the deposition process of a debris-flow failure, accompanying with the decreasing kinetic energy and the increasing stabilized zones inside the deformed geometry, decreasing granular temperature in the flow slide retards the growth of random particle movement and allows particles to settle and form stable regions. Consequently, kinetic energy further dissipates from the lack of movement within the stable regions. Eventually, movement is slowly decreased and the structure develops its post-failure geometry. However, some of the residual liquefied area may still exist inside the deformed debris with high excess pore water pressure. The consolidation process then takes place, rearranging the particles and forming a more stable configuration.

The failure materials are transformed to this post-failure configuration from their pre-failure positions by lacking resistance to the driving stresses and the kinetic energy. After the post-failure consolidation process, the soils resistance (provided by the non-liquefied and liquefied materials) will be more than sufficient to maintain stability in the post-failure configuration.

4.2.2.2 Kinetic Effect in the Macro Scale

When materials that have reached the strain-softening stage fail to regain strength from the surrounding soils, the progressive-type failure may eventually produce tremendous deformations. During the failure process, one or several failure surfaces, or localized sheared zones, force materials to slide downward. Davis et al. (1988) used a sliding block model to illustrate the failure process of the flow-slide failure with the kinetic effect (Figure 4-2). The model demonstrates how kinetic energy accumulates and wanes.

In this schematic illustration of the flow-slide failure, the mass of the total failure materials and their movement is represented at the center of gravity. When the failure mass slides along the failure surface, the movement of the center of gravity is assumed to be parallel to the failure surface. At the failure surface, liquefied soils suddenly lose their strength and cannot maintain the stability of the original configuration. To account for the soil resistance (τ_r) in the analysis of the flow-slide failure, the mobilized soil strength depends on both the liquefied material and the non-liquefied material. Because liquefied materials are weakly supported, the driving stress (τ_d) at Point A produces a large unbalanced force that accelerates the failure materials downward. This downward movement produces kinetic energy, which increases until the point at which the soil resistance is equal to the driving stress (Point B). At this instant, the velocity at the center of gravity reaches its maximum value in the entire failure process. Considering only the forces acting on the failure mass, the mass would be in equilibrium at this point, and no further displacement would be expended. However, the kinetic energy associated with the non-zero velocity of the mass produces additional displacement. After this point, the failure mass decelerates on the sliding path becomes a more gentle slope. Decreased kinetic energy permits the soil to regain resistance, and it overcomes the driving stress. The center of gravity slows until the failure materials reach their final resting positions (Point C). In this representation, the displacement of the failure mass from Point A to Point B can be thought of a resulting from the loss of strength, and the displacement from Point B to Point C as resulting from the inertia of the failure.

4.2.3 Soil Behavior of Flow-Slide Material

4.2.3.1 Influence of Pore Water on Soil Behavior

In the evaluation of soil liquefaction hazards, the condition of pore water migration plays an important role. In the case of level ground, when excess pore water pressure is produced within a liquefied soil, the pore water tends to migrate toward the ground surface. Soil particles move downward and produce looses areas at the upper portion of the liquefied area (Kramer, 1996). When less-permeable layer exists above the liquefied layer, experimental and field studies suggest that water films can be created between the impermeable layer and the liquefied layer (Fiegel and Kutter, 1994; Boulanger and Truman, 1996; Kokusho et al., 1999; Kokusho and Fujita, 2002). When water films occur in the case of level ground, they deform the ground because materials can collapse and fall into the loosened liquefied layer (Fiegel and Kutter, 1994). In the case of sloping ground, the undrained condition reduces the shear strength of soil to that of the residual strength after soil liquefaction. Combined with the effect of water film accumulation, loosening of the upper part of the liquefied layer may produce lateral spreads (Kokusho, 1999). In the case of the flow-slide failure, less-permeable material exists above the liquefiable materials may increase the extent of soil liquefaction because they retard excess pore water migration after the initiation of liquefaction. Subsequently, water films trapped below less permeable zones can be sheared with little resistance resulting in large deformation.

When a less permeable layer does not exist above the liquefiable layer, partial drainage can allow the liquefied materials to regain strength by dissipating the excess pore water pressure. Figure 4-3 demonstrates the possible behavior of liquefied soils under partially drained conditions. In the initial field condition (Point A), the flow-slide failure can be initiated by monotonic or cyclic loading where the stress path reaches the flow liquefaction surface. Points B_{mono} and B_{cyc} represent the initiation of flow liquefaction under monotonic and cyclic loading, respectively. Under undrained conditions, the liquefied soils mobilize their residual strengths (Point C) at large strain levels. During the flow-slide failure, undrained deformation persists until the partial drainage occurs (Point D). When partial drainage occurs, the escape of the excess pore water pressure causes liquefied soils to become denser and, therefore, the soils to increase in strength. With the decrease in void ratio, the residual strength of the liquefied soils is increased (i.e. to Point C'). Because a slight change of void ratio may produce a large increase in the residual strength, the difference between the residual strength value under undrained condition and partially drained conditions can be dramatic.

4.2.3.2 Stress-Strain Behavior of Flow-Slide Material

In laboratory testing, an entire sample can be fully liquefied and sheared under steady-state conditions. However, this kind of testing can only represent the soil behavior in a small portion of an actual soil structure that has failed. In the field, soil liquefaction is initially triggered within a localized area. While the liquefaction may eventually move outside the initially-liquefied area, the large deformation that occurs in a limited area may affect other portions of the structure that remain relatively intact. During a flow-slide failure, when the liquefied soils are sheared and large deformation occurs, some of the materials in the failure debris may still remain relatively intact. Additionally, various drainage conditions may also affect the soil behavior in the liquefied area. Figure 4-4 illustrates several possible stress-strain behaviors among the failure debris.

Two types of stress-strain relationship that include the behavior of liquefied and non-liquefied soil are introduced in Figure 4-4. The plots of Cases 1 to 4 represent the soil behaviors of the non-liquefied materials, while the plots of Cases 5 to 7 represent the behaviors of the liquefied materials. In some case histories, such as the collapse of the Lower San Fernando Dam in 1971, most of the non-liquefied materials within the failure debris broke down into huge blocks that drifted among the liquefied materials. Case 1 represents the small amount of deformation that is produced by the fluctuation of dynamic stress from the sliding movement; the materials inside the block remain relatively intact throughout the sliding process. For those materials located near the boundaries between blocks, Case 2 illustrates the separation that can occur between blocks. Because soil has little or no tensile strength, tension cracks occur when blocks collide and grind. Case 3 illustrates another situation when the blocks push other blocks down the slope. The dynamic movements of blocks can produce rapid loading and unloading forces near the boundaries. Usually the outer shells of an earth-filled dam are composed of coarser materials. When straining occurs in those areas, the soil is usually assumed to be loaded under drained conditions because they are able to dissipate excess pore water pressure during the failure process. As indicated in Case 3, the loading and unloading forces result in strain-hardening soil behavior under drained conditions. In comparison, Case 4 demonstrates another example of non-liquefied materials strained under the drained condition, but in a region under high effective vertical stress with concentrated shearing (i.e. a relative thin sheared zone). In addition to high shearing stresses, localized stress fluctuations occur from particle breakage or highly-agitated, random particle collisions. This type of stress fluctuation can be seen when the materials are under rapid shearing – for instance, a fully developed flow slide.

Compared with the stress-strain behaviors of the non-liquefied materials described above, liquefied materials are strongly affected by both undrained and the partially-drained conditions. In Case 5, strain-softening occurs because of the contractive behavior of the liquefied materials under undrained conditions. With the less permeable sliding bed, this region may still contain a large amount of excess pore water pressure after sliding has terminated. Consolidation process then dissipates the remaining excess pore water pressure. However, some regions of the liquefied area may be able to partially drain the excess pore water pressure during the failure process. Case 6 illustrates that materials located near the boundary between the non-liquefied and liquefied areas can regain at least some of their strength by partial drainage. The mechanism of this case was explained in Section 4.2.3.1. In a different situation, Case 7 illustrates the behavior of materials located near toe area that eventually lose their strength and flatten out. Excess pore water pressure in this area is drained to nearby non-liquefied materials or outside the slope, and the liquefied materials near the toe area may eventually flatten out because the soil strength is reduced. Research has found that the residual strength of the liquefied materials is the function of the effective vertical stress, for this instance, in Stark and Mesri (1992). At the end of deformation process, the flattened, liquefied material within the toe has its residual strength reduced to a less amount because of the decreasing effective vertical stress. To explain this phenomenon on the micro-scale level, the action of materials flowing down and flattening out near the toe decreases the load that is transferred from the upper to lower materials. The reduction of load decreases the contact forces between the moving particles. This action leads to the overall weakening of the soil resistance in this area. Unlike Case 6, Case 7 reveals that the decrease of vertical effective stress can diminish the residual strength even after the partial drainage creates the strain-hardening behavior.

4.2.4 Ideal Analytical Approach to Evaluate Flow-Slide Failure

Back-calculating the residual strength involves several steps, combining all the analytic resources for evaluating of flow-slide failure. First, the pre-failure condition should be estimated by determining the proper geometric configurations, soil properties, and correct pre-failure stress conditions. Second, when the soil structure is struck by the sudden reduction of soil resistance in the liquefied area, soil should be evaluated by the severity of the structural deformation. The proper evaluation should include the acceleration, velocity, and deformation profiles that reflect the actual failure process. Finally, with the estimated residual strength of liquefied soil, the calculated resting geometry should match the observed post-failure geometry. Several attempts may be required in order to bracket the results to the observed post-failure geometry. By following those steps, the back-calculation produces the accurate value of residual strength.

Uncertainty involved in defining parameters is another important factor to characterize a case history. In the back-calculation procedure, estimating the stability of slope requires parameters to describe a case history. These parameters include soil structure configuration (exterior geometry, interior geometry, water table, and failure surface) and soil properties (density, friction angle, cohesion, and in-situ testing results). Information for these parameters usually is obtained from existing documentation. A systematical procedure should be established to characterize those parameters based on their quality and quantity obtained from documentation. For example, parameters acquired from well-documented case histories should carry lower uncertainty level compared with parameters acquired from poorly-documented case histories.

4.2.5 Summary of Flow-Slide Failure

Catastrophic failures caused by flow slides reveal the critical nature of residual strength evaluation. Because of the soil liquefaction, the shear strength of the material in a flow slide can be dramatically reduced from its pre-failure shear strength to its residual strength. Without sufficient resistance from the soil in any non-liquefied zones, the soil structure can no longer maintain its original configuration, which leads to a deformation process. Kinetic effects affect valuation of the residual strength of the soil. Kinetic energy is accumulated from the unbalanced force that drives the failure debris down the slope. With increased kinetic energy, the deformation process is prolonged, until the failure debris has sufficient soil resistance to oppose the driving stress.

Because soil liquefaction causes flow-slide failures, back-calculating the residual strength from the flow-slide case history can provide useful information about the residual strength under field conditions. To better understand the mechanism of soil behavior, this section examined various soil behaviors and explained the occurrence of the flow-slide failure.

4.3 FACTORS AFFECTING BEHAVIORS OF LIQUEFIED SOILS

In laboratory and in-situ observations, several important factors have proven to affect the behavior of liquefied soils. In this section, the factors are classified into four groups: initiation conditions, testing conditions, material physical properties, and residual conditions.

In terms of initial conditions, the factors include initial effective stress, initial void ratio (or initial relative density), and sample preparation procedure. The major concern of this group is to retain the inherent history from the deposition process in the soil fabric. This inherent history usually will be destroyed as the particles rearrange their positions under the applied loading condition.

In the group of testing conditions, factors include testing apparatus and stress path. This group considers the destroying of initial soil fabric created from the deposition process, and restriction on soil particle rearrangement. Researchers can ascertain a steady-state condition only by using the proper testing apparatus and following an appropriate stress path, as it exists in the field.

With respect to the group of material physical properties, this group considers the fines content, the particle size, the particle angularity, and the particle surface roughness. When liquefied materials are sheared under the steady-state condition, those physical attributes will influence random particle collisions in the flow structure.

In the steady-state deformation, the group of residual conditions includes the residual effective stress and the residual void ratio, also known as the residual relative density. These factors help to identify the location of residual strength on the steady-state line. With controlled laboratory testing, undrained conditions can be maintained throughout the test. Therefore, the void ratio can be kept constant from the initial stage to the final stage. Under in-situ conditions, however, partially-drained conditions are possible. Because the residual strength relies on the effective stress and the void ratio partial drainage can affect the residual strength mobilized in the field.

To understand the effects of each factor, soil stress-strain behavior is divided into three regions (Figure 4-5). In the small strain region, the applied stresses contribute to destruction of the soil fabric produced by the depositional history of the particle assembly. Under certain conditions, a local peak strength may be produced (in Cases 1 and 2). When the soil fabric has been totally or partially destroyed, subsequent loads displace particle and create the temperate instability (reducing effective confining stress and/or shear stress), which is define by terms "phase transformation" or "quasi-steady state". An example of quasi-steady state, shown in Cases 1 and 2, produces a temperate reduction on shear stress. In this region, particles are forced to rearrange their position in order to establish a stable configuration. When the particles are further deformed beyond the quasi-steady state, a flow structure can eventually develop at the stage of steady-state deformation. This section introduces the factors that affect the residual strength, based on effects in these three regions.

4.3.1 Effects of Initial Conditions

4.3.1.1 Initial Effective Stress

As mentioned in Chapter 2, the state of the soil, i.e. its combination of initial density and effective stress, will affect its susceptibility to liquefaction. In Figure 2-15, when the initial state plots to the right of the critical void ratio line, the soil exhibits a tendency to contract under undrained conditions. This strain-softening behavior can produce static liquefaction when static loading is applied. When the initial effective stress falls to the left side of the line, the tendency to dilation in strain-hardening behavior prevents static liquefaction.

The initial effective stress also influence the type of liquefaction induced by monotonic or cyclic loading. By locating the initial effective stress condition within the stress-path space (Figure 2-26), soil liquefaction can be classified by flow liquefaction and cyclic mobility. Details about this classification were explained in Sections 2.4.2.2 and 2.4.2.3.

4.3.1.2 Initial Void Ratio

Under undrained conditions, the void ratio of a liquefied soil remains constant throughout the process of deformation. In Figure 2-23, given a constant void ratio, tests with various initial effective stresses always arrive at the same point on the critical void ratio line. By projecting the same behaviors on the stress-path space with the same initial void ratio, various initial effective stresses and various stress paths are always mobilized to the same residual strength at the steady-state condition.

However, in-situ conditions may contradict this prediction of the soil behavior, because undrained conditions may not exist throughout the deformation process in the field. When partial drainage occurs, the value of the void ratio can change, leading to misleading predictions the steady-state strength (Figure 2-23). In this instance, the residual strength is determined by the actual void ratio and effective stress at large deformations.

4.3.1.3 Sample Preparation

To simulate liquefied soil behavior, samples used for laboratory testing are usually reconstituted from materials collected from the field. The most common sample preparation procedures are water pluviation, dry pluviation, and moist tamping. However, different preparation procedures produce different fabrics among soil particles, which can affect response under loading. As a result, the use of undisturbed samples collected from the field is highly desired for soil liquefaction evaluation. For current advance of technology, the in-situ ground freezing technique can allow engineers to retrieve undisturbed samples from field. This section gives a brief introduction to each method of sample preparation. Soil behaviors based on various sample preparation procedures are then compared.

Dry Pluviation

The dry pluviation method uses oven-dried soil to fill the sample space confined by a mold. Soils are dropped through a funnel or a screened tube with a controlled drop height to form the specimen. It should be noted that if soils were dropped from a constant height, the lower portion of the sample may be densified by subsequent soil deposition . Vaid and Negussey (1988) showed that the initial specimen density can be significantly affected by the drop height. To reach the desired initial density, tapping can be applied on the mold to densify the dry soil. After the sample space has been filled, soils are sealed and flushed with de-aired water to saturate the specimen.

Water Pluviation

Preparing a specimen by water pluviation simulates the process of soil deposition through water, e.g. by hydraulic filling. The sample is made by pouring oven-dried soils into a mold that has been previously filled with an adequate amount of water. During the entire sample preparation process, the proper level of water should be maintained to allow soils to settle through the water. The initial density of the sample can be increased by tapping on the side of mold. It should be noticed that the process of depositing soils through water may produce particle segregation when the material contains silts or well-graded soils (Ladd, 1974). Other similar procedures can be found in publications made by Kolbuszewski (1948), Chaney and Mulilis (1978), and Kuerbis and Vaid (1988).

Moist Tamping

Compared with other three procedures, the specimens made by the moist tamping can be reduced to the loosest state. Because liquefaction is caused by the contractive behavior of loosely-filled soils, many loose samples made by the moist tamping procedure can exhibit highly contractive behavior. A moist-tamped sample is prepared by mixing oven-dried soils with de-aired water (water content at about 5%) (Ishihara, 1996). Moist soil is then placed into several layers in the mold. The moisture creates a capillary effect among particles that characterizes the extremely loose fills. The density is controlled by tamping the top of each layer. Under certain circumstances, this method can produce samples with negative initial relative density. With proper densification of the sample, this procedure can produce specimens that cover a wide range of the initial void ratio values. The typical procedure of the moist tamping founding described in an article by Ladd (1978).

In-Situ Ground Freezing

Loose, liquefied soils are very difficult to sample without causing disturbance (i.e. densification), even using thin-walled tube or block samplers. In order to preserve the original fabric, in-situ ground freezing is preferred. This process can form a stiff mass and retain the fabric history by freezing pore water in the target area. This permits laboratory testing on undisturbed samples. Yoshimi et al. (1989) described a typical in-situ ground freezing procedure with the sample retrieving procedure and the laboratory testing results. The proper procedure of thawing the frozen sample was described by Vaid et al. (1996). The restriction to using this technique is that it is expensive and complicated.

Effects of Sample Preparation

Figure 4-6a shows resulting soil behaviors with various remolded sample preparation procedures under the same initial effective confining stress and approximately the same initial void ratio. Tests were done with an undrained, simple–shear test in an NGI-type device. The figure shows that the specimen made by moist tamping is highly contractive. Because the initial fabric is supported by the capillary forces, the specimen can be easily broken down after capillary forces are removed in saturation process. Compared with other two procedures, the sample made by moist tamping has less dilative behavior toward the large strain region.

Because the technique of water pluviation for reconstituting specimens is similar to the natural deposition process of most potential liquefiable soils, this technique is considered more reliable for soil liquefaction evaluation. To verify the accuracy of the sample preparation procedures, soil behaviors of remolded samples made by water pluviation were compared with the results from the undisturbed frozen samples. Figure 4-6b shows a good agreement between these two techniques.

4.3.2 Effects of Testing Conditions

4.3.2.1 Testing Apparatus

To examine in-situ soil behavior, numerous laboratory experiments have been conducted using various testing apparatuses. The most commonly-used apparatuses are the triaxial device, the simple shear device, the direct shear device, and the ring shear device. Each of these devices involves different loading conditions, boundary conditions, and failure mechanisms. Because testing conditions differ, the failure mechanisms developed in the test specimens are different. For example, Figure 4-7 shows the response of Toyoura sand tested using triaxial and simple shear devices. With the same initial effective stress and the similar initial relative density, soil behavior varies greatly between the apparatuses.

4.3.2.2 Stress Path

In most naturally-deposited soils, soil layers extend horizontally, which means soil properties vary greatly in the vertical direction compared to the horizontal direction. When remolded or undisturbed samples are tested in the laboratory, the soil fabric also has its own, unique formation. The variations of soil behavior can be seen on the stress path according to the interactions between the soil deposition history and the loading conditions. The effect on soil behaviors caused by the various stress paths has been studied by Miura and Toki (1982), Vaid and Thomas (1995), Vaid et al. (1990), Uthayakumar and Vaid (1998), Yoshimine et al. (1998), Yoshimine et al. (1999), Vaid and Sivathayalan (2000), and Vaid et al. (2001).

The effects of a stress path on soil behavior can be defined by the inclination of the major principal stress to the vertical direction (α), and the parameter defined by the principal stresses, $b = (\sigma_2 - \sigma_3)/(\sigma_1 - \sigma_3)$. The symbols σ_1, σ_2, and σ_3 represent the major, intermediate, and the minor principal stresses, respectively. For example, the triaxial compression test has parameters of $\alpha = 0°$ and $b = 0$, whereas the triaxial extension test has parameters $\alpha = 90°$ and $b = 1$. Figure 4-7 clearly shows that strain-hardening behavior occurred during the compression test, while strain-softening occurred during the extension test. Figure 4-8 shows examples of the various α and b values that characterize the various loading conditions.

4.3.3 Effects of Material Physical Properties

4.3.3.1 Particle Size, Angularity, and Surface Roughness

The effects of physical properties of the soil particle, which include size, angularity, and surface roughness, play an important role in the development of large deformations. As previously shown in Figure 3-8a, the stress components are produced between two particles with rounded shape and smooth surface texture. When particles have irregular shapes and rough surface texture, the stress components developed at the particle contacts can be more complicated. In order to disturb the initial packing geometry in the region of a small deformation, a relatively considerable amount of shear stress is required to mobilize angular particles with rough surface texture, compared to the amount of stress needed to mobilize movement among rounded particles with smooth surface texture. After the initial packing history has been totally or partially destroyed, the particle size directly affects the amount of stress dilation. Rowe (1962) demonstrated that stress dilatancy is strongly affected by particle size within various particle assemblies. In addition, the tendency of particle rearrangement may be affected by the variation of the particle angularity and surface roughness. When increased deformation tends to mobilize shear strength from stress dilation, the interlocking created from the previous particle rearranging may retard this action. A slight difference in spatial variation in the void ratio, and the tendency to failure can causes a localized sheared zone at the region with the high void ratio.

When large deformation has occurred, rapid stress fluctuations can be observed under steady-state conditions. The magnitude and frequency of stresses that fluctuate around the average value increase with increasing particle size, angularity, and surface roughness. These stress fluctuations may eventually reflect on the plot of the steady-state line, which is described by the relationship between the residual strength (S_r) and the residual void ratio (e_r).

Researchers at the University of Washington have run various types of sand through laboratory testing programs. A new laboratory testing apparatus has been able to shear the specimens uniformly with the shear strain of over 100%. By observing the behavior of various types of sand under the various initial conditions, the effects of the particle physical properties agree with the descriptions above.

4.3.3.2 Fines Content

Research has been widely conducted to understand the effect that fines content has on the evaluation of the residual strength of liquefied soils (e.g. Lade and Yamamuro, 1997; Yamamuro and Lade, 1997 and 1998; Thevanayagam, 1998; Guo and Prakash, 1999; Polite and Martin, 2001). Yamamuro and Covert (2001) gave a good description of how to perform liquefaction evaluation on soil with both high and low non-plastic silts content.

Yamamuro and Covert (2001) used the Nevada 50/200 sand (grain size gradation between the No. 50 and the No. 200 sieves) mixed with ATC silts (non-plastic quartz grains with an insignificant amount of mica). The results shown here are from undrained triaxial compression tests on the Nevada 50/200 sand with low fines content (7%) and high fines content (40%). When the clean sands were mixed with low fines content (Figure 4-9a), the specimen initially had a high tendency for contraction because the silt particles were pushed into the voids. The quasi-steady state was created by the significant drop in the shear strength between the larger particles. After the quasi-steady state, the contacts among particles of various sizes increased the stress dilatancy. In Yamamuro and Covert's tests, the high magnitude of stress dilation resulted mainly from the contacts among the larger-sized particles. When the fines content was increased, the finer particles lodged between the larger particles, thereby decreasing the contacts between the larger particles even in the quasi-steady state and the steady state. When the specimen was prepared with a high fines content (Figure 4-9b), the tendency for contraction toward the quasi-steady state was influenced by the compressibility of the silts. With limited contacts between larger particles, or none at all, the stress dilation after the quasi-steady state was significantly decreased, compared with the behavior of the soil with the low fines content. Figure 4-10 shows the results of tests with various initial effective confining pressures in groups with low and high fines contents. Comparing Figures 4-10a with 4-10b, under the same initial effective confining pressure and at approximately the same void ratio, the soil behavior of the specimen with a low fines content had a higher peak stress difference (q) and a larger amount of stress dilation after the quasi-steady state.

Figure 4-11 shows the stress-strain behaviors of the undrained test results with the low and high fines content by comparing the ratio of the minimum stress difference, $q(min)$, to the peak stress difference, $q(peak)$, and the ratio of the peak stress difference, $q(peak,)$ to the steady-state stress difference, $q(ss)$. In Figure 4-11a, both groups show increasing values of $q(min)/q(peak)$ when the initial effective confining stress is increased. This can be explained by the effect of frustration (term explained in Section 3.2.3.2) that is caused by high initial effective stress. The interlocking effect from frustration reduces the mobility within particles for rearrange themselves. To change this condition, a larger load is required, which initiates stress dilatancy. The difference between the samples with high and low fines content is that, because of the dominance of the larger particles, the tests with low fines content have an early tendency to show stress dilatancy. In Figure 4-11b, the trend of $q(peak)/q(ss)$ shows reversed direction in the tests with low and high fines content. In the group with high fines content, undergoing as increase in initial effective confining stress, finer particles suspend larger particles during the steady-state deformation. The residual strength therefore depends on the interaction among the smaller, rather than larger, particles. As mentioned in Section 3.2.2, the stress in the particulate flow, or the flow structure of the liquefied soils, depends on the frequency of random particle collisions. Smaller particles have a greater chance of random particle contact than the larger particles. In each individual test, when the fines content is increased, the value of $q(peak)/q(ss)$ decreases because the high magnitude of inter-particle stress occurs with effective stress at the steady state because the frequency of random particle collision is increases. When the sample space is mostly occupied by large particles, the early failure concentrates on the localized sheared zones within larger particles because larger effort is required to overcome frustration developed within other regions. The chance of developing early localized shear zones increases when effective stress is increased.

4.3.4 Effects of Residual Condition

In controlled laboratory tests, an undrained condition is maintained in order to evaluate the behavior of liquefied soils. The argument is that the failure process is so rapid that any excess pore water pressure is inhibited from migrating outside the liquefied zone. In this circumstance, the initial void ratio can be preserved throughout the entire deformation process. With constant volume, the residual void ratio remains equal to the initial void ratio. The residual effective stress, however, is decreased by the excess pore water pressures that develop during the deformation process. With the contractive behavior of the liquefied soil, the residual effective stress can be considerably reduced from the initial effective stress.

In the field, although the process of liquefaction-related failure (e.g. flow-slide failure) has been reported to persist for only seconds to minutes, the complicated in-situ drainage condition can create partial drainage during the deformation process (Stark and Mesri, 1992). As indicated in Section 4.1.3.1, partial drainage can dramatically change the behavior of liquefied soils. In this instance, the residual void ratio can be changed from its initial condition, consequently affecting the residual strength. Evaluation of residual strength should take into account of potential volume change during this transformation from initial condition to residual condition.

4.3.5 Summary of the Factors Affecting Residual Strength

In the laboratory approach, various testing apparatuses have been used to conduct research on liquefied soil behavior. Soil specimens are collected from the field in disturbed or undisturbed form. In order to simulate the behaviors of liquefied soil, undrained loading conditions are often applied to the specimens, which then mobilize their residual strength at the steady-state deformation. Section 4.3 introduced a number of factors that can affect soil behavior. These factors were classified into four groups: initial conditions, testing conditions, material physical properties, and residual conditions. Table 4-1 lists the corresponding factors in each group. In laboratory tests, soil behavior can be divided into three major stages -- peak strength, quasi-steady state or phase transformation, and steady-state of deformation. Table 4-1 also points out the stages with which each factor is associated. The factors in the initial condition and the testing condition affect soil behavior in the peak strength and the quasi-steady state or phase transformation. These two stages correspond to the process in which the original soil structure (or fabric) is destroyed and the spatial positions of particles are subsequently rearranged (the quasi-steady state or phase transformation). It should be noted that, because of the limitation of some testing apparatuses, the steady-state deformation may never be reached in laboratory. Finally, group that describes the material physical properties usually affects the overall soil behavior (peak strength, quasi-steady state or phase transformation, and steady-state deformation). The last group refers to the residual condition, which corresponds to large deformations.

In the residual condition, residual strength is created by random particle collisions in liquefied soil. A similar phenomenon can be observed in debris-flow failures. Because the steady-state deformation involves the momentum of the constant shearing rate, stress fluctuations through agitated particle interactions are anticipated. In Figure 4-12, a steady-state band, instead of a distinct steady-state line, characterizes the relation between residual strength and residual void ratio. To characterize the scattering effect caused by this stress fluctuation, the steady-state band is described by the average steady-state line with lower and upper bounds. The position of the average steady-state line for each type of soil is uniquely governed by material physical properties and residual condition. The positions of the lower and upper bounds are similarly affected.

4.4 EVALUATION OF RESIDUAL STRENGTH

Over the years, engineers have developed a variety of ways to evaluate the residual strength of liquefied soils. In this section, the efforts that have been made on the evaluation of residual strength are introduced in two approaches: the laboratory-based approach and the field-based approach. Several methods are introduced in each approach.

4.4.1 Laboratory-Based Approach

To simulate the liquefaction behavior in the laboratory, the proper experimental procedure needs to be capable of several important functions. The applied stress conditions should be able to simulate actual field conditions, such as monotonic and cyclic loading. The stress path of the specimen should also reflect in-situ soil behavior under applied loads. A reasonable sample preparation procedure should be followed in order to reconstitute remolded specimens. During the experiment, the apparatus should be able to apply uniform stress and strain conditions to the entire specimen, especially when the loading condition strains the specimen to large deformations. At the same time, the system should be able to accurately monitor the stress and strain conditions in both the small and large strain regions. By satisfying these conditions, the residual strength of the liquefied soil should be characterized correctly. However, most laboratory apparatuses can only satisfy some of these requirements. In other words, an individual apparatus can only approximate soil conditions and field behavior. Furthermore, complications have been made by using different apparatuses because of the variety of the testing capacities of each apparatus to simulate the in-situ conditions.

This section introduces several common laboratory apparatuses that have been used in residual strength evaluation, including the triaxial, the simple shear, and the ring shear tests. This introduction focuses on their advantages and disadvantages in evaluating residual strength.

4.4.1.1 Triaxial Test

The triaxial test is one of the most commonly-used laboratory apparatuses for observing the soil behavior. The soil specimen is prepared in a cylindrical column (usually with an aspect ratio of about 2 height:1 diameter) surrounded by water in a chamber. During the test, an axial load is applied to simulate the actual loading condition in the field, while the confining pressure is applied through the water that surrounds the specimen. Under monotonic or cyclic loading conditions, the specimen may be tested under strain- or stress-controlled conditions. To simulate a flow-slide failure, the stress-controlled method is preferred because the constant stress condition represents the constant load that drives the failure mass in the downslope direction.

The most significant advantage of using a triaxial test is the availability of a large body of data with which results may be compared. Several major types of sand have been widely tested around the world. Some typical sands are Nevada Sand, Ottawa Sand, and Toyoura Sand. In addition, the system of monitoring and controlling stress conditions has been substantially improved over the years. Soil behavior can now be observed with high accuracy, which is important because of the high deformation rate after the initiation of liquefaction. The improved triaxial test describes the conditions at the peak stress, the quasi-steady state, and the phase transformation. This advantage allows researcher to examine the soil behavior under uniform stress conditions at low strain level.

The weakness of the triaxial test is that it cannot produce the uniform strain and stress conditions within the entire specimen to large strains, and therefore it cannot properly estimate residual strength. Even with some detailed monitoring equipment (e.g. Presti et al., 2000), the reasonable stress-strain relationship can only be observed in the range of an axial strain of 15 to 25% before the specimen is too badly deformed. In this strain range, it is difficult to characterize the soil behavior in most liquefaction-related failures, such as the lateral spreads. Under the drained loading conditions, Oda (1972) reported that the spatial distribution of the non-uniform void ratio started to increase after the peak stress had been reached. Various zoning effects were then produced within the specimen. The regions at the top and the bottom of the specimen were described as the dead domain, implying that soils within these regions only showed a small deformation compared to other regions. The soils at the center showed an increase in void ratio after the peak stress. The dilation in volume produced a weaker region that developed concentrated shearing deformation in the middle of specimen.

When the void ratio is non-uniformly distributed within the specimen, the external monitoring system can only response to the average behaviors, not actual localized behaviors. The applied incremental axial stress usually is updated according to the axial strain that reflects the average value of cross-section area in deformed specimen. The deformed specimen usually has larger cross-section area at the center of specimen. Because load is uniformly applies to the entire specimen, the actual stress at the center of deformed specimen is lower than the stress at the top and bottom portions. This suggests that the non-uniformly distributed void ratio produces stresses that non-uniformly distribute within a deformed specimen. .

4.4.1.2 <u>Simple Shear Test</u>

A simple shear test specimen is placed in a cylindrical container, usually with the aspect ratio of 3 diameter:1 height (Kramer and Elgamal, 2001). The container provides horizontal restraint that allows no lateral strain in the specimen. After the vertical stress is applied, the horizontal shear stress is then provided to mobilize shear strain. The horizontal shear stress can be produced by monotonic or cyclic loading.

In design of earthquake resistance, SH-wave usually is considered to be the major cause for structural damage. The most advantage of using simple shear test is that the sample is exposed to the vertically propagating SH-wave rather than other types of wave. To evaluate soil behaviors under the effects of the seismic loads, the cyclic simple shear test provides a better simulation than the cyclic triaxial test. Another advantage of the simple shear test is that the distributions of the shear strain and shear stress are relatively uniform, compared to the triaxial test.

The disadvantage of the simple shear test to evaluate the residual strength is the limitation of maximum shear strain. Most experimental data show a maximum shear strain of less than 30% (e.g. Finn et al., 1971; Budhu, 1984 and 1988; and Lau and Powell, 1991). The non-uniformity of shear strain starts to develop with increasing shear strain (Budhu, 1984). Zone of less movement are formed at the top and bottom under the large strain condition, which is similar to the triaxial test. Before the test is terminated at large strain, the arching effect (stress concentration) at the corners of specimen also limits the development of uniform shear strain beyond 15 to 20% (Kramer and Elgamal, 2001).

4.4.1.3 Ring Shear Test

In a triaxial test, the orientation of the shear plane generally follows the rule of ($45°+\phi/2$), the relationship of the angle to the horizontal plane. However, the location of the development of the shear plane is not controlled or restrained. In some cases, failure produces bulging of the sample with no obvious development of a specific shear plane. In the simple shear test, because the specimen is ideally sheared with the uniform shear stress, the shear strain is so uniform that there is no obvious development of a specific shear plane. Unlike the other tests, the soil specimen in a ring shear test is confined in a donut-shaped annular space within rigid side walls. The soils in the specimen are divided into upper and lower parts. Initially, vertical stress is applied to the top of specimen. Torque is then applied either to the upper or lower part of the specimen, while the other part is hold in a fixed position. The shear plane is therefore forced to develop on the horizontal interface between the upper and lower parts. With the design of the annular specimen, the ring shear test has no limitation on the shear strain.

Figure 4-13 shows a specific type of the ring shear that was built by Sassa and his colleagues to test soils under drained and undrained conditions. The loading system is able to shear the specimen in the single-direction (monotonic loading) and bi-direction (cyclic loading). Figure 4-14 shows an enlarged cross-section view with detailed illustrations of the pore water measuring and controlling system. The annular specimen has an outside diameter of 31 cm and an inside diameter of 21 cm. The sample thickness above and below the shearing plane is 7 cm and 4 cm, respectively. The specifications for this device were documented by Sassa (1997); this device has been used to evaluate the soil behaviors of landslide and debris-flow materials (Sassa, 1984, 1988, and 1992; Shoaei and Sassa, 1994; Lee and Sassa, 1996; Fukuoka et al., 1997; and Wang et al., 2000)

The disadvantage of the ring shear test is the concentrated failure plane that develops from stress concentration. As a result, the shear strain develops mostly near the shear plane while the other regions remain relatively intact. The concentrated failure plane also affects the generation and migration of excess pore water pressure. When the interface between the upper and lower parts is sheared, the contractive behavior generates excess pore water pressure at the localized shear plane. After the specimen has been sheared, the excess pore water pressure can migrate toward the relatively intact regions above and below the failure plane. As indicated in Figure 4-14, pore water pressure measurement is taken between the upper and lower parts. The pore water pressure reading can only reflect the local variation, and not the global migration. To evaluate residual strength, the ring shear device shows a promising advantage to shear a specimen to the large strain region. However, the development of a concentrated shear plane conflicts the natural process of liquefaction-related failures.

Another major concern is the actual stress-strain behavior within the sample. The concentrated shearing caused particles to be highly disturbed near the failure surface, which develops soil liquefaction. However, particles located away from this area may only experience a small amount of movement because of the lateral restrains. The actual stress-strain relationship near the failure surface may demonstrate the behavior through small (peak strength), intermediate (phase transformation or quasi-steady state), to large strain (steady state) regions. This process describes a strain-softening behavior of liquefied soil. At the same time, particles located above and below the failure surface only have limited effect from shearing. The soils may still under the effect of strain-hardening. Moreover, particle movement in these areas is also affected by those particles move vertically from the failure surface. This action of vertical particle movement further escalates the variability of stress-strain relationship within the truly liquefied area – the concentrated failure plane. As a result, the external observation of the ring shear test is a combined effect caused by the strain-softening and strain-hardening behaviors, and also the interaction between the liquefied and non-liquefied areas.

4.4.2 Field-Based Approach

Relationships have also been established between measurements from in-situ tests and back-analyzed residual strength of liquefied soils. The field-based approach includes the procedure used estimates residual strength based on this relationship. The first section introduces several most commonly-used methods involved in back-analyzing residual strength, including limit-equilibrium stability analysis, Newmark method, and normalized residual strength ration method. The second section introduces two major in-situ testing techniques for site exploration: the standard penetration test and the cone penetration test. Finally, the in-situ-testing results are related to the back-analyzed residual strength from the actual flow-slide case histories. The last section introduces several previously established relationships that allows engineer to use field data and assess the residual strength of liquefiable-susceptive soil.

4.4.2.1 Methods in Back-Analyzing of Residual Strength

Limit-Equilibrium Back-Calculation Method

The limit-equilibrium method of evaluating the stability of slope is based on Coulomb's failure criterion to satisfy equilibrium of a failure mass along a prescribed failure surface. The shape of the failure surface can be a planar surface, circular surface, spiral surface, randomly-searched surface, or an observed surface. To evaluate the safety of the slope, equilibrium is evaluated by estimating the soil weight, water weight, boundary surcharge, and soil resistance. The most common way to describe the stability of the slope is in terms of the factor of safety (*FS*). The basic form of the factor of safety can be described as

$$FS = \frac{\text{Available Shear Strength}}{\text{Shear Stress Reaquired to Maintain Equilibrium}}. \tag{4.1}$$

Stability is provided by the soil shearing resistances, including both the cohesional and frictional components of shearing resistance. The driving stresses that cause instability are contributed by soil weight, water weight, and boundary surcharge loads. The slope is considered to be safe when *FS* is greater or equal to one. Some commonly-used limit-equilibrium methods include the Taylor's method, Bishop's method, Morgenstern's method, Spencer's method, and Hunter and Schuster's method. A well-documented summary of the limit-equilibrium methods can be found in Fang and Mikroudis (1991)

Several assumptions are used in the limit-equilibrium method of evaluating slope stability. First, the failure soil mass is usually divided into several slices. Evaluation of equilibrium is based on the forces between adjacent slices, between slices and failure surface, and boundary loads. This represents the soil mass failure as a rigid block for each individual slice. Second, the assumption of the sliding block implies that the materials within the block are assumed to remain intact. The failure criterion only applies to the interaction between the failure mass and the failure surface, and interaction between adjacent slices. Last, the factor of safety describes the overall safety of the soil structure along the failure surface. A localized unstable zone cannot be characterized by this approach.

To evaluate the residual strength of liquefied soil, the conventional procedure is to back-calculate residual strength from actual flow-slide failure case histories using the limit-equilibrium method with documented geometry and soil properties. Using a process of trial-and-error, the residual strength is back-calculated as the cohesion value assigned to the liquefied materials that provides a *FS* value of 1.0. Usually, the residual strength is back-calculated as the upper and lower bound values according to selected slope geometries.

At the point at which the strength of the liquefied soil is reduced to the residual strength, the original geometry fails because of insufficient the soil resistance. Application of the conventional back-calculation on the pre-failure geometry, therefore, yields an estimated residual strength that is higher than the actual residual strength. The upper bound of residual strength is thus defined by the back-calculated value from the pre-failure geometry. As described in Section 4.2, the post-failure geometry of the flow-slide failure is the combined effect of the reduced residual strength and kinetic momentum. The kinetic effect that extends the deformation process cannot be accounted for by applying the limited-equilibrium method to the post-failure geometry. Because of this deficiency, the conventional back-calculation procedure on the post-failure geometry usually produces a residual strength value that is lower than the actual residual strength.

The lower bound of residual strength is therefore defined by the back-calculated value from post-failure geometry.

In cases such as the flow-slide failures of a tailings dam, the post-failure geometry may be seriously deformed to an extremely gentle slope. Ishihara et al. (1990) suggested simply treating the post-failure geometry as an infinite slope. For that case, the residual strength was approximately formulated as

$$S_r = \gamma_t H \sin\alpha \cos\alpha \tag{4.2}$$

where γ_t is the total soil density, H is the soil thickness above the sliding surface, and α is the inclination of the sliding surface. This simplified approach assumes that the failure surface is coincident with the sliding surface. The value of H is calculated as the average thickness of the post-failure geometry. The residual strength estimated by this approach also represents a lower bound value.

Newmark Method

In static stability analysis, the driving stress results mainly from the soil weight and boundary surcharge load. Under a seismic event, ground shaking produces dynamic driving stresses that reduce the safety of the slope. Pseudostatic stability analyses consider the effects of both static and the dynamic driving stress. Figure 4-15a shows a simple slope subjected to a horizontal downslope dynamic force $K_h W$, where K_h is the horizontal, dimensionless, pseudostatic coefficient, and W is the weight of the potential failure area. In this manner, the complex, transient nature of earthquake shaking is represented very simply by a constant force. In this case, only the downslope dynamic force is considered because the upslope dynamic force increases the stability of slope. In the pseudostatic stability analysis, Equation (4.1) is revised to the form of

$$FS = \frac{\text{Available Shear Strength}}{\text{Static Driving Stresses} + \text{Pseudostatic Driving Stresses}}. \tag{4.3}$$

The slope is considered to become unstable when the *FS* drops below one. However, the pseudostatic stability analysis can only provide a factor of safety for the slope. It provides no information about the amount of deformation caused by the seismic event, which is an important index of structural serviceability.

Newmark (1965) suggested a sliding block approach to estimate the approximate amount of deformation caused by a seismic event. The failure process of the unstable slope is simulated by a rigid block (as the potential failure mass) that slides on an inclined surface (as the failure surface) in the downslope direction because of the combined effects of static and seismic driving forces, as shown in Figure 4-15b. The soil resistance, in this case, exists between the block and the sliding surface. The triggering of sliding is defined by the point that the combination of the static and dynamic stresses produces a pseudostatic *FS* of one. This yield seismic force is expressed as $K_y W$, where K_y is the pseudostatic coefficient that causes yielding (i.e. a *FS* = 1.0). In the seismic deformation-type analysis, the seismic input is described by a series of acceleration values in an accelerogram (time history of seismic acceleration values). The yield acceleration, a_y, then defines the triggering of deformation, in which $a_y = K_y g$. In Figure 4-16, acceleration values that are higher than a_y drive the block to slide toward the downslope direction. The amount of velocity values are calculated by integrating the acceleration values that exceed a_y. The integration is then applied again to calculate the amount of deformation accumulated from the velocities.

Appropriate usage of the Newmark method can provide estimates of the deformation accumulated from dynamic loading. A trial residual strength is first assigned to the soil resistance to estimate the yield acceleration by the pseudostatic stability analysis. The accumulated deformation can then be calculated from the double-integration process based on the Newmark method. This process can be repeated in a series of trial residual strength values until the calculated deformation matches the observed value.

Precautions should be taken when using the Newmark method to estimate the residual strength value by back-analyzing of flow-slide case history. First, soil resistance is assumed to be constant during the sliding. This assumption is not suitable for the strain-softening behavior of liquefied soil. Second, the amount of deformation is assumed to be at the center of gravity of the failure mass, or the corresponding sliding block. The observed deformation should also occupy at the center of gravity in the deformed post-failure geometry. The confliction is that the sliding block model describes the movement of rigid block. This approach cannot simulate the deformation process inside the failure mass. Finally, the Newmark method only estimates the deformation generated by the dynamic loading. For example, Castro et al. (1989) used the Newmark method to estimate the deformation of the Lower San Fernando Dam during the 1971 San Fernando Earthquake motion. However, for a flow-slide failure, the deformation generated during a seismic loading is only a fraction of the total deformation. The large deformations of flow-slide failure are caused by the static driving stress in the post-triggering process. For this reason, the Newmark method is not adequate to back-calculate the residual strength of the flow-slide failure.

Normalized Residual Strength Ratio Method

Poulos et al. (1985) proposed a procedure to estimate the field residual strength based on the difference of void ratio value in field and laboratory conditions, and the steady-state line that was established in laboratory tests. The procedure required that the steady-state line be established from a series of consolidated-undrained triaxial tests on reconstituted specimens. It was assumed that the inclination of the laboratory-determined steady-state line was parallel to the field steady-state line. The field residual strength was then estimated based on the difference between the void ratio in the field and the laboratory. This procedure implies several assumptions of the steady-state line. First, it assumes that the inclination of the steady-state line is parallel to the consolidation line. The consolidation line reflects the deposition history of the soil (e.g. the in-situ void ratio). Second, it assumes that the inclination of the steady-state line is unique and not affected by the sample preparation procedure or testing apparatus. Third, it assumes that the relationship between the residual strength and void ratio is unique for each individual type of sand.

Because the void ratio reflects the history of the field condition, this unique relationship can also be applied to the residual strength and the initial vertical effective stress (σ'_{vo}). This relationship is termed the normalized residual strength ratio, S_r/σ'_{vo}. Research has shown evidence that the value of S_r/σ'_{vo} may be unique for an individual sand. Laboratory experiments made by Baziar and Dobry (1995) suggested that the S_r/σ'_{vo} values of the liquefied soil in Lower San Fernando Dam ranged from 0.04 to 0.2. Ishihara (1993) indicated that two types of sand, Tia Juana silty sand and Lagunillas sand silt, had S_r/σ'_{vo} values ranging from 0.146 to 0.181 and from 0.086 to 0.134, respectively. However, it should be noted that the results concluded by Ishihara (1993) was based on the strength at the quasi-steady state. It was his belief that for design purposes, the lower strength at the quasi-steady state rather then the strength at the steady-state condition should be used, in certain conditions.

4.4.2.2 In-Situ Testing Techniques

Standard Penetration Test

The Standard Penetration Test (SPT) is probably the most common in-situ test in geotechnical engineering. This test can be used for site exploration, foundation design, and geotechnical earthquake design. The test is carried out by advancing a split-barrel sampler connected to the end of a drilling rod to the bottom of the pre-drilled boring hole. At ground level, the hammer with a weight of 140 lb (63.6 kg) is dropped repeatedly (30 to 40 blows/minute) on the top of the drill rod from a drop height of 30 inches (76 cm). The energy delivered by the hammer advances the SPT sampler into the soil at the bottom of the boring. At each desired depth, the sampler is driven 18 inches into soils. Because of the potential for soil disturbance during drilling, the SPT blowcount (N) is taken as the number of drops required for the last 12 inches of penetration. In common practice, the dropping of the hammer is terminated when the SPT blowcount is higher than 100. At the end of test, the sampler can be retrieved to collect the soils that have been trapped inside the split-barrel space. Those soils although disturbed, can be used in laboratory tests. Several factors may affect the blowcount number, that is, the driving energy, such as the soil type, confining pressure, and soil density (Kramer, 1996). Human and mechanical errors may also reduce the driving energy (Kulhawy and Mayne, 1990; and Canadian Geotechnical Society, 1992).

In geotechnical practice, the SPT blowcount is normalized by the overburden pressure and the energy level in the form of

$$(N_1)_{60}=N\frac{ER}{60}C_N \tag{4.3}$$

where $(N_1)_{60}$ is the normalized SPT blowcount, ER is the energy ratio, $ER/60$ is the rod energy ratio normalized to 60%, and C_N is the correction factor of the effective overburden pressure. In North America, the most common hammer types are the safety and donut hammers. The value of ER is based on the type of the hammer, the release method, rod length, number of rods, and the region of practice. Table 4-2 lists values corresponded to these factors. Besides those correction values in Table 4-2, the driving energy actually can be directly measured by a pile driving analyzer. Liao and Whitman (1986) recommended the value of C_N in the form of

$$C_N = \sqrt{1/\sigma'_{vo}} \tag{4.4}$$

where σ'_{vo} is the effective vertical stress in tons/ft^2 at the soil where SPT blowcount is measured.

For evaluation of soil liquefaction susceptivity, it is believed that the present of fines inhibits liquefaction occurrence. Value of $(N_1)_{60}$ is then further corrected to the equivalent clean-sand SPT resistance, $(N_1)_{60\text{-CS}}$. The value of $(N_1)_{60\text{-CS}}$ is estimated based on the value of $(N_1)_{60}$ with a correction for fines content, i.e.

$$(N_1)_{60\text{-CS}} = (N_1)_{60} + \Delta(N_1)_{60} \tag{4.5}$$

where $\Delta(N_1)_{60}$ is the fines content correction of the SPT resistance. Table 4-3 summarizes the recommended values for the fines content corrections recommended by Seed (1987), Seed and Harder (1990), and Stark and Mesri (1992). It should be noted that the $\Delta(N_1)_{60}$ values provided by Stark and Mesri (1992) was intended for the correction to the yield strength, or the peak strength.

Cone Penetration Test

The Cone Penetration Test (CPT), once called the Dutch cone test, has been used widely in recently years. The test is carried out by pushing the penetrometer into the ground to measure the tip resistance (q_c) and the sleeve resistance (f_s). The advantage of CPT is that it can provide continuous data, providing beneficial details about the subsurface materials. A modified version of the CPT can even measure the pore water pressure or the wave propagation velocity by adding sensors to the penetrometer. Although no soil is retrieved from subsurface in this method, the measurements provided by CPT can still help to identify the soil properties and the soil type. However, very dense soils that consist of larger particles (e.g. gravels, cobbles, and boulders) may limit the use of the CPT.

The CPT's strength is the accuracy of the tip resistance measurement. The tip resistance is usually corrected based on the effective vertical stress in the form of

$$q_{cN} = C_q q_c \tag{4.6}$$

where q_{cN} is the corrected tip resistance, and C_q is the effective overburden stress correction factor. Seed et al. (1983) proposed the form of this factor as

$$C_q = \frac{1.8}{0.8 + \left(\sigma'_{vo} / p_a\right)} \tag{4.7}$$

where p_a is one atmosphere pressure (approximately 100 kPa).

When sand contents more than 5% of fines, Ishihara (1993) suggested that the value of q_{cN} should be increased to the equivalent clean-sand CPT tip resistance. Table 4-4 lists the values of tip resistance increment in various levels of fines content.

4.4.2.3 Typical Relationships between Field Data and Back-Analyzed Residual Strength of Liquefied Soil

To directly estimate soil strength in laboratory, the soil behavior can be closely monitored by various pieces of testing equipment. However, because of the limitations of the devices themselves, the soil behavior is recorded under limited dimensions and with restrictions from the loading and boundary conditions. Another method to directly estimate the residual strength is the back-analyzing methods. These methods usually use various parameters to conclude results from simulation on the full-scaled geometry. The back-analyzing methods, therefore, have been invented to overcome the disadvantages that exist in the laboratory tests. When site investigations are conducted in field, in-situ test is the only technique to describe the field soil condition. For soil liquefaction assessment, it benefits designer to obtain residual strength directly from the in-situ testing results, such as SPT and CPT resistances. This section introduces several important establishments on relating in-situ testing results to the estimated residual strength of liquefied soil: SPT-based assessment and CPT-based assessment.

SPT-Based Assessment

Seed (1987) developed a relationship between the representative $(N_1)_{60\text{-CS}}$ value obtained within liquefied area and the residual strength of liquefied soils, by back-calculating the residual strength from flow-slide failures induced by soil liquefaction. Figure 4-17 shows the original relationship between the residual strength and $(N_1)_{60\text{-CS}}$ proposed by Seed (1987). He stated that the scattered results may be affected by the water content redistribution within different degrees of soil stratification, and the values that determined from conditions at the beginning of failure or at the end of failure. He also stated that there is a considerable degree of judgment involved in establishing this relationship. However, after many years of extensive uses by engineering practice, this relationship has been proven to be extremely valuable.

After Seed's pioneering establishment, various researchers updated the database with improved results. Seed and Harder (1990) reevaluated this relationship and added new case histories to establish the relationship between residual strength and $(N_1)_{60\text{-CS}}$. Figure 4-18 shows Seed and Harder's updated plot. In this updated relationship, $(N_1)_{60\text{-CS}}$ was corrected as the same method as Seed (1987). Some of the residual strength values presented are slightly different from the Seed's original results. One reason is the dynamic effect (e.g. momentum) was considered in the evaluation. Another reason is additional information were available for several case histories.

Idriss (1998) also compiled the data published by Seed (1987) and Seed and Harder (1990) and proposed another relationship between SPT resistance and residual strength. In Figure 4-19, a trend was established to show the representative average relationship between residual strength of liquefied soil and SPT resistance. This representative averaging trend implies an exponential relationship is existed. It also implies that the trend crosses the 50 psf at zero SPT resistance.

The S_r/σ'_{vo} value has also been calibrated according to the representative SPT resistance. Stark and Mesri (1992) established the relationship between S_r/σ'_{vo} and SPT resistance based on the back-calculation of soil liquefaction case histories. The relationship shows

$$\frac{S_r}{\sigma'_{vo}}=0.0055\,(N_1)_{60\text{-}CS}\,. \tag{4.8}$$

Table 4-5 summarizes the case histories with their causes of failure for studies made by Seed (1987), Seed and Harder (1990), Stark and Mesri (1992), and Idriss (1998).

Table 4-6 summarizes the back-calculated results, including residual strength of liquefied soil, the representative $(N_1)_{60\text{-CS}}$ values obtained within liquefied area, and S_r/σ'_{vo}.

Olson and Stark (2002) proposed the updated relationship between S_r/σ'_{vo} and SPT resistance. The relationship is

$$\frac{S_r}{\sigma'_{vo}} = 0.03 + 0.0075(N_1)_{60} \pm 0.03 \qquad for\ (N_1)_{60} \le 12\,\text{bpf} \tag{4.9}$$

The SPT resistance used in Equations (4.9) is based on values with no correction for the fines content. Olson and Stark (2002) indicated that the capability of silty sand to maintain the truly undrained condition compensates for the lower uncorrected values of the SPT resistances. The truly undrained condition produced lower residual strength values, corresponding to lower values of SPT resistance. Soil with lower fines content was suggested to be in the partially-drained condition, leading to higher residual strength values (Stark and Mesri, 1992).

CPT-Based Assessment

CPT-based liquefaction evaluation procedures have been established by, for example, Olson and Stark (1998), Robertson and Wride (1997), and Stark and Olson (1995). Generally, the relationship is established in charts to show the value of q_{cN} versus the cyclic resistance ratio, CRR. CRR represents the capability of soils to resist liquefaction induced by cyclic loading. Usually, CRR is set to equal to the value of the cyclic stress ratio, CSR. Seed and Idriss (1971) defined the simplified equation to estimate the equivalent CSR as

$$CSR = \frac{\tau_{ave}}{\sigma'_{vo}} \approx 0.65\frac{\tau_{max}}{\sigma'_{vo}} \approx 0.65\frac{a_{max}}{g}\frac{\sigma_{vo}}{\sigma'_{vo}}r_d \qquad (4.10)$$

where τ_{ave} is the average value of earthquake-induced shear stress, τ_{max} is the maximum value of the earthquake-induced shear stress, a_{max} is the peak seismic acceleration at the ground level, g is the acceleration of gravity; σ_{vo} is the total vertical stress, and r_d is the stress reduction coefficient in function of depth. Equation (4.10) represents the CSR value at the earthquake (moment) magnitude of 7.5. Recently, Equation (4.10) was updated by Idriss (1998) in the form of

$$CSR \approx 0.65\frac{a_{max}}{g}\frac{\sigma_{vo}}{\sigma'_{vo}}\frac{r_d}{MSF} \qquad (4.11)$$

where MSF is the magnitude scaling factor. When MSF equals to 1.0 with the earthquake (moment) magnitude (M_w) of 7.5, MSF was defined as

$$\begin{aligned} MSF &= 37.9\left(M_w\right)^{-1.81} & M_w &> 5.75 \\ &= 1.625 & M_w &\le 5.75 \end{aligned} \qquad (4.12)$$

Idriss (1998) also proposed the value of r_d in the form of

$$\mathrm{Ln}(r_d) = \alpha(z) + \beta(z) M_w$$

$$\alpha(z) = -1.012 - 1.126 \sin[(z/38.5) + 5.133] \tag{4.13}$$
$$\beta(z) = 0.106 + 0.118 \sin[(z/37.0) + 5.142]$$

where z is the depth.

Stark and Olson (1995) compiled 180 case histories and established a chart (Figure 4-20) to show the relationship between the corrected CPT tip resistance and the seismic shear stress ratio at the earthquake (moment) magnitude of 7.5. In Figure 4-16, the term "seismic shear stress ratio" is equivalent to the definition of CSR. In Stark and Olson's database, the 180 case histories were classified into three groups according to mean grain size (D_{50}) and the fines content ($F.C.$). Each line marks the boundary between liquefied case histories (left side of line) and non-liquefied case histories (right side of line).

Olson and Stark (2002) also proposed the updated relationship between S_r/σ'_{vo} and CPT tip resistance. The relationships is

$$\frac{S_r}{\sigma'_{vo}} = 0.03 + 0.0143 q_{cN} \pm 0.03 \qquad for\ q_{cN} \leq 6.5\text{MPa} \tag{4.14}$$

The same reason as Equation (4.9), the CPT tip resistance is not corrected for fines content.

4.4.2.4 <u>Uncertainties for Establishing the Relationship between Field Data and Back-Analyzed Residual Strength of Liquefied Soil</u>

It is valuable to back-calculate the residual strength from the case histories because the natural failure process reflects the true soil behavior. However, the importance of reflecting the true nature of each failure complicates the back-calculation process because the level at which the conditions of each case history is documented is highly variable, and frequently poor. Table 4-7 (Stark et al., 1997) reveals that the back-calculation procedure should involve a careful process to define input parameters with accurate values. The database created from a series of careful evaluations can then be used with confidence. Generally, the parameters involved in the back-calculation procedure can be classified into several groups, such as the structural configuration, source of failure triggering, descriptions of failure in the post-triggering process, site history, and soil properties. Several important factors are discussed in the following paragraphs, including the geometry, failure surface, SPT and CPT resistances, water table, and soil properties.

The geometry (exterior configuration and interior soil layers) may be the most critical factor for the back-calculation procedure. Usually, a well-documented case history records the structural configuration in the pre-failure and post-failure conditions. In the conventional back-calculation method, the upper and lower bound of residual strength values are determined by analyzing stability for those two geometries as discussed in Section 4.4.2.1. When kinetic energy is involved, the geometry should be corrected according to the deformation process. The residual strength can be back-calculated only when kinetic is accounted for.

For using the limit-equilibrium back-calculation procedure, the process involves the force equilibrium among the slices that rest above the failure surface. The locations of the failure surface and the weight of the slice affect the soil resistance at the base of the slice. The location of the failure surface is usually documented according to the discrete measurements made by the in-situ borings. While only a single failure surface is required for the limit-equilibrium approach, the actual location of the concentrated failure area is uncertain because of the information from the discrete measurements.

In each case history, the SPT and CPT resistances are usually represented by one representative value. This SPT or CPT resistance value is determined from the available data, which may include a series of tests at various locations and depths. Descriptions of previous residual strength evaluation procedures indicate that this value has usually been determined by engineering judgment. An estimation of the representative SPT or CPT resistance from several measured values should involve a systematic statistical procedure with corrections for the spatial variation, scattered soil types, and human and device errors. In some cases, the SPT and CPT resistances should be corrected because data were made in different time periods, or in the similar soil stratum but not liquefied. For example, the SPT resistances of the Lower San Fernando Dam were conducted in 1971, and also in 1985. The 1971 SPT data were obtained immediately after the major flow-slide failure, but in the non-liquefied zone. The correction should be made based on the variation of consolidation process in the liquefied and non-liquefied areas. The 1985 SPT data were obtained in the similar locations as the 1971 data. However, the 1971 failure debris had been buried under the reconstructed dam. Besides the correction of non-liquefied SPT resistance to the liquefied SPT resistance, extra correction of 1985 SPT resistance should also involve the degree of consolidation over various timeframes and disturbance caused by reconstruction.

The location of water table an important factor because only the liquefiable soils that are submerged under water can be liquefied and because it controls effective stress levels in the slope. For those case histories that involve the failure of dikes or dams, the water level in the reservoir usually was relatively well documented. However, the location of the water table, or the phreatic surface, inside the soil structure was usually not monitored. Some well-documented case histories provide an approximate position of the water level inside the slope as recorded by monitoring wells during construction, before failure, or after failure. In most of case histories, the water level inside the soil structure can only be estimated according to the soil permeability, water level in reservoir, or judgment.

In the limit-equilibrium stability method, the soil resistance is caused by the cohesional or the frictional resistances. The parameters that define the soil resistance, including the cohesion value and friction angle, can be estimated by the in-situ test or the laboratory test. For some case histories, some degree of objective judgments is involved because of a lack of specific strength information. In this situation, a range of parameter values is used to estimate the range of residual strength.

To summarize the back-calculation procedure, the outcome of the limit-equilibrium stability analysis is dependent upon the quality and quantity of information provided by available documentation. For well-documented case histories, the necessary information for back-calculation procedure is sufficient to produce an estimation with a high degree of confidence. The database created by those cases should provide highly accurate for further predictions. On the other hand, when the poorly-documented case histories are involved in the database, the predictions made from those cases should be considered less reliable. Unfortunately, most of the available case histories are poorly documented. The back-calculation process consequently requires a high degree of judgment based on researchers' own knowledge, or similar information collected from other cases.

In order to treat every case history systematically, the required parameters for the back-calculation procedure should be produced with the highest consistency in documentation and judgment. The best approach is to collect the required parameter data and produce the statistical matrices (e.g. the average value and standard deviation). Consequently, a prescribed distribution (e.g. uniform, normal, or log-normal distribution) should be assigned to each parameter during the back-calculation process. Certain types of parameter, such as the SPT resistance, should be scattered according to their expected spatial variability. As a result, the relationship developed between the residual strength and the SPT resistance can then be systematically established with statistical confidence.

4.4.3 Summary of Evaluation of Residual Strength

Section 4.4 summarizes existing approaches to evaluate the residual strength of the liquefied soils. These include the laboratory-based approach, and the field-based approach. In each approach, several important methods were introduced. Table 4-8 lists the methods that have been discussed in each approach.

In general, the method to evaluate residual strength should be able to take into account the in-situ condition in order to make the best estimation. The in-situ conditions include the failure-triggering agents (e.g. construction load, seismic load, and water table fluctuation), the boundary conditions (e.g. a stiff soil layer and a less permeable boundary), the failure process (e.g. the description of deformation process and the drainage pattern of liquefied soils), and the soil properties (e.g. soil density, cohesion, and friction angle). The laboratory-based approach recreates the in-situ conditions and simulates the process of the soil liquefaction; hence, soil strength can be directly measured. However, the laboratory-based approach to simulate the residual strength still has restrictions because of sample preparation quality, the specimen dimension, and the device limitations. The advantage of the field-based approach can then compensate for the weakness of the laboratory-based approach, because the field-based approach combines advantages from both the in-situ testing technique and the back-analyzing methods. The in-situ testing techniques uses mechanical equipment to characterize the resistance of soils at their original positions, preventing the possible disturbance during the transportation of soils from field to laboratory, and the variation of soil fabric caused by different sample preparation procedures. The in-situ testing results also reflect the soils confined by their natural environment. The disadvantage of in-situ testing is that no soil strength can be directly measured, like the laboratory testing does. Besides, the in-situ testing methods can only be conducted in the discrete spatial locations. The spatial variation of soil properties should be considered when in-situ testing results are used for design. Consequently, evaluation of residual strength in the full-scale in-situ environment can be accomplished using the back-analyzing methods. The back-analyzing methods are to evaluate the residual strength according to the overall geometry and soil properties. The evaluation can therefore be performed under the proper assumption with actual soil behavior and site parameters. Characterizing the parameters for analysis, however, presents a difficulty. The parameters include the exterior and interior geometries, and soil properties. They also include the boundary conditions and the post-triggering failure process. By combining the in-situ testing results and the back-analyzed results, the relationship has been established between the SPT and CPT resistance and the residual strength of liquefied soil. Examples of these relationships was showed in studies made by Seed (1987), Seed and Harder (1990), Stark and Miser (1992), Stark and Olson (1995), Idriss (1998), and Olson and Stark (2002).

4.5 SUMMARY OF RESIDUAL STRENGTH OF LIQUEFIED SOIL

After reviewing particulate flow and debris flow, this chapter started with an introduction of the flow-slide failure, which is often caused by soil liquefaction. Flow-slide failure can be triggered by a sudden reduction in the strength of liquefied soils. The body weight of the soil structure itself starts to accelerate the deformation and kinetic energy prolongs the effect. It is important to understand that kinetic energy, when develops during flow-slide failure, helps transform the soil from the pre-failure geometry to a deformed post-failure geometry. A number of factors affect the behavior of the liquefied soils in both in-situ and laboratory conditions. These factors include the initial conditions (initial effective stress, initial void ratio, and sample preparation procedure), laboratory testing conditions (type of testing apparatus and stress path), material physical properties (particle size, particle surface texture, particle angularity, and fines content), and residual conditions (residual effective stress and residual void ratio). Only the material physical properties and the residual conditions can influence the position of the steady-state line.

The last section in this chapter was a summary of the current common approaches to estimate residual strength. Those approaches include the laboratory-based approach (triaxial test, simple shear test, and ring shear test), the field-based approach. The laboratory-based approach is to reconstruct the field conditions in laboratory and directly estimate the residual strength of liquefied soils. In the field-based approach, a relationship has been established to relate the results from the in-situ tests (standard penetration test (SPT) and cone penetration test (CPT)) to the back-analyzing procedure (limit-equilibrium back-calculation method, Newmark method, and the normalized residual strength ratio method). Databases and relationships have been established by previous researches to use SPT and CPT resistances to estimate residual strength of liquefied soil.

Although some drawbacks still exist in each approach, those approaches can still provide the adequate procedure to evaluate the residual strength. However, the deterministic back-calculation procedure could be improved by involving the uncertainty to define the input parameters, including the soil structure configuration and soil property. Among the case histories, parameters are reported with various quality and quantity. A systematic back-calculation procedure should be established according to various levels of uncertainty involved in defining parameter values. The back-calculated residual strength can then be reported with statistical significance.

	Peak Strength	Quasi-Steady State or Phase Transformation	Steady-State Deformation
Initial Condition			
Initial Effective Stress	×	×	
Initial Void Ratio	×	×	
Sample Preparation	×	×	
Testing Condition			
Testing Apparatus	×	×	?
Stress Path	×	×	
Material Physical Property			
Particle Size	×	×	×
Particle Angularity	×	×	×
Particle Surface Roughness	×	×	×
Fines Content	×	×	×
Residual Condition			
Residual Effective Stress			×
Residual Void Ratio			×

"?": The capacity of testing apparatus to reach large strain

Table 4-1 Classification of factors that affect the residual strength in various stages.

Geographic Region	Hammer Type	Release Method	*ER (%)*	***ER/*60**
North and South America	Donut	2 turns of rope	45	0.75
	Safety	2 turns of rope	55	0.92
	Automatic	Trip	55 to 83	0.92 to 1.38
Japan	Donut	2 turns of rope	65	1.08
	Donut	Auto-trigger	78	1.30
U.K.	Safety	2 turns of rope	50	0.83
	Automatic	Trip	60	1.00
Italy	Donut	Trip	65	1.08
China	Donut	2 turns of rope	50	0.83
	Automatic	Trip	60	1.00

Table 4-2 Energy correction of SPT blowcount (after Canadian Geotechnical Society, 1992).

Fines Content (%)	$\Delta(N_1)_{60}$ (bpf) Seed (1987) and Seed and Harder (1990)	Stark and Mesri (1992)
0	0	0
10	1	2.5
15	-	4
20	-	5
25	2	6
30	-	6.5
35	-	7
50	4	7
75	5	7

Table 4-3 Recommended values of $\Delta(N_1)_{60}$ for various levels of fines content.

Fines Content (%)	Increment of CPT Tip Resistance (ton/ft^2)
≤ 5	0
≈ 10	12
≈ 15	22
≈ 35	40

Table 4-4 Recommended values of tip resistance increment for various levels of fines content (Ishihara, 1993).

Case History	Cause of Failure	Seed (1987)	Seed and Harder (1990)	Stark and Mesri (1992)	Idriss (1998)
Calaveras Dam	1918 Construction	×	×	×	×
Fort Peck Dam	1938 Construction	×	×	×	×
Heber Road	1979 Imperial Valley Earthquake			×	
Kawagishi - Cho Buildings	1964 Niigata Earthquake	×	×	×	×
Koda Numa Highway Embankment	1968 Tokachi-Oki Earthquake	×	×	×	×
La Marquesa Dam, Downstream	1985 Chilean Earthquake		×	×	×
La Marquesa Dam, Upstream	1985 Chilean Earthquake		×	×	×
La Palma Dam	1985 Chilean Earthquake		×	×	×
Lake Ackerman	1987 Seismic Reflection Survey			×	
Lower San Fernando Dam	1971 San Fernando Earthquake	×	×	×	×
Mochi-Koshi Tailings Dam	1978 Izu-Oshima-Kinkai Earthquake	×	×	×	×
Nerlerk Embankment	1990 Construction			×	
River Park, Lake Merced	1979 Imperial Valley Earthquake	×	×	×	×
San Fernando Juvenile Hall Slide	1971 San Fernando Earthquake	×	×	×	×
Sheffield Dam	1925 Santa Barbara Earthquake	×	×	×	×
Snow River Bridge Fill	1964 Alaska Earthquake	×	×	×	×
Solfatara Canal Dike	1940 El Centro Earthquake	×	×	×	×
Uetsu Railway Embankment	1964 Niigata Earthquake	×	×	×	×
Upper San Fernando Dam	1971 San Fernando Earthquake		×	×	×
Whiskey Springs Fan	1983 Borah Peak Earthquake		×	×	×

Table 4-5 Database compiled by Seed (1987), Seed and Harder (1990), Stark and Mesri (1992), and Idriss (1998) to establish relationship between residual strength and $(N_1)_{60\text{-CS}}$.

Case History	Seed (1987) $(N_1)_{60\text{-CS}}$ (bpf)	Seed (1987) S_r (psf)	Seed and Harder (1990) $(N_1)_{60\text{-CS}}$ (bpf)	Seed and Harder (1990) S_r (psf)	Stark and Mesri (1992) $(N_1)_{60\text{-CS}}$ (bpf)	Stark and Mesri (1992) S_r/σ'_{vo}	Stark and Mesri (1992) S_r (psf)
Calaveras Dam	12	750	12	650±50	12	0.228	650±50
Fort Peck Dam	11	600	10	350±100	10	0.032	350±100
Heber Road					1.5	0.125	100
Kawagishi - Cho Buildings	4	120	4	120	4	0.098	120
Koda Numa Highway Embankment	3	50	3	50	3	0.032	50
La Marquesa Dam, Downstream			11	400±150	11	0.224	400±150
La Marquesa Dam, Upstream			6	200±100	6	0.125	200±100
La Palma Dam			4	200±100	4	0.120	200±100
Lake Ackerman					4	0.117	215±45
Lower San Fernando Dam	15	750	13.5	400±100	13.5	0.102	400±100
Mochi-Koshi Tailings Dam	6	250	5	250±150	5	0.092	250±150
Nerlerk Embankment					11 - 11.5	0.148	
River Park, Lake Merced	5	100	6	100	6	0.105	100
San Fernando Juvenile Hall Slide	6	140	10.5	130±70	10.5	0.067	130±70
Sheffield Dam	6	50	6	75±25	6	0.038	75±25
Snow River Bridge Fill	5	50	7	50	7	0.024	50
Solfatara Canal Dike	5	130	4	50±25	4	0.052	50±25
Uetsu Railway Embankment	3	35	3	40	3	0.015	40
Upper San Fernando Dam			15	600±100	15	0.202	600±100
Whiskey Springs Fan			11	150±10	11	0.057	150±10

Table 4-6 Database of $(N_1)_{60\text{-CS}}$, S_r, and S_r/σ'_{vo}, proposed by Seed (1987), Seed and Harder (1990), and Stark and Mesri (1992).

Field Data to be Obtained	Flow Slides	Lateral Spreads
Pre-Failure Geometry	Important/Critical	Critical
Post-Failure Geometry	Critical	Critical
Movements:		
Magnitude, distribution, and area extent of displacements	Critical	Critical
Sequence/Time Rate	Important	Critical
Type/Mechanism of Movement	Important	Critical
Distress/Cracking/Bulging	Important	Critical
Stratigraphy	Critical	Critical
In-situ Properties:		
Penetration Resistance	Critical	Critical
Unit Weights	Relevant	Relevant
Gradation	Important	Important
Plasticity	Important	Important
Static Shear Strength	Relevant	Relevant
Shear Wave Velocity	Relevant	Relevant
Gradational Changes	Critical	Critical
Stress History	Critical	Critical
Identification and delineation of liquefied soil layer	Critical	Critical
Three-Dimensional Effects	Important	Important
Location of phreatic surface/saturation	Critical	Critical
General Earthquake Characteristics:		
Time Histories	Important	Critical
Magnitude	Important	Critical
Peak Acceleration	Important	Critical
Depositional History	Important	Important
Historic Seismic Performance	Important	Important
Consideration of modified inertial loading through liquefied layer	Relevant	Critical

Table 4-7 Importance of field data to evaluate residual strength based on case histories (The Workshop of Shear Strength of Liquefied Soils, Stark et al., 1997)

Laboratory-Based Approach	Field-Based Approach	
	In-Situ Testing Techniques	**Back-Analyzing Methods**
Triaxial Test	Standard Penetration Test	Limit-Equilibrium Back-Calculation Method
Simple Shear Test	Cone Penetration Test	Newmark Method
Ring Shear Test		Normalized Residual Strength Ratio Method

Table 4-8 List of methods to evaluate the residual strength of the liquefied soil.

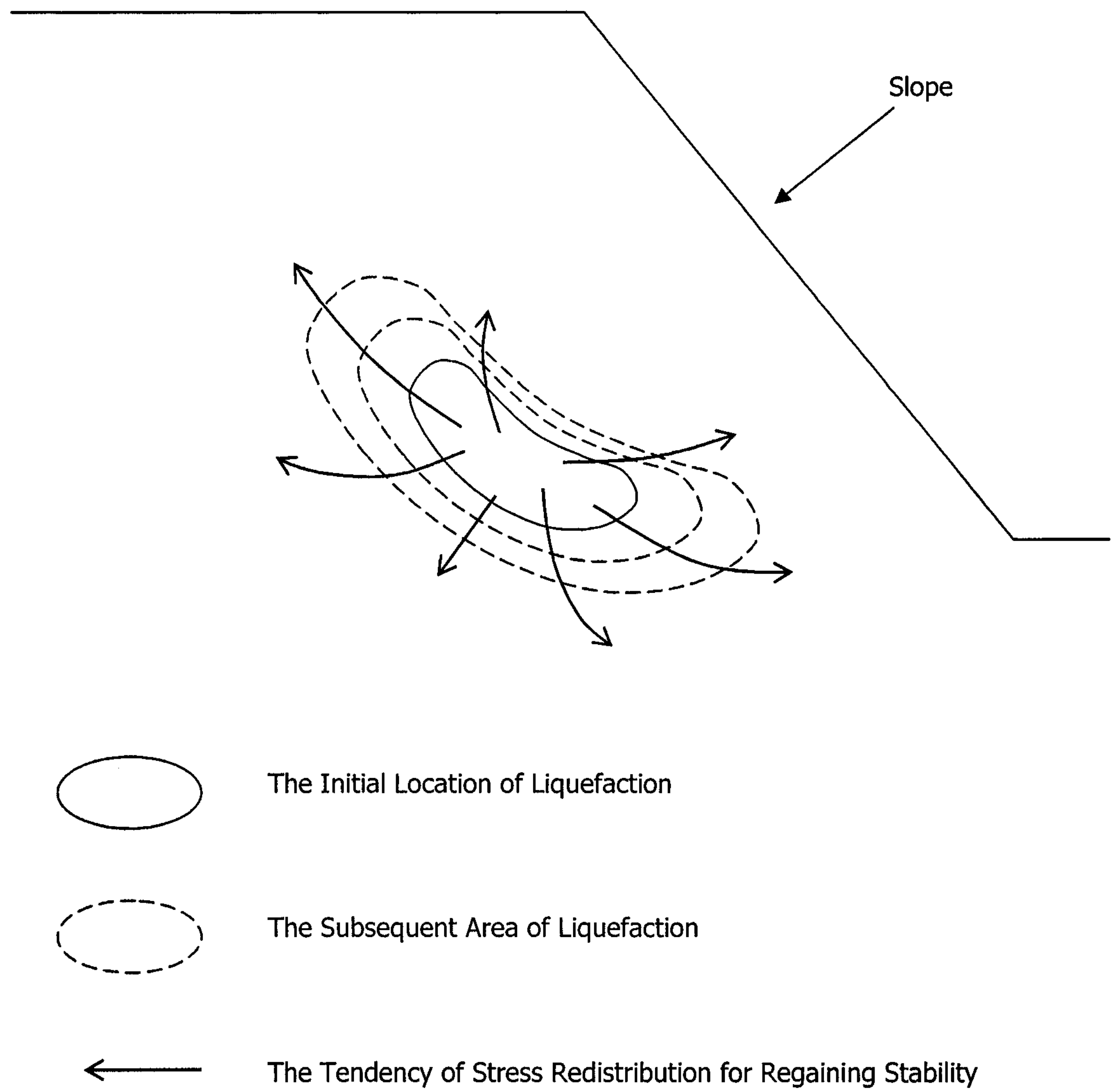

Figure 4-1 Propagation of stress redistribution during the initiation of the flow-slide failure.

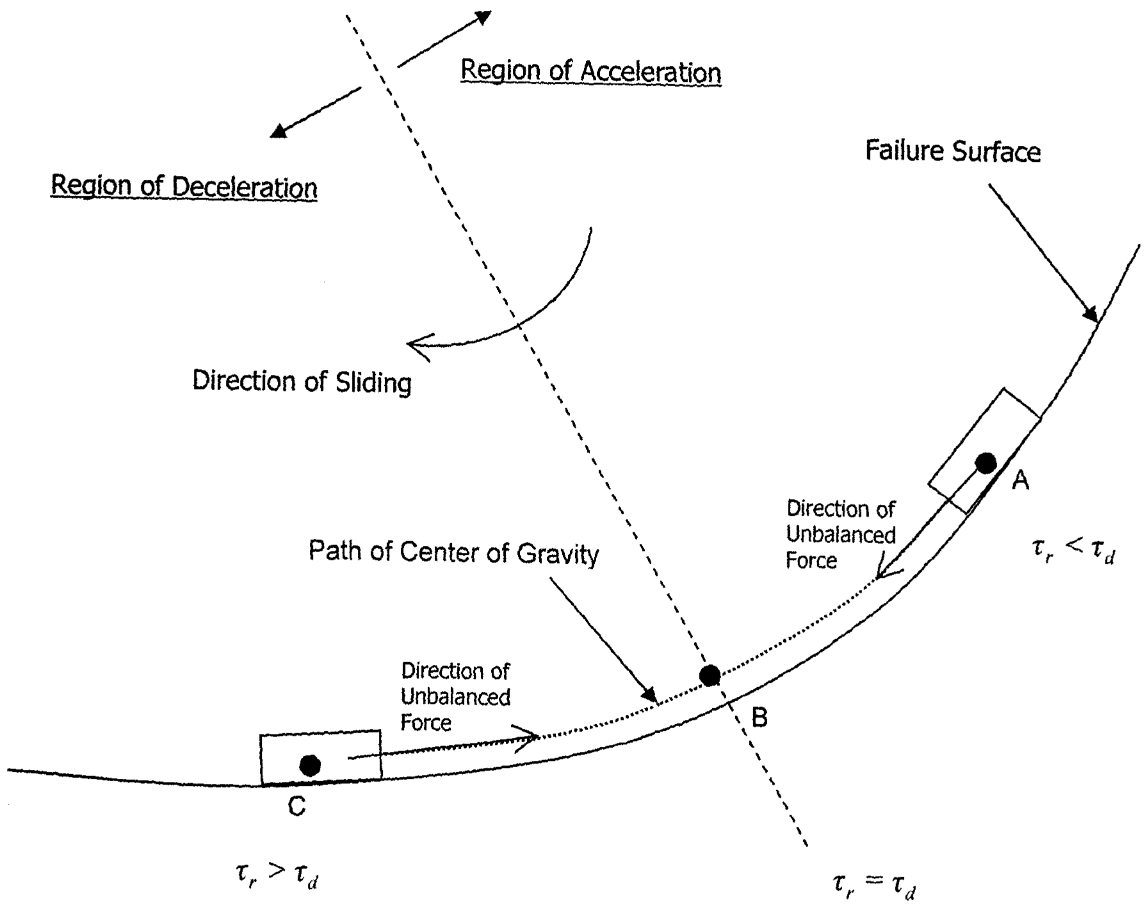

Figure 4-2 Scheme of the flow-slide failure model with the kinetic effect (after Davis et al., 1988).

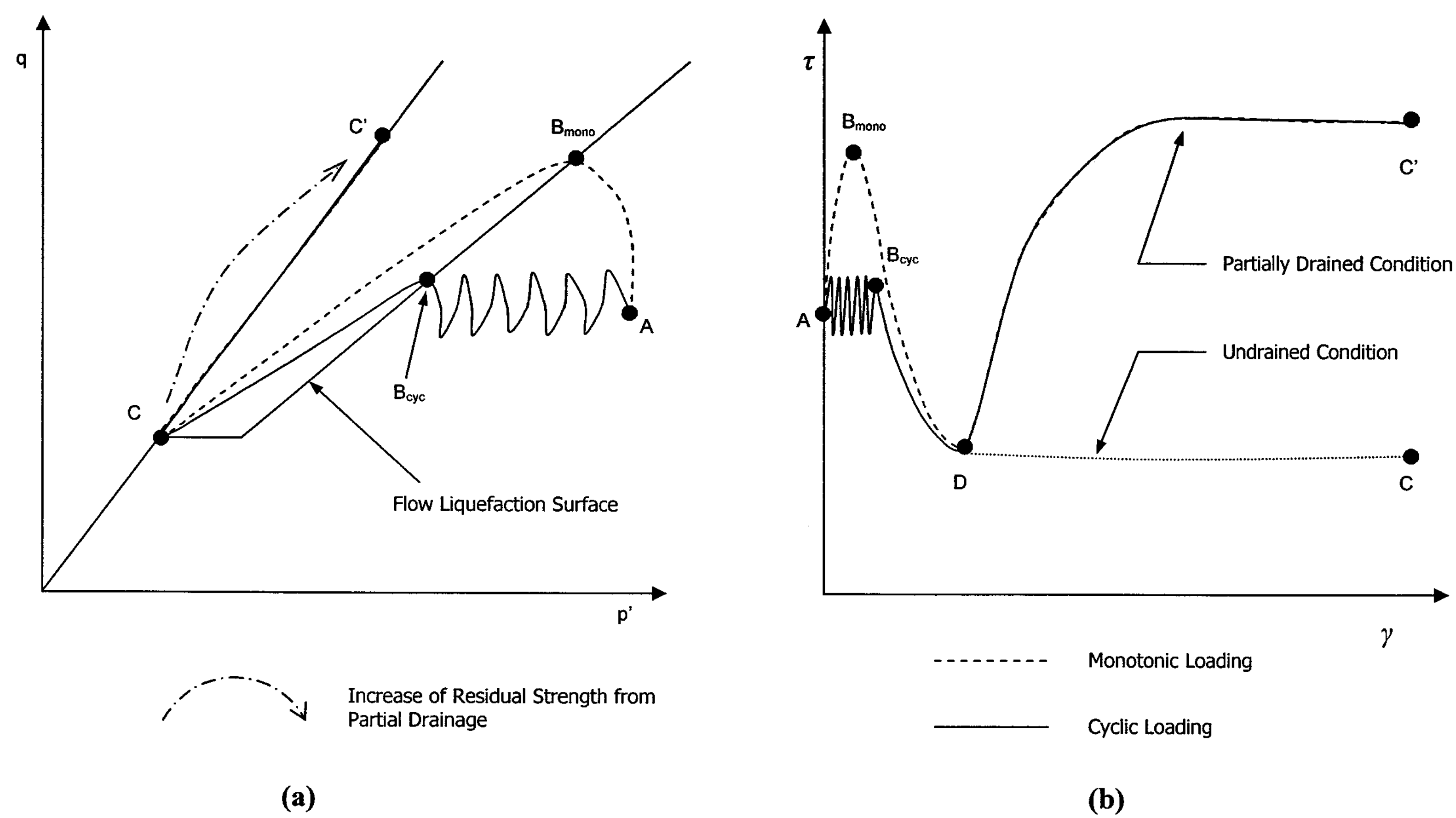

Figure 4-3 Liquefied soil behavior under the influence of the partial drainage, illustrated by (a) stress path and (b) shear stress (τ) versus shear strain (γ).

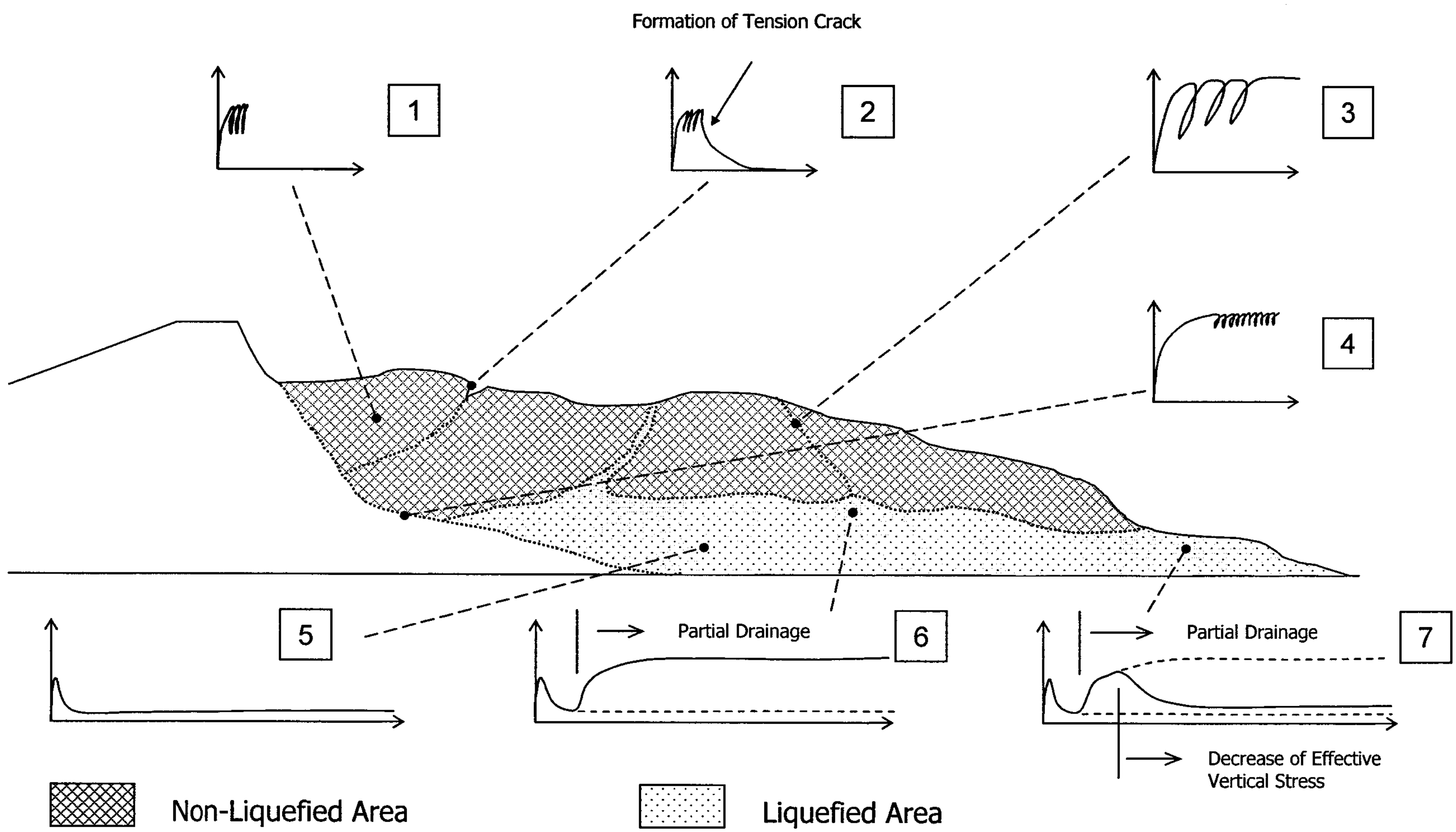

Figure 4-4 Various soil behaviors within the flow-slide debris.

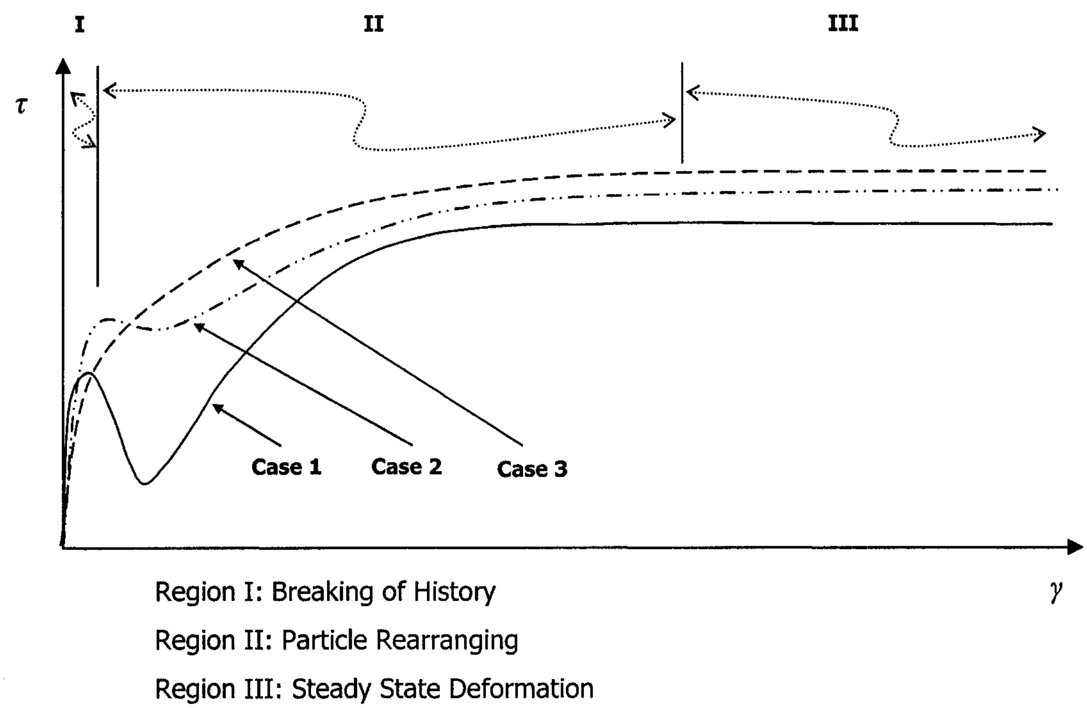

Figure 4-5 Scheme of various regions defined in shear stress (τ) versus shear strain (γ).

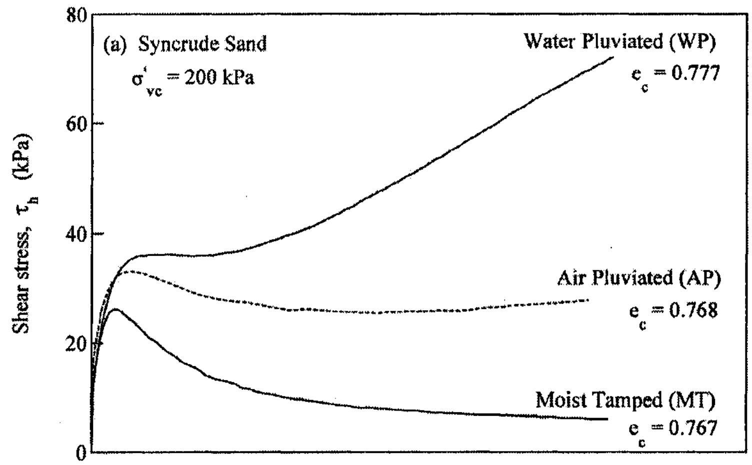

(a)

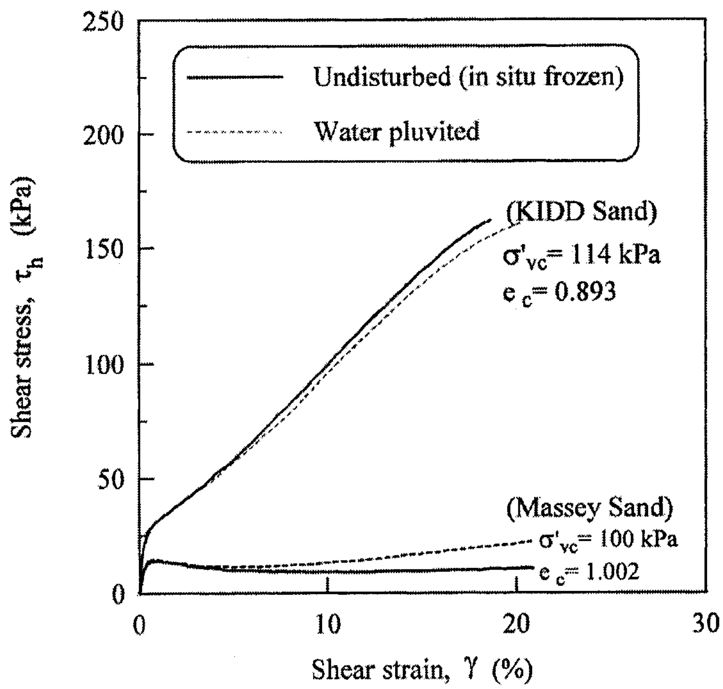

(b)

Figure 4-6 Soil behaviors based on various sample preparation techniques (a) water pluviation, dry pluviation, and moist tamping and (b) water pluviation and in-situ ground freezing (Vaid et al., 1999).

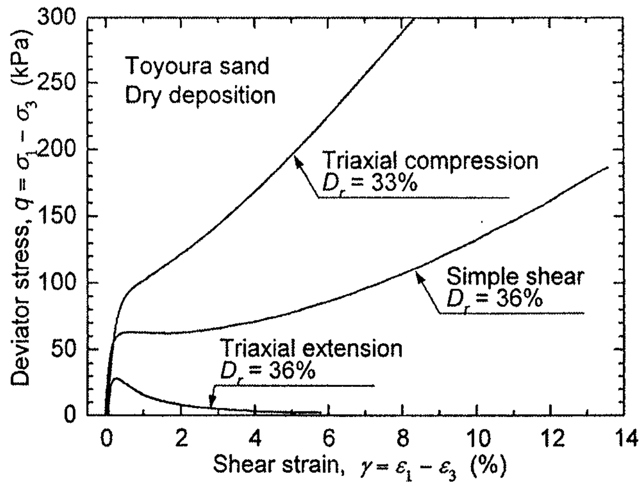

(a)

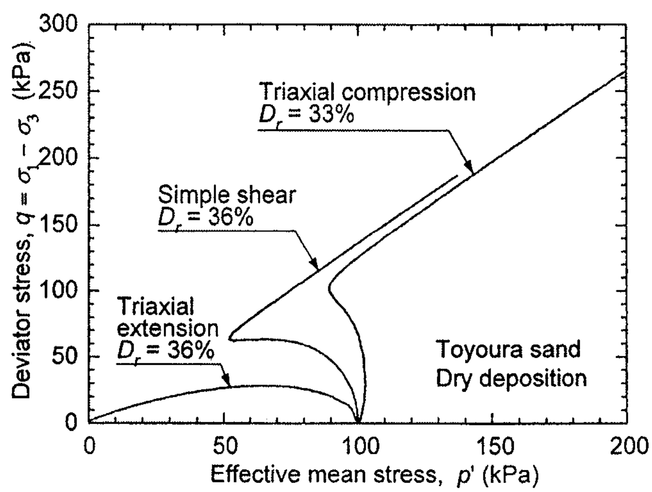

(b)

Figure 4-7 Soil behaviors affected by various testing devices (Yoshimine et al., 1999).

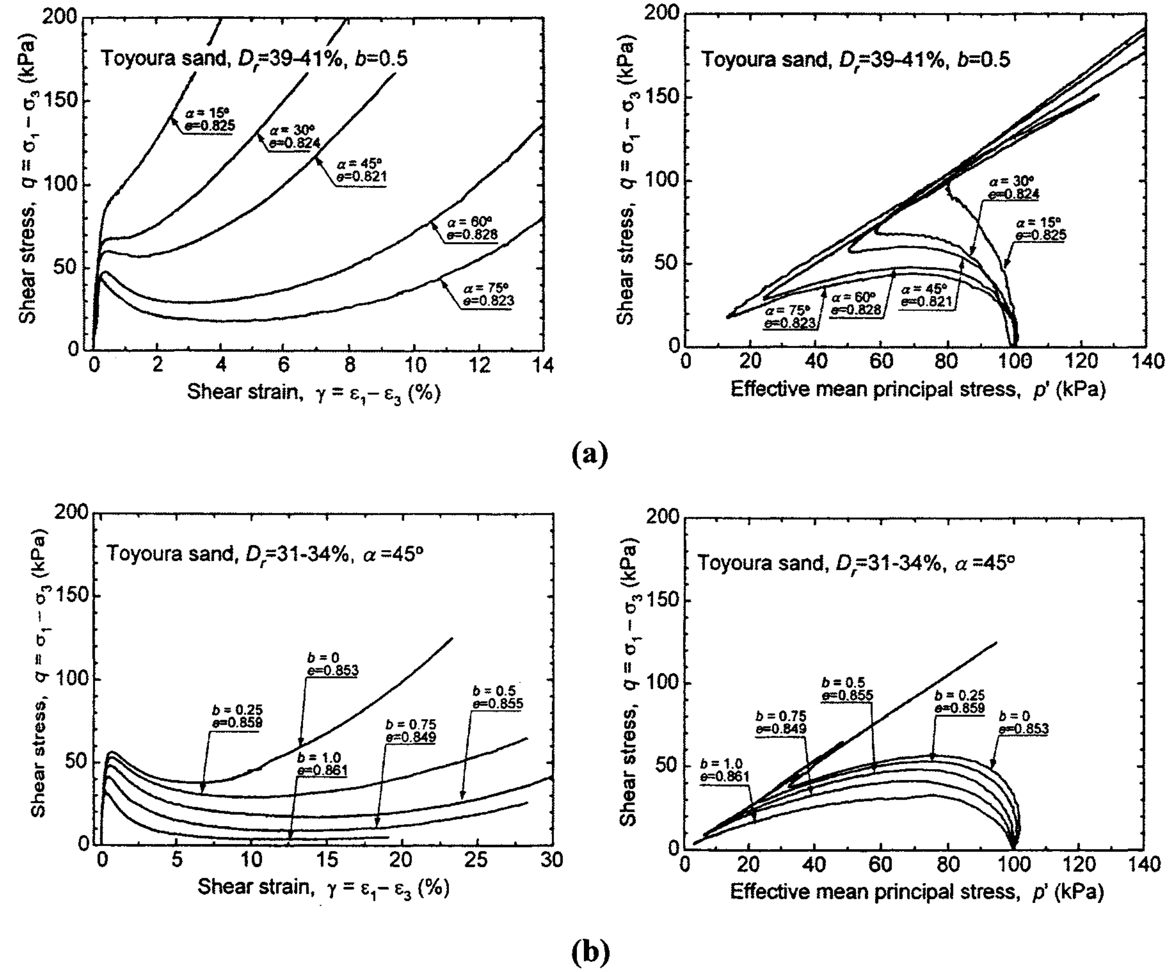

Figure 4-8 Soil Befaviors affected by stress path (Yoshimine et al., 1998).

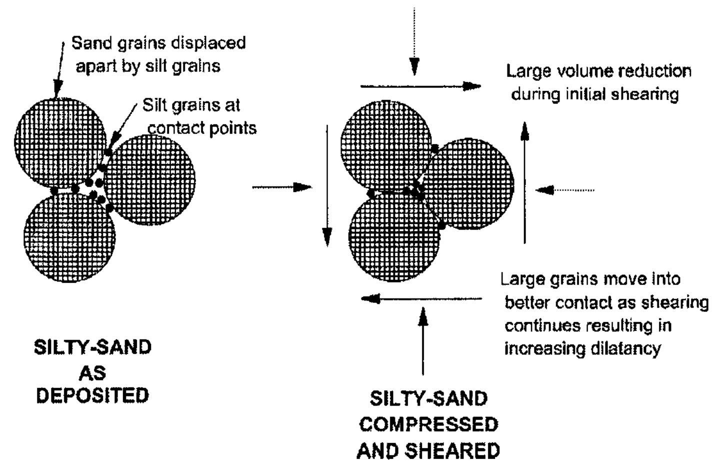

(a)

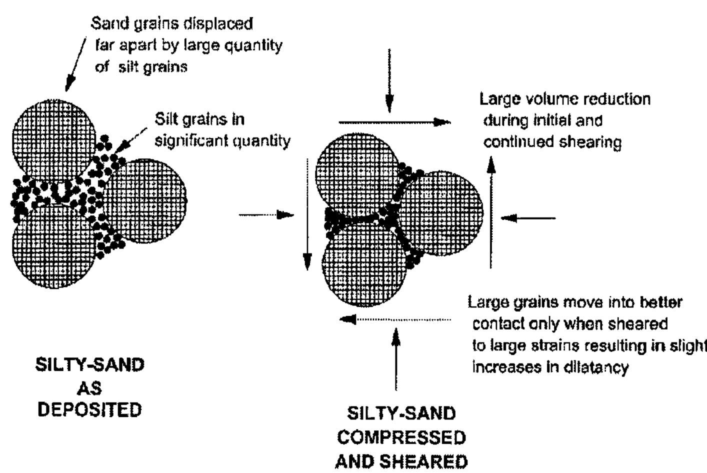

(b)

Figure 4-9 Schemes of soil sassemblies composed by (a) low silts content (Yamamuro and Lade, 1997) and (b) high silts content (Yamamuro and Covert, 2001).

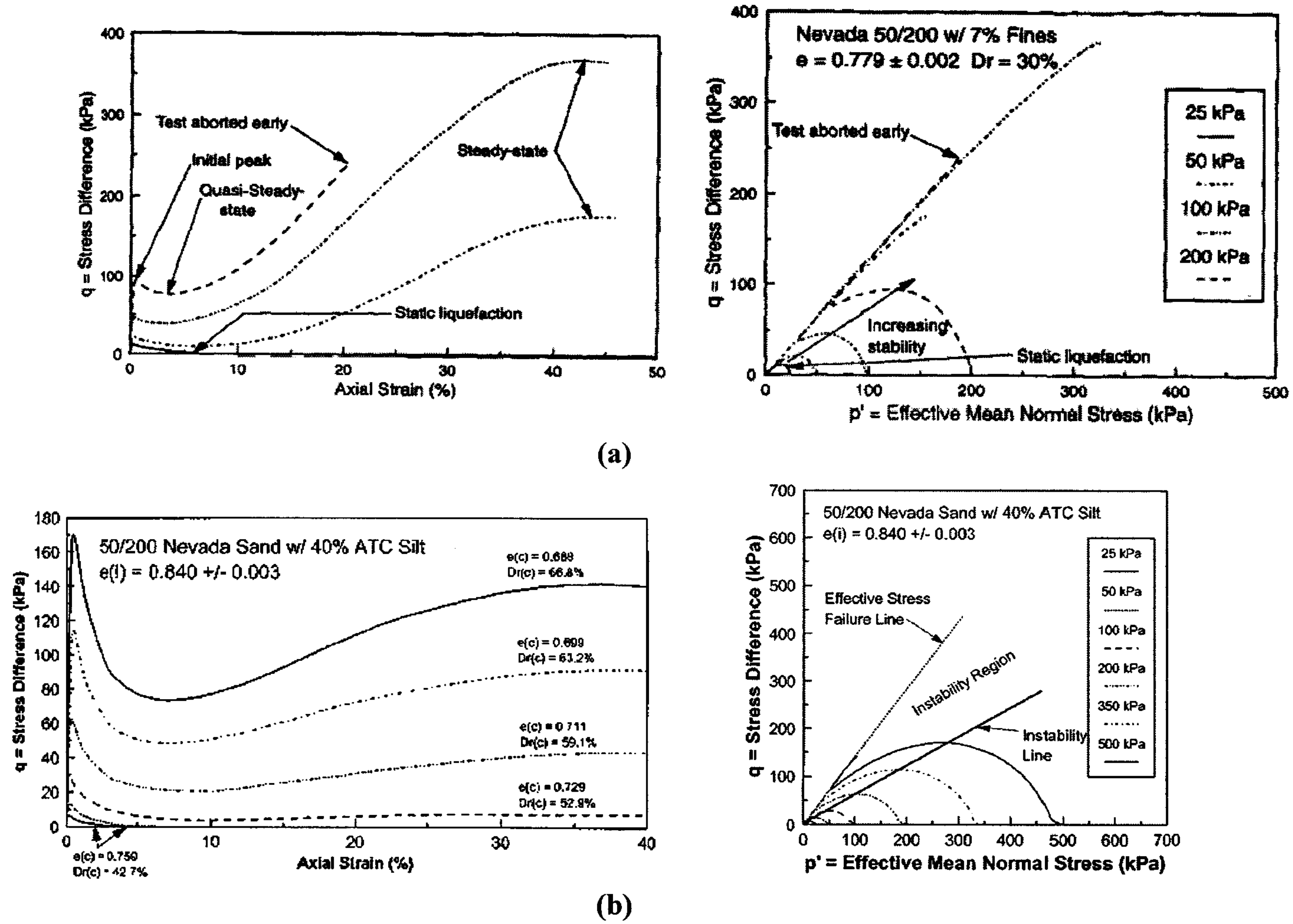

Figure 4-10 Undrained triaxial test results of specimens with (a) 7% of silts content (Yamamuro and Lade, 1998) and (b) 40% of silts content (Yamamuro and Covert, 2001).

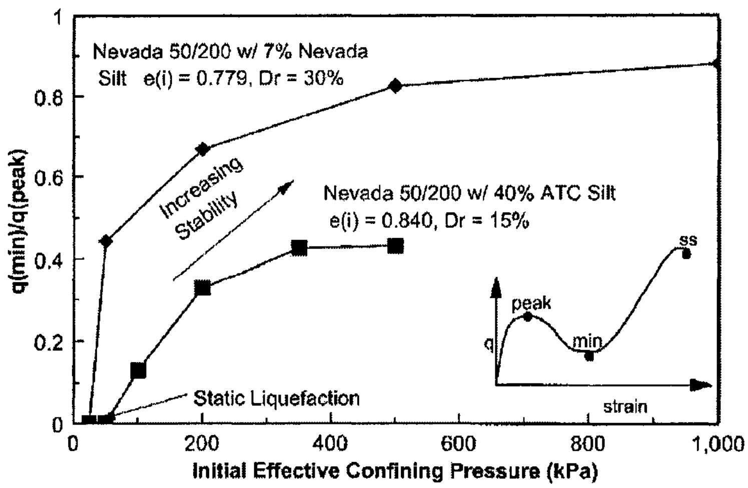

(a)

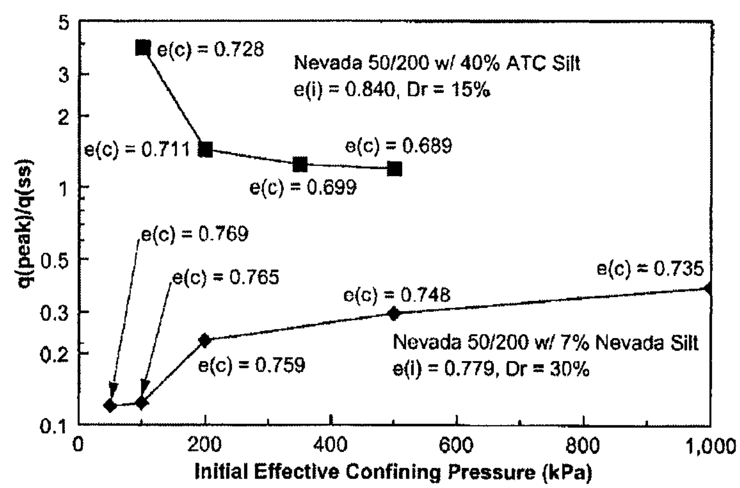

(b)

Figure 4-11 Effect of silts content on the stress ratio with various initial effective stress, (a) stresses at quasi-steady state to peak and (b) stresses at steady state to peak (Yamamuro and Covert, 2001).

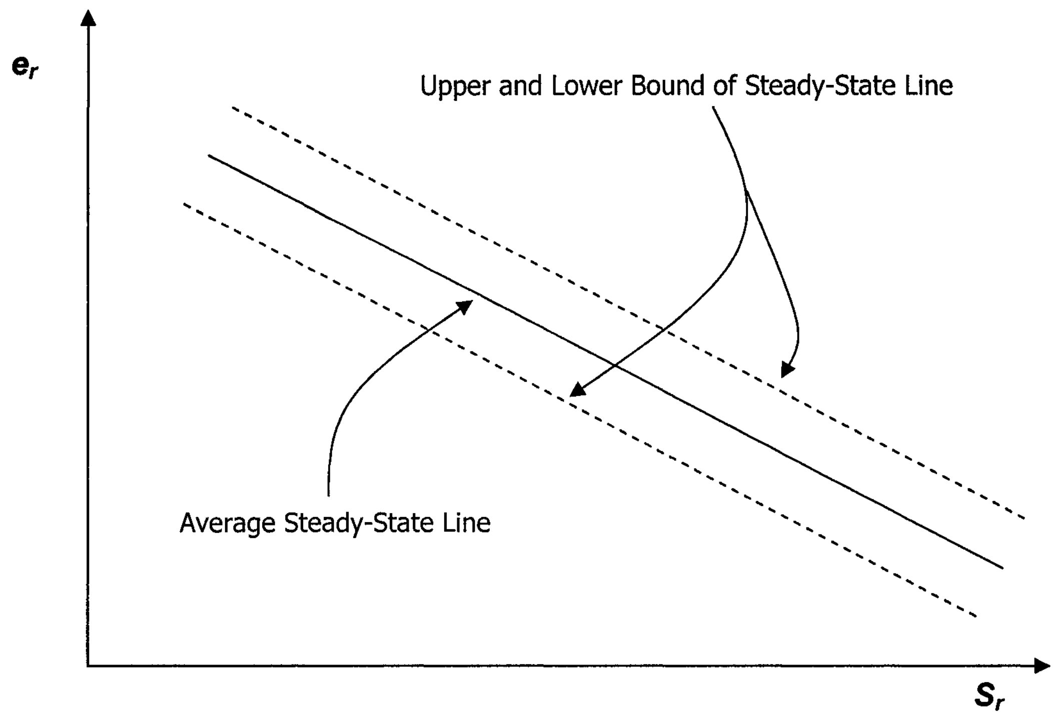

——	Affected by particle size, particle angularity, particle surface roughness, fines content, residual effective stress, and residual void ratio.
- - - - - -	Affected by particle size, particle angularity, and particle surface roughness.

Figure 4-12 Ideal steady-state band described by the average steady-state line with the upper and lower bounds.

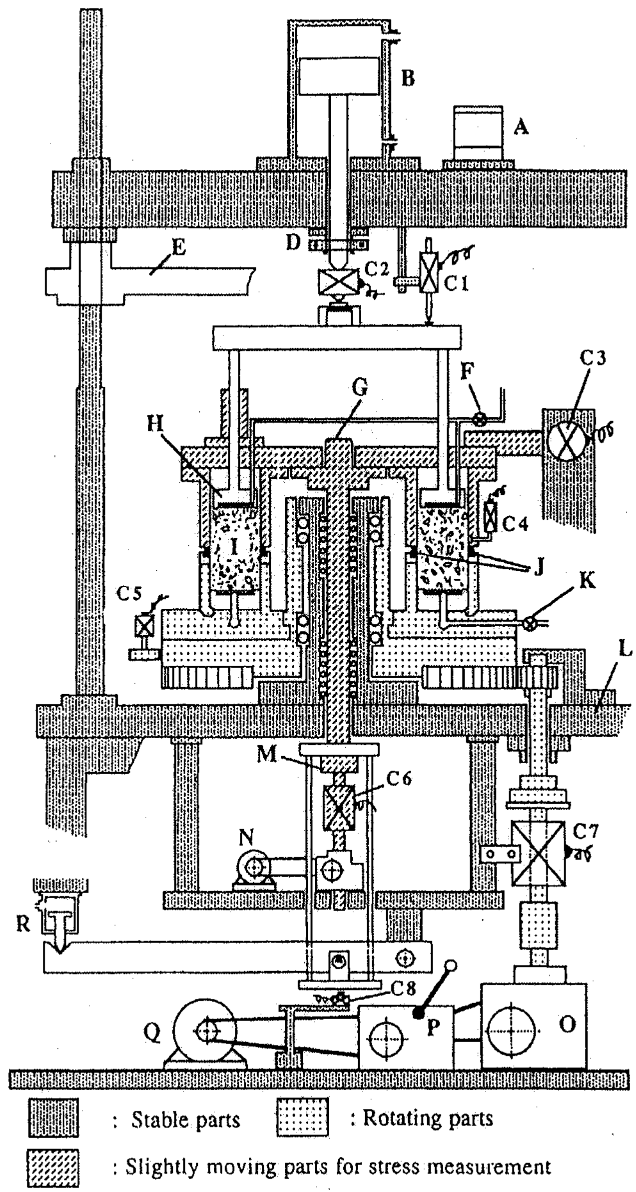

A: Lifting-crane motor, B: Air piston, C_1: Sample-height linear transducer, C_2: Vertical load cell (VL1), C_3: Shear resistance load cell, C_4: Pore pressure transducer, C_5: Shear displacement rotary transducer, C_6: Vertical load cell (VL2), C_7: Torque transducer, C_8: Gap sensor for gap controlling, D: Piston-axis stopper, E: Lifting arm, F: Upper draining valve, G: Central axis, H: Loading plate, I: Sample, J: Rubber edges, K: Lower draining valve, L: Base, M: Rotary joint, N: Gap control servo motor, O: Transmission gear box, P: Reducer gear box, Q: Shearing servo motor, R: Air piston cylinder for counter dead-weight.

Figure 4-13 Schematic diagram of the undrained cyclic ring shear apparatus (Shoaei and Sassa, 1994).

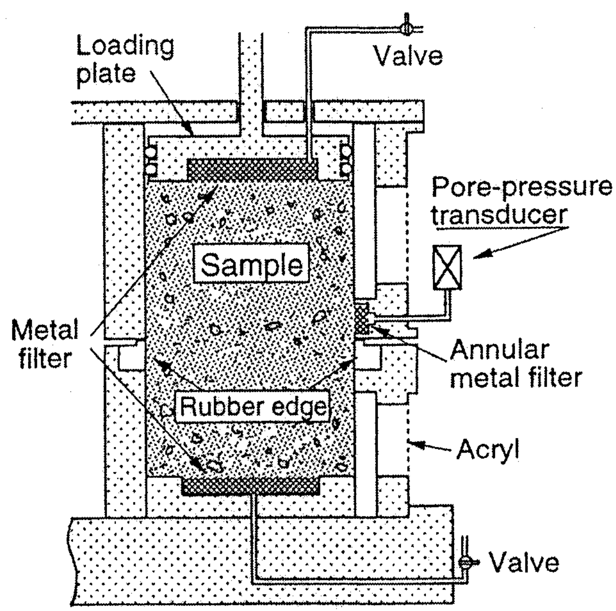

Figure 4-14 The enlarged cross-section view of the sample space (Lee and Sassa, 1996).

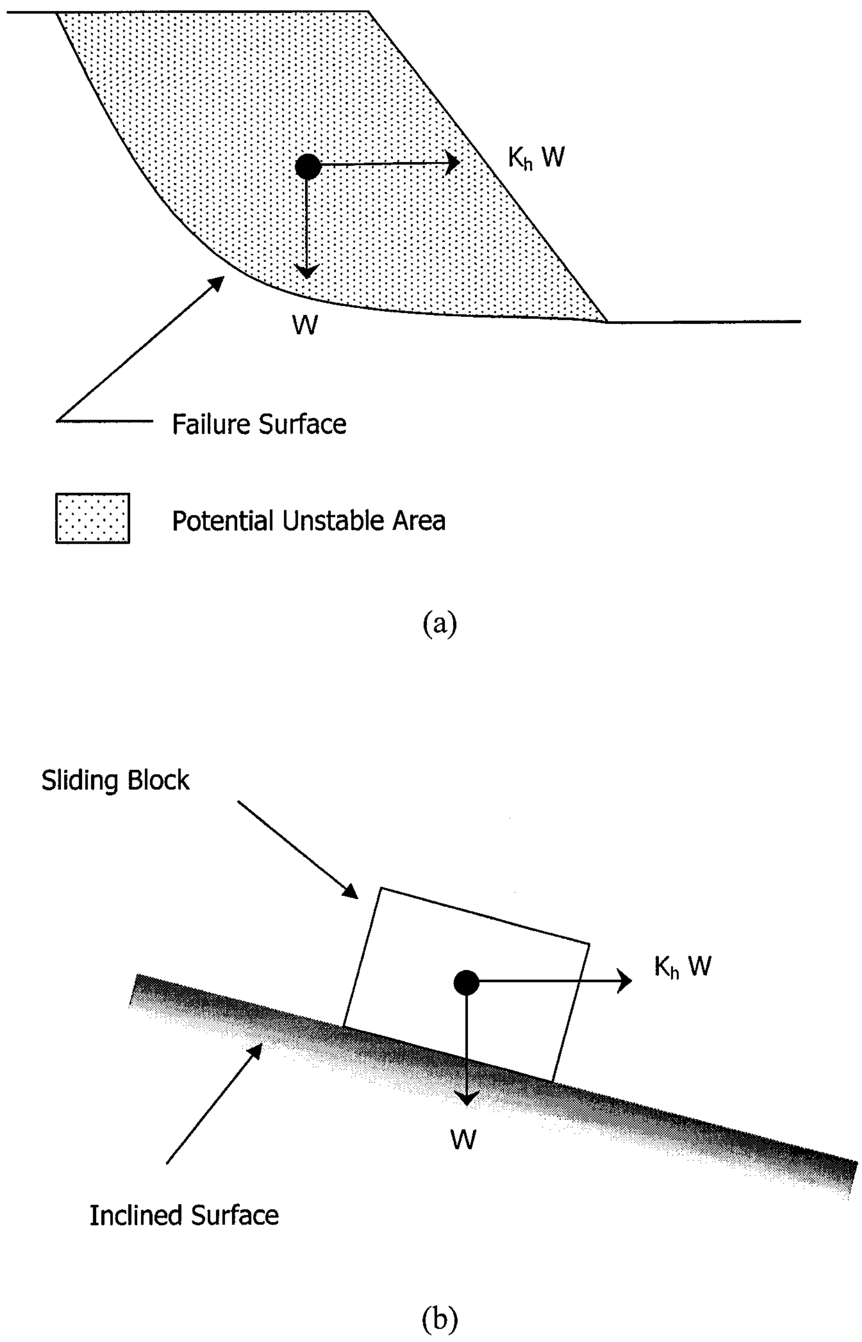

Figure 4-15 Schemes of stability analysis, (a) pseudostatic stability analysis and (b) sliding block analysis.

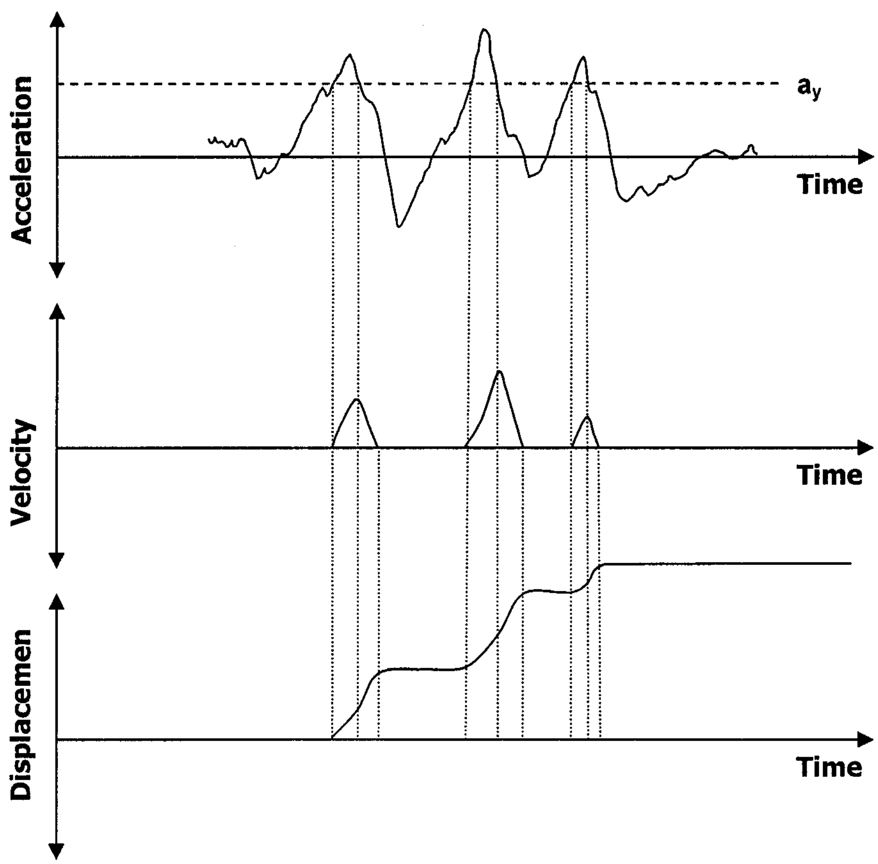

Figure 4-16 Newmark method to estimate deformation caused by seismic forces.

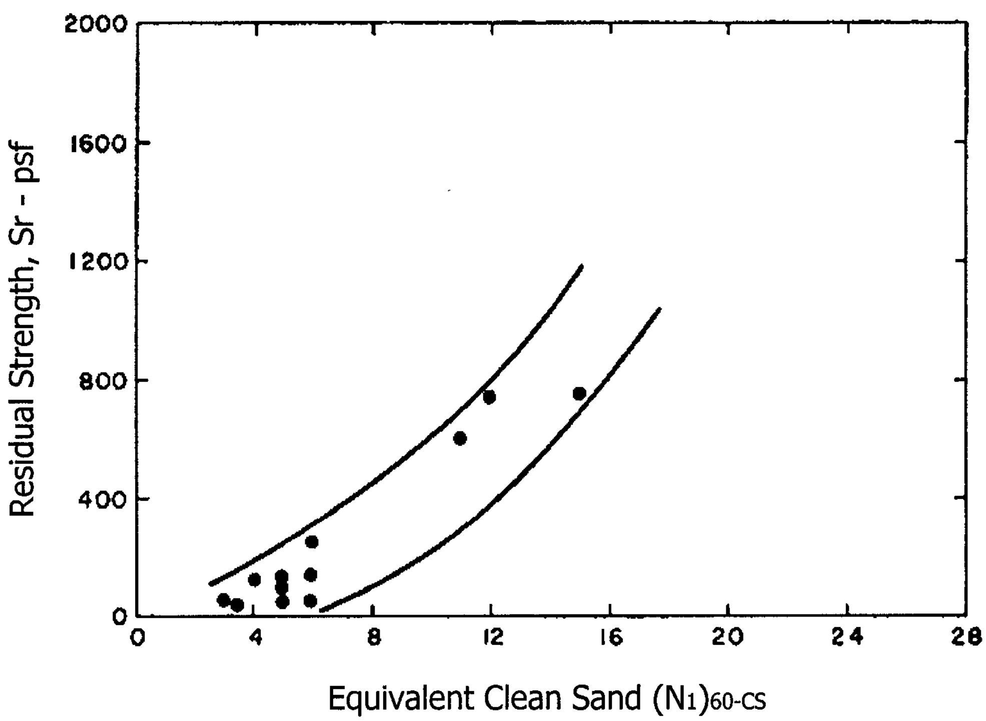

Figure 4-17 Back-calculation results of residual strength versus $(N_1)_{60\text{-CS}}$, proposed by Seed (1987).

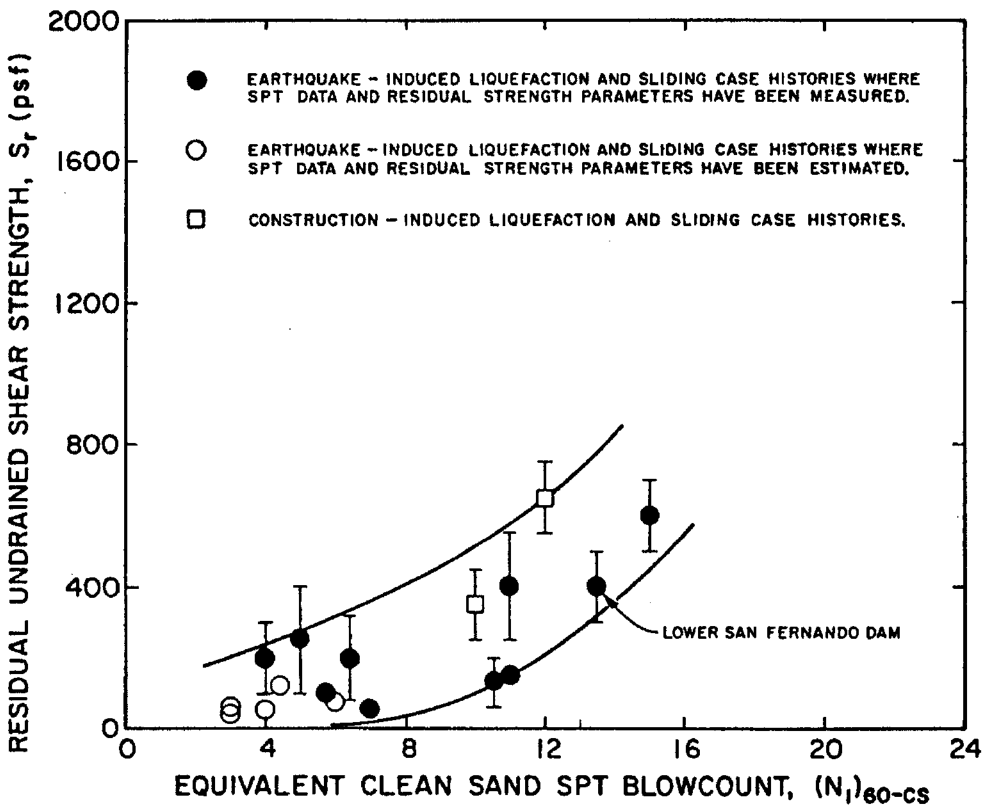

Figure 4-18 Back-calculation results of residual strength versus $(N_1)_{60\text{-CS}}$, proposed by Seed and Harder (1990).

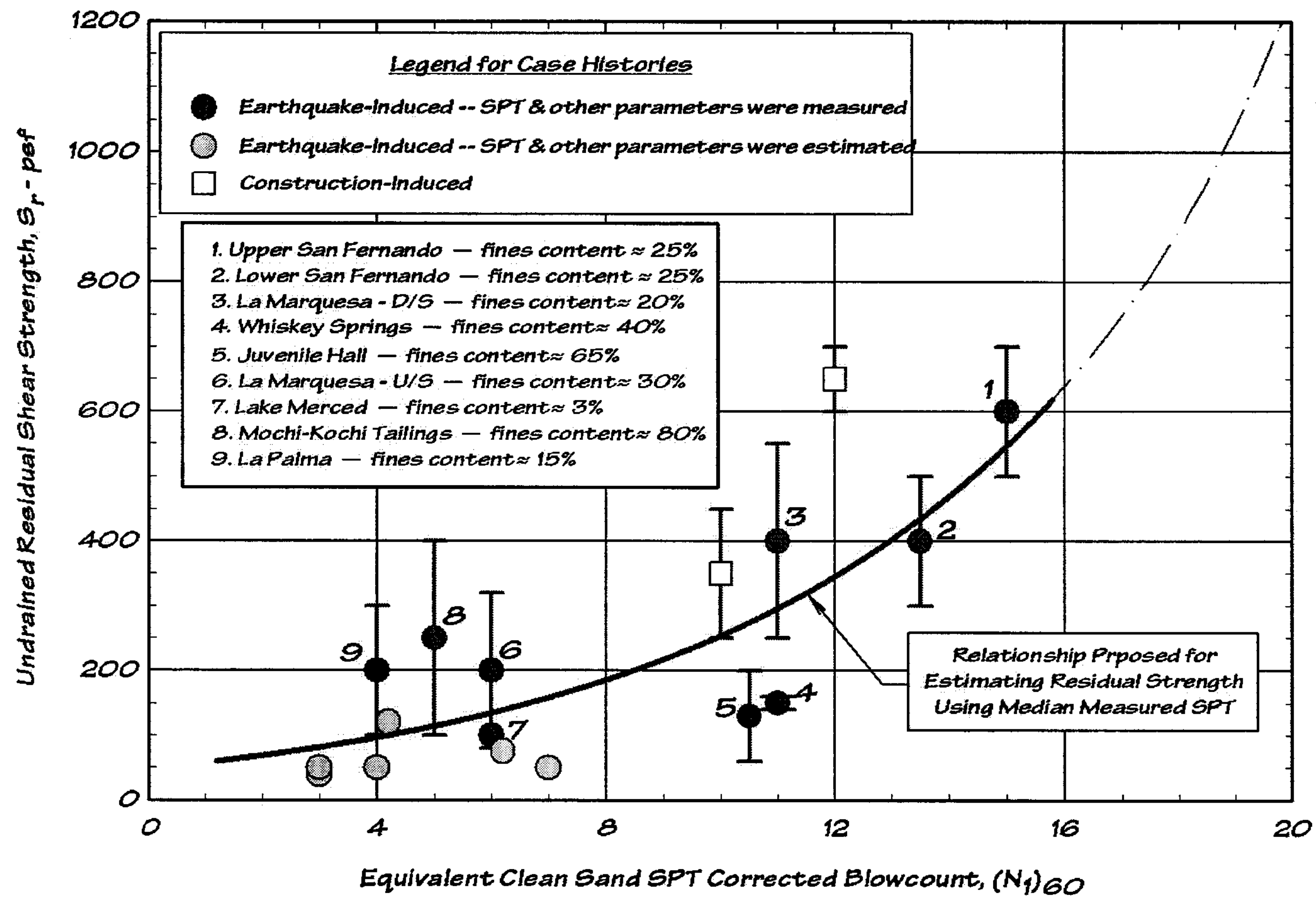

Figure 4-19 Relationship between the residual strength and $(N_1)_{60\text{-CS}}$, proposed by Idriss (1998).

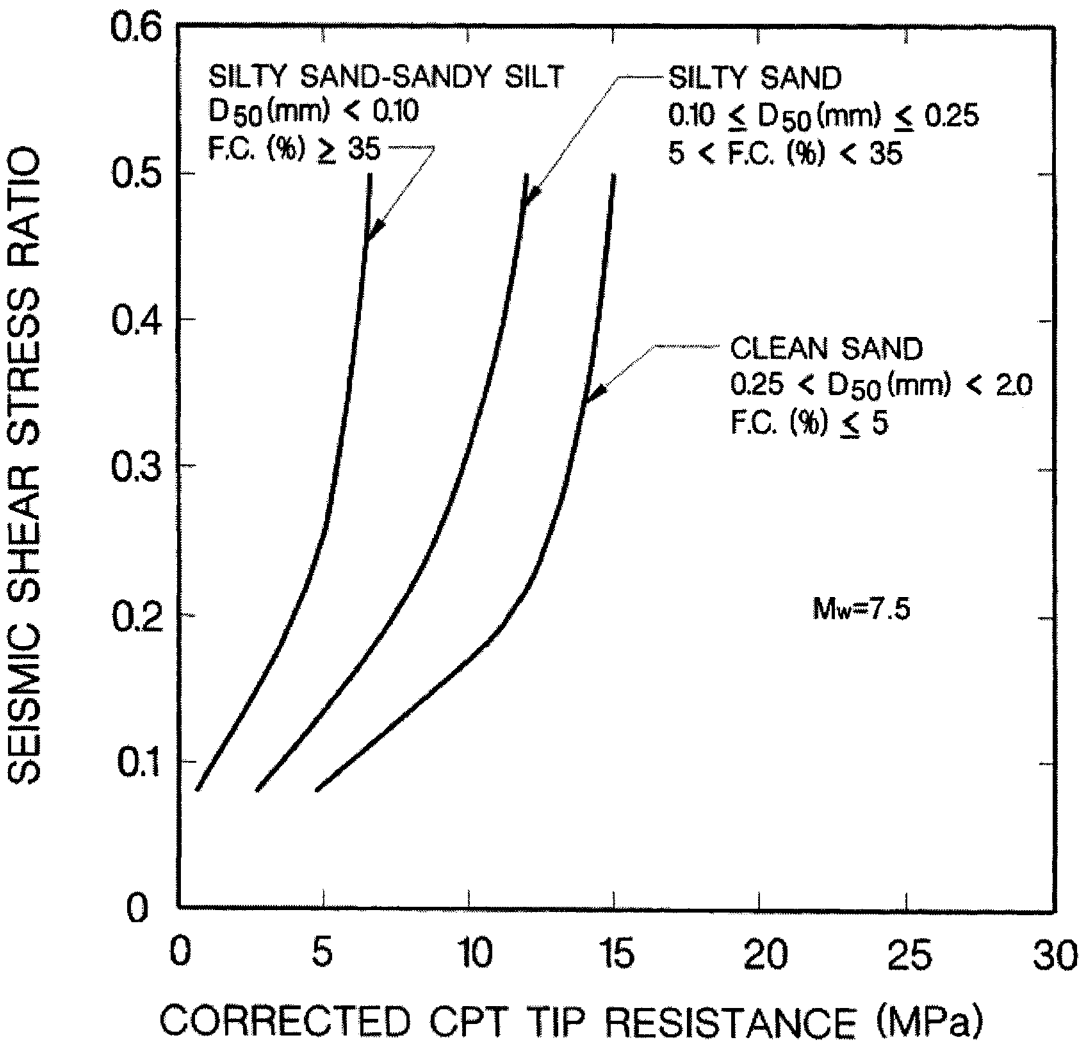

Figure 4-20 Relationship between the corrected CPT tip resistance versus the seismic shear stress ratio (Stark and Olson, 1995).

Chapter 5

Case History Back-Calculation

5.1 INTRODUCTION

As discussed in previous chapters, the residual strength of liquefied soil has frequently been estimated by analysis of flow slide case histories. These analyses have generally consisted of two primary elements: (1) determination of some "representative" value of penetration resistance and (2) back-calculation of a residual strength that is consistent with the observed failure. The resulting penetration resistance/residual strength "pair" provides a single data point that represents the relationship between residual strength and penetration resistance for that case history. Determination of that relationship for multiple case histories results in a set of data points which several researchers have used to establish procedures for predicting residual strength as a function of penetration resistance.

A limited number of flow slide case histories are available for interpretation, and these case histories span a range of slope sizes, material types, and failure conditions. Of the available case histories, some are well documented and some are poorly documented. In the development of existing procedures for residual strength prediction, all available case histories have been analyzed and their results combined for development of predictive relationships. The case histories have not explicitly been distinguished between on the basis of size, failure mechanism, or the quantity and quality of available supporting data. Thus, all case histories – small and large, well-documented and poorly-documented – have implicitly been given equal weight in the development of residual strength predictive relationships.

This chapter presents a procedure that can be used to develop predictions of residual strength that reflect the quantity and quality of available data, and implicitly give more weight to case histories for which data of good quality and quantity are available.

The procedure requires explicit identification and characterization of uncertainty in the variables that contribute to residual strength, and incorporation of the uncertainty in those variables in the back-calculation process. The application of this procedure to a specific case history, that of the flow slide at Wachusett Dam, is described in the following chapter.

5.2 IDENTIFICATION AND CHARACTERIZATION OF UNCERTAIN VARIABLES

The stability of slopes, like many other problems of geotechnical and structural engineering, is a function of geometry and material properties. Analysis of slope stability, therefore, requires characterization of the geometry and material properties of a slope. Geometric variables include those that describe the external geometry of the slope, the geometry of individual layers of soil/rock within the slope, the geometry of any phreatic surface within the slope, and the geometries of potential failure surfaces. Material property variables include measures of density and available shearing resistance.

5.2.1 Geometric Variables

The external geometry of a slope plays a major role in determination of its stability. All other things, in particular available shear strength, being equal, it is obvious that steep slopes are less stable than flat slopes. The converse of that statement provides a fact often used in geologic interpretation – steep slopes are likely to contain stronger soils than flat slopes. In the context of back-calculation of shear strength from case history data, therefore, accurate characterization of slope geometry is necessary for back-calculation of reliable shear strengths.

The following sections describe factors that influence the geometry of slopes used in flow slide back-calculation. These factors are more important for flowslides than geometric factors in back-calculation exercises for more typical failures due to two primary reasons: (1) flow slide case histories involve larger displacements than conventional failures, hence, the difference between the pre-failure geometry and the post-failure geometry is often very large, and (2) the materials involved in flow slides can travel at much higher velocities than those involved in conventional failures, hence, the role of dynamic effects must be considered in the interpretation of these case histories.

5.2.1.1 Kinetic Effects

When a soil mass liquefies, the residual strength may drop below the shear stress required to maintain static equilibrium. If this occurs, the soil mass is acted upon by an unbalanced force equal to the difference between the resultant of the driving stress and the resultant of the soil resistance. When acted upon by this unbalanced force during failure, the unstable mass initially accelerates and then decelerates until it comes to rest in its final, post-failure geometry. Inertial forces act on the unstable mass while it is accelerating and decelerating. During acceleration, the inertial force acts in the uphill direction, and during deceleration it acts in the downhill direction. Therefore, the final geometry reflects the residual strength of the liquefied soil, but also the inertial force during deceleration. If the failure took place very slowly, there would be no inertial forces and the unstable zone would come to rest at the point where the inertial force was zero. At the point at which it is neither accelerating nor decelerating – i.e. when it reaches its maximum velocity – there are no inertial forces acting on the mass. Accurate back-calculation of the residual strength of a liquefied soil, if performed using static slope stability analyses, should be performed using the slope geometry that corresponds to this condition of no inertial forces.

Simplified Analysis of Kinetic Effects

Davis et al. (1988) used a simple sliding block analogy to account for the kinetic effect on residual strength by using Newton's second law of motion to describe the movement of the center of gravity of the failure soil mass :

$$F = m\,a \tag{5.1}$$

where F is the unbalanced force acting on the failed soil mass, m is the mass of failed soil mass, and a is the acceleration. Using a hyperbolic function, Davis et al. (1988) described the path for failed soil mass during its transformation from its pre-failure to post-failure geometry. Olson et al. (2000) and Olson (2001) chose a third-order polynomial to describe the path, and assumed that the center of gravity moved along a path parallel to the estimated failure surface. The third-order polynomial was approximately expressed as

$$y=c_1x^3+c_2x^2+c_3x+c_4 \tag{5.2}$$

where c_1 - c_4 are constants that describe the path of the center of gravity between its pre-failure and post-failure positions.

Figure 5-1a shows the scheme for back-calculation of residual strength with the kinetic effect. The net force (unbalanced force), F, acts on the block that simulates the failed soil mass as it moves downslope on the path described by Equation (5.2). The net force driving the movement can be described as

$$F=W\,sin\theta\text{-}S_r\,L = m\,a \tag{5.3}$$

where W is the weight of the failed soil mass, θ describes the local slopes, S_r is the residual strength, and L is the length of the failure path within the liquefied zone. When the resistance of the non-liquefied materials is involved in the calculation, Equation (5.3) is revised as

$$F=[W\sin\theta - S_r L_1+(C_{NL}+\sigma'_{vo}\tan\varphi')L_2]=ma \tag{5.4}$$

where σ_{vo} is the vertical effective stress at the sliding surface, φ is the effective stress friction angle of the non-liquefied material, C_{NL} is the cohesion of the non-liquefied material, and L_1 and L_2 are the length corresponding to the resistances of the liquefied and non-liquefied materials, respectively.

By defining the constants in Equation (5.2), the curvature of the path of the center of gravity can be computed as

$$sin\theta = \frac{dy/dx}{\sqrt{1+(dy/dx)^2}} \tag{5.5}$$

where dy and dx are the vertical and horizontal incremental displacement on the path of the center of gravity. The acceleration of the center of gravity can be further defined as the second derivative of displacement, Δ, with respect to time, t, or

$$a = \frac{d^2\Delta}{d^2t}. \tag{5.6}$$

By substituting Equation (5.6) into Equation (5.4), the complete equation for failure analysis with the kinetic effect is expressed as

$$[W\sin\theta - S_r L_1 + (C_{NL} + \sigma'_{vo}\ \tan\varphi')L_2] = m\ \frac{d^2\Delta}{d^2 t}. \tag{5.7}$$

By expressing the second derivative in finite difference form, Equation (5.7) can be integrated by a time-stepping procedure to obtain the displacement of the center of gravity with time. During evaluation of the residual strength, a trial value of S_r was used in order to calculate the final displacement. The residual strength was then determined by comparing the final displacement with the observed data at the center of gravity.

Identification of Zero-Inertia Geometry

During a flow slide, the driving stresses act against the available soil resistance to produce deformation of the unstable soil. An unstable slope can regain its stability when the geometry changes sufficiently to reduce the driving stress to the available soil resistance; however, momentum associated with the velocity of the soil at that point causes additional deformation. The geometry that would allow the soil resistance to regain stability without inertial loads will hereafter be referred to as the "zero-inertia geometry" (ZIG). The ZIG represents the geometry of the slope at the point at which the acceleration of the failing soil mass is zero; hence, the point at which the velocity reaches its maximum value. Applying limit-equilibrium slope stability analysis with the ZIG captures the residual strength without interference from the inertia component.

It is therefore assumed that back-calculation of residual strength from flow slide case histories using static limit equilibrium procedures should most logically be based on the ZIG rather than the pre-failure or post-failure geometries. The problem then becomes one of estimating the ZIG for a particular case history.

Olson et al. (2000) and Olson (2001) provided acceleration and velocity profiles for kinetic effect evaluation of a number of case histories using the sliding block procedure described in the previous section. For the case shown in Figure 5-1b, those profiles indicated that the maximum velocity occurred at a time of approximately 3.7 seconds, or when 43.3% of the total slope movement had occurred. The deformed shape of the slope at this point can therefore be taken as corresponding to a "zero-inertia factor," or ZIF, of 0.433.

Knowing the pre- and post-failure geometries, and the ZIF, the ZIG can then be estimated. The process can be performed in the following steps:

1. Several pairs of points that describe the pre-failure geometry and their corresponding locations on the post-failure geometry are selected. These points are selected on the basis of the degree of confidence with which their positions both before and after failure can be estimated.
2. Paired points that describe the pre-failure and post-failure geometry of any phreatic surfaces are also selected.
3. As indicated in Figure 5-2, a number of paired paths are defined by the pre- and post-failure points and by representative paths drawn between them. The paths are drawn in a manner considered to be consistent with the failure mechanism; obviously, some degree of judgment is required in construction of these paths. The assumption is that the points on the pre-failure geometry followed the paired paths as they moved to their final locations on the post-failure geometry.
4. The ZIF is determined by means of sliding block or more advanced analyses.

5. A point on each paired path is at the point corresponding to the ZIF is identified. For the case shown in Figure 5-3, the points are located 43.3% of the way between the pre-failure and post-failure points on each paired path.

6. The points located in Step 5 are connected in a manner consistent with the known geometry of the slope between the identified geometry points.

7. Identification of the ZIF for each pair of points, therefore, allows graphical construction of the ZIG, including the position of the phreatic surface at the point at which inertial forces are absent.

The ZIG can then be used for static back-calculation analyses. However, it is important to recognize that there is significant uncertainty in the ZIG. This uncertainty results from selection of the paired pre- and post-failure geometry points, from estimation of the paths upon which selected geometry points are assumed to travel from the pre-failure geometry to the post-failure geometry, and from the sliding block model upon which the ZIF is computed. This uncertainty is accounted for by assigning a distribution to the ZIF and then by assigning uncertainty to the horizontal and vertical positions of the various points used to specify the geometry of the slope conditional upon the ZIG.

Uncertainty in the ZIF

The ZIF is obtained by a procedure that is rational and objective, but very approximate. As a result, it is unreasonable to assign a specific ZIF to any particular case history. Furthermore, available case histories differ in the level of documentation of pre- and post-failure geometries and the complexity of the failure mechanisms that govern the transformation from pre-failure to post-failure geometry. A procedure for estimation of the uncertainty in the ZIF that recognizes these factors was developed.

The uncertainty in the ZIF is a function of the level of documentation of the individual flow slide and of the degree to which the failure mechanism is consistent with the simplified sliding block model used in estimation of the ZIF. Based on judgment, a minimum coefficient of variation of 10% was assigned to the ZIF – this was considered to reflect the minimum level of uncertainty that would exist for a very well documented flow slide in which failure occurred on a single failure surface whose position was well known. For a poorly documented flow slide with a failure mechanism that does not correspond well to the assumptions of the sliding block model, a coefficient of variation of 30% was judged to be reasonable. The actual coefficients of variation used in the analyses were determined as

$$COV_{\mathrm{ZIF}} = 0.10 + 0.20 Q_{\mathrm{ZIF}} \tag{5.8}$$

where Q_{ZIF} is a quality factor estimated from Table 5-1a.

Once the value of COV_{ZIF} had been determined, the uncertainty was characterized by a discrete probability mass function (pmf) that was formulated in a manner that would match the first two moments of a continuous normal distribution. The "weights" associated with the pmf were as tabulated in Table 5-1b.

The weights were applied by sub-sampling from the distribution of $(N_1)_{60}$ - S_r pairs generated from the Monte Carlo analyses. If, for example, 50,000 simulations were performed for a geometry based on the mean value of the ZIF, or $\overline{\mathrm{ZIF}}$, 10,000 values sampled randomly from that pool of 50,000 values were applied with their mean residual strength set equal to the deterministic value of residual strength obtained for ZIF values of $\overline{\mathrm{ZIF}} - 1.7\sigma_{\mathrm{ZIF}}$ and $\overline{\mathrm{ZIF}} + 1.7\sigma_{\mathrm{ZIF}}$; similarly 15,000 values were applied at the deterministic strengths corresponding to $\overline{\mathrm{ZIF}} - 1.1\sigma_{\mathrm{ZIF}}$ and $\overline{\mathrm{ZIF}} + 1.1\sigma_{\mathrm{ZIF}}$. This procedure assumed that the variance of S_r was not sensitive to the value of ZIF within the range of ZIFs considered.

The procedure of applying uncertainty of ZIF involves several steps.

1. The strength of liquefied soil is back-calculated based on the pre- and post-failure geometries.

2. The average residual strength of liquefied is backcaculated by the Monte Carlo analyses. This average residual strength value corresponds to the condition at ZIG.

3. As shown in Figure 5-4a, a trendline that represents the back-calculated soil strength values of pre-failure, ZIG, and post-failure is established.

4. The residual strength values that correspond to various degrees of ZIF (e.g. $\overline{\text{ZIF}}-1.7\sigma_{\text{ZIF}}$, $\overline{\text{ZIF}}-1.1\sigma_{\text{ZIF}}$, $\overline{\text{ZIF}}$, $\overline{\text{ZIF}}+1.1\sigma_{\text{ZIF}}$, and $\overline{\text{ZIF}}-1.7\sigma_{\text{ZIF}}$) can then be estimated based on the trendline.

5. The entire distribution of $(N_1)_{60}$ - S_r pairs is then sub-sampled to describe the uncertainty caused by the various degrees of ZIF.

6. The result of the sub-sampling process then generates the final distribution of $(N_1)_{60}$ - S_r pairs, as shown in Figure 5-4b. In Figure 5-4b, the oval shape indicates the distribution of $(N_1)_{60}$ - S_r pairs at various degrees of ZIF.

5.2.1.2 Uncertainty in Slope Geometry Point Locations

Definition of the slope geometry in each case history was accomplished by specification of the locations of points that represent the exterior geometry and interior geometry of the slope. In view of potential human and measurement errors, some uncertainty exists in the documented post-failure and pre-failure geometry. The exterior geometry is then estimated by surveying, which defines locations with relatively good measurement accuracy. The geometries of subsurface layers, however, are usually estimated from a limited number of subsurface borings. Therefore, a higher degree of uncertainty should be assigned to the locations of the points that define the interior geometry.

The exterior geometry and interior geometry are defined by points with X (horizontal) and Y (vertical) coordinates. Each point is assigned with normally distributed position errors in the vertical and horizontal directions; the mean values of these errors are zero for both exterior and interior geometry. The standard deviations were defined by procedures consistent with the information on geometry determination available for each case history.

5.2.1.3 Uncertainty in Phreatic Surface Position

Uncertainty in the location of the water table is separated into three parts: the water level in the reservoir (when appropriate), the exit point of the phreatic surface on the slope, and the position of the phreatic surface within the slope. As previously mentioned, flow slide failures are assumed to produce undrained conditions in all liquefied soils. The position of the phreatic surface inside the slope is allowed to vary from the water level in the reservoir. Consequently, two sets of normally distributed random numbers separately characterize the water level in the reservoir and the phreatic surface point on the boundary. Figure 5-5 shows the scheme for defining the variation of the water table in the ZIG.

Another group of normally distributed random numbers is generated to describe the possible shift of the phreatic surface. The purpose of this randomization is to simulate potential seepage conditions during initial filling of a reservoir and the deformation of liquefied area during failure movement. A transition zone is made between the shifted phreatic surface and the point defining the intersection of the phreatic surface with the face of the slope (Figure 5-5). This transition zone is characterized by a single-ended Butterworth type spatial taper (Figure 5-6a).

A transition zone is made between the shifted phreatic surface and the starting point of fluctuated phreatic surface on the slope. This zone is characterized by the single-ended Butterworth type spatial taper (Figure 5-6a), in which the region of minimum shift provides a smooth transition to the region of maximum shift. The overall inclination of the fluctuated phreatic surface is the same as the inclination of the original phreatic surface in the ZIG.

5.2.1.4 Uncertainty in Position of Failure Surface

Conventional deterministic back-calculation procedures usually use a single estimated failure surface for limit-equilibrium evaluation, despite the fact that the position of a single, actual failure surface is not well known, and perhaps not even very appropriate, for many case histories. For the current Monte Carlo analyses, simulations incorporated uncertainty in failure surface position by adding uncertainty to the shape and position of the documented failure surface. The position of the failure surface in each Monte Carlo realization was assembled in three steps:

1. The failure surface was shifted by an amount defined by the shape of a half-cycle sinusoidal curve spanning from the beginning of the failure surface (at the top of the slope) to the end (at the exit point at the bottom of the slope). This shift placed the trendlines of the failure surfaces within a distributed region around the most likely failure surface.
2. A degree of spatial variability was added to the shape of the failure surface to account for the fact that failure surfaces in real materials are seldom as smooth as idealized. The sinusoidally shifted failure surface was overlain on a random field mesh to characterize a failure surface with reasonable properties of spatial variation.
3. A double-ended Butterworth-type taper (Figure 5-6b) was used to reduce the uncertainty in failure surface position near the two ends of failure surface where field observations are generally more accurate.

Half-Sine Wave Variability

An objective procedure was developed to allow consistent estimation of standard deviation applied to the half-sine wave randomization function that was applied to the mean failure surface position. The purpose of the half-sine wave randomization function was to reflect uncertainty in the basic position of the failure surface. This uncertainty was specified in terms of the mean and standard deviation of the amplitude of the half-sine wave that was added to the mean failure surface position.

Because the mean failure surface was interpreted as a best estimate, the mean value of the half-sine wave amplitude was set to zero. The standard deviation of the half-sine wave amplitude was selected by a procedure that was intended to account for both the "size" of the failure surface and the quality of information on which the mean failure surface location was based.

After review of the case histories, the following expression was developed to estimate the standard deviation (in ft) of the half-sine wave function, or $\sigma_{\text{half-sine}}$:

$$\sigma_{\text{half-sine}} = (1.0 + 0.015H)Q_{\text{half-sine}} \tag{5.9}$$

where H is the height of slope (in ft) and $Q_{\text{half-sine}}$ is the information quality factor determined from Table 5-2.

This procedure results in standard deviations of at least 1 ft, which is considered to represent a reasonable lower bound consistent with the error involved in measuring a relatively well defined failure surface in an excavation following failure.

Spatial Variability of Failure Surface

To account for spatial variability along the length of the failure surface, a two-dimensional random field mesh of failure surface deviations was pre-generated. These deviations were defined by a mean value of zero, a standard deviation of 1.0 ft, and a scale of fluctuation that varied with the length of the failure surface. The scale of fluctuation is assumed to be the same in the vertical and horizontal directions. Several values of scale of fluctuation were used to test the effect on the overall procedure. It was determined that an appropriate value of the scale of fluctuation was about half the length of the failure surface. Throughout the Monte Carlo analyses, sinusoidally shifted failure surfaces were imaged on the mesh in a simulation sequence. The fluctuation values of points on failure surface were estimated by a two-dimensional mapping technique, as indicated in Figure 5-7. The fluctuation value at Point P was interpolated from the random values in Grid Points G1, G2, G3, and G4. Point P was then displaced radially in the direction of maximum local curvature.

Taper Function

Finally, in order to minimize excessive deviations at the two ends of the failure surface where failure surface positions are more readily observed in the field, a double-ended Butterworth spatial taper (Figure 5-6b) was applied in these areas. Figure 5-8 shows an example of the fluctuated failure surface with the spatial taper. The purpose of the spatial taper was to simulate the quick transition into the liquefied soil with a relatively wide, concentrated high strain region. The characteristics of the spatial taper functions had to be defined on a case-by-case basis. The application of a taper function assumed the development of a distinct "scarp" at the top of the slope. The existence of such features minimizes uncertainty in the position of the failure surface at the top of the slope.

A number of case histories, however, involve failure mechanisms that did not produce a clear "scarp" or other form of visual evidence of the failure surface position.

An objective procedure was developed to allow consistent estimation of the location of the point at which the failure surface intersected the top of the slope. Some case histories, for example, included considerable settlement in addition to lateral movement; the "slump" nature of these failures makes identification of the point at which the failure surface intersected the top of the slope uncertain. Other case histories may have involved some degree of progressive failure in which case the final geometry may not accurately reflect the geometry of the initial failure that mobilized the residual strength of the soil.

The position of the point at which the failure surface intersected the top of the slope was assumed to be uniformly distributed; therefore, it can be characterized by the mean and range of the horizontal position of that point. Because the mean failure surface was interpreted as a best estimate, the mean value of the top-of-slope failure surface position was set to zero. The range of the top-of-slope failure surface position was selected by a procedure that was intended to account for both the "size" of the failure surface and the quality of information on which the mean failure surface location was based.

After review of data for the case histories, the following expression was developed to estimate the range of the top-of-slope position distribution, $W_{\text{top-of-slope}}$:

$$W_{\text{top-of-slope}} = 0.06 L Q_{\text{top-of-slope}} \tag{5.10}$$

where L is the length of failure surface (in ft) and $Q_{\text{top-of-slope}}$ is the information quality factor determined from Table 5-3.

For the majority of case histories, the position of the intersection of the failure surface with the top of the slope was sufficiently well defined that a high quality rating was assigned; in these cases, the numerical value of the quality factor specifies that the uncertainty in the location of the intersection point is negligible. For some cases, however, principally those involving slump-type failures, the range was significant.

5.2.2 Material Property Variables

Soil deposits often show great variability in their physical properties (e.g. bonding history, and particle packing) because of the complex process of deposition, transporting, and construction that form them. As a result, the mechanical properties (e.g. strength and stiffness) of soils also show a degree of inherent variability with respect to their spatial locations.

Phoon and Kulhawy (1999) classified uncertainty in estimated soil properties in three major groups: inherent soil variability, measurement error, and transformation model error. The uncertainty of soil itself is characterized by the inherent soil variability. This variability is usually caused by the natural deposition process or the construction procedure for man-made structures. The second uncertainty, measurement error, is caused by testing apparatus, procedure, and testing effects. This uncertainty can apply to field testing or laboratory testing. The third uncertainty, transformation model error, occurs when data from field and laboratory are calibrated with constitutive models.

Spatial variability of soil properties is influenced by the deposition history, weathering conditions, transportation agents, or by construction processes for man-made soil deposits. Besides the probability distributions of purely randomized numbers, some soil parameters require quantitative description of their spatial distribution. Davis (1986) defined the term of "regionalized variable" to characterize the variation between truly random numbers and deterministic numbers. The values of regionalized variables should be correlated with separation distance by estimating their auto-correlation functions. Figure 5-9 demonstrates a hypothetical soil property with spatial variation. The trend of the soil variable describes the expected value as a function of depth. The regionalized variable drifts away from this expected value with a certain deviation, which can be characterized by a set of normally distributed random numbers with a zero mean. While the randomized values scatter around the trend, the scale of fluctuation describes the distance between values that have the strongest correlation. The example shown in Figure 5-9 represents the scale of fluctuation in terms of the distance between values with zero deviation from the trend. A rapid spatial variation represents corresponds to a small value of the scale of fluctuation, e.g. the SPT blowcount in the vertical direction. A large value of the scale of fluctuation describes a parameter that fluctuates from the trend over relatively long distances, for example, the SPT blowcount in the horizontal direction. Figure 5-9 shows that the scale of fluctuation changes locally at various depths. The representative value of the scale of fluctuation is calculated from the auto-correlation function obtained from observed data.

In the current research, spatial variability concepts were used to generate spatial fluctuations of the failure surfaces and randomized SPT values along the failure surface in the liquefied area. Because of the large computational effort involved in simulation with the Monte Carlo analyses, two-dimensional random field meshes were pre-generated. The generation of two-dimensional random fields was based on the procedure of Yamazaki and Shinozuka (1988). The resulting random fields consisted of normally distributed random numbers with a prescribed mean value, standard deviation, and scale of fluctuation value. For geotechnical materials, the scale of fluctuation may be different in vertical and horizontal directions. An example mesh is shown in Figure 5-10.

5.2.2.1 Shear Strength of Non-Liquefied Soil

In almost all flow slide case histories, the flow slide occurs by a failure mechanism that involves non-liquefied as well as liquefied soils. The total resistance to sliding, therefore, depends on the shear strength of the non-liquefied soil as well as the residual strength of the liquefied soil. In some cases, the non-liquefied soil consists of soil similar to the liquefied soil, but exists above the water table. In other cases, the non-liquefied soil is too cohesive or too dense to have liquefied under the level of loading that produced liquefaction in the liquefied soil. In this research, the strength properties of the non-liquefied soils were assigned coefficients of variation equal to those recommended by Phoon and Kulhawy (1998) unless case-specific information that suggested other values were more appropriate.

5.2.2.2 SPT Resistance

The SPT blowcount is commonly correlated to the residual strength of liquefied soil. However, the reliability of this correlation can vary depending on the quality of documentation. In order to establish a reliable and consistent method for Monte Carlo analyses, estimation of statistical parameters for SPT blowcount was based on the quantity and quality of available data. Field generation of randomized SPT blowcounts with spatial variation was accomplished in two steps. The first step was to generate a distribution of SPT resistance for each simulation. The second step was to sample the random number on a pre-generated random field mesh. The random numbers represent the spatial variation of SPT resistance on the fluctuated failure surface. The random field mesh used a lognormal distribution of SPT resistance in order to prevent the occurrence of negative blowcount values in the Monte Carlo simulations.

In the first step to generate a normal distribution of random numbers for SPT variation, the mean SPT value is calculated by averaging the available measured SPT data,

$$\overline{N} = \frac{1}{m} \sum_{i=1}^{m} N_i \tag{5.11}$$

where $\overline{N}$ is the mean value of field data, m is the number of SPT tests in the liquefied zone, and N_i is the individual SPT blowcount value.

Estimation of the uncertainty in SPT resistance was complicated by the widely-varying amounts of measured SPT data in the various case histories. Some case histories include substantial amounts of well-documented SPT data, while others have very little measured SPT data. As a result, a procedure was developed to allow consistent and objective estimation of the uncertainty in SPT resistance. The procedure, which estimates the standard deviation of SPT resistance by weighted average of three different procedures for standard deviation estimation, is described in the following paragraphs.

The first method was used when the availability of existing data were limited or non-existent. In such cases, the coefficient of variation (COV) was assumed to be 150% in order to reflect the large uncertainty about SPT resistance that would exist in this case. The estimated standard deviation (σ_{est}) was defined as

$$\sigma_{est} = 1.5\overline{N} . \tag{5.12}$$

The second method, which corresponded to cases in which a small amount of SPT data was available, estimated the standard deviation from the range of the available SPT data. In the three-sigma rule, the difference between the maximum and minimum observed values is assumed to represent six standard deviations. Burlington and May (1970) suggested an improved method to calculate the standard deviation based on the range of available data divided by a value that increases as the number of measurements increases (Table 5-4). The standard deviation estimated from the range of available data (σ_{range}) was defined by

$$\sigma_{range} = \frac{SPT_{max} - SPT_{min}}{N_{range}} \tag{5.13}$$

where SPT_{max} and SPT_{min} are the maximum and minimum values of the available data, and N_{range} is the recommended value from Table 5-4.

The third method, which applied to cases in which SPT data was plentiful, was to calculate the standard deviation directly from the available data. The calculated standard deviation (σ_{calc}) is defined as

$$\sigma_{calc}=\sqrt{\frac{1}{m\text{-}1}\sum_{i=1}^{m}\left(N_i\text{-}\overline{N}\right)^2}\ . \tag{5.14}$$

Based on the actual amount of available SPT data, weighting factors were applied to the values of standard deviation generated from the three methods to produce a single standard deviation. The standard deviation used for the case history (σ_{used}) was then computed as

$$\sigma_{used} = w_{est}\,\sigma_{est} + w_{range}\,\sigma_{range} + w_{calc}\,\sigma_{calc} \tag{5.15}$$

where w_{est}, w_{range}, and w_{calc} are weighting factors for the estimated, range, and calculated standard deviation, respectively. The expressions of weighting factors are tabulated in Table 5-5. Figure 5-11 shows the plots of weighting factors versus the availability of SPT data.

The weighting factors were set up so that all of the weight will be given to σ_{est} for case histories with zero or one SPT measurement, and all to σ_{calc} for case histories with more than 30 SPT measurements. For case histories with 3 to 5 SPT measurements, σ_{used} is based equally on σ_{est} and σ_{range}. For case histories in between 6 to 30 SPT measurements, σ_{used} is based on linearly varying weighting factors; the influence of σ_{calc} increases and the influence of σ_{est} and σ_{range} decrease as the number of available measurements increases.

The estimated mean is also a random variable with a standard deviation that depends on the number of measured values used to obtain it. The standard deviation of $\overline{N}$, or $\sigma_{\overline{N}}$, was computed as

$$\sigma_{\overline{N}} = \frac{1}{\sqrt{m}}\sigma_{used}. \tag{5.16}$$

In order to account for the possible negative SPT resistance generated from the probability procedure, a lognormal distribution was generated. The standard deviation, $\sigma_{\ln\overline{N}}$, and mean value, $\overline{\ln N}$, for the lognormal distribution were defined (Benjamin and Cornell, 1970) as

$$\sigma_{\ln\overline{N}} = \sqrt{\ln(1+(\frac{\sigma_{\overline{N}}}{\overline{N}})^2)} \tag{5.17}$$

and

$$\overline{\ln N} = \ln\overline{N} - \frac{1}{2}\sigma_{\ln\overline{N}}^{2}. \tag{5.18}$$

A set of lognormally distributed random numbers was then generated for a mean SPT blowcount in the Monte Carlo analyses. Each random number in this distribution represented the mean SPT resistance in lognormal distribution ($\overline{\ln N_{mean}}$) for each Monte Carlo simulation.

The second step was to define random fields to represent the spatial variation of SPT resistance for each Monte Carlo analysis. The technique of generating the random field mesh was basically the same as that used for failure surface fluctuation. However, because the deposition process of soil usually spreads out in a horizontal direction, the scale of fluctuation for SPT resistance in the horizontal direction is usually longer than it is in the vertical direction. Currently, the method for generating a random field mesh adopted from Yamazaki and Shinozuka (1988) can only assign an equal value of scale of fluctuation in both the vertical and horizontal directions. In order to simulate the anisotropic property of SPT resistance, the size of the mesh was scaled in the vertical direction when sampling random numbers to fit the correct scale of fluctuation. The random field mesh was generated by the scale of fluctuation of 39.37 ft (12 m) in both directions. The true values of the scale of fluctuation are 7.87 ft (2.4 m) and 39.37 ft (12 m) in the vertical and horizontal directions, respectively.

The definition of standard deviation for the lognormally-distributed random field mesh ($\sigma_{\bar{Y}}$) is termed as (Benjamin and Cornell, 1970)

$$\sigma_{\bar{Y}} = \sqrt{\ln(1+\mathrm{COV}^2)} \qquad (5.19)$$

Phoon and Kulhawy (1999) compiled available SPT data and showed that typical COV values ranged from 19% to 62%, with an average value of 54%. The SPT resistance compiled in their database included no correction for overburden stress and energy ratio. The mean value of this random field mesh is zero.

Random numbers ($\Delta \ln N$) were then sampled from the random field mesh, similar to the procedure described in Figure 5-7. The only difference was that the fluctuated failure surface was imaged on the two-dimensional mesh instead of the sinusoidally shifted failure surface.

In Monte Carlo simulations, the spatial variation of SPT blowcount number was generated based on those two steps. In each simulation, the logarithmic value of mean blow count number ($\overline{Y}$) (Benjamin and Cornell, 1970) was assigned as

$$\overline{Y} = \overline{\ln N_{mean}} - \frac{1}{2}\ln(1+\mathrm{COV}^2). \qquad (5.20)$$

Each randomized SPT logarithmic number on the fluctuated failure surface is converted to its exponential value (N^*) by

$$N^* = e^{(\overline{Y}+\Delta \ln N)} + \Delta(N_1)_{60} \qquad (5\text{-}21)$$

where $\Delta(N_1)_{60}$ is the fines content correction. Because of the variety of soil grain distribution, the Monte Carlo analysis is applied to the fines content correction as well. The mean value of $\Delta(N_1)_{60}$ is estimated based on the study of Seed and Harder (1990) corresponded to the appropriate estimated fines content. A normal distribution of $\Delta(N_1)_{60}$ is characterized by a mean value and a standard deviation defined by COV 0f 0.3.

Figures 5-12a and Figure 5-12b show examples of possible fluctuated failure surfaces with corresponding $(N_1)_{60\text{-CS}}$ values along the surface within the liquefied zone. Owing to the anisotropy of the scale of fluctuation, the $(N_1)_{60\text{-CS}}$ values fluctuate rapidly at the left side of Figure 5-12b, where the failure surface has a steeper slope.

5.2.3 Failure Mechanism Variables

Additional uncertainties can be associated with the failure mechanism itself. No two flow slides occur in exactly the same manner, and the differences between flow slides lead to some uncertainty in the residual strength predictions obtained by back-calculation procedures. Potential uncertainties related to failure mechanisms are described in the following sections.

5.2.3.1 Hydroplaning

Debris flows, which are gravity-driven flows of mixtures of solid particles and fluid, are known to occur in both subaerial (above water) and subaqueous (below water) environments. Subaerial debris flows frequently occur following periods of heavy rainfall in steep, mountainous terrain, and can produce tremendous damage to surface structures and facilities. Subaqueous flows can cause damage to submarine structures, produce tsunamis, and contribute to turbidity currents.

Both subaerial and subaqueous debris flows can travel over very large distances. Subaerial debris flows typically come to rest on slopes of 1°-9° (Suwa and Okuda, 1983; Costa, 1984; Whipple and Dunne, 1992). Subaqueous debris flows, however, have traveled from 10 km to several hundred km on slopes of less than 1° (Embley, 1982; Shor and Piper, 1989; Aksu and Hiscott, 1992; Masson et al., 1993; Laberg and Vorren, 1995). Differences in the runout distances of subaerial and subaqueous debris flows have been attributed to basal lubrication of the subaqueous flows, which can occur by a process known as hydroplaning (Horne and Dreher, 1963; Horne and Joyner, 1965; Browne, 1975; Browne and Whicker, 1983; Mohrig et al., 1998; Mohrig et al., 1999). Hydroplaning occurs when a debris flow moves so quickly that the fluid in front of it cannot be displaced from its contact with the seabed and becomes trapped under the leading edge of the debris flow (Figure 5-13).

Hydroplaning requires that the debris flow material be of sufficiently low permeability that water can be trapped beneath it during the flow process; this implies that hydroplaning would be more likely beneath fine-grained materials than coarse-grained materials. Mohrig et al. (1998) reported the results of a series of laboratory flume experiments in which different amounts of dye were added to the debris flow material to distinguish it from the native material on which the debris flow material came to rest. The dye affected the rheological characteristics of the debris flow material; Mohrig et al. observed that the more plastic and viscous debris flows exhibited greater tendencies for hydroplaning than the less plastic and viscous debris flows.

Hydroplaning is caused by the development of hydrodynamic water pressures that develop along the advancing surface of a debris flow. These pressures act on all parts of the surface that are in contact with the fluid. When the pressure at the point where the debris flow is in contact with the stable underlying soils becomes greater than the stress between the debris flow and the underlying soil, the water will lift the debris flow and penetrate beneath it, leading to hydroplaning. The phenomenon is similar to that which can occur beneath automobile tires on wet pavement.

Experimental studies have shown that debris flows tend to form when values of the densimetric Froude number

$$Fr_d = \frac{v}{\sqrt{\left(\frac{\rho_d}{\rho_a} - 1\right) gh\cos\theta}} \tag{5.22}$$

exceeds values of 0.3-0.4. In this equation, v is the velocity of the head of the flow, ρ_d and ρ_a are the densities of the debris flow and ambient fluid (water), h is the thickness of the head of the flow, and θ is the angle of the slide. In the laboratory, the maximum distance that water penetrated beneath a hydroplaning debris flow was approximately 10 times the thickness of the debris flow; the distance was observed to increase with increasing Froude number (Mohrig et al., 1998). The maximum Froude number in the reported experiments was 1.6.

From the standpoint of interpretation of liquefaction flow slide case histories, the literature on hydroplaning offers some insights into the conditions under which hydroplaning is most likely to occur. Unfortunately, documentation of case histories does not typically provide all of the information needed to determine whether or not hydroplaning was likely to have occurred and had an impact on back-calculated residual strengths. In particular, the flow velocity required to compute the densimetric Froude number is generally not known with high accuracy.

As a result, an approximate procedure for estimating the degree of potential influence of hydroplaning on back-calculated residual strength was developed. The procedure involves a number of assumptions and approximations, but it can be applied consistently to all flow slide case histories to obtain rational predictions of the effects of hydroplaning. The procedure involves (a) estimation of the densimetric Froude number, (b) use of the estimated Froude number to estimate the distance to which hydroplaning effects extend back beyond the head of the flow slide, and (c) development of a reduction factor by which the strength of the interface influenced by hydroplaning should be reduced in the back-calculation process. The procedure was implemented in the following steps:

1. Assume $\rho_d/\rho_a = 1.6$ and $g = 32.2$ ft/sec^2.
2. Take h as the average thickness of the liquefiable layer. Take θ as the average slope of the failure surface within the liquefied layer.
3 Estimate the maximum velocity, v, of the sliding material from available information. This step involves a combination of subjective and objective information. In cases where eyewitness accounts provide a reasonable indication of the speed of the failure, that information is used to estimate a

maximum velocity. In other cases, the maximum velocity obtained from the kinetics analysis is used as the best estimate of the maximum velocity.

4 Compute the densimetric Froude number, F_{rd}.

5 Compute the hydroplaning distance, d_{hp} , to which the effects of hydroplaning are expected to extend from the toe of the slide in the upslope direction as

$$d_{hp} = 7.692 F_{rd} h - 2.308 \tag{5.23}$$

which, in accordance with experimental results, corresponds to a hydroplaning distance of zero for $F_{rd} = 0.3$ and $10\,h$ for $F_{rd} = 1.6$.

7. Apply a hydroplaning factor, α, to the portion of the failure surface within d_{hp} of the toe of the slope. The value of α, which reflects the nature of the materials involved in the failure with a weighting factor of 0.5 – 0.9 that can be interpreted as a degree-of-belief (or epistemic uncertainty) that hydroplaning actually occurred, is obtained from the Table 5-6.
8. Perform the back-calculation analyses using the hydroplaning factor and take that factor into account in the residual strength averaging procedure.

Because the failure process usually was reported with personal opinions, the failure duration described in previous investigations was highly unreliable. In current research, the value of d_{hp} is characterized by the uncertainty of ν that was estimated by Olson (2001). After examining all available case histories, the value of ν calculated by Olson (2001) is further reduced to ν_{used}, which ν_{used} ranges between 0.25ν to 0.75ν. As a result, in the Monte Carlo analyses, the uncertainty of d_{hp} is characterized by a uniform distribution defined by random values of ν_{used}.

5.3 MONTE CARLO SIMULATION IN LIMIT-EQUILIBRIUM SLOPE STABILITY ANALYSIS

The Monte Carlo analyses used a large number of simulations to represent the uncertainties in input parameters with appropriate statistical characteristics. By using the ZIG to eliminate inertial effects, the back-calculation procedure represented uncertainties in the friction angle of the non-liquefied soils, external and internal geometry, water table, failure surface geometry, and SPT resistance. Each uncertain parameter was characterized by a probability distribution. Spatial variability of the failure surface and SPT resistance were also modeled. An iterative limit-equilibrium slope stability analysis was then carried out to back-calculate the residual strength and the normalized residual strength ratio (NRSR).

In limit-equilibrium slope stability analyses (Spencer's method), force equilibrium is calculated by dividing the failed soil mass into slices above each of a series of segments along the failure surface. The SPT resistance at the bottom of each segment was used to characterize the soil resistance. To iteratively back-calculate the residual strength and NRSR for cases in which the SPT resistance was allowed to vary along the length of the failure surface (which has not been attempted by previous investigators), equations to relate the residual strength (S_r) in the liquefied zone to SPT resistance were required. Two equations were used for this purpose:

$$S_r = 50\, e^{(k_1 N^*)} \tag{5.24}$$

and

$$\frac{S_r}{\sigma'_{vo}} = k_2\, N^* \tag{5.25}$$

The form of Equation (5.24) is consistent with the general shape of the graphical relationships proposed to bracket the residual strength data compiled by Seed and Harder (1990). The coefficient of 50 represents the residual strength (in psf) corresponding to $N^* = 0$, and is consistent with the results of an interpretation of case history data by Idriss (1998). For the current analyses, however, the coefficient k_1 was treated as an unknown quantity whose value was sought (by iteration to the FS = 1 condition) in each Monte Carlo realization. This allowed the analyses to use variable residual strength values that were consistent with the variable SPT resistance along the length of the failure surface. The form of Equation (5.25) was suggested by Stark and Mesri (1992) with the parameter $k_2 = 0.0055$. For the current project, the coefficient, k_2, was treated as an unknown, again to allow the use of a variable residual strength along the length of the failure surface. This form implies that the steady state line is parallel to the one-dimensional consolidation curve, which allowed the residual strength value to vary with depth in the liquefied soil. In each Monte Carlo simulation, the single value of k_1 or k_2 that produced a safety factor of 1.0 for the entire liquefied zone was computed. With the same randomized SPT resistance, the residual strength value of each segment of the failure surface was varied, based on Equations (5.24) and (5.25). The values of k_1 and k_2 that produce FS = 1.0 were then computed. Using those k_1 and k_2 values and Equations (5.24) or (5.25), the variable residual strength along the failure surface was computed. The average values of SPT resistance, $(\overline{N}_1)_{60\text{-}CS}$, residual strength, $\overline{S}_r$, and vertical effective stress, $\overline{\sigma}_{vo}$, over the length of the failure surface were then computed. The evaluation of $\overline{\sigma}_{vo}$ is estimated as

$$\overline{\sigma}'_{vo} = \frac{\sum_{i=1}^{n} \sigma'_{vo,i} L_i}{L_{total}} \tag{5.26}$$

where $\sigma'_{vo,i}$ is the vertical effective stress of the individual segment, L_i is the length of the ith segment in the liquefied area, and L_{total} is the summation of all segment lengths in the liquefied area. The value of $(\overline{N}_1)_{60\text{-CS}}$ was accomplished using a procedure similar to that described in Equation (5.26).

The value of $\overline{S}_r$, however, required involving the effect of hydroplaning. The value of $\overline{S}_r$ was estimated by

$$\overline{S}_r = \frac{\sum_{i=1}^{n} S_{hr,i} L_i}{\sum_{i=1}^{n} \alpha_i L_i}$$

and (5.27)

$$S_{hr,i} = \alpha_i S_{r,i}$$

where $S_{r,i}$ is the trial residual strength according to Equations (5.24) and (5.25) at the base of slice, $S_{hr,i}$ is the trial residual strength after the reduction from hydroplaning, and α_i is the reduction factor of hydroplaning. The value of α_i was equal to 1.0 for slices that were not subject to hydroplaning. When the hydroplaning effect was accounted for, a random number was assigned to α_i in each simulation.

By this procedure, each Monte Carlo realization produced a single $\{(\overline{N}_1)_{60\text{-CS}}, \overline{S}_r\}$ or $\{(\overline{N}_1)_{60\text{-CS}}, \overline{S}_r/\overline{\sigma}'_{vo}\}$ pair.

In Equation 5.25, the residual strength value was assumed to be proportional to the vertical effective stress, σ_{vo}, within each segment at its location on the pre-failure geometry. Figure 5-14 demonstrates the method to trace the pre-failure position of segment from its ZIG position. In the pre-failure geometry, the portion of failure surface within the liquefied zone is bounded by Points WL and Point WR. During the flow slide failure, the stretching of the failure surface in this region is referenced by the paired path on the exterior geometry. The term "paired path" describes a specific point in the deformation process that moves from the pre-failure geometry to the ZIG. For example, two sets of paired paths, Point A to Point A' and Point B to Point B', bound Points P and P' in the pre-failure geometry and ZIG, respectively. The relative position of Point P' between Point A' and Point B' is calculated in order to estimate the position of Point P between Point A and Point B. In each Monte Carlo simulation, the failure surface is defined between Point WL and Point WR'. Point P' on the fluctuated failure surface is then traced back to its pre-failure position of Point P. By following the trend of failure surface, the same approach is repeated for all segments on ZIG to estimate their positions in the pre-failure geometry. The values of σ_{vo} in the pre-failure geometry can then be computed.

5.4 SUMMARY

This chapter has described the procedures used to identify and characterize the main sources of uncertainty that can influence the results of residual strength back-calculation from flow slide case histories. Uncertainties can result from both geometric and material parameters, and both can strongly influence the values of back-calculated residual strength.

The geometry of the slope upon which back-calculation analyses are performed is critically important in developing a reasonable estimate of residual strength. It has been shown that kinetic effects, associated with the inertial forces that can act upon a rapidly moving flow slide, can have a very strong influence on back-calculated residual strength. A procedure for identifying a slope geometry that is intermediate between the pre-failure and post-failure geometries was described; because the procedure involved significant simplifications of the actual failure process, a procedure for estimating the uncertainty in that intermediate geometry was also developed. Procedures for incorporating additional uncertainties associated with slope and phreatic surface geometry were also developed and described.

In all flow slide case histories, uncertainties in material properties also exist. These uncertainties are related to natural randomness of soil properties, which are also spatially variable, and to lack of information/data about the properties. Substantial uncertainty exists in values of the critical parameter, SPT resistance, upon which residual strength predictive procedures are to be developed, in many case histories; some case histories for which data have been presented in the literature actually have no measurements of SPT resistance. A procedure for estimation of the uncertainty in SPT resistance, given the amount of available SPT data, was described. A procedure for simulation of spatially variable soil properties, and for using those spatially variable properties in back-calculation analyses, was also described.

Description	Q_{ZIF}	Comments
Very good	0.0	Block-type failure on well-defined failure surface
Good	0.3	Relatively coherent block(s) of soil above relatively well-defined failure surface
Fair	0.6	Predominantly broken up failure mass with straining on several surfaces
Poor	1.0	Slumping failure or highly distributed zone of shear strain producing poorly-defined failure surface

(a)

ZIF value	$\overline{ZIF} - 1.7\sigma_{ZIF}$	$\overline{ZIF} - 1.1\sigma_{ZIF}$	$\overline{ZIF}$	$\overline{ZIF} + 1.1\sigma_{ZIF}$	$\overline{ZIF} + 1.7\sigma_{ZIF}$
Weight	0.10	0.15	0.50	0.15	0.10

(b)

Table 5-1 Estimation of ZIF (a) quality factor and (b) weights.

Quality Rating	$Q_{\text{half-sine}}$	Description
High	1.0	Shearing occurred within well-defined zone. Failure surface exposed by post-failure excavation; location surveyed during failure investigation
Medium	2.0	Failure surface position well constrained at top and bottom of slope. Subsurface conditions provide reasonable constraint to location within slope. No post-failure excavation to provide specific location.
Low	3.0	Failure surface position not well constrained (e.g. slump-type failure). No post-failure investigation. No clear indication of failure surface position in case history reports.

Table 5-2 Information quality factor that defines the half-cycle sinusoidal curve for randomizing failure surface.

Quality Rating	$Q_{\text{top-of-slope}}$	Description
High	0.0	Shearing occurred within well-defined zone. Failure surface intersected top of slope at well constrained location identified during failure investigation.
Low	1.0	Failure surface position not well constrained (e.g. slump-type failure). No clear indication of point of intersection of failure surface with top of slope in case history reports.

Table 5-3 Information quality factor that defines the range of the top-of-slope position distribution for the mean failure surface.

m	N_{range}
2	1.128
3	1.693
4	2.059
5	2.326
6	2.534
7	2.704
8	2.847
9	2.970
10	3.079
15	3.472
20	3.735
30	4.090

Table 5-4 Estimation of standard deviation of SPT resistance from number of measurements, m, and N_{range} (Burlington and May, 1978).

Weighting Factor	$m = 0 - 2$	$m = 3 - 5$	$m = 6 - 30$	$m > 30$
w_{est}	1	0.5	$0.5 - (m - 5)/50$	0
w_{range}	0	0.5	$0.5 - (m - 5)/50$	0
w_{calc}	0	0	$(m - 5)/25$	1

Table 5-5 Weighting factor for estimation of standard deviation for SPT resistance.

Material at toe of slope	Hydroplaning factor, α
Very permeable (rockfill, cobbles, clean gravel)	0.9
Permeable (clean sand, silty gravel)	0.7
Low permeability (silty sand or finer)	0.5

Table 5-6 Information quality factor that defines the reduction factor for estimating the hydroplaning distance.

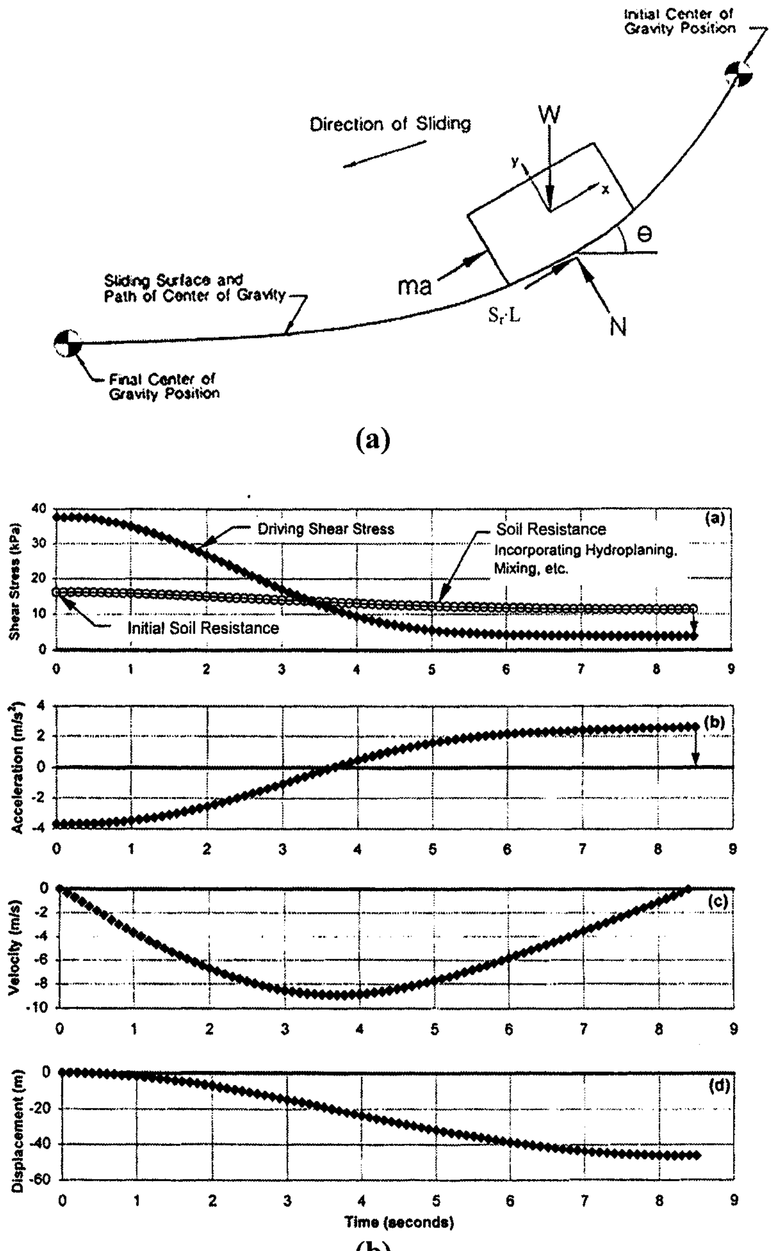

Figure 5-1 Failure analysis with kinetic effect on North Dike of Wachusett Dam (a) soil mass movement on the path described by a third-order polynomial and (b) soil mass movement profiles (after Olson et al., 2000).

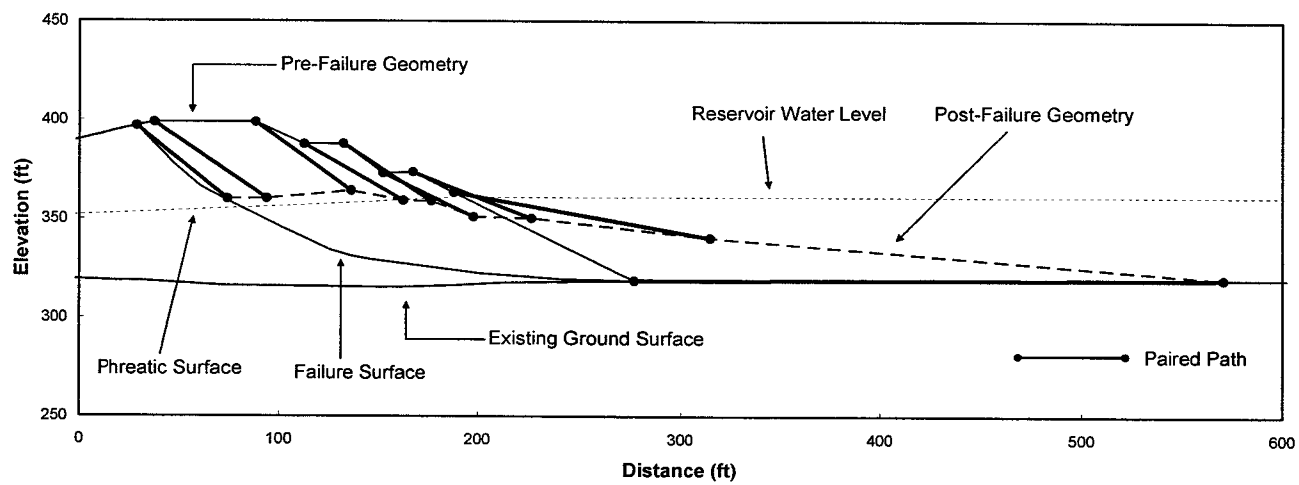

Figure 5-2 Paired Path shown with Pre-failure and Post-failure Geometry of the North Dike of Wachusett Dam.

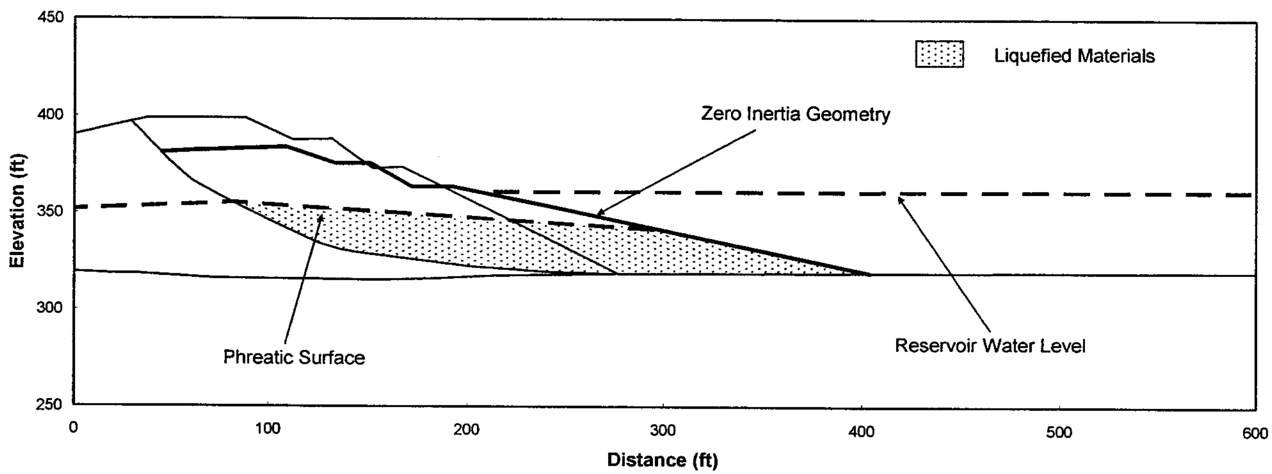

Figure 5-3 Zero Inertia Geometry of the North Dike of Wachusett Dam.

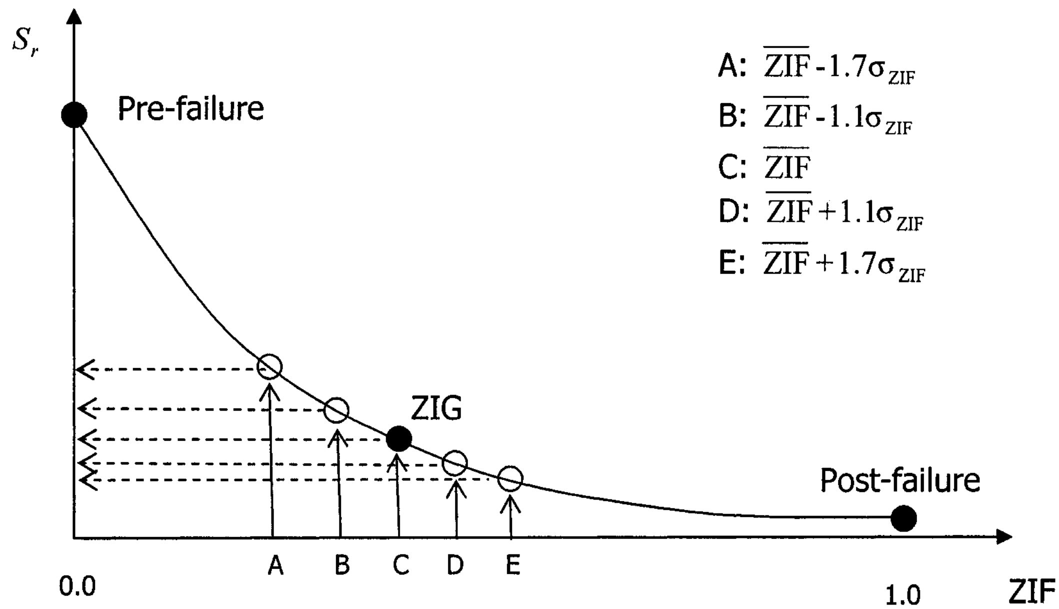

(a)

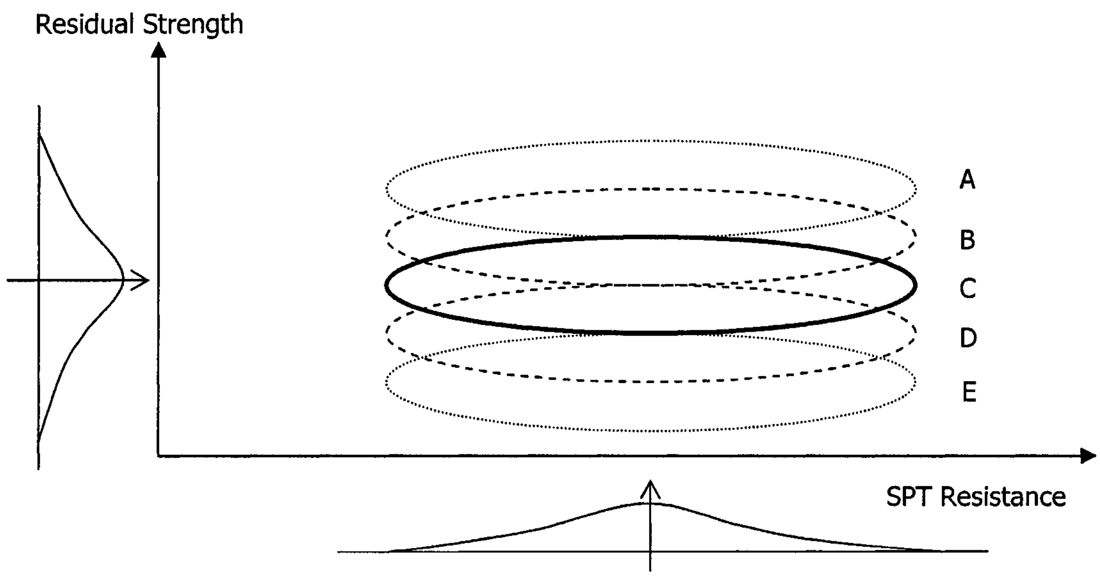

(b)

Figure 5-4 Scheme for applying uncertainty on ZIF.

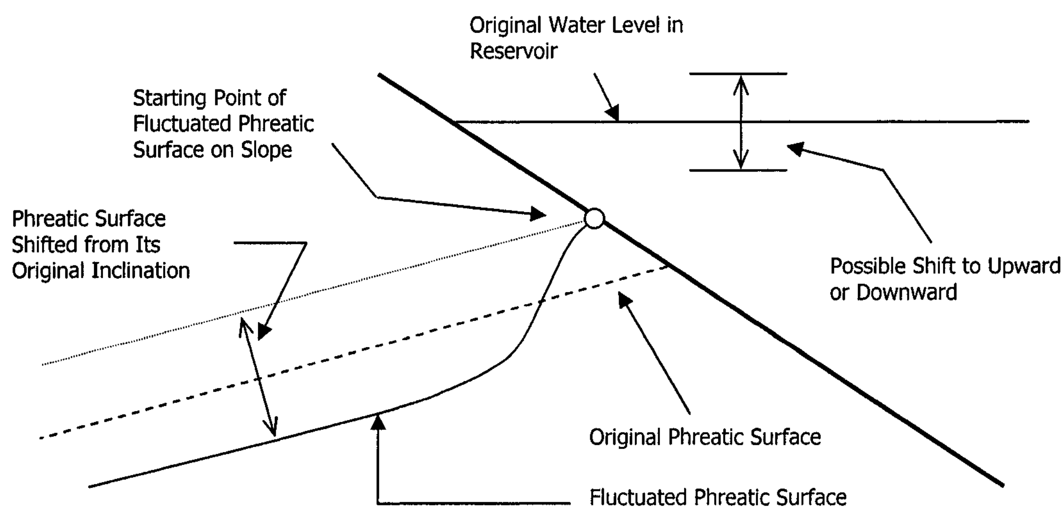

Figure 5-5 Scheme for description of water table position.

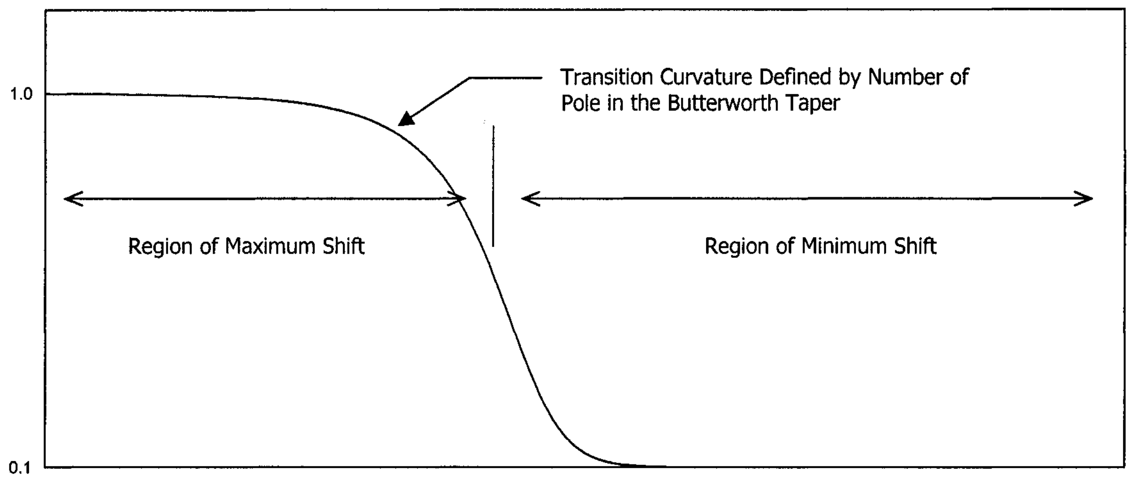

(a)

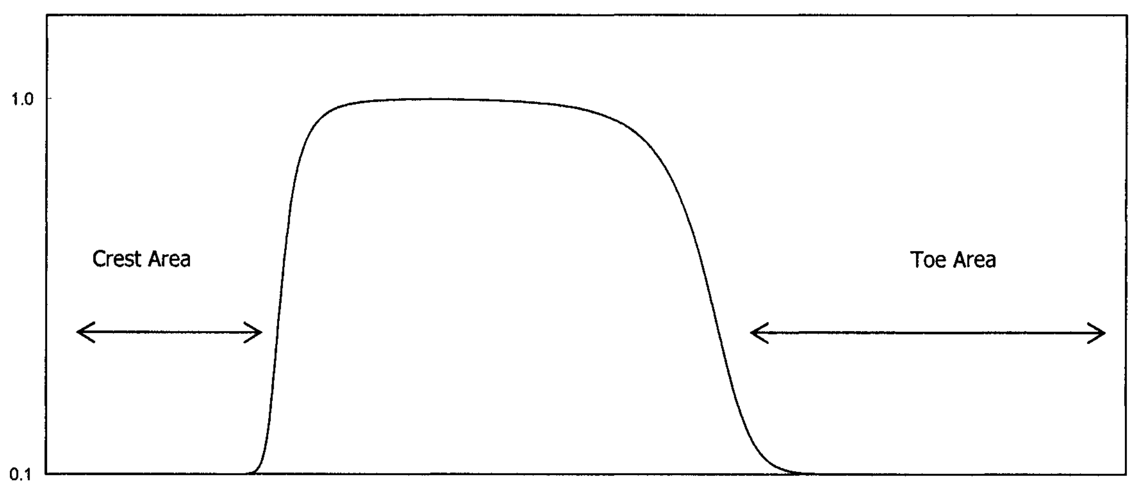

(b)

Figure 5-6 Butterworth type spatial taper for (a) fluctuated phreatic surface and (b) fluctuated failure surface.

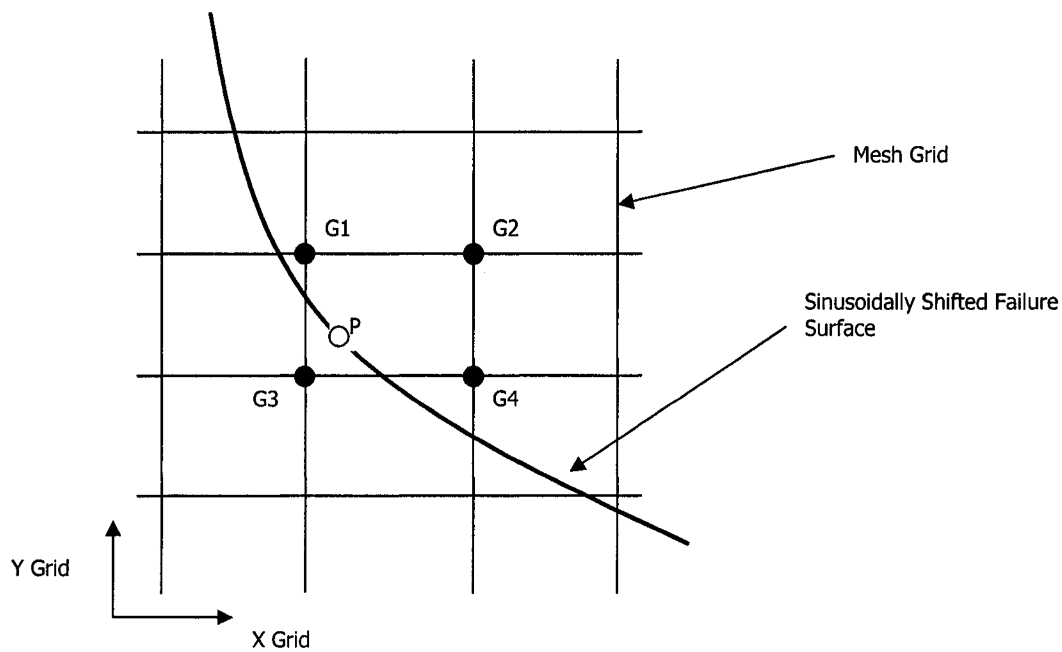

Figure 5-7 Interpolation of failure surface fluctuation from random field mesh.

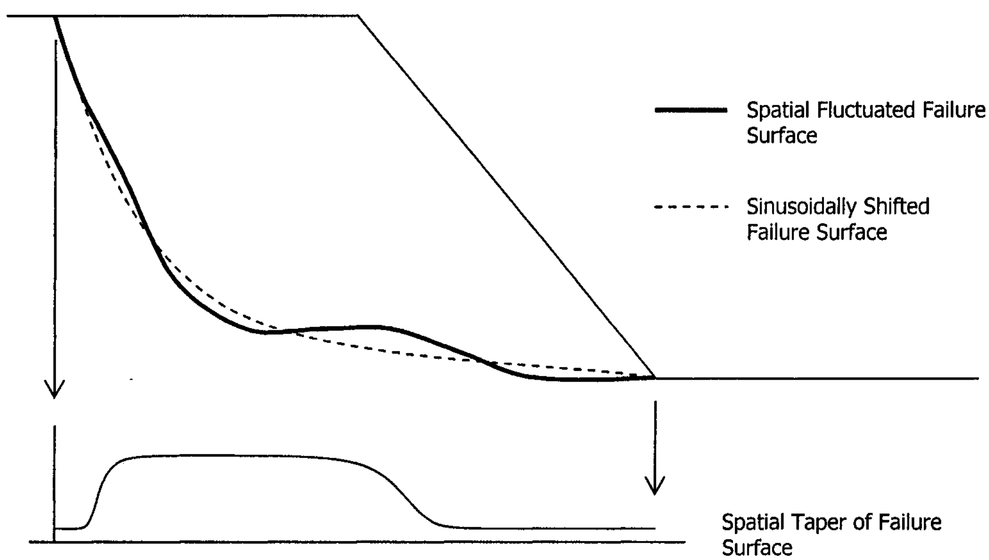

Figure 5-8 Generation of spatial fluctuated failure surface. Deviations are exaggerated from sinusoidally shifted surface for illustrative purposes.

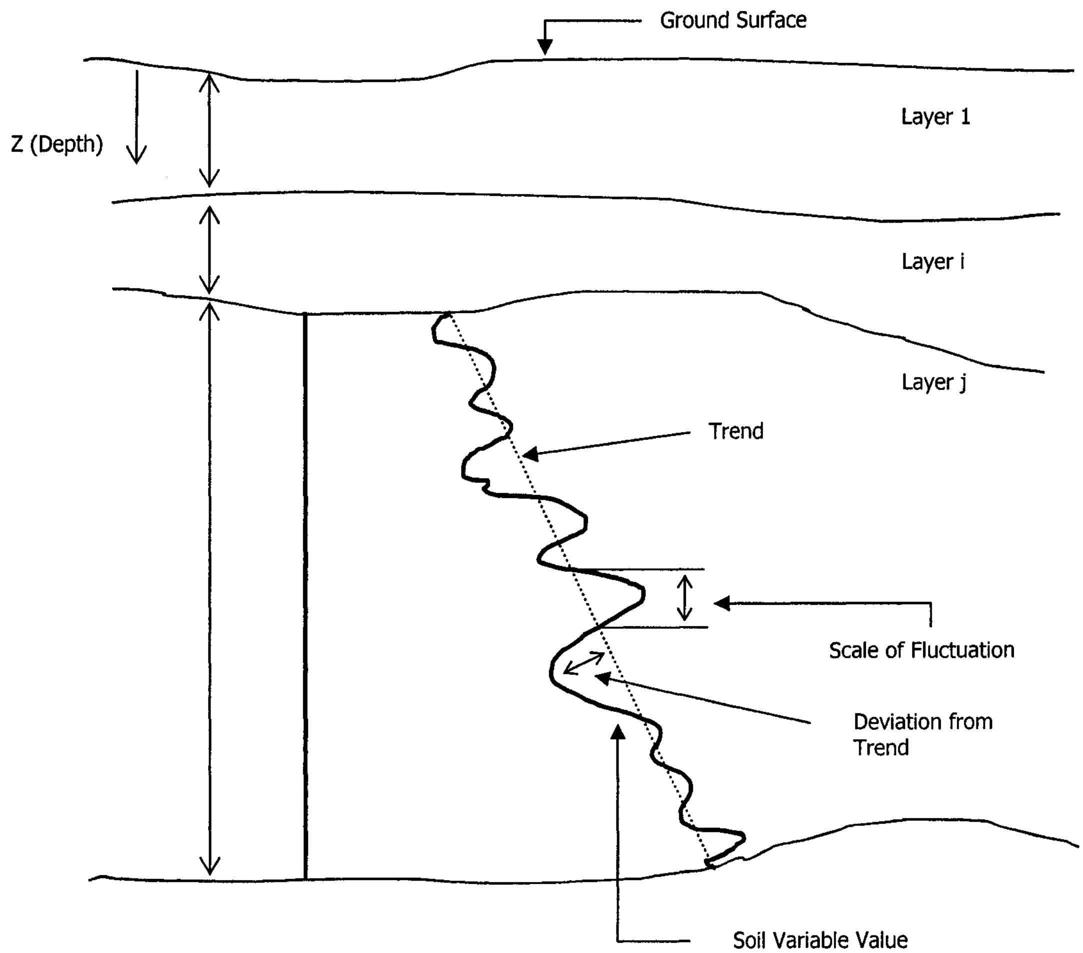

Figure 5-9 Inherent Soil Variability (after Phoon and Kulhawy, 1999).

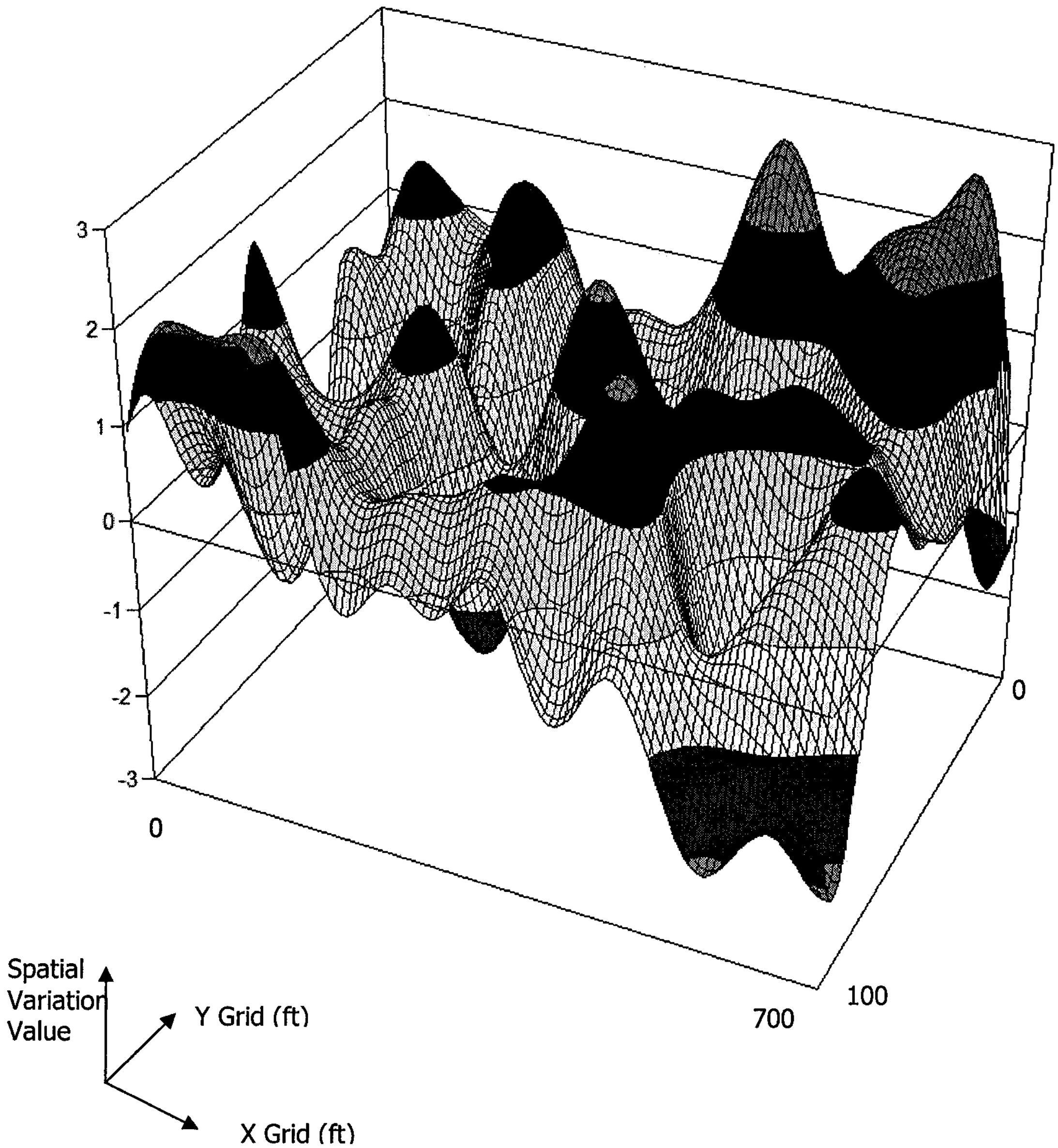

Figure 5-10 Example of random field mesh used for defining spatial fluctuation of failure surface and SPT. The vertical coordinate represents the spatial variable deviation from the mean.

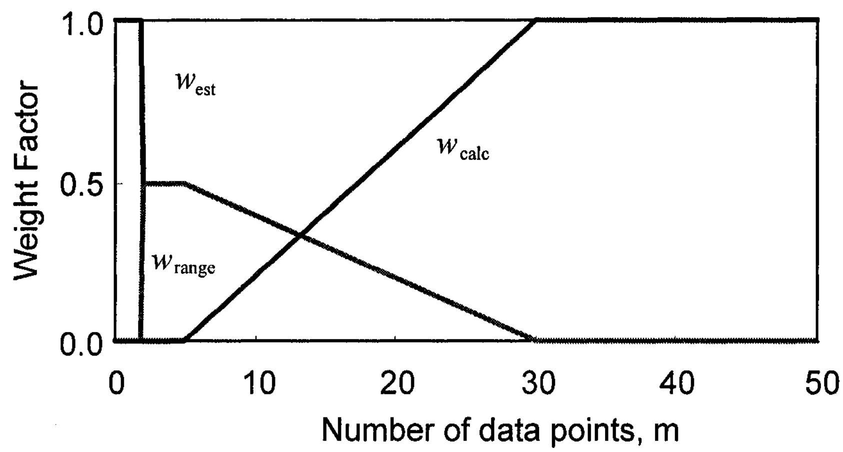

Figure 5-11 Estimation of weighting factor for used standard deviation of SPT, estimation from estimated value, range value, and calculated value.

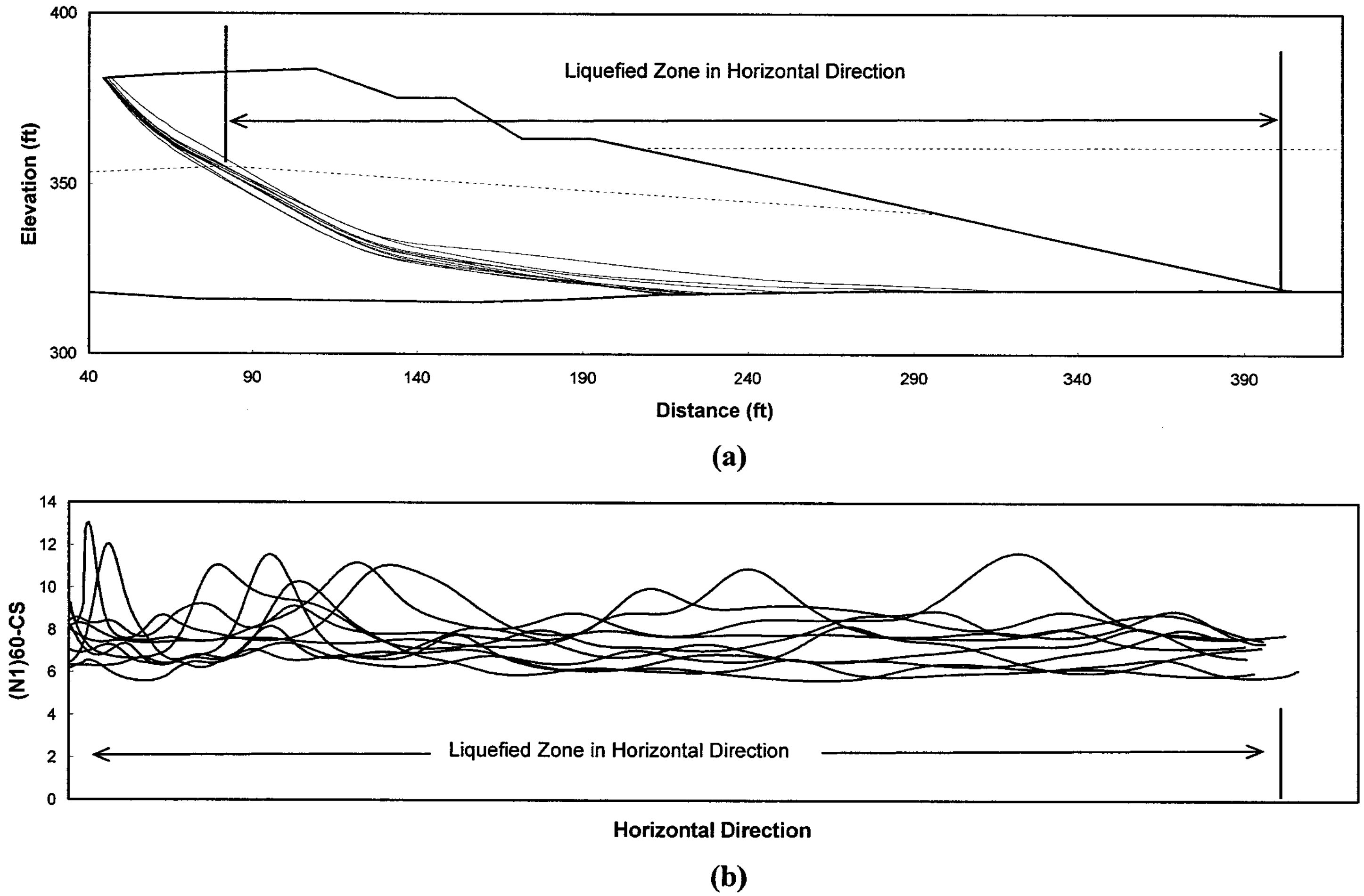

Figure 5-12 Examples of (a) fluctuated failure surface and (b) $(N_1)_{60\text{-CS}}$ along the surface within the liquefied zone.

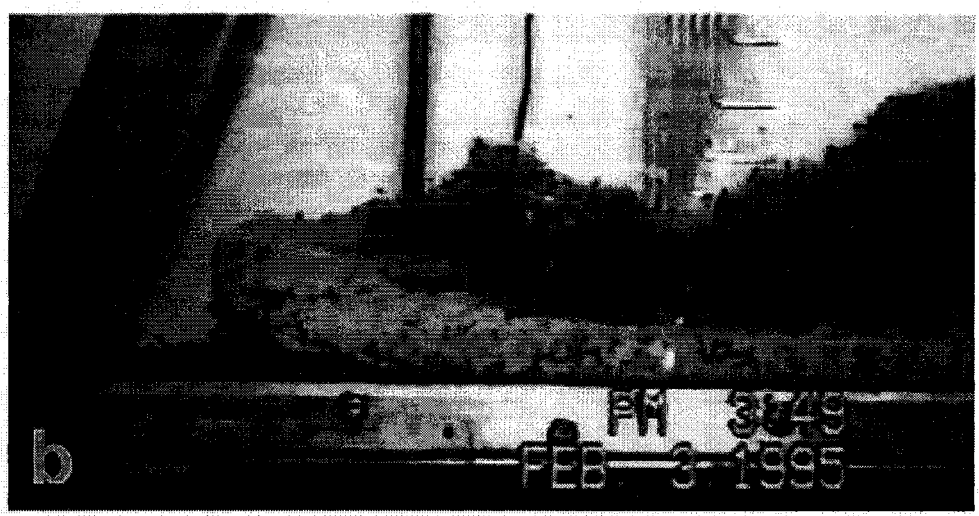

Figure 5-13 Video image of hydroplaning in a laboratory model of a subaqueous flow slide. Note that the leading edge of the flow slide is underlain by a wedge-shaped region of trapped fluid (Mohring et al., 1999).

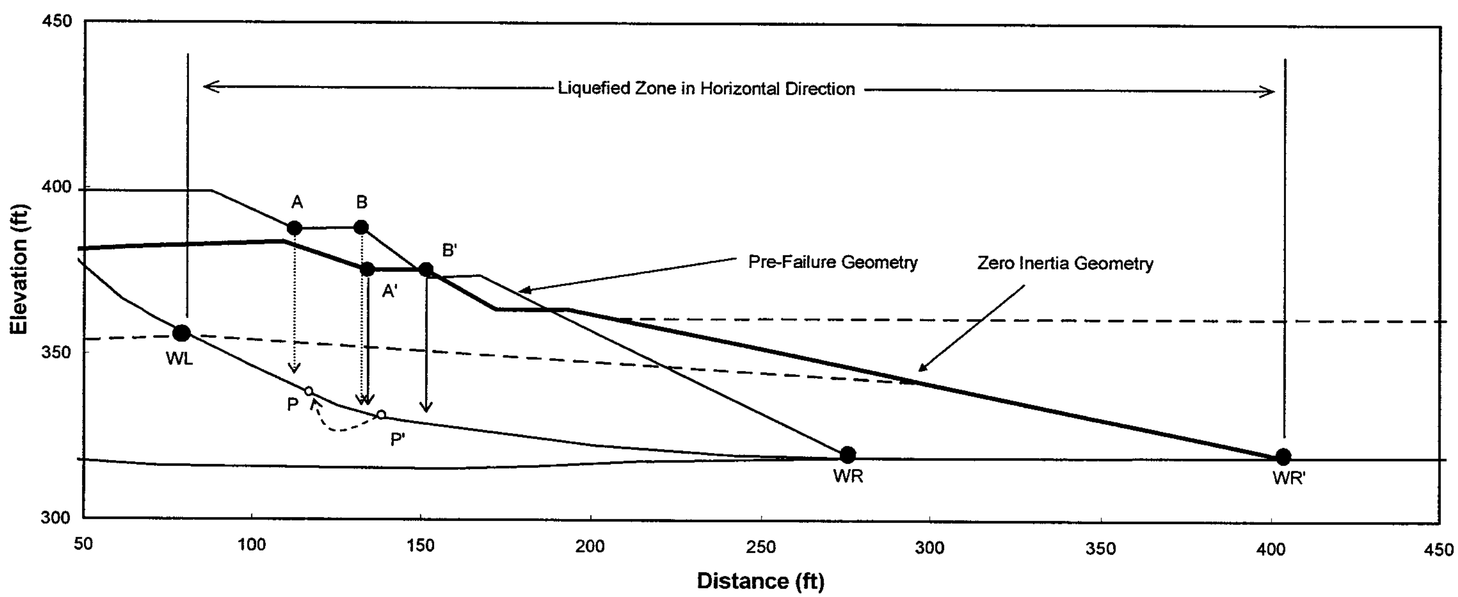

Figure 5-14 Scheme for calculation of effective stress from pre-failure geometry.

Chapter 6

Back-Calculation of Flow Slide Case Histories

6.1 INTRODUCTION

The preceding chapter presented the basic procedures used to perform Monte Carlo simulations of flow slide case histories for the purpose of investigating the effects of uncertainties in input parameters on uncertainty in the residual strength of the soil. The application of those procedures is presented in this chapter, first in a detailed example for the Wachusett Dam case history and then in summaries of other significant case histories. Finally, procedures for estimation of the uncertainty in residual strength for smaller and less well-documented case histories are presented.

6.2 NORTH DIKE OF WACHUSETT DAM

Constructed from 1898 to 1907, Wachusett Reservoir in Clinton, Massachusetts, is retained by a main dam and two dikes. Wachusett Reservoir provided water supply to the metropolitan Boston area for 33 years until the construction of Quabbin Reservoir. Figure 6-1 shows the location of Wachusett Reservoir and the surrounding area. The main Wachusett dam was constructed as a stone masonry gravity structure, 43 m high and 259 m long, with a crest elevation of 125.7 m (the reference elevation in the Boston area is 1.72 m below sea level). The North Dike extends 3,200 m along the reservoir rim against a glacial lake with a crest elevation ranging from 123.6 m to 125.9 m. The South Dike is 760 m long a with crest elevation of 123.7 m, constructed along the Carville Basin. These two dikes were constructed with sandy silt and silty sand in the central core, and mostly fine sand in the shells.

On April 11, 1907, three years after its construction had been completed, the upstream slope of the North Dike failed during initial filling of the reservoir. The failure involved approximately 46,500 cubic meters of material from a 213 m long-section of the dike. The final geometry showed displacements of approximately of 100 m horizontally at the toe and approximately 12 m vertically at the crest. Taking into consideration factors such as the change of effective stress (by filling the reservoir), the type of failure (large deformations), and the existing liquefiable soil (sandy fills in shells), the failure of North Dike is classified as a flow slide caused by a sudden reduction of strength within liquefied soils.

Details of this case history were described in Olson et al. (2000) and Olson (2001). The following pages describe the case history, and its use in previous investigations of residual strength behavior.

6.2.1 Construction and Geometry of the North Dike

Construction of the North Dike started in 1902 and ended in 1904. The dike was constructed on a glacial river channel deposit mainly comprised of dense to very dense sands, gravels, and non-plastic silts. Along the centerline of the dike, a cut-off wall and core were constructed using materials removed from the reservoir area. Sandy silt and silty sand were placed as core materials in lifts of 0.15 m thickness and rolled by horse-drawn carts. Fine sand from cut-off trenches made up a large portion of the shells. The downstream shells were placed in lifts of 2.3 m thickness and then compacted and flooded with water. Following saturation, about 15 to 30 cm of settlement was observed in each lift. The downstream shells consisted of sand to silty sand, with some gravel. Unlike the downstream shells, the upstream shells were built without compacting and flooding with water. The upstream was also constructed of silty sand to sand with gravel.

The flow slide occurred above a former river channel between Stations 22+50 and Station 25+00. The cross-section for current study used the profile at Station 23+20, at approximately the central line of the flow slide. At the time of failure, the final elevation at the crest for this station was approximately 125 m (Figure 6-2). The core and cut-off wall were built toward the upstream direction with a slope of 1 horizontal to 1 vertical

(1H:1V). Its maximum width was 30.5 m, measured approximately at the top of the core area. The downstream slope was built toward Coachlace Pond with a 4H:1V slope immediately from the crest. The slope was decreased to 30H:1V at elevations below 122.5 m, gently extending to the channel of the Nashua River. The upstream slope was built at a 2H:1V to 3H:1V slope, immediately below the crest toward the reservoir. A 6 m-wide bench was placed at about Elevation 122.5 m with riprap at a slope of 1.25H:1V. Below this riprap bench, the shell started at Elevation 117 m with a 2H:1V slope above the foundation.

Prior to the failure, the cross-section of the dike at Station 23+20 had reached its maximum height of 24.4 m and the reservoir had been filled to a depth of 12.8 m. The position of the phreatic surface, however, was not measured, and therefore its location must be estimated. The North Dike was built of silty sand to sandy silt in the core and silty sand to sand in the shells. The reasonably high permeability of these soils established hydraulic equilibrium almost immediately upon filling the reservoir. Because of the relatively lower permeability of the core, a change in the slope of the phreatic surface was expected. However, the estimated failure zone only went through the core above the phreatic surface. As the result, detailed information about the phreatic surface in core material is not required for this study. The phreatic surface defined by Olson et al. (2000) and Olson (2001) was assumed to be parallel to the steady state slope of the phreatic surface reported by GZA GeoEnvironmental, Inc. in 1991.

6.2.2 Description of Failure

As shown in Figure 6-3, the flow slide induced by filling the reservoir produced tremendous deformation of the embankment's upstream shell. Compared to the initial slope of 1.25H:1V to 3H:1V in the pre-failure geometry, the average slope of the post-failure geometry was reduced to approximately 11H:1V below the reservoir water level, or 5° to 6°. The slide produced displacements of 100 m horizontally at the toe and 12 m vertically at the crest.

Because of the highly permeable soils in the upstream shell, the water table in the shell rose almost immediately with the filling of reservoir. The rising phreatic surface caused the effective stress to decrease in the shell soils. Because of the lack of compaction during construction, the shell materials that consisted of sand to silty sand were highly contractive and liquefiable. The gravitational stresses within the dike induced anisotropic stress conditions within the very loose upstream shell soils, which amplified the tendency for liquefaction. Once the affected area had liquefied, the soils strained toward the steady state deformation at which point the available strength was reduced to the residual strength. The large deformations in this failure primarily involved upstream shell materials below the phreatic surface.

6.2.3 Soil Properties

Shortly after the flow failure, reconstruction of the North Dike was accomplished by placing soils on top of the failed section without removing any of the remaining debris. The reconstructed geometry at Station 23+20 is shown in Figure 6-4. Fill was dumped over the remaining debris under the post-failure reservoir level without any compaction. The average thickness for this dumped mass was approximately 4.6 m (maximum thickness of 5.1 m). It formed a gentle slope of 4H:1V to 5H:1V, which was considerably flatter than the pre-failure 2H:1V slope. Above this level, a new berm was built at a slope of 2H:1V by placing saturated granular fill with a lift thickness of 0.3 m, compacted by horse-drawn carts. Above the new berm level, high-pressure water jets were used along the interface between the new and old materials to assure proper mixing and cosedimentation. The area affected by water jetting is shown in Figure 6-3, which also presents the pre-failure and post-failure geometries.

In the 1980s and 1990s, numerous borings and standard penetration tests (SPT) were conducted by GZA GeoEnvironmental, Inc. This investigation provided valuable soil property parameters. However, those in-situ tests were conducted over the reconstructed section of the North Dike some 80 years after the failure. Soil properties that were evaluated in this investigation did not account for the effects of soil liquefaction, reconsolidation after liquefaction, construction disturbance, and consolidation under reconstruction that had taken place. However, efforts to correct for these disturbances have not been discussed.

As indicated in Figure 6-4, six borings were located along Station 23+20. The SPT procedure used a donut ring hammer with an energy ratio (ER) of 45%; energy corrections were made to estimate $(N_1)_{60}$ values. In those borings, 30 SPT tests were performed within the shell soils involved in the 1907 failure. The average $(N_1)_{60}$ value was reported as 8 blows per foot (bpf) by Olson et al. (2000) and Olson (2001) with a range from 1 bpf to 21 bpf. In Figure 6-4, 13 open circles represent the blowcount number near the estimated failure surface; the average of these values is 6 bpf to 7 bpf. Olson et al. (2000) and Olson (2001) used 7 bpf as the representative value for $(N_1)_{60}$. Olson et al. (2000) and Olson (2001) clarified that, the jetting of water was done along the failure zone in the region above the phreatic surface (Figure 6-4). The blowcount numbers from WND-1, WND-2, and WND-105 were assumed to have had no disturbance from the jetting, while the blowcount numbers from WND-3 were considered to have been affected by jetting.

Because no direct measurements were made during initial construction or reconstruction, no representative soil property values at the time of failure are available. However, the investigation that took place in the 1990s provides some useful information. Tube samples taken from the core area indicated that the saturated unit weight was between 18.9 to 20.4 kN/m^3 (120 to 130 lb/ft^3). In studies by Olson et al. (2000) and Olson (2001), a unit weight of 18.1 kN/m^3 (115 lb/ft^3) was used for all soil types in limit-equilibrium slope stability analyses. The representative median grain size, D50, was approximately 0.42 mm for the liquefied material, with a fines content of 5% - 10%. The permeability of the shell material was measured to be approximately 1×10^{-5} m/s. The core material was expected to have lower permeability than the shell material.

For stability analysis, the non-liquefied zone was assumed to be the drained frictional material during failure, which was above the phreatic surface. The friction angle was estimated to range from 30° to 35°.

6.3 PREVIOUS RESIDUAL STRENGTH ANALYSES

A detailed investigation of the flow slide in the North Dike of Wachusett Dam was reported by Olson et al. (2000), with additional information provided by Olson (2001). The following sections provide a summary of the residual strength back-calculation analyses reported in these publications, both to put the case history into perspective and to provide a deterministic comparison for the results of the probabilistic analyses performed in this research.

6.3.1 Kinetic Effect Analysis

Olson et al. (2000) and Olson (2001) paid careful attention to inertial effects in their analysis of the North Dike of Wachusett Dam, and reported the results of a kinetic analysis to estimate those effects. Figure 6-5 illustrates the kinetic effects analysis for Wachusett Dam. The kinetic effects analysis was performed using the simplified sliding block approach described in Section 6.1.1.1. In this approach, the residual strength was varied until the computed displacement of the sliding block was consistent with the observed displacement of the center of gravity of the unstable soil. A large, unbalanced force at the beginning of failure, due to the strength loss associated with soil liquefaction, causes the sliding block to accelerate. At a time of about 3.7 sec, the point at which the driving shear stress is equal to the soil resistance, the unstable soil reaches its maximum velocity and then begins to decelerate. A total duration of about 8.5 seconds was required for the center of gravity of the unstable soil mass go from its pre-failure to its post-failure position. The final calculated displacement of the center of gravity was approximately 9.4 m vertically and 44.5 m horizontally, which was in excellent agreement with the observed displacement at the center of gravity, approximately 9.4 m vertically and 44.8 m horizontally.

6.3.2 Other Considerations in Wachusett Dam Residual Strength Evaluation

Olson et al. (2000) and Olson (2001) made adjustments to some of the parameters used in the residual strength evaluation to account for various factors that were considered to have potential effects on residual strength.

6.3.2.1 Hydroplaning, Mixing, and Other Large-Deformation Effects

The residual strength mobilized in the liquefied area of the North Dike of Wachusett Dam was considered to have been affected by hydroplaning, mixing with water, and changing of its void ratio at large deformation. Olson et al. (2000) and Olson (2001) suggested that these factors might reduce residual strength by 50% in the portion of the failed materials that extended beyond the pre-failure geometry. No explicit justification for the amount or geometric extent of this effect was provided. The trial residual strength value was reduced by 25% and 100% to investigate the sensitivity of the residual strength to this effect. The results of these sensitivity tests were reflected in the range of residual strengths reported for this case history.

6.3.2.2 Buoyancy Effects

The buoyant force acting on the failed soil mass was varied with time as the mass slides into the reservoir. When the deformed failure mass slid and submerged into water, the increase of volume of soil mass that fell under water increases the buoyant force. The increase affected the net unbalanced force that acted upon the sliding block. This effect was incorporated into Equation (5.7) as the function of distance of block movement.

6.3.2.3 Geometric Changes

As expressed in Equation (5.7), the values of L_1 and L_2 were updated because the deformation associated with failure changes the length of the failure surface. In this case history, the value of L_2, which represents the length of non-liquefied region on failure surface, was estimated to be 12% of the total length. This region was originated from the area above the phreatic surface prior to failure.

6.3.2.4 Strength of Non-Liquefied Soils

In the study of Olson et al. (2000) and Olson (2001), a representative strength value had to be assigned to the non-liquefied material. In the case of the North Dike of Wachusett Dam, an average strength based on an assumption of friction angles ranging from 30° to 35°. As a result, the estimated residual strength from Equation (5.7) was corrected to obtain a final residual strength, $S_r(LIQ)$ as

$$S_r(LIQ) = \frac{S_r - (\frac{L_d}{100} S_d)}{(1 - \frac{L_d}{100})} \tag{6.1}$$

where S_r is the residual strength based on the kinetic correction, L_d is the percentage of the non-liquefied length to the total failure surface length (which was approximately 12% for Wachusett Dam), S_d is the cohesion value for the non-liquefied materials (which was approximately 47.8 kPa to 57.4 kPa).

The estimated residual strength with consideration of kinetic effects for the North Dike of Wachusett Dam was reported as varying from 10.4 kPa (217 lb/ft^2) to 19.1 kPa (399 lb/ft^2), with an average value of 15.0 kPa (334 lb/ft^2).

6.3.3 Normalized Residual Strength Ratio Evaluation

Stark and Mesri (1992) defined the term "liquefied strength ratio", which is equivalent to the normalized residual strength ratio (NRSR), as the ratio of the residual strength mobilized during flow failure to the pre-failure vertical effective stress. A discussion of NRSR can be found in Section 4.4.2.1. In a conventional back-calculation for residual strength, the estimated residual strength is defined as the value assigned to the liquefied zone in a limit-equilibrium slope stability analysis that produces a factor of safety of unity. In the NRSR approach, the residual strength is not constant within the liquefied zone, rather it is assumed to be proportional to the initial vertical effective stress. This requires that the pre-failure vertical effective stress be estimated for all elements of soil on the failure surface; because the analyzed (e.g. post-failure) geometry may differ greatly from the pre-failure geometry, this step can require a great deal of judgment and interpretation.

In their study of the North Dike of Wachusett Dam, Olson et al. (2000) and Olson (2001) assumed that the initial failure surface passed through the center of the liquefied zone. In the back-calculation of the lower-bound value of residual strength, Figure 6-6 illustrates the manner in which pre-failure vertical effective stress values were assigned to slices in the post-failure geometry. The total failure surface of the post-failure geometry was divided into 16 segments that comprised the bases of slices above the failure surface. Segments 1-13 were within the liquefied area while Segments 14-16 were initially above the phreatic surface. Before liquefaction, only Segments 1-5 were on the failure surface below the phreatic surface. Segments 6-9 were located below the estimated failure surface approximately at the center of liquefied area, while Segments 10-13 were above the failure surface. While the criteria for assigning these segment locations is not clear, Olson et al. (2000) and Olson (2001) indicated that further rearranging of slice location around the center of the liquefied zone only slightly affected the back-calculated residual strength.

To evaluate the NRSR, the initial vertical effective stresses on Segments 1-13 were calculated based on their pre-failure locations. By assigning a single value of the NRSR for the total liquefied portion of the failure surface, different vertical effective stress values for each slice on its post-failure location produced different residual strengths along the failure surface. Segments 14-16, the non-liquefied segments, were treated as frictional materials in the stability analyses.

The methods of using conventional back-calculation of residual strength and NRSR on the post-failure geometry yielded a lower-bound residual strength of approximately 3.8 kPa (79 lb/ft^2) and a lower-bound strength ratio of approximately 0.025. In order to confirm the accuracy and correlation between these two approaches, the weighted average vertical effective stress, or $\sigma'_{vo,ave}$, was calculated in a similar way as it was described in Equation (5.26). Equation (5.26) calculated $\sigma'_{vo,ave}$ as 151.2 kPa (3158 lb/ft^2) for Segments 1–13 in which liquefaction occurred. By multiplying the NRSR of 0.026 by the $\sigma'_{vo,ave}$ value, the average residual strength yielded a value of 3.9 kPa (81 lb/ft^2), which was consistent with the back-calculated residual strength of 3.8 kPa.

A similar approach was used for back-calculation of residual strength and NRSR for the pre-failure geometry. Unlike the analysis of post-failure geometry, the vertical effective stress of each segment of the pre-failure geometry was directly calculated based on its location on the failure surface. The ranges of the back-calculated the upper-bound residual strength and the upper-bound NRSR were 37.6 kPa to 41.9 kPa and 0.26 to 0.30, respectively.

As mentioned in Section 5.2.1.1, the evaluation of residual strength with the kinetic effect was based on Equation (5.7). In this equation, the amount of displacement is estimated by residual strength value, weight of soil, local slopes, length of failure surface that represents the liquefied material or the non-liquefied material, and other factors listed in Section 6.3.2. Olson et al. (2000) and Olson (2001) suggested that NRSR is not able to fit in this time-marching calculation. Therefore, the evaluation of NRSR was based on the estimated residual strength divided by the average vertical effective stress calculated from the pre-failure geometry. The value of $\sigma'_{vo,ave}$ was chosen as 151.2 kPa (3158 lb/ft^2), which was estimated by evaluating NRSR of the post-failure geometry. By dividing the residual strength with range from 10.4 to 19.1 kPa (average of 16.0 kPa) to $\sigma'_{vo,ave}$, the NRSR with kinetic effect correction yielded the range of 0.07 to 0.126 (average of 0.106).

6.4 MONTE CARLO SIMULATION OF RESIDUAL STRENGTH EVALUATION

The current research project used Monte Carlo simulation to represent the effects of uncertainties in input parameters on back-calculated residual strength. Spencer's method was used for limit-equilibrium slope stability analysis in the back-calculation of residual strength and NRSR. As described in Chapter 5, the primary uncertain parameters considered in this work included the interior and exterior geometry, water level in the reservoir, phreatic surface, friction angle for non-liquefied zone, failure surface geometry, and SPT blowcount. Spatial variability was also considered in modeling uncertainties in failure surface geometry and SPT blowcount.

6.4.1 Zero-Inertia Geometry

Olson et al. (2000) and Olson (2001) provided acceleration and velocity profiles for their kinetic effect evaluation of Wachusett Dam. Those profiles indicated that the acceleration was zero at a time of 3.7 seconds, or when 43.3% of the total slope movement had occurred, yielding a ZIF value of 0.433.

Figure 6-7 shows the paired points on the pre-failure and post-failure geometries for the North Dike of Wachusett Dam. Figure 6-8 shows the ZIG constructed from the paths between those paired points at a ZIF of 0.433. The figure shows that the water level in the reservoir remained at the same elevation. The phreatic surface, however, moved in a manner consistent with the movement of the slope. Because the flow slide produced large deformation in a short period of time, undrained conditions were assumed for the liquefied materials even though the materials of dike were relatively permeable.

Uncertainty in the geometry of the North Dike of Wachusett Dam was accounted for by using a coefficient of variation of the ZIF of 0.16 (Q_{ZIF} = 0.3).

6.4.2 Uncertainties in Monte Carlo Type Analysis

Monte Carlo analyses were introduced to establish an analytical procedure for case histories. This analytical procedure provides a general approach for back-calculating the residual strength of liquefied soil. Parameters that influence the residual strength back-calculated from a case history, such as friction angle, geometry, water table, failure surface, and SPT blowcount, are characterized as random variables. The uncertainty in each random variable is specified by a probability distribution. Statistical parameters are best calculated from data provided in documented case histories. However, when well-documented case histories are rare, a certain degree of judgment is needed to estimate those statistical parameters.

6.4.2.1 Uncertainty in Slope Geometry Point Locations

As indicated in Section 5.2.1.2, potential measurement errors in the points defining the geometry of the slope were accounted for by adding vertical and horizontal "coordinate shifts" to the best estimates of the coordinates of these points. The standard deviations of the coordinate shifts were 0.25 ft vertically and 1.0 ft horizontally for exterior geometry points, and 1.0 ft vertically and 4.0 ft horizontally for interior geometry points. In the case of North Dike of Wachusett Dam, a constant value of soil density was used; hence, no interior boundaries were assigned.

6.4.2.2 Uncertainty in Phreatic Surface Position

The statistical parameters used to characterize the uncertainty in water level in the reservoir and in the position of the phreatic surface point on the boundary were a mean value of 0.0 and a standard deviation of 0.33 ft. Within the embankment, the normally distributed phreatic surface elevations were characterized by mean value of 0.0 and standard deviation of 3.33 ft. The single-ended, three-pole Butterworth-type taper function (Figure 5-6a) produced a minimum shift zone of 25 ft. In the current case history, the amount of minimum shift was taken as 10% of the maximum shift. All parameters described for uncertainties in the position of the phreatic surface were made by reasonable assumptions for this case history.

The overall inclination of the fluctuated phreatic surface was the same as the inclination of the original phreatic surface in the ZIG. Examples of fluctuated phreatic surfaces for the North Dike of Wachusett Dam are shown in Figure 6-10.

6.4.2.3 Uncertainty in Position of Failure Surface

In the case of the North Dike of Wachusett Dam, the mean and standard deviation of the half-sine function amplitude were 0.0 ft and 2.2 ft, respectively. The value of 2.2 ft was estimated based on Equation (5.9) with H of 80 ft and $Q_{\text{half-sine}}$ of 1. As indicated in Figure 6-10, the span of the half-cycle sinusoidal curve was set equal to the entire length of the documented failure surface.

The region of minimum shift and the number of poles, for the upper portion of the failure surface were 25 ft and 5, respectively. At the toe area, the failed soil mass was assumed to slide along the existing ground surface, so only a small shift was appropriate for an extensive region. The region of minimum shift and the number of poles for the failure surface near the toe were 150 ft and 10, respectively.

In the failure description of the North Dike of Wachusett dam, the value of $W_{\text{top-of-slope}}$ was set to zero because a distinct scarp was observed at the top of the slope.

6.4.2.4 Shear Strength of Non-Liquefied Soils

For the North Dike of Wachusett dam, Olson et al. (2000) and Olson (2001) assumed that the materials above the phreatic surface failed under drained loading conditions. The friction angle of the non-liquefied soil was assumed to range from 30° to 35°. In the current research, the distribution of friction angle is generated based on the three-sigma rule. The maximum value or minimum value of the observed data is three standard deviations (sigma) apart from the mean value. In this case history, mean value and standard deviation are 32.5° and 0.86°, respectively.

6.4.2.5 SPT Resistance

Table 6-1 lists the Wachusett Dam $(N_1)_{60}$ values as digitized from the hollow circles in Figure 6-4. The 13 available data points yielded a mean $(N_1)_{60}$ value of 6.3 bpf and a standard deviation of 5.2 bpf. Table 6-6 lists the weighting factors and standard deviation calculated from the three methods. The σ_{used} and COV were computed by the procedure described in Section 5.2.2.2 as 6.9 bpf and 110.3%, respectively. The values of $\sigma_{\overline{N}}$ was estimated as 1.9 bpf.

The liquefied soil in this case history was estimated to have a fines content of 5-10%. The Monte Carlo analysis is applied to the fines content correction as well. A normal distribution is generated with the mean value of $\Delta(N_1)_{60}$ as 1 bpf, according to the study of Seed and Harder (1990). The COV is 0.3, which yields a standard deviation of 0.3 bpf.

6.4.3 Results of Monte Carlo Analyses

A total of 50,000 Monte Carlo simulations were conducted for the North Dike of Wachusett Dam. In each simulation, a set of uncertain parameter values was generated and used to back-calculate the residual strength and NRSR.

6.4.3.1 Back-calculated Residual Strength

The 50,000 Monte Carlo simulations produced 50,000 pairs of mean SPT resistance and mean residual strength values. A scatter plot of the 50,000 $(\overline{N}_1)_{60\text{-CS}}$ - $\overline{S}_r$ pairs is presented in Figure 6-11; it should be noted that the SPT resistance is plotted on a logarithmic scale.

The Monte Carlo simulations produce a "cloud" of data points that are distributed in a manner that reflects the effects of uncertainties in the inputs to the back-calculation analyses. By using $\overline{\text{ZIF}}$ of 0.433, the mean values of $(\overline{N}_1)_{60\text{-CS}}$ and $\overline{S}_r$ are 7.3 bpf and 345 psf, respectively. The representative values of $(N_1)_{60}$ and S_r reported by Olson et al. (2000) and Olson (2001) were 8.0 bpf and 217 psf to 398 psf, respectively. Therefore, the mean SPT resistance from the Monte Carlo analyses was somewhat lower than the representative SPT resistance interpreted by Olson et al. (2000) and Olson (2001), and the mean residual strength was toward the upper end of the range reported by Olson et al. (2000) and Olson (2001).

Using the approach described in Section 5.2.1.1, with σ_{ZIF} of 0.0693, the results that include uncertainty in the ZIF produce a marginal distribution of $\overline{S}_r$ with a mean and standard deviation of 348 psf and 74.8 psf, respectively.

The Monte Carlo analyses provide useful insight into the effects of uncertainties in input parameters on back-calculated residual strengths. The residual strengths obtained from this process were approximately normally distributed with a coefficient of variation of approximately 21.5%. The fact that the Wachusett Dam case history is one of the most thoroughly investigated and well-documented flow slide case histories available in the literature suggests that the coefficients of variation of other case histories is likely to be greater than 21.5%.

6.4.3.2 Back-calculated NRSR

The 50,000 Monte Carlo simulations also produced 50,000 mean normalized residual strength ratio values. A scatter plot of the 50,000 $(\overline{N}_1)_{60\text{-CS}}$ - $\overline{S}_r/\overline{\sigma}'_{vo}$ pairs is presented in Figure 6-12; it should be noted that the SPT resistance is again plotted on a logarithmic scale.

The Monte Carlo simulations produce a "cloud" of data points that are distributed in a manner that reflects the effects of uncertainties in the inputs to the back-calculation analyses. By using $\overline{\text{ZIF}}$ 0f 0.433, the values of $(\overline{N}_1)_{60\text{-CS}}$ and $\overline{S}_r/\overline{\sigma}'_{vo}$ are 7.3 bpf and 0.134, respectively. The representative values of $(N_1)_{60\text{-CS}}$ and S_r/σ'_{vo} reported by Olson et al. (2000) and Olson (2001) were 8.0 bpf and 0.070 to 0.126, respectively. Therefore, the mean SPT resistance from the Monte Carlo analyses was somewhat lower than the representative SPT resistance interpreted by Olson et al. (2000) and Olson (2001), and the mean NRSR was above the range reported by Olson et al. (2000) and Olson (2001).

As discussed in Section 5.2.1.1, with σ_{ZIF} of 0.0693, the final results that involve uncertainty of ZIF produce a marginal distribution of $\overline{S}_r/\overline{\sigma}'_{vo}$ that has a mean and standard deviation of 0.1358 and 0.0284, respectively. By using Equation (5.25) from the Monte Carlo analyses, the average value of $\overline{\sigma}'_{vo}$ is estimated as 2544 psf in the pre-failure condition. This value gives the strength ratio values of 0.340 and 0.032 for the pre- and post-failure geometry, respectively.

The Monte Carlo analyses provide useful insight into the effects of uncertainties in input parameters on back-calculated normalized residual strength ratios. The normalized residual strength ratios obtained from this process were approximately normally distributed with a coefficient of variation of approximately 20.9%, which is slightly lower than the coefficient for the residual strength, $\overline{S}_r$. The fact that the Wachusett Dam case history is one of the most thoroughly investigated and well-documented flow slide case histories available in the literature suggests that the coefficients of variation of other case histories is likely to be greater than 20.9%.

6.4.4 Discussion

The results of the Monte Carlo simulations illustrate the effects of uncertainties in the input parameters to a back-calculation analysis on the results of the back-calculation analysis. The "clouds" of data points shown in Figures 6-11 and 6-12 provide a somewhat limited view of these effects because the density of plotted points is so large that the points overlap over much of the region of interest. Figure 6-13 shows two additional plots of the $(\overline{N}_1)_{60\text{-CS}}$ - $\overline{S}_r$ data, both of which better illustrate the shape of the distribution. Figure 6-14 shows similar plots for the $(\overline{N}_1)_{60\text{-CS}}$ - $\overline{S}_r/\overline{\sigma}'_{vo}$ data. Table 6-2 summarizes the results of the Monte-Carlo-type analyses. Table 6-3 summarizes the results concluded by other researchers.

The preceding sections have presented a detailed description of the application of the Monte Carlo back-calculation methodology to the Wachusett Dam case history. The same methodology was applied to eight other case histories for which sufficient information on geometric and material properties, and on kinetic effects, was available. The results of Monte Carlo analyses of those case histories are briefly described in Section 6.5. Finally, approximate procedures for estimation of the effects of uncertainties in other case histories, for which less information was available, are described in Section 6.6.

6.5 ADDITIONAL CASE HISTORIES INVOLVING KINETIC EFFECTS

A number of flow slides have caused enough damage to warrant some level of post-failure investigation. Many of the larger of these flow slides involved flow velocities sufficient to induce significant inertial forces in the unstable soil. Proper back-calculation of residual strength from these case histories, therefore, requires consideration of kinetic effects. This section presents brief reviews of the circumstances of these slides, and of the results of the Monte Carlo back-calculation processes.

6.5.1 Calaveras Dam

Calaveras Dam was constructed just south of San Francisco in 1914. The dam was constructed by hydraulic filling, but suffered a flow slide in its upstream slope when it was within 40 ft of its intended 210 ft height. The slide caused the upstream toe to move more than 650 ft and the height of the embankment to decrease by 80 – 100 ft.

6.5.1.1 Available Information

The Calaveras Dam failure was described in several publications (Hazen, 1918, Hazen and Metcalf, 1918, and Hazen, 1920), each of which contributes some useful information. Because the failure occurred nearly 90 years ago, however, the amount of quantitative data is relatively small. Cross-sections through the failed section appear to provide a good indication of the external geometry before and after failure. However, the geometry of the internal boundaries, in particular the boundaries between the core and shells, is not well defined. The densities of the soils had to be estimated, as did the undrained strength ratio of the core material.

Notably, no SPT measurements were made at Calaveras Dam. Previous attempts at back-calculation of residual strength for this case history have assigned representative $(N_1)_{60\text{-CS}}$ values ranging from 2 bpf (Poulos, 1988) to 12 bpf (Seed, 1987, Seed and

Harder, 1990, and Stark and Mesri, 1992). These assignments were made based on various assumptions about the in-situ relative density of the soil and about the relationship between relative density and SPT resistance, but the details of those assumptions have not been reported.

Olson (2001) used the information of relative compaction of shell material (75% to 85 %) and estimated the possible relative density to range from 20 to 50 %, which showed the average relative density to be 35%. Combined with the estimated average vertical effective stress of 6422 psf, he estimated a representative $(N_1)_{60}$ of 8.0 bpf. Current research agreed with Olson's procedure and set $\overline{N}$ equal to 8.0 bpf.

6.5.1.2 Previously Back-calculated Residual Strengths

The Calaveras Dam case history has been analyzed by Seed (1987), Poulos (1988), Seed and Harder (1990), Stark and Mesri (1992), and Olson (2001). The residual strengths obtained from these investigations were generally on the order of 650 – 750 psf, although Olson (2001) implied a high degree of uncertainty in his reported residual strength range of 75 – 1600 psf.

With consideration of kinetic effects, Olson (2001) reported S_r and S_r/σ'_{vo} values of 722 psf (with a range of 600 – 791 psf) and 0.112 (with a range of 0.095 – 0.123), respectively.

6.5.1.3 Monte Carlo Analyses

Monte Carlo back-calculation analyses were performed for Calaveras Dam. The uncertainty in the input parameters for the Monte Carlo analyses had to reflect the significant uncertainty in geometric and material properties associated with the available information for this relatively old failure. These uncertainties were considerably higher than for some of the other case histories, particularly in comparison to the well-documented Wachusett Dam case history.

Table 6-4 illustrates the manner in which uncertainty was characterized for the Calaveras Dam. The uncertainty in SPT resistance, for example, was very large since no SPT measurements were available. Uncertainties in geometric factors were also significant.

6.5.1.4 Results of Monte Carlo Analyses

A total of 50,000 Monte Carlo simulations produced 50,000 pairs of mean SPT resistance and mean residual strength values. A scatter plot of the 50,000 $(\overline{N}_1)_{60\text{-CS}}$ - $\overline{S}_r$ pairs is presented in Figure 6-15; it should be noted that the SPT resistance is plotted on a logarithmic scale.

The Monte Carlo simulations produced a "cloud" of data points that are distributed in a manner that reflects the effects of uncertainties in the inputs to the back-calculation analyses. By using $\overline{\text{ZIF}}$ = 0.404 and σ_{ZIF} = 0.089, the mean values of $(\overline{N}_1)_{60\text{-CS}}$ and $\overline{S}_r$ were 10.5 bpf and 637 psf, respectively. Therefore, both the mean SPT resistance and the mean residual strength from the Monte Carlo analyses of Calaveras Dam were somewhat lower than the values interpreted by previous investigators. The standard deviation of Sr was 223 psf.

The 50,000 Monte Carlo simulations also produced 50,000 mean normalized residual strength ratio values, shown in Figure 6-16. By using $\overline{\text{ZIF}}$ of 0.404, the mean value of $\overline{S}_r/\overline{\sigma}'_{vo}$ was 0.099 and the standard deviation was 0.034. The values of $(N_1)_{60}$ and S_r/σ'_{vo} estimated by Olson (2001) were 8.0 bpf and 0.112 (with a range of 0.012 – 0.270). Therefore, the mean NRSR was within the range reported by Olson (2001), but lower than the mean value presented by Olson.

The Monte Carlo analyses provide useful insight into the effects of uncertainties in input parameters on back-calculated residual strengths. The residual strengths obtained from this process were approximately normally distributed with a coefficient of variation of approximately 35%, which corresponds to a standard deviation of 223 psf. The NRSR values were approximately normally distributed, also with a coefficient of variation of about 34%. Uncertainty in the SPT resistance for this case history was quite large, particularly in comparison to the Wachusett Dam case history.

6.5.2 Fort Peck Dam

Located on the Missouri River in Montana, the Fort Peck Dam was planned to be hydraulic-filled to a designed height of about 240 ft with crest length over 10,000 ft. On September 22, 1938, after the dam collapsed near the end of construction, the flow-slide failure produced the displacement at upstream toe over 1200 ft and the crest drop of about 120 ft. Numerous investigations were conducted and produced a large amount of in-situ testing, laboratory experiments, and computer simulations to back-analyze the failure mechanism. Several possible reasons have been considered to be the trigger of the failure. Among them, the static liquefaction induced within the hydraulic-filled materials has been proven to be the cause of this failure.

6.5.2.1 Available Information

Tremendous efforts have been made by various researcher and agencies to investigate the failure of the Fort Peck Dam. Some important references include U.S Army Corps of Engineers (1939), Middlebrooks (1942), Casagrande (1965; 1976), Marcuson and Krinitzsky (1976), Marcuson et al. (1978), and Kramer (1985). Because of the plentiful information to describe this case, the back-analyses involves relatively low uncertainty compared with other cases.

U.S Army Corps of Engineers (1939) and Middlebrooks (1942) showed the well defined external and internal geometries with a distinct failure surface scarp. The uncertainty of the geometric parameters is relative low in this case.

Marcuson and Krinitzsky (1976) documented a series of in-situ and laboratory tests conducted by the U.S Army Corps of Engineers. Among those data, a relatively large number of SPT blowcount values provides the information with good quality and quantity for the back-analyses procedure.

The representative $(N_1)_{60\text{-CS}}$ value for Fort Peck Dam has been estimated as 5.3 bpf (Poulos, 1988), 10 bpf (Seed and Harder, 1990; Stark and Mesri, 1992), and 11 bpf (Seed, 1987). Olson (2001) estimated the representative $(N_1)_{60}$ at 8.5 bpf.

6.5.2.2 Previous Back-Calculated Residual Strengths

The Fort Peck Dam case history has been analyzed by Lucia et al. (1982), Seed (1987), Davis et al. (1988), Poulos (1988), Seed and Harder (1990), Stark and Mesri (1992), and Olson (2001). By using the conventional back-calculation procedure, the residual strengths obtained from these investigations were generally on the order of 250 – 700 psf, although Olson (2001) implied a high degree of uncertainty in his reported residual strength range of 79 – 1731 psf.

Some conventional back-calculation results also showed the NRSR values. Stark and Mesri (1992) show the best estimated NRSR with value of 0.032. By back-calculating on the pre- and post-failure geometries, Olson (2001) estimated the NRSR values has a range between 0.011 to 0.255.

Using a sliding block model, Davis et al. (1988) and Olson (2001) provided the back-calculation results including the kinetic effect. Davis et al. (1988) suggested the best estimated residual strength of 700 psf. Olson (2001) reported S_r and S_r/σ'_{vo} values of 571 psf (with a range of 352 – 711 psf) and 0.078 (with a range of 0.048 – 0.097), respectively.

6.5.2.3 Monte Carlo Analyses

Monte Carlo back-calculation analyses were performed for Fort Peck Dam. The uncertainty in the input parameters for the Monte Carlo analyses had to reflect the relatively low uncertainty in geometric and material properties associated with the relatively large amount of available information. Table 6-4 illustrates the manner in which uncertainty was characterized for the Fort Peck Dam.

6.5.2.4 Results of Monte Carlo Analyses

A total of 50,000 Monte Carlo simulations produced 50,000 pairs of mean SPT resistance and mean residual strength values. A scatter plot of the 50,000 $(\overline{N}_1)_{60\text{-CS}}$ - $\overline{S}_r$ pairs is presented in Figure 6-17; it should be noted that the SPT resistance is plotted on a logarithmic scale.

The Monte Carlo simulations produced a "cloud" of data points that are distributed in a manner that reflects the effects of uncertainties in the inputs to the back-calculation analyses. By using $\overline{\text{ZIF}}$ = 0.36 and σ_{ZIF} = 0.0576, the mean values of $(\overline{N}_1)_{60\text{-CS}}$ and $\overline{S}_r$ were 15.8 bpf and 672 psf, respectively. The mean $(\overline{N}_1)_{60\text{-CS}}$ value, which is estimated based on Marcuson and Krinitzsky (1976), has a higher value compared to results interpreted by previous investigators. The mean $\overline{S}_r$ values show good agreement with others. The standard deviation of residual strength was 130 psf.

The 50,000 Monte Carlo simulations also produced 50,000 mean normalized residual strength ratio values, shown in Figure 6-18. By using $\overline{\text{ZIF}}$ of 0.36, the mean value of $\overline{S}_r/\overline{\sigma}'_{vo}$ was 0.094 and the standard deviation was 0.017. The mean NRSR was within the range reported by Olson (2001), but higher than the value presented by Olson.

The Monte Carlo analyses provide useful insight into the effects of uncertainties in input parameters on back-calculated residual strengths. The residual strengths obtained from this process were approximately normally distributed with a coefficient of variation of approximately 19.2. The NRSR values were approximately normally distributed, also with a coefficient of variation of about 18.3%. The back-calculation results show a relatively low degree of uncertainty because this case was thoroughly investigated and well documented.

6.5.3 Hachiro-Gata Roadway Embankment

The 1983 Nihonkai-Chubu earthquake triggered a slump-type flow failure near the Akita area in Japan. The specific site for the Monte-Carlo-type analyses is the Hachiro-Gata roadway embankment. The failure produced some 4-ft drop of the roadway from its original height of about 15 ft above a firm soil stratum.

6.5.3.1 Available Information

Ohya et al. (1985) provided information to describe the case history. These information included the pre- and post-failure geometries, construction method, and various in-situ testing results. The representative SPT resistance of this case was converted from the data that were conducted by the Japan system to the $(N_1)_{60}$ values.

Generally, this case was documented with limited information. As a result, certain assumptions had to be made to define the soil properties (e.g. density), location of the water table, and geometric parameters (e.g. exterior and interior geometries, and location of failure surface).

6.5.3.2 Previously Back-calculated Residual Strengths

Olson (2001) estimated a representative $(N_1)_{60}$ of 4.4 bpf and a S_r range of 29 – 100 psf using the conventional back-calculation approach. His conventional back-calculation approach also estimated S_r/σ'_{vo} value ranging from 0.16 to 0.033. With consideration of kinetic effects, Olson (2001) reported S_r and S_r/σ'_{vo} values of 42 psf (with a range of 21 – 67 psf) and 0.062 (with a range of 0.03 – 0.092), respectively.

6.5.3.3 Monte Carlo Analyses

Monte Carlo back-calculation analyses were performed for the Hachiro-Gata roadway embankment flow slide case history. Table 6-4 illustrates the manner in which uncertainty was characterized for this case.

6.5.3.4 Results of Monte Carlo Analyses

A total of 50,000 Monte Carlo simulations produced 50,000 pairs of mean SPT resistance and mean residual strength values. A scatter plot of the 50,000 $(\overline{N}_1)_{60\text{-CS}}$ - $\overline{S}_r$ pairs is presented in Figure 6-19; it should be noted that the SPT resistance is plotted on a logarithmic scale.

The Monte Carlo simulations produced a "cloud" of data points that are distributed in a manner that reflects the effects of uncertainties in the inputs to the back-calculation analyses. By using $\overline{\text{ZIF}}$ = 0.5 and σ_{ZIF} = 0.15, the mean values of $(\overline{N}_1)_{60\text{-CS}}$ and $\overline{S}_r$ were 5.7 bpf and 65 psf, respectively. Therefore, the mean residual strength from the Monte Carlo analyses of Hachiro-Gata roadway was somewhat higher than the values interpreted by previous investigator. The standard deviation of residual strength was 25 psf.

The 50,000 Monte Carlo simulations also produced 50,000 mean normalized residual strength ratio values, shown in Figure 6-20. The mean value and standard deviation of $\overline{S}_r/\overline{\sigma}'_{vo}$ was 0.164 and 0.064, respectively.

The Monte Carlo analyses provide useful insight into the effects of uncertainties in input parameters on back-calculated residual strengths. The residual strengths obtained from this process were approximately normally distributed with a coefficient of variation of approximately 38%. The NRSR values were approximately normally distributed, with a coefficient of variation of about 39.1%. Uncertainty in the SPT resistance for this case history was relatively high due to the generally limited quantity and quality of available information.

6.5.4 Lake Ackerman Road Embankment

Hryciw et al. (1990) documented an unusual flow slide at the location of a road embankment along the shore of Lake Ackerman on the upper peninsula of Michigan. The site experienced a flow slide when a series of six geophysical exploration trucks generated vibrations for a deep seismic reflection exploration. The flow slide involved a 300-ft long section of the embankment and underlying soil that moved some 60 ft horizontally and 10 ft vertically.

6.5.4.1 Available Information

The Lake Ackerman failure was investigated shortly after the failure and reported in a single publication (Hryciw et al., 1990). The geometry of the site is well established, and the geometry of the failure surface is reasonably well known. Subsurface investigations following the failure made use of SPT and DMT testing in the field, and of laboratory testing. SPT measurements were taken both within and just outside of the area involved in the failure. In general, the amount and quality of available information for the Lake Ackerman flow slide case history was good.

6.5.4.2 Previously Back-calculated Residual Strengths

The Lake Ackerman case history has been analyzed by Hryciw et al. (1990) and Olson (2001). Hryciw et al. (1990) reported a representative $(N_1)_{60}$ of 3 bpf and a S_r range of 170 – 260 psf. Olson (2001) reported a representative SPT resistance of 3 bpf and a residual strength range of 71 – 211 psf. Considering kinetic effects, Olson (2001) reported S_r and S_r/σ'_{vo} values of 82 psf (with a range of 71 – 98 psf) and 0.076 (with a range of 0.092 – 0.066), respectively.

6.5.4.3 Monte Carlo Analyses

Monte Carlo back-calculation analyses were performed for the Lake Ackerman flow slide case history. Table 6-4 illustrates the manner in which uncertainty was characterized for the Lake Ackerman case history.

6.5.4.4 Results of Monte Carlo Analyses

A total of 50,000 Monte Carlo simulations produced 50,000 pairs of mean SPT resistance and mean residual strength values. A scatter plot of the 50,000 $(\overline{N}_1)_{60\text{-CS}}$ - $\overline{S}_r$ pairs is presented in Figure 6-21; it should be noted that the SPT resistance is plotted on a logarithmic scale.

The Monte Carlo simulations produced a "cloud" of data points that are distributed in a manner that reflects the effects of uncertainties in the inputs to the back-calculation analyses, shown in Figure 6-22. By using $\overline{\text{ZIF}}$ = 0.46 and σ_{ZIF} = 0.074, the mean values of $(\overline{N}_1)_{60\text{-CS}}$ and $\overline{S}_r$ were 4.8 bpf and 98 psf, respectively. Therefore, the mean SPT resistance was somewhat higher and the mean residual strength from the Monte Carlo analyses of Lake Ackerman were somewhat lower than the values interpreted by previous investigators. The standard deviation of residual strength was 20 psf.

The 50,000 Monte Carlo simulations also produced 50,000 mean normalized residual strength ratio values. The mean value and standard deviation of $\overline{S}_r/\overline{\sigma}'_{vo}$ was 0.1126 and 0.022, respectively.

The Monte Carlo analyses provide useful insight into the effects of uncertainties in input parameters on back-calculated residual strengths. The residual strengths obtained from this process were approximately normally distributed with a coefficient of variation of approximately 20.8%. The NRSR values were approximately normally distributed, with a coefficient of variation of about 19.6%. Uncertainty in the SPT resistance for this case history was relatively low due to the generally good quantity and quality of available information.

6.5.5 Lower San Fernando Dam

After the 1971 San Fernando earthquake (magnitude 6.6), Lower San Fernando Dam suffered serious damage from a flow slide failure. The flow slide failure produced displacement of the upstream toe of over 150 ft and a drop in the crest of about 50 ft. Numerous investigations have been conducted ever since. As a result, the failure of the Lower San Fernando Dam becomes one of the most important cases for evaluation of the residual strength of liquefied soil. Furthermore, because the available information to describe this case is plentiful, consequently the uncertainty of this case is relatively low.

6.5.5.1 Available Information

Tremendous efforts have been made by various researchers and agencies to investigate residual strength from the failure of the Lower San Fernando Dam. Some important references include Seed et al. (1973), Seed et al. (1975a, b), Lee et al. (1975), Seed (1987), Davis et al. (1988), Castro et al. (1989), Seed et al. (1989), Marcuson et al. (1990), Seed and Harder (1990), and Stark and Mesri (1992). With plenty of information, this case has been illustrated with high quality and quantity.

Seed et al. (1973) presented the first publication that described this case in details, which included the geometries, soil property investigation, and back-analyses of the failure mechanism. The level of details even showed the various soil strata in their pre- and post-failure positions. These efforts gave the back-analyses procedure a high degree of confidence on defining the required geometric parameters.

Castro et al. (1989) and Seed et al. (1989) re-evaluated this case and provided further information by conducting additional in-situ and laboratory testing. By combining both accomplishments both in 1973 and 1989, the process of defining a representative SPT resistance was provided with good quality and sufficient quantity. Various values had been proposed by different researchers. The representative SPT resistance has been chosen as $(N_1)_{60\text{-CS}}$ = 4.0 – 17.5 bpf (Seed, 1987, Davis et al., 1988, Seed et. al., 1988, Poulos, 1988, Seed and Harder, 1990, Stark and Mesri, 1992, and McRoberts and Sladen, 1992), and $(N_1)_{60}$ = 5.5 – 11.5 bpf (Davis et al., 1988, Seed et al., 1988, Seed and Harder, 1990, Stark and Mesri, 1992, and Olson, 2001).

6.5.5.2 Previously Back-calculated Residual Strengths

Using the conventional back-calculation procedure, the residual strength of liquefied soil has been estimated to have a range from 400 – 750 psf (Seed, 1987, Seed et al., 1988, Poulos, 1988, Seed and Harder, 1990, and Stark and Mesri, 1992, and Olson, 2001).

Some conventional back-calculation results also showed the NRSR values. Stark and Mesri (1992) show the best estimated NRSR with value of 0.102. By back-calculating on the post-failure geometry, Olson (2001) estimated the NRSR value has a range between 0.026 to 0.076.

By using the sliding block model, Davis et al. (1988) and Olson (2001) provided the back-calculation involving kinetic effects. Davis et al. (1988) suggested the best estimated residual strength of 510 psf. Olson (2001) reported S_r and S_r/σ'_{vo} values of

391 psf (with a range of 331 – 456 psf) and 0.112 (with a range of 0.095 – 0.131), respectively.

6.5.5.3 Monte Carlo Analyses

Monte Carlo back-calculation analyses were performed for Lower San Fernando Dam. The uncertainty in the input parameters for the Monte Carlo analyses had to reflect the low uncertainty in geometric and material properties associated with the relatively large amount of available information. Table 6-4 illustrates the manner in which uncertainty was characterized for the Lower San Fernando Dam.

6.5.5.4 Results of Monte Carlo Analyses

A total of 50,000 Monte Carlo simulations produced 50,000 pairs of mean SPT resistance and mean residual strength values. A scatter plot of the 50,000 $(\overline{N}_1)_{60\text{-CS}}$ - $\overline{S}_r$ pairs is presented in Figure 6-23; it should be noted that the SPT resistance is plotted on a logarithmic scale.

The Monte Carlo simulations produced a "cloud" of data points that are distributed in a manner that reflects the effects of uncertainties in the inputs to the back-calculation analyses. By using $\overline{\text{ZIF}}$ = 0.446 and σ_{ZIF} = 0.098, the mean values of $(\overline{N}_1)_{60\text{-CS}}$ and $\overline{S}_r$ were 14.5 bpf and 485 psf, respectively. The mean $(\overline{N}_1)_{60\text{-CS}}$ value, which is estimated based on Seed et al. (1973), Castro et al. (1989), and Seed et al. (1989), shows good agreement with others. The mean $\overline{S}_r$ values, however, falls toward the lower bound of the previous investigations. The standard deviation of residual strength was 111 psf.

The 50,000 Monte Carlo simulations also produced 50,000 mean normalized residual strength ratio values, shown in Figure 6-24. By using $\overline{\text{ZIF}}$ of 0.446, the mean value and standard deviation of $\bar{S}_r/\bar{\sigma}'_{vo}$ were 0.133 and 0.029, respectively. The mean NRSR was higher than the representative value suggested by Stark and Mesri (1992).

The Monte Carlo analyses provide useful insight into the effects of uncertainties in input parameters on back-calculated residual strengths. The residual strengths obtained from this process were approximately normally distributed with a coefficient of variation of approximately 22.9%. The NRSR values were approximately normally distributed, also with a coefficient of variation of about 21.6%. The back-calculation results show a low degree of uncertainty because this case was documented with high quality and quantity.

6.5.6 Route 272 Roadway Embankment

A portion of Route 272 at Higashiarekinai, Japan, was seriously damaged by flow-slide failure caused by the 1993 Kushiro-oki earthquake (magnitude 7.8). The post-failure geometry showed a displacement of about 80 ft at toe and a crest drop of about 8 ft. Geographically, this site is similar to another case history at the Shibecha-Cho embankment (discussed in Section 6.5.7).

6.5.6.1 Available Information

Because of a citation error, the original reference could not be located. The information proved for this case history is mainly obtained from Olson (2001) and from information provided for the case of Shibecha-Cho embankment.

Generally, the case history of the Route 272 roadway embankment is moderately documented. Embankment geometries were provided in their pre- and post failure forms. Other information, such as soil properties and in-situ testing data (SPT), were also provided by Olson (2001).

6.5.6.2 Previously Back-calculated Residual Strengths

Olson (2001) estimated a representative $(N_1)_{60}$ of 6.3 bpf and S_r range of 61 – 274 psf using the conventional back-calculation approach. His conventional back-calculation approach also estimated S_r/σ'_{vo} ranging from 0.059 to 0.25. Considering kinetic effects, Olson (2001) reported S_r and S_r/σ'_{vo} values of 100 psf (with a range of 63 – 119 psf) and 0.097 (with a range of 0.061 – 0.117), respectively.

6.5.6.3 Monte Carlo Analyses

Monte Carlo back-calculation analyses were performed for the Route 272 flow-slide case history. Table 6-4 illustrates the manner in which uncertainty was characterized for the Route 272 roadway embankment case history.

6.5.6.4 Results of Monte Carlo Analyses

A total of 50,000 Monte Carlo simulations produced 50,000 pairs of mean SPT resistance and mean residual strength values. A scatter plot of the 50,000 $(\overline{N}_1)_{60\text{-CS}}$ - $\overline{S}_r$ pairs is presented in Figure 6-25; it should be noted that the SPT resistance is plotted on a logarithmic scale.

The Monte Carlo simulations produced a "cloud" of data points that are distributed in a manner that reflects the effects of uncertainties in the inputs to the back-calculation analyses. By using $\overline{\text{ZIF}}$ = 0.446 and σ_{ZIF} = 0.098, the mean values of $(\overline{N}_1)_{60\text{-CS}}$ and $\overline{S}_r$ were 8.5 bpf and 131 psf, respectively. Therefore, the mean residual strength from the Monte Carlo analyses of Route 272 roadway embankment was somewhat higher than the values interpreted by previous investigator. The standard deviation of residual strength was 34 psf.

The 50,000 Monte Carlo simulations also produced 50,000 mean normalized residual strength ratio values, shown in Figure 6-26. By using $\overline{\text{ZIF}}$ of 0.446, the mean value and standard deviation of $\overline{S}_r/\overline{\sigma}'_{vo}$ were 0.125 and 0.030, respectively.

The Monte Carlo analyses provide useful insight into the effects of uncertainties in input parameters on back-calculated residual strengths. The residual strengths obtained from this process were approximately normally distributed with a coefficient of variation of approximately 26%. The NRSR values were approximately normally distributed, with a coefficient of variation of about 23.6%.

6.5.7 Shibecha-Cho Embankment

The 1993 Kushiro-oki earthquake (magnitude 7.8) produced serious damage near Hushiro city in Hokkaido, Japan. Among these damages, a 640-ft long embankment collapsed in the Shibecha-Cho area. A flow-slide failure was triggered at one specific site and produced a displacement of 80 ft at the toe and a crest drop of about 10 ft.

This case is geographically similar to the case history of Route 272 roadway embankment (discussed in Section 6.5.6).

6.5.7.1 Available Information

Available information for this case can be found in Miura et al. (1995; 1998). This case was relatively well-documented with history of construction, soil properties, and pre- and post-failure geometries. The in-situ soil investigation was made by the Swedish sounding. A proper procedure was used to convert the in-situ soil resistance from the Swedish sounding results to the SPT resistance. In the description of failure surface, however, was not reported with distinctive locations. A relatively high uncertainty was applied to fluctuate the failure surface locations.

6.5.7.2 Previously Back-calculated Residual Strengths

Olson (2001) estimated a representative $(N_1)_{60}$ of 5.6 bpf and S_r range of 104 – 330 psf using the conventional back-calculation approach. His conventional back-calculation approach also estimated S_r/σ'_{vo} values ranging from 0.078 to 0.24. Considering kinetic effects, Olson (2001) reported S_r and S_r/σ'_{vo} values of 117 psf (with a range of 81 – 173 psf) and 0.086 (with a range of 0.061 – 0.123), respectively.

6.5.7.3 Monte Carlo Analyses

Monte Carlo back-calculation analyses were performed for the Shibecha-Cho embankment flow slide case history. Table 6-4 illustrates the manner in which uncertainty was characterized for the Shibecha-Cho embankment case history.

6.5.7.4 Results of Monte Carlo Analyses

A total of 50,000 Monte Carlo simulations produced 50,000 pairs of mean SPT resistance and mean residual strength values. A scatter plot of the 50,000 $(\overline{N}_1)_{60\text{-CS}}$ - $\overline{S}_r$ pairs is presented in Figure 6-27; it should be noted that the SPT resistance is plotted on a logarithmic scale.

The Monte Carlo simulations produced a "cloud" of data points that are distributed in a manner that reflects the effects of uncertainties in the inputs to the back-calculation analyses. By using $\overline{\text{ZIF}}$ = 0.46 and σ_{ZIF} = 0.101, the mean values of $(\overline{N}_1)_{60\text{-CS}}$ and $\overline{S}_r$ were 5.6 bpf and 209 psf, respectively. Therefore, the mean residual strength from the Monte Carlo analyses of Shibecha-Cho embankment was somewhat higher than the values interpreted by previous investigator. The standard deviation of residual strength was 39 psf.

The 50,000 Monte Carlo simulations also produced 50,000 mean normalized residual strength ratio values, shown in Figure 6-28. By using $\overline{\text{ZIF}}$ of 0.46, the mean value and standard deviation of $\overline{S}_r/\overline{\sigma}'_{vo}$ were 0.200 and 0.031, respectively.

The Monte Carlo analyses provide useful insight into the effects of uncertainties in input parameters on back-calculated residual strengths. The residual strengths obtained from this process were approximately normally distributed with a coefficient of variation of approximately 18.5%. The NRSR values were approximately normally distributed, with a coefficient of variation of about 15.6%. Uncertainty in the SPT resistance for this case history was relatively high due to the SPT resistance was converted from the Swedish sounding results.

6.5.8 Uetsu-Line Railway Embankment

The 1964 Niigata earthquake (magnitude 7.7) produced numerous instances of damage in and near the Niigata Prefecture, Japan. Various forms of damage were observed along several railway lines including settlement, rock falls, cracking, and flow slide. Among those failures, a flow-slide failure produced serious damage at the Uetsu-Line railway embankment. The post-failure geometry showed a displacement of about 340 ft at the toe of the embankment and a drop of the crest of about 17 ft. The original height of embankment was about 27 ft above the native ground surface.

6.5.8.1 Available Information

Yamada (1966) documented the various failures produced by the 1964 Niigata earthquake. The failure at the Uetsu-Line railway was a typical flow slide-type failure. However, only limited information was provided besides the pre- and post-failure geometries. As a result, the parameters describing this case had a relatively high level of uncertainty.

Unfortunately, no in-situ testing data had been conducted for this case. According to previous researches on this case (Seed, 1987; Seed and Harder, 1990, Stark and Mesri, 1992; Olson, 2001), the representative $(N_1)_{60}$ was generally agreed to be 3 bpf. It is believed the previous process of choosing the representative SPT resistance was made according to the nature of the local soil type and some reasonable judgments.

6.5.8.2 Previously Back-calculated Residual Strengths

The Uetsu-Line railway embankment case history has been analyzed by Lucia et al. (1982), Seed (1987), Davis et al. (1988), Seed and Harder (1990), Stark and Mesri (1992), and Olson (2001). The residual strengths obtained from these investigations were generally on the order of 35 – 40 psf. Among them, Davis et al. (1988) and Olson (2001) used the sliding block model for the back-calculation.

The back-calculation of S_r/σ'_{vo} was conducted by Stark and Mesri (1992) and Olson (2001). By using the conventional back-calculation procedure, Stark and Mesri (1992) presented a best estimate value of 0.015. Olson (2001) estimated the value of S_r/σ'_{vo} ranging from 0.009 to 0.21. By using the sliding block model, Olson (2001) calculate that the best estimation for S_r/σ'_{vo} is 0.027.

6.5.8.3 Monte Carlo Analyses

Monte Carlo back-calculation analyses were performed for the Uetsu-Line railway embankment flow slide case history. Table 6-4 illustrates the manner in which uncertainty was characterized for the Uetsu-Line Railway embankment case history.

Because the available information for this case is limited, the parameters used in the back-calculated procedure of this case carry a high level of uncertainty.

6.5.8.4 Results of Monte Carlo Analyses

A total of 50,000 Monte Carlo simulations produced 50,000 pairs of mean SPT resistance and mean residual strength values. A scatter plot of the 50,000 $(\overline{N}_1)_{60\text{-CS}}$ - $\overline{S}_r$ pairs is presented in Figure 6-29; it should be noted that the SPT resistance is plotted on a logarithmic scale.

The Monte Carlo simulations produced a "cloud" of data points that are distributed in a manner that reflects the effects of uncertainties in the inputs to the back-calculation analyses. By using $\overline{\text{ZIF}}$ = 0.28 and σ_{ZIF} = 0.084, the mean values of $(\overline{N}_1)_{60\text{-CS}}$ and $\overline{S}_r$ were 2.9 bpf and 44 psf, respectively. Therefore, both the mean residual strength and the representative SPE resistance from the Monte Carlo analyses of Uetsu-Line railway embankment agree with the values interpreted by previous investigator. The standard deviation of residual strength was 25 psf.

The 50,000 Monte Carlo simulations also produced 50,000 mean normalized residual strength ratio values, shown in Figure 6-30. By using $\overline{\text{ZIF}}$ of 0.28, the mean value and standard deviation of $\overline{S}_r/\overline{\sigma}'_{vo}$ were 0.048 and 0.027, respectively.

The Monte Carlo analyses provide useful insight into the effects of uncertainties in input parameters on back-calculated residual strengths. The residual strengths obtained from this process were approximately normally distributed with a coefficient of variation of approximately 56.8%. The NRSR values were approximately normally distributed, with a coefficient of variation of about 55%. Uncertainty in the SPT resistance for this case history was relatively high due to no SPT resistance is available for this case. Furthermore, the back-calculated results on residual strength and NRSR have high levels of uncertainty because the high uncertainties that were inherited from the geometric parameters.

6.6 ADDITIONAL CASE HISTORIES

A second set of flow-slide case histories, hereafter referred to as the secondary case histories, has been analyzed by multiple investigators but at a lesser level of detail than the primary case histories described in the previous section. These case histories typically involve smaller slopes and/or lower levels of failure investigation/documentation, which tend to reduce the need for detailed analyses. Most of these case histories have been interpreted using simplified back-calculation models such as infinite slope models, and involve more extensive assumptions about representative material and geometric properties.

The approach taken to estimate the uncertainties in these case histories is consistent with the simplified procedures used by previous investigators; detailed Monte Carlo analyses of individual case histories that were not thoroughly investigated and/or documented were not judged to be warranted. Instead, the knowledge gained during the detailed Monte Carlo analyses of the primary case histories was used to estimate the uncertainty in SPT resistance and residual strength in a manner that would be consistent with the primary case histories while reflecting the additional uncertainty in the secondary case histories.

The procedures used to estimate uncertainties in the secondary case histories are described in the following section. Application of those procedures to the individual case histories is then described in Section 6.6.2.

6.6.1 Estimation of Distributions

The joint distributions of SPT resistance and residual strength for the secondary case histories were assumed to be of the same form as those of the primary case histories – lognormal with respect to $(N_1)_{60\text{-CS}}$ and normal with respect to S_r. The $(N_1)_{60\text{-CS}}$ and S_r values were taken, for consistency with those from the primary case history back-calculation, to be uncorrelated.

The marginal distribution of $(N_1)_{60\text{-CS}}$ was determined in exactly the same manner as in the primary case histories – as a weighted average of three potential methods for estimating the coefficient of variation. This procedure was described in Section 5.2.2.2 and is not repeated here.

The marginal distribution of S_r can be described by two parameters – the mean and coefficient of variation of the residual strength. The mean value of S_r for each secondary case history was taken as the average of the applicable back-calculated residual strengths from previous investigations. Given the relatively simple back-calculation procedures used in past investigations, and the generally good agreement between back-calculated residual strengths obtained by others, repetition of the same types of analyses was not considered necessary. Estimation of the coefficient of variation of residual strength for the secondary case histories involved a more complicated process.

The procedure for estimation of the dispersion in residual strength estimates was developed to: (a) provide general consistency with the estimated levels of dispersion in the primary case histories, and (b) account for the increased uncertainty associated with the use of simplified models that may not accurately represent actual failure mechanisms in the secondary case histories. Toward this end, the coefficient of variation for the secondary case histories ($COV_{\text{secondary}}$) was taken to be composed of two components

$$COV^2_{\text{secondary}} = COV^2_{\text{primary}} + COV^2_{\text{model}} \tag{6.2}$$

where COV_{primary} is the estimated coefficient of variation for a primary case history with a consistent level of information/documentation and COV_{model} is an estimated coefficient of variation associated with modeling uncertainty.

The estimated coefficient of variation for a primary case history was obtained by a two-step process. The first step was to determine which parameters contributed most strongly to uncertainty in residual strength from the primary case histories. The parameters considered were $\sigma_{\text{half-sine}}$, $W_{\text{top-of-slope}}$, σ_{ZIF}, and the hydroplaning parameters, d_{hp} and α. This was accomplished by regressing the following equation on the results of the primary case history back-calculation analyses.

$$COV^2_{\text{primary}} = a + b\left\{\sigma_{\text{half-sine}}/H\right\}^2 + c\left\{W_{\text{top-of-slope}}/L\right\}^2 + d\,I_{\text{kinetic}}\,\sigma^2_{\text{ZIF}} + e\,I_{\text{HP}}\left\{d_{\text{hp}}/L\right\}(1-\alpha) \tag{6.3}$$

where I_{kinetic} is a kinetic effects importance factor (=1.0 for all primary case histories), I_{HP} is a hydroplaning importance factor and a - e are coefficients for which multiple linear regression analyses produced the following values: $a = 0$, $b = 0$, $c = 0$, $d = 2.22$, $e = 0$. In other words, the value of COV_{primary} was found to be dominated by σ_{ZIF}; this observation results from the fact that the criteria used to estimate $\sigma_{\text{half-sine}}$ and $W_{\text{top-of-slope}}$ are similar to those used to estimate σ_{ZIF}, and the fact that hydroplaning has a relatively small effect on the total amount of uncertainty in the primary case histories. The coefficient of variation from the primary case histories was then estimated by the simpler equation

$$COV^2_{\text{primary}} = 0.0056\exp\left[1.177 + 2.353\,Q_{\text{ZIF}}\right] \tag{6.4}$$

where Q_{ZIF} was estimated as described in Table 5-1a.

The coefficient of variation for modeling uncertainty was determined by a process that was not without some subjectivity; because of the variable levels of documentation of the case histories, a purely objective procedure was not possible. Because of the unavoidable subjectivity, a relatively simple and coarse rating (1-5 scale) of the appropriateness of the model was used to assign coefficients of variation for modeling uncertainty. The values produced by this procedure were as indicated in Table 6-5.

6.6.2 Statistical Parameters for Secondary Case Histories

The procedures described in the preceding section were applied to all of the secondary case histories for the purpose of estimating the joint distributions of $(N_1)_{60}$ and S_r for each. The parameters are summarized in the following sections.

6.6.2.1 Mean SPT Resistances

Each of the secondary case histories was investigated with different levels of detail. In some cases, SPT measurements were made in the liquefied zone and in other cases SPT values had to be estimated. For each of the secondary case histories, the mean SPT resistances were taken as those shown in Table 6-6.

6.6.2.2 Coefficients of Variation of SPT Resistances

The coefficients of variation for SPT resistance in the secondary case histories were obtained as the weighted averages of σ_{est}, σ_{range}, and σ_{calc} as described in Section 5.2.2.2. The values obtained for the secondary case histories are shown in Table 6-7.

6.6.2.3 Mean Residual Strength and Normalized Residual Strength Ratio

The mean residual strengths and residual strength ratios for the secondary case histories were simply taken as the average values of the residual strengths and residual strength ratios reported by previous investigators. In almost all cases, the residual strengths back-calculated by others were obtained from similar analyses and fell in a relatively narrow range. The values obtained for the secondary case histories are shown in Tables 6-8 and 6-9 for the mean residual strength and normalized residual strength ratio, respectively.

6.6.2.4 Coefficient of Variation of Residual Strength and Normalized Residual Strength Ratio

As described previously, the coefficient of variation for residual strength in the secondary case histories was estimated by a procedure intended to provide general consistency with the primary case histories and to account for the increased effects of modeling uncertainty in these more simplified analyses. The former objective was addressed by estimating Q_{ZIF} from which COV_{primary} could be computed, or Equation (6.4), in the same manner used for the primary case histories. Model uncertainty was judged in a semi-qualitative manner with consideration of the degree to which the available information supported the applicability of the chosen analytical model (one-dimensional, two-dimensional, etc.) to the individual case history. The coefficients of variation assigned to the secondary case histories were then obtained from Equation (6.2). The values obtained by this process are summarized in Table 6-10. The coefficients of variation for the residual strength ratios were assumed to be equal to those for residual strength.

6.6.3 Generation of Secondary Case History Data

Having determined the parameters describing the distributions of $(N_1)_{60\text{-CS}}$ and S_r, and made the assumption of independence (consistent with observations from the results of the primary case history back-calculations), secondary case history data could be generated. For each secondary case history, 50,000 $(N_1)_{60\text{-CS}} - S_r$ and 50,000 $(N_1)_{60\text{-CS}} - S_r/\sigma'_{vo}$ pairs with the desired distributions were generated.

6.7 COMBINATION OF PRIMARY AND SECONDARY CASE HISTORY DATA

With both the primary and secondary case histories, a complete database of case history data that reflects uncertainties can be assembled. For individual case, the distributions of data are shown in the form of contour plots in Figures 6-31 – 6-60. This database, which contains a total of 1,550,000 individual data points is shown graphically in Figures 6-61 (three-dimensional plot) and 6-62 (contour plot) for residual strength and in Figures 6-63 (three-dimensional plot) and 6-64 (contour plot) for residual strength ratio. The plots show considerable scatter, although it should be noted that data points from many of the individual case histories overlap each other in these plots. There is, however, a distinct trend of increasing residual strength with increasing SPT resistance. Determination of the form of this trend is described in the following chapter.

Table 6-11 summarizes the statistical parameters of the $(\overline{N}_1)_{60\text{-CS}}$, $\overline{S}_r$, and $\overline{S}_r/\overline{\sigma}'_{vo}$ for the generated, clouded data of each case in the database.

$(N_1)_{60}$
10.7
21.0
5.6
5.8
5.1
9.0
4.2
4.3
5.5
1.9
1.9
0.9
5.7

Table 6-1 Available $(N_1)_{60}$ within liquefied area of the North Dike of Wachusett Dam.

	$(\overline{N}_1)_{60\text{-CS}}$ (bpf)	$\overline{S}_r$ (1) (psf)	$\overline{S}_r/\overline{\sigma}'_{vo}$ (2)
Mean Value	7.3	348	0.1358
Standard Deviation	1.9	74.8	0.0284
COV	0.260	0.215	0.209

(1) Based on Equation (5.24)
(2) Based on Equation (5.25)

Table 6-2 Statistic parameter summary of Monte Carlo analyses on the North Dike of Wachusett Dam.

	S_r (psf)	S_r/σ'_{vo}
Post-failure Geometry Analysis	79	0.026
Pre-failure Geometry Analysis	785 - 875	0.26 - 0.30
Kinetic Effect Analysis	334 (217 - 399)	0.106 (0.070 - 0.126)

Table 6-3 Summary of back-calculation on the North Dike of Wachusett Dam, made by Olson et al. (2000) and Olson (2001).

	Calaveras Dam	Fort Peck Dam	Hachiro-Gata Roadway	Lake Ackerman Roadway	Lower San Fernando Dam	Route 272 Roadway	Shibecha-Cho Embankment	Uetsu Railway	Wachusett Dam
Uncertainty of Geometry									
$\overline{ZIF}$	0.404	0.360	0.500	0.460	0.446	0.446	0.460	0.280	0.433
COV_{ZIF}	0.22	0.16	0.30	0.16	0.22	0.22	0.22	0.30	0.16
σ_{ZIF}	0.0889	0.0576	0.15	0.0736	0.0981	0.0981	0.1012	0.084	0.0693
Exterior σ_X (ft)	0.25	0.25	0.5	0.25	0.25	0.25	0.25	0.25	0.25
Exterior σ_Y (ft)	1.0	1.0	2.0	1.0	1.0	1.0	1.0	1.0	1.0
Interior σ_X (ft)	1.0	1.0			1.0				
Interior σ_Y (ft)	4.0	4.0			4.0				
Uncertainty of Water Table									
Water Table in Reservoir $\sigma =$ (ft)	0.33	0.33	1.0	1.0	0.33				0.33
Phreatic Surface at Boundary $\sigma =$ (ft)	0.33	0.33	1.0	1.0	0.33				0.33
Phreatic Surface inside Embankment $\sigma =$ (ft)	3.33	3.33	3.33	1.0	3.33	3.33	2.0	3.33	3.33

Table 6-4 Summary of parameters used in Monte-Carlo-type analyses for flow slide case histories.

Table 6-4 continued.

	Calaveras Dam	Fort Peck Dam	Hachiro-Gata Roadway	Lake Ackerman Roadway	Lower San Fernando Dam	Route 272 Roadway	Shibecha-Cho Embankment	Uetsu Railway	Wachusett Dam
Uncertainty of Failure Surface									
$Q_{\text{half-sine}}$	2.0	2.0	3.0	2.0	1.0	2.0	3.0	3.0	1.0
Height of Slope H (ft)	170.0	200.0	15.0	19.0	100.0	28.0	30.0	26.0	80.0
$\sigma_{\text{half-sine}}$ (ft)	7.1	8.0	3.675	2.57	2.65	2.84	4.35	4.17	2.2
Random Field for Failure Surface $\sigma =$ (ft)	1.0	1.0	1.0	1.0	1.0	1.0	1.0	1.0	1.0
Scale of Fluctuation of Failure Surface (ft)	550	870	35	60	230	63	75	155	150
Length of Failure Surface L (ft)	1100	1740	70	120	460	126	150	310	300
$Q_{\text{top-of-slope}}$	0.0	0.0	1.0	0.0	1.0	0.0	1.0	1.0	0.0
$W_{\text{top-of-slope}}$ (ft)	0.0	0.0	4.2	0.0	27.6	0.0	9.0	18.6	0.0
Uncertainty of SPT Resistance									
Scale of Fluctuation of SPT, Horizontal (ft)	39.37	39.37	39.37	39.37	39.37	39.37	39.37	39.37	39.37
Scale of Fluctuation of SPT, Vertical (ft)	7.78	7.78	7.78	7.78	7.78	7:78	7.78	7.78	7.78
Number of SPT measurements (bpf)	0	46	2	10	42	6	5	0	13
σ_{used} (bpf)	12.0	3.7	4.0	3.9	5.8	6.6	4.8	4.5	6.9
$\sigma_{\bar{N}}$ (bpf)	12.0	0.5	2.8	1.2	0.9	2.7	2.2	4.5	1.9

Q_{model}	**Applicability**	COV_{model}
5	High	0.05
4	Medium High	0.10
3	Medium	0.15
2	Medium Low	0.20
1	Low	0.25

Table 6-5 Information quality factor Q_{model} and COV_{model} that define the quality of the secondary flow-slide case history.

Case	Available $(N_1)_{60}$ Values	**Fines Content (%)**	**Mean** $\Delta(N_1)_{60}$ (bpf)	**STD** $\Delta(N_1)_{60}$ (bpf)	**Estimated Mean** $(N_1)_{60}$ (bpf)
Asele Road	None	32	2.5	0.75	9
Chonan Middle School	5	18	1.5	0.45	5
El Cobre	0, 1, 2.5	90 - 100	5.6	0.03	1.2
Helsinki Harbor	None	0	0	0	6
Hokkaido Tailings	None	50	4	1.2	1.1
Kawagishi-cho	2.4, 1.9, 1.9, 4.4, 5.5, 7.1, 6.9	<5	0	0	4.3
Koda Numa	None	13 - 68	3	0.6	3
La Marquesa Downstream	8.7, 11.0, 10.1, 6.4, 5.2, 7.7	20	1.7	0.51	8.2
La Marquesa Upstream	4.9, 3.3	30	2.4	0.72	4.1
La Palma Dam	1.3, 3.0, 4.4	15	1.3	0.39	2.9
Lake Merced	None	0	0	0	6
Metoki Road	None	0	0	0	2
Mochi Koshi Dike 1	1.6, 3.1, 4.2, 3.1, 4.2, 3.4, 5.5, 3.6, 1.7, 1.4, 2.5, 1.3, 3.6, 2.7, 6.0, 5.1, 5.0, 3.9, 8.4, 9.5, 3.9	60 - 85	4.9	0.17	4
Mochi Koshi Dike 2	13.5, 4.0, 3.9, 3.9, 5.9, 16.7, 8.4, 4.6, 6.1, 4.8, 4.3, 3.1, 0.8, 0.8, 2.8, 2.5, 1.2	60 - 85	4.9	0.17	5.1
Nalbland	4	30	2.4	0.72	4
Nerlerk Berm	None	10	1	0.3	10.5
Sheffield Dam	None	33 - 48	3.35	0.2	5
Snow River	None	10 - 30	1.7	0.2	7
Solfatara Canal	None	0	0	0	5
Soviet Tajik	None	15	1.3	0.39	7.6
Tar Island Dike	None	10 - 15	1.2	0.05	8
Zeeland	None	11	1	0.3	7.5

Table 6-6 The SPT resistance of the secondary flow-slide case histories.

Case	No. of SPT Values in Liquefied Zone	σ_{range}	σ_{calc}	σ_{used}	COV_{used}
Asele Road	0	0	0	13.5	1.5
Chonan Middle School	1	0	0	7.5	1.5
El Cobre	3	1.5	1.3	0.9	0.75
Helsinki Harbor	0	0	0	9.0	1.5
Hokkaido Tailings	0	0	0	0.825	0.75
Kawagishi-cho	7	1.9	1.3	1.5	0.349
Koda Numa	0	0	0	2.25	0.75
La Marquesa Downstream	6	2.3	2.2	2.9	0.354
La Marquesa Upstream	2	1.4	1.1	2.7	0.659
La Palma Dam	3	1.8	1.6	1.8	0.621
Lake Merced	0	0	0	9.0	1.5
Metoki Road	0	0	0	1.5	0.75
Mochi Koshi Dike 1	21	2.2	2.1	0.6	0.15
Mochi Koshi Dike 2	17	4.4	4.3	1.3	0.255
Nalbland	1	0	0	6.0	1.5
Nerlerk Berm	0	0	0	1.575	0.15
Sheffield Dam	0	0	0	7.5	1.5
Snow River	0	0	0	10.5	1.5
Solfatara Canal	0	0	0	7.5	1.5
Soviet Tajik	0	0	0	5.7	0.75
Tar Island Dike	0	0	0	12.0	1.5
Zeeland	0	0	0	5.625	0.75

Table 6-7 Uncertainty parameters of SPT resistance for the secondary flow-slide case histories.

Case	*References*	S_r **Values** (psf)	**Mean** S_r (psf)
Asele Road	Konrad and Watts (1995) Olson (2001)	11 241	164
Chonan Middle School	Ishihara et al (1990) Ishihara (1993) Olson (2001)	167 194 178	179
El Cobre	Olson (2001)	195	195
Helsinki Harbor	Olson (2001)	53	53
Hokkaido Tailings	Ishihara et al (1990a) Olson (2001)	408 172	251
Kawagishi-cho	Seed (1987) Seed and Harder (1990) Stark and Mesri (1992)	120 120 120	120
Koda Numa	Lucia (1981); Lucia et al (1982) Seed (1987) Seed (1987) Olson (2001)	25 50 50 66	48
La Marquesa Downstream	De Alba et al (1987) Seed and Harder (1990) Stark and Mesri (1992) Olson (2001)	423 400 400 190	344
La Marquesa Upstream	De Alba et al (1987) Seed and Harder (1990) Stark and Mesri (1992) Olson (2001)	208 200 200 129	181
Lake Merced	Seed (1987) Seed and Harder (1990) Stark and Mesri (1992) Olson (2001)	100 100 100 257	139
La Palma Dam	De Alba et al (1987) Seed and Harder (1990) Stark and Mesri (1992) Olson (2001)	210 200 200 156	189

Table 6-8 Information of residual strength for the secondary flow-slide case histories.

Table 6-8 continued.

Case	***References***	S_r **Values** (psf)	**Mean** S_r (psf)
Metoki Road	Olson (2001)	113	113
Mochi Koshi Dike 1	Poulos (1988) Davis et al (1988) Olson (2001)	60 60 258	159
Mochi Koshi Dike 2	Lucia (1981); Lucia et al (1982) Seed (1987) Seed (1987) Poulos (1988) Davis et al (1988) Seed and Harder (1990) Stark and Mesri (1992) Olson (2001)	210 210 210 250 250 250 250 223	234
Nalbland	Yegian et al (1994) Olson (2001)	117 152	140
Nerlerk Berm 1	Sladen et al (1985a) Jeffries et al (1990) Stark and Mesri (1992) Olson (2001)	42 308 300 54	179

Table 6-8 continued.

Case	***References***	S_r **Values** (psf)	**Mean** S_r (psf)
Sheffield Dam	Seed (1987) Seed and Harder (1990) Stark and Mesri (1992) Olson (2001)	50 75 75 198	100
Snow River	Seed (1987) Seed and Harder (1990) Stark and Mesri (1992)	50 50 50	50
Solfatara Canal	Seed (1987) Seed and Harder (1990) Stark and Mesri (1992) Olson (2001)	130 50 50 88	77
Soviet Tajik – May 1 Slide	Ishihara et al (1990b) Olson (2001)	167 418	334
Tar Island Dike	Plewes et al (1989) Konrad and Watts (1995) Olson (2001)	305 80 500	346
Zeeland	Olson (2001)	226	226

Case	References	S_r/σ'_{vo} Values	Mean S_r/σ'_{vo}
Asele Road	Olson and Stark (2002)	0.104	0.104
Chonan Middle School	Olson and Stark (2002)	0.091	0.091
El Cobre	Olson and Stark (2002)	0.020	0.020
Helsinki Harbor	Olson and Stark (2002)	0.060	0.060
Hokkaido Tailings	Olson and Stark (2002)	0.074	0.074
Kawagishi-cho	Stark and Mesri (1992) Olson and Stark (2002)	0.098 0.075	0.087
Koda Numa	Stark and Mesri (1992) Wride et al. (1999) Olson and Stark (2002)	0.032 0.032 0.040	0.045
La Marquesa Downstream	Stark and Mesri (1992) Wride et al. (1999) Olson and Stark (2002)	0.224 0.223 0.110	0.186
La Marquesa Upstream	Stark and Mesri (1992) Wride et al. (1999) Olson and Stark (2002)	0.125 0.125 0.070	0.107
Lake Merced	Stark and Mesri (1992) Wride et al. (1999) Olson and Stark (2002)	0.105 0.105 0.108	0.106
La Palma Dam	Stark and Mesri (1992) Olson and Stark (2002)	0.120 0.120	0.120

Table 6-9 Information of normalized residual strength ratio for the secondary flow-slide case histories.

Table 6-9 continued.

Case	**References**	S_r/σ'_{vo} **Values**	**Mean** S_r/σ'_{vo}
Metoki Road	Olson and Stark (2002)	0.043	0.043
Mochi Koshi Dike 1	Stark and Mesri (1992) Wride et al. (1999) Olson and Stark (2002)	0.092 0.015 0.060	0.091
Mochi Koshi Dike 2	Stark and Mesri (1992) Wride et al. (1999) Olson and Stark (2002)	0.092 0.048 0.104	0.081
Nalbland	Olson and Stark (2002)	0.109	0.109
Nerlerk Berm	Jeffries et al (1990) Stark and Mesri (1992) Olson and Stark (2002)	0.150 0.148 0.086	0.124
Sheffield Dam	Stark and Mesri (1992) Wride et al. (1999) Olson and Stark (2002)	0.038 0.038 0.053	0.043
Snow River	Stark and Mesri (1992)	0.024	0.024
Solfatara Canal	Stark and Mesri (1992) Wride et al. (1999) Olson and Stark (2002)	0.052 0.052 0.080	0.063
Soviet Tajik – May 1 Slide	Olson and Stark (2002)	0.082	0.082
Tar Island Dike	Olson and Stark (2002)	0.058	0.058
Zeeland	Olson and Stark (2002)	0.048	0.048

Case	H (ft)	Q_{ZIF}	COV_{primary}	COV_{model}	$COV_{\text{secondary}}$
Asele Road	23	0.6	0.27	0.20	0.336
Chonan Middle School	20	0.1	0.15	0.10	0.180
El Cobre	98	0.6	0.27	0.20	0.336
Fraser River Delta	131	0.3	0.19	0.20	0.276
Helsinki Harbor	10	0.6	0.27	0.25	0.368
Hokkaido Tailings	30	0.6	0.27	0.10	0.288
Kawagishi-cho	0	1.0	0.44	0.25	0.506
Koda Numa	10	0.6	0.27	0.20	0.336
La Marquesa Downstream	23	0.6	0.27	0.20	0.336
La Marquesa Upstream	26	1.0	0.44	0.20	0.483
La Palma Dam	36	1.0	0.44	0.20	0.483
Lake Merced	32	0.6	0.27	0.15	0.301
Mochi Koshi 1	98	0.6	0.27	0.15	0.301
Mochi Koshi 2	66	0.6	0.27	0.20	0.336
Motoki Road	10	1.0	0.44	0.25	0.506
Nalbland	18	0.6	0.27	0.10	0.288
Nerlerk Berm	79	0.1	0.15	0.10	0.180
Sheffield Dam	25	0.6	0.27	0.15	0.301
Snow River	10	0.6	0.27	0.20	0.336
Solfatara Canal	7	0.6	0.27	0.20	0.336
Soviet Tajik	98	0.6	0.27	0.20	0.336
Tar Island Dike	289	0.6	0.27	0.20	0.336
Zeeland	131	0.6	0.27	0.20	0.336

Table 6-10 Information of coefficients of variation for the residual strength ratios of the secondary flow-slide case histories.

	$(\overline{N}_1)_{60\text{-CS}}$ (bpf)		$\overline{S}_r$ (psf)		$\overline{S}_r/\overline{\sigma}'_{vo}$	
	Mean	**STD**	**Mean**	**STD**	**Mean**	**STD**
Primary Case History						
Calaveras Dam	10.5	9.7	636.9	223.1	0.0993	0.0337
Fort Peck Dam	15.8	0.9	671.6	130.2	0.0914	0.0167
Hachiro-Gata Road Embankment	5.7	2.8	65.0	24.7	0.1639	0.0641
Lake Ackerman Roadway	4.8	1.2	98.0	20.4	0.1140	0.0224
Lower San Fernando Dam	14.5	1.1	484.7	111.0	0.1329	0.0287
Route 272 at Higashiarekinai	8.5	2.6	130.5	33.5	0.1250	0.0295
Shibecha-Cho Embankment	5.6	2.2	208.9	38.6	0.1996	0.0312
Uetsu-Line Railway Embankment	2.9	4.2	43.7	24.8	0.0480	0.0265
Wachusett Dam	7.3	1.9	348.0	74.8	0.1358	0.0284
Secondary Case History						
Asele Road	11.0	10.7	163.6	54.6	0.1040	0.0345
Chonan Middle School	6.4	6.9	178.7	32.0	0.0911	0.0163
El Cobre Tailings Dam	6.8	0.9	195.2	64.8	0.0200	0.0066
Helsinki Harbor	5.9	8.0	53.2	19.0	0.0602	0.0215
Hokkaido Tailings	5.1	1.4	250.6	71.9	0.0741	0.0212
Kawagishi-Cho Building	4.3	1.2	123.5	56.7	0.0894	0.0411
Koda Numa Embankment	3.6	4.1	48.0	15.9	0.0451	0.0150
La Marquesa Downstream	9.9	3.0	343.5	113.8	0.1861	0.0615
La Marquesa Upstream	6.5	2.8	185.1	82.1	0.1098	0.0489
La Palma Dam	4.2	1.8	193.3	86.3	0.1229	0.0547
Lake Merced Bank	5.9	8.0	139.5	41.4	0.1060	0.0316
Metoki Road	2.0	1.5	116.8	53.7	0.0442	0.0204
Mochi Koshi Tailings Dam 1	8.9	0.6	158.9	47.7	0.0911	0.0272
Mochi Koshi Tailings Dam 2	10.0	1.3	233.6	78.0	0.0812	0.0269
Nalbland Railway Embankment	6.3	5.6	139.9	40.2	0.1089	0.0311
Nerlerk Berm	11.4	7.7	179.1	32.1	0.1239	0.0222
Sheffield Dam	8.2	6.8	100.0	29.8	0.0720	0.0215
Snow River Bridge Fill	8.5	9.0	50.1	16.6	0.0240	0.0080
Solfatara Canal Dike	4.9	6.9	77.1	25.6	0.0630	0.0210
Soviet Tajik - May 1 Slide	8.9	5.7	334.3	110.9	0.0822	0.0274
Tar Island Dyke	8.9	9.7	364.2	115.6	0.0580	0.0193
Zeeland	8.5	5.5	226.0	75.0	0.0481	0.0160

Table 6-11 Summary of mean and standard deviation (STD) values of $(\overline{N}_1)_{60\text{-CS}}$, $\overline{S}_r$, and $\overline{S}_r/\overline{\sigma}'_{vo}$ of all case histories.

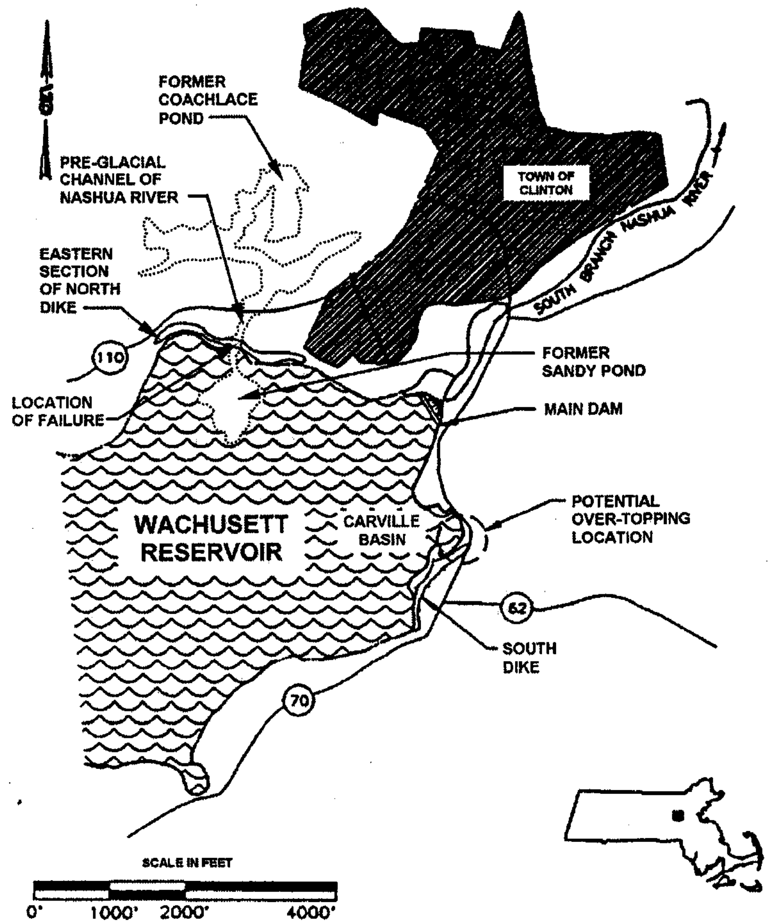

Figure 6-1 Wachusett Reservoir prior to 1907 flow slide failure (after Baril et a., 1992).

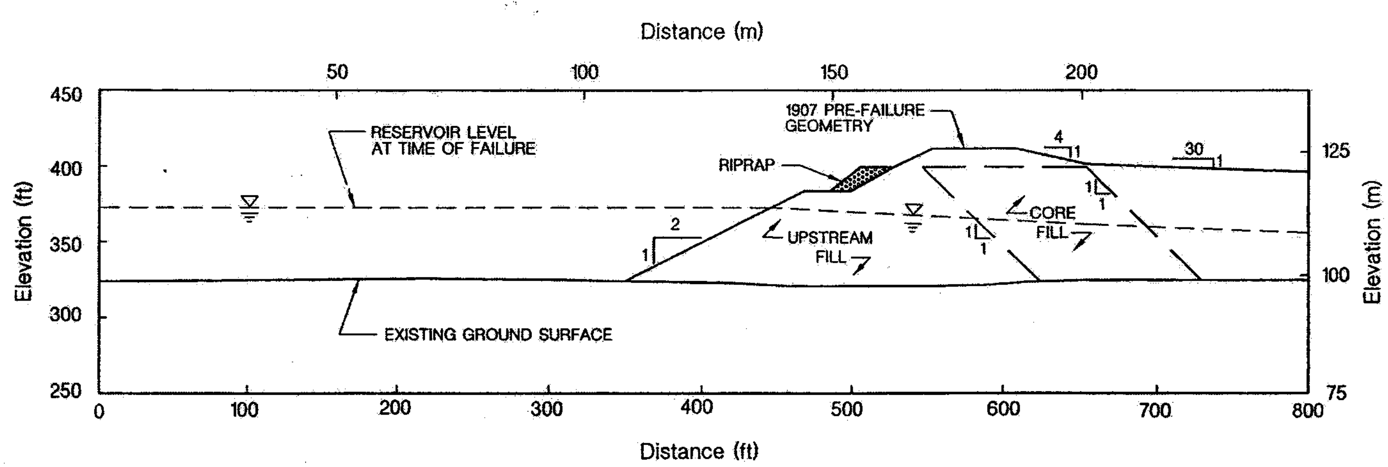

Figure 6-2 Pre-failure geometry at Station 23+20 with slope inclination (Olson et al., 2000).

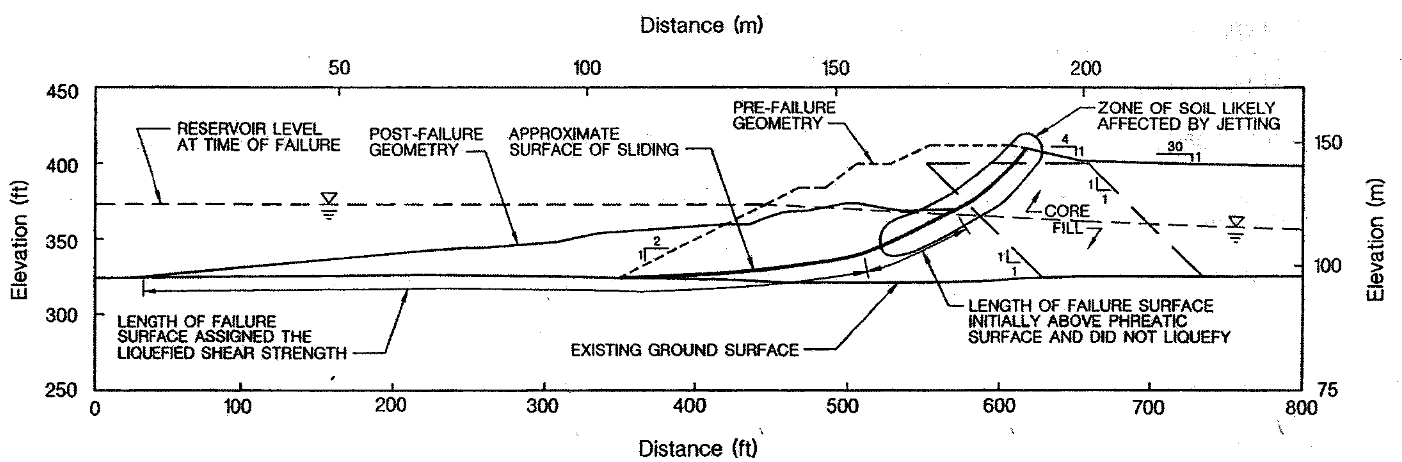

Figure 6-3 Post-failure geometry at Station 23+20 with indication of water jetting area (Olson et al., 2000).

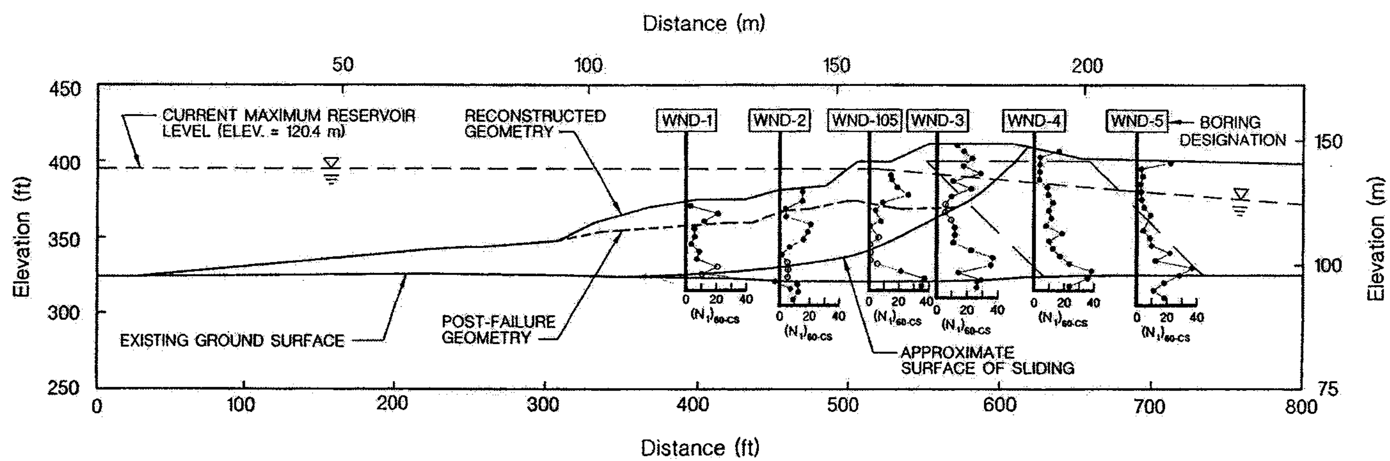

Figure 6-4 Reconstruction at Station 23+20 with borings and SPT (Olson et al., 2000).

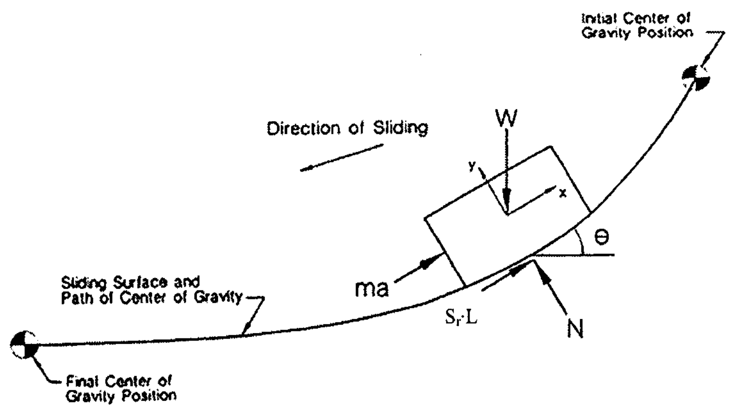

(a)

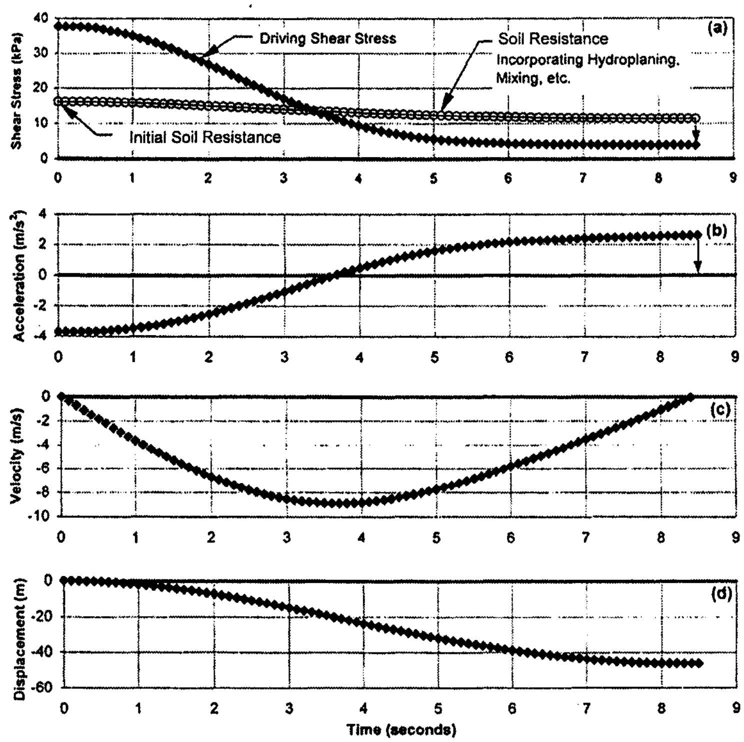

(b)

Figure 6-5 Failure analysis with kinetic effect on North Dike of Wachusett Dam (a) soil mass movement on the path described by a third-order polynomial and (b) soil mass movement profiles (after Olson et al., 2000).

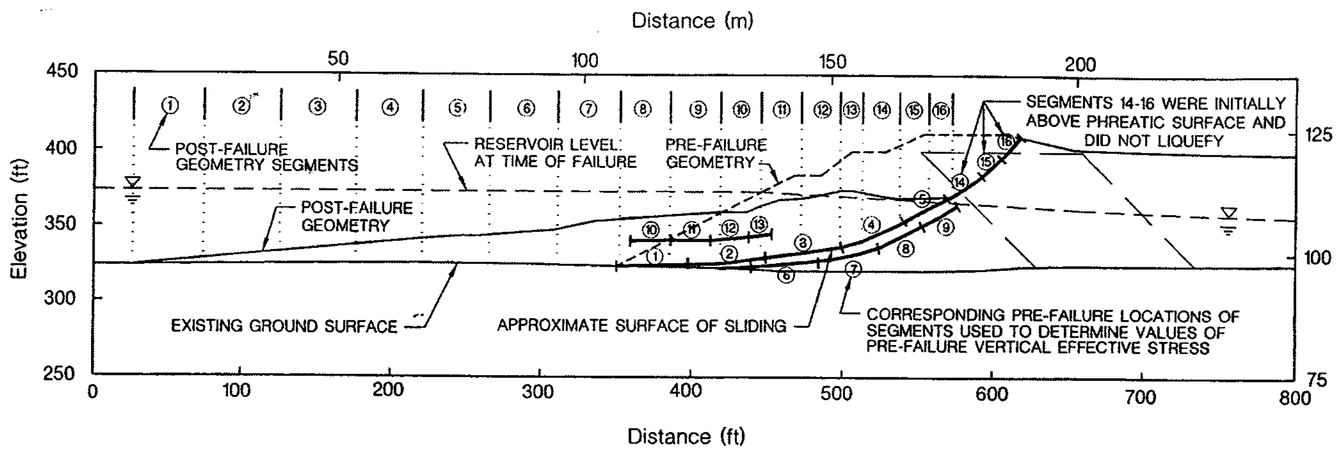

Figure 6-6 Indication of post-failure slices on pre-failure geometry for residual strength ratio evaluation (Olson et al., 2000).

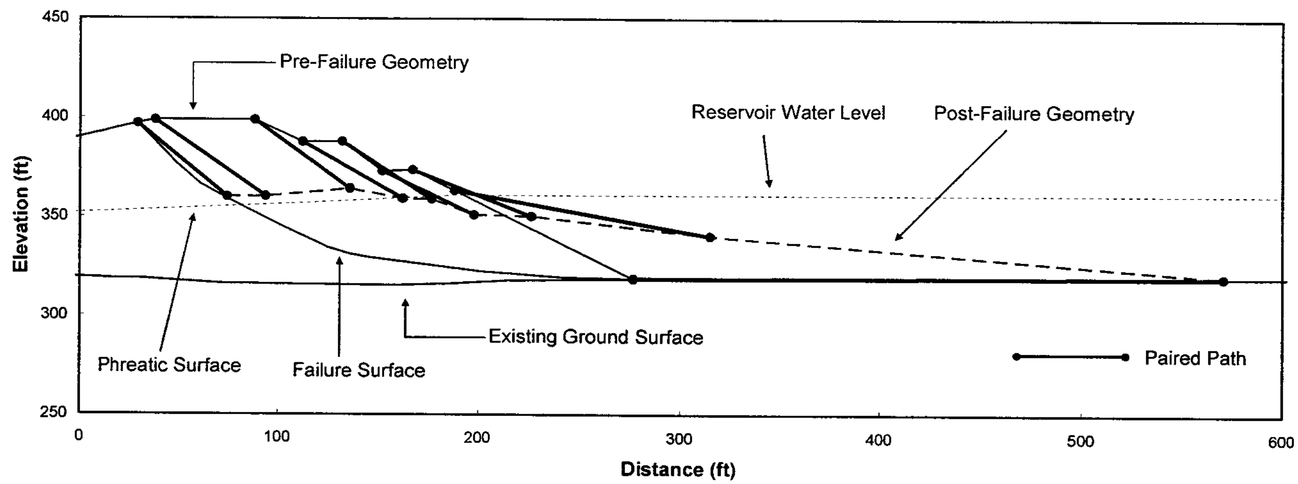

Figure 6-7 Paired Path shown with Pre-failure and Post-failure Geometry of the North Dike of Wachusett Dam.

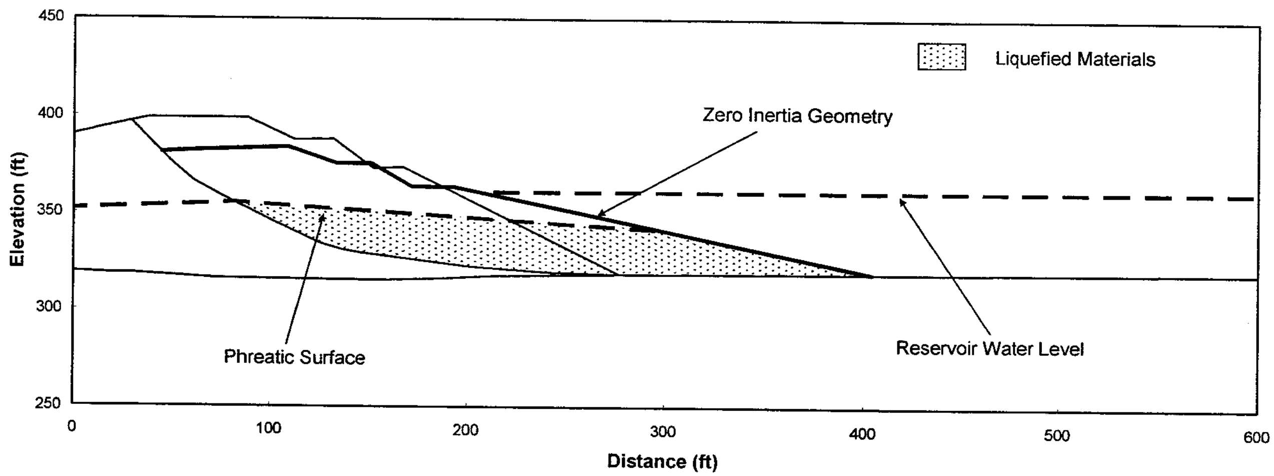

Figure 6-8 Zero Inertia Geometry of the North Dike of Wachusett Dam.

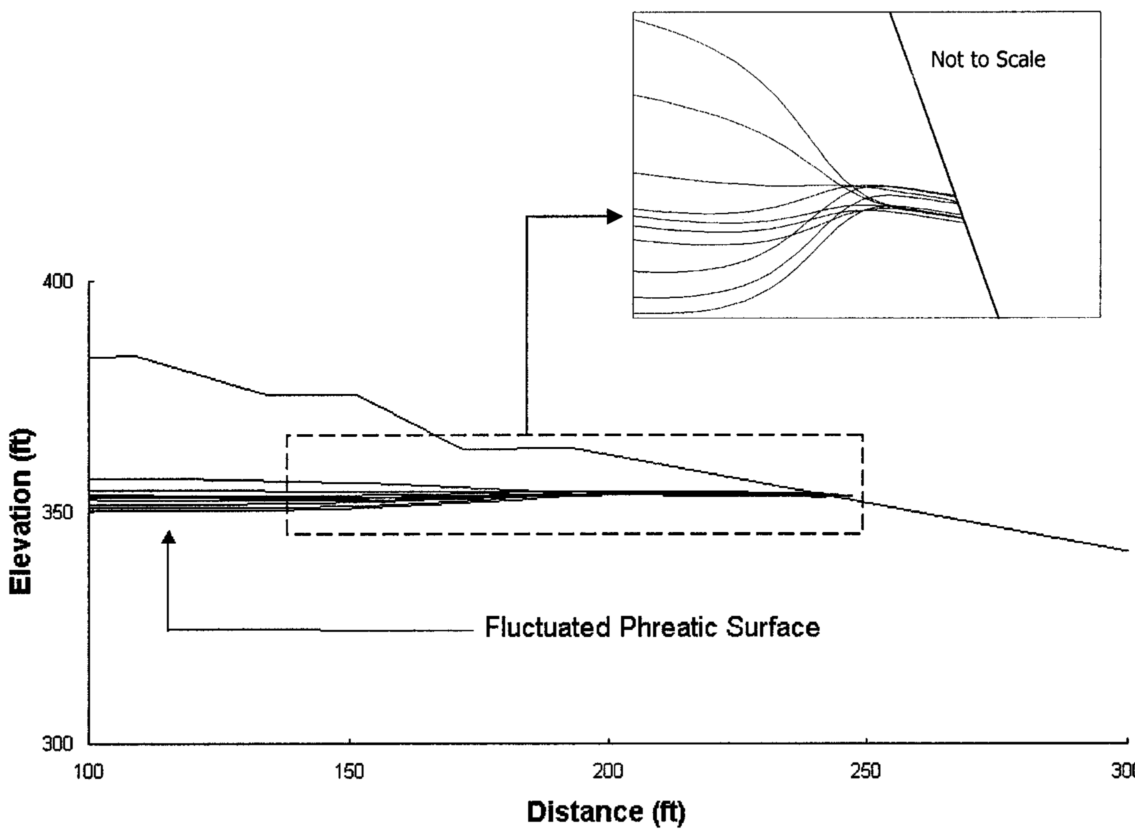

Figure 6-9 Examples of 10 fluctuated phreatic surfaces.

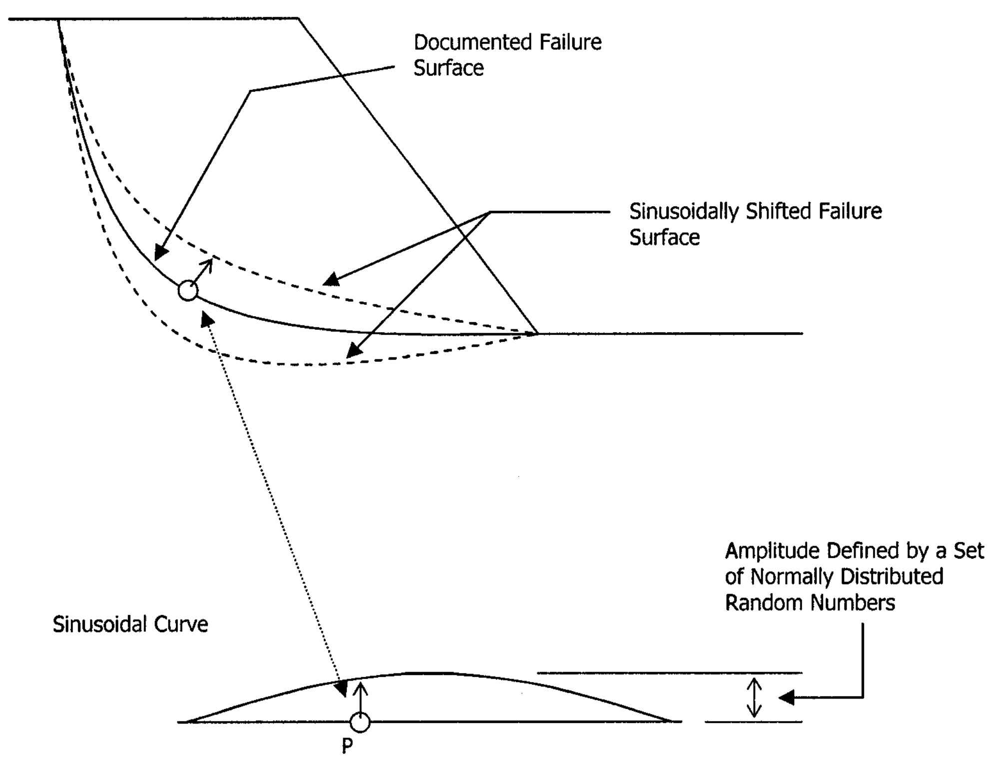

Figure 6-10 Scheme of defining sinusoidally shifted failure surface.

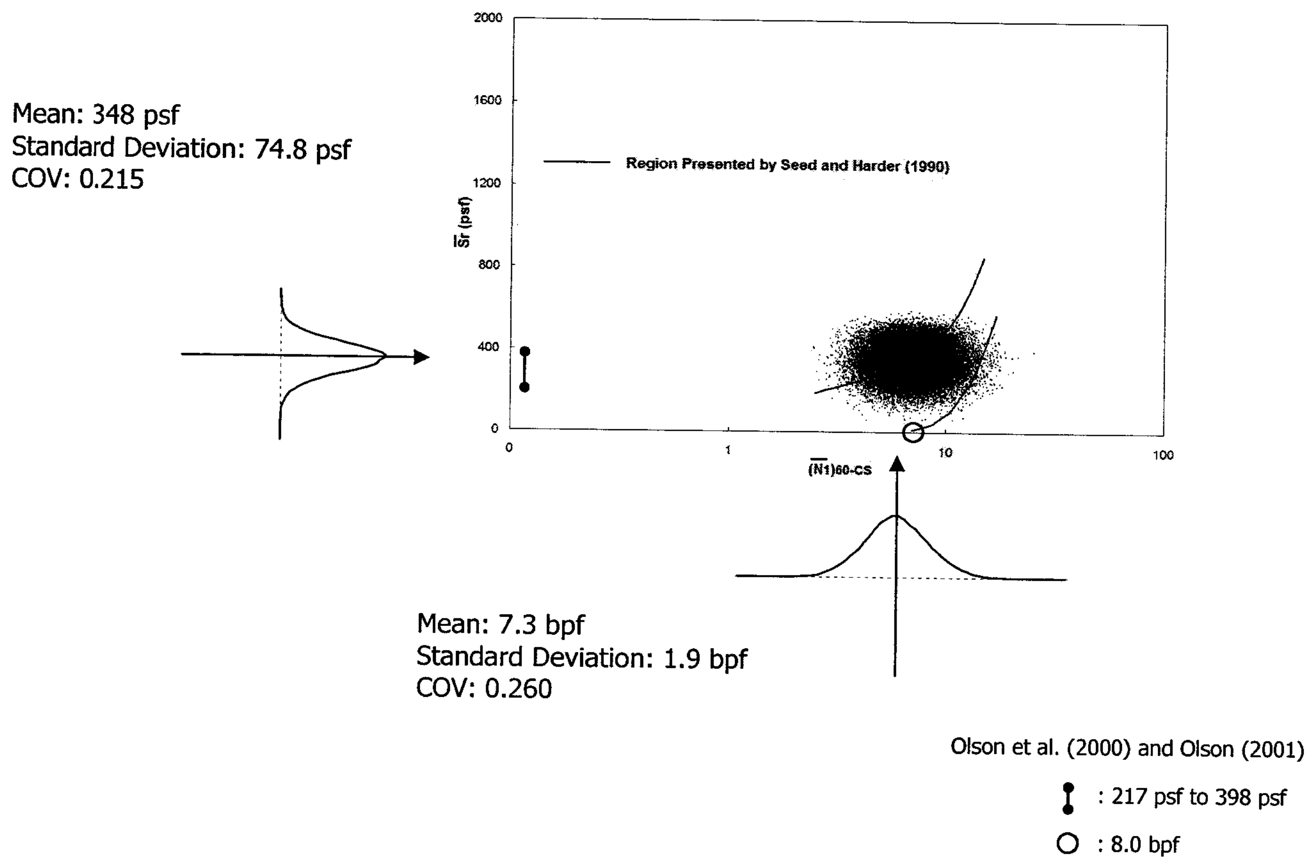

Figure 6-11 $\overline{S}_r$ versus $(\overline{N}_1)_{60\text{-}CS}$ for the North Dike of Wachusett Dam, based on Equation (5.24). A total of 50,000 data points are shown.

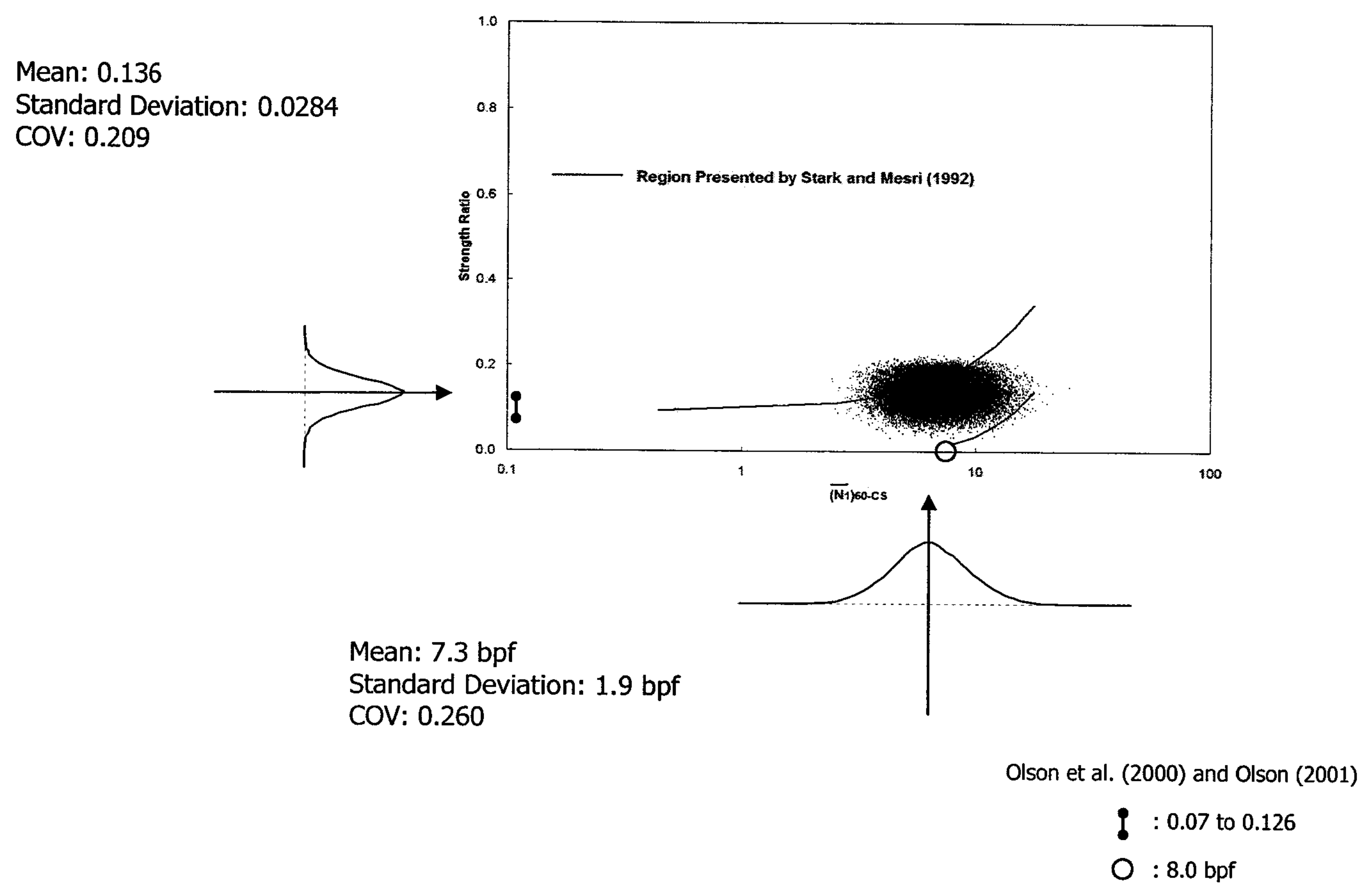

Figure 6-12 $\overline{S}_r/\overline{\sigma}'_{vo}$ versus $(\overline{N}_1)_{60\text{-}CS}$ for the North Dike of Wachusett Dam. A total of 50,000 data points are shown.

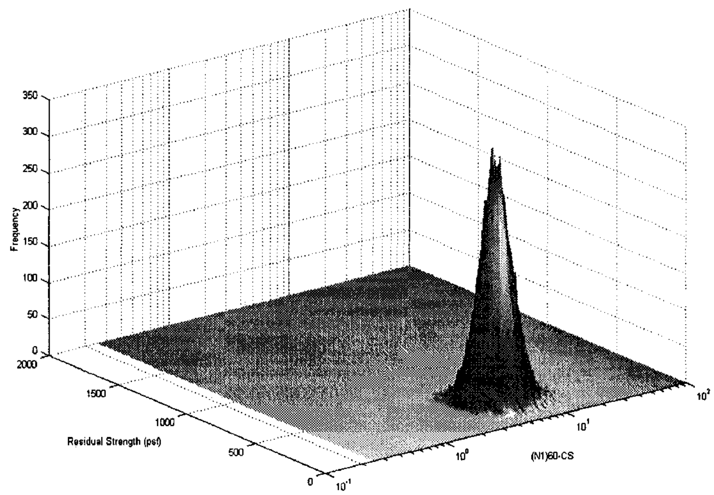

(a)

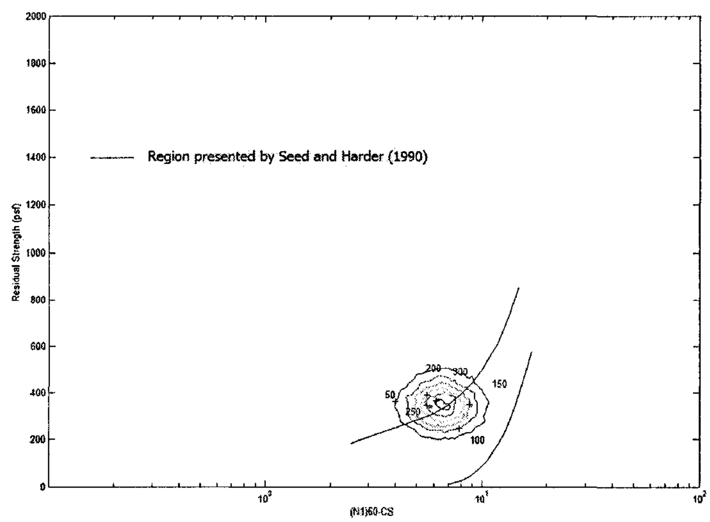

(b)

Figure 6-13 (a) Three-dimensional histogram and (b) contour plot of $\overline{S}_r$ versus $(\overline{N}_1)_{60\text{-CS}}$ for the North Dike of Wachusett Dam, based on Equation (5.24).

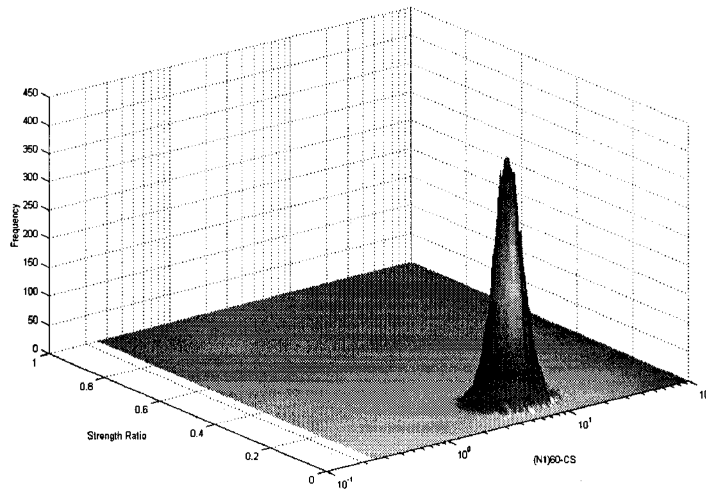

(a)

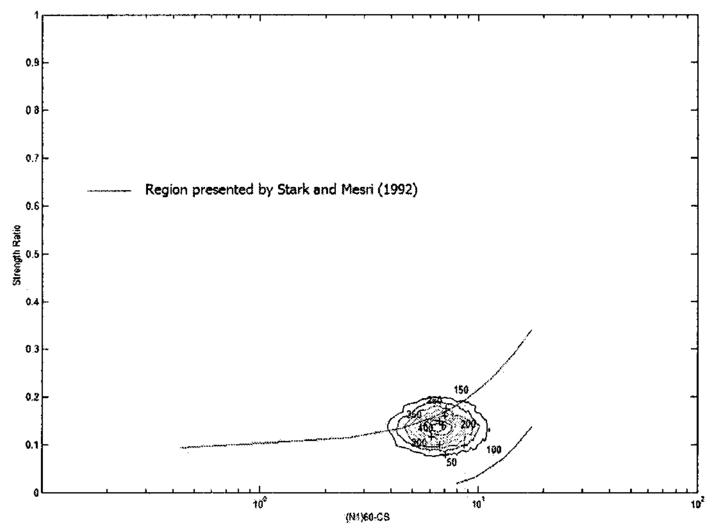

(b)

Figure 6-14 (a) Three-dimensional histogram and (b) contour plot of $\overline{S}_r/\overline{\sigma}'_{vo}$ versus $(\overline{N}_1)_{60\text{-}CS}$ for the North Dike of Wachusett Dam.

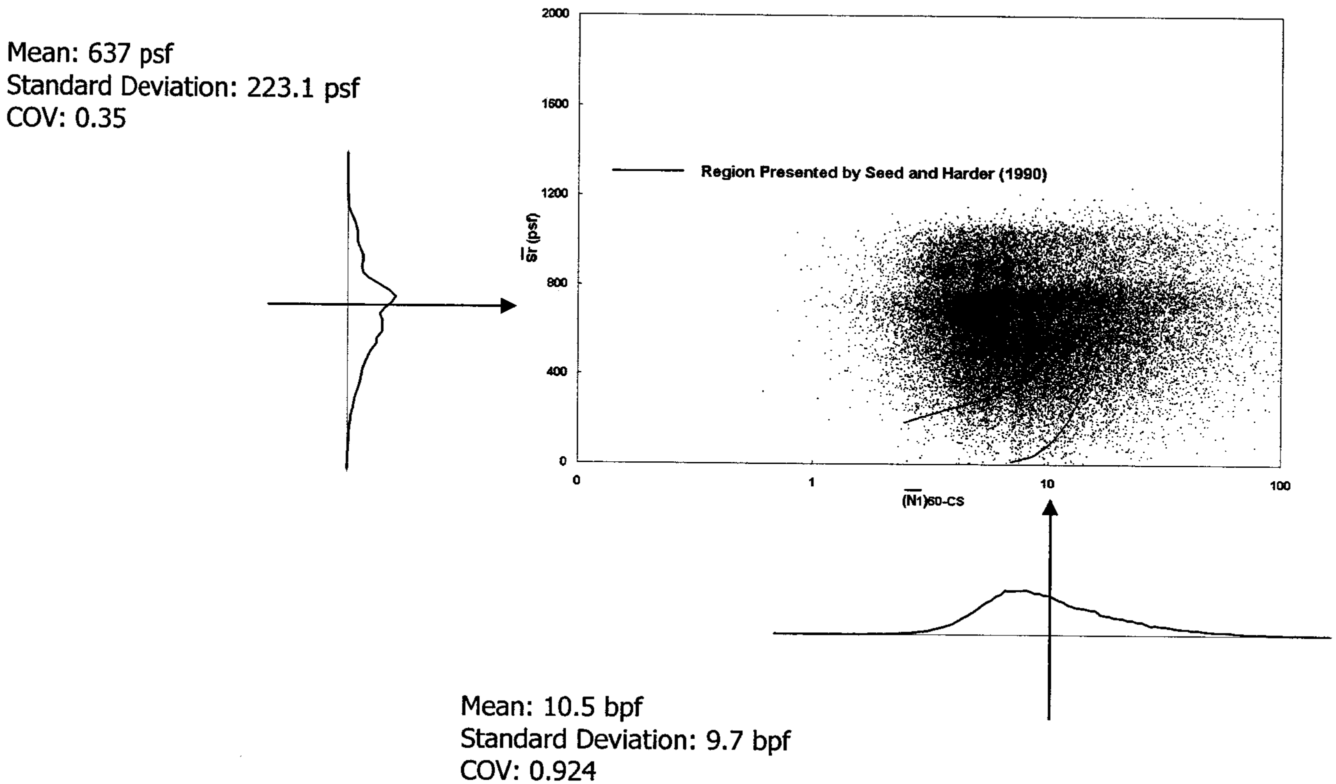

Figure 6-15 $\overline{S}_r$ versus $(\overline{N}_1)_{60\text{-CS}}$ for the Calaveras Dam, based on Equation (5.24). A total of 50,000 data points are shown.

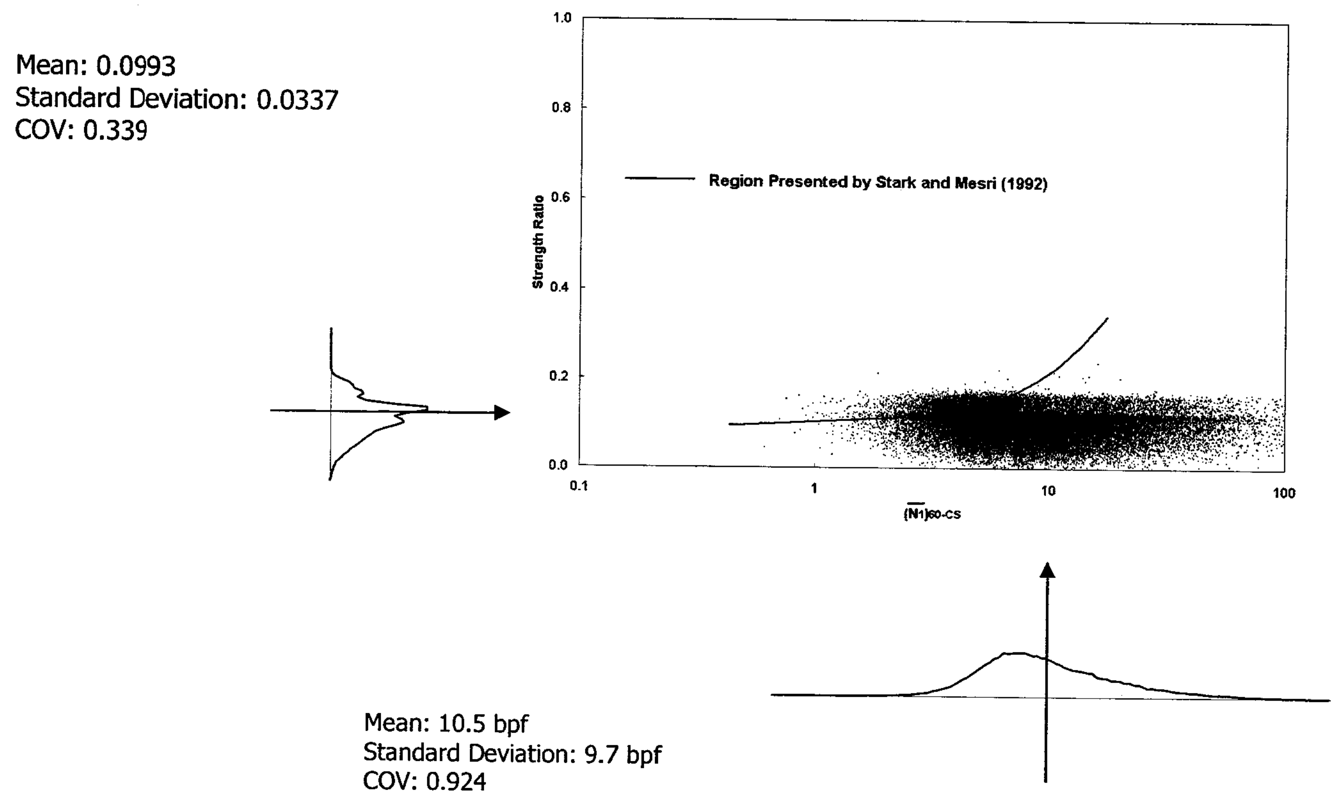

Figure 6-16 $\bar{S}_r/\bar{\sigma}'_{vo}$ versus $(\bar{N}_1)_{60\text{-}CS}$ for the Calaveras Dam. A total of 50,000 data points are shown.

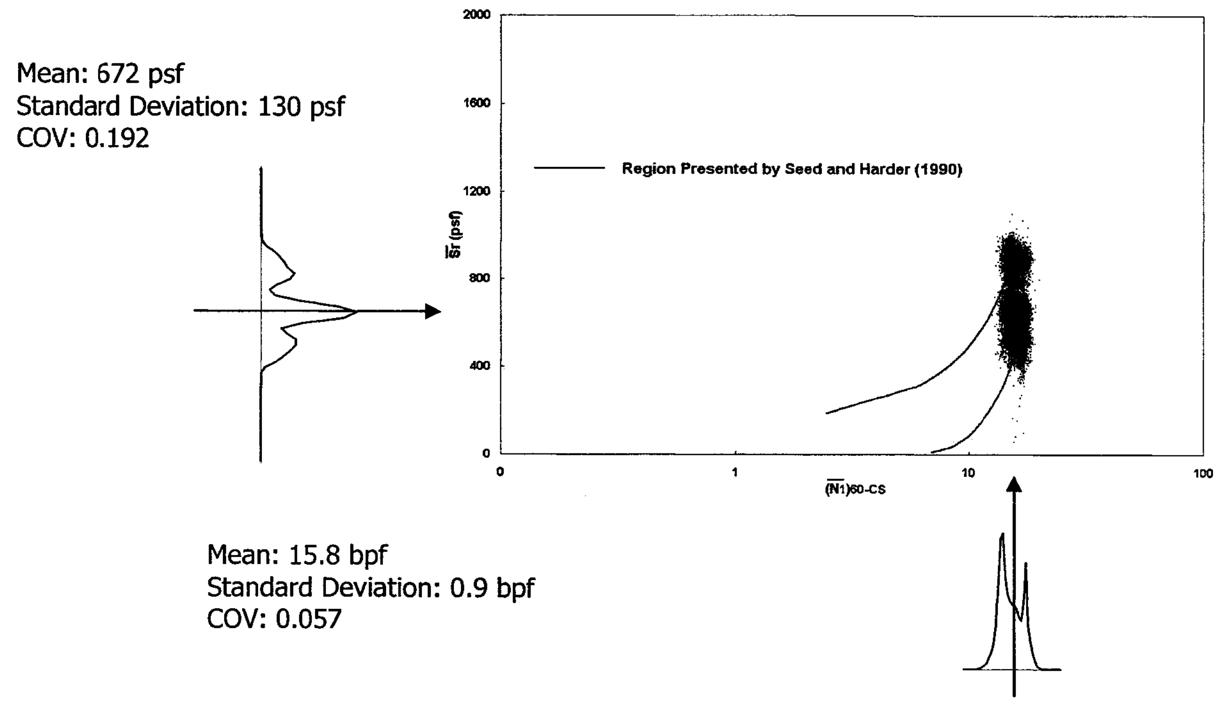

Figure 6-17 $\overline{S}_r$ versus $(\overline{N}_1)_{60\text{-CS}}$ for the Fort Peck Dam, based on Equation (5.24). A total of 50,000 data points are shown.

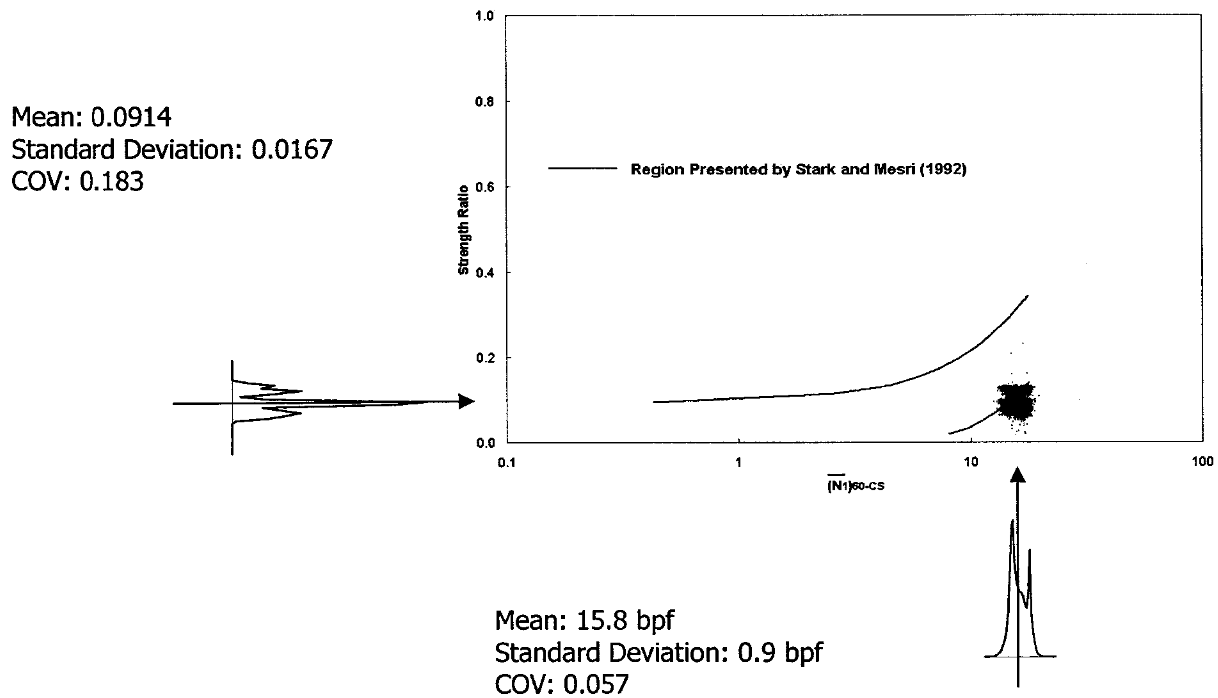

Figure 6-18 $\overline{S}_r/\overline{\sigma}'_{vo}$ versus $(\overline{N}_1)_{60\text{-CS}}$ for the Fort Peck Dam. A total of 50,000 data points are shown.

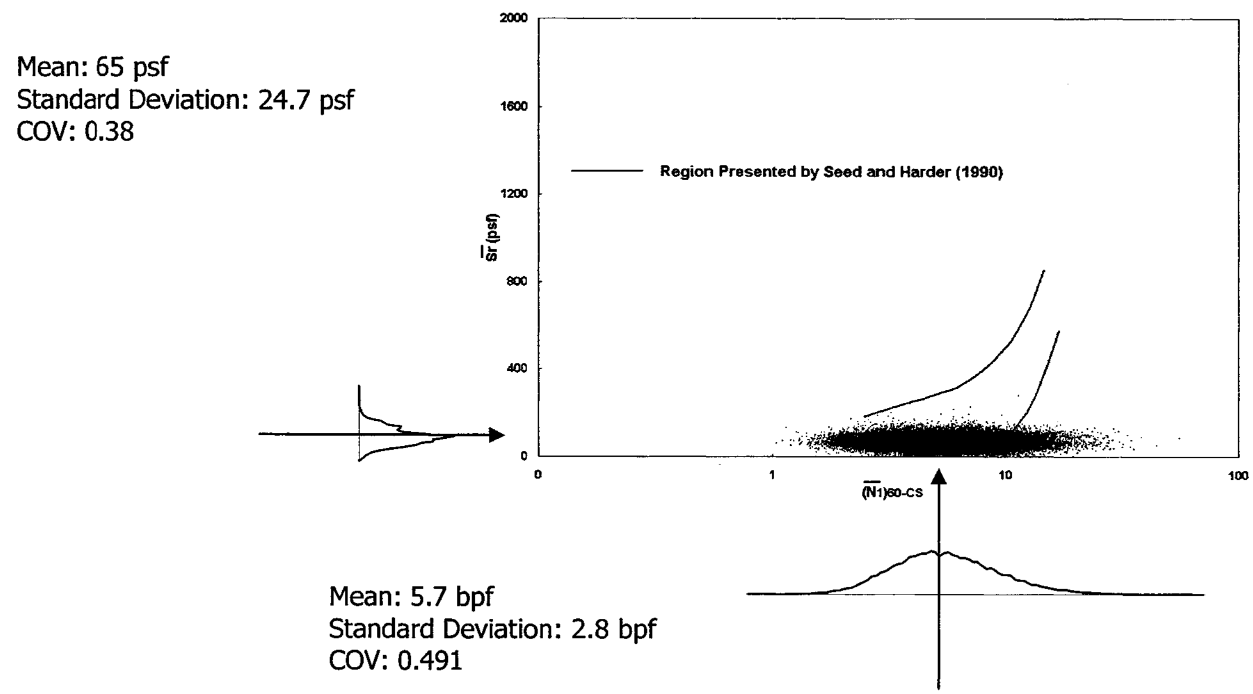

Figure 6-19 $\overline{S}_r$ versus $(\overline{N}_1)_{60\text{-CS}}$ for the Hachiro-Gata roadway embankment, based on Equation (5.24). A total of 50,000 data points are shown.

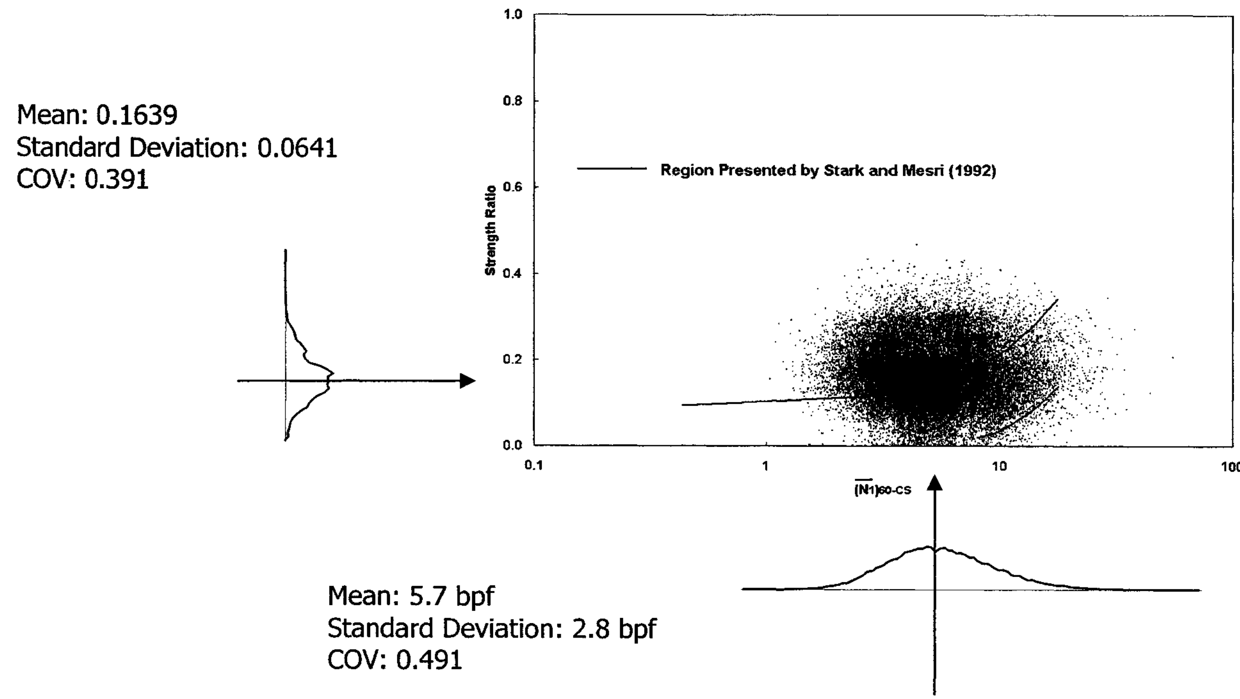

Figure 6-20 $\overline{S}_r/\overline{\sigma}'_{vo}$ versus $(\overline{N}_1)_{60\text{-CS}}$ for the Hachiro-Gata roadway embankment. A total of 50,000 data points are shown.

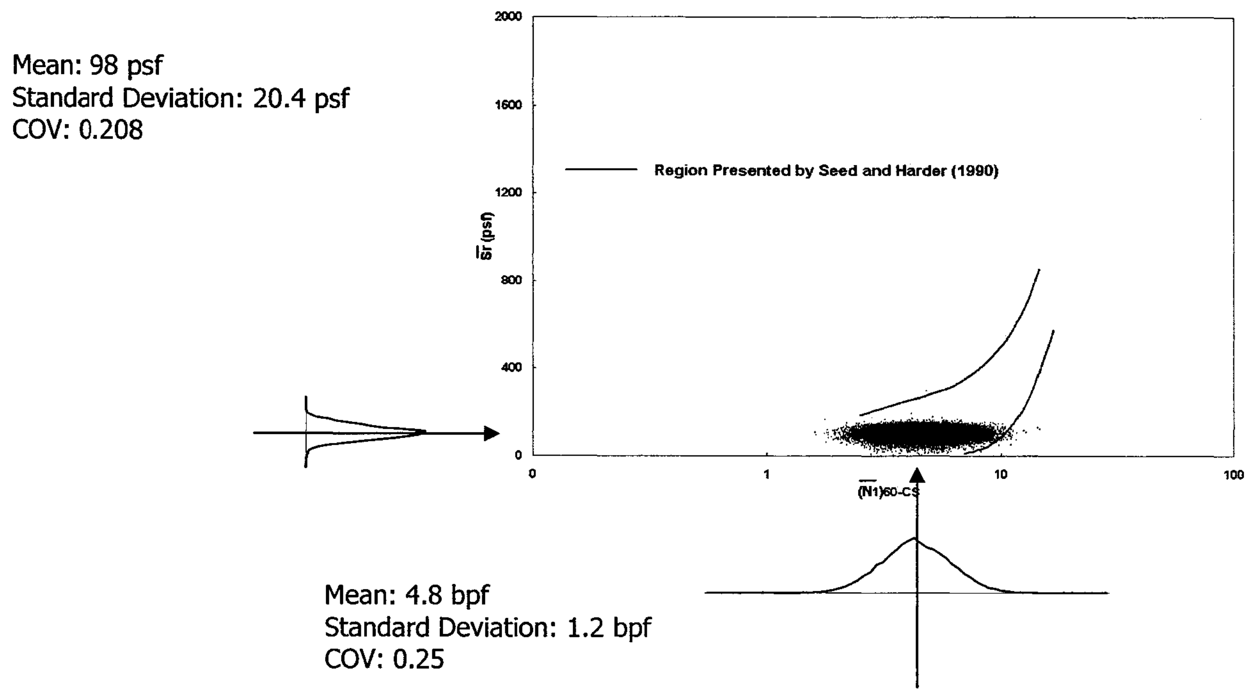

Figure 6-21 $\overline{S}_r$ versus $(\overline{N}_1)_{60\text{-CS}}$ for the Lake Ackerman roadway embankment, based on Equation (5.24). A total of 50,000 data points are shown.

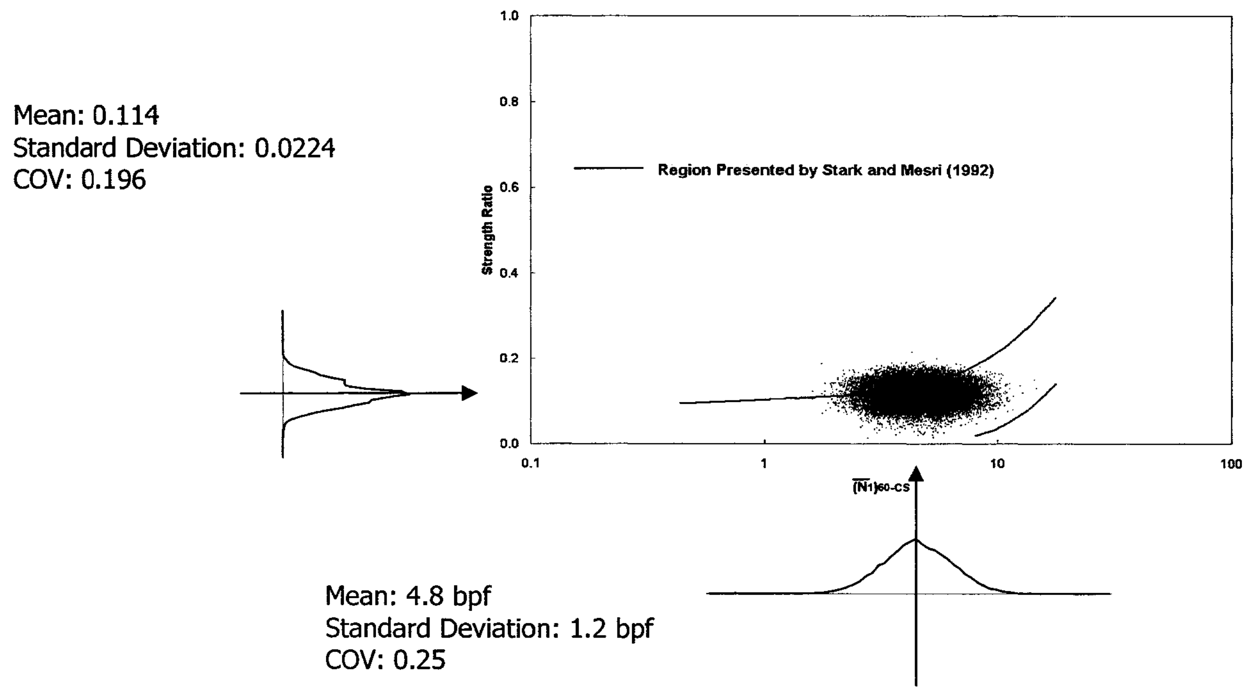

Figure 6-22 $\overline{S}_r/\overline{\sigma}'_{vo}$ versus $(\overline{N}_1)_{60\text{-CS}}$ for the Lake Ackerman roadway embankment. A total of 50,000 data points are shown.

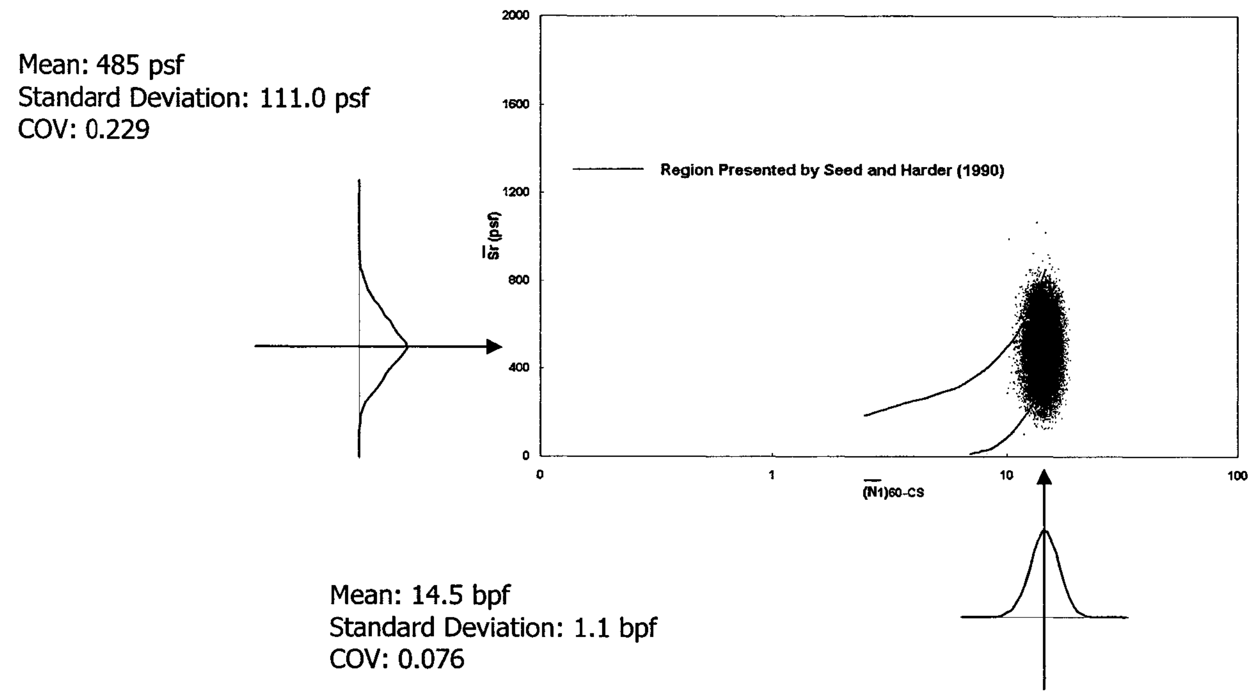

Figure 6-23 $\overline{S}_r$ versus $(\overline{N}_1)_{60\text{-CS}}$ for the Lower San Fernando Dam, based on Equation (5.24). A total of 50,000 data points are shown.

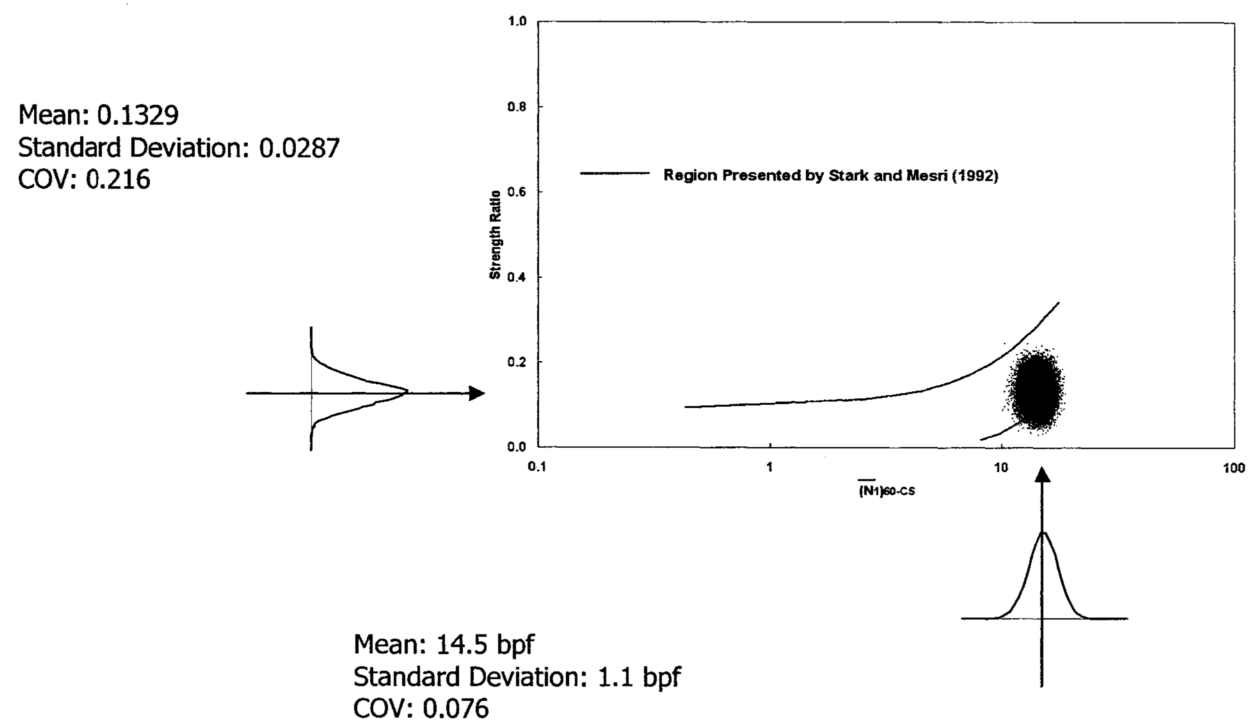

Figure 6-24 $\overline{S}_r/\overline{\sigma}'_{vo}$ versus $(\overline{N}_1)_{60\text{-CS}}$ for the Lower San Fernando Dam. A total of 50,000 data points are shown.

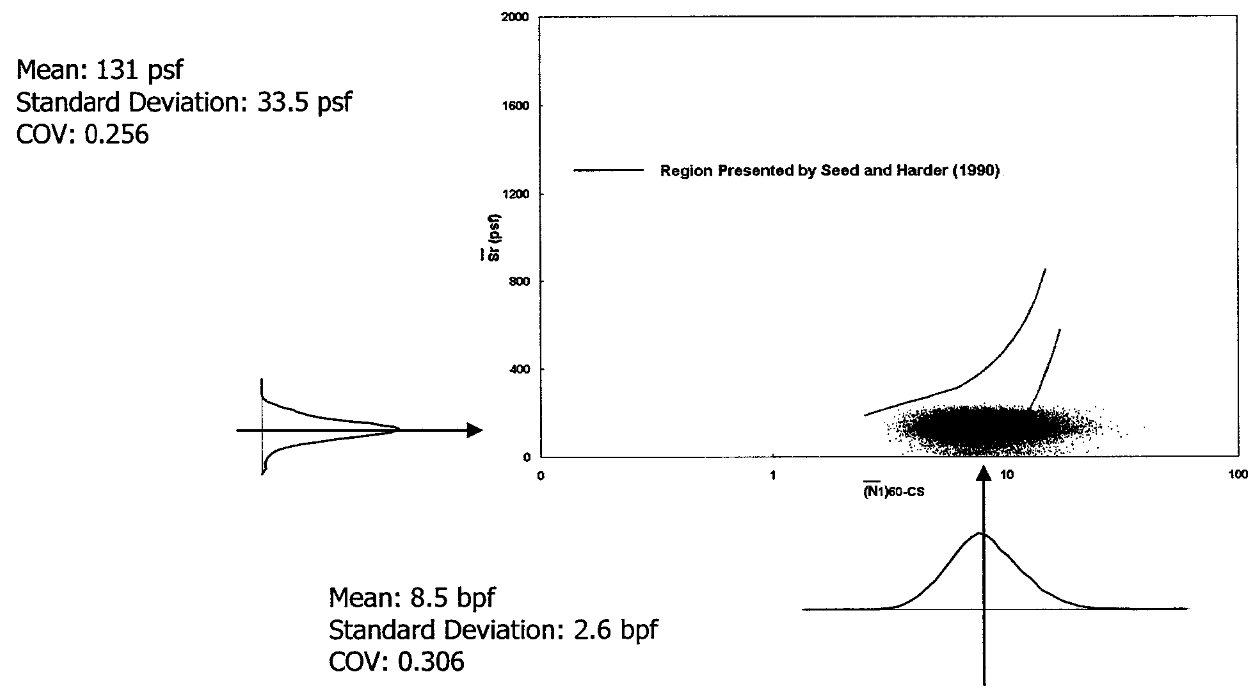

Figure 6-25 $\overline{S}_r$ versus $(\overline{N}_1)_{60\text{-CS}}$ for the Route 272 roadway embankment, based on Equation (5.24). A total of 50,000 data points are shown.

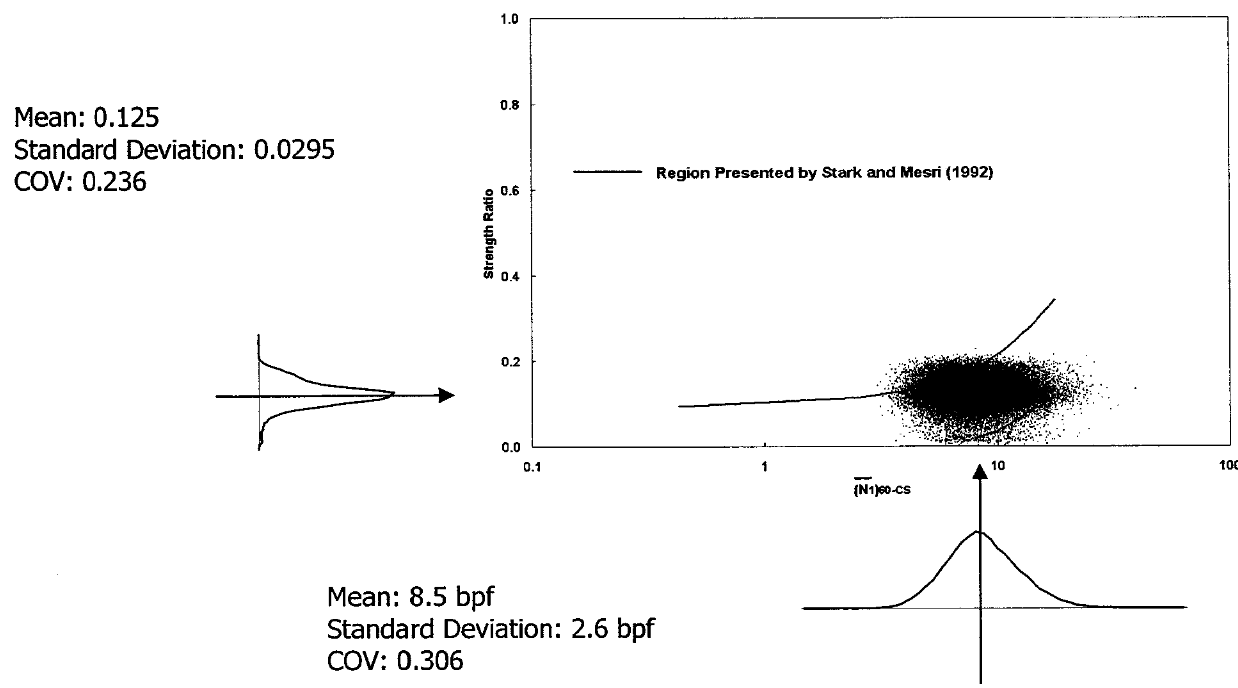

Figure 6-26 $\overline{S}_r/\overline{\sigma}'_{vo}$ versus $(\overline{N}_1)_{60\text{-CS}}$ for the Route 272 roadway embankment. A total of 50,000 data points are shown.

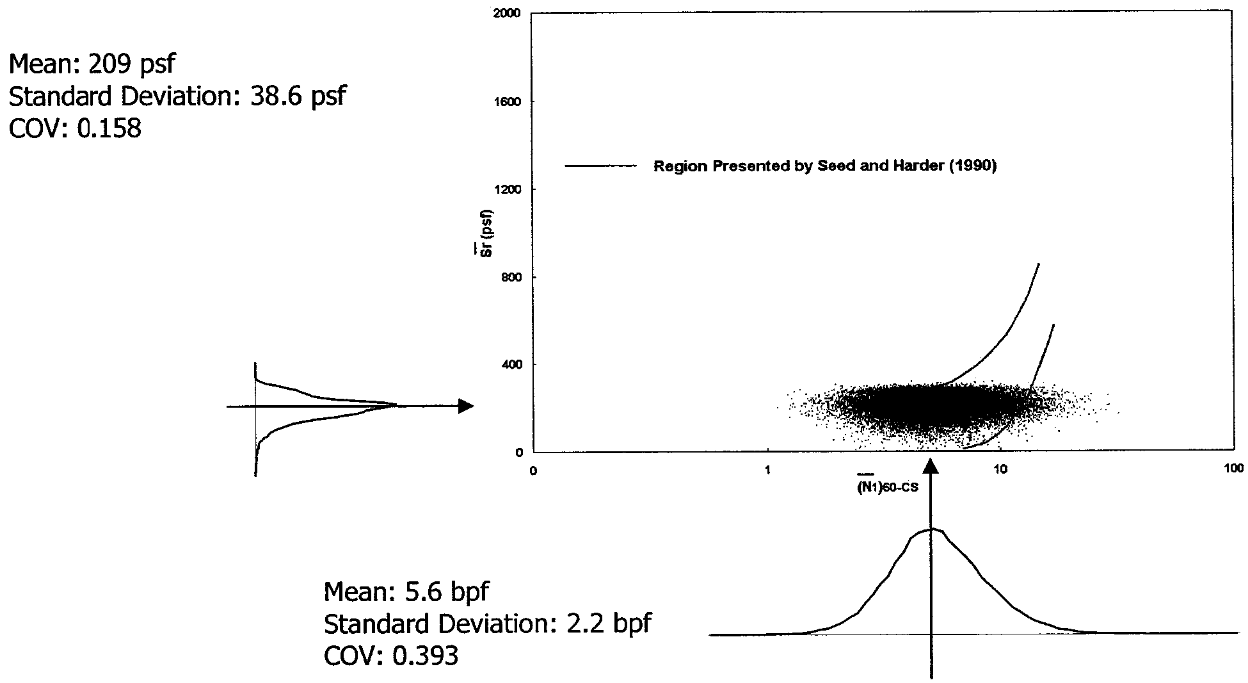

Figure 6-27 $\overline{S}_r$ versus $(\overline{N}_1)_{60\text{-CS}}$ for the Shibecha-Cho embankment, based on Equation (5.24). A total of 50,000 data points are shown.

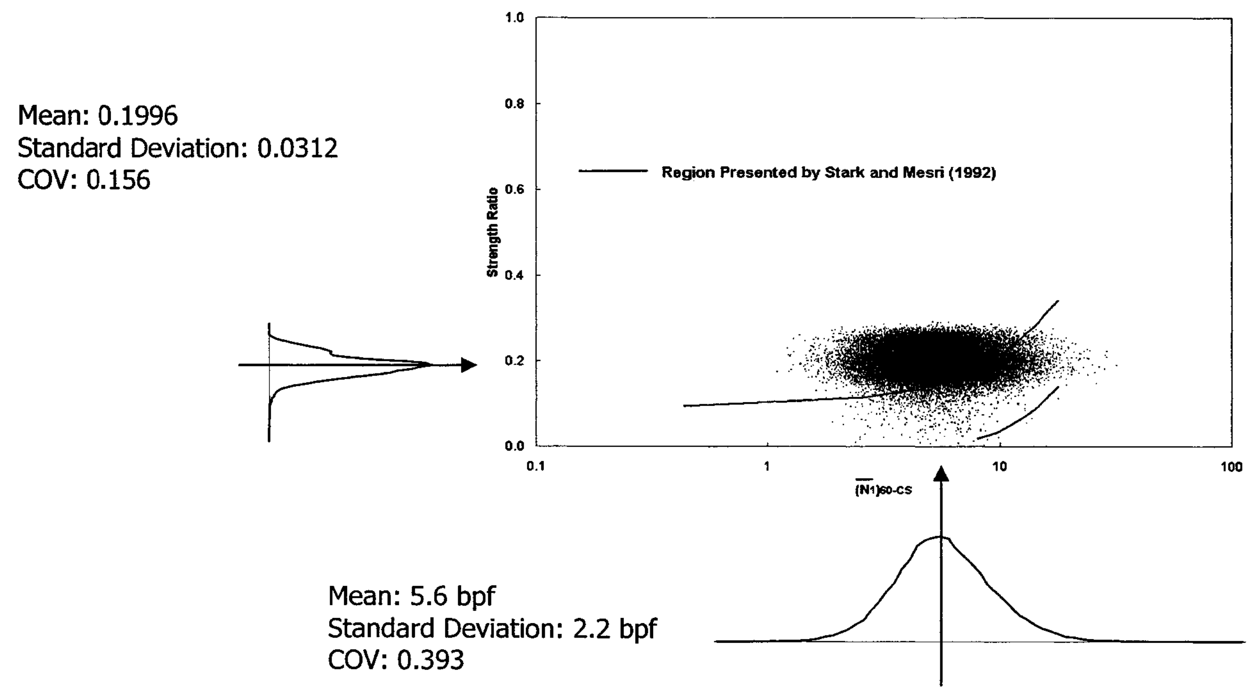

Figure 6-28 $\overline{S}_r/\overline{\sigma}'_{vo}$ versus $(\overline{N}_1)_{60\text{-CS}}$ for the Shibecha-Cho embankment. A total of 50,000 data points are shown.

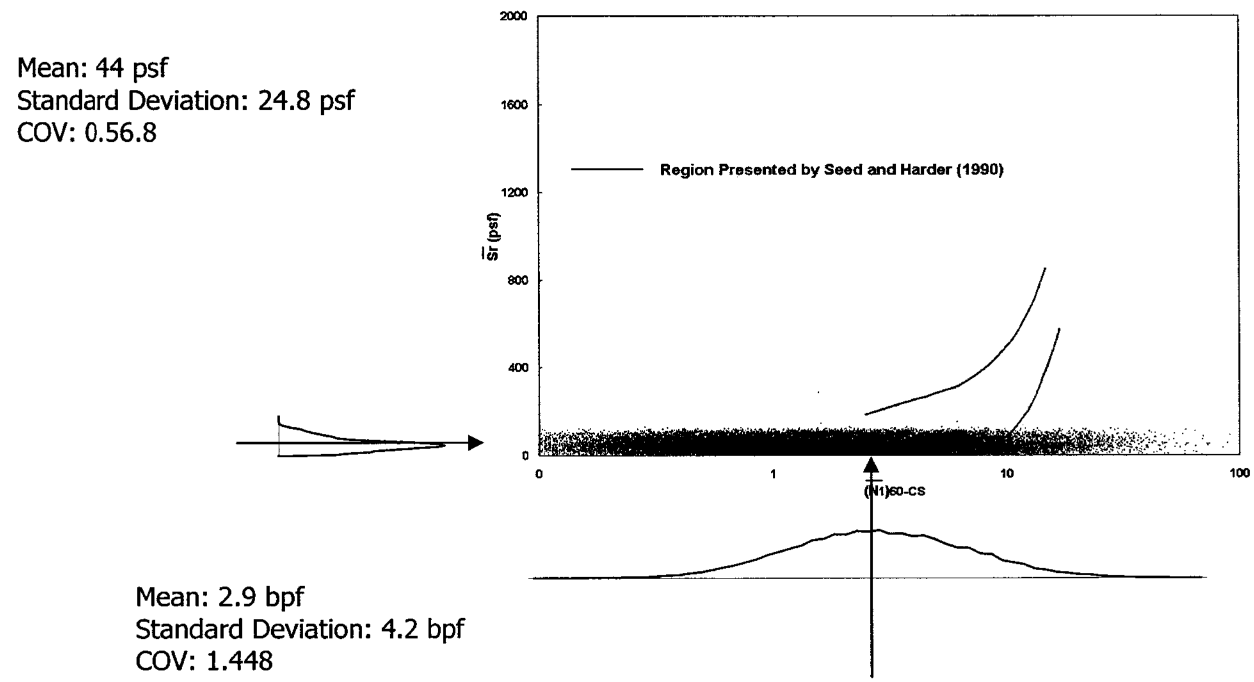

Figure 6-29 $\overline{S}_r$ versus $(\overline{N}_1)_{60\text{-CS}}$ for the Uetsu-Line railway embankment, based on Equation (5.24). A total of 50,000 data points are shown.

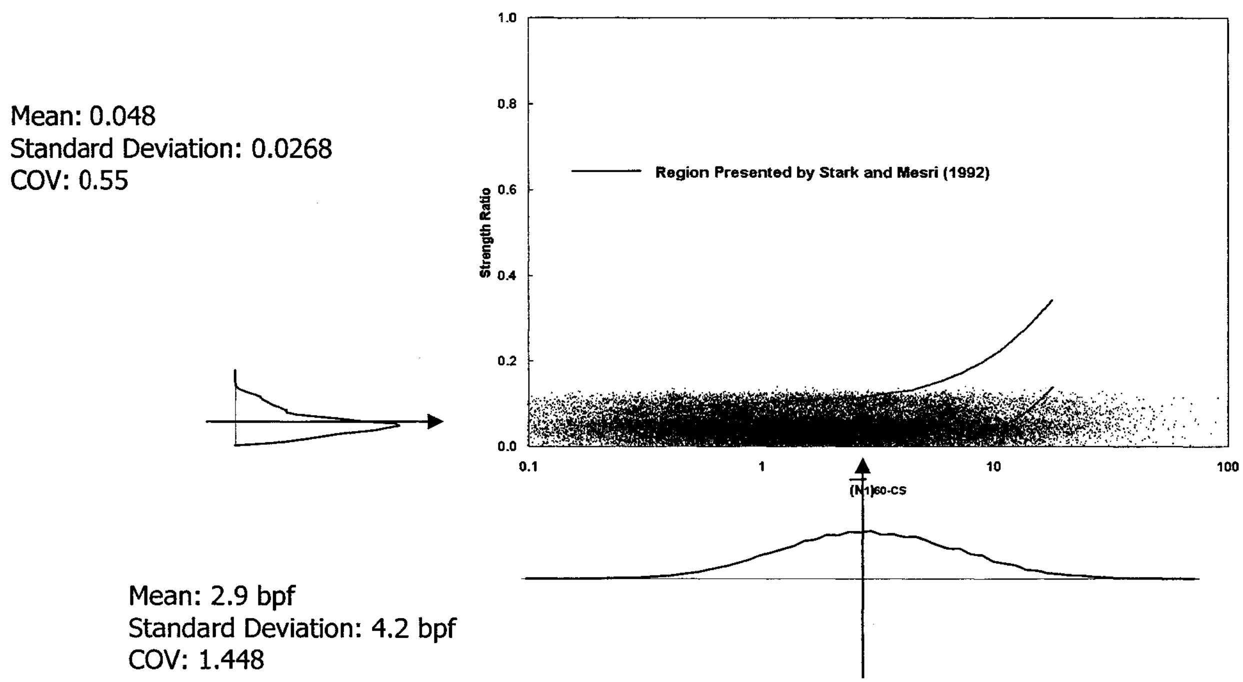

Figure 6-30 $\overline{S}_r/\overline{\sigma}'_{vo}$ versus $(\overline{N}_1)_{60\text{-CS}}$ for the Uetsu-Line railway embankment. A total of 50,000 data points are shown.

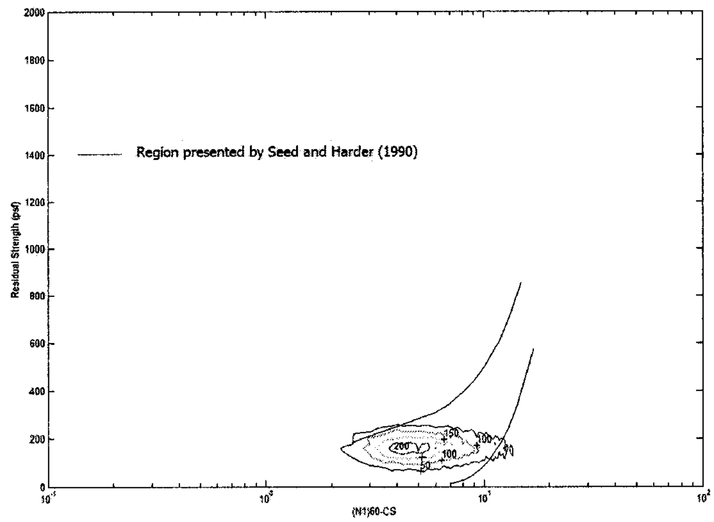

(a)

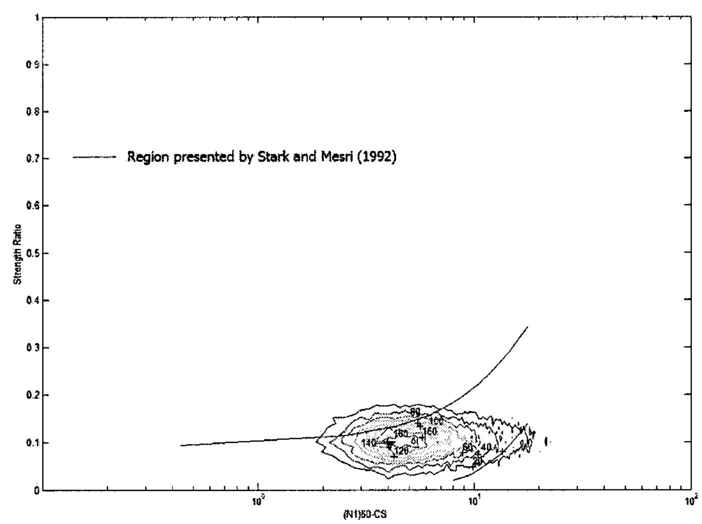

(b)

Figure 6-31 Contour plots of **(a)** $\overline{S}_r$ versus $(\overline{N}_1)_{60\text{-CS}}$ and (b) $\overline{S}_r/\overline{\sigma}'_{vo}$ versus $(\overline{N}_1)_{60\text{-CS}}$ for the Asele Road.

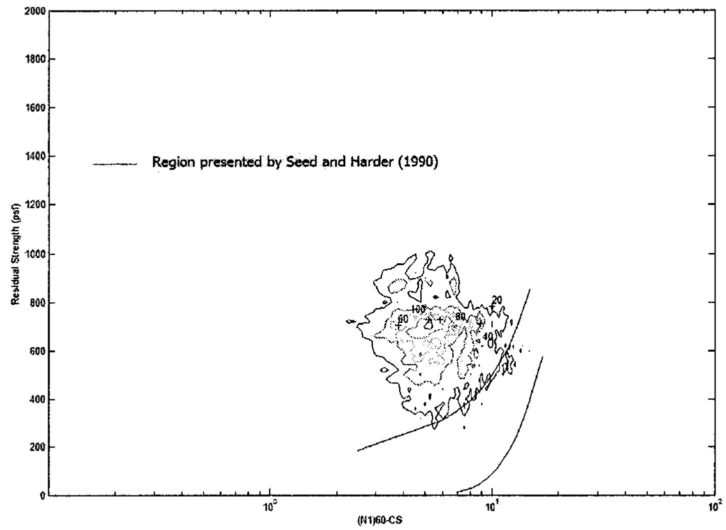

(a)

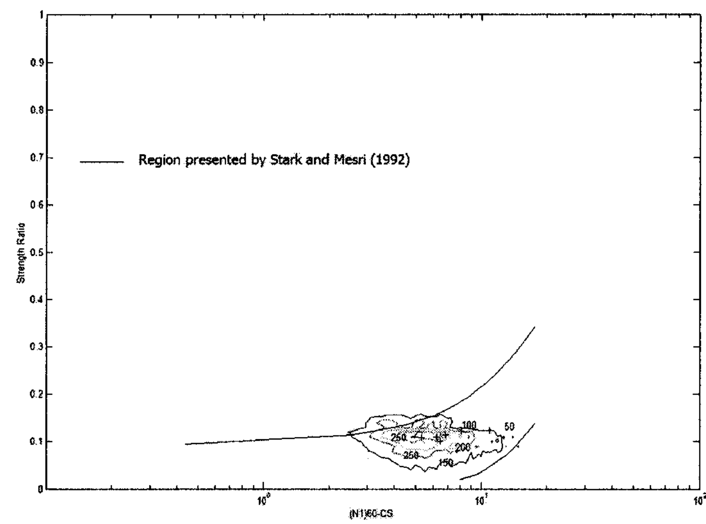

(b)

Figure 6-32 Contour plots of **(a)** $\overline{S}_r$ versus $(\overline{N}_1)_{60\text{-CS}}$ and (b) $\overline{S}_r/\overline{\sigma}'_{vo}$ versus $(\overline{N}_1)_{60\text{-CS}}$ for the Calaveras Dam.

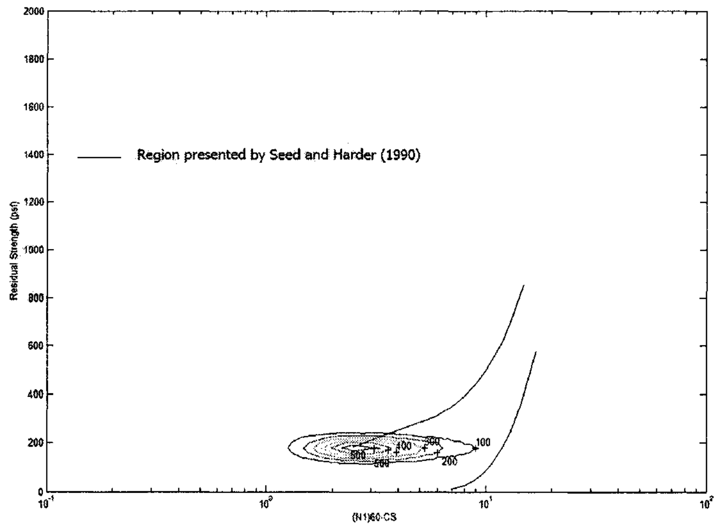

(a)

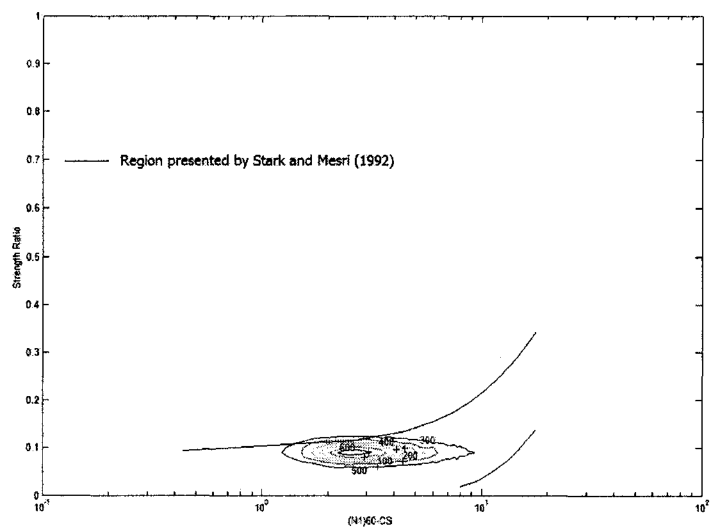

(b)

Figure 6-33 Contour plots of **(a)** $\overline{S}_r$ versus $(\overline{N}_1)_{60\text{-CS}}$ and (b) $\overline{S}_r/\overline{\sigma}'_{vo}$ versus $(\overline{N}_1)_{60\text{-CS}}$ for the Chonan Middle School.

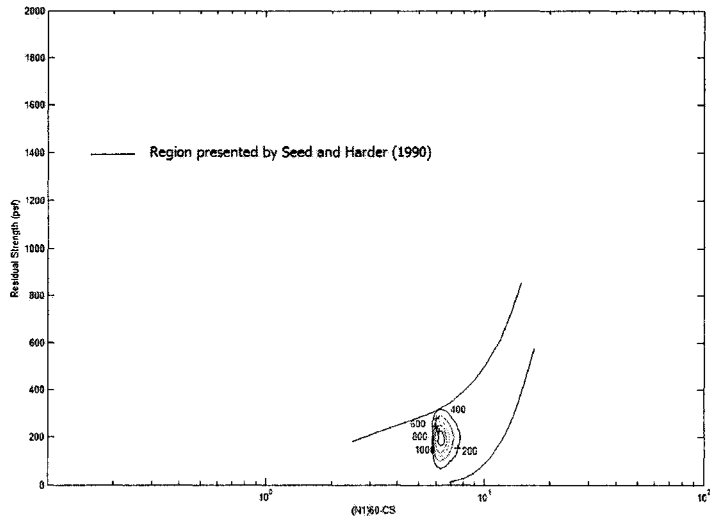

(a)

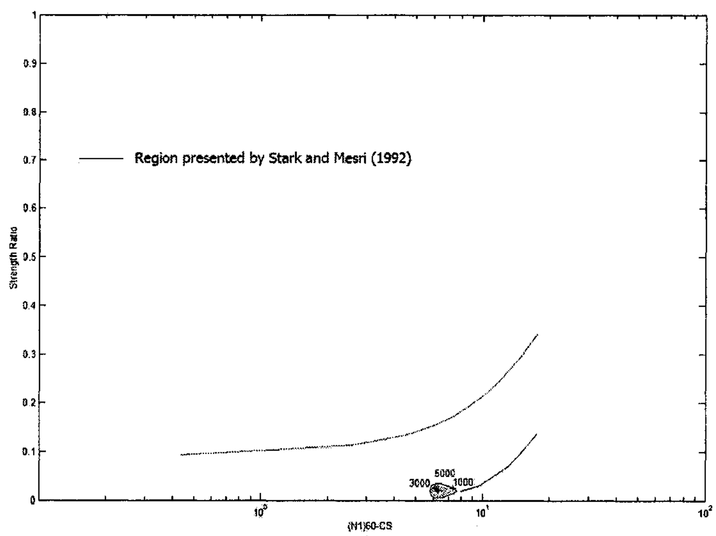

(b)

Figure 6-34 Contour plots of **(a)** $\overline{S}_r$ versus $(\overline{N}_1)_{60\text{-CS}}$ and (b) $\overline{S}_r/\overline{\sigma}'_{vo}$ versus $(\overline{N}_1)_{60\text{-CS}}$ for the El Cobre Tailings Dam.

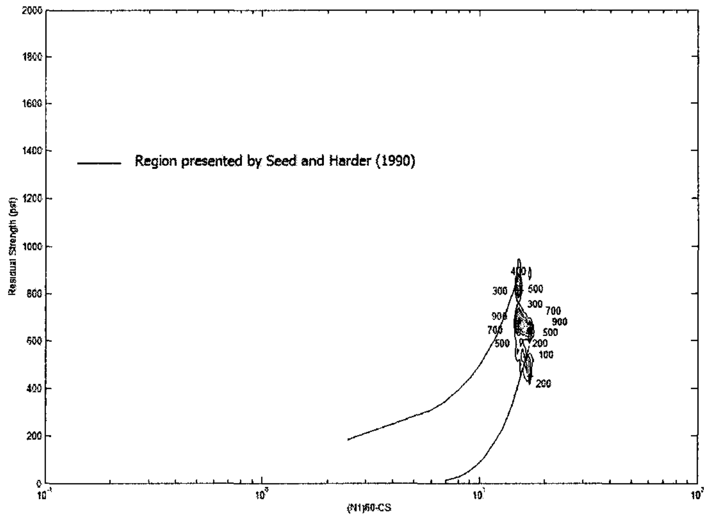

(a)

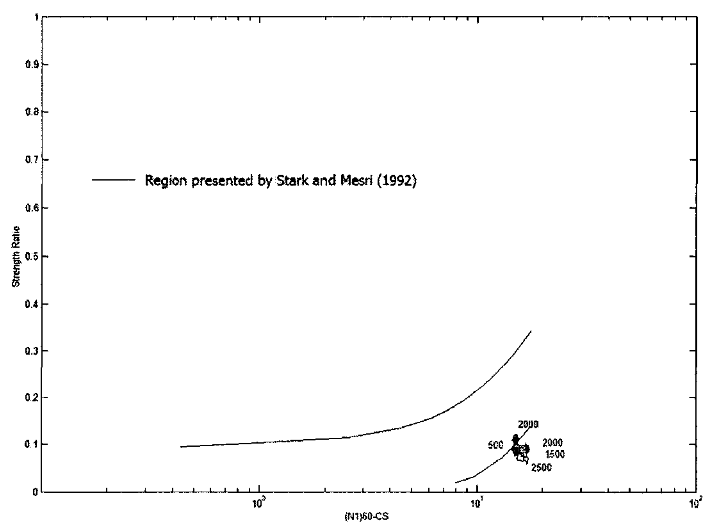

(b)

Figure 6-35 Contour plots of **(a)** $\overline{S}_r$ versus $(\overline{N}_1)_{60\text{-CS}}$ and (b) $\overline{S}_r/\overline{\sigma}'_{vo}$ versus $(\overline{N}_1)_{60\text{-CS}}$ for the Fort Peck Dam.

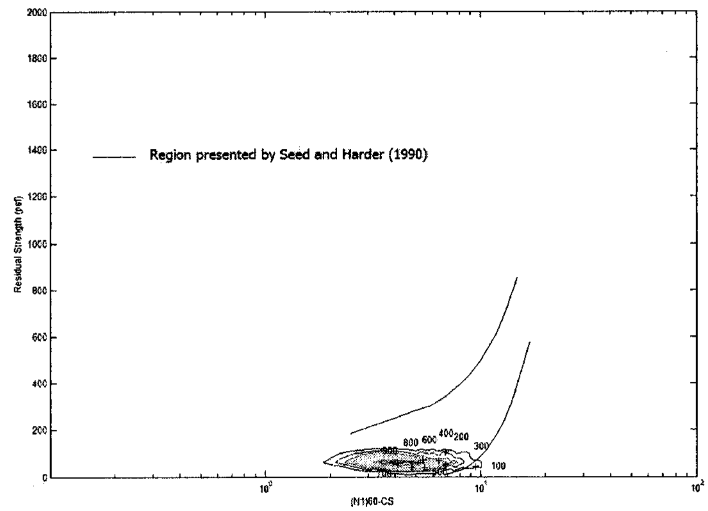

(a)

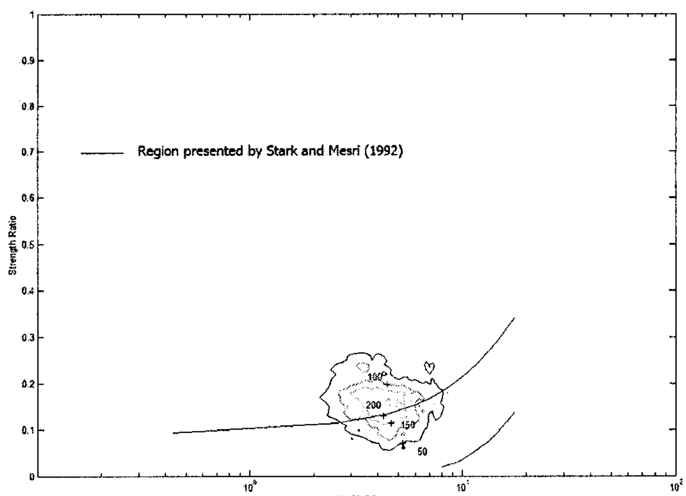

(b)

Figure 6-36 Contour plots of **(a)** $\overline{S}_r$ versus $(\overline{N}_1)_{60\text{-CS}}$ and (b) $\overline{S}_r/\overline{\sigma}'_{vo}$ versus $(\overline{N}_1)_{60\text{-CS}}$ for the Hachiro-Gata Roadway.

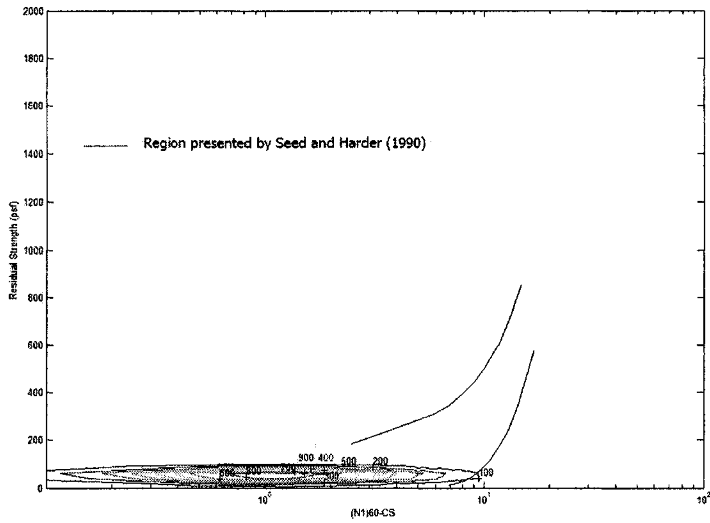

(a)

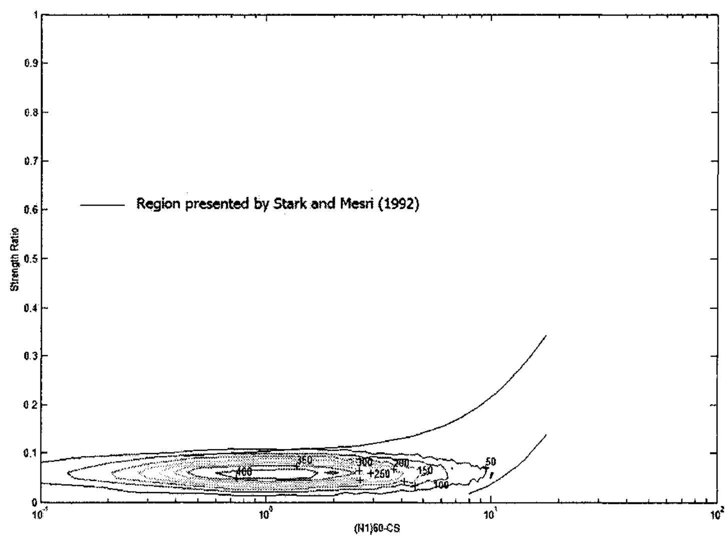

(b)

Figure 6-37 Contour plots of **(a)** $\overline{S}_r$ versus $(\overline{N}_1)_{60\text{-CS}}$ and (b) $\overline{S}_r/\overline{\sigma}'_{vo}$ versus $(\overline{N}_1)_{60\text{-CS}}$ for the Helsinki Harbor.

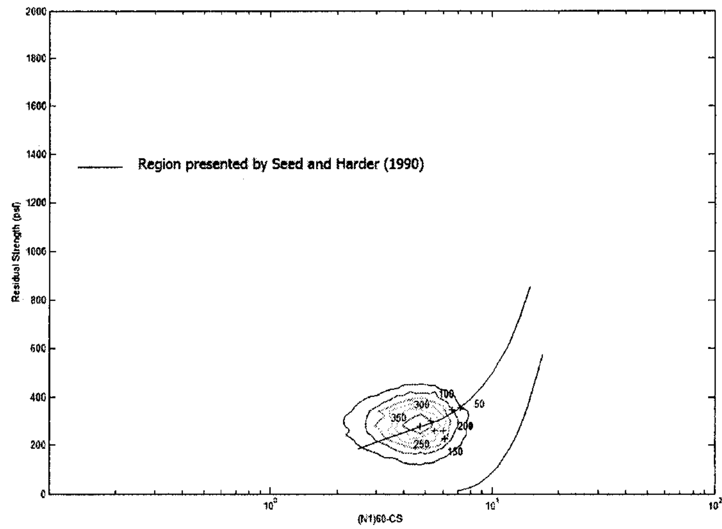

(a)

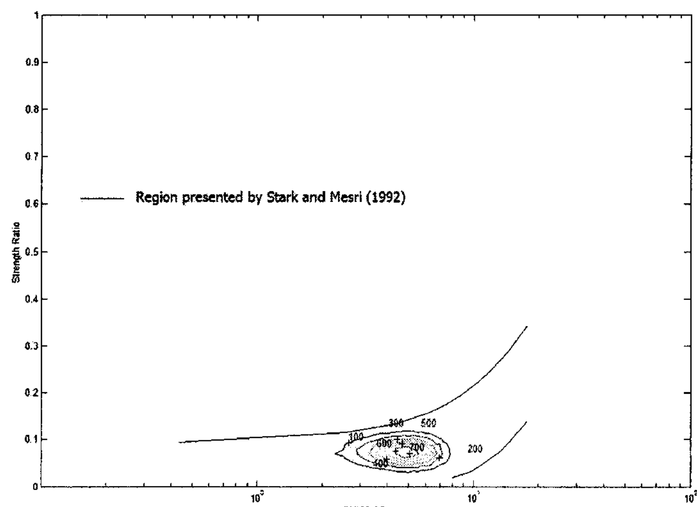

(b)

Figure 6-38 Contour plots of **(a)** $\overline{S}_r$ versus $(\overline{N}_1)_{60\text{-CS}}$ and (b) $\overline{S}_r/\overline{\sigma}'_{vo}$ versus $(\overline{N}_1)_{60\text{-CS}}$ for the Hokkaido Tailings Dam.

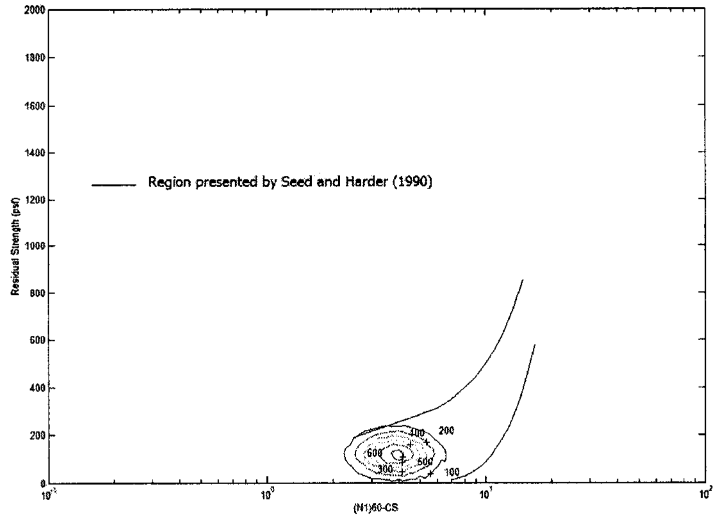

(a)

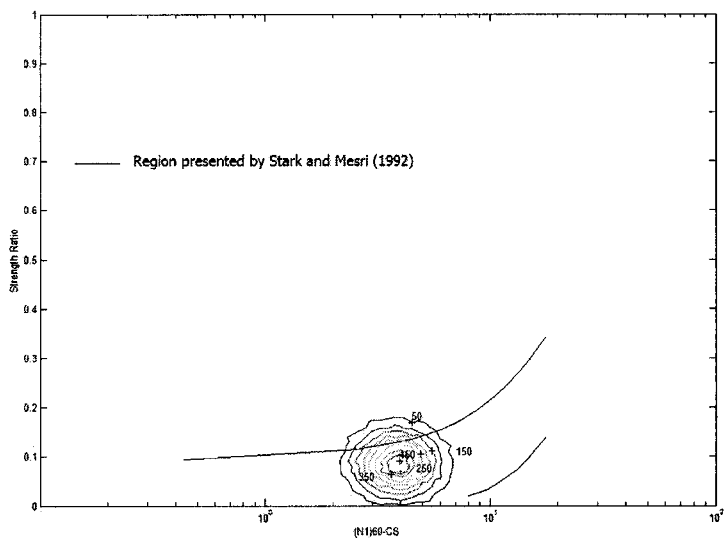

(b)

Figure 6-39 Contour plots of **(a)** $\overline{S}_r$ versus $(\overline{N}_1)_{60\text{-CS}}$ and (b) $\overline{S}_r/\overline{\sigma}'_{vo}$ versus $(\overline{N}_1)_{60\text{-CS}}$ for the Kawagich-Cho buildings.

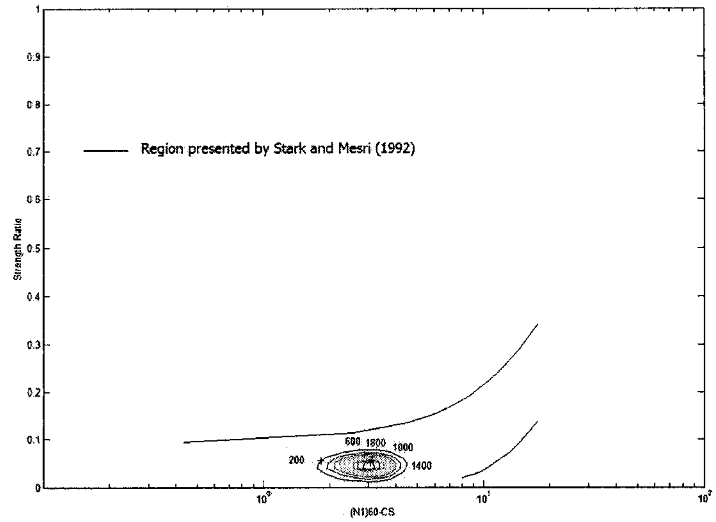

(a)

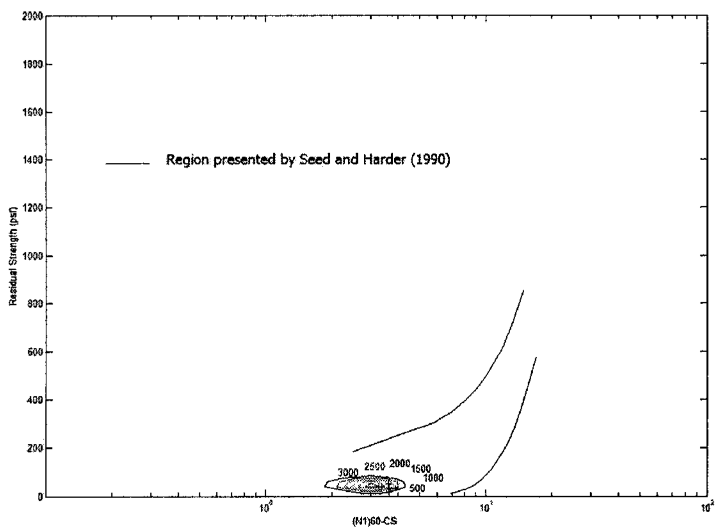

(b)

Figure 6-40 Contour plots of **(a)** $\overline{S}_r$ versus $(\overline{N}_1)_{60\text{-CS}}$ and (b) $\overline{S}_r/\overline{\sigma}'_{vo}$ versus $(\overline{N}_1)_{60\text{-CS}}$ for the Koda Numa embankment.

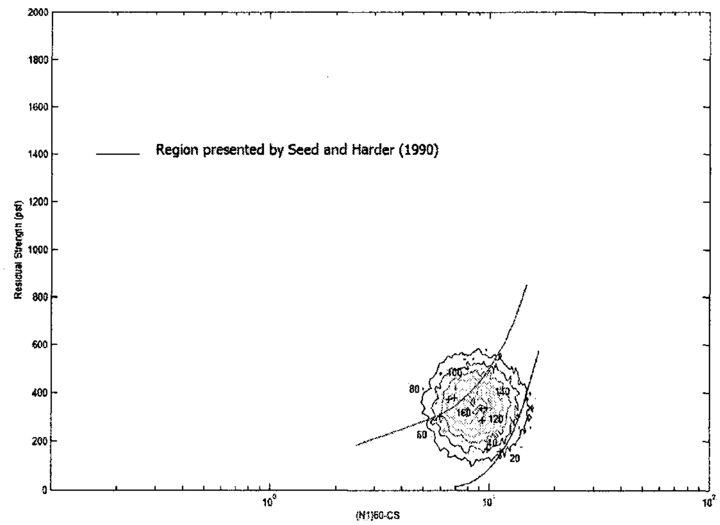

(a)

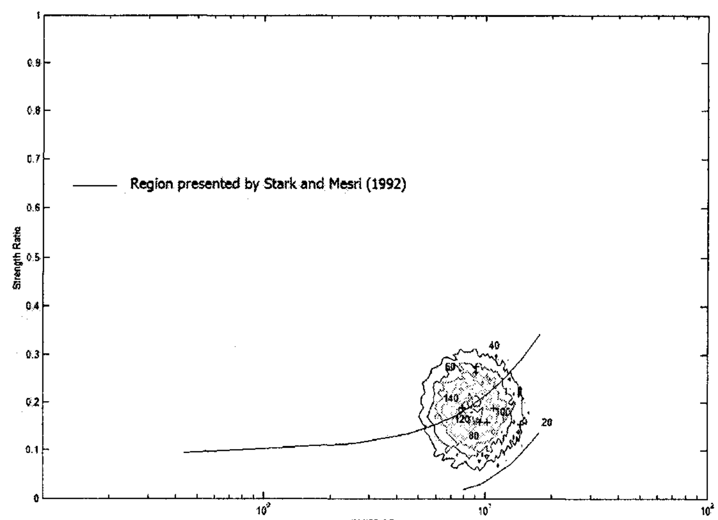

(b)

Figure 6-41 Contour plots of **(a)** $\overline{S}_r$ versus $(\overline{N}_1)_{60\text{-CS}}$ and (b) $\overline{S}_r/\overline{\sigma}'_{vo}$ versus $(\overline{N}_1)_{60\text{-CS}}$ for the La Marquesa Dam downstream.

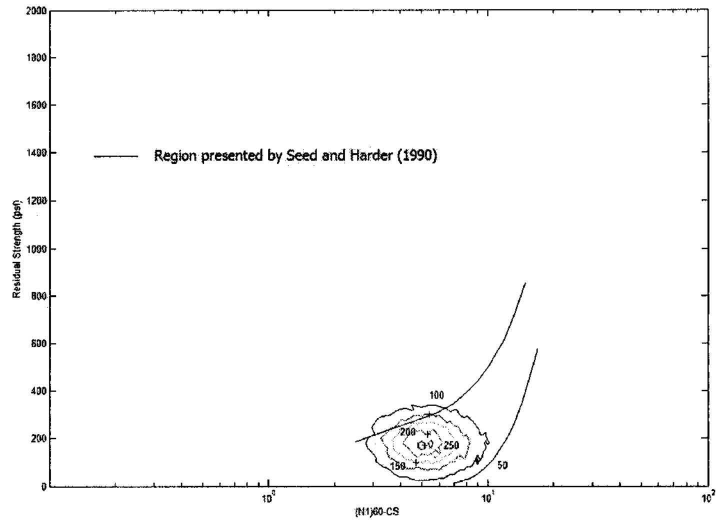

(a)

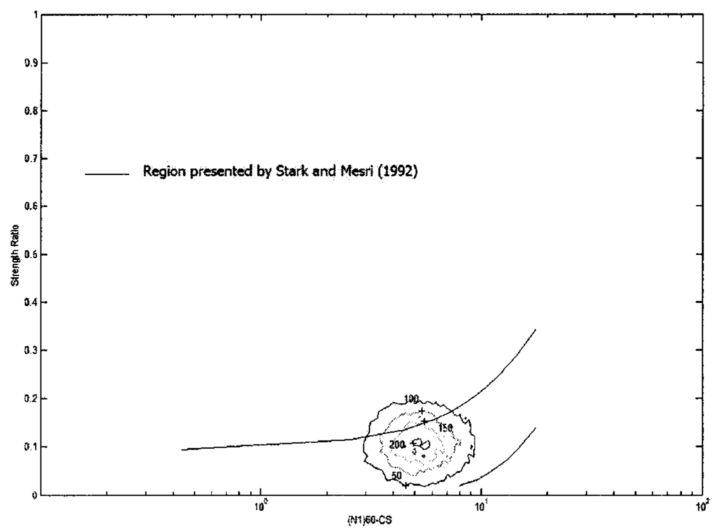

(b)

Figure 6-42 Contour plots of **(a)** $\overline{S}_r$ versus $(\overline{N}_1)_{60\text{-CS}}$ and (b) $\overline{S}_r/\overline{\sigma}'_{vo}$ versus $(\overline{N}_1)_{60\text{-CS}}$ for the La Marquesa Dam upstream.

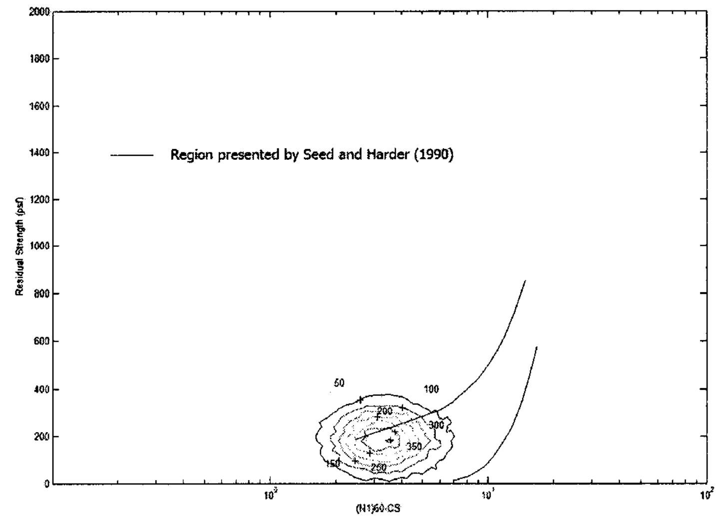

(a)

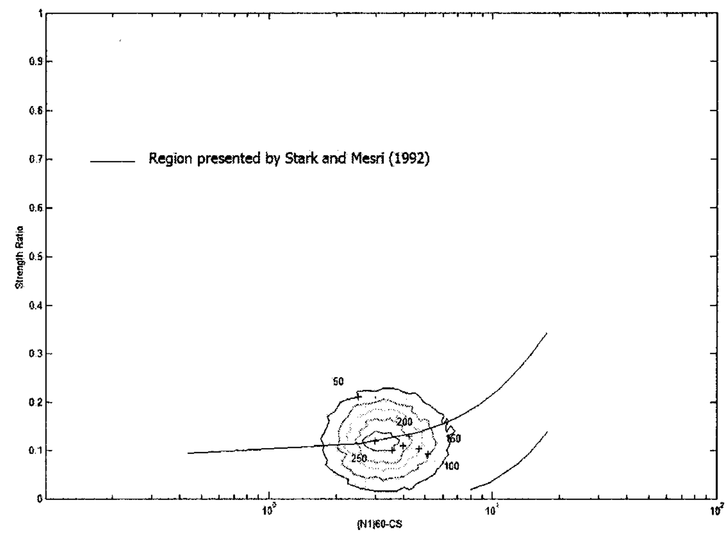

(b)

Figure 6-43 Contour plots of **(a)** $\overline{S}_r$ versus $(\overline{N}_1)_{60\text{-CS}}$ and (b) $\overline{S}_r/\overline{\sigma}'_{vo}$ versus $(\overline{N}_1)_{60\text{-CS}}$ for the La Palma Dam.

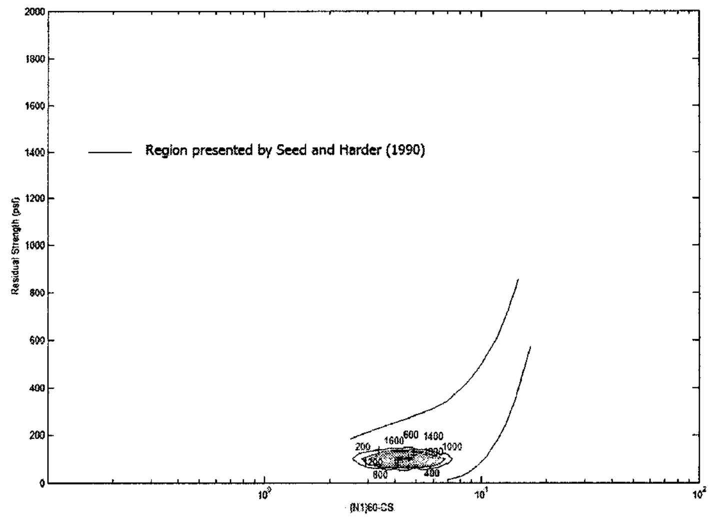

(a)

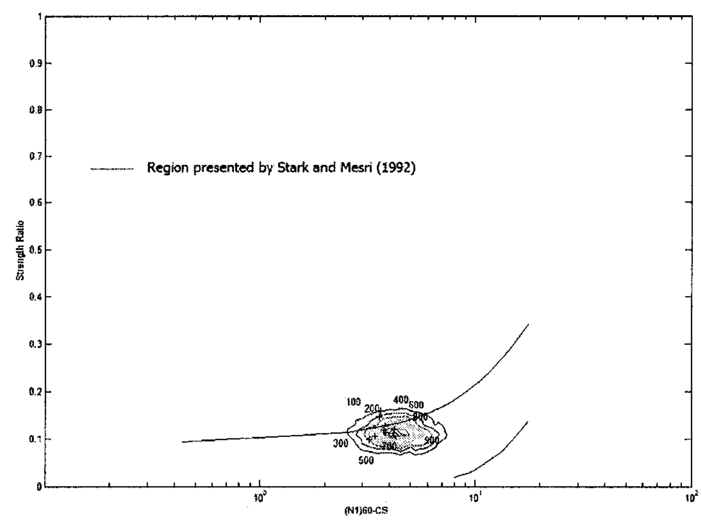

(b)

Figure 6-44 Contour plots of **(a)** $\overline{S}_r$ versus $(\overline{N}_1)_{60\text{-CS}}$ and (b) $\overline{S}_r/\overline{\sigma}'_{vo}$ versus $(\overline{N}_1)_{60\text{-CS}}$ for the Lake Ackerman roadway.

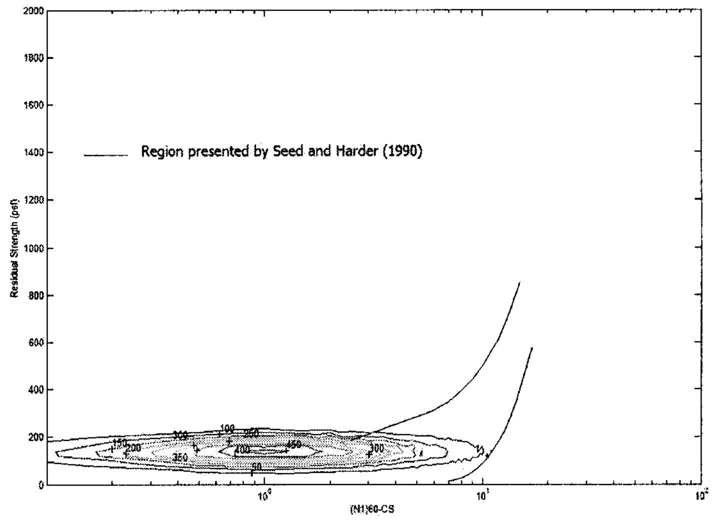

(a)

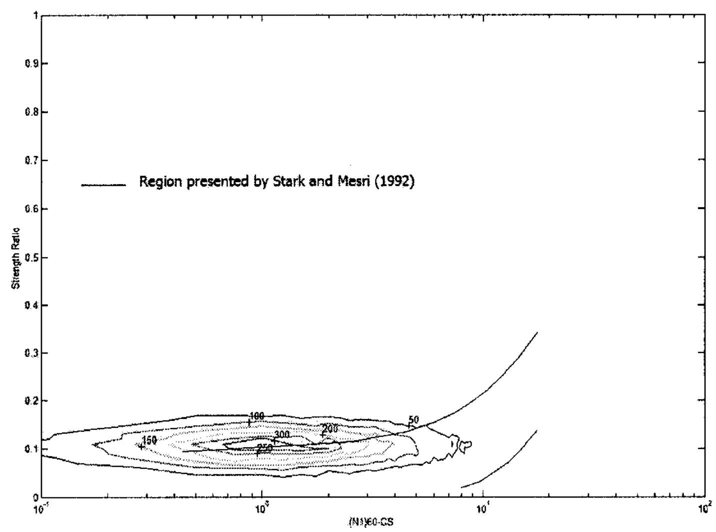

(b)

Figure 6-45 Contour plots of **(a)** $\overline{S}_r$ versus $(\overline{N}_1)_{60\text{-CS}}$ and (b) $\overline{S}_r/\overline{\sigma}'_{vo}$ versus $(\overline{N}_1)_{60\text{-CS}}$ for the Lake Merced bank.

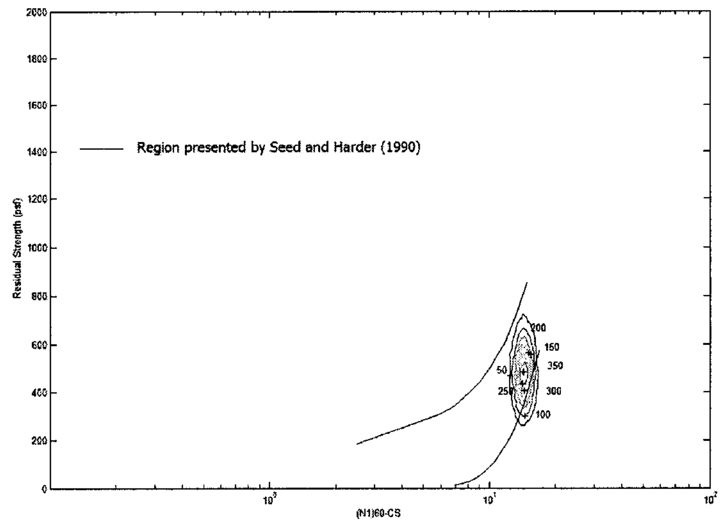

(a)

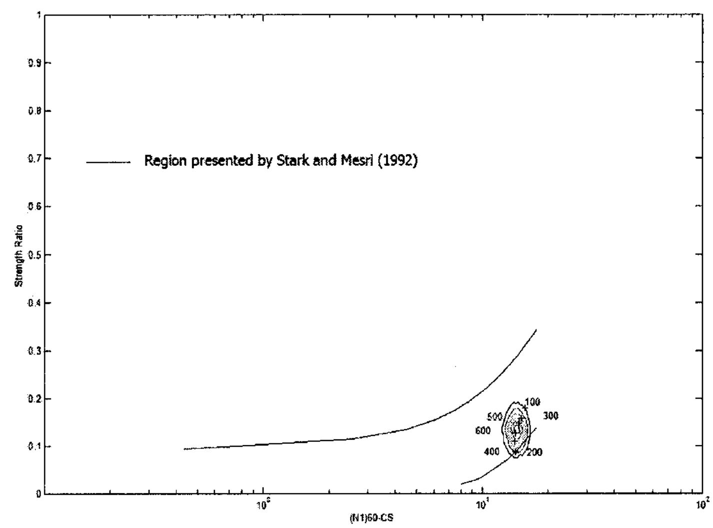

(b)

Figure 6-46 Contour plots of **(a)** $\overline{S}_r$ versus $(\overline{N}_1)_{60\text{-CS}}$ and (b) $\overline{S}_r/\overline{\sigma}'_{vo}$ versus $(\overline{N}_1)_{60\text{-CS}}$ for the Lower San Fernando Dam upstream.

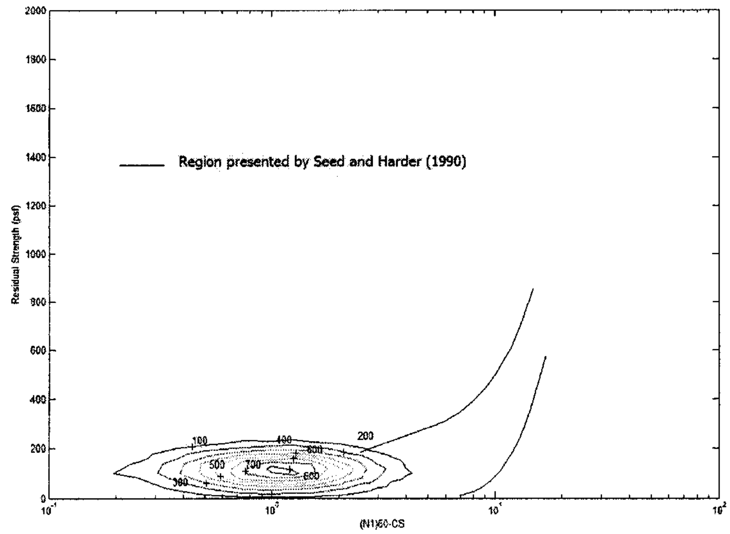

(a)

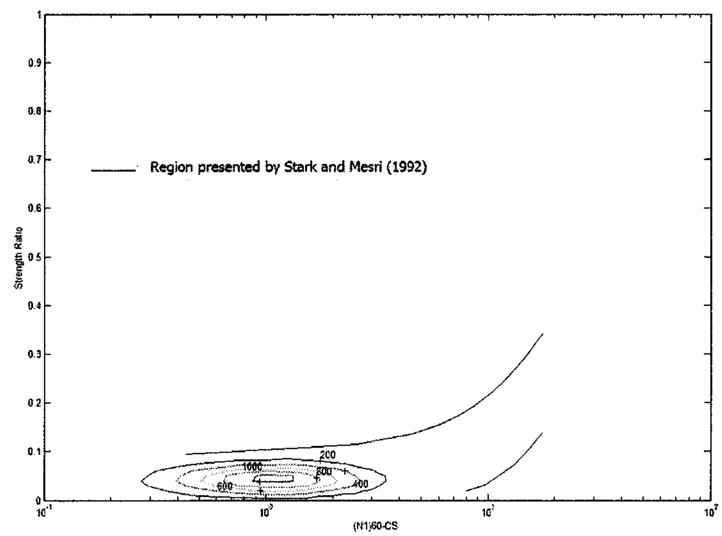

(b)

Figure 6-47 Contour plots of **(a)** $\overline{S}_r$ versus $(\overline{N}_1)_{60\text{-CS}}$ and (b) $\overline{S}_r/\overline{\sigma}'_{vo}$ versus $(\overline{N}_1)_{60\text{-CS}}$ for the Metoki roadway.

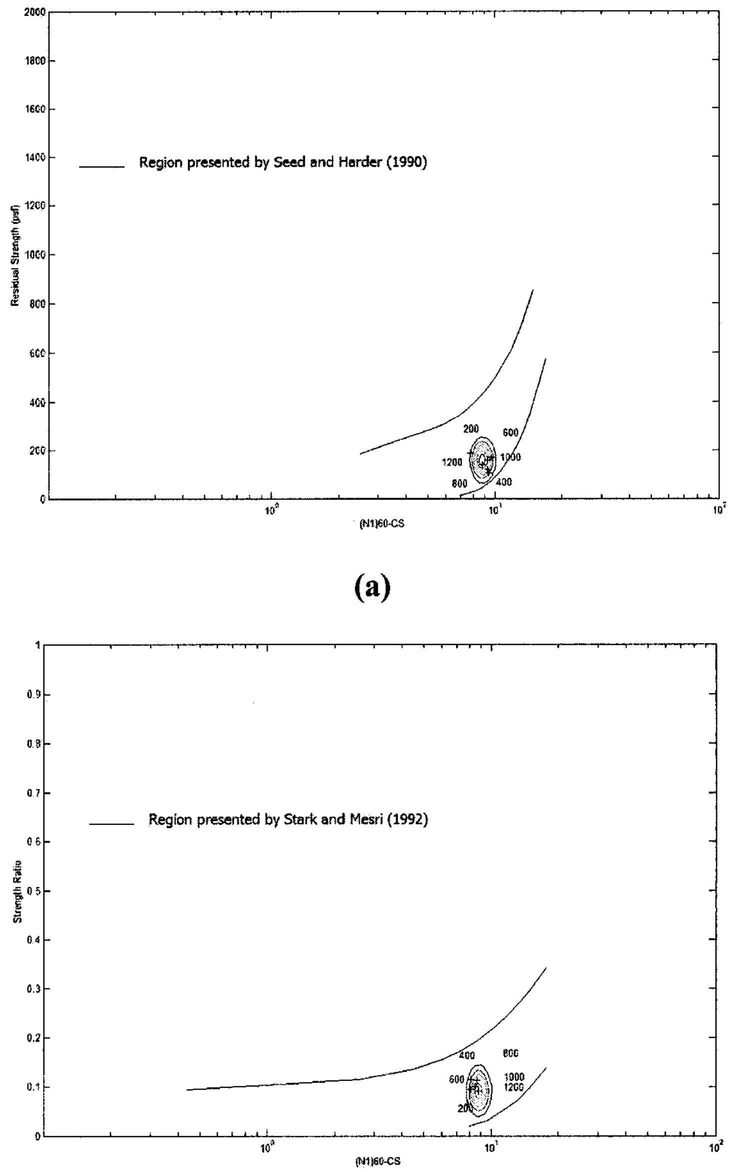

(a)

(b)

Figure 6-48 Contour plots of **(a)** $\overline{S}_r$ versus $(\overline{N}_1)_{60\text{-CS}}$ and (b) $\overline{S}_r/\overline{\sigma}'_{vo}$ versus $(\overline{N}_1)_{60\text{-CS}}$ for the Mochi Koshi Tailings Dam 1.

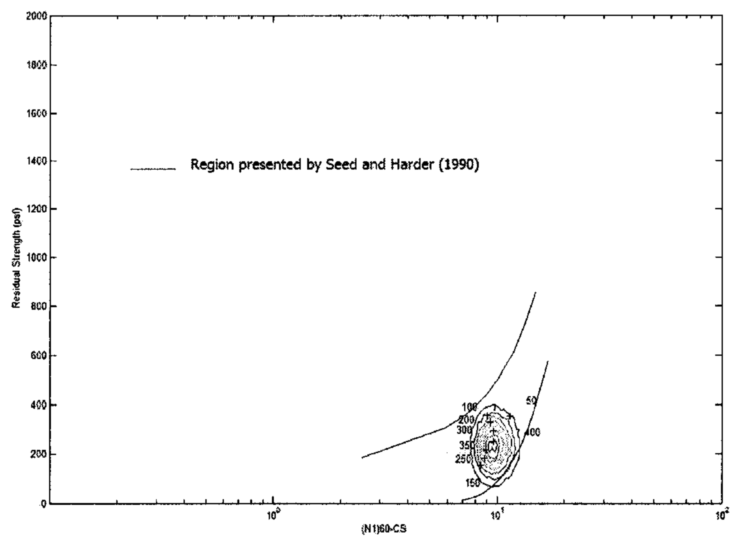

(a)

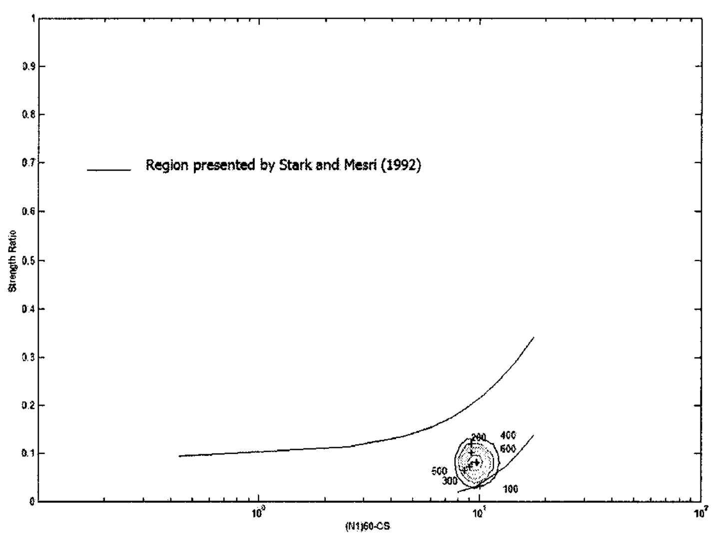

(b)

Figure 6-49 Contour plots of **(a)** $\overline{S}_r$ versus $(\overline{N}_1)_{60\text{-CS}}$ and (b) $\overline{S}_r/\overline{\sigma}'_{vo}$ versus $(\overline{N}_1)_{60\text{-CS}}$ for the Mochi Koshi Tailings Dam 2.

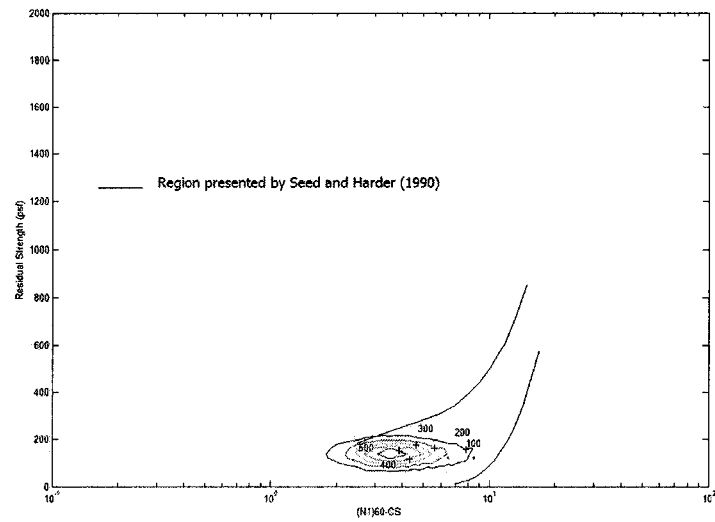

(a)

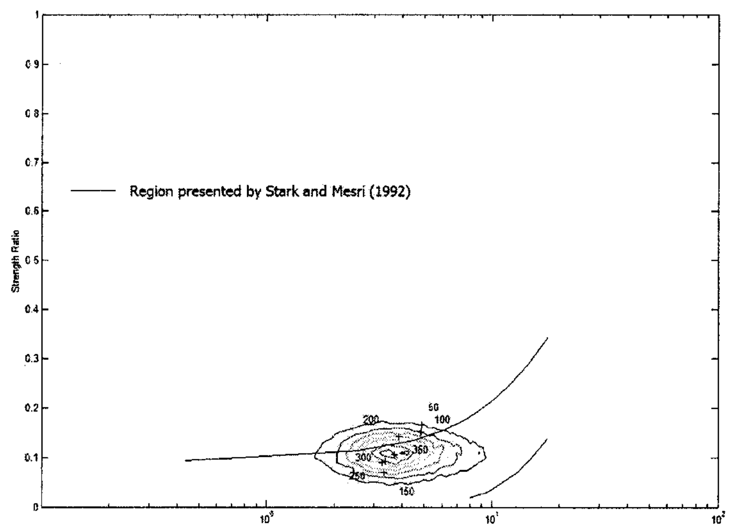

(b)

Figure 6-50 Contour plots of **(a)** $\overline{S}_r$ versus $(\overline{N}_1)_{60\text{-CS}}$ and (b) $\overline{S}_r/\overline{\sigma}'_{vo}$ versus $(\overline{N}_1)_{60\text{-CS}}$ for the Nalband railway embankment.

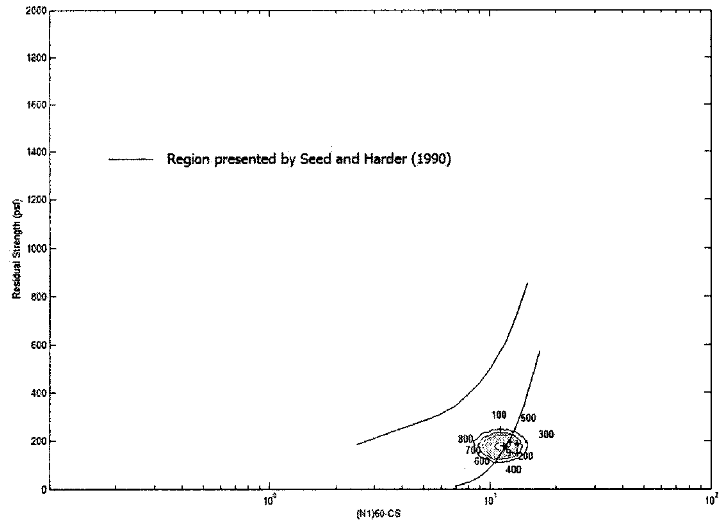

(a)

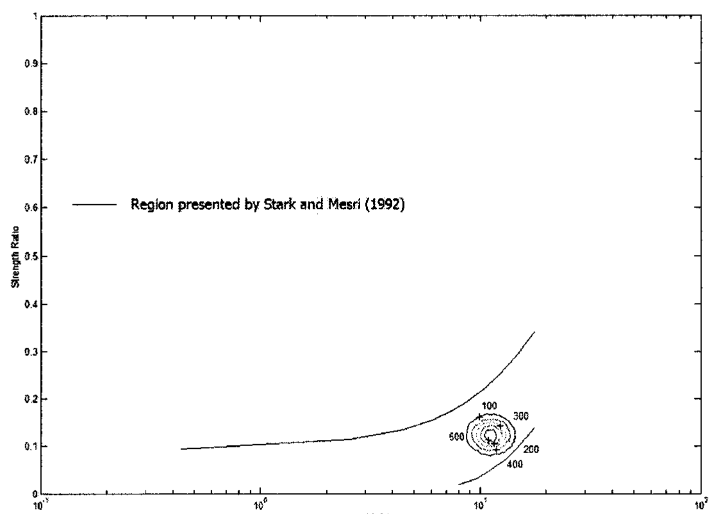

(b)

Figure 6-51 Contour plots of **(a)** $\overline{S}_r$ versus $(\overline{N}_1)_{60\text{-CS}}$ and (b) $\overline{S}_r/\overline{\sigma}'_{vo}$ versus $(\overline{N}_1)_{60\text{-CS}}$ for the Nerlerk Berm.

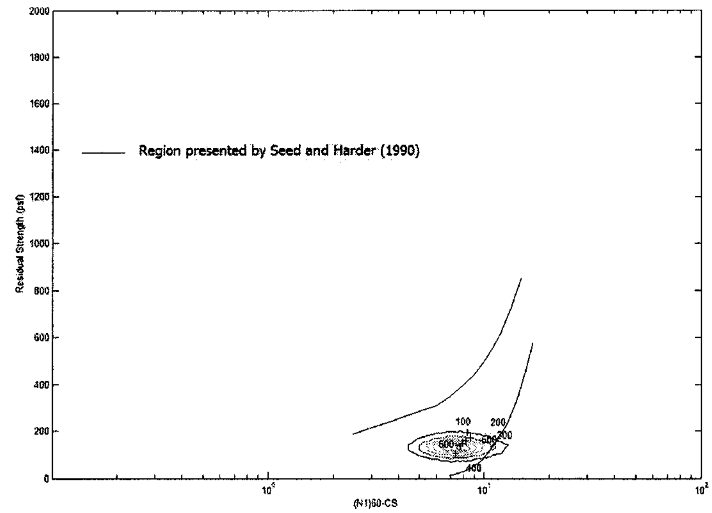

(a)

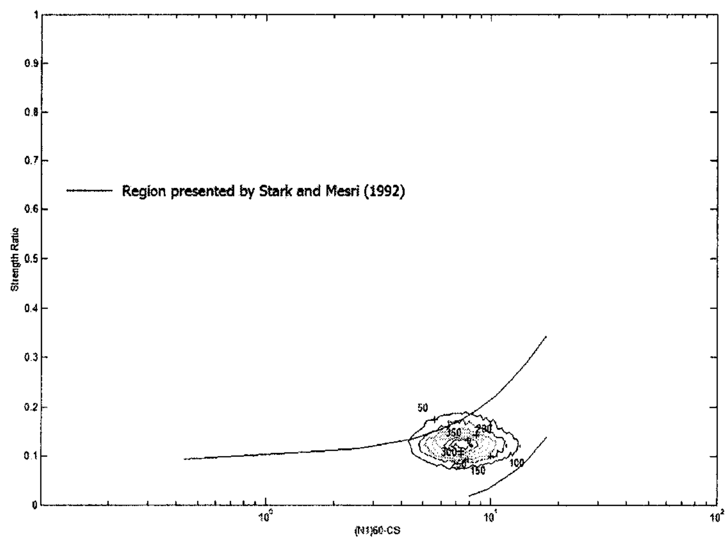

(b)

Figure 6-52 Contour plots of **(a)** $\overline{S}_r$ versus $(\overline{N}_1)_{60\text{-CS}}$ and (b) $\overline{S}_r/\overline{\sigma}'_{vo}$ versus $(\overline{N}_1)_{60\text{-CS}}$ for the Route 272 roadway embankment.

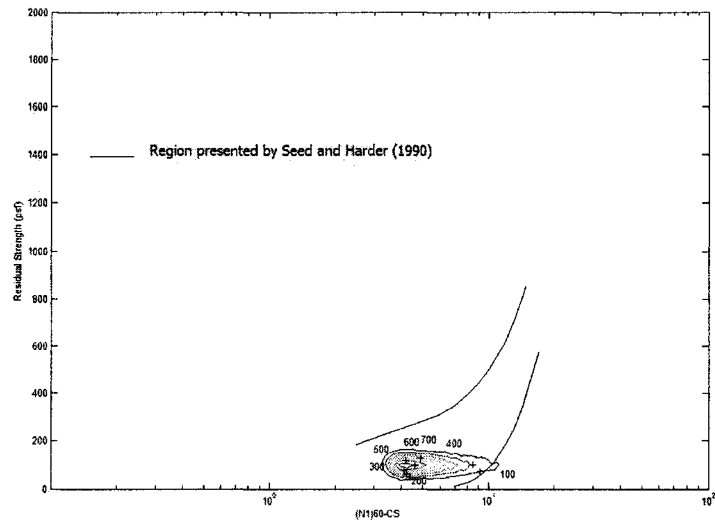

(a)

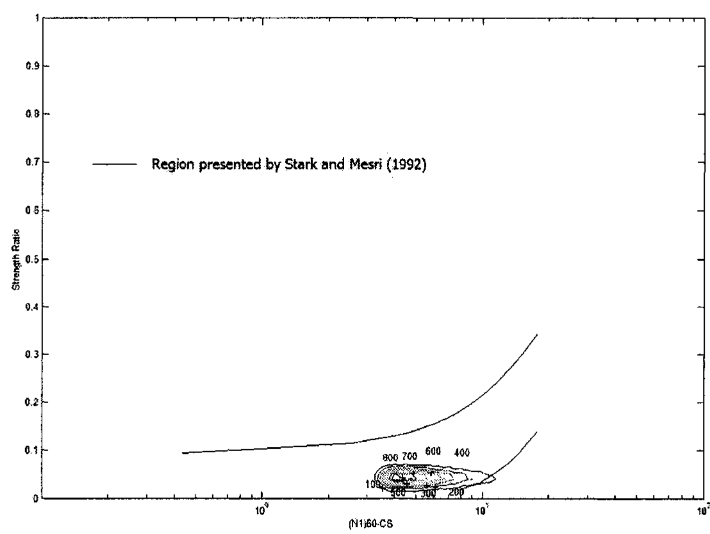

(b)

Figure 6-53 Contour plots of **(a)** $\overline{S}_r$ versus $(\overline{N}_1)_{60\text{-CS}}$ and (b) $\overline{S}_r/\overline{\sigma}'_{vo}$ versus $(\overline{N}_1)_{60\text{-CS}}$ for the Sheffield Dam.

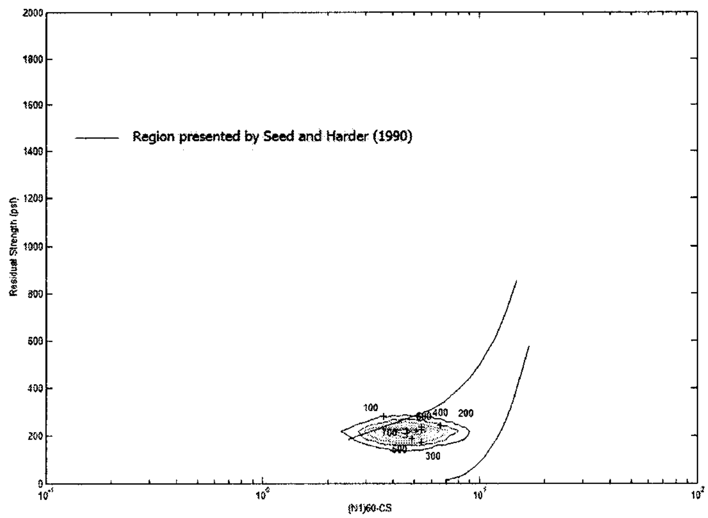

(a)

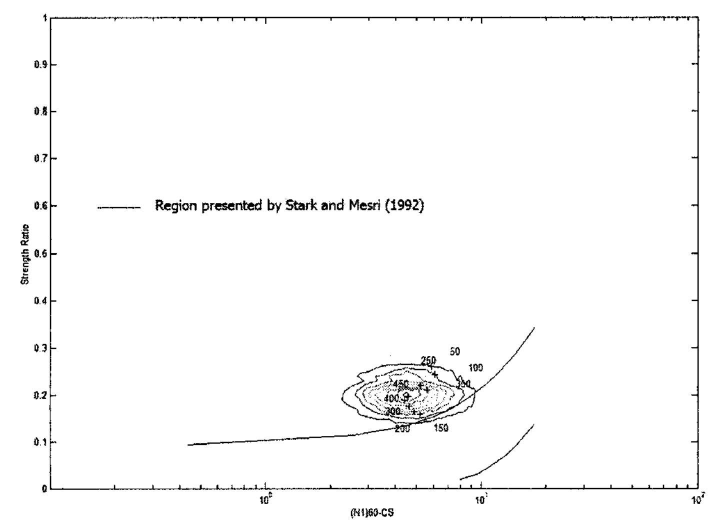

(b)

Figure 6-54 Contour plots of **(a)** $\overline{S}_r$ versus $(\overline{N}_1)_{60\text{-CS}}$ and (b) $\overline{S}_r/\overline{\sigma}'_{vo}$ versus $(\overline{N}_1)_{60\text{-CS}}$ for the Shibecha-Cho embankment.

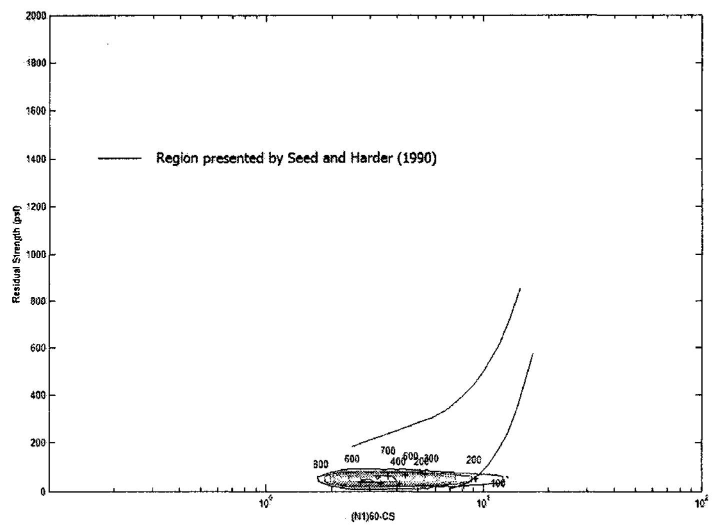

(a)

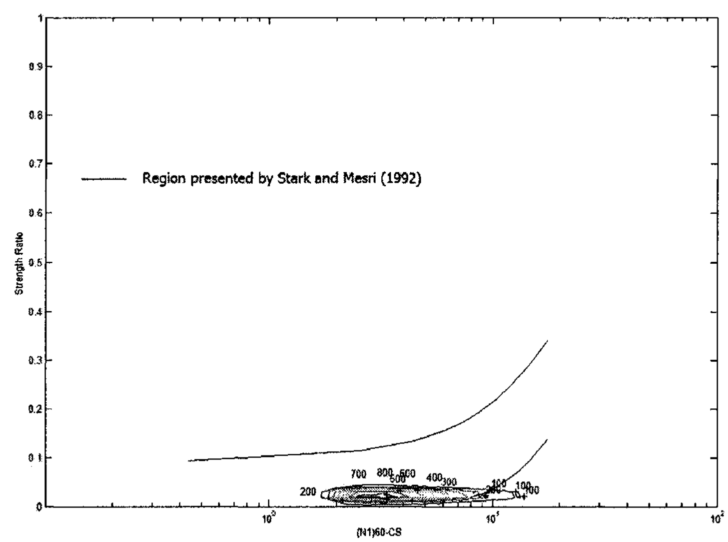

(b)

Figure 6-55 Contour plots of **(a)** $\overline{S}_r$ versus $(\overline{N}_1)_{60\text{-CS}}$ and (b) $\overline{S}_r/\overline{\sigma}'_{vo}$ versus $(\overline{N}_1)_{60\text{-CS}}$ for the Snow River bridge fill.

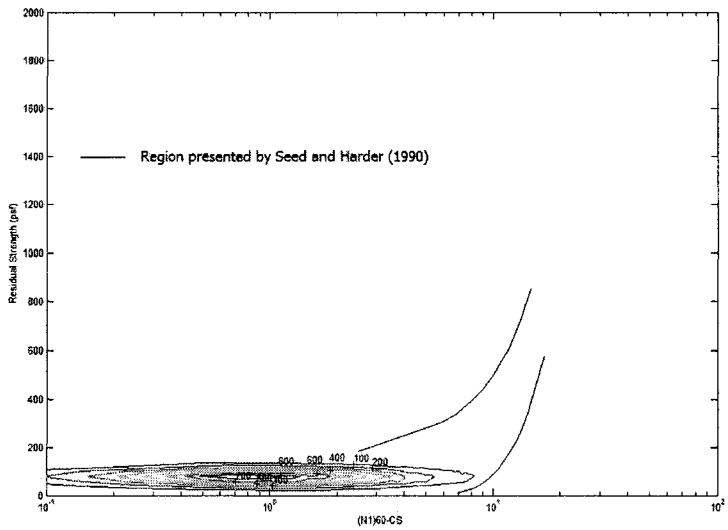

(a)

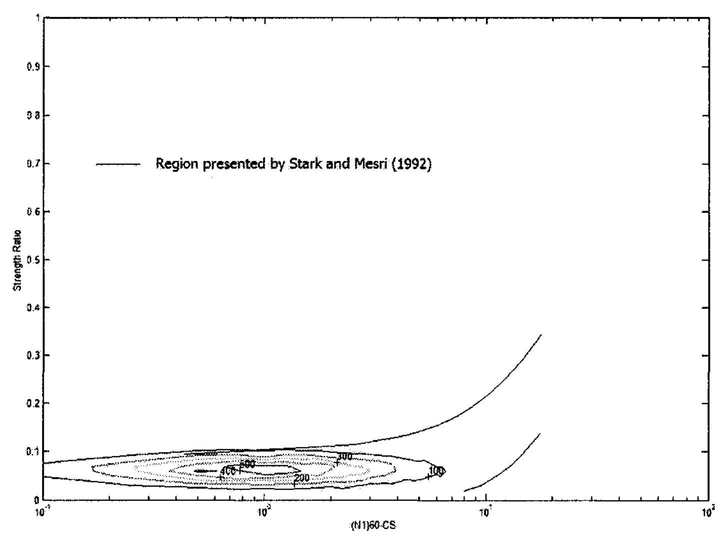

(b)

Figure 6-56 Contour plots of **(a)** $\overline{S}_r$ versus $(\overline{N}_1)_{60\text{-CS}}$ and (b) $\overline{S}_r/\overline{\sigma}'_{vo}$ versus $(\overline{N}_1)_{60\text{-CS}}$ for the Solfatara Canal Dike.

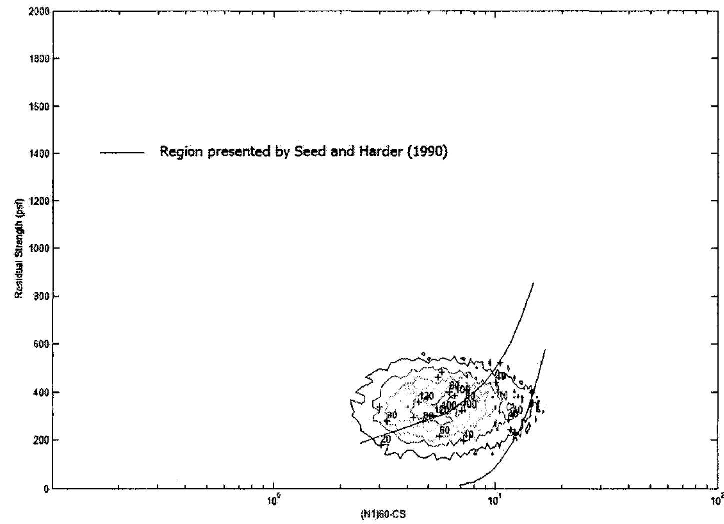

(a)

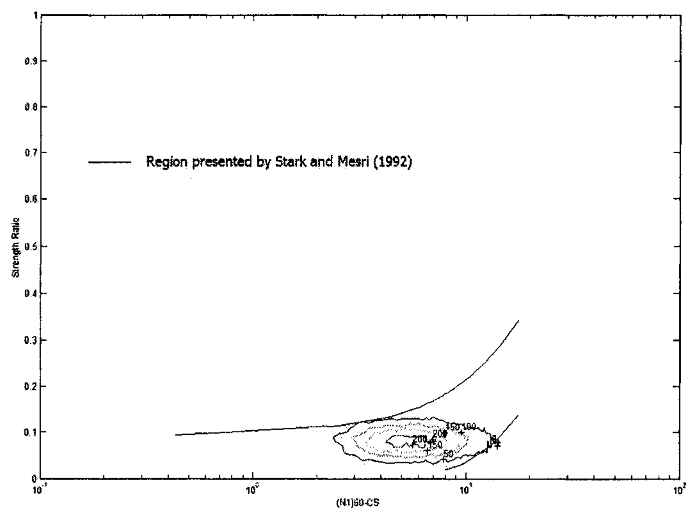

(b)

Figure 6-57 Contour plots of **(a)** $\overline{S}_r$ versus $(\overline{N}_1)_{60\text{-CS}}$ and (b) $\overline{S}_r/\overline{\sigma}'_{vo}$ versus $(\overline{N}_1)_{60\text{-CS}}$ for the Soviet Tajik, May 1 Slide.

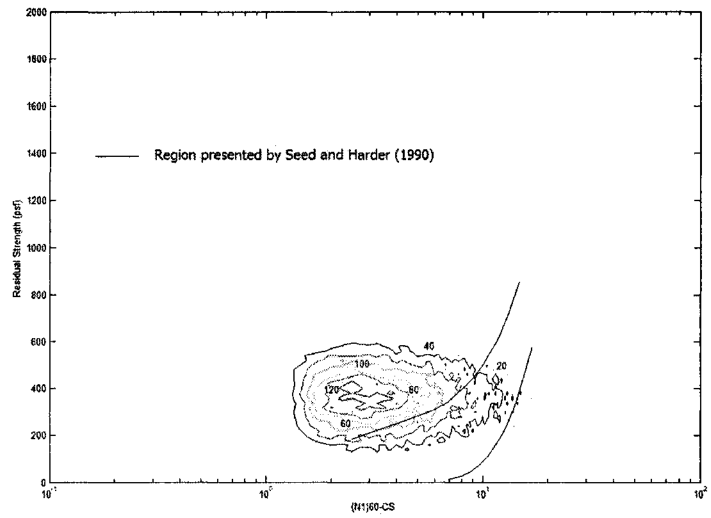

(a)

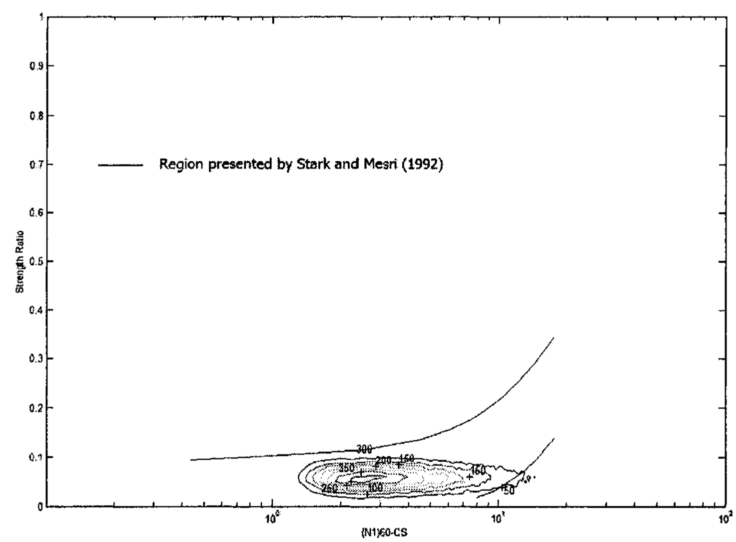

(b)

Figure 6-58 Contour plots of **(a)** $\overline{S}_r$ versus $(\overline{N}_1)_{60\text{-CS}}$ and (b) $\overline{S}_r/\overline{\sigma}'_{vo}$ versus $(\overline{N}_1)_{60\text{-CS}}$ for the Tar Island Dyke.

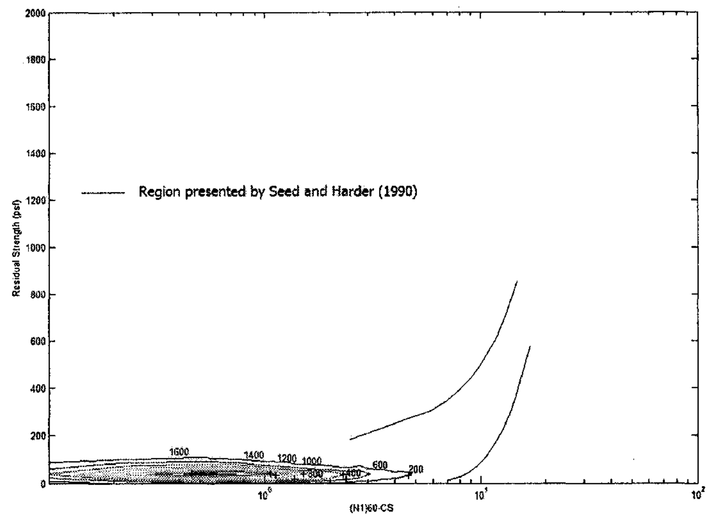

(a)

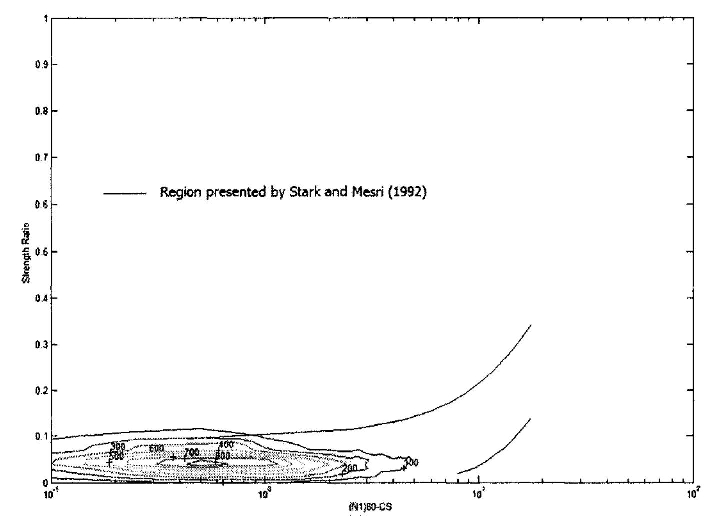

(b)

Figure 6-59 Contour plots of **(a)** $\overline{S}_r$ versus $(\overline{N}_1)_{60\text{-CS}}$ and (b) $\overline{S}_r/\overline{\sigma}'_{vo}$ versus $(\overline{N}_1)_{60\text{-CS}}$ for the Uetsu-Line railway embankment.

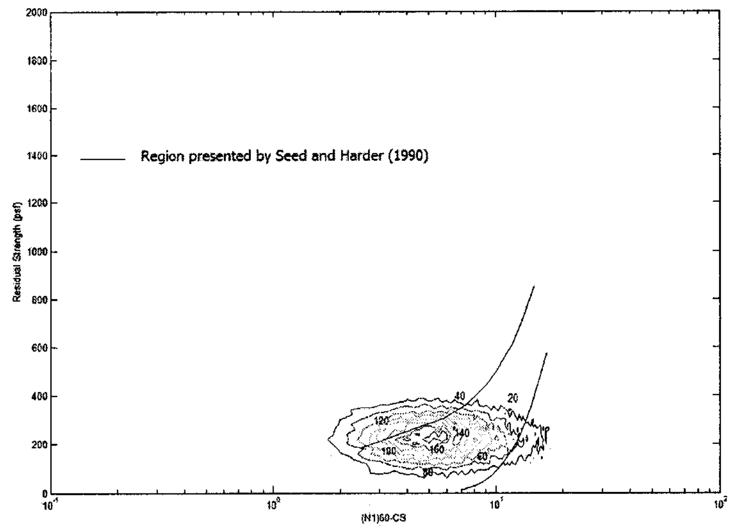

(a)

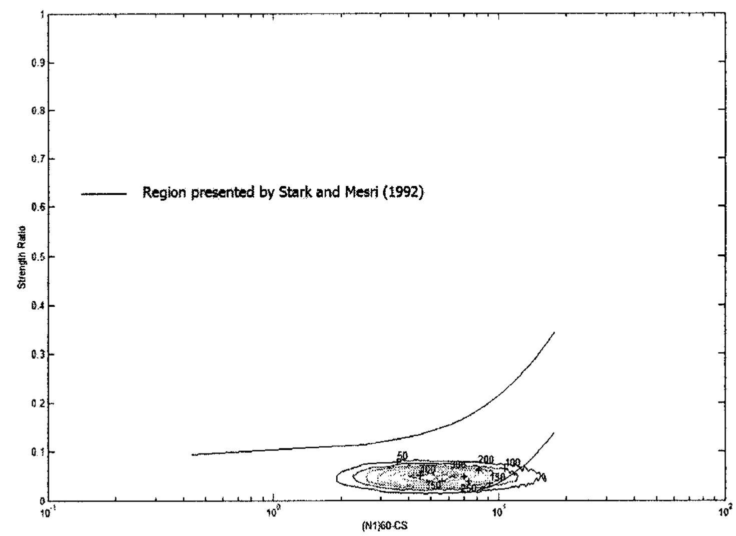

(b)

Figure 6-60 Contour plots of **(a)** $\overline{S}_r$ versus $(\overline{N}_1)_{60\text{-CS}}$ and (b) $\overline{S}_r/\overline{\sigma}'_{vo}$ versus $(\overline{N}_1)_{60\text{-CS}}$ for the Zeeland slide.

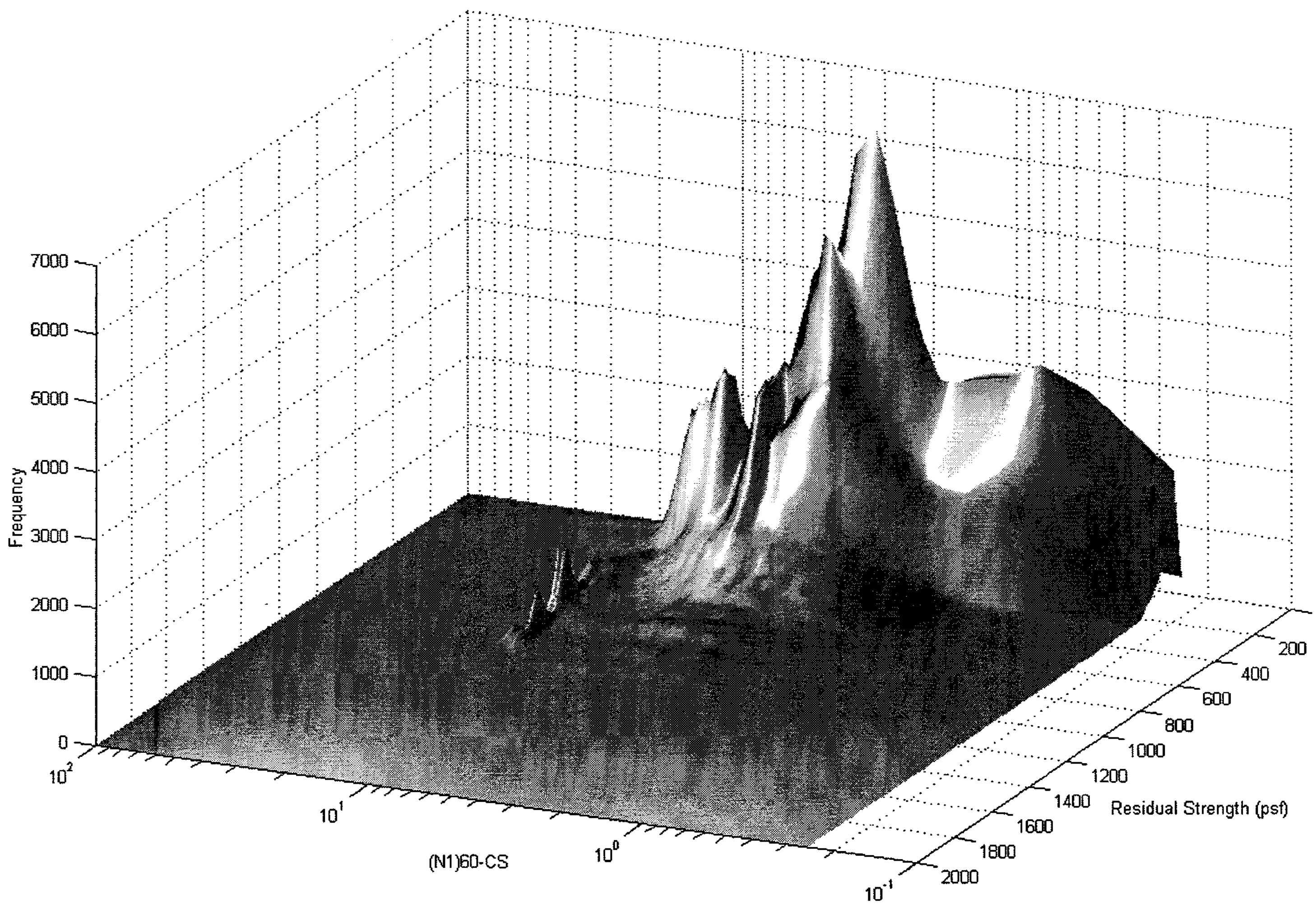

Figure 6-61 Three-dimensional histogram of $\overline{S}_r$ versus $(\overline{N}_1)_{60\text{-CS}}$ of the database for current study.

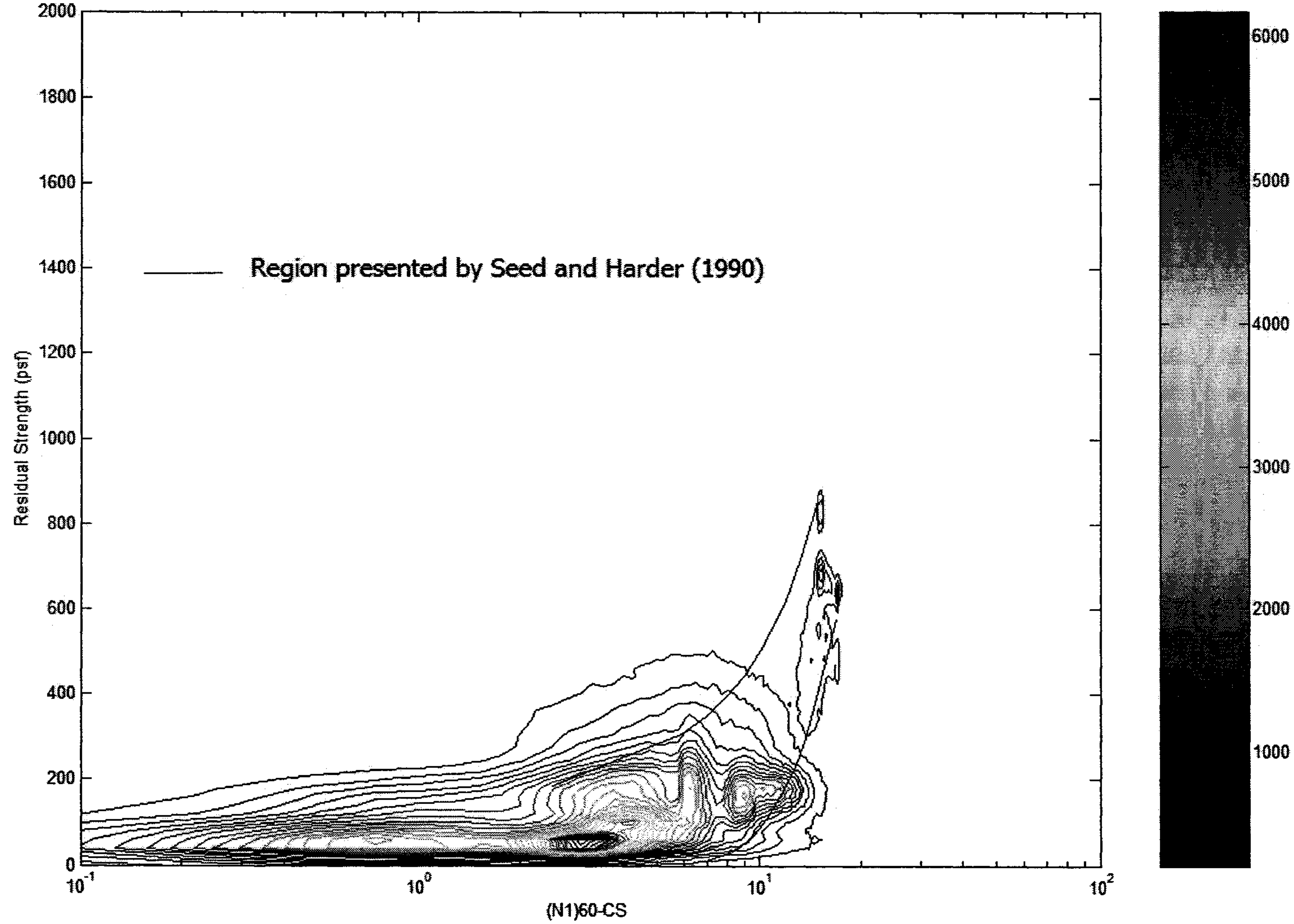

Figure 6-62 Contours plot of the database of $\overline{S}_r$ versus $(\overline{N}_1)_{60\text{-}CS}$ of the database for current study.

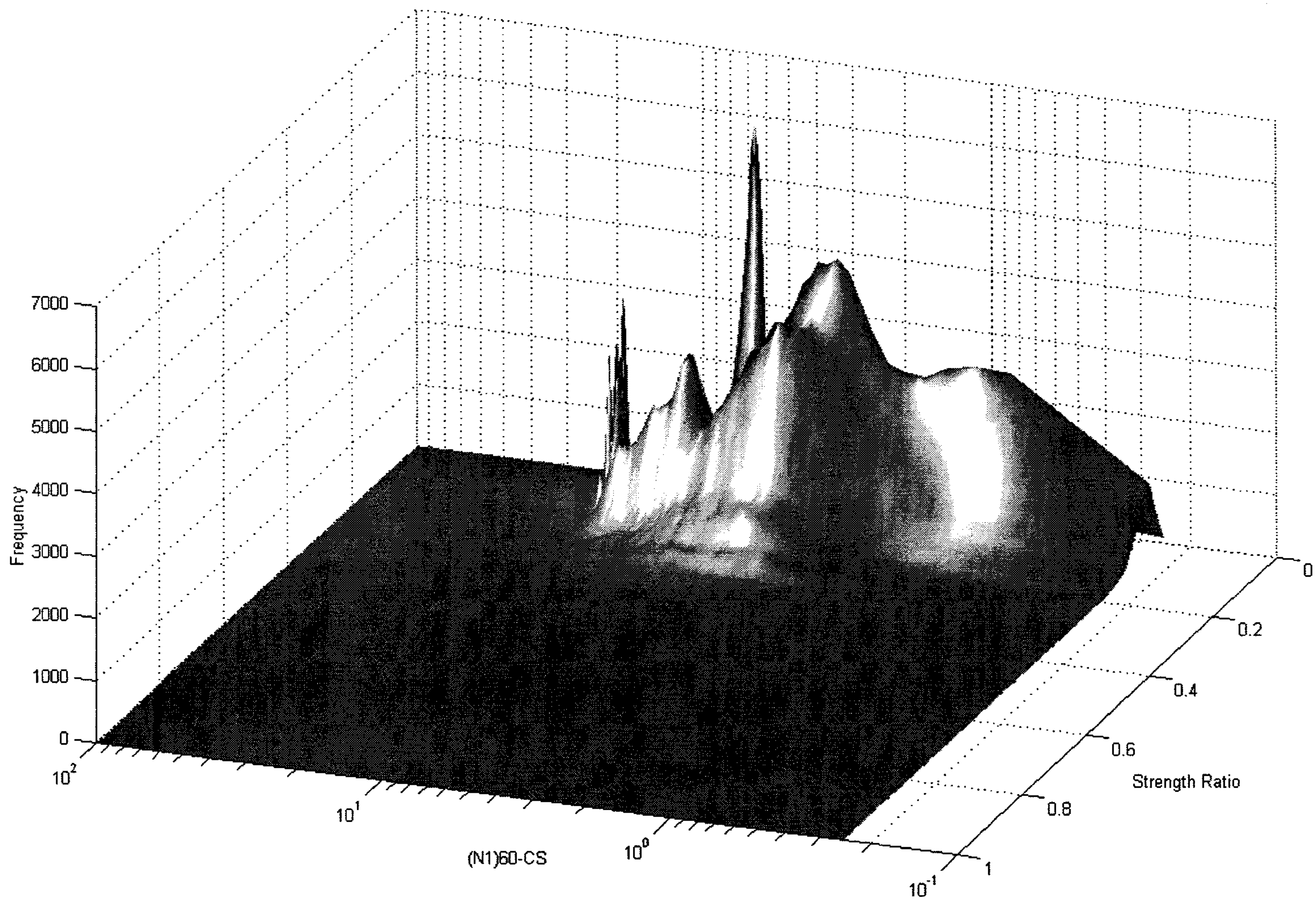

Figure 6-63 Three-dimensional histogram of $\overline{S}_r/\overline{\sigma}'_{vo}$ versus $(\overline{N}_1)_{60\text{-CS}}$ of the database for current study.

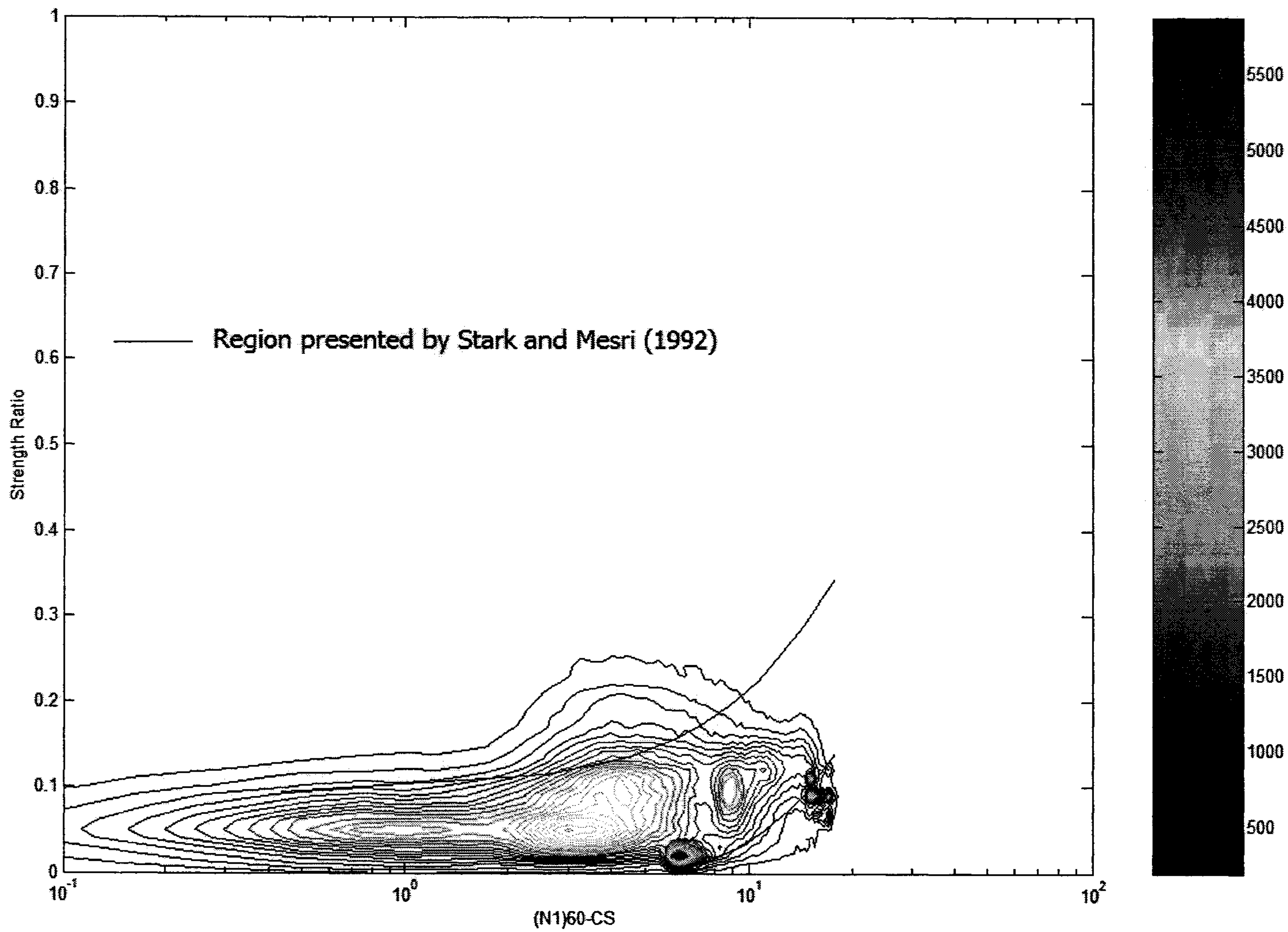

Figure 6-64 Contour plot of $\overline{S}_r/\overline{\sigma}'_{vo}$ versus $(\overline{N}_1)_{60\text{-CS}}$ of the database for current study.

Chapter 7

Residual Strength Prediction Model

7.1 INTRODUCTION

Geotechnical engineers are frequently faced with the problem of predicting the residual strength of a liquefied soil given some measure of penetration resistance such as $(N_1)_{60}$. Given the scarcity of available case history data, and the inconsistent levels of detail with which the case histories have been investigated and documented, it is clear that precise predictions of residual strength are not possible. Therefore, this study has focused on the development of procedures for quantifying and estimating the uncertainty in case history-based residual strength predictions.

Development of predictive models for residual strength involve three primary tasks: (1) identification of the proper form of the predictive model, (2) assembly of the data against which the predictive model is to be calibrated, and (3) calibration of the model. The manner in which these three tasks were accomplished in this research is described in the remainder of this chapter.

A total of four different predictive models have been developed. Two methods of residual strength estimation, the classical S_r vs. $(N_1)_{60}$ approach made popular by Seed (1987) and Seed and Harder (1990) and the normalized strength approach (Stark and Mesri, 1992), have been considered. In addition, two different case history weighting schemes have been used – one in which all case histories are weighted equally, and one in which the data from different case histories are weighted according to their "quality."

7.2 FORM OF THE PREDICTIVE MODEL

It would be possible to fit any number of arbitrary mathematical functions to the data produced by the Monte Carlo back-calculation analyses, and some of those functions would likely produce a good mathematical match to the available data. When data results from some physical process, however, the physics of that process will control the relationship between the predicted quantity and the variables used to predict it. A predictive relationship that is based on the physics of the process being modeled has the advantage of producing more realistic behavior in regions of sparse data and of doing so with a smaller number of calibration parameters than an arbitrary mathematical function.

7.2.1 Classical Residual Strength Model

Fundamental aspects of soil mechanics can be used to gain insight into the basic form of the relationship between S_r and $(N_1)_{60}$. Since an element of soil mobilizes a constant shearing resistance when it is neither dilating nor contracting, the residual strength occurs at the critical state. Bolton (1986) used the results of axisymmetric and plane strain laboratory tests on 17 types of sand to develop an expression for a relative dilatancy index, I_{RD}, of a sand as

$$I_{RD} = D_r\left(Q - \ln\frac{100p'}{p_a}\right) - R \tag{7.1}$$

where D_r = relative density, p' = mean effective confining pressure, p_a = atmospheric pressure, and Q and R are empirical parameters found to have values of approximately 10 and 1, respectively, for quartzitic sands. At the critical state, I_{RD} = 0, so

$$D_{r,ss}\left(Q - \ln\frac{100p'}{p_a}\right) = R \tag{7.2}$$

where $D_{r,ss}$ = relative density at the critical (steady) state. Rearranging, we can express the mean effective confining pressure as

$$p' = \frac{p_a \exp\left[Q - R/D_{r,ss}\right]}{100} \tag{7.3}$$

Now, letting $p' = \sigma'_1(1+2K_o)/3$ and $q' = \sigma'_1(1-K_a)/2$ the residual strength can be expressed as

$$S_r = \frac{1-K_a}{2} \cdot \frac{3}{1+2K_o} \cdot \frac{p_a \exp\left[Q - R/D_{r,ss}\right]}{100} \tag{7.4}$$

which allows prediction of residual strength as a function of relative density (for a given sand). Using the well-established graphical relationship of Holtz and Gibbs (1979), which can be approximated by the relationship

$$D_r \approx A N^B \tag{7.5}$$

where A = 0.0645 and B = 0.6636, the residual strength can be estimated as

$$S_r = \frac{1-K_a}{2} \cdot \frac{3}{1+2K_o} \cdot \frac{p_a}{100} \cdot \exp\left[Q - \frac{R}{A} N^{-B}\right] \tag{7.6}$$

For a given sand, the terms K_a, K_o, Q, and R will be constant, and the terms p_a, A, and B are always constants, so Equation 7.4 can be written as

$$S_r = a\exp\left(bN^c\right) \tag{7.7}$$

where

$$a = \frac{1-K_a}{2} \cdot \frac{3}{1+2K_o} \cdot \frac{p_a}{100} \cdot \exp[Q]$$

$$b = -R/A$$

$$c = -B$$

This expression will lead to a value of zero residual strength at zero SPT resistance, which is inconsistent with the general trend observed in previous back-calculation analyses (at least if the low SPT blowcount data is extrapolated backward to zero SPT resistance). To provide the opportunity for a calibrated predictive relationship to have a non-zero strength intercept, the basic form of the classical residual strength model was taken as

$$S_r = a\exp\left(bN^c\right) + d \tag{7.8}$$

where a - d are coefficients to be obtained by nonlinear regression.

7.2.2 Normalized Residual Strength Model

The normalized residual strength model cannot be justified by concepts as fundamental to soil mechanics as critical state concepts. Because critical state concepts imply that the shear strength of the soil at the critical (steady) state is only a function of void ratio, the basic concept of a normalized residual strength is flawed. If one assumes, however, that the critical (steady) state line is parallel to the one-dimensional consolidation curve, and that the friction angle of the soil is independent of the effective confining pressure, then the ratio of critical (steady) state strength to initial effective stress should be constant. The validity of this assumption was discussed in Section 4.4.2.1.

The available residual strength on a horizontal plane can be computed as

$$\frac{S_r}{\sigma'_{vo}} = tan\,\varphi' \tag{7.9}$$

where σ'_{vo} = initial vertical effective stress and φ' = effective stress friction angle of liquefied soil. The friction angle of sand soils, however, has been observed to vary with soil density and effective confining pressure. The graphical relationship of Schmertmann (1975) relates triaxial friction angle to SPT resistance and vertical effective stress. This relationship can be approximated (Kulhawy and Mayne, 1990) as

$$\phi' = \tan^{-1}\left[\frac{N}{12.2 + 20.3\dfrac{\sigma'_{vo}}{p_a}}\right]^{0.34} \tag{7.10}$$

Rearranging Equation (7.10) and substituting it into Equation (7.9) gives

$$\frac{S_r}{\sigma'_{vo}} = \left(12.2 + 20.3\,\sigma'_{vo}/p_a\right)^{-0.34} N^{0.34} \tag{7.11}$$

This equation implies that the normalized strength ratio is not a constant for a given sand, since the initial vertical effective confining pressure appears on the right side of the equation. However, the vertical effective stress on the right side is raised to a relatively small fractional power (doubling σ'_{vo} from 500 psf to 1000 psf, for example, causes a change of less than 10% in the right side of Equation (7.11)), and the average effective stresses in many of the case histories fall within a moderate range of values, so is reasonable to assume that the first portion of the right side of Equation (7.11) is constant. Then, allowing for the possibility of a strength ratio intercept, the basic form of the normalized residual strength model can be taken as

$$\frac{S_r}{\sigma'_{vo}} = aN^b + c \tag{7.12}$$

where $a - c$ are coefficients to be determined by nonlinear regression.

7.3 ASSEMBLY OF BACK-CALCULATION DATA

The residual strength prediction models were developed on the basis of the back-calculation data generated by the analyses described in Chapter 6. This data consisted of pairs of SPT resistance and residual strength values from Monte Carlo simulations of multiple case histories. Each case history was simulated using 50,000 Monte Carlo realizations, therefore, there are a total of 1.55 million data points for the 31 case histories described in Chapter 6.

As previously described, the back-calculation data was examined in two ways. First, all of the back-calculation data was equally weighted, an approach that implies that all of the case histories are equally valid. This approach is consistent with past investigations in which each of the back-calculated S_r - $(N_1)_{60\text{-CS}}$ and S_r/σ'_{vo} - $(N_1)_{60\text{-CS}}$ points are implicitly considered to be of equal significance.

In the second approach, the individual case histories were evaluated for their "quality," a process that produced weighting factors comprised of three elements. The first involved a necessarily qualitative evaluation that considered the level of detail with which the individual case histories were investigated and documented on a 1-5 scale. Case histories that were thoroughly investigated and well documented and that clearly involved flow sliding on a well-defined failure surface were given high ratings. Case histories that were not thoroughly investigated, were poorly documented, potentially involved lateral spreading or progressive failure, or involved significantly interbedded soils received lower ratings. The quality ratings were used to develop weighting factors (w_{case}) that ranged from 0.40 (for Q_{case} = 1) to 1.0 (for Q_{case} = 5). The next element was based on the number of residual strength evaluations that were used to compute the average residual strength. This element was intended to recognize the greater validity of multiple case history evaluations, i.e. to assign a higher weight for a case history for which four evaluations have produced consistent results than to one for which only one evaluation has been performed. In this approach, weighting factors (w_{number})of 0.7, 0.8. 0.9, and 1.0 were assigned to cases with one, two, three, and four or more residual strength evaluations, respectively. Finally, a weighting factor to account for the level of agreement between different investigators was introduced; this weighting factor is a function of the coefficient of variation of the reported residual strengths. This factor(w_{COV}), computed as 1-COV/2, is intended to give more weight to case histories for which all previous investigators obtained similar residual strengths. The quality ratings and weighting factors for each of the case histories are shown in Table 7-1. Note that the total weighting factors (w_{total}) range from 0.20 to 1.00, with a mean value of 0.46 and a coefficient of variation of 0.37; this wide range reflects the great variation in quality of the various secondary case histories.

7.4 CALIBRATION OF RESIDUAL STRENGTH PREDICTION MODELS

Predictive models were developed by nonlinear regression analyses on the data generated in the back-calculation analyses. The regression analyses were performed using the functional forms of the relationship between S_r (or S_r/σ'_{vo}) and $(N_1)_{60\text{-CS}}$ described in Section 7.2. Because these functions required the identification of only three or four constants, a relatively simple and straightforward grid search procedure was used to find the values of the constants that produced the best fit to the back-calculation data.

Prior to performing regression analyses, preliminary investigations of the basic form of the data were performed. These investigations were intended to gain insight into the results of the back-analyses that might prove useful in further data analysis.

7.4.1 Behavior of Mean Values

Each case history produced a set of data points that approximate the joint distribution of residual strength (or residual strength ratio) and SPT resistance. Insight into the results of the back-calculation analyses performed in this research can be obtained by comparing the mean values from these distributions with the data points determined by previous investigators.

Figure 7-1 presents the mean S_r - $(N_1)_{60\text{-CS}}$ data pairs obtained from this research along with the corresponding values obtained by Seed (1987), Seed and Harder (1990), Stark and Mesri (1992), and Olson (2001). The results are generally consistent and show a similar trend in the variation of S_r with $(N_1)_{60\text{-CS}}$. A few of the case histories show a noticeable difference in S_r and/or $(N_1)_{60\text{-CS}}$. The reasons for the most significant differences are briefly described in Table 7-2.

Figure 7-2 presents the mean S_r/σ'_{vo} - $(N_1)_{60\text{-CS}}$ data pairs obtained from this research along with the corresponding values obtained by Stark and Mesri (1992), Wride et al. (1999), and Olson (2001). The results are generally consistent and show a similar trend in the variation of S_r/σ'_{vo} with $(N_1)_{60\text{-CS}}$. A few of the case histories show a noticeable difference in S_r/σ'_{vo} and/or $(N_1)_{60\text{-CS}}$. The reasons for the most significant differences are briefly described in Table 7-3.

7.4.2 Variation of Mean with SPT Resistance and Homoscedasticity of Residuals

Both the residual strength and normalized residual strength ratio data shown in Figures 6-61 and 6-63 were divided into one-blowcount intervals within which the mean value and 16th and 84th percentile values were computed. The results, presented in Figures 7-3 and 7-4 for the unweighted data and Figures 7-5 and 7-6 for the weighted data, show the general variation of residual strength and residual strength ratio with $(N_1)_{60\text{-CS}}$.

The mean values show a trend of increasing residual strength with increasing SPT resistance. The trend appears to follow a form that could be reasonably represented by the basic form of Equation (7.8). The 16th and 84th percentile curves are, except at very low SPT resistances, approximately parallel to the mean value curve, indicating that the dispersion is nearly constant over a range of $(N_1)_{60\text{-CS}}$ values, i.e. that the data is homoscedastic (constant variance of residuals).

With respect to normalized residual strength, the mean values, however, does not show an obvious trend with the increasing of SPT resistance.

7.4.3 Nonlinear Regression Analyses

Calibration of the various residual strength prediction models was accomplished by nonlinear regression analysis. The regression analyses sought to identify the set of predictive model parameters (the coefficients $a - d$ in Equation (7.8) and $a - c$ in Equation (7.12)) that minimized an objective function that reflected the "error" of the predictions.

7.4.3.1 Definition of Objective Function

A least squares objective function was used to define the error that comprised the objective function. Such a function can be defined in different ways for the present study – as the sum of squared differences between predicted and observed residual strengths (i.e. the "vertical" error), as the sum of squared differences between predicted and observed SPT resistances (i.e. the "horizontal" error), or as some combination of the two. Consultation with the UW Statistics Department did not bring resolution of the question of which approach is optimal in time for the completion of this dissertation, so the objective function was taken as the sum of squared errors in residual strength prediction; this issue should be revisited to determine the practical benefits of an alternative objective function formulation.

The objective function was therefore defined as

$$F = \sum_{i=1}^{N} \sum_{j=1}^{M_i} w_i \left[S_j - \hat{S}(N_j) \right]^2 \qquad (7.13)$$

where N = number of case histories, M_i = number of data points in the i^{th} case history, w_i = weighting factor for the i^{th} case history, S_j = residual strength for the j^{th} point, $\hat{S}(N_j)$ = predicted residual strength based on SPT resistance of the j^{th} point, and N_j = $(N_1)_{60\text{-CS}}$ value of the j^{th} point. For the equally weighted cases, all w_i values were set equal to 1.0. For the weighted cases, the values of w_i were set to the weighting factor values described previously.

7.4.3.2 Optimization

Identification of the parameters that minimize the objective function involves multivariate optimization. The predictive models described in Section 7.2 are relatively simple, involving either 3 or 4 unknown coefficients. This simplifies the optimization process and allows the use of straightforward optimization schemes. For this research, a grid search procedure was used to identify the optimal model coefficients; such an approach is often less computationally efficient than other approaches, but the simplicity of the objective function and small number of unknown parameters made it a practical choice.

As it was discussed in Chapter 6, the values of SPT resistance was generated between 0 – 100 bpf. However, by observing the plots of Figures 61 to 64, the large SPT resistance is mainly contributed from the secondary cases. Those cases usually carry long '"tails", or large, SPT resistance, while the residual strength is relatively low. Only the cases of Lower San Fernando Dam and Fort Peck Dam provide a higher quality data to describe the trend of increasing residual strength with increasing SPT resistance. For those two cases, because of the high quality of available SPT data, the spread of SPT resistance only extend a limited amount beyond 18 bpf. To regress S_r - $(N_1)_{60\text{-CS}}$ and

S_r/σ'_{vo} - $(N_1)_{60\text{-CS}}$ pairs beyond 18 bpf will only involve the low quality data that produced by the high uncertainty of SPT resistance from the secondary cases. Because of this consideration, current study only uses the data that correspond to $(N_1)_{60\text{-CS}}$ less than 18 bpf. Table 7-4 shows the statistical parameters of all cases after removing S_r - $(N_1)_{60\text{-CS}}$ and S_r/σ'_{vo} - $(N_1)_{60\text{-CS}}$ pairs that have $(N_1)_{60\text{-CS}}$ value greater than 18 bpf.

The grid search was initiated from a set of model parameters that produced an optimal fit to the equally weighted mean values shown in for the residual strength and normalized residual strength. The initial grid was then obtained by computing objective function values for all combinations of the unknown parameters with values of 0.8, 0.9, 1.0, 1.1, and 1.2 times the initial parameter values. This involved 625 (=5^4) objective function evaluations for the residual strength and 125 (=5^3) evaluations for the normalized residual strength cases. The minimum objective function value was determined and the parameter values that produced it used as the starting point for a new search on a more refined grid. This procedure was repeated until a set of model parameters that minimized the objective function was identified.

7.4.3.3 Results of Optimization Processes

The results of the optimization processes produced four sets of model parameters – parameters with unweighted and weighted case histories for both residual strength and normalized residual strength ratio. The values of the parameters are listed in Table 7-5, and the relationships they predict are illustrated graphically in Figures 7-6 and 7-7.

Mean Values

The results of the optimization process for residual strength shows that curves of the form of Equation (7.8) provide a good fit to the Monte Carlo back-analysis data. Regression on the unweighted data produces a curve that is consistent with the curve for the weighted data at low SPT resistances, but lower than the curve for the weighted data at high SPT resistances. This is due primarily to the Nerlerk Berm case history, for which a low residual strength was back-calculated by some investigators in a sand with a moderately high SPT resistance. The significant disagreement in back-calculated residual strength for that case history produced a lower weighting factor, which allowed the regression based on weighted data to predict a higher residual strength at higher SPT resistances.

Residuals

In order to predict the likelihood of a particular value of residual strength (or residual strength ratio) being exceeded, it is necessary to examine the scatter in the data about the best fit regression curve. This scatter can be expressed in terms of the residuals of the regression analysis. The i^{th} residual in a set of x-y data is defined as

$$e_i = y_i - \hat{y}(x_i) \tag{7.14}$$

where y_i is the y-value of the i^{th} data point (either residual strength or normalized residual strength ratio in this case) and $\hat{y}(x_i)$ is the predicted value of y for the x-value of the i^{th} data point (SPT resistance in this case).

Figure 7-9 shows the distribution of residuals for the entire data set, i.e. for SPT resistances ranging up to 18 blows/ft. The residuals can be seen to be centered about zero, but distributed in a skewed manner. Although the variance is reasonably constant over the range of SPT resistances considered, the shapes of the residuals distributions vary somewhat, particularly at the highest blowcount levels. After unsuccessfully attempting to fit lognormal distributions to the residuals, beta distributions were fit to the normalized residuals histograms for SPT resistances of 2, 4, 6, 8, 10, 12, 14, 16, and 18. The beta distributions were expressed in the form

$$f\left(e_{Sr+1000}\right)=\frac{1}{\lambda}\left(e_{Sr+1000}-a\right)^{c}\left(b-e_{Sr+1000}\right)^{d} \tag{7.15}$$

where $e_{Sr+1000}$ is the value of the residual plus 1000 psf (which was required to produce a variable with all positive values, as required for a beta distribution), λ is a normalizing factor that produces a unit integral of the distribution over its full range, and *a-d* are model coefficients that define the range and shape of the distribution. The beta distributions determined to provide the best fit to the individual distributions are shown in Figure 7-10.

The beta distribution model parameters were then plotted as functions of SPT resistance and quadratic equations used to provide a smooth approximation of their variation with SPT resistance. These relationships were as follows:

$$a = -2.2186N^2 + 14.539N + 827.86 \tag{7.16a}$$

$$b = -6.6558N^2 + 127.28N + 1186.9 \tag{7.16b}$$

$$c = 0.0272N^2 - 0.3734N + 2.099 \tag{7.16c}$$

$$d = -0.041N^2 + 0.4591N + 6.5652 \tag{7.16d}$$

where $N = (N_1)_{60\text{-}cs}$. These expressions were then used to generate cumulative distribution functions for the residual, from which residual values at the 10^{th}, 20^{th}, … , 90^{th} percentile values were obtained.

7.4.4 Discussion

The results of the model calibration have some interesting implications with respect to the suitability of the classical and normalized approaches to the estimation of residual strength. The first section of this chapter presented derivations of the general form of the expected relationships between residual strength and SPT resistance, and between normalized residual strength ratio and SPT resistance. Notwithstanding a few mild assumptions, both of these derivations indicate the form of the respective equations that would be consistent with the geotechnical engineering profession's current understanding of the mechanics of liquefiable soil. The fact that the curve regressed on residual strength produced a much better fit to the case history data than the curved regressed on normalized residual strength ratio suggests that the classical approach, i.e. relating residual strength itself directly to penetration resistance, is more consistent with both the basic principles of soil mechanics and available case history data than is the normalized residual strength ratio approach.

The effects of uncertainty also have a systematic effect on the predictive relationship obtained by least squares regression. Because the form of the equation for residual strength is concave up, equal deviations above and below the mean value of SPT resistance produce a larger residual on the high side than on the low side of the mean. Therefore, a least squares objective function will tend to predict a residual strength value at the mean SPT resistance that is lower than the data suggests.

7.5 PREDICTIVE MODEL

The studies described in this dissertation have allowed development of a predictive model for residual strength from measured standard penetration resistance. The model allows not only prediction of the mean value of residual strength, but also prediction of the probability distribution of residual strength, conditional upon standard penetration resistance. In doing so, it allows an engineer the capability of selecting a residual strength value with an expected probability of being exceeded. While the determination of that probability level is the responsibility of the engineer, who must consider the consequences of a failure in his/her selection process, the capability of doing so is a very useful feature of the proposed model.

The model allows the mean value of residual strength to be expressed as

$$\bar{S}_r = 88\exp\left[0.076\left(\bar{N}_1\right)_{60-cs}^{1.122}\right] + 28.05 \tag{7.17}$$

The results of the analyses of residuals were then used to develop the curves shown in Figure 7-11.

These curves allow construction of a cumulative distribution function (CDF) for residual strength given some SPT resistance; the percentage values associated with the different residual strengths at the void ratio of interest represent the ordinates of the CDF. To give the engineer the ability to determine the probability that a particular residual strength will be exceeded (or not exceeded), which can be used to estimate the probability of failure for a particular slope. In a design or soil improvement situation, the residual strength that is consistent with a prescribed probability of failure can be determined and used in the design of the slope or of the hazard mitigation efforts.

7.6 PRACTICAL EXAMPLE

Consider the slope shown in Figure 7-12a, for which an extensive subsurface investigation has indicated the presence of a liquefiable zone within which corrected SPT resistances are normally distributed with a mean value of 10 and a standard deviation of 2. Limit equilibrium stability analyses show that the factor of safety of the slope is sensitive to the residual strength of the liquefied soil; Figure 7-12b shows the variation of factor of safety with residual strength. The engineer is faced with the problem of determining the factor of safety of the slope if liquefaction has occurred.

Using the recommendations of Seed and Harder (1990) with the mean SPT value, the engineer would conclude that the residual strength is somewhere between approximately 100 psf and 500 psf, which would yield factors of safety ranging from 0.83 to 1.08. In practice, many engineers use a residual strength corresponding to the lower third-point of the range prescribed by Seed and Harder – this residual strength of 233 psf would yield a factor of safety of 0.92.

Using the chart of Idriss (1998), which presents a curve closely approximated by the equation

$$S_r = 50e^{0.16N} \tag{7.17}$$

and the mean SPT value, the implied residual strength of 248 psf produces a factor of safety of 0.93. The chart, however, provides no indication of the reliability of that estimate.

Using the recommendations of Olson and Stark (2002), the residual strength varies with initial vertical effective stress. For the slope shown in Figure 7-12a and the mean SPT resistance value, the indicated residual strengths result in a factor of safety of 0.94. Again, there is no indication of how reliable this value is.

Finally, using the residual strength model developed in this research, Equation (7.17), with the mean SPT resistance, one directly obtains the distribution of residual strength shown in Figure 7.-13a, which yields the distribution of factor of safety shown in Figure 7-13b. The mean value of residual strength from this distribution is 288 psf, and the mean value of the factor of safety is 0.95. The distribution also shows an 80% probability that $FS < 1.0$.

If we then account for the uncertainty in the SPT resistance, the probability that the residual strength exceeds some particular value, S_r^*, is given by

$$P\left[S_r > S_r^*\right] = \int G[S_r \mid N] \, df_N(N) \tag{7.18}$$

where G[.] is the complementary conditional cumulative distribution for residual strength given corrected SPT resistance and $f_N(N)$ is the probability density function for corrected SPT resistance. Integrating numerically, the probability can be computed as

$$P\left[S_r > S_r^*\right] = \sum P\left[S_r > S_r^* \mid N = N_i\right] P\left[N = N_i\right] \tag{7.19}$$

The results of these analyses show that the proposed residual strength prediction model allows an engineer to express the residual strength, and its implications on stability, in a manner that other approaches are unable to. With this model, probabilities of various residual strength values can be computed, and used to compute probabilities of various factor of safety values. This, in turn, allows evaluation of the probability of failure for an existing slope, or design of a new slope to achieve a desired probability of failure.

Case	Q_{case}	w_{case}	w_{number}	w_{COV}	w_{total}
Asele Road	3	0.70	0.80	0.35	0.20
Calaveras Dam	2	0.55	1.00	1.00	0.55
Chonan Middle School	4	0.85	0.90	0.96	0.74
El Cobre Tailings Dam	4	0.85	0.70	1.00	0.60
Fort Peck Dam	4	0.85	1.00	1.00	0.85
Hachiro-Gata Roadway	2	0.55	1.00	1.00	0.55
Helsinki Harbor	2	0.55	0.70	1.00	0.39
Hokkaido Tailings	2	0.55	0.80	0.71	0.31
Kawagishi-cho Building	2	0.55	0.90	1.00	0.50
Koda Numa Embankment	2	0.55	1.00	0.79	0.44
Lake Ackerman Roadway	5	1.00	1.00	1.00	1.00
La Marquesa Downstream	4	0.85	1.00	0.85	0.72
La Marquesa Upstream	4	0.85	1.00	0.90	0.76
La Palma Dam	4	0.85	1.00	0.94	0.80
Lake Merced Bank	2	0.55	1.00	0.72	0.39
Lower San Fernando Dam	5	1.00	1.00	1.00	1.00
Metoki Road	2	0.55	0.70	1.00	0.39
Mochi Koshi Tailings Dam 1	3	0.70	0.90	0.55	0.34
Mochi Koshi Tainilgs Dam 2	3	0.70	1.00	0.96	0.67
Nalbland Railway	3	0.70	0.80	0.91	0.51
Nerlerk Berm	3	0.70	1.00	0.58	0.41
Route 272 Roadway	3	0.70	1.00	1.00	0.70
Sheffield Dam	2	0.55	1.00	0.66	0.37
Shibeca-cho Embankment	3	0.70	1.00	1.00	0.70
Snow River Bridge Fill	2	0.55	0.90	1.00	0.50
Solfatara Canal Dike	2	0.55	1.00	0.76	0.42
Soviet Tajik – May 1 Slide	1	0.40	0.80	0.70	0.22
Tar Island Dike	2	0.55	0.90	0.64	0.32
Uetsu-Line Railway	2	0.55	1.00	1.00	0.55
Wachusett Dam	5	1.00	1.00	1.00	1.00
Zeeland	2	0.55	0.70	1.00	0.39

Table 7-1 Summary of cases history quality factors.

Case History	Difference	Explanation
Fort Peck Dam	SPT Resistance Residual Strength	Other studies did not indicate the sources that the SPT values were obtained from. The SPT values of this study are gathered from the boring log that penetrated the liquefied zone. The difference of residual strength can be caused by the configuration of geometry. For this study, this difference also involves the uncertainty of ZIF.
Lower San Fernando Dam	Residual Strength	The progressive-type failure causes high uncertainty on evaluation of kinetic effect. A large difference of back-calculated residual strength exists when the pre- or post geometry is used. This increases the difficulty to make a estimation by using the conventional back-calculation process.
Lake Ackerman	Residual Strength	The difference between current study and Stark and Mesri (1990) is unknown, because no detailed information was provided by Stark and Mesri (1990).
Shibecha-Cho Embankment	SPT Resistance Residual Strength	The Swedish sounding is the only available in-situ testing data. The difference can be the method used to convert the Swedish sounding data to SPT resistance. Difference of residual is contributed from the difference assigned soil density.

Table 7-2 Descriptions of difference of primary case histories in back-calculated S_r between the current research to previous investigations.

Case History	Difference	Explanation
Calaveras Dam	NRSR	This is a relatively poor-documented case. Soil properties (e.g. soil density) may be the contribution of this difference.
Fort Peck Dam	SPT Resistance	Same as it was described in Table 7-2
Hachiro-Gata Road Embankment	NRSR	Difference is caused by using different density.
Shibecha-Cho Embankment	NRSR	Difference is caused by using different density.

Table 7-3 Descriptions of difference of primary case histories in back-calculated S_r/σ'_{vo} between the current research to previous investigations.

	$(\overline{N}_1)_{60\text{-CS}}$ (bpf)		$\overline{S}_r$ (psf)		$\overline{S}_r/\overline{\sigma}'_{vo}$	
	Mean	**STD**	**Mean**	**STD**	**Mean**	**STD**
Primary Case History						
Calaveras Dam	7.6	3.6	632.7	189.5	0.099	0.3078
Fort Peck Dam	15.8	0.9	671.5	130.1	0.091	0.1666
Hachiro-Gata Road Embankment	5.7	2.6	65.0	24.7	0.164	0.0641
Lake Ackerman Roadway	4.8	1.2	98.0	20.4	0.114	0.2245
Lower San Fernando Dam	14.5	1.1	484.7	11010	0.133	0.0287
Route 272 at Higashiarekinai	8.5	2.4	130.5	33.5	0.125	0.0295
Shibecha-Cho Embankment	5.6	2.1	208.9	38.6	0.200	0.0312
Uetsu-Line Railway Embankment	2.6	2.8	43.5	24.7	0.048	0.0264
Wachusett Dam	7.2	1.9	348	75.4	0.136	0.0284
Secondary Case History						
Asele Road	7.6	3.8	163.7	54.5	0.104	0.3446
Chonan Middle School	5.2	3.4	178.7	32.0	0.091	0.0163
El Cobre Tailings Dam	6.8	0.9	195.2	64.8	0.020	0.0066
Helsinki Harbor	4.3	3.8	52.4	19.0	0.067	0.0843
Hokkaido Tailings	5.1	1.4	250.6	71.9	0.074	0.0212
Kawagishi-Cho Building	4.3	1.2	123.5	56.7	0.089	0.0411
Koda Numa Embankment	3.2	1.2	48.0	15.9	0.045	0.0265
La Marquesa Downstream	9.7	2.7	343.5	113.8	0.186	0.0614
La Marquesa Upstream	6.4	2.5	185.2	82.2	0.110	0.0490
La Palma Dam	4.2	1.8	193.3	86.3	0.123	0.0547
Lake Merced Bank	4.3	3.8	139.5	41.4	0.106	0.0316
Metoki Road	2.0	1.5	116.8	53.7	0.044	0.0204
Mochi Koshi Tailings Dam 1	8.9	0.6	158.9	47.7	0.091	0.0272
Mochi Koshi Tailings Dam 2	10.0	1.3	233.6	78.0	0.081	0.2694
Nalbland Railway Embankment	5.5	3.1	139.9	40.2	0.109	0.0311
Nerlerk Berm	11.5	1.6	178.5	31.8	0.124	0.0222
Sheffield Dam	6.9	3.1	99.8	29.8	0.043	0.1750
Snow River Bridge Fill	6.3	3.7	50.0	16.5	0.025	0.3303
Solfatara Canal Dike	3.8	3.6	77.1	25.6	0.063	0.0214
Soviet Tajik - May 1 Slide	7.8	3.6	334.2	110.9	0.082	0.0274
Tar Island Dyke	6.2	3.9	364.2	115.4	0.058	0.0193
Zeeland	7.5	3.6	226.1	75.1	0.048	0.0160

Table 7-4 Summary of mean and standard deviation (STD) values of $(\overline{N}_1)_{60\text{-CS}}$, $\overline{S}_r$, and $\overline{S}_r/\overline{\sigma}'_{vo}$ of all case histories, after removing data that have $(\overline{N}_1)_{60\text{-CS}}$ value greater than 18 bpf.

Case	S_r parameters				S_r/σ'_{vo} parameters		
	a	b	c	d	a	b	c
Unweighted	81.634	0.09	1.04	36.3	0.54	0.0257	-0.47
Weighted	88.0	0.076	1.122	28.05	0.71442	0.01779	-0.635

Table 7-5 Summary of results of optimization processes – parameters defined in Equations (7.8) and (7.12).

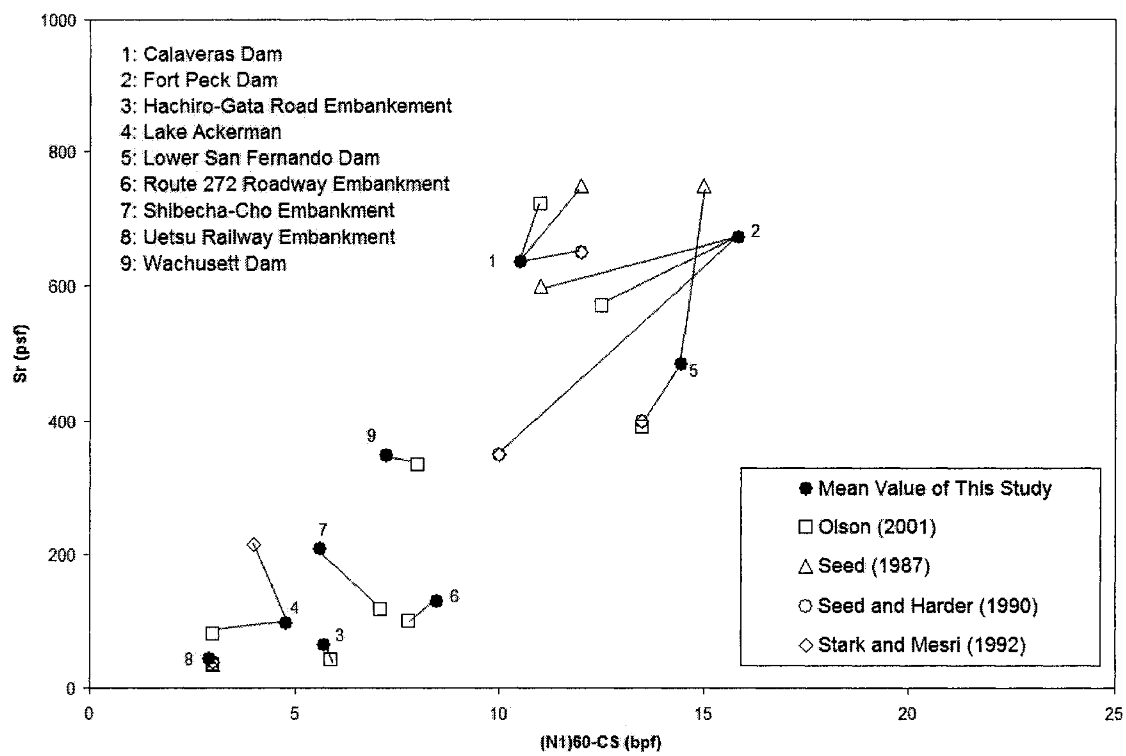

Figure 7-1 Comparison of mean S_r - $(N_1)_{60\text{-CS}}$ data pairs of primary cases histories with corresponding values obtained by other researcher.

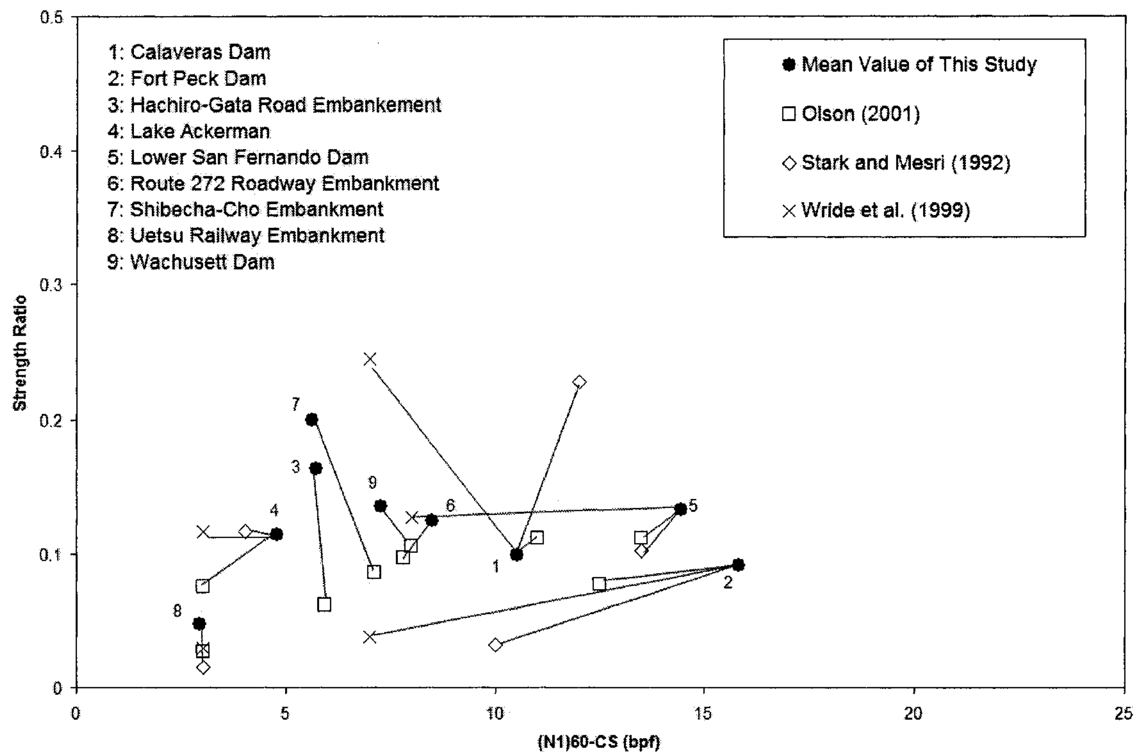

Figure 7-2 Comparison of mean S_r/σ'_{vo} - $(N_1)_{60\text{-CS}}$ data pairs of primary cases histories with corresponding values obtained by other researcher.

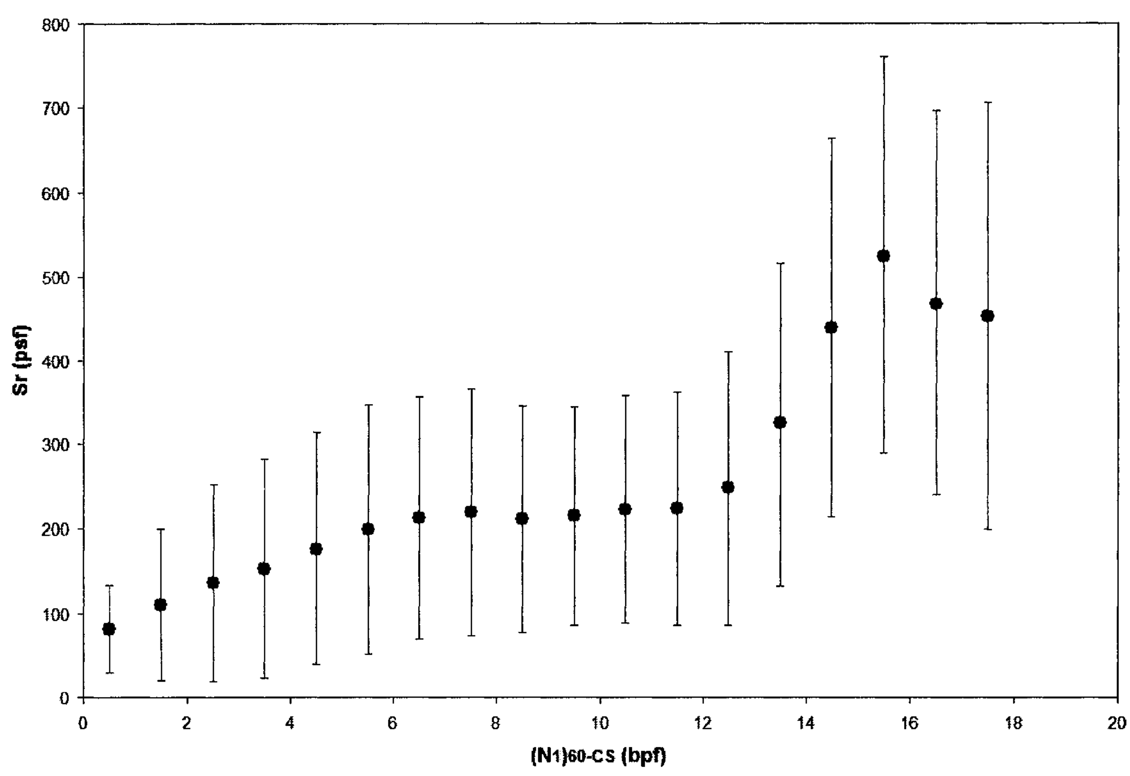

Figure 7-3 Unweighted data shown residual strength at the mean value and 16th and 84th percentile values.

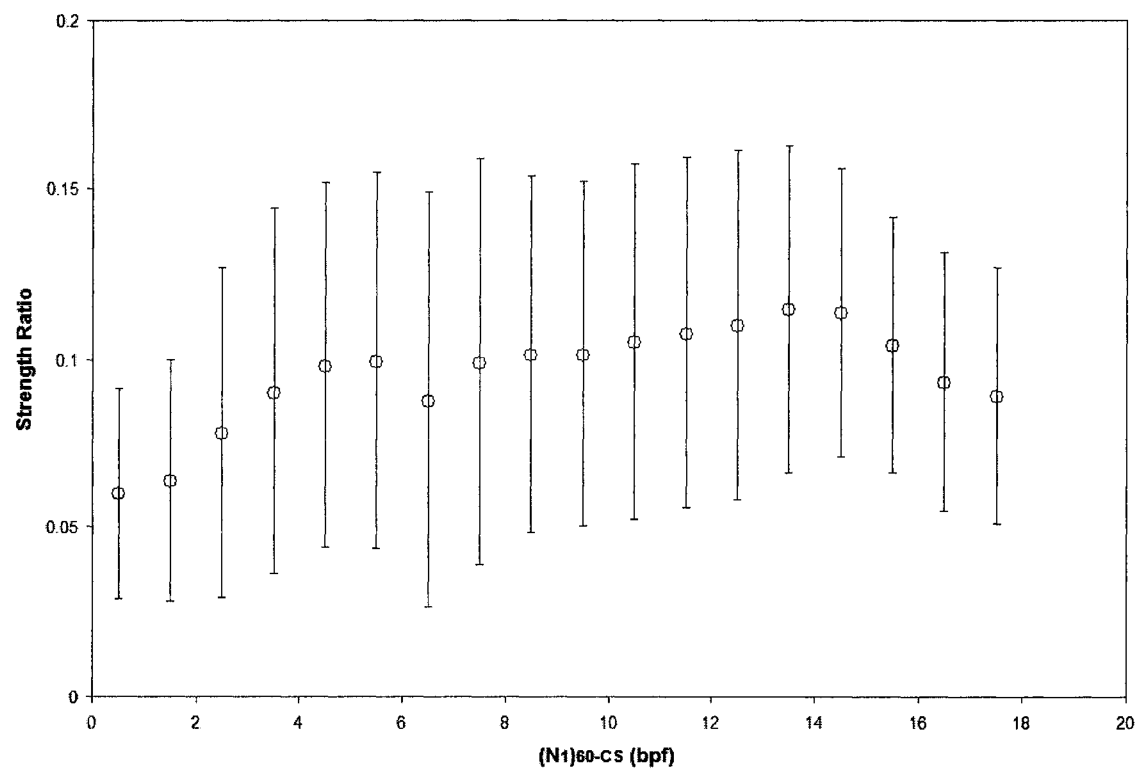

Figure 7-4 Unweighted data shown NRSR at the mean value and 16th and 84th percentile values.

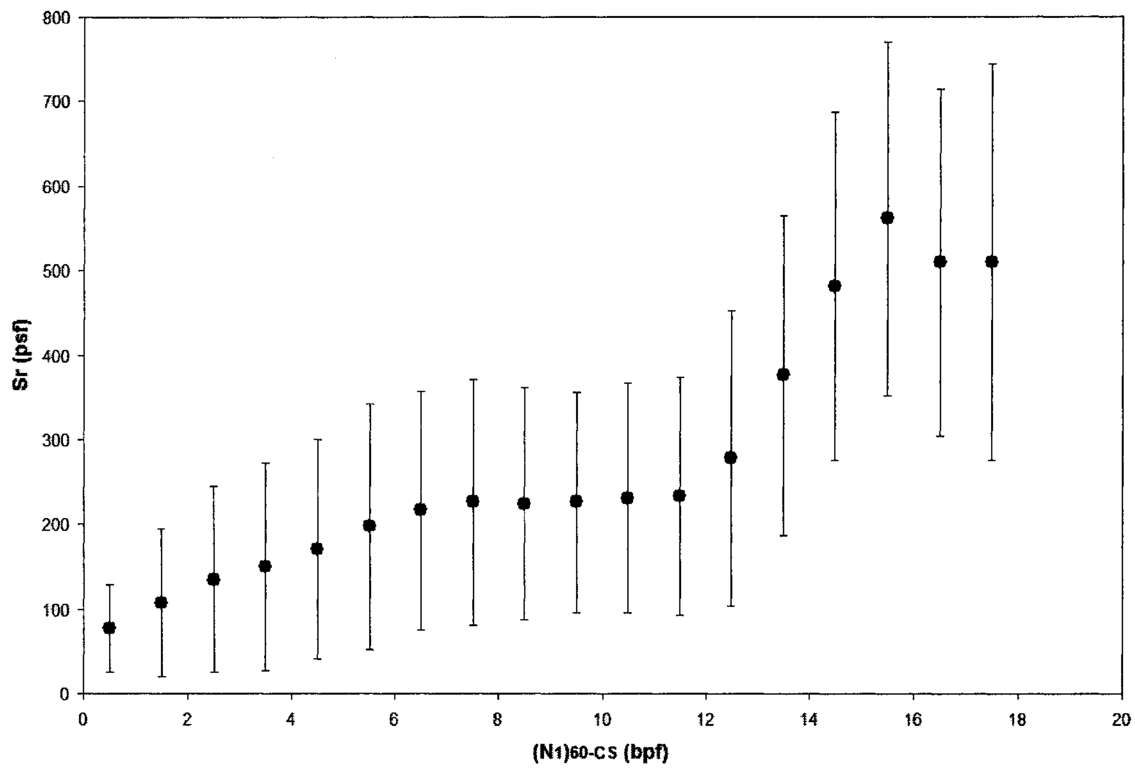

Figure 7-5 Weighted data shown residual strength at the mean value and 16th and 84th percentile values.

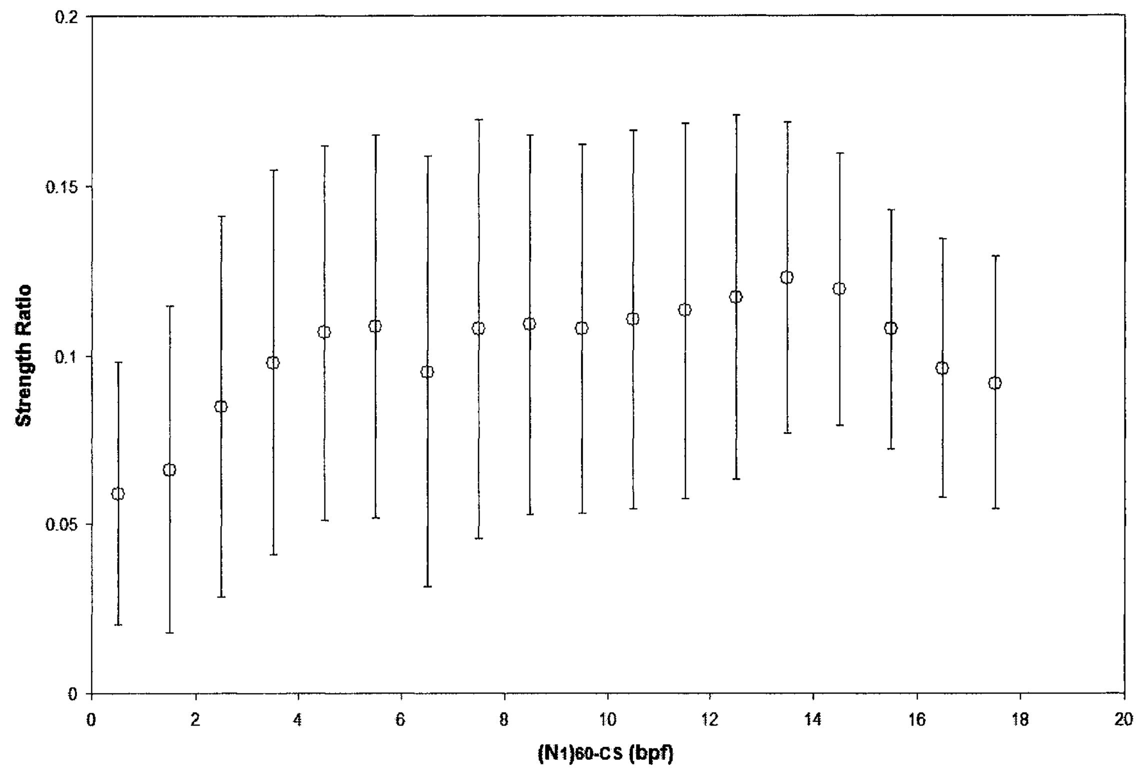

Figure 7-6 Weighted data shown NRSR at the mean value and 16th and 84th percentile values.

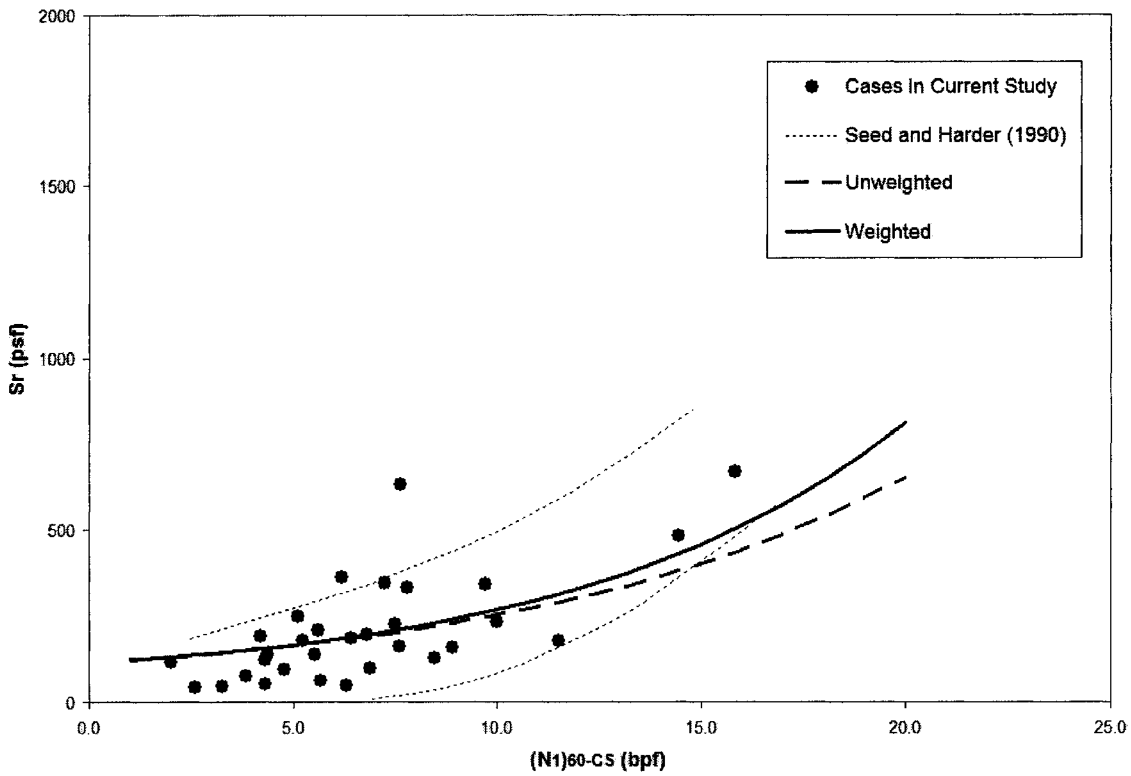

Figure 7-7 Predication of relationship between S_r and $(N_1)_{60\text{-CS}}$.

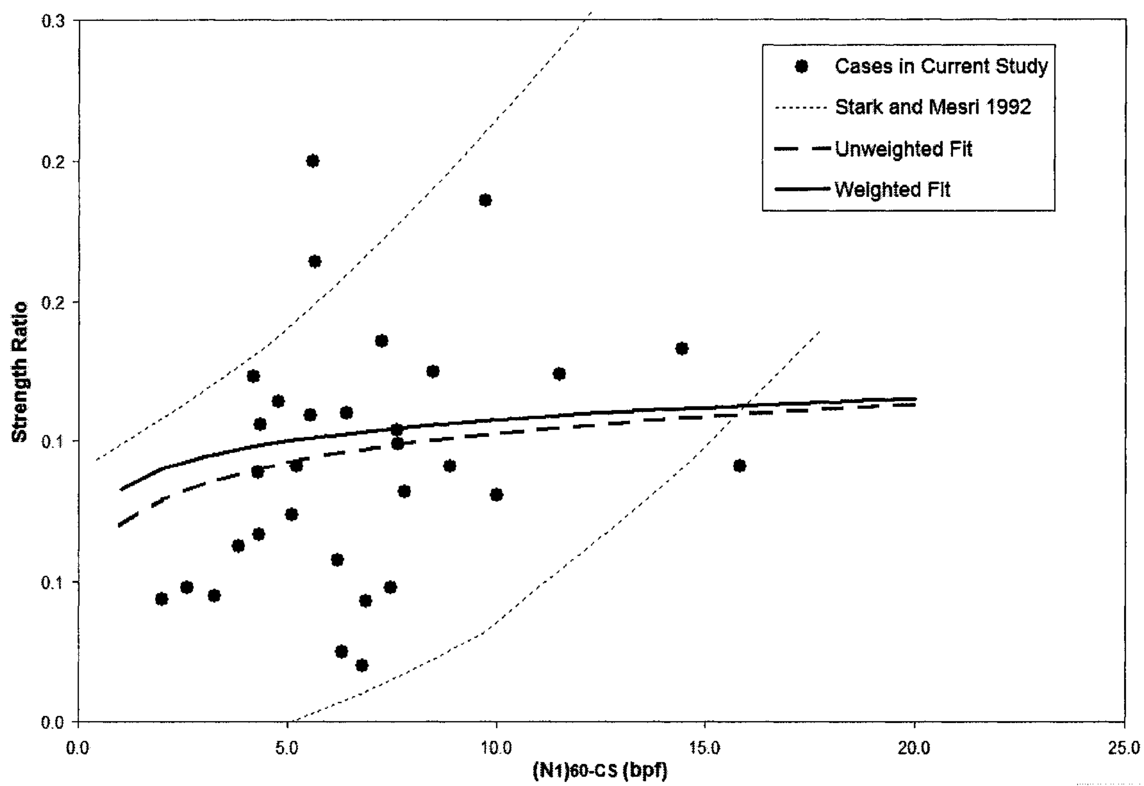

Figure 7-8 Predication of relationship between S_r/σ'_{vo} and $(N_1)_{60\text{-CS}}$.

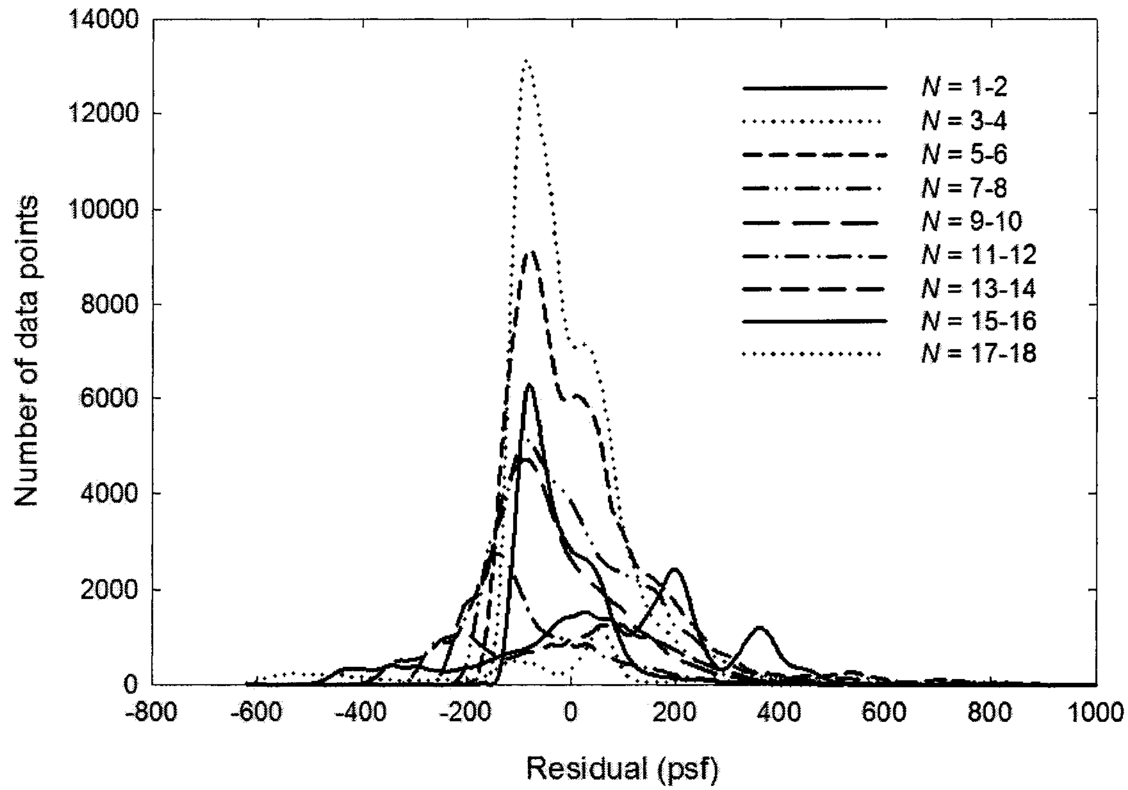

Figure 7-9 Plot of residuals from regression analyses.

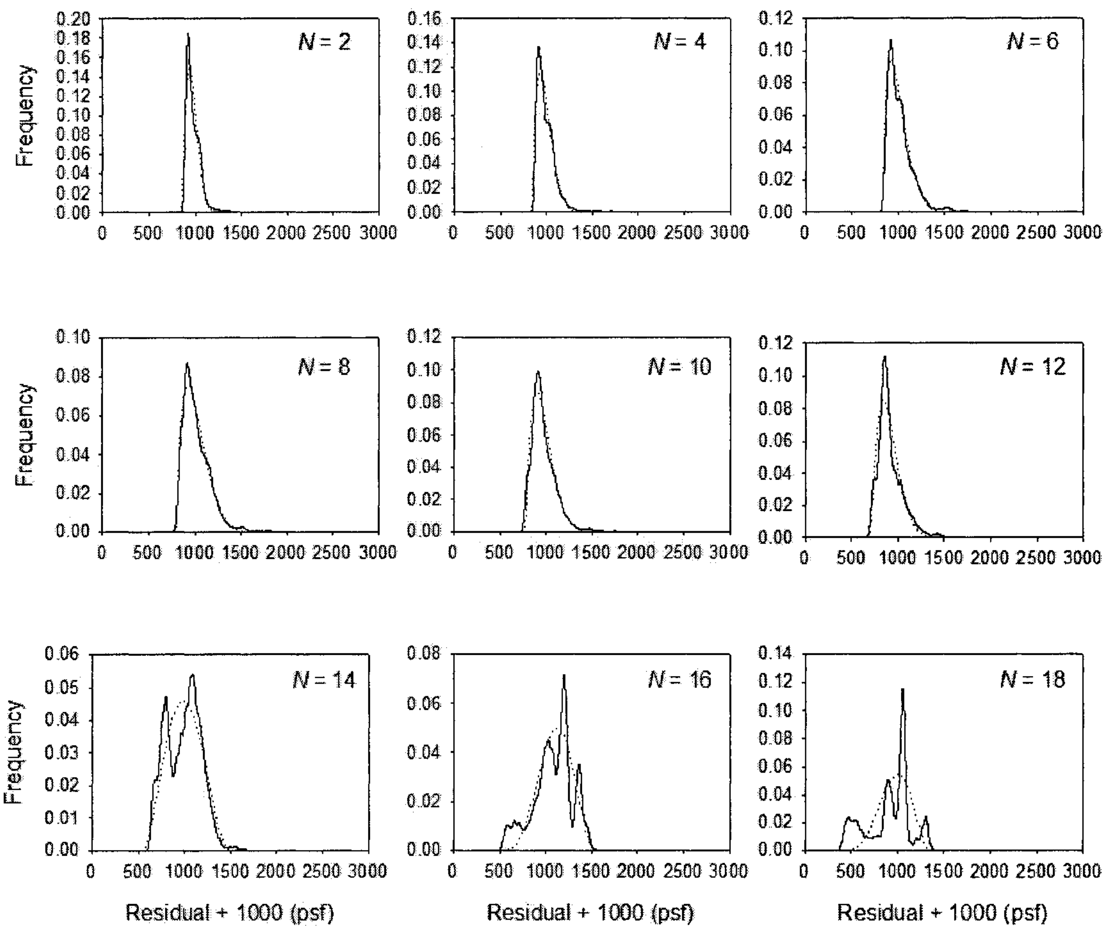

Figure 7-10 Fitted data distributions to the e+1000 data from the regression analyses (solid curve represents normalized histogram from back-calculation data, dashed line represents best fit beta distribution).

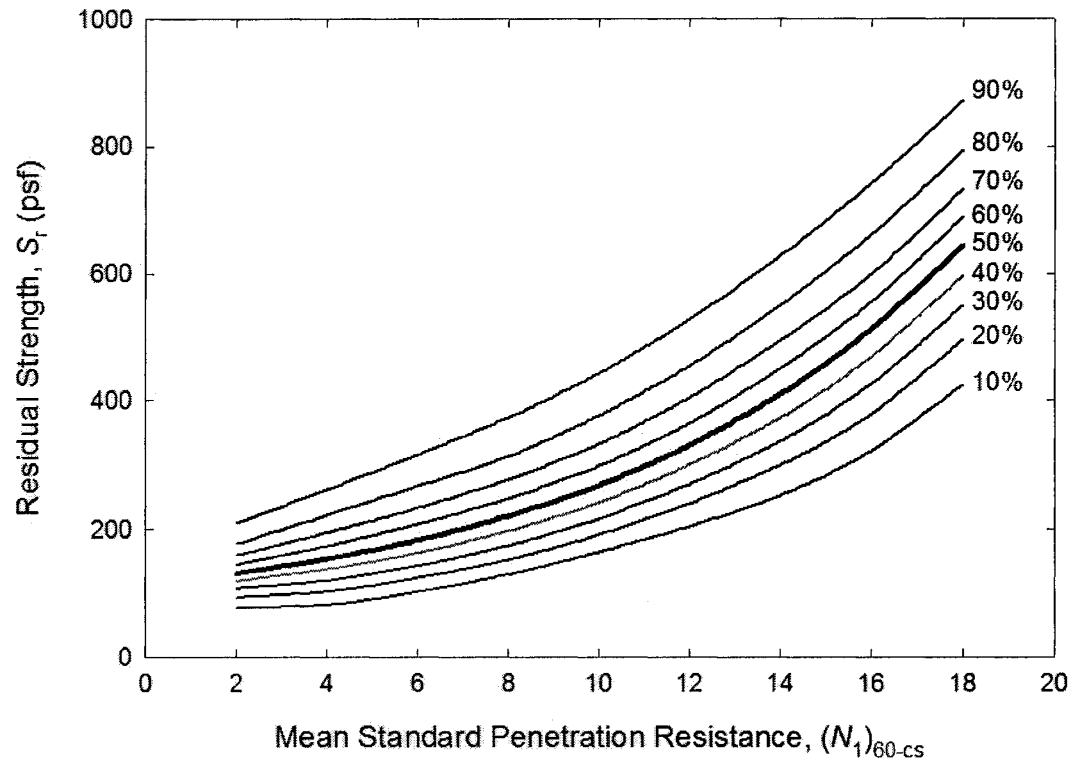

Figure 7-11 Curves indicating percent probability that actual residual strength will be lower than value given by curve.

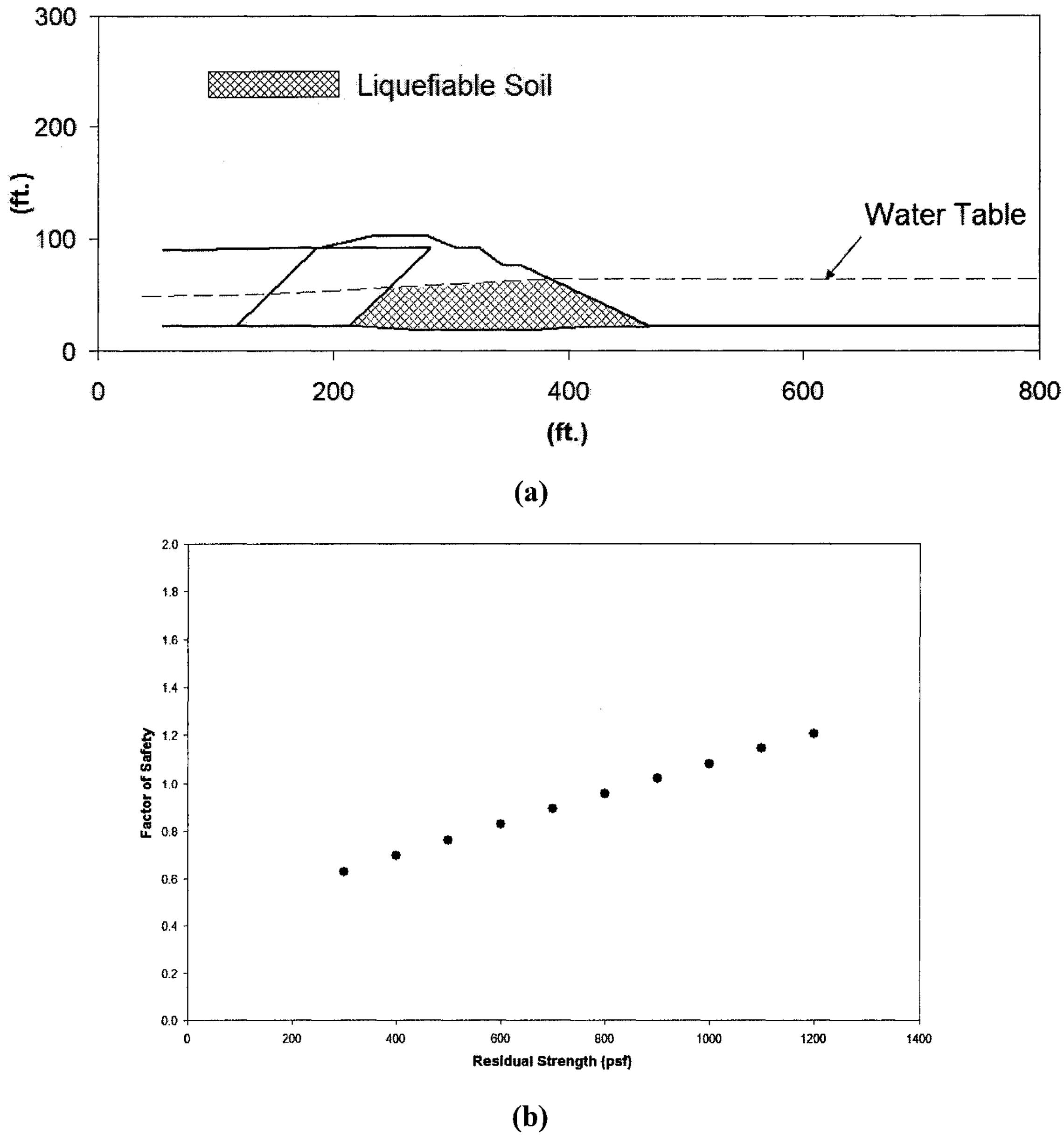

Figure 7-12 Example slope for practical evaluation of residual strength of liquefied soil, (a) geometry of slope and (b) results of limit equilibrium stability analyses.

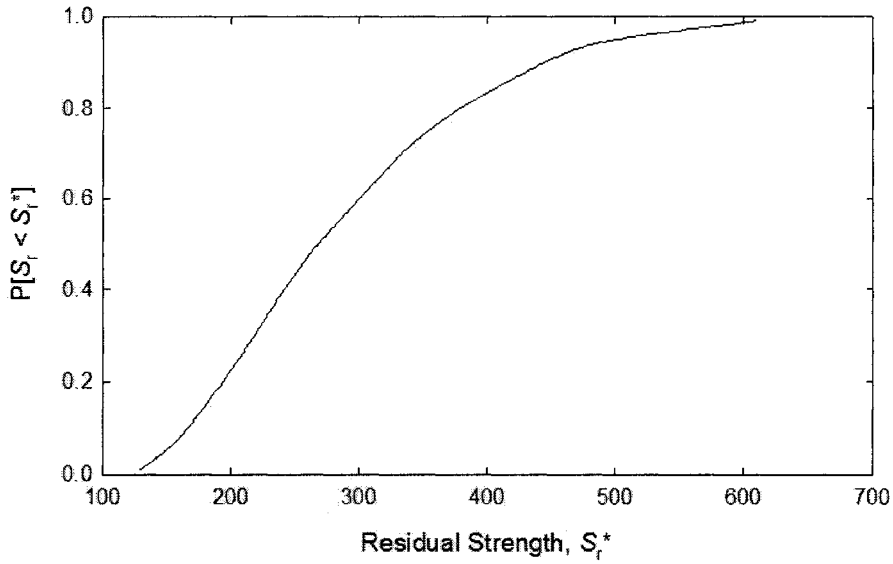

(a)

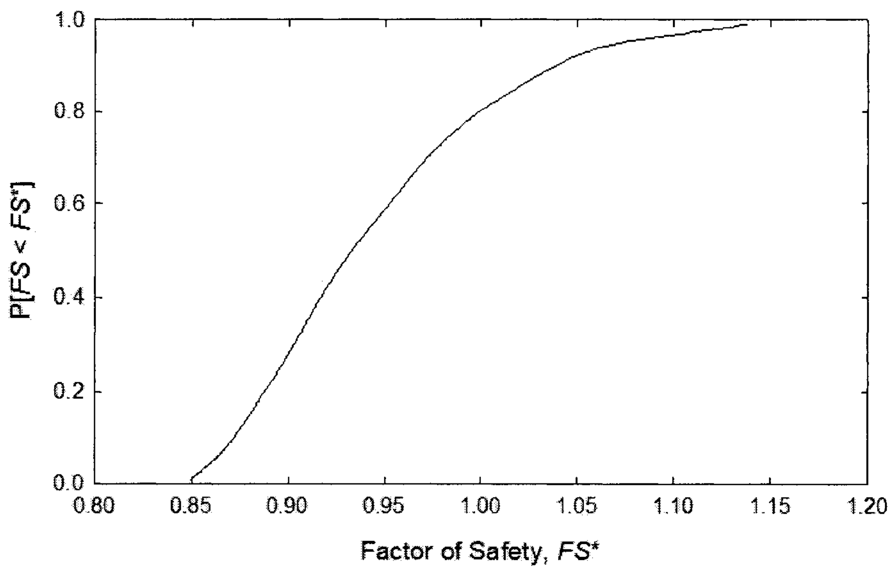

(b)

Figure 7-13 Predicted (a) residual strength distribution and (b) factor of safety for the example slope.

Chapter 8

Summary, Conclusions, and Recommendations for Further Research

Soil liquefaction has been recognized as an important seismic hazard for many years, but only in the last 40 years has it been investigated in great detail. During that 40 years, however, the geotechnical engineering profession's understanding of liquefaction has increased greatly. Geotechnical engineers now have practical tools to predict the occurrence of liquefaction, and past experience has shown that these tools nearly always predict liquefaction at sites where liquefaction is observed. On the other hand, these tools frequently predict liquefaction to occur at sites where it is not actually observed during earthquakes; this bias toward overconservative prediction of liquefaction is well recognized, and probably appropriate for design purposes.

An important aspect of liquefaction that additional attention is required for is the prediction of the effects of liquefaction. Given that liquefaction occurs, a geotechnical engineer needs to be able to predict what the effects of that liquefaction will be. Research on several aspects of this problem has been performed, and further research is currently underway. Prediction of liquefaction effects is one of the most important current topics in geotechnical earthquake engineering.

The potential effect of liquefaction that has proven to be most difficult to deal with is the evaluation of the residual strength of liquefied soil. Evaluation of the residual strength is required for evaluation of the potential for flow slide instability following soil liquefaction. Flow slides have caused tremendous damage in past earthquakes, and the potential for their occurrence depends directly on the residual strength of the liquefied soil. This pressing need provided the motivation for this research.

8.1 SUMMARY

Chapter 2 presents an overview of soil liquefaction. It starts by showing some case studies of earthquake-induced liquefaction failures. These cases give a good picture of how soil liquefaction causes some devastated hazards and produce great damages. To realize the mechanism of soil liquefaction, the following sections explain the terminology and evaluation of susceptibility for soil liquefaction. The main focus is to illustrate the frame work in theory of how the soils react with water in laboratory and field conditions, thus causing liquefaction phenomena. The last section of this chapter describes several typical types of failure that are caused by soil liquefaction

Chapter 3 describes the behavior of liquefied soil at the micro- and macro-scale levels. Because liquefaction-susceptible material is usually granular (sandy), the soil matrix comprising liquefiable soil and other materials can be treated as a particulate assembly. During soil liquefaction, at the micro-scale level, the particulate behavior within an assembly is introduced according to the inter-particle and particle-fluid interactions. At the macro-scale level, the behavior of debris-flow material is presented as an extreme case of soil liquefaction. The flow behavior is examined according to the strong agitation within the particle-fluid mixture.

Chapter 4 explains various approaches to evaluate the residual strength of liquefied soil. This chapter begins with a review of flow-slide failures. Several possible soil behaviors were introduced. Unlike the element test in laboratory, the flow-slide failure, which usually involves a large amount of mass, has more complicated failure patterns. Those patterns usually are spatially varied among failure debris. The knowledge learned from studies of the particulate flow and the debris-flow failure helps to understand the failure mechanisms that cause the initiation and failure process of flow-slide failure. Numerous approaches to evaluate the residual strength have been proposed, and this chapter reviews the laboratory-based and field-based approaches for doing the evaluations.

Chapter 5 described a procedure that would allow consideration of the uncertainties in the input parameters to a case history-based residual strength evaluation, and provide insight into the effects of those uncertainties on the back-calculated residual strength. The procedure recognized potential uncertainties in geometric variables including the geometry of the slope at the point at which inertial effects are non-existent, the initial and final geometries, the position of the phreatic surface within the slope, and the position of the failure surface. It also recognized uncertainties in material properties including spatial variability effects in the liquefied soil. It used a procedure for estimation of uncertainty in SPT resistance that accounted for the number of SPT measurements in the liquefied soil, a variable that ranges from zero to a relatively high number for the various flow slide case histories available for residual strength back-calculation. Finally, a procedure for estimating the effects of hydroplaning on the back-calculated residual strength of slopes that slid into bodies of water was developed. Chapter 5 then described a Monte Carlo simulation procedure that allowed representation of the effects of the various uncertainties on the back-calculated residual strength of liquefied soil. The Monte Carlo simulations allowed the results of a back-calculation to be expressed as a "cloud" of data points with dispersion in both SPT resistance and residual strength, rather than as a single, deterministic point as expressed by previous investigators.

The application of the procedure developed in Chapter 5 was described, with the Wachusett Dam flow-slide used as a detailed example, in Chapter 6. The methodology was then applied to 8 additional case histories for which sufficient information to justify detailed analyses was available. These primary case histories were analyzed in detail with full accounting for uncertainties, inertial effects, and other factors through Monte Carlo simulation. An additional set of case histories, termed secondary case histories, were insufficiently well documented to allow the type of detailed analyses applied to the primary case histories. Procedures for estimation of the uncertainties in the residual strength and normalized residual strength ratio, and in the SPT resistance, were developed and applied to the secondary case histories. The result of all of these analyses was a database of some 1,550,000 data points expressing the relationship between back-calculated residual strength and SPT resistance, and another database with the same number of points expressing the relationship between back-calculated normalized residual strength ratio and SPT resistance. The data in both cases was not uniformly distributed with respect to SPT resistance, but showed a general trend of increasing residual strength with increasing SPT resistance.

Chapter 7 describes the development of a predictive model for residual strength based on the results of the simulations described in Chapter 6. Derivations based on fundamental concepts of soil mechanics were used to identify the proper forms of the relationships between residual strength and SPT resistance, and between normalized residual strength ratio and SPT resistance. These derivations showed that, to be consistent with the basic principles of soil mechanics, a predictive model for residual strength should be an exponential function of SPT resistance, and that a model for normalized residual strength ratio should be a power function of SPT resistance. Both of these basic forms were modified by the addition of a constant term intended to act as an intercept (strength or strength ratio value at zero SPT resistance) if the data suggested that such a value was appropriate. In this sense, the functional forms of the predictive relationships could be thought of as vertically shifted exponential and power functions. The data was then compiled and weighted according to the perceived level of quality of the individual case histories; the intent of this step was to assign more weight to flow slides that were thoroughly investigated and well documented than to cases that were not. This was a major departure from past investigations which implicitly treated all case histories equally. Finally, the predictive models were calibrated against the back-calculation data, and the results for the two approaches to residual strength prediction compared. Finally, a simple example was used to illustrate how the results of the research can be used by practicing engineers.

8.2 CONCLUSIONS

The unique nature of the research described in this dissertation has led to a number of conclusions regarding the residual strength of liquefied soil and the development of procedures for its prediction. A careful review and interpretation of previous work on residual strength allows formation of some general conclusions regarding residual strength and the factors that influence it. The results of the research conducted in this investigation allow some additional conclusions to be formed. These conclusions are described in the following sections.

8.2.1 General Conclusions

1. The residual strength of liquefied soil is an extremely difficult property to measure physically because of difficulties in sampling, transporting, and sample preparation without densifying or otherwise damaging the structure of the soil, and because laboratory testing apparatuses are largely unable to mobilize residual strengths under accurately measurable stress and strain conditions.
2. Residual strength prediction procedures based on back-calculation of residual strength from reported case histories of actual flow slides represents the most reasonable approach to the estimation of residual strength at the present time.
3. A number of flow slide case histories have been reported in the literature, but the level of investigation and documentation associated with each varies widely. Some flow slides, such as the one in Lower San Fernando Dam, had millions of dollars spent on their investigation; others had only cursory investigations. The thoroughly investigated flow slides are typically very well documented with careful measurements of the parameters required for residual strength back-calculation; others have only sketches with little or no direct measurement of geometric conditions or material properties.
4. Because of the relatively small number of flow slides reported in the literature, all flow slides must be considered in a comprehensive investigation of residual strength. It is not necessary or advisable, however, to consider all as being of equal value. Thoroughly investigated and well documented flow slide case histories provide more useful information than flow slides that were not well investigated or documented.
5. The results of a back-calculation-based residual strength evaluation are sensitive to a number of soil/slope characteristics, and these characteristics are not always known with certainty. As a result, many of the inputs to a back-calculation analysis are uncertain, and therefore lead to uncertainty in the back-calculated

residual strength. To judge the effects of these uncertainties on the expected value and dispersion of residual strength about that expected value, uncertainty in the input parameters must be characterized and considered in the back-calculation process.

6. Inertial effects are very important for some case histories, and the results of a back-calculation process are sensitive to the manner in which inertial effects are handled. Past investigations have analyzed response based on pre-failure and post-failure geometries (in which inertial effects are not important because the slope is not moving) to obtain upper and lower bound estimates of residual strength. These investigations then used approximate procedures to estimate the most likely value of residual strength between the upper and lower bound estimates. In reality, a failing slope first accelerates and then decelerates on its way from it pre-failure geometry to its post-failure geometry. At some point, it is neither accelerating nor decelerating; at this point inertial effects are non-existent. This zero-inertia-geometry is the most appropriate geometry on which to base the residual strength back-calculation.

7. The position of the zero-inertia-geometry is uncertain because the available procedures for estimation of the dynamics (i.e. acceleration and deceleration) of a flow slide are very approximate. Because the back-calculated residual strength may be sensitive to the geometry that is analyzed, this uncertainty must be accounted for. Uncertainty in the pre- and post-failure geometries can be approximated by considering the coordinates that define the zero-inertia-geometry to be uncertain.

8. The position of the failure surface is often difficult to determine after a flow slide has occurred, hence it must also be considered to be uncertain. In some cases, failures occur on relatively well-defined surfaces, which is consistent with the assumptions of the limit equilibrium procedures used to back-calculate residual strength. In other cases, failure involves shearing that is distributed through a wide band or zone of soil, which introduces additional uncertainty into the position of the failure surface. Because the back-calculated residual strength is nearly always sensitive to the position of the failure surface, uncertainty in the position of the failure surface must be accounted for.

9. Some flow slides involve soil sliding into bodies of water, in which case the phenomenon of hydroplaning may cause the mobilized strength to be lower than it would have been in the absence of hydroplaning. Although hydroplaning is not a well understood phenomenon, neglecting its potential existence will introduce an overly conservative bias in the back-calculated residual strength. Procedures based on particulate flow mechanics can be used to develop a consistent and objective procedure for treating hydroplaning in the back-calculation process.

8.2.2 Additional Conclusions

1. Monte Carlo simulation procedures are well-suited for the propagation of uncertainties in input parameters through the back-calculation process. By assigning probability distributions to the uncertain input parameters and generating multiple realizations of the back-calculated residual strength, a joint distribution of residual strength and SPT resistance can be developed for a given flow slide case history. This distribution reflects the uncertainty in both parameters associated with the case history. Thoroughly investigated and well-documented case histories tend to have relatively narrow and compact distributions, and poorly investigated and documented case histories have highly dispersed distributions. The results of such analyses show very weak correlation between residual strength and SPT resistance for a given case history because it is only the correlation between SPT resistance and soil density that relates residual strength to back-calculated residual strength, and the dependence of residual strength on the density of the liquefied soil, again for a single case history, is quite weak.
2. Soil mechanics principles suggest that the residual strength should be an exponential function of SPT resistance, and that normalized residual strength ratio should be approximately a power function of SPT resistance. Functions of these types were calibrated against the Monte Carlo back-calculation data to find the values of the function parameters that provided the best least-squares fit to the data. The exponential form provided a good fit to the residual strength data, and the power function provided a relatively poor fit to the normalized residual strength ratio data. These results suggest that the classical residual strength model is more consistent with the basic principles of soil mechanics, as evidenced by actual flow slide behavior, than the normalized strength approach.
3. The residual strength of liquefied soil can be predicted as a function of corrected SPT resistance using the predictive relationship presented in this dissertation. The relationship allows prediction of the conditional probability distribution of residual strength given mean SPT resistance. This relationship can be propagated through a probabilistic analysis to express stability hazards in terms of a probability of failure instead of a simple single-valued factor of safety. The probability of failure can be used to estimate potential economic risk, or to determine the level of site improvement required to reduce the risk at an existing site to an acceptable value.

8.3 RECOMMENDATIONS FOR FURTHER RESEARCH

The research described in this dissertation provides a new approach to the estimation and of residual strength of liquefied soil. There are, however, additional elements that could extend and improve the work, and efforts toward their accomplishment are planned for the near future. The primary efforts that could be made include:

1. Adding correlation between SPT resistance and the unit weight of the liquefied soil – the effect on the back-calculated residual strength will be small; this change will essentially rotate the joint distributions in the counter-clockwise direction, but sensitivity analyses have indicated that the rotation will be very slight. Nevertheless, this would make the analyses more correct.
2. Investigate in more detail the anticipated distribution of SPT resistance – the assumption of lognormality provides the benefit of eliminating negative SPT resistances, but it introduces a skew to the distribution that produces a significant tail at high SPT values. The tails of some of the secondary case history distributions tend to reduce the predicted residual strength at high SPT resistances; the reasonableness of the influence of these case histories should be confirmed.
3. Extend the predictive model to include residual strength predictions on the basis of cone penetration test (CPT) tip resistances. The current results can, of course, be used with a suitable CPT-SPT conversion, but the availability of flow slide case histories with CPT data is increasing and will likely continue to increase in the future.
4. Develop procedures to account for the information provided by sites subjected to strong historical earthquake shaking at which flow sliding did not occur. There are undoubtedly many sites in areas of high seismic activity that have been subjected to earthquake shaking strong enough to initiate liquefaction, but which have not developed flow failures. These case histories could be analyzed to obtain the information they contain about minimum residual strength values; this information could be used to update the distributions developed in this research. A Bayesian approach could likely be developed to add this information.

List of References

ALARCON-GUZMAN, A., LEONARDS, G.A., AND CHAMEANU, J.L. (1988). "Undrained monotonic and cyclic strength of sands," *Journal of Geotechnical Engineering Division*, American Society of Civil Engineers, VOL. 114, No. 10, pp 1089-1109.

AMBRASEYS, N.N. (1988). "Engineering Seismology," *Earthquake Engineering and Structural Dynamics,* Vol. 17, pp 1-105.

AKAI, K., BRAY, J.D., BOULANGER, R.W, CHRISTIAN, J.T., FINN, W.D.L., HARDER, L.F., JR.,IDRISS, I.M., ISHIHARA, K., IWASAKI, J.K., MITCHELL, J.K., MORIWAKI, Y., NAKAGAWA, K., O'ROURKE, T.D., SEED, R.B., SITAR, N., SOGO, K., SOMERVILLE, P., TOWHATA, I., AND YOUD, T.L. (1995). *Geotechnical Reconnaissance of the Effects of the January 17, 1995, Hyogoken-Nanbu Earthquake, Japan,* Report No. UCB/EERC-95/01, University of California at Berkeley, California, 151pp.

AKSU, A.E. AND HISCOTT, R. (1992). "Shingled quaternary debris flow bases on the north-east Newfoundland slope," *Sedimentology,* Vol. 39, pp 193-206.

BAGNOLD, R.A. (1954). "Experiments on a gravity-free dispersion of large solid spheres in a Newtonian fluid under shear," *Proceedings of the Royal Society of London,* Vol. 225A, pp. 49-63.

BARDET, J.P. AND PROUBET, J. (1991). "A numerical investigation of the structure of persistent shear bands in granular media," *Geotechnique,* Vol. 41, No. 4, pp 599-613.

BARIL, P.H., WOOD, D.W., AND WALTON, W.H. (1992). 'The Wachusett dam in the 21st century: modifications after 100 years of service,' *Twelfth Annu. U.S. Comm. On Large Dams (USCOLD) Lecture Series,* Fort Worth, Texas, Vol. 1, pp 1-22.

BARTLETT, S.F. AND YOUD, T.L. (1992). "Case histories of lateral spreads caused by the 1964 Alaska Earthquake," *Case Studies of Liquefaction and Lifeline Performance During Past Earthquake, Volume 2,* National Center for Earthquake Engineering Research, Buffalo, New York.

BARTLETT, S.F. AND YOUD, T.L. (1990). "Empirical analysis of horizontal ground displacement generated by liquefaction-induced lateral spread," *Technical Report NCEER-92-0021*, National Center of Earthquake Engineering Research, Buffalo, New York.

BAZIAR, M.H. AND DOBRY, R. (1995). "Residual strength and large-deformation potential of loose silty sands," *Journal of Geotechnical Engineering*, American Society of Civil Engineers, Vol. 121, No. 12, pp 896-906.

BEEN, K., CONLIN, B.H., CROOKS, J.H.A., FITZPATRICK, S.W., JEFFERIES, M.G., ROGERS, B.T., AND SHINDE, S. (1987). "Back analysis of the Nerlerk berm liquefaction slides: Discussion," *Canadian Geotechnical Journal,* Vol. 24, pp. 170-179.

BENJAMIN, J.R. AND CORNELL, C.A. (1970). *Probability, Statistics, and Decision for Civil Engineers*, McGraw-Hill, New York, 684 pp.

BINGHAM, E.C. (1922). *Fluidity and Plasticity*, McGraw-Hill Book Company, 440 pp.

BOLT, B.A. AND GOPALAKRISHNAN, B.S. (1975). "Magnitude, aftershocks and fault dynamics," *San Fernando, California Earthquake of 9 February, 1971, Bulletin 196,* California Division of Mines and Geology, Sacramento, California, pp. 369-380.

BOLTON, M.D. (1986). "The strength and dilatancy of sands," *Geotechnique*, Vol. 36, No. 1, pp 65-78.

BOULANGER, R.W AND TRUMAN, S.P. (1996). "Void redistribution in sand under post-earthquake loading," *Canadian Geotechnical Journal,* Vol. 33, No. 5, pp 829-834.

BROWNE, A. L. (1975). "Mathematical analysis for pneumatic tire hydroplaning," *Surface texture versus skidding: Measurements, frictional aspects, and safety features*, American Society for Testing and Materials Special Technical Publication 583, pp 75–94.

BROWNE, A.L., AND WHICKER, D. (1983). "An interactive tire-fluid model for dynamic hydroplaning," *Frictional Interaction of Tire and Pavement*, American Society for Testing and Materials Special Technical Publication 793, pp 130-150.

BUDHU, M. (1984). "Nonuniformities imposed by simple shear apparatus," *Canadian Geotechnical Journal*, Vol. 20, No. 1, pp 125-137.

BUDHU, M. (1988). "Failure state of sand in simple shear," *Canadian Geotechnical Journal*, Vol. 25, No. 2, pp 395-400.

BURLINGTON, R.S. AND MAY, D.C., JR. (1970). *Handbook of Probability and Statistics*, McGraw-Hill, New York, 463pp.

CAMPBELL, C.S. (1990). "Rapid granular flows," *Annual Review of Fluid Mechanics,* Vol. 22, pp 57-92.

CANADIAN GEOTECHNICAL SOCIETY (1992). *Canadian Foundation Engineering Manual*, third edition, Canadian Geotechnical Society, pp 512.

CASAGRANDE, A. (1936). "Characteristics of cohesionless soils affecting the stability of slopes and earth," *Contributions to Soil Mechanics, 1925-1940,* Boston Society of Civil Engineering, pp. 257-276.

CASAGRANDE, A. (1965). "Second Terzaghi Lecture: the role of "calculated risk" in earthwork and foundation engineering." *Journal of the Soil Mechanics and Foundations Division,* American Society of Civil Engineers, Vol. 91, No. SM4, pp 1-40.

CASAGRANDE, A. (1976). "Liquefaction and cyclic deformation of sands, a critical review," *Harvard Soil Mechanics Series 88*, Harvard University, Cambridge, Massachusetts.

CASTRO, G. (1969). "Liquefaction of sands," *Harvard Soil Mechanics Series 87*, Harvard University, Cambridge, Massachusetts.

CASTRO, G. AND Poulos, S.J. (1977). "Factors affecting liquefaction and cyclic mobility," *Journal of the Geotechnical Engineering Division,* American Society of Civil Engineers, Vol. 103, No. GT6, pp. 501-516.

CASTRO, G., KELLER, T.O., AND BOYNTON, S.S. (1989). "Re-evaluation of the Lower San Fernando Dam: Report 1, an investigation of the February 9, 1971 slide," *U.S. Army Corps of Engineers Contact Report GL-89-2,* Vol. 1 and 2, U.S. Army Corps of Engineers Waterways Experiment Station, Vicksburg, Mississippi.

CASTRO, G., SEED, R.B., KELLER, T.O., AND SEED, H.B. (1992). "Steady-state strength analysis of Lower San Fernando Dam slide." *Journal of Geotechnical Engineering,* American Society of Civil Engineers, No. 118, Vol. 3, pp 406-427.

CHANEY, R. AND MULILIS, J.P. (1978). "Suggested method for soil specimen remolding by wet-raining," *Geotechnical Testing Journal*, Vol. 1, No. 2, pp 107-108.

CHEN, C.J. AND JUANG, C.H. (2000). "Calibration of SPT- and CPT- based liquefaction evaluation methods," *Innovation and Applications in Geotechnical Site Characterization,* Geotechnical Special Publication No. 97, American Society of Civil Engineers.

CHILLARIGE, A.V., ROBERTSON, P.K., MORGENSTERN, N.R., AND Christian, H.A. (1997). "Evaluation of the in situ state of Fraser River sand," *Canadian Geotechnical Journal,* Vol. 34, pp. 510-519.

CHILLARIGE, A.V., MORGENSTERN, N.R., ROBERTSON, P.K., AND Christian, H.A. (1997). "Seabed instability due to flow liquefaction in the Fraser River delta," *Canadian Geotechnical Journal,* Vol. 34, pp. 520-533.

CHRISTIAN, H.A., Woeller, D.J., ROBERTSON, P.K., AND COURTNEY, R.C. (1997). "Site investigations to evaluate flow liquefaction slides at Sand Heads, Fraser River delta," *Canadian Geotechnical Journal,* Vol. 34, pp. 384-397.

CLOUD, W.K. AND HUDSON, D.E. (1975). "Strong-motion data from the San Fernando, California, earthquake of February 9, 1971," *San Fernando California, Earthquake of 9 February 1971,* Division of Mines and Geology, California, pp 273-303.

COFFMAN, K.L., VON HAKE, C.A., AND STOVER, C.W. (1982). *Earthquake History of the United States, Publication 541-1,* U.S. National Oceanic and Atmospheric Administration, U.S. Geological Survey, Boulder, Colorado.

COSTA, J. E. (1984). "Physical geomorphology of debris flows," *Developments and applications of geomorphology*, Berlin, Springer-Verlag, pp 268–317.

DAVIS, J.C. (1986). *Statistics and Data Analysis in Geology*, John Wiley and Sons, Inc., 664 pp.

DAVIS, A.P., CASTRO, G., AND POULOS, S.J. (1988). 'Strength backfigured from liquefaction case histories,' *Proc., 2nd Int. Conf. on Case Histories in Geotech. Engrg.,* St. Louis, Vol. IV, pp 1693-1701.

DE ALBA, P., SEED, H.B., RETAMAL, E., AND SEED, R.B. (1987). "Residual strength of sand from dam failures in the Chilean Earthquake of March 3, 1985," *Earthquake Engineering Research Center Report No. UCB/EERC-87-11,* University of California, Berkeley, CA.

DOBRY, R. AND NG, T.-T. (1992). "Discrete modeling of stress-strain behaviour of granular media at small and large strains," *Engineering Computations,* Vol. 9, pp 129-143.

EMBLEY, R.W. (1982). "Anatomy of some Atlantic margin sediment slides and some comments on ages and mechanisms," *Marine slides and other mass movements*, New York, Plenum Press, pp 189–213.

FALLGREN, R.B. AND SMITH, J.L. (1973). "Ground displacement at San Fernando Valley Juvenile Hall during San Fernando Earthquake," *San Fernando, California, Earthquake of February 9, 1971, Volume 3,* U.S. Department of Commerce, National Oceanic and Atmospheric Administration, Washington, D.C.

FANG, H.-Y. AND MIKROUDIS, G.K.M. (1991). "Stability of earth slopes," *Foundation Engineering Handbook*, second edition, Van Nostrand Reinhold, 923 pp.

FIEGEL, G.L. AND KUTTER, B.L. (1994). "Liquefaction mechanism for layered soils," *Journal of Geotechnical Engineering,* American Society of Civil Engineers, Vol. 120, No. 4, pp 737-755.

FINN, W.D.L., PICKERING, D.J., AND BRANSBY, P.L. (1971). "Sand liquefaction in triaxial and simple shear tests," *Journal of Soil Mechanics and Foundation Division*, American Society of Civil Engineers, Vol. 97, No. SM4, pp 639-659.

FROST, J.D., CARROL, D.P., AND ROCKAWAY, T.D. (1997). "Spatial liquefaction analysis," *Spatial Analysis in Soil Dynamics and Earthquake Engineering,* Geotechnical Special Publication No. 67, American Society of Civil Engineers, pp 70-86.

FROST, J.D. AND JANG, D.-J. (2000). "Evolution of sand microstructure during shear," *Journal of Geotechnical and Geoenvironmental Engineering,* American Society of Civil Engineers, Vol. 126, No. 2, pp 116-130.

FUKUOKA, H., SASSA, K., AND SCARASCIA-MUGNOZZA, G. (1997). "Distribution of landslides triggered by the 1995 Hyogo-Ken Nanbu earthquake and long runout mechanism of the Takarazuka golf course landslide," *Journal of Physics of the Earth*, Vol. 45, No. 2, pp 83-90.

GZA Geoenvironmental, Inc. (1991). 'Wachusett Dam – Clinton, Massachusetts – north dike stability,' *Stage I report, Report to the Commonwealth of Massachusetts,* Vol. II, Metropolitan District Commission, Boston.

GUO, T. AND PRAKASH, S. (1999). "Liquefaction on silts and silty-clay mixtures," *Journal of Geotechnical and Environmental Engineering,* American Society of Civil Engineers, Vol. 125, No. 8, pp 706-710.

HAMADA, M. (1992). "Large ground deformation and their effects on lifelines: 1964 Niigata Earthquake," *Case Studies of Liquefaction and Lifeline Performance During Past Earthquake, Volume 1,* National Center for Earthquake Engineering Research, Buffalo, New York.

HANES, D.M. AND INMAN, D.L. (1985a). "Experimental evaluation of a dynamic yield criterion for granular fluid flows," *Journal of Geophysical Research,* Vol. 90, No. B5, pp 3670-3674.

HANES, D.M. AND INMAN, D.L. (1985b). "Observations of rapidly flowing granular-fluid materials," *Journal of Fluid Mechanics,* Vol. 150, pp 357-380.

HARDIN, B.O. (1985). "Crushing of soil particles," *Journal of Geotechnical Engineering,* American Society of Civil Engineers, Vol. 111, No. 10, pp 1177-1192.

HAZEN, A. (1918). "A study of the slip in the Calaveras Dam," *Engineering News-Record*, Vol. 81, No. 26, pp 1158-1164.

HAZEN, A. (1920). "Hydraulic-fill dams," *Transactions of the American Society of Civil Engineers*, Paper No. 1458, pp 1713-1821 (including discussions).

HAZEN, A. AND METCALF, L. (1918). "Middle section of upstream side of Calaveras dam slips into reservoir," *Engineering News-Record*, Vol. 80, No. 14, pp 679-681.

HEISKANEN, K. (1993). *Particle Classification,* Powder Technology Series, Chapman and Hall, 321 pp.

HERTZ, H. (1896). "On the contact of elastic solids,' *Miscellaneous papers*, Macmillan, and Co., 340 pp.

HICKS, M.A. AND BOUGHRAROU, R. (1998). "Finite element analysis of the Nerlerk underwater berm failures," *Geotechnique,* Vol. 48, No. 2, pp. 169-185.

HORNE, W.B., AND DREHER, R.C. (1963). "Phenomena of pneumatic tire hydroplaning," *Washington, D.C., National Aeronautics and Space Administration Technical Note D-2056*, 52 p.

HORNE, W.B., AND JOYNER, U.T. (1965). "Pneumatic tire hydroplaning and some effects of vehicle performance," *Society of Automotive Engineers Technical Paper 970C*, 51 p.

HRYCIW, R.D., VITTON, S., AND THOMANN, T.G. (1990). "Liquefaction and flow failure during seismic exploration," *Journal of Geotechnical Engineering,* American Society of Civil Engineers, Vol. 116, No. 12, pp. 1881-1899.

HUTTER, K. (1999). "Order and disorder in granular materials," *Kinetic and Continuum Theories of Granular and Porous Media,* CISM Courses and Lectures NO. 400, International Centre for Mechanical Science, Springer Wien New York, pp 1-65.

IDRISS, I.M. (1998). "Evaluation of liquefaction potential, consequences and mitigation – An update," Presentation Notes, Vancouver Geotechnical Society Meeting, February 17, Vancouver, B.C.

ISHIHARA, K. (1984). "Post-earthquake failure of a tailings dam due to liquefaction of pond deposit," *Proc. Inter. Conf. On Case Histories in Geotechnical Engineering,* Rolla, Missouri, May 6 to 11, Vol. 3, pp 1129-1143.

ISHIHARA, K. (1993). "Liquefaction and flow failure during earthquakes," *Geotechnique*, Vol. 43, No. 3, pp. 351-415.

ISHIHARA, K. (1996). *Soil Behaviour in Earthquake Geotechnics*, Oxford Science Publications, 350 pp.

ISHIHARA, K., OKUSA, S., OYAGI, N., AND ISCHUK, A. (1990b). "Liquefaction-induced flow slide in the collapsible loess deposit in Soviet Tajik," *Soils and Foundations,* Vol. 30, No. 4, pp. 73-89.

ISHIHARA, K., TATSUOKA, F., AND YASUA, S. (1975). "Undrained deformation and liquefaction of sand under cyclic stresses," *Soils and Foundations,* Vol. 15, No. 1, pp 29-44.

ISHIHARA, K., YASUDA, S., AND YOSHIDA, Y. (1990a). "Liquefaction-induced flow failure of embankments and residual strength of silty sands," *Soils and Foundations,* Vol. 30, No. 3, pp 69-80.

IVERSON, R.M. (1997). "The physics of debris flows," *Reviews of Geophysics,* Vol. 35, pp 245-296.

IVERSON, R.M. (2000). "Landslide triggering by rain infiltration," *Water Resources Journal,* No. 207, pp 59-82.

IVERSON, R.M. AND LAHUSEN, R.G. (1989). "Dynamic pore-pressure fluctuations in rapidly shearing granular materials," *Science,* New Series, Vol. 246, Issue, 4931, pp 796-799.

IVERSON, R.M. AND LAHUSEN, R.G. (1993). "Friction in debris flows: inferences from large-scale flume experiments," *Proceedings of the 1993 Conference of the Hydraulics Division of the American Society of Civil Engineers,* Vol. 2, pp 1604-1609.

IVERSON, R.M., REID, M.E., AND LAHUSEN, R.G. (1997). "Debris-flow mobilization from landslides," *Annual Review of Earth and Planetary Sciences,* Vol. 25, pp 85-138.

IWASHITA, K. AND ODA, M. (1999). "Micro-deformation mechanism of shear banding development on modified distinct element method," *Powder Technology,* Vol. 109, pp 192-205.

JACOBY, G.C., BUNKER, D.E., AND BENSON, B.E. (1997). "Tree-ring evidence for an A.D. 1700 Cascadia earthquake in Washington and northern Oregon," *Geology,* Geological Society of America, Vol. 25, No. 11, pp 999-1002.

JAEGER, H.M. AND NAGEL, S.R. (1992). "Physics of granular state," *Science,* New Series, Vol. 255, Issue. 5051, pp 1523-1531.

THE JAPANESS GEOTECHNICAL SOCIETY. (1998). *Remedial Measures Against Soil Liquefaction, from Investigation and Design to Implementation,* A.A. Balkema, 443 pp.

JEFFERIES, M.G., BEEN, K., AND HACHEY, J.E. (1990). "Influence of scale on the constitutive behavior of sand." *Proc. Canadian Geotechnical Engineering Conference*, Laval University, Quebec, Canada, Vol. 1, pp 263-273.

JENKINS, J.T. AND SAVAGE, S.B. (1983). "A theory for the rapid flow of identical, smooth, nearly elastic, spherical particles," *Journal of Fluid Mechanics,* Vol. 130, pp 187-202.

JONES, A.L., KRAMER, S.L., AND ARDUINO, P. (2001). *Estimation of Uncertainty in Geotechnical Properties for Performanced-Based Earthquake Engineering*, PEER Report 2001/03, Pacific Earthquake Engineering Research Center, College of Engineering, University of California, Berkeley, 98 pp.

JOHNSON, A.M. (1965). *A Model for Debris Flow,* Ph.D. Dissertation, The Pennsylvania State University, 233pp.

JOHNSON, A.M. (1970). *Physical Processes in Geology*, Freeman, Cooper and Co., 577pp.

JOHNSON, A.M. AND RODINE, J.R. (1984). "Debris flow," *Slope Instability,* John Wiley and Sons, pp 257-361.

JUANG, C.H., CHEN, C.J., AND JIANG, T. (2001). "Probabilistic framework for liquefaction potential by shear wave velocity," *Journal of Geotechnical and Environmental Engineering,* American Society of Civil Engineers, Vol. 127, No. 8, pp 670-678.

JUANG, C.H., CHEN, C.J., TANG, W.H., AND ROSOWSKY, D.V (2000a). "CPT-based liquefaction analysis, Part 1: Determination of limit state function," *Geotechnique,* Vol. 50, No. 5, pp 583-592.

JUANG, C.H., CHEN, C.J., ROSOWSKY, D.V., AND TANG, W.H. (2000b). "CPT-based liquefaction analysis, Part 2: Reliability for design," *Geotechnique,* Vol. 50, No. 5, pp 593-599.

JUANG, C.H. AND JIANG, T. (2000). "Assessing probabilistic methods for liquefaction potential evaluation," *Soil Dynamics and Liquefaction 2000,* Geotechnical Special Publication No. 107, American Society of Civil Engineers, pp 148-162.

JUANG, C.H., ROSOWSKY, D.V., AND TANG, W.H. (1999). "A reliability-based method for assessing liquefaction potential of sandy soils," *Journal of Geotechnical and Geoenvironmental Engineering,* American Society of Civil Engineers, Vol. 125, No. 8, pp 684-689.

JULIEN, P.Y. AND LAN, Y. (1991). "Rheology of hyperconcentrations," *Journal of Hydraulic Engineering,* American Society of Civil Engineers, Vol. 117, No. 3, pp 346-353.

KANAMORI, H. (1995). "The Kobe (Hyogo-ken Nanbu), Japan, earthquake of January 16, 1995," *Seismological Research Letters*, Vol. 66, No. 2, pp 6-10.

KONRAD, J.M. AND WATTS, B.D. (1995). "Undrained shear strength for liquefaction flow failure analysis." *Canadian Geotechnical Journal*, Vol. 32, pp 783-794.

KRAMER, S.L. (1985). *Liquefaction of Sands Due to Non-seismic Loading,* Ph.D. Dissertation, University of California, Berkeley, 369 pp.

KRAMER, S.L. (1988). "Triggering of liquefaction flow slides in coastal soil deposits," *Engineering Geology*, Vol. 26, pp 17-31.

KRAMER, S.L. (1996). *Geotechnical Earthquake Engineering,* Prentice Hall, Upper Saddle River, New Jersey, 653 pp.

KRAMER, S.L. AND ELGAMAL, A.-W. (2001). *Modeling soil liquefaction hazards for performance-based earthquake engineering*, PEER Report 2001, Pacific Earthquake Engineering Research Center, University of California, Berkeley, 156 pp.

KRAMER, S.L. AND SEED, H.B. (1988). "Initiation of soil liquefaction under static loading conditions," *Journal of Geotechnical Engineering,* American Society of Civil Engineering, Vol. 114, No. 4, pp 412-430.

KOLBUSZEWSKI, J.J. (1948). "An experimental study of the maximum and minimum porosities of sands," *Proceedings, Second International Conference on Soil Mechanics and Foundation Engineering*, Rotterdam, Vol. 1, pp 158-165.

KOKUSHO, T. (1999). "Water film in liquefied sand and its effect on lateral spread," *Journal of Geotechnical and Geoenvironmental Engineering,* American Society of Civil Engineers, Vol. 125, No. 10, pp 817-826.

KOKUSHO, T AND FUJITA, K. (2002). "Site investigation for involvement of water films in lateral flow in liquefied ground," *Journal of Geotechnical and Environmental Engineering,* American Society of Civil Engineers, Vol. 128, No. 11, pp 917 – 925.

KOKUSHO, T., KOJIMA, T., AND NONAKA, N. (1999). "Emergence of water film in liquefied sand and its role in lateral flow," *12th World Conf. on Earthquake Engineering,* No. 0946, Auckland, New Zealand.

KONAGAI, K. AND RANGELOW, P. (1994). "Real-time observation of dynamic changes in the fabric of granular material structures through Laser-Aided Tomography," *Proceedings Tenth European Conference Earthquake Engineering, Vienna,* pp 459-465.

KONAGAI, K. AND TAMURA, C. (1992). "Visualization and analysis of dynamic behavior of underwater granular structure models," *Proceedings of the Tenth World Conference on Earthquake Engineering,* Vol. 5, pp 2731-2736.

KONAGAI, K., TAMURA, C., RANGELOW, P., AND MATSUSHIMA, T. (1992). "Laser-Aided Tomography: A tool for visualization of changes in the fabric of granular assemblage," *Structural Engineering/Earthquake Engineering,* Vol. 9, No. 3, pp 193-201.

KONRAD, J.M. (1991). "The Nerlerk berm case history: some considerations for the design of hydraulic sand fills," *Canadian Geotechnical Journal,* Vol. 28, pp. 601-612.

KOVACS, W.D. AND SALOMONE, L.A. (1982). "SPT hammer energy measurement," *Journal of the Geotechnical Division*, American Society of Civil Engineers, Vol. 108, No. GT4, pp 599-620.

KUERBIS, R. AND VAID Y.P. (1988). "Sand sample preparation – The slurry deposition method," *Soils and Foundations*, Vol. 28, No. 4, pp 107-118.

KULHAWY, F.H. AND MAYNE, P.W. (1990). *Manual on Estimating Soil Properties for Foundation Design*, EL-6800, Research Project 1493-6, Electric Power Research Institute.

KURIBAYASHI, E. AND TATSUOKA, F. (1975). "Brief review of liquefaction during earthquakes in Japan," *Soils and Foundations,* Vol. 15, No. 4, pp 81-92.

LABERG, J.S. AND VORREN, T.O. (1995). "Late wWeichselian submarine debris flow deposits on the Bear Island Trough Mouth Fan," *Marine Geology*, Vol. 127, pp 45–72.

LADD, C.C. (1991). "Stability evaluation during staged construction," *Journal of the Geotechnical Engineering*, American Society of Civil Engineers, Vol. 117, No. 4, pp 540-615.

LADD, R.S. (1974). "Specimen preparation and liquefaction of sands," *Journal of the Geotechnical Engineering Division*, American Society of Civil Engineers, Vol. 100, No. GT10, pp 1180-1184.

LADD, R.S. (1978). "Preparing test specimen using undercompaction," *Geotechnical Testing Journal*, Vol. 1, No. 1, pp 16-23.

LADE, P.V. (1993). "Initiation of static instability in the submarine Nerlerk berm," *Canadian Geotechnical Journal,* Vol. 30, pp. 895-904.

LADE, P.V. AND YAMAMURO, J.A. (1997). "Effects of nonplastic fines on static liquefaction of sands," *Canadian Geotechnical Journal,* Vol. 34, No. 6, pp 918-928.

LADE, P.V., YAMAMURO, J.A., AND BOPP, P.A. (1996). "Significance of particle crushing in granular materials," *Journal of Geotechnical Engineering,* American Society of Civil Engineers, Vol. 122, No. 4, pp 309-316.

LAU, J.H.A. AND POWELL, J.J.M. (1991). "Measurement of soil strength in simple shear tests," *Canadian Geotechnical Journal*, Vol. 28, No. 2, pp 255-262.

LEE, K.L. AND FARHOOMAND, I. (1967). "Compressibility and crushing of granular soils in anisotropic triaxial compression," *Canadian Geotechnical Journal,* Vol. 4, No. 1, pp 68-86.

LEE, K.L. AND SEED, H.B. (1967). "Drained strength characteristics of sand," *Journal of Soil Mechanics and Foundations Division,* American Society of Civil Engineers, Vol. 93, No. SM6, pp 117-141.

LEE, K.L., SEED, H.B., IDRISS, I.M., AND MAKDISI, F.I. (1975). "Properties of soil in the San Fernando hydraulic fill dams," *Journal of the Geotechnical Engineering Division,* American Society of Civil Engineers, Vol. 101, No. GT8, pp. 801-821.

LEE, J.-H. AND SASSA, K. (1996). "A study on the apparent friction angle mobilized during the undrained loading in long run-out landslides," *Bulletin of the Disaster Prevention Research Institute*, Kyoto University, Vol. 45, Part 4, No. 393, pp 99-124.

LI, X.S. AND DAFALIAS, Y.F. (2000). "Dilatancy for cohesionless soils," *Geotechnique,* Vol. 50, No. 4, pp 449-460.

LI, X.S., DAFALIAS, Y.F., AND WANG, Z.L. (1999). "State dependent dilatancy in critical state constitutive modeling of sands," *Canadian Geotechnical Journal,* Vol. 36, No. 4, pp 599-611.

LIAO, S.C. AND WHITMAN, R.V. (1986). "Overburden correction factors for SPT in sand," *Journal of Geotechnical Engineering*, American Society of Civil Engineers, Vol. 112, No. 3, pp 373-377.

LIN, X. AND NG, T.-T. (1997). "A three-dimensional discrete element model using arrays of ellipsoids," *Geotechnique*, Vol. 47, No. 2, pp 319-329.

LUCIA, P.C. (1981). "Review of experiences with flow failures of tailings dams and waste impoundments." *Ph.D. Thesis*, University of California, Berkeley, California.

LUCIA, P.C., DUNCAN, J.M., AND SEED, H.B. (1982). "Summary of research on case histories of flow failures of mine tailings impoundments," *Proceedings of the Bureau of Mines technology transfer workshop on Mine waste disposal technology,* Bureau of Mines Information Circular. 8857, pp. 46-53.

MAEDA, K., MIURA, K., AND TOKI, S. (1995). "Mechanical properties of elliptic microstructure formed in granular materials" *Soils and Foundations,* Vol. 35, No. 2, pp 1-13.

MAJOR, J.J. AND PIERSON, T.C. (1992). "Debris flow rheology: experimental analysis of fine-grained slurries," *Water Resources Research,* Vol. 28, No. 3, pp841-857.

MANDL, G., JONG, L.N., AND MALTHA, A. (1977). "Shear Zones in granular materials," *Rock Mechanics,* Vol. 9, pp 95-144.

MARCUSON, W.F., BALLARD, R.F., JR., AND LEDBETTER, R.H. (1979). "Liquefaction failure of tailings dams resulting from the near Isu Oshima Earthquake, 14 and 15 January 1978," *Proc. 6th Pan-American Conf. On Soil Mechanics and Foundation Engineering,* Lima Peru, Vol. 2, pp. 69-80.

MARCUSON, W.F., III, HYNES, M.E., AND FRANKLIN, A.G. (1990). "Evaluation and use of residual strength in seismic safety analysis of embankments," *Earthquake Spectra,* Vol. No. 3, pp. 529-572.

MARCUSON, W.F., III, AND KRINITZSKY, E.L. (1976). "Dynamic analysis of Fort Peck dam." *Technical Report S-76-1*, U.S. Army Engineer Waterways Experiment Station, Vicksburg, Mississippi, March.

MARCUSON, W.F., III, BALLARD, R.F., JR., AND COOPER, S.S., (1978). "Comparison of penetration resistance values to in situ shear wave velocities." *Proc., 2nd International Conf. on Microzonation for Safer Construction – Research and Application*, San Francisco, CA, Nov. 26 – Dec. 1, Vol. 2, pp 1013-1023.

MARSAL, R.J. (1967). "Large scale testing of rockfill materials," *Journal of Soil Mechanics and Foundations Division,* American Society of Civil Engineers, Vol. 93, No. 2, pp 27-43.

MASSON, D.G., HUGGETT, Q.J., AND BRUNSDEN, D. (1993). "The surface texture of the Saharan Debris Flow and some speculations on submarine debris flow processes," *Sedimentology*, Vol. 40, pp 583–598.

MCKENNA, G.T., LUTERNAUER, J.L., AND KOSTASCHUK, R.A. (1992). "Large-scale mass-wasting event on the Fraser River delta front near Sand Heads, British Columbia," *Canadian Geotechnical Journal,* Vol. 29, pp. 151-156.

MCROBERTS, E.C. AND SLADEN, J.A. (1992). "Observations on static and cyclic sand liquefaction methodologies." *Canadian Geotechnical Journal*, Vol. 29, pp 650-665.

MIDDLEBROOKS, T.A. (1942). "Fort Peck Slide," *Transactions,* American Society of Civil Engineers, Vol. 107, pp 723-764.

MIDDLETON, G.V. AND HAMPTON, M.A. (1976). "Subaqueous sediment transport and deposition by sediment gravity flows," *Marine Sediment Transport and Environmental Management,* John Wiley and Sons, pp197-218.

MINDLIN, R.D. (1949). "Compliance of elastic bodies in contact," *Journal of Applied Mechanics*, September, pp 259-268.

MIURA, K., YOSHIDA, N., AND WAKAMATSU, K. (1995). "Damage to fill embankment during the1993 Kushiro-oki earthquake." *Proc., 1st International Conf. on Earthquake Geotechnical Engineering*, Nov. 14-16, Tokyo, Japan, Vol. 2, pp 1057-1062.

MIURA, K., YOSHIDA, N., NISHIMURA, M., AND WAKAMATSU, K. (1998). "Stability analysis of the fill embankment damaged by recent two major earthquakes in Hokkaido, Japan." *Proc., 1998 Geotechnical Earthquake Engineering and Soil Dynamics Specialty Conference*, American Society of Civil Engineers Geo-Institute Geotechnical Special Publication No. 75, Vol. 2, August 3-6, Seattle, Washington, pp 926-937.

MISHUMA, S. AND. KIMURA, H (1970). "Characteristics of landslides and embankment failures during the Tokachioki earthquake," *Soils and Foundations,* Vol. 10, No. 2, pp. 39-51.

MITCHELL, D.E. (1984). "Liquefaction slides in hydraulically sands," *Canadian Case Histories, Landslides* : preprint volume for 37th Canadian Geotechnical Conference, Monday, September 17, 1984, Toronto, Canada, pp. 141-146.

MITCHELL, J.K. (1993). *Fundamentals of Soil Behavior,* John Wiley and Sons, Inc., 437 pp.

MIURA, K., MADEA, K., FURUKAWA, M., AND TOKI, S. (1997). "Physical characteristics of sands with different primary properties," *Soils and Foundations,* Vol. 37, No. 3, pp. 53-64.

MIURA, K., YOSHIDA, N., AND WAKAMATSU, K. (1995). "Damage to fill embankment during the 1993 Kushiro-oki earthquake." *Proc., 1st International Conf. on Earthquake Geotechnical Engineering*, Nov. 14-16, Tokyo, Japan, Vol. 2, pp 1057-1062.

MIURA, K., YOSHIDA, N., NISHIMURA, M., AND WAKAMATSU, K. (1998). "Stability analysis of the fill embankment damaged by recent two major earthquakes in Hokkaido, Japan." *Proc., 1998 Geotechnical Earthquake Engineering and Soil Dynamics Specialty Conference*, ASCE Geo-Institute Geotechnical Special Publication No. 75, Vol. 2, August 3-6, Seattle, Washington, pp 926-937.

MIURA, N. AND O-HARA, S. (1979). "Particle-crushing of a decomposed granite soil under shear stresses," *Soils and Foundations,* Vol. 19, No. 3, pp 1-14.

MIURA, S. AND TOKI, S. (1982). "A sample preparation method and its effect on static and cyclic deformation-strength properties of sand," *Soils and Foundations*, Vol. 22, No. 1, pp 61-77.

MOGAMI, T. AND KUBU, K. (1953). "The behavior of soil during vibration," *Proceedings, 3rd International Conference on Soil Mechanics and Foundation Engineering,* Zurich, Vol. 1, pp 152-155.

MOHRIG, D., ELVERHØI, A., AND PARKER, G. (1999), "Experiments on the relative mobility of muddy subaqueous and subaerial debris flows, and their capacity to remobilize," *Marian Geology*, Vol. 154, pp 117-129.

MOHRIG, D., WHIPPLE, K.X., HONDZO, M., ELLIS, C., AND PARKER, G. (1998). "Hydroplaning of subaqueous debris flows," *GSA Bulletin*, Vol. 110, No. 3, pp 387-394.

MÜHLHAUS, H.B. AND VARDOULAKIS, I. (1987). "The thickness of shear bands in granular materials," *Geotechnique,* Vol. 37, No. 3, pp 271-283.

NEWMARK, N.M. (1965). "Effects of earthquakes on dams and embankments," *Geotechnique*, Vol. 15, No. 2, pp 139-159.

NG, T.-T. (1994). "Numerical simulations of granular soil using elliptical particles," *Computers and Geotechnics,* Vol. 16, pp 153-169.

NG, T.-T. (1999). "Fabric study of granular material after compaction," *Journal of Engineering Mechanics*, American Society of Civil Engineers, Vol. 125, No. 12, pp 1390-1394.

NG, T.-T. AND LIN, X. (1993). "Numerical simulations of naturally deposited granular soil with ellipsoidal elements," *Second Conference on Discrete Element Methods, Boston, Masseshusett,* pp 122-133.

O'BRIEN, J.S. AND JULIEN, P.Y. (1985). "Physical properties and mechanics of hyperconcentrated sediment flows," *Proc., ASCE Specialty Conference on Delineations of Landslide, Flashflood, and Debris Flow Hazards in Utah,* Logan, Utah, pp 260-279.

O'ROURKE, T.D., ROTH, B.L., AND HAMADA, M. (1992). "Large ground deformations and their effects on lifeline facilities: 1971 San Fernando Earthquake," *Case Studies of Liquefaction and Lifeline Performance During Past Earthquake, Volume 2,* National Center for Earthquake Engineering Research, Buffalo, New York.

ODA, M. (1972). "Deformation mechanism of sand in triaxial compression tests," *Soils and Foundations*, Vol. 12, No. 4, pp 45-63.

ODA M. AND IWASHITA, K. (1999). *Mechanics of Granular Materials: An Introduction,* A.A. Balkema, 383 pp.

ODA, M. AND KAZAMA, H. (1998). "Microstructure of shear bands and its relation to the mechanisms of dilatancy and failure of dense granular soils," *Geotechnique,* Vol. 48, No. 4, pp 465-481.

ODA, M., KAWAMOTO, K., SUZUKI, K., FUJIMORI, H., AND SATO, M. (2001). "Microstructural interpretation on reliquefaction of saturated granular soils under cyclic loading," *Journal of Geotechnical and Geoenvironmental Engineering,* American Society of Civil Engineers, Vol. 127, No. 5, pp 416-423.

ODA, M. AND KOISHIKAWA, I. (1977). "Anisotropic fabric of sands," *Proceedings of Ninth International Conference on Soil Mechanics and Foundation Engineering,* Vol. 1, pp 235-238.

ODA, M., KONISHI, J., AND NEMAT-NASSER, S. (1982). "Experimental micromechanical evaluation of strength of granular materials: Effect of particle rolling," *Mechanical of Materials,* Vol. 1, pp 267-283.

OKUSA, S. AND ANMA, S. (1980). "Slope failures and tailings dam damage in the 1978 Izu-Ohshima-Kinkai Earthquake," *Engineering Geology,* Vol. 16, pp. 195-224.

OLSON, S.M. (2001). 'Liquefaction analysis of level and sloping ground using field case histories and penetration resistance,' *Ph.D. Dissertation*, University of Illinois at Urbana-Champaign.

OLSON, S.M. AND STARK, T.D. (1998). "CPT based liquefaction resistance of sandy soils," *Proc., 1998 Geotechnical Earthquake Engineering and Soil Dynamic Specialty Conference,* ASCE Geo-Institute Geotechnical Special Publication No. 75, Vol. 1, August 3-6, Seattle, Washington, pp 325-336.

OLSON, S.M. AND STARK, T.D. (2002). "Liquefied strength ratio from liquefaction flow failure case histories," *Canadian Geotechnical Journal*, Vol. 39, No. 5, pp 629-647.

OLSON, S.M., STARK, T.D., WALTON, W.H., AND CASTRO, G. (2000). "1907 static liquefaction flow failure of the North Dike of Wachusett Dam," *J. of Geotechnical and Environmental Engineering,* American Society of Civil Engineers Vol. 126, No. 12, pp. 1184-1193.

OHYA, S., IWASAKI, T., AND WAKAMATSU, M. (1985). "Comparative study of various penetration tests in ground that underwent liquefaction during the 1983 Nihon-Kai-Chubu and 1964 Niigata earthquakes." *Proc., Workshop on In-Situ Testing Methods for Evaluation of Soil Liquefaction Susceptibility*, San Francisco, California, Vol. 1, pp 56-88.

ORTIZ, J.D., TAMURA, C., AND KONAGAI, K. (1992). "Three-dimensional stress and strain detection by photoelasticity using laser-light-sheet," *Proceedings of the Tenth World Conference on Earthquake Engineering,* Vol. 5, pp 2719-2724.

PERLOFF, W.H. AND BARON, W. (1976). *Soil Mechanics: Principles and Applications,* John Wiley and Sons, 745 pp.

PHOON, K.-K. AND KULHAWY, F.H. (1999). 'Characterization of geotechnical variability,' *Canadian Geotechnical Journal,* Vol. 36, pp. 612-624.

PLAFKER, G. AND ERICKSEN, G.E. (1978). "Nevados Huascaran avalanches," *Peru. In Rockslides and Avalanches Vol. 1: Natural Phenomena,* pp 277-314.

PLEWES, H.D., O'NEIL, G.D., MCROBERTS, E.C., AND CHAN, W.K. (1989). "Liquefaction considerations for Suncor tailings pond." *Proc., Dam Safety Seminar*, Edmonton, Alberta, Sept., Vol. 1, pp 61-89.

POLITO, C.P. AND MARTIN, J.R. II (2001). "Effects nonplastic fines on the liquefaction resistance of sands," *Journal of Geotechnical and Environmental Engineering,* American Society of Civil Engineers, Vol. 127, No. 5, pp 408-415.

POULOS, S.J. (1981). "The steady state of deformation," *Journal of Geotechnical Engineering Division,* American Society of Civil Engineers , Vol. 107, No. GT5, pp 553-562.

POULOS, S.J. (1988). "Liquefaction and related phenomena," in *Advanced Dam Engineering for Design, Construction, and Rehabilitation,* R.B. Jansen, ed., Van Nostrand Reinhold, New York, pp 292-320.

POULOS, S.J., CASTRO, G., AND FRANCE, J.W. (1985). "Liquefaction evaluation procedure," *Journal of Geotechnical Engineering,* American Society of Civil Engineers, Vol. 111, No. 6, pp 772-792.

PRESTI, D.C.F.L., PUCI, I., PALLARA, O., MANISCALCO, R., AND PEDRONI, S. (2000). "Experimental laboratory determination of the steady state of sands," *Soils and Foundations*, Vol. 40, No. 1, pp 113-122.

REID, M.E., LAHUSEN, R.G., AND IVERSON, R.M. (1997). "Debris-flow initiation using diverse hydrologic triggers," *Debris-Flow Hazards Mitigations: Mechanics, Prediction, and Assessment*, Proceedings of First International Conference, August 7-9, San Francisco, California, pp 1-11.

ROBERTSON, P.K. AND WRIDE, C.E. (1998). "Evaluating cyclic liquefaction potential using the cone penetration test," *Canadian Geotechnical Journal*, Vol. 35, No. 3, pp 442-459.

ROGERS, B.T., BEEN, K., Hardy, M.D., JOHNSON, G.J., AND HACHEY, J.E. (1990). "Re-analysis of Nerlerk B-67 berm failures," *Prediction and Performance in Geotechnique,* 43rd Canadian Geotechnical Conference, October 10 to 12, 1990, Quaebec, Canada, pp. 227-237.

ROSCOE, K.H. (1970). "The influence of strains in soil mechanics," *Geotechnique,* Vol. 20, No. 2, pp 127-170.

ROSS, G.A., SEED, H.B., AND MIGLIACCIO, R.R. (1969). "Bridge foundation behavior in Alaska earthquake," *Journal of the Soil Mechanics and Foundations Division,* American Society of Civil Engineers, Vol. 95, No. SM4, pp. 1007-1036.

ROSS, G.A., SEED, H.B., AND MIGLIACCIO, R.R. (1973). "Performance of highway bridge foundations," *The Great Alaska Earthquake Of 1964,* National Academy Sciences, Washington, D.C.

ROWE, P.W. (1962). "The stress-dilatancy relation for static equilibrium of an assembly of particles in contact," *Proceedings of the Royal Society,* Vol. A269, pp 500-527.

SANTAMARINA, J.C., KLIEN, K.A., AND FAM, M.A. (2001). *Soils and Waves: Particulate Materials Behavior, Characterization and Process Monitoring,* John Wiley and Sons, 488 pp.

SASAKE, K, SHIMAZAKI, K., TSUJI, Y., AND UEDA, K. (1996). "Time and size of a giant earthquake in Cascadia inferred from Japanese tsunami records of January 1700," *Nature*, Vol. 379, No. 6562, pp 246-249.

SASSA, K. (1984). "The mechanism starting liquefied landslides and debris flows," *IV International Symposium on Landslides*, Vol. 2, pp 349-354.

SASSA, K. (1988). "Special lecture: Geotechnical model of the motion of landslides," *Proc., 5th International Symposium on Landslides*, Landslide, Vol. 1, pp 37-55.

SASSA, K. (1992). "Landslide Volume – apparent friction relationship in the case of rapid loading on alluvial deposits," *Landslide News*, Vol. 6, pp 16-19.

SASSA, K. (1997). "A new intelligent-type dynamic loading ring shear apparatus," *Landslide News*, No. 10, pp 33.

SAVAGE, S.B. AND JEFFREY, D.J. (1981). "The stress tensor in a granular flow at high shear rates," *Journal of Fluid Mechanics,* Vol. 110, pp 255-272.

SAVAGE, S.B. AND MCKEOWN, S. (1983). "Shear stresses developed during rapid shear of concentrated suspensions of large spherical particles between concentric cylinders," *Journal of Fluid Mechanics,* Vol. 127, 453-472.

SAVAGE, S.B., AND SAYED, M. (1984). "Stresses developed in dry cohesionless granular materials sheared in an annular shear cell," *Journal of Fluid Mechanics*, Vol. 142, pp. 391-430.

SCARPELLI, G. AND WOOD, D.M. (1982). "Experimental observations of shear band patterns in direct shear tests," *Proceedings of IUTAM Symposium on Deformations and Failure of Granular Materials,* pp 473-484.

SCHMERTMANN, J.H. (1975). "Measurement on in-situ shear strength," *Proceedings, ASCE Conference on In-situ Measurement of Soil Properties,* Vol. 2, pp 57-138.

SCOTT, R.F. (1971). "San Fernando Earthquake, 9 February, 1971 preliminary soil engineering report," *Engineering Features of the San Fernando Earthquake February 9, 1971,* EERL 71-01, California Institute of Technology, California.

SEED, H.B. (1987). "Design problems in soil liquefaction," *Journal of the Geotechnical Engineering Division,* American Society of Civil Engineers, Vol. 113, No. 8, pp. 827-845.

SEED, H.B. AND IDRISS, I.M. (1971). "Simplified procedure for evaluating soil liquefaction potential," *Journal of the Soil Mechanics and Foundation Division,* American Society of Civil Engineers, Vol. 97, No. SM9, pp. 1249-1273.

SEED, H.B., IDRISS, I.M., AND ARANGO, I. (1983). "Evaluation of liquefaction potential using field performance data," *Journal of Geotechnical Engineering Division*, American Society of Civil Engineers, Vol. 109, No. 3, pp. 458-452.

SEED, H.B., IDRISS, I.M., LEE, K.L., AND MAKDISI, F. (1975b). "Dynamic analysis of the slide in the Lower San Fernando Dam during the Earthquake of February, 9, 1971," *Journal of the Geotechnical Engineering Division,* American Society of Civil Engineers, Vol. 101, No. GT9, pp 889-911.

SEED, H.B. AND LEE, K.L. (1966). "Liquefaction of saturated sands during cyclic loading," *Journal of Soil Mechanics and Foundation Division*, American Society of Civil Engineers, Vol. 92, No. SM6, pp 105-134.

SEED, H.B., LEE, K.L., IDRISS, I.M., AND MAKDISI, F. (1973). "The slides in the San Fernando Dams during the earthquake of Feb. 9, 1971," *Journal of the Geotechnical Engineering Division,* American Society of Civil Engineers, Vol. 101, No. GT7, pp 651-688.

SEED, H.B., LEE, K.L., IDRISS, I.M., AND MAKDISI, F. (1975a). "Analysis of the slides in the San Fernando Dams during the earthquake of Feb. 9, 1971," *Report No. UCB/EERC 73-2,* University of California, Berkeley, CA.

SEED, H.B., SEED, R.B., HARDER, L.F., AND JONG, H.-L. (1989)." Re-evaluation of the slide in the Lower San Fernando Dam in the earthquake of Feb. 9, 1971," *Report No. UCB/EERC-88/04*, University of California, Berkeley, CA.

SEED, R.B., DICHENSON, S.E., REIMER, M.F.,BRAY, J.D., SITAR, N., MITCHELL, J.K., IDRISS, I.M., KAYEN, R.E., KROPP, A., HARDER, L.F., Jr., AND POWER, M.S. (1990). "Preliminary report on the principal Geotechnical aspects of the October 17, 1989 Loma Prieta Earthquake," *Report No. UCB/EERC-90/05,* Earthquake Engineering Research Center, College of Engineering, University of California a Berkeley, 137p.

SEED, R.H. AND HARDER, L.F. (1990). 'SPT-based analysis of cyclic pore pressure generation and undrained residual strength,' *Proc., H.B. Seed Memorial Symp.*, Bi-Tech Publishing Ltd., Richmond, British Columbia, Vol. 2, pp 351-376.

SHEAER, M. AND SCHAEFFER, D.G. (1997a). "Models for stress fluctuations in plasticity," *Proceedings of the Third International Conference on Powers and Grains,* A.A. Balkema.

SHEAER, M. AND SCHAEFFER, D.G. (1997b). "Stress fluctuations in granular materials," *Mechanics of Deformation and Flow of Particulate Materials,* American Society of Civil Engineers, 458 pp.

SHOAEI, Z. AND SASSA, K. (1994). "Basic study on the shear behavior of landslides during earthquakes," *Bulletin of the Disaster Prevention Research Institute*, Kyoto University, Vol. 44, Part 4, No. 378, pp 1-43.

SHOR, A.N. AND PIPER, D.J.W. (1989). "A large late Pleistocene blocky debris flow on the central Scotian Slope," *Geo-Marine Letters*, Vol. 9, pp 153–160.

SKEMPTON, A.W. (1964). "Long-term stability of clay slopes," *Geotechnique,* Vol. 14, No. 2, pp 77-101.

SLADEN, J.A. (1989). "Problems with interpretation of sand state from cone penetration test," *Geotechnique,* Vol. 39, No. 2, pp. 323-332.

SLADEN, J.A., D'HOLLANDER, R.D., AND KRAHN, J. (1985a). "The liquefaction of sands, a collapse surface approach," *Canadian Geotechnical Journal,* Vol. 22, pp. 564-578.

SLADEN, J.A., D'HOLLANDER, R.D., KRAHN, J., AND MITCHELL, D.E. (1985b). "Back analysis of the Nerlerk berm liquefaction slides," *Can. Geotech. J.,* Vol. 22, pp. 579-588.

SLADEN, J.A., D'HOLLANDER, R.D., KRAHN, J., AND MITCHELL, D.E. (1987). "Back analysis of the Nerlerk berm liquefaction slides: Reply," *Canadian Geotechnical Journal,* Vol. 24, pp. 179-185.

STAR, J. AND ESTES, J. (1990). *Geographic Information Systems: An Introduction,* Prentice-Hall, Inc., 303 pp.

STARK, T.D. AND MESRI, G. (1992). "Undrained shear strength of liquefied sands for stability analysis," *Journal of Geotechnical Engineering,* American Society of Civil Engineers, Vol. 118, No. 11, pp. 1727-1747.

STARK, T.D., AND OLSON, S.M. (1995). "Liquefaction resistance using CPT and field case histories," *Journal of Geotechnical Engineering*, American Society of Civil Engineers, Vol. 121, No. 12, pp 856-869.

STARK, T.D., OLSON, S.M., KRAMER, S.L., AND YOUD, T.L. (1997). *Proceedings, The Workshop of Shear Strength of Liquefied Soils,* April 17-18, Urbana, Illinois, National Science Foundation.

STEINBRUGGE COLLECTION. Earthquake Engineering Research Center, University of California, Berkeley.

STONE, K.J.L., RANDOLPH, M.F., TOH, S., AND SALES, A.A. (1994). "Evaluation consolidation behavior of mine tailings," *Journal of Geotechnical Engineering,* American Society of Civil Engineers, Vol. 120, No. 3, pp 473-490.

SUWA, H. AND OKUDA, S. (1983). "Deposition of debris flows on a fan surface, Mt. Yakedake, Japan," *Zeitschrift fur Geomorphologie Supplement band N.F.*, Vol. 46, pp 79–101.

TAKAHASHI, T. (1978). "Mechanical characteristics of debris flow," *Journal of the Hydraulic Division,* American Society of Civil Engineers, Vol. 104, No. HY8, pp 1153-1169.

TAKAHASHI, T. (1980). "Debris flow on prismatic open channel," *Journal of the Hydraulic Division,* American Society of Civil Engineers, Vol. 106, No. HY3, pp 381-396.

TAKAHASHI, T. (1981). "Debris flow," *Annual Review of Fluid Mechanics,* Vol. 13, pp57-77.

TAKAHASHI, T. (1991). *Debris Flow,* A.A. Balkema, Rotterdam, 165pp.

TAKAHASHI, T. (1993). "Dynamic of inertial and viscous flows," *Proc., International Workshop on Debris Flow, Kagoshima*, pp 43-55.

TAKAHASHI, T., SATOFUKA, Y., AND CHISHIRO, K. (1997). "Dynamic of debris flows in the internal regime," *Debris-Flow Hazards Mitigations: Mechanics, Prediction, and Assessment*, Proceedings of First International Conference, August 7-9, San Francisco, California, pp 239-248.

TAMURA, T. AND YAMADA, Y. (1996). "A rigid-plastic analysis for granular materials," *Soils and Foundations,* Vol. 36, No. 3, pp 113-121.

TAYLOR, D.W. (1948). *Fundamental of Soil Mechanics*, John Wiley and Sons, 700 pp.

TERZAGHI, K., PECK, R.B., AND MESRI, G. (1996). *Soil Mechanics in Engineering Practice*, John Wiley and Sons, 549 pp.

THEVANAYAGAM, S. (1998). "Effect of fines and confining stress on undrained shear strength of silty sands," *Journal of Geotechnical and Environmental Engineering,* American Society of Civil Engineers, Vol. 124, No. 6, pp 479-491.

THOMPSON, J.H. (1973). "San Fernando Valley Juvenile Hall," *San Fernando, California, Earthquake of February 9, 1971, Volume 3,* U.S. Department of Commerce, National Oceanic and Atmospheric Administration, Washington, D.C.

U.S. ARMY CORPS OF ENGINEERS. (1939). "Report on the slide of a portion of the upstream face of the Fort Peck Dam, Fort Peck, Montana." *United States Government Printing Office*, Washington, D.C.

UENG, T.-S. AND CHEN, T.-J. (2000). "Energy aspects of particle breakage in drained shear of sands," *Geotechnique,* Vol. 50, No. 1, pp 65-72.

UTAHAYAKUMAR, M. AND VAID, Y.P. (1998). "Liquefaction of sand under multi-axial stresses," *Canadian Geotechnical Journal*, Vol. 35, No. 2, pp 273-283.

VAID, Y.P., CHUNG, E.K.F., AND KUREBIS, R.H. (1990). "Stress path and steady state," *Canadian Geotechnical Journal,* Vol. 27, pp 1-7.

VAID, Y.P., ELIADORANI, A., SIVATHAYALAN, S., AND UTHAYAKUMAR, M. (2001). "Laboratory characterization of stress-strain behavior of soils by stress and/or strain path loading," *Geotechnical Testing Journal*, Vol. 24, No. 2, pp 200-208.

VAID, Y.P. AND NEQUSSEY, D. (1988). "Preparation of constituted sand specimens," *Advanced Triaxial Testing of Soil and Rock,* ASTM STP 977, American Society for Testing and Materials, pp 405-417.

VAID, Y.P. AND THOMAS, J. (1993). "Liquefaction and postliquefaction behavior of sand," *Journal of Geotechnical Engineering,* American Society of Civil Engineers, Vol. 121, No. 2, pp 163-173.

VAID, Y.P. AND SIVATHAYALAN, S. (2000). "Fundamental factors affecting liquefaction susceptibility of sand," *Canadian Geotechnical Journal,* Vol. 37, pp 592-606.

VAID, Y.P., SIVATHAYALAN, S., ELIADORANI, A, AND UTHAYAKUMAR, M. (1996). *Canadian liquefaction experiment – Sand characterizing for static and dynamic liquefaction*, Canlex Laboratory Testing at U.B.C., Report No. CANLEX 04/96.

VAID, Y.P., SIVATHAYALAN, S., AND STEDMAN, D. (1999). "Influence of specimen-reconstituting method on the undrained response of sand," *Geotechnical Testing Journal,* Vol. 22, No. 3, pp 187-195.

VAN WAZAR, J.R., LYONS, J.W., KIM, K.Y., AND COLWELL, R.E. (1963). *Viscosity and Flow Measurement,* Wiley Interscience, New York, 406pp.

VASQUEZ-HERRERA, A., BOBRY, R., AND BAZIAR, M. (1990). "Re-evaluation of liquefaction triggering and flow sliding in the Lower San Fernando Dam during the 1971 earthquake," *Proceedings of the Fourth U.S. National Conference on Earthquake Engineering,* May 20-24, Palm Springs, California, Vol. 3, pp. 783-792.

VERDUGO, R. AND ISHIHARA, K. (1996). "The steady state of sandy soils," *Soils and Foundations,* Vol. 36, No. 2, pp 81-89.

WAN, R.G. AND GUO, P.J. (1999). "A pressure and density dependent dilatancy model for granular materials," *Soils and Foundations,* Vol. 39, No. 6, pp 1-11.

WANG, F.-W., SASSA, K., AND FUKUOKA, H. (2000). "Geotechnical simulation test fro the Nikawa Landslide induced by January 17, 1995 Hyogoken-Nambu earthquake," *Soils and Foundations*, Vol. 40, No. 1, pp 35-46.

WHIPPLE, K.X. AND DUNNE, T. (1992). "The influence of debrisflow rheology on fan morphology," *Geological Society of America Bulletin*, Vol. 104, pp 887–900.

WONG, R.C.K. (2000). "Shear deformation of locked sand in triaxial compression," *Geotechnical Testing Journal,* Vol. 23, No. 2, pp 158-170.

WRIDE (FEAR), C.E., MCROBERTS, E.C., AND ROBERTSON, P.K. (1999). "Reconsideration of case histories for estimating undrained shear strength in sandy soils." *Canadian Geotechnical Journal*, Vol. 36, pp 907-933.

YAMAMURO, J.A. AND COVERT, K.M. (2001). "Monotonic and cyclic liquefaction of very loose sands with high silt content," *Journal of Geotechnical and Environmental Engineering,* American Society of Civil Engineers, Vol. 127, No. 4, pp 314-324.

YAMAMURO, J.A. AND LADE, P.V. (1997) "Static liquefaction of very loose sands," *Canadian Geotechnical Journal,* Vol. 34, No. 6, pp 905-917.

YAMAMURO, J.A. AND LADE, P.V. (1998) "Steady-state concepts and static liquefaction of silty sands," *Journal of Geotechnical and Environmental Engineering,* American Society of Civil Engineers, Vol. 124, No. 9, pp 868-877.

YAMAZAKI, F. AND SHINOZUKA, M. (1988). 'Digital generation of non-Gaussian stochastic fields,' *Journal of Engineering Mechanics,* American Society of Civil Engineers, Vol. 114, NO. 7, pp 1183-1197.

YEGIAN, M.K., GHAHRAMAN, V.G., AND HARUTIUNYAN, R.N. (1994). "Liquefaction and embankment failure case histories, 1988 Armenia Earthquake," *Journal of Geotechnical Engineering,* American Society of Civil Engineers, Vol. 120, No. 3, pp. 581-596.

YOSHIMI, Y., TOKIMATSU, K., AND YOSHINORI, H. (1989). "Evaluation of liquefaction resistance of clean sands based on high-quality undisturbed samples," *Soils and Foundations*, Vol. 29, No. 1, pp 93-104.

YOSHIMINE, M. AND ISHIHARA, K. (1998). "Flow potential of sand during liquefaction," *Soils and Foundations,* Vol. 38, No. 3, pp 189-198.

YOSHIMINE, M., ISHIHARA, K., AND VARGAS, W. (1998). "Effects of principal stress direction and intermediate principal stress on undrained shear behavior of sand," *Soils and Foundations*, Vol. 38, No. 3, pp 179-188.

YOSHIMINE, M., ROBERTSON, P.K., AND WRIDE, C.F. (1999). "Undrained shear strength of clean sands to trigger flow liquefaction," *Canadian Geotechnical Journal*, Vol. 36, No. 5, pp 891-906.

YOUD, T.L. AND PERKINS, D.M. (1978). " Mapping liquefaction-induced ground failure potential," *Journal of the Geotechnical Engineering Division,* American Society of Civil Engineers, Vol. 104, No. GT4, pp 433-446.

YOUD, T.L. AND PERKINS, D.M. (1987). " Mapping of liquefaction severity index," *Journal of the Geotechnical Engineering,* American Society of Civil Engineers, Vol. 113, No. 11, pp 1374-1392.

Vita

Chwen-Huan (C.H.) Wang was born in Taiwan, Republic of China. He received his B.S. in Civil Engineering from the Feng Chia University (1993), M.S. in the Civil and Environmental Engineering (Geotechnical Engineering) from the Utah State University (1996), and Ph.D. in Civil and Environmental Engineering (Geotechnical Engineering) from the University of Washington (2003).